UNIVERSITAT DE BARCELONA

Novel chemical tools for Cancer therapy and imaging: from targeted photoactivatable Pt(IV) complexes to coumarin-based fluorophores and caging groups

Albert Gandioso Ubieto

Albert Gandioso Ubieto

NOVEL CHEMICAL TOOLS FOR CANCER THERAPY AND IMAGING:

FROM TARGETED PHOTOACTIVATABLE Pt(IV) COMPLEXES TO COUMARIN-BASED FLUOROPHORES AND CAGING GROUPS

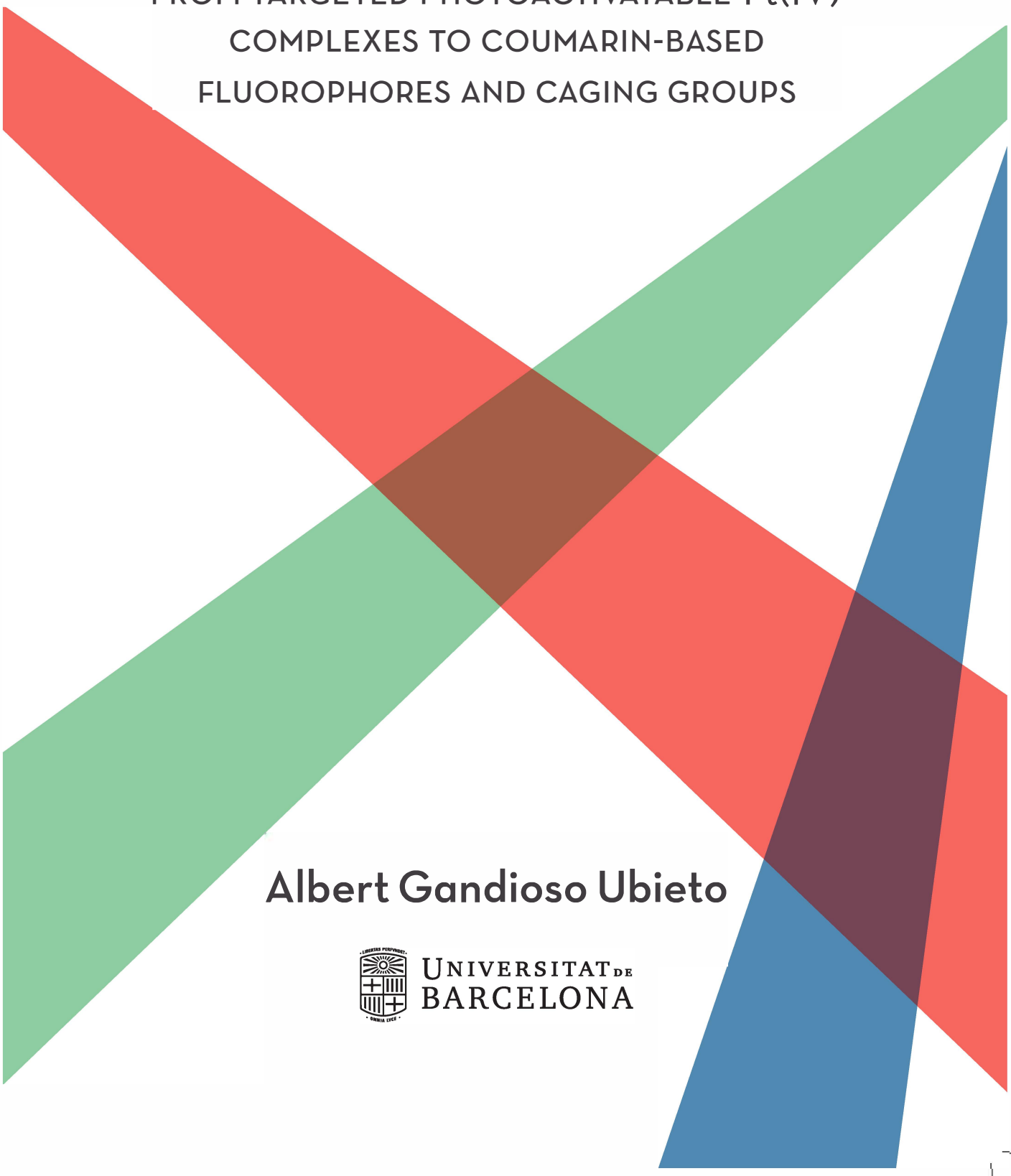

Albert Gandioso Ubieto

UNIVERSITAT DE BARCELONA

TESIS DOCTORAL

2018

NOVEL CHEMICAL TOOLS FOR CANCER THERAPY AND IMAGING:

FROM TARGETED PHOTOACTIVATABLE Pt(IV) COMPLEXES TO COUMARIN-BASED FLUOROPHORES AND CAGING GROUPS

Albert Gandioso Ubieto

UNIVERSITAT DE BARCELONA

Programa de Doctorado de Química Orgánica

Tesis doctoral

Novel chemical tools for Cancer therapy and imaging: from targeted photoactivatable Pt(IV) complexes to coumarin-based fluorophores and caging groups

Memoria presentada por
Albert Gandioso Ubieto

Dirigida y revisada por:

Dr. Vicente Marchán Sancho
(Universidad de Barcelona)

Universidad de Barcelona
Barcelona, 2018

The present thesis has been developed at the Department of Inorganic and Organic Chemistry located at the Faculty of Chemistry of the University of Barcelona (September 2014- July 2018). This work was supported by funds from the Spanish “Ministerio de Economía y Competitividad” (Grants CTQ2014-52658-R, CTQ2017-84779R). The PhD student has been supported by a fellowship from the University of Barcelona (“Ajuts de Personal Investigador predoctoral en Formació” (APIF)).

A mis héroes,

"Un científico en su laboratorio
no es sólo un técnico:
es también un niño colocado
ante fenómenos naturales
que le impresionan
como un cuento de hadas."

Marie Curie

Agradecimientos

En primer lugar, quiero agradecerle, y también dedicarle la tesis, a mi compañero de guerra durante estos años, a quien me ha ayudado y me ha enseñado todo, que me ha aconsejado como un jefe y como un amigo, a ti Vicente. Si tuviera que volver a empezar, sin ninguna duda sería un honor volver a hacerlo contigo.

Quería agradecer también a todos los jefes del grupo: Anna, Enrique, Nuria y Jordi, por compartir conmigo estos años y hacer que me sienta uno más del grupo de Oligos. Gracias también a Montse T, Francisco, Irene, Laura, Manel, Anna M por ayudarme durante la tesis.

No puedo olvidarme de todos mis compañeros de laboratorio que han ido pasando durante estos años: Ana Z, Omar, Tomeu, Clément, Natalia, Alex, Anna R, Jordi, Ivanna, Alex, Marta, y un largo número de nombres…gracias a todos.

During my short stay in Frederick, I want to say thanks to everybody, thanks Martin to host me in your group and permit me to know more every day. Specially, Tsuyoshi and the rest of the group: Gabby, Venu, Erin, Mike and Saghar. Maybe one day I will come back. Thanks also John and Jordan to make me feel like at home.

Tampoco me quiero olvidar de todos mis compañeros de carrera: Ester, Aixa, Nuria, a todos los mayores y todos los pequeños, esto también es un pequeño granito de arena vuestro. Y a todos los profesores, en especial, Margarita C y Laura R.

Que voy a decir de vosotr@s; Anna, Esther, Tamar, Laia, Marta, Eli, Jas y Gerard esto también es vuestro y nunca podré dar las gracias por todo lo que me dais día a día. También a esas personas nuevas: Joseju, Vicent, Kilian, Carlos, Ciscu, Marco y un infinito nombre de personas.

Por último, y no menos importante. Gracias de manera infinita a vosotros, **a mis héroes**, que han hecho que luche siempre por mi sueño, y por poder poner mi granito de arena. Sé que estarás muy orgullosa y, esto es por ti y para ti.

Os quiero a todos.

Thesis Outline

This Thesis is structured as a compendium of publications, being organized around four published articles and one manuscript submitted for publication (see below), together with the corresponding supporting information material. The Thesis contains a General Introduction where we have reviewed the state-of-the-art of the main topics related with the Objectives of the research work presented here (metal-based anticancer drugs, targeted drug delivery strategies, and imaging and caging applications of organic-based chromophores). After the Results and Discussion section, which contains the five publications, the Conclusions of the Thesis can be found. Finally, according to the guidelines of the University of Barcelona for Thesis presented as a compendium of publications, a summary of the main results of the Thesis written in Spanish is provided.

List of publications:

- **Gandioso, A**.; Shaili, E.; Massaguer, A.; Artigas, G.; González-Cantó, A.; Woods, J. A.; Sadler, P. J.; Marchán, V. "An integrin-targeted photoactivatable Pt(IV) complex as a selective anticancer pro-drug: Synthesis and photoactivation studies". *Chem. Commun.* **2015**, *51*(44), 9169-9172.

- **Gandioso, A**.; Cano, M.; Massaguer, A.; Marchán, V. "A green light-triggerable RGD peptide for photocontrolled targeted drug delivery: Synthesis and photolysis studies". *J. Org. Chem.* **2016**, *81*(23), 11556-11564.

- **Gandioso, A**.; Palau, M.; Nin-Hill, A.; Melnyk, I.; Rovira, C.; Nonell, S.; Velasco, D.; García-Amorós, J.; Marchán, V. "Sequential uncaging with green light can be achieved by fine-tuning the structure of a dicyanocoumarin chromophore". *ChemistryOpen.* **2017**, *6*(3), 375–384.

- **Gandioso, A**.; Bresolí-Obach, R.; Nin-Hill, A.; Bosch, M.; Palau, M.; Galindo, A.; Contreras, S.; Rovira, A.; Rovira, C.; Nonell, S.; Marchán, V. "Redesigning the coumarin scaffold into small bright fluorophores with far-red to NIR emission and large Stokes' shifts useful for cell imaging". *J. Org. Chem.* **2018,** *83*(3), 1185–1195.

- Rovira, A.; **Gandioso, A**.; Goñalons, M.; Galindo, A.; Massaguer, A.; Bosch, M.; Marchán, V. Straightforward solid-phase approaches for labelling targeting peptides with far-red/NIR emitting coumarin fluorophores. *Manuscript submitted for publication.*

Index

Abbreviations and Acronyms

ACN	Acetonitrile
Alloc	Allyloxycarbonyl
Arg	Arginine
Asp	Aspartic acid
br	Broad
BSA	Bovine serum albumin
Boc	*tert*-Butyloxycarbonyl
COSY	Correlation spectroscopy
Cys	Cysteine
d	Doublet
DCM	Dichloromethane
DEACM	7-(*N,N*-Diethylamino)-coumarin
DEACE	7-(*N,N*-Diethylamino)-4-(1-hydroxyeth-1-yl)-coumarin
DEATCM	7-(*N,N*-Diethylamino)-2-thiocoumarin
DEATCE	7-(*N,N*-Diethylamino)-4-(1-hydroxyeth-1-yl)-2-thiocoumarin
DEAdcCM	2-(Dicyanomethylene)-7-(*N,N*-diethylamino)-coumarin
DEAdcCE	2-(Dicyanomethylene)-7-(*N,N*-diethylamino)-4-(1-Hydroxyeth-1-yl)-coumarin
DIPC	*N,N*'-Diisopropylcarbodiimide
DIPEA	*N,N*'-Diisopropylethylamine
DMAP	4-Dimethylaminopyridine
DMEM	Dubelcco's modified Eagle's medium
DMF	*N,N*'-Dimethylformamide
DMSO	Dimethylsulfoxide
DNA	Deoxyribonucleic acid
DU-145	Human prostate cancer cell line

EDC·HCl	1-Ethyl-3-(3-dimethylaminopropyl)carbodiimide hydrochloride
EDT	1,2-Ethanedithiol
ESI MS	Electrospray ionization mass spectrometry
Fmoc	9-Fluorenylmethoxycarbonyl
FR	Folate receptor
Gly	Glycine
GMP	Guanosine monophosphate
HATU	1-[Bis(dimethylamino)methylene]-1H-1,2,3-triazolo[4,5-b] pyridinium 3-oxidhexafluorophosphate
HeLa	Human cervical carcinoma cell line
HOAt	1-Hydroxy-7-azabenzotriazole
HOBt	1-Hydroxybenzotriazole
HPLC	High-performance liquid chromatography
HPLC-MS	High-performance liquid chromatography – mass spectrometry
ICT	Intramolecular charge transfer
LED	Light-emitting diode
Lys	Lysine
m	Multiplet
m/z	Mass to charge ratio
MDA-MB-468	Triple-negative human breast cancer cell line
NIR	Near infrared light
NHS	*N*-Hydroxysuccinimide
NMR	Nuclear magnetic resonance
NOESY	Nuclear overhauser effect spectroscopy
Oct	Octreotide
PACT	Photoactivated chemotherapy
Pbf	2,2,4,6,7-Pentamethyl-2,3-dihydrobenzofuran -5-sulfonyl
PBS	Phosphate-buffered saline
PDT	Photodynamic theraphy

PEG	Polyethylenglycol
Phe	Phenylalanine
PI	Phototoxic index
PPG	Photocleavable protecting group
PyBOP	Benzotriazol-1-yl-oxytripyrrolidinophosphonium hexafluorophosphate
RNA	Ribonucleic acid
ROS	Reactive oxygen species
RT	Room temperature
s	Singlet
SK-MEL-28	Human melanoma cancer cell line
SPPS	Solid-phase peptide synthesis
SST	Somatostatin
SSTR	Somatostatin receptor
t	Triplet
TFA	Trifluoroacetic acid
TFE	2,2,2-Trifluoroethanol
Thr	Threonine
TMS	Tetramethylsilane
TICT	Twisted intramolecular charge transfer
TIS	Triisopropylsilane
UV	Ultraviolet

Introduction and Objectives

0. Cancer disease

Cancer is one of the most important health problems worldwide with more than 3.7 million of new cases diagnosed per year. This disease represents the second cause of death and morbidity in Europe and in the United States, with more than 1.9 millions of deaths each year. On a global scale, cancer accounted for 8.2 million deaths (around 13% of the total) in 2012 according to the World Health Organization (WHO) (**Figure 1**),[1] and it is expected that the number of new cancer cases will rise to 22 million within the next two decades. In Spain, The *Asociación Española Contra el Cáncer* (AECC) has estimated more than 200.000 new cases in Spain on 2017, which represents an increase of approximately 13% over the last 10 years.

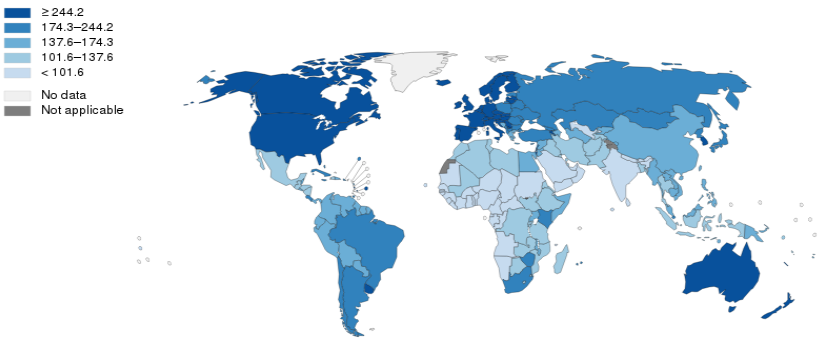

Figure 1 General representation about the estimated age-standardized rates (world) of incidence of cancer according to WHO.

Despite significant progress in the development of anticancer therapies (involving prevention, tumor detection, surgery, and chemotherapeutic treatments), there is still no efficient cure for all patients with such malignant disease. One of the major drawbacks of current chemotherapy is related with the lack of selectivity of most cytotoxic drugs, either metallodrugs or organic drugs, which usually do not accurately discriminate between healthy and malignant cells, leading to systemic toxicity.[2]

Most clinically approved anticancer drugs are characterized by a narrow therapeutic window, poor bioavailability, high-dose requirements, adverse side-effects and low therapeutic indices. To limit the onset of toxic side-effects, anticancer agents are often administered at suboptimal doses, thus preventing their ability to reach tumor-destroying drug concentrations while prompting, after prolonged treatments, the development of resistance phenomena. At present, the design and development of novel anticancer strategies is based on two main premises: targeted drug delivery and controlled release of the drug at the tumor site.[2,3]

Targeted drug delivery strategies usually consist on attaching a tumor recognition moiety to a cytotoxic drug, either directly or through a suitable linker. The resulting conjugate should be sufficiently stable while in bloodstream to be selectively internalized into the target cancer cell. The success of this strategy requires a detailed knowledge of the specific morphological and physiological differences distinguishing malignant from healthy tissues. Rapidly dividing cancer cells require various nutrients and vitamins to maintain their rapid growth. Therefore, receptors involved in the uptake of essential vitamins for cell growth are often overexpressed on the surface of malignant cells.[4,5] In recent years, the use of light, heat or magnetic fields has also demonstrated great potential in the field of oncology as non-invasive external regulatory elements.

The development of new diagnostic techniques is another challenge that needs to be addressed in the next years. Over the past two decades, synergistic innovations in imaging technologies have resulted in a revolution in which a range of biomedical applications are now benefiting from fluorescence imaging. Specifically, advances in fluorophore chemistry and imaging hardware, and the identification of targetable biomarkers have now positioned intraoperative fluorescence as a highly specific real-time detection modality for surgeons in oncology.[6–8]

In particular, the deep tissue penetration and limited autofluorescence of near-infrared (NIR) fluorescence imaging improves the translational potential of this modality over visible-light fluorescence imaging. Rapid developments in fluorophores with improved characteristics, detection instrumentation, and targeting strategies led to the clinical testing in the early 2010s of the first targeted NIR fluorophores for intraoperative cancer detection.

In the following sections, we will first introduce a brief overview of **platinum-based anticancer drugs**, in particular some novel approaches based on photoactivatable platinum(IV) pro-drugs. Next, we will discuss the concepts and recent applications of **targeted drug delivery strategies**, specifically the use of ligands based on RGD peptides, folic acid and octreotide to selective deliver cytotoxic drugs into the cancer cells. Finally, we will introduce **the imaging and caging applications of chromophores** based on organic molecules, particularly those of **coumarin derivatives**.

1. Metal-based anticancer drugs

1.1. Platinum(II) complexes

Platinum-based anticancer therapies represent one of the most remarkable advances on the therapies against cancer. Three platinum-containing drugs are approved worldwide by the FDA for treating cancer: cisplatin (1978), carboplatin (1989) and oxaliplatin (2002). In addition, many other Pt-based drugs have entered clinical trials or have been approved for use in specific countries (**Figure 2**).[9,10]

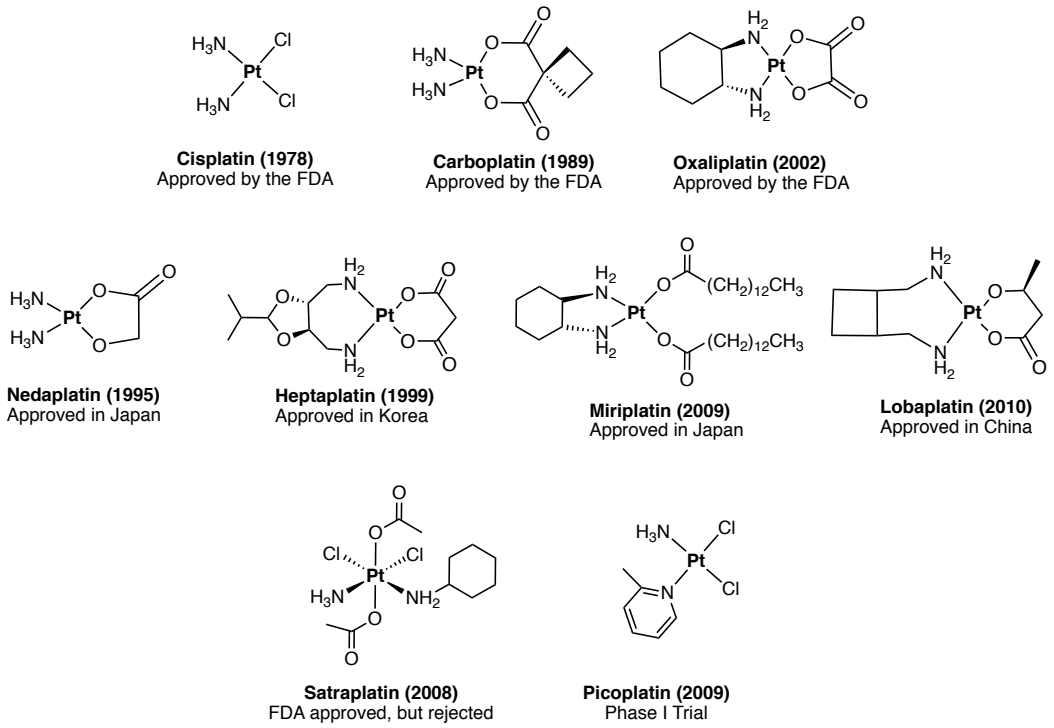

Figure 2 Structures of Pt-based anticancer drugs.[10]

Since the introduction of cisplatin (*cis*-diamminedichloridoplatinum(II)) for the treatment of testicular cancer, its use in combination with other chemotherapeutic drugs has been extended to many other types of cancers including ovarian, cervical, heck and neck and non-small-cell lung cancer.[9]

Cisplatin-related drugs are based on a square-planar neutral structure with two *cis* ammino ligands and two *cis* anionic ligands, in the case of cisplatin, chlorido ligands. The generally accepted mechanism of action for this type of Pt(II) drugs involves three key steps (**Scheme 1**):[10]

1. **Cellular uptake (i).** The entrance of platinum complexes within the cell combines passive diffusion and active transport, the latter being mediated mainly by membrane proteins such as the copper transporter CTR1.
2. **Aquation/activation (ii).** Once inside the cytoplasm, the chlorido ligands of cisplatin are quickly substituted by water due to a decrease in the concentration of the chloride ion (< 10 mM) with respect to the bloodstream (~ 100 mM), where hydrolysis is mainly suppressed.
3. **DNA binding (iii)**. The cationic aquated activated species enter into the cell nucleus where the DNA nucleobases replace the coordinated water molecules. The most nucleophilic sites of DNA, the *N7* atoms of purine residues, guanine and adenine, are preferentially platinated. Among the different types of adducts that can be formed, 1,2-d(GpG) and 1,2-d(ApG) intrastrand adducts are the major platinated products. These adducts interfere with cellular metabolism, such as DNA replication and transcription, thereby triggering cell death.[9,11]

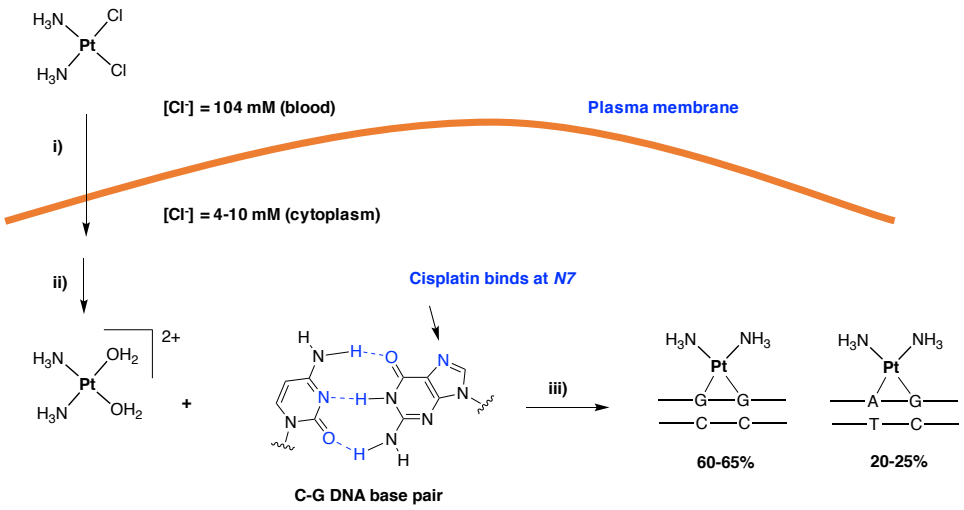

Scheme 1 Schematic representation of the mechanism of action of cisplatin.[12]

There are several deactivation pathways that can sequester platinum complexes or prevent them from triggering apoptosis (**Figure 3**). Because current platinum drugs are administrated intravenously, they can interact with the blood components, such as human serum albumin (HSA). HSA, the most abundant protein in the human bloodstream, contains a cysteine residue that can interact with metal complexes.[9,11]

Platinum complexes can also interact with glutathione (GSH). Such adducts with GSH are eliminated from the cytoplasm by the ATP7B pumps and, consequently, this process has been implicated in cisplatin resistance. Another mechanism of deactivation is caused by proteins that are able to recognize and interact with DNA-cisplatin adducts, such as nucleotide-excision repair (NER), mismatch repair (MMR), kinases and HMG (High mobility group) proteins.[9,11]

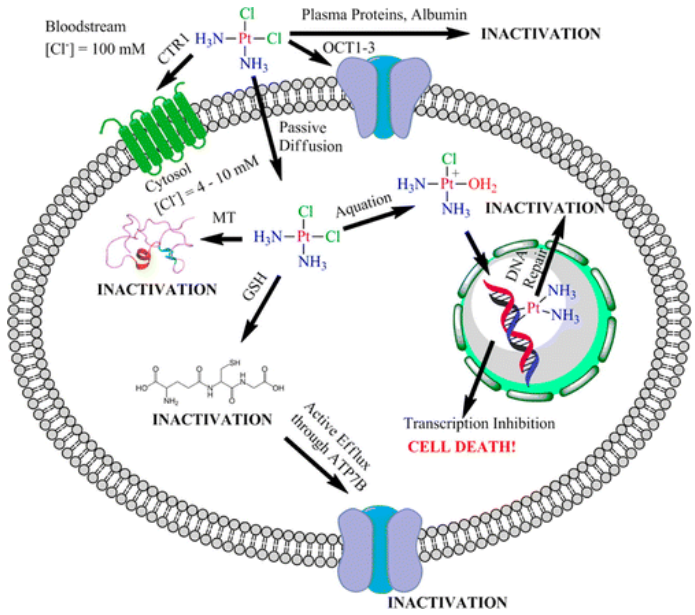

Figure 3 Extracellular and intracellular events that influence cisplatin activity.[13]

Cisplatin mainly affects rapidly dividing cells such as tumor cells, although not specifically. Since cisplatin also affects healthy cells such as the epithelium, bone marrow or intestine, one of the main limitations of this drug is related with its high toxicity. Another important disadvantage of cisplatin is the high nephrotoxicity, since the urine is one of the principal ways to eliminate it. The administration of cisplatin is also associated with neurotoxicity and ototoxicity, but to a lesser degree.

Taking into account the intrinsic or acquired resistance and the high toxicity of cisplatin, many analogues of this drug have been synthesized and screened in an attempt to overcome such limitations as well as to broaden the range of treatable tumors. The structure of second (carboplatin) and third (oxaliplatin) generation of platinum(II) drugs was conceived to improve the stability of the complexes before they reach their ultimate target, the nuclear DNA. In both cases, the reactivity of the metal center was modified because of the chelating effect of the leaving group ligand. Thus, the half-life for the aquation reaction of these analogs, which is approximately 2 h for cisplatin, was drastically decreased to make carboplatin and oxaliplatin stable to aquation for over a period of weeks to months.[9,10,14]

The general molecular framework of cisplatin (*cis*-geometry) has also been modified more drastically in order to uncover novel mechanisms of cell killing, alter the spectrum of activity and render new cancers susceptible to platinum therapy (**Figure 4**). There is a broad range of compounds with such non-conventional structures, including *trans* geometries (**Figure 4, A**), compounds that bind non covalently to DNA (**Figure 4, B**), monofunctional Pt(II) complexes (**Figure 4, C**) and polynuclear Pt(II) species (**Figure 4, D**). [10,15]

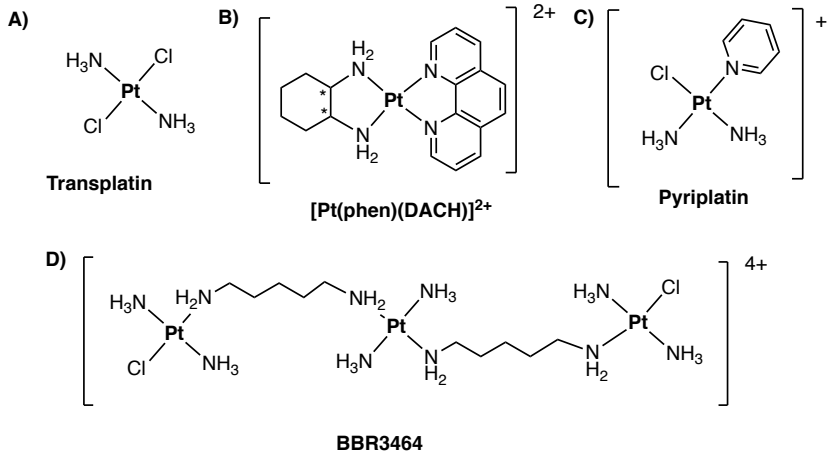

Figure 4 Examples of non-conventional Pt(II) complexes.[13]

1.2. Platinum(IV) complexes

The anticancer potential of platinum(IV) agents has been recognized from the time of the original discovery of the biological properties of cisplatin, but their clinical value was not realized until several years later. At present, there is a growing interest in the development of Pt(IV) anticancer agents because of the inertness of the low-spin d^6 Pt(IV) center to ligand substitution reactions, which minimizes undesired side-reactions with biomolecules prior to DNA binding. The Pt(IV) complexes are usually composed by six ligands: two are classified as non-leaving groups, two as leaving groups (such as in conventional Pt(II) complexes), and two extra ligands which occupy the two-axial positions.[10,16] These two additional positions offer the possibility of modifying the lipophilicity and solubility of the complex, as well as facilitate the attachment of targeting ligands. The structures of four relevant examples of Pt(IV) complexes (Ormaplatin, Iproplatin, Satraplatin and LA-12) are shown in **Figure 5**.

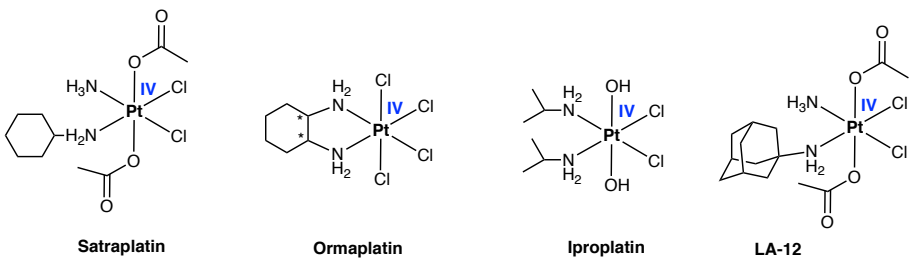

Figure 5 Examples of some platinum(IV) anticancer agents.

The reduction of the Pt(IV) complexes to Pt(II), which is accompanied by the loss of the two axial ligands, is thought to be essential for the anticancer activity of these pro-drugs. The resulting Pt(II) species bind DNA, inhibit transcription and replication, and induce apoptosis in a similar way than cisplatin and related Pt(II) complexes. This activation process depends on the nature of the ligands of the Pt(IV) complex which modulate the reduction potential. Moreover, the reduction time depends on the biological agents that are involved in the process (glutathione or ascorbic acid).[10,17]

Trans,cis,cis-bis(acetate)amminecyclohexylaminedichloridoplatinum(IV) (Satraplatin) was the first platinum agent reported to have oral activity, which was accomplished by improving lipophilicity and stability. The half-life of reduction of this complex by 5 mM ascorbate is 50 min, which is adequate for absorption by the gastrointestinal mucosa in the Pt(IV) form once ingested. Upon uptake into the bloodstream, Satraplatin is reduced to six different platinum(II) species (**Scheme 2**).[18,19]

In preclinical studies, Satraplatin showed a better toxicity profile than cisplatin, including in cisplatin-resistant human tumor cell lines. In the same way as cisplatin, the mechanism of action of this Pt(IV) pro-drug involves the formation of DNA cross-links by the Pt(II) species, DNA distortion, and subsequent inhibition of DNA transcription and replication. [18,19]

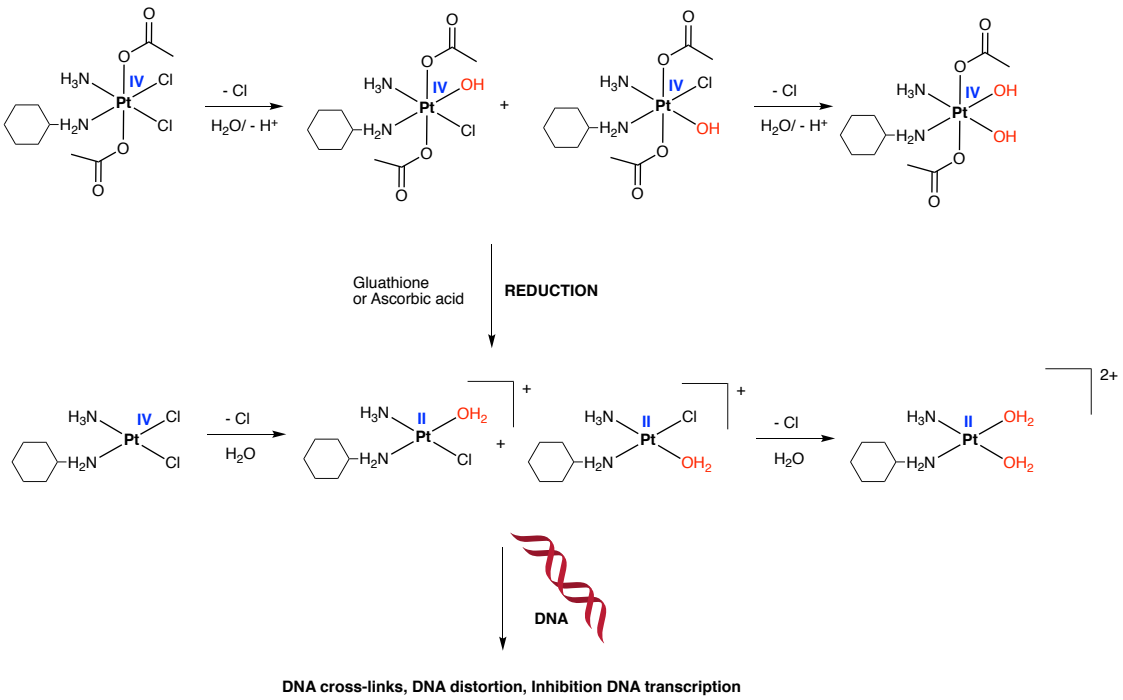

Scheme 2 Schematic representation of the activation of Satraplatin.[9]

1.3. Photoactivatable metallodrugs.

The use of light holds enormous potential in chemotherapy since offers the possibility of controlling, at a desire time and place, the release of cytotoxic species from an inert pro-drug. For this reason, much efforts have been dedicated to the development of photoactivatable metal–based anticancer complexes for improving drug efficacy and, more importantly, to reduce the toxic side-effects associated with current platinum drugs.[20–22]

The light-mediated activation of anticancer metallodrugs can be generally divided in two categories: photoactivated chemotherapy (PACT) and photodynamic therapy (PDT). PACT exploits different mechanisms to induce cell death such as ligand ejection, DNA crosslinking and caging approaches. On the other hand, PDT relies mainly on the generation of toxic reactive oxygen species (ROS) like singlet oxygen ($^1O_2$).

Photoactivation offers the possibility for initiating unusual ligand substitution and redox reactions in transition metal complexes. Moreover, the process may produce novel types of DNA adducts that can not be readily achieved by chemical reactions alone. These novel lesions may avoid repair mechanisms of the DNA, which are important variables to overcome inherent or acquired resistance to cisplatin, thereby offering new mechanism of anticancer activity. In this emerging field, several examples of novel metal complexes activatable with UV-visible light have been described (**Figure 6**), including Pt(IV) complexes,[23,24] Ru(II) arene complexes,[25,26] Ru(II) polypyridyl complexes,[27,28] and Re(I) complexes.[29,30]

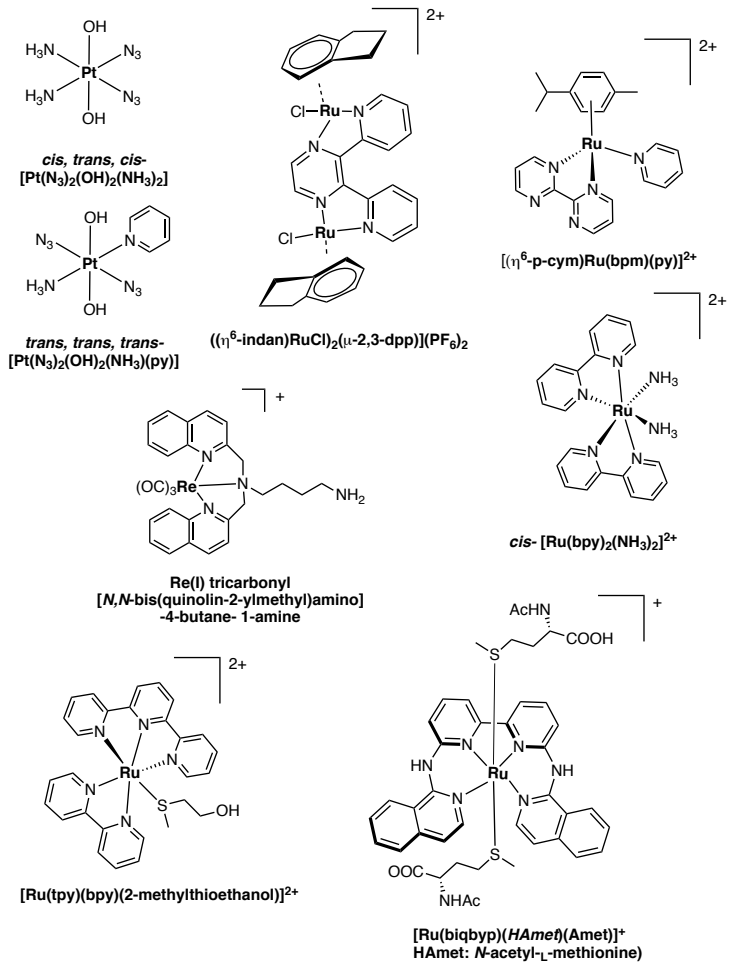

Figure 6 Examples of photoactivatable metal-based anticancer complexes

Photodynamic therapy (PDT) usually consists of three components: a photosensitizer (PS) (organic or inorganic PSs), light, and tissue with presence oxygen. The light-activated PS transfers its excited-state energy to the surrounding oxygen for generating reactive oxygen species (ROS). Although most PDT processes are oxygen-dependent and are only initiated in oxygenated conditions, some PDT can take place even in hypoxic environments, without the participation of oxygen. Based on the different photochemical reaction processes, PDT can be divided into two types: type I PDT and type II PDT.[31–34]

After light activation, the photosensitizer is transformed from the ground singlet state (S_0) to the excited singlet state (S_1), and then to an electronically excited triplet state (T_1); T_1 triggers the photochemical reaction via two different (type I and type II) paths. For type I PDT, T_1 participates in a hydrogen- or electron-transfer process to react directly with a biological substrate to form free radicals, which can interact with triplet oxygen ($^3O_2$) and water to produce superoxide anions ($O_2^{\cdot-}$) and hydroxyl radicals ($OH^{\cdot}$), respectively. During the type II PDT process, T_1 undergoes a type II photochemical reaction to convert the surrounding $^3O_2$ into cytotoxic singlet oxygen ($^1O_2$) via direct energy transfer. Therefore, type II PDT dominates in well-oxygenated environments, while type I PDT can occur under hypoxic conditions (**Scheme 3**).[35]

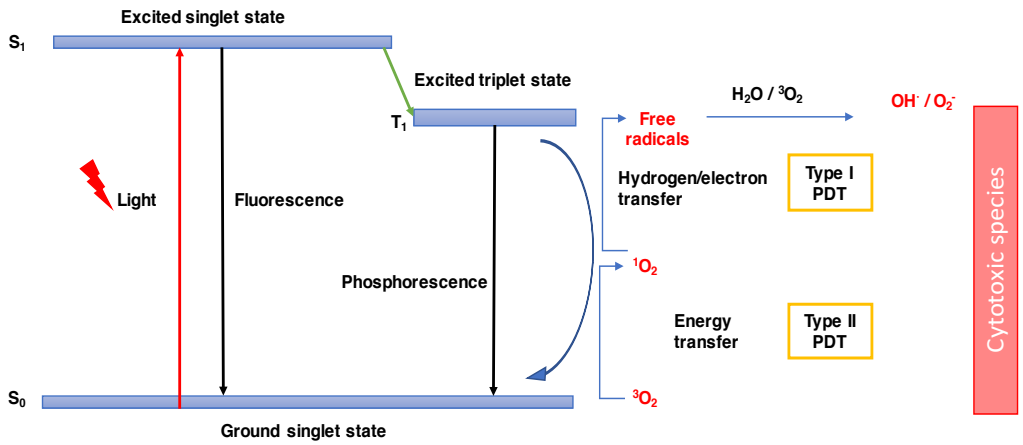

Scheme 3 Scheme of the photochemical reactions for type I and type II PDT processes. .

Some representative examples of PDT systems based on metal complexes are shown in **Figure 7**: Pd(II)-porphyrin complex has progressed to phase III clinical trial[36] and Ru polypyridyl complexes[34] and Ir(III) complexes have just started to be studied as PDT agents.[33,37,38]

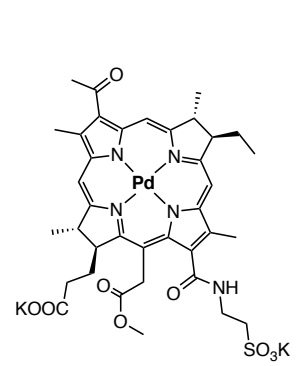

TOOKAD (phase III cllinical trials)

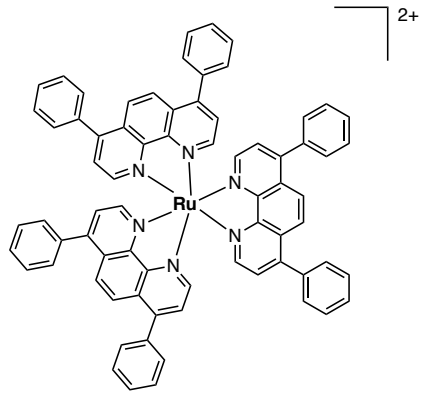

[Ru(bathophenanthroline)$_3$]$^{2+}$

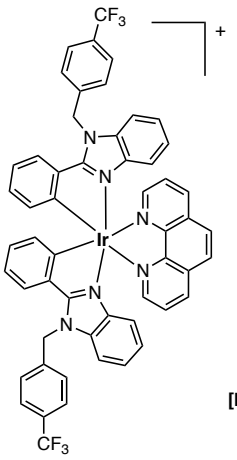

[Ir(2-phenyl-1-[4-(trifluoromethyl)benzyl)$_2$(phen)]$^+$

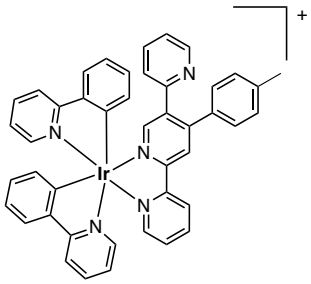

[Ir(2-phenyl-pyridine)$_2$(3-py,4-methylphenyl-by)]$^+$

Figure 7 Examples of photosensitizers based on metal complexes.

1.3.1. Photoactivatable Platinum(IV) complexes

Octahedral Pt(IV) complexes can be activated with UV-visible light to induce ligand-exchange and photoreduction reactions. This strategy has been explored by Bernaski and collaborators who described one of the first photoactivatable platinum(IV) complexes, *trans,cis*-[$Pt(OH)_2I_2(en)$] and *trans,cis*-[$Pt(OAc)_2I_2(en)$].[16] Stability studies in the dark revealed that no covalent binding to DNA occurred. However, when irradiated at <370 nm, the formation of adducts with DNA was observed, which confirmed the photoreduction (**Scheme 4**).[39]

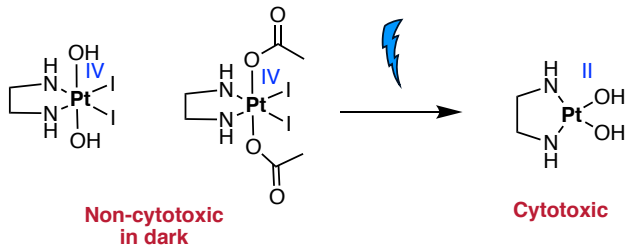

Scheme 4 Chemical structures of photoactivatable diiodido-platinum(IV) complexes.

A similar approach has been widely explored by Sadler's group for the generation of a novel class of photoactivatable Pt(IV) anticancer pro-drugs. A promising example was the discovery that the novel diazido platinum(IV) complex *trans,trans,trans*-[$Pt(N_3)_2(OH)_2(py)_2$][24] (**Figure 8**) can be photoactivated with low doses of UV light, but also with blue and green light, to give potent cytotoxic species. In fact, this complex is 13–80 times more cytotoxic than cisplatin, and approximately 15 times more cytotoxic towards cisplatin-resistant human ovarian cancer cells.[23,24,40] This Pt(IV) pro-drug is more thermally stable than some other analogs (**Figure 8**) and decomposes only at high temperatures. It also has good aqueous solubility, and it is highly stable in buffer solutions and in the presence of glutathione.[23,24,40,41]

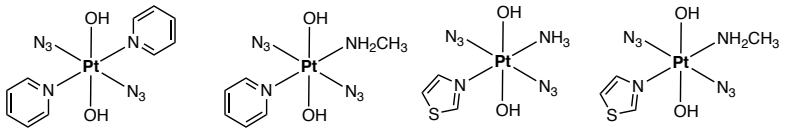

Figure 8 Examples of Sadler's photoactivatable Pt(IV) anticancer pro-drugs.

In addition, when *trans,trans,trans*-$[Pt(N_3)_2(OH)_2(py)_2]$ was irradiated (350, 420 and 450 nm) in the presence of 5'GMP, the corresponding Pt(II) adducts with this nucleotide were identified by ESI-MS and ^{1}H and ^{195}Pt NMR, which confirmed that the photoreduction occurs (**Scheme 5**).[23,24] These studies reveled that one azido ligand and the two axial hydroxyl groups were released during irradiation. The azido ligand is likely to be released as an azidyl radical with a further electron being donated resulting in reduction of Pt(IV) to Pt(II) and formation of Pt(II)-5'-GMP adducts. In addition, the second azido ligand can also be lost to form a bis-GMP adduct. Interestingly, the acute photocytotoxicity can be switched off by low doses (500 µM) of L-tryptophan. EPR and NMR spectroscopic experiments using spin traps showed that this amino acid quenches the formation of azidyl radicals, probably by acting as an electron donor.[42]

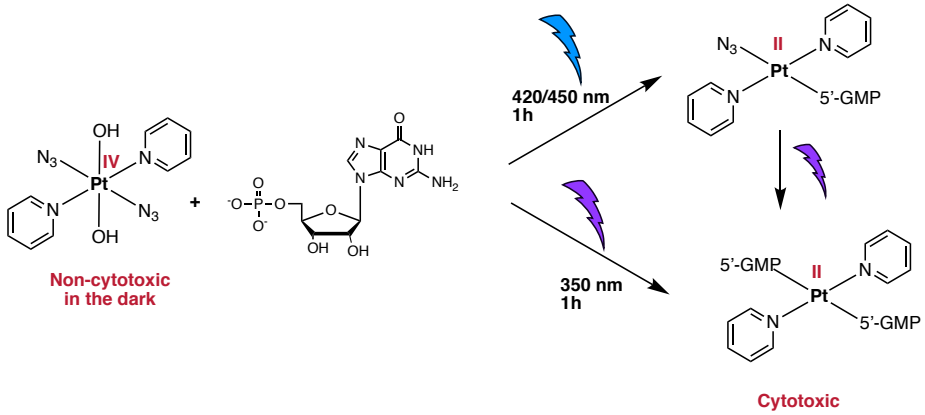

Scheme 5 Photo-activation of *trans,trans,trans*-$[Pt(N_3)_2(OH)_2(py)_2]$ in the presence of 5'-GMP.

When photo-activated, *trans,trans,trans*-[$Pt(N_3)_2(OH)_2(py)_2$] accumulates in tumor cells, penetrates the nucleus, and binds strongly to nuclear DNA under conditions in which it exhibits cytotoxicity. The nature of the DNA adducts, generated by this Pt(IV) pro-drug are distinct from those produced by cisplatin or transplatin. Another critical difference between this Pt(IV) complex and cisplatin emerged with respect to the ability of their DNA adducts to inhibit transcription by stalling RNA pol II. Hence, *trans,trans,trans*-[$Pt(N_3)_2(OH)_2(py)_2$] proved to be a significantly more potent inhibitor of RNA synthesis than cisplatin.[41]

Another interesting approach for achieving the photoactivation of Pt(IV)-pro-drugs with near-infrared (NIR) light has been explored by the Bednarski's and Salassa's groups, who recently reported the preparation and surface modification of upconversion nanoparticles (UCNPs) with light-sensitive diiodido–Pt(IV)[43] (**Scheme 16**) and *cis,cis,trans*-[$Pt(NH_3)_2(Cl)_2(succ)_2$][44] complexes, respectively. UCNPs are innovative materials which have the capability to overcome some of the main drawbacks of transition metal complexes. They have unique optical features allowing efficient conversion of NIR photons into visible and UV light via multiphotonic energy transfer processes. Potentially, light emitted by UCNPs can be used to excite metal complexes and prompt their photochemistry upon 980 nm excitation

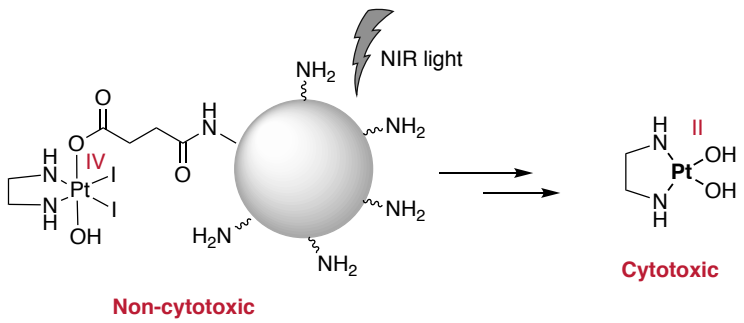

Scheme 6 Upconversion nanoparticles attached to a light sensitive diiodido–Pt(IV) complex.

Very recently, Salassa and co-workers have reported the photoactivation of Pt(IV) derivatives of cisplatin and carboplatin, as well as of Ru(II) complexes, with low doses of visible light in the presence of electron donors (flavoproteins). These findings offer new opportunities for the design of chemically and light-activated metal-based pro-drugs, whose biological effects could be triggered endogenously by bio-orthogonal flavoprotein catalysts (**Scheme 7**). [45,46]

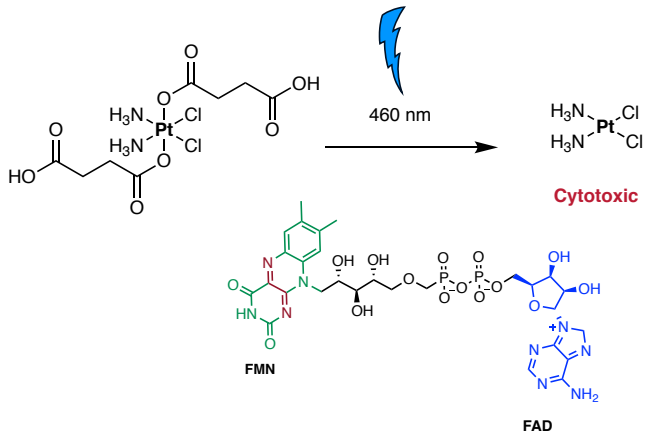

Scheme 7 Photoreduction of Pt(IV) derivatives of cisplatin mediated by flavoproteins.

2. Targeted drug delivery strategies

As previously stated in section 1, platinum-based anticancer drugs occupy an important role in the treatment of a wide variety of malignant tumors. However, the efficacy of platinum(II) drugs is often restricted by systemic toxicity due to their poor ability to differentiate between cancer and healthy cells, as well as by inherent or acquired resistance. In this context, different drug targeting and delivery strategies have been developed to minimize the toxicity related with chemotherapy and a rapidly growing class of anticancer drugs, both organic molecules and metallodrugs, incorporate a targeting moiety to deliver them selectively into malign cells.[47] Targeted drug delivery can be generally divided into two main strategies: active and passive.[48]

Active targeted drug delivery is based on specific biomolecular interactions between a targeting moiety conjugated to a drug and certain cell or tissue elements. Although cancer cells share many common characteristics with normal cells, certain receptors are overexpressed on their surface (e.g, folate receptors, somatostatin receptors, epidermal growth factor receptors, integrins, transferring receptors, etc.), thereby offering an opportunity to deliver cytotoxic agents into human tumors through attachment to a suitable carrier agent with high binding affinity and selectivity for those receptors.[6,7] A wide variety of targeting ligands have been used in active targeted drug delivery strategies including antibodies, aptamers, small protein scaffolds, peptides and low-molecular-weight non-peptidic ligands **(Figure 9).**

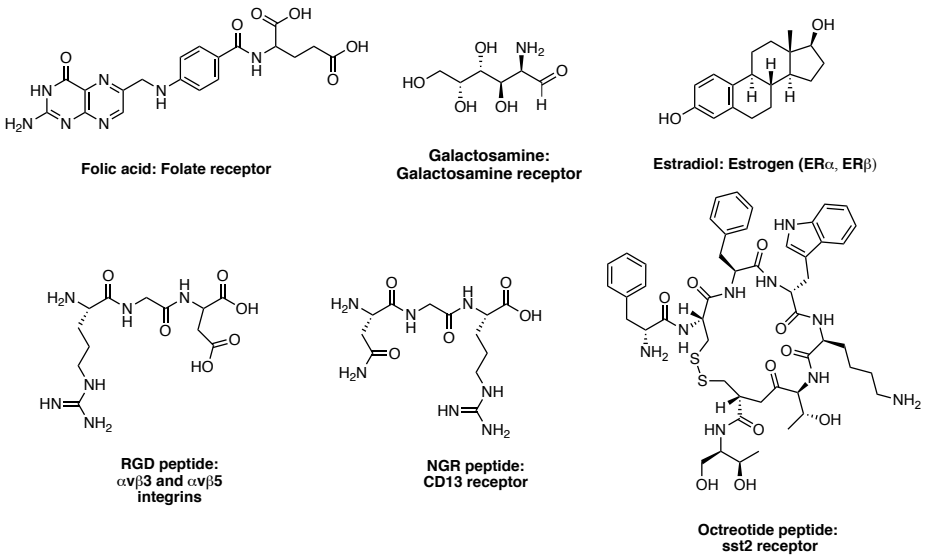

Figure 9 Examples of targeting ligands.

In such a context, it is remarkable that two antibody-drug conjugates (ADCs), trastuzumab emtansine and brenutuximab vedotin, are currently in clinical trials, as well as several conjugates incorporating smaller targeting ligands: i) a NGR peptide conjugated to the protein of tumor necrosis factor (TNF) is being evaluated in Phase I for treatment of solid tumors and in Phase II for kidney and ovarian cancer treatment,[4,48] and ii) vintafolide, which is composed by folic acid and a doxorubicin analog, is being used for the treatment of platinum-resistant ovarian cancer (**Figure 10**).[5,48]

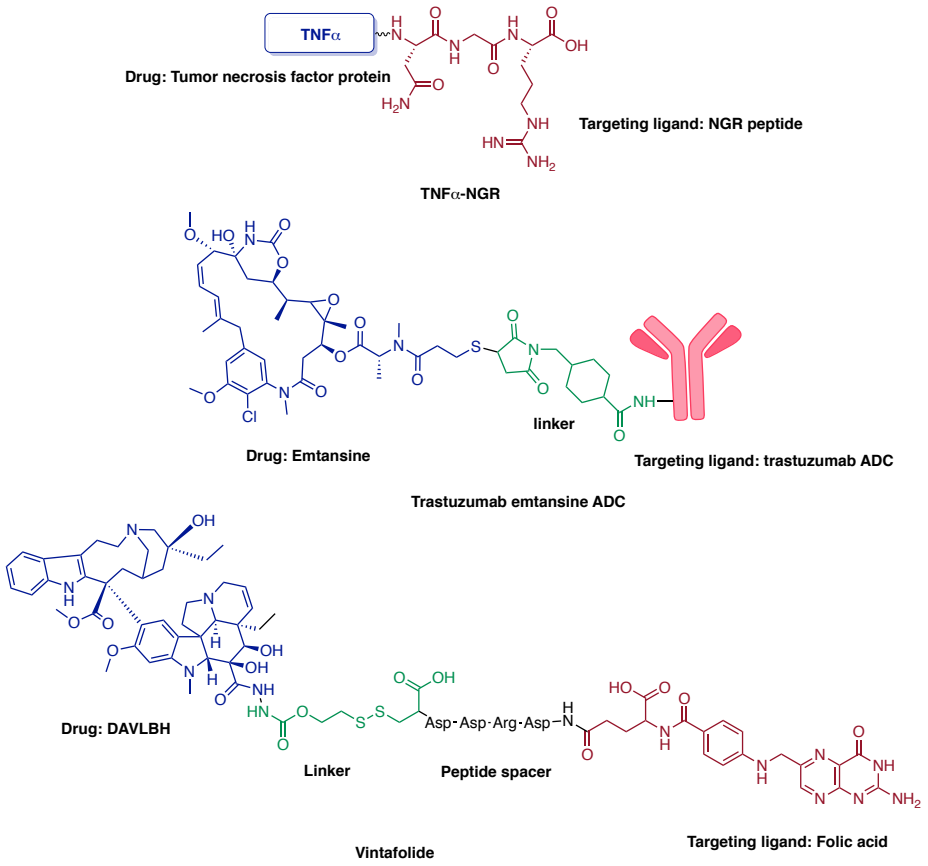

Figure 10 Examples of targeted drugs that have entered in clinical trials.

During the design and development of ligand-targeted anticancer therapeutics, several points need to be addressed such as the selection of the targeted receptor and the design of the targeting ligand, as well as the optimization of the therapeutic payload and of the spacer linking it to the ligand.[48]

- **Level and location of cancer-specific receptor expression**. To be useful for targeted drug delivery, the receptor must be overexpressed on cancer cells relative to normal cells. In addition, the level of expression must be sufficient high to enable delivery of therapeutic quantities of the desired drug. Ideally, targeted receptors should be expressed on the surface of cancer cells and not within cytoplasm or nucleus.

As the availability of empty receptors on the plasma membrane will depend on the rate of return of unoccupied receptors from intracellular endosomes, an ideal receptor will be one that either recycles frequently or it is resynthesized rapidly following degradation.

- **Optimal features for the ligand**. The targeting ligand must have high binding affinity and target selectivity for the receptor, as well as easy derivatizability to attach the cargo drug.

- **Physicochemical properties of the linker.** Linkers or spacers that are situated between the drug and the targeting ligand should not interfere with the pharmacokinetics and pharmacodynamics of the conjugate. The drug should not alter the kinetics of the ligand, and the ligand should not interference with the mechanism of action of the drug. In general, PEG spacers are selected to increase the solubility in water of the conjugate.

- **Criteria for payload selection.** The cytotoxicity depends on the intrinsic toxicity of the therapeutic agent. In addition, it is important to achieve an efficient release of the therapeutic agent to reach its intended intracellular target.

In active targeted drug delivery approaches, the conjugate between the drug and the targeting ligand enters the cell by receptor-mediated endocytosis. After ligand-receptor recognition, internalization occurs via endocytosis, leading to the formation of an intracellular compartment called CURL (receptor and ligand uncoupling compartment). Within a CURL, the conjugate and the receptor can be dissociated from each other and distributed in different intracellular compartments, allowing the receptor to be degraded or returned to the cell surface for another round of endocytosis **(Figure 11**).[48]

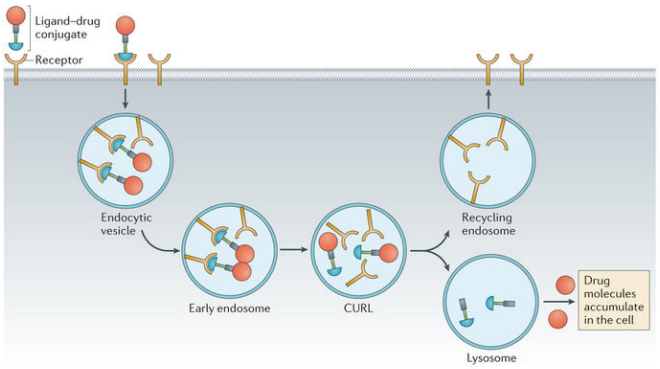

Figure 11 Ligand-drug conjugate entry into the cell.[48]

Passive targeted drug delivery is based on the enhanced permeability and retention effect (EPR) that is generally increased in tumors. The vasculature of the tumor is markedly disorganized and twisted in comparison to the vasculature of normal cells. Vascular endothelium in tumors proliferate rapidly and discontinuously, resulting in a greater number of open fenestrations and unions than in normal vessels. As a consequence, the EPR effect permits the accumulation of molecules of certain size (typically liposomes, nanoparticles, and macromolecular drugs) in tumor tissues much more than they do in normal tissues.[10,47,49]

2.1. Active targeted drug delivery strategies

In this section, we will introduce some representative examples of ligands that recognize three relevant receptors (integrins, folate receptor and sstr2), which are overexpressed in certain tumor cells, and we will describe some recent examples of drug-ligand conjugates targeting such receptors.

2.1.1. Integrins: RGD peptides

Integrins are overexpressed in cancer cells and contribute to tumor progression and metastasis by increasing migration, invasion, proliferation and survival of malign cells.

The malign microenvironment is comprised of many host cell types, like endothelial cells, perivascular cells, fibroblasts and inflammatory cells, which contribute to tumor progression by mediating angiogenesis, lymphanogiogenesis and inflammation.[49–52] Integrins are heterodimers composed by two different types of subunits, the α subunit and the β subunit, which are assembled non-covalently. There are several types of integrins (αvβ3, αvβ5, α5β1, α6β4, α4β1 and αvβ6) and their expression has been correlated with disease progression in various tumor types (**Table 1**).

Table 1 Expression of integrins in different types of cancer.

Tumor type	Integrins expressed	Associated phenotypes
Melanoma	αvβ3 and α5β1	Vertical growth phase and lymph node metastasis
Breast	α6β4 and αvβ3	Increased tumor size (α6β4). Increased bone metastasis (αvb3)
Prostate	αvβ3	Increased bone metastasis
Pancreatic	αvβ3	Lymph node metastasis
Ovarian	α4β1 and αvβ3	Increased peritoneal metastasis (α4β1) and tumor proliferation (αvβ3)
Cervical	αvβ3 and αvβ6	Decreased patient survival
Glioblastoma	αvβ3 and αvβ5	Both are expressed at the tumor–normal tissue margin
NSC lung carcinoma	α5β1	Decreased survival in patients with lymph node-negative tumors
Colon	αvβ6	Reduced patient survival

Integrins αvβ3 and αvβ5 are upregulated in both tumor cells and angiogenic endothelial cells, making them particularly attractive pharmacological targets. Integrin agonists currently in clinical trials include monoclonal antibodies (8A2 and P4G11)[53] and RGD peptides. When the arginine-glycine-aspartic acid (RGD) (**Figure 12, A**) sequence was discovered as cell attachment site in fibronectin about 20 years ago, it was unexpected that a fundamental recognition site for cells and proteins could be formed by only three amino acids.[54] Soon thereafter, RGD-recognition sites were also reported in other extracellular matrix (ECM) proteins.[55] In parallel, the receptors for these ECM proteins were identified and organized in the integrin family.[4]

In such a context, the rigidity conferred by cyclization was exploited to develop RGD peptides with higher stability, potency and specificity. [49,56] In addition, non-natural modifications such as the introduction of *D*-amino acids and *N*-methylation, as well as the replacement with peptidomimetic structures, have yielded RGD-peptide ligands with increased specificity and nanomolar or even higher integrin affinity.[53] Cyclization of a linear RGD-containing pentapeptide incorporating one of the amino acids in the *D*-configuration (*D*-Phe) resulted in two revelant cyclic peptides: c(RGDf[*N*-methyl]V), also known as Cilengitide (**Figure 12, B**), and c(RGDfK) (**Figure 12, C**).

Cilengitide has entered phase III clinical trials for fighting against glioblastoma. This peptide is an inhibitor of $\alpha v\beta 3$ and $\alpha v\beta 5$ integrins and it is also being tested in phase II trials in patients with lung and prostate cancer.[53] On the other hand, **c(RGDfK)** is often used for the delivery of drugs, thanks to the lysine residue (K) which allows conjugation. In recent years, several integrin targeted drugs and imaging constructs, bearing either one or more c(RGDfK) ligands, have been developed.[50]

RGD4C (**Figure 12, D**) and RGD10 (**Figure 12, E**) are also representative RGD-peptide derivatives that have been exploited as targeting ligands for the delivery of cytostatic drugs. However, one disadvantage of these of is that they can fold into different cyclic structures.[4,56] Finally, RGD peptidomimetics (**Figure 12, F**) have been also reported with improved integrin binding affinity. Peptidomimetics are small protein-like chains designed to mimic peptide sequences and to target receptors with higher affinity than the natural ligands. Peptidomimetics offer several advantages when compared to natural peptides such as increased physiological half-lives and oral bioavailability.[49] Most RGD peptidomimetics contain a guanidine that replaces arginine, while the aspartic acid has been substituted by a carboxylic acid. These two essential groups have been linked together by various tethers and constraints, yielding compounds with low nanomolar or even picomolar affinities for $\alpha v\beta 3$ integrin.

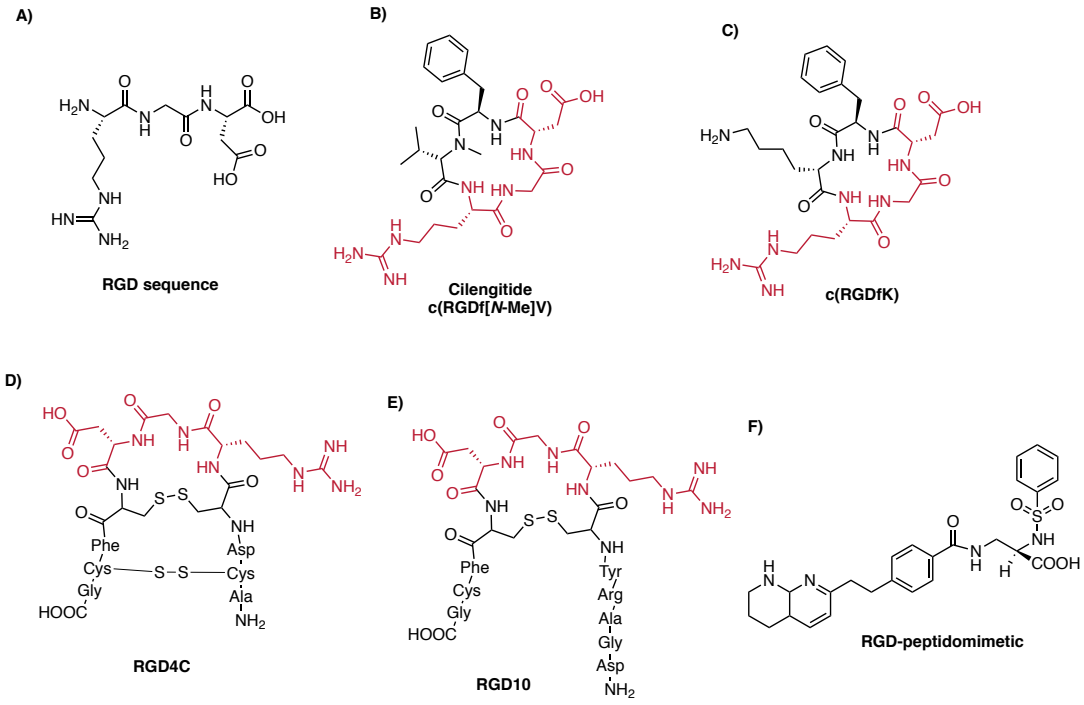

Figure 12 Examples of RGD-containing peptides and analogs.

One of the first approaches in which the RGD motif was used for drug targeting was focused on the delivery of doxorubicin to angiogenic endothelial cells. A doxorubicin-RGD4C conjugate (doxo-RGD4C) proved to be equally effective as free doxorubicin *in vitro* and, more importantly, demonstrated improved inhibition of tumour growth and spreading of metastases in mice. Besides improving efficacy, a reduced toxicity to liver and heart was observed.[57]

In recent years, several other examples of drug conjugates with the RGD peptide sequence have been reported, which include a large variety of anticancer organic drugs such as doxorubicin (**Figure 13, A**),[58] paclitaxel (**Figure 13, B**),[59] camptothecin (**Figure 13, C**)[60] , as well as metallodrugs (**Figure 14**).[20,61-63]

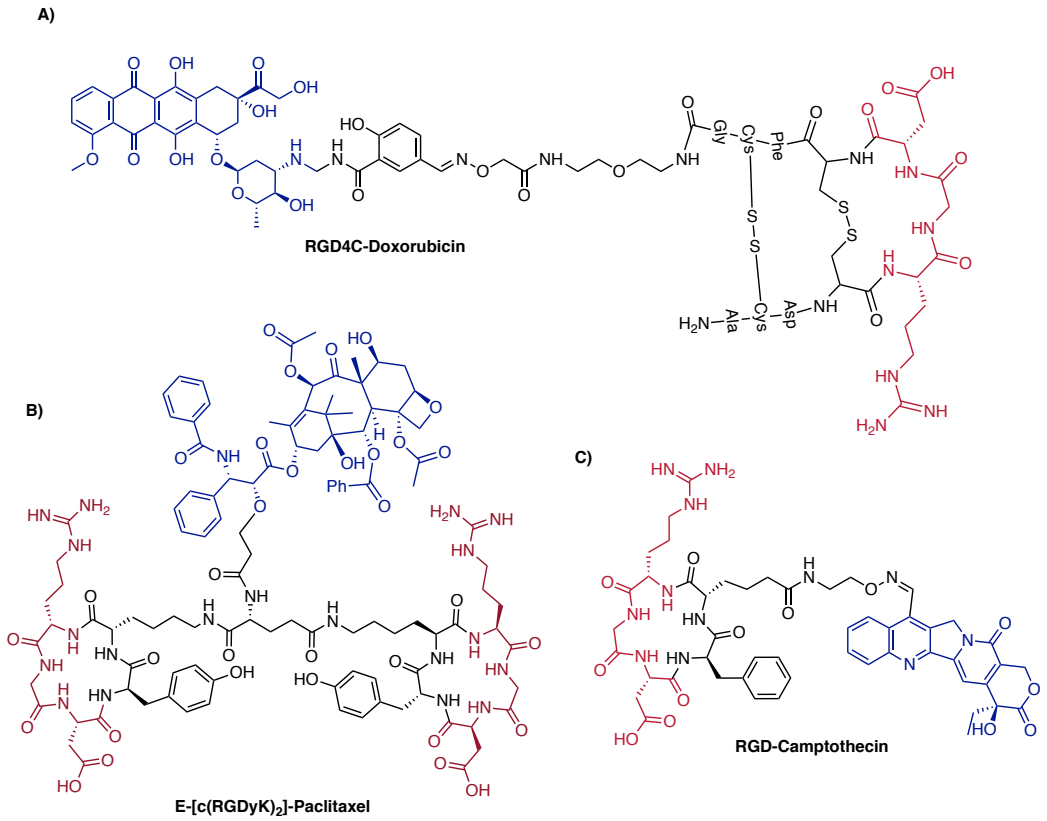

Figure 13 Examples of integrin-targeted anticancer drug conjugates.

In the field of metal-based anticancer drugs, Lippard and collaborators were pioneering in describing a series of mono- and difunctionalized platinum(IV) complexes conjugated to the cyclic RGD motif, c(RGDfK) (**Figure 14, A**), or to NGR.[61] Such RGD-tethered Pt(IV) complexes are potent inhibitors of cellular proliferation when compared to non-targeted platinum(IV) compounds and to the unconjugated RGD peptide moieties. Other recent examples of the conjugation of the RGD motif to metal-based anticancer complexes include a Pt(IV) derivative of picoplatin[63] (**Figure 14, B**) and ruthenium(II) complexes.[26,62] (**Figure 14, C and D**).

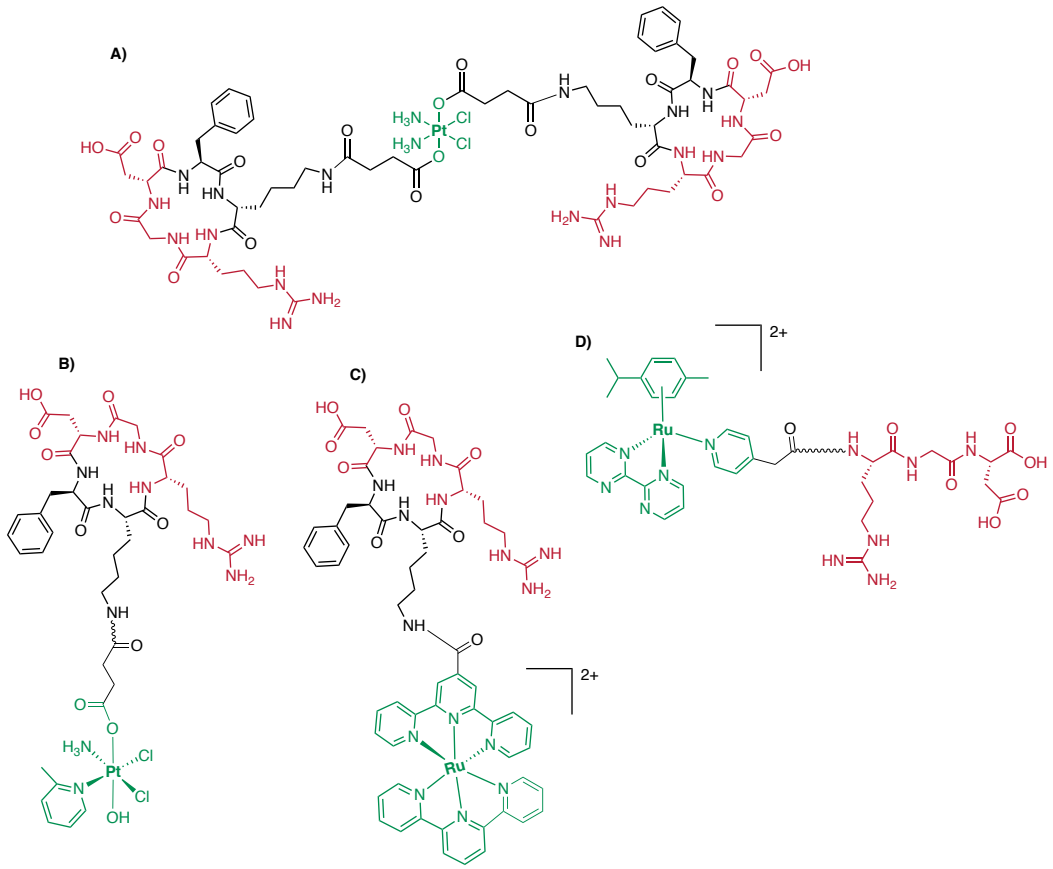

Figure 14 Examples of integrin-targeted metal-based anticancer complexes**.**

Finally, it is worth noting that nanocarriers such as liposomes, nanoparticles and micelles have been also grafted at their surface with targeting ligands based on RGD peptides. One of the main advantages of these nanocarriers is their size (20−400 nm) that allows: i) high drug loading capacity and water solubility, ii) high stability in blood vessels and drug retention time in tumors. RGD-targeted nanocarriers may specifically address drugs into cancer cells by the binding of the RGD peptide to αvβ3 integrins, which conduces to an active targeted drug delivery approach within the tumors via receptor-mediated endocytosis.[64] The fact that this strategy is not possible with non-targeted nanocarriers is particularly interesting for the selective delivery of drugs into cancer cells. RGD-targeted nanocarriers have been recently applied to the delivery of several drugs such as doxorubicin,[64] paclitaxel,[65] gemcitabine[66] and metal-based anticancer drugs,[67,68] as summarized on **Table 2**.[49]

Table 2 Examples of recent preclinical studies of RGD-targeted nanocarriers

Nanocarrier	Therapeutic agent	Targeting motif	Tumor model
Nanoparticle	doxorubicin	cRGD	Pancreatic/renal tumors
Nanoparticles	paclitaxel	GRGDS	TLT hepatocarcinoma
Albumin NP	gemcitabine	RGD	BxPC3 pancreatic cancer
Micelles	paclitaxel	c(RGDfK)	U87MG glioblastoma
HPMA conjugates	geldanamycin	c(RGDfK)	DU145 prostate tumor
Liposomes	paclitaxel	cRGD	A549 lung adenocarcinoma

2.1.2. Folate receptor: Folic Acid

Folate receptor, which is involved in the uptake of folic acid (vitamin B9, **Figure 15**), exists in three different isoforms: FR-α, FR-β, and FR-γ. Among them, FR-α is often up-regulated on the cell surface of a wide variety of human carcinomas, including ovary, brain, kidney, breast, colon, and lung malignancies, but it is more rarely expressed on normal cells. FR-β is expressed on activated macrophages and on the surface of malignant cells of hematopoietic origin.[69-71] FR-γ has been detected principally in normal and leukemic hematopoietic tissues, including bone marrow, spleen and thymus and in some carcinoma explant cells. Folate backbone is composed by three different fragments: pterin, *p*-aminobenzoate (pABA), and glutamate.

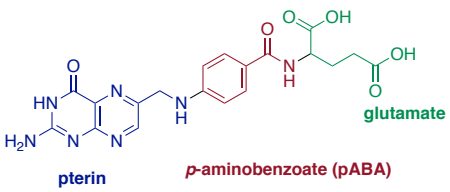

Figure 15 Chemical structure of folic acid.

Folate receptors (FR-α) are also expressed on the apical surface of healthy epithelial cells. However, previous studies have demonstrated that folic acid has higher affinity for receptors in malignant cells because the surface of the epithelial cells is tightly packed and form a continuous sheet with no intercellular spaces that could facilitate the access of folate (**Figure 16**).[48,70]

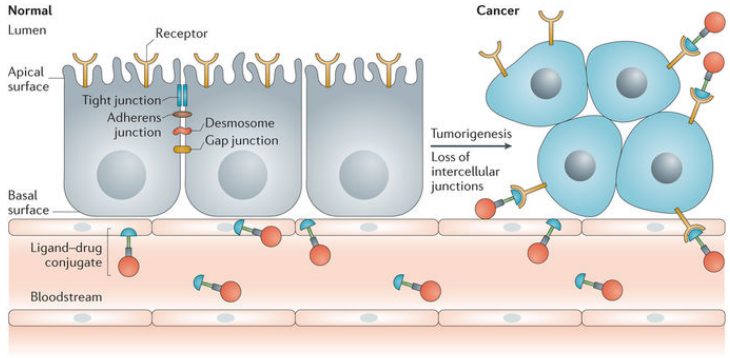

Figure 16 The effect of epithelial-cell transformation on the accessibility of apical receptor.[48]

Owing to the frequent overexpression of folate receptors (FRs) on the surface of malignant cells, the conjugation of cytotoxic agents to folic acid via suitable linkers has been widely explored to achieve selective drug delivery within tumors. Conjugates covalently linked via folate's γ-carboxyl group maintain a high affinity for FRs, and their mechanism of cellular internalization is as effective as that displayed by folic acid in its free form. Indeed folate-conjugates enter cells by FR-mediated endocytosis and move through many organelles supplying transported materials to cell cytoplasm. Due to recycling of the unligated FR back to the cell surface, the uptake process can be reiterative, allowing a continuous supply of folate-linked drugs into the cell.[71,72]

Several chemotherapeutic agents have been conjugated to folic acid for active targeted drug delivery. One of the first examples was reported by Gibson and co-workers who developed long-circulating PEGylated carboplatin analogues with improved cell permeation abilities, by conjugating the platinum moiety to folate-targeted PEG carriers.[69,73] Similarly, folate has been conjugated to small organic drugs such as Chlorambucil,[74] Paclitaxel,[75] and Mitomycin C,[76] as well as to other platinum-based complexes (**Figure 17**).[77]

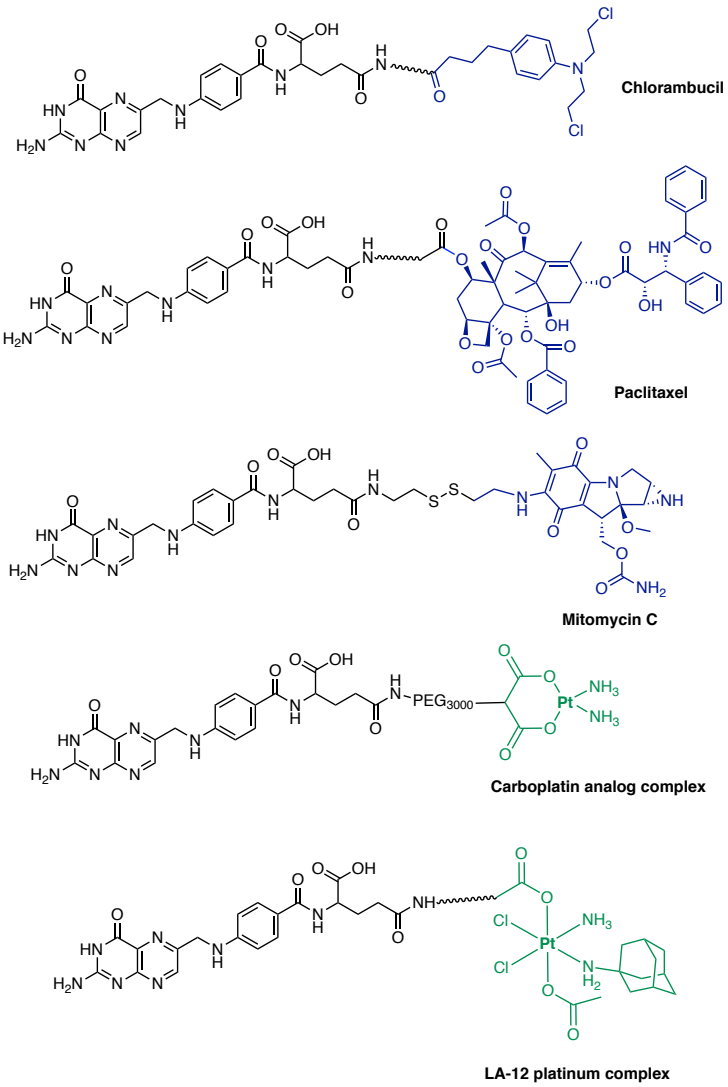

Figure 17 Examples of folate-drug conjugates.

In this context, Lippard and collaborators have described Pt(IV) complexes containing a folic acid derivative at one of the axial positions to specifically target folate receptor-enriched tumor cells, and a delivery system based on nanoparticles at the other axial position. The conjugate exhibited enhanced cell-killing properties when conjugated to nanoparticles, which facilitate delivery via endocytosis. The internalization studies showed high and specific binding to FRα (**Figure 18**).

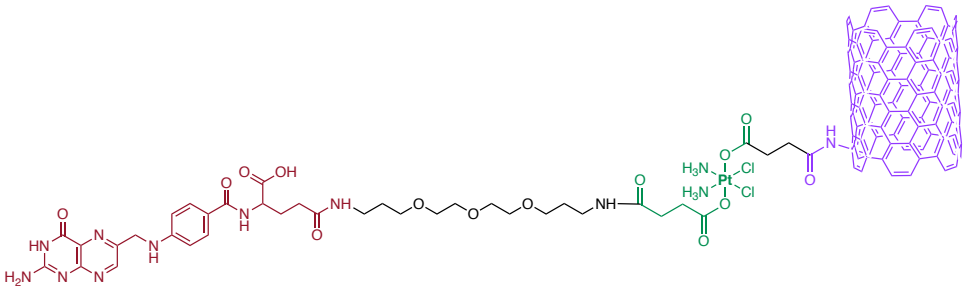

Figure 18 Structure of a folate-conjugate with Pt(IV) drug and nanoparticles.[77]

Finally, it is worth noting that two folate conjugates that have entered in clinical trials: Vintafolide (**Figure 10, page 25**) and Epofolate (**Figure 19**). Vintafolide is in Phase III for the treatment of platinum-resistant ovarian cancer (PROCEED trial) and in a Phase IIb trial for non-small-cell lung carcinoma (NSCLC).[48] On the other hand, Epofolate has completed Phase I and II assessments for the treatment of advanced solid tumors.[78]

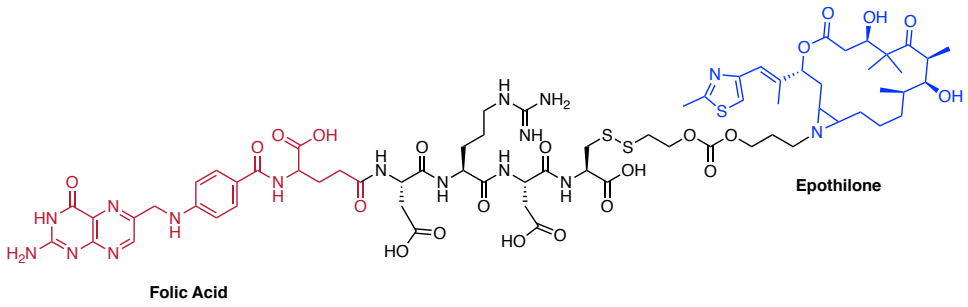

Figure 19 Chemical structure of Epofolate.

2.1.3. $SSTR_2$: Octreotide

Somatostatin subtype-2 receptor ($sstr_2$) as well as other somatostatin receptors ($sstr_1$, $sstr_3$, $sstr_4$ y $sstr_5$) are expressed on the cell membrane matrix. In addition, the SSTR family is localized on tissues in the periphery that include gastrointestinal and pancreatic tissues, and a high level of expression of this type of receptors can also be detected in the brain. The main receptor subtype is $sstr_2$, which mediates both anti-secretory and anti-proliferative actions. Most tumor tissues preferentially express $sstr_2$, less frequently sstr $_{1,3,5}$, and the $sstr_4$ receptor is only rarely detected in tumor tissues. $Sstr_2$ is expressed on several types cancer, including small-cell lung and gastro-entero-pancreatic tumors and mediates tumor cell growth inhibition. The somatostatin receptors, in turn, are classified within the family of G protein receptors, a superfamily of receptors with seven transmembrane domains of alpha helical structure.[79–81]

Somatostatin (SST) is a regulatory peptide that was isolated for the first time in the early 1970s from the hypothalamus ovine.[82] SST is produced by neuroendocrine, inflammatory, and immune cells in response to ions, nutrients, neuropeptides, neurotransmitters, thyroid and steroid hormones, growth factors, and cytokines. Somatostatin has broad inhibitory effects on the secretion of hormones such as growth hormone, insulin and glucagon. These effects have formed the basis for the clinical use of SST analogues in the treatment of endocrine tumors. In addition, Somatostatin functions as a neurotransmitter in the brain and inhibits the release of thyroid stimulating hormone (TSH).[81,83–85]

All five somastostatin receptor subtypes bind their natural somatostatin ligands, SST-14 and SST-28 (**Figure 20**), with nanomolar affinity. Cortistatin is, like somatostatin, a high-affinity universal agonist of human sstr receptors ($sstr_{1–5}$) and, in addition, binds with moderate affinity to the growth hormone secretagogue receptor (GHSR). A more selective binding profile was found for the short synthetic SST analogues: octreotide, lanreotide, vapreotide and MK-678, that we will explain in more detail next.[86,87]

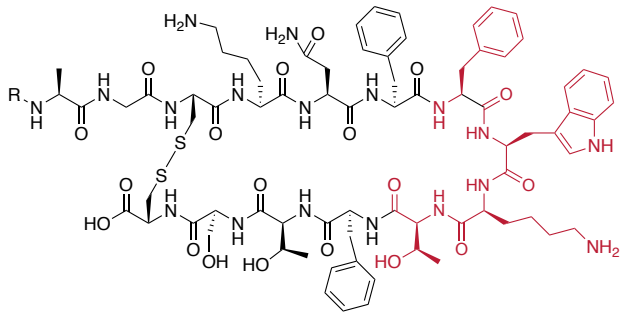

SST-14 R = H
SST-28 R= Ser-Ala-Asn-Ser-Asn-Pro-Ala-Met-Ala-Pro-Arg-Glu-Arg-Lys.

Figure 20 Chemical structures of the two main somatostatin hormones.

The use of somatostatin as a vehicle in targeted drug delivery strategies is highly problematic since it is very easily degraded by the proteases found in the bloodstream, which difficults clinical applications. For this reason, many somatostatin analogs have been developed over the past years.[83,88,89]

One of the first and most important SST derivatives was described by Bauer and collaborators who found that **Octreotide** (Oct, **Figure 21, A**) has higher inhibitory capacity of the growth hormone than somatostatin. Octreotide is currently approved by the FDA for use in diagnostic imaging applications and for the treatment of hormone-secreting pituitary adenomas and gastro-enteropancreatic (GEP) tumours. Other cyclooctapeptide analogs such as Lanreotide (**Figure 21, B**) and Vapreotide (**Figure 21, C**) have found clinical applications, mainly in the treatment of tumor symptoms such as carcinoma. Finally, the synthesis of cyclohexapeptide (MK-678, **Figure 21, D**) and β-peptides is also highlighted.[79,80,89] On the one hand, MK-678 shows a reduced size compared to common agonist peptides of somatostatin receptors, exhibiting an even more selective profile than octreotide, with higher binding affinity to $sstr_2$ and reduced affinity for $sstr_3$ and $sstr_5$.[76,77] On the other hand, β–peptides analogs, which also have a reduced number of backbone amide bonds, are useful as potential somatostatin agonists.[86]

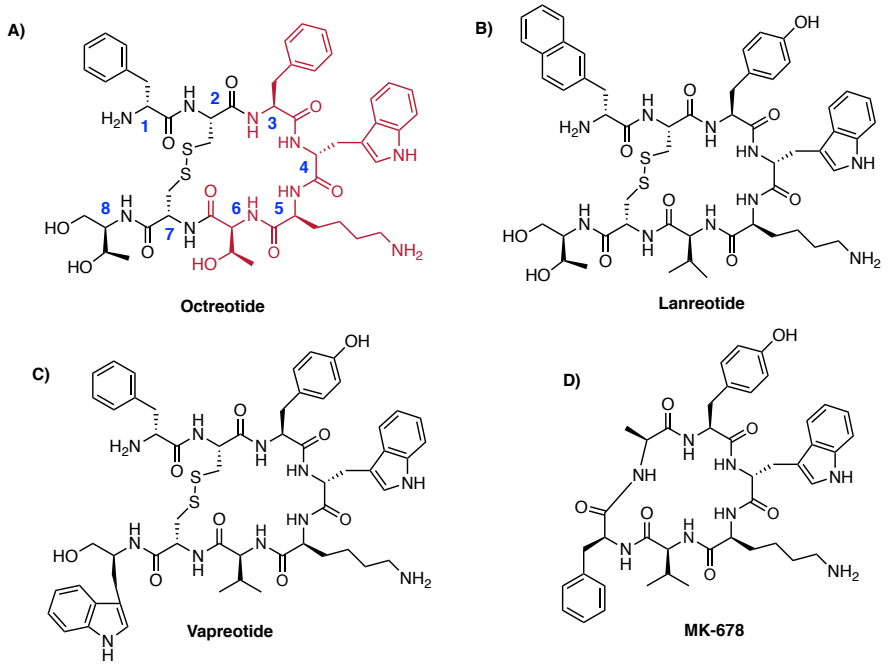

Figure 21 Chemical structure of some representative analogs of somatostatin.

The amino acid sequence Phe^3-*D*-Trp^4-Lys^5-Thr^6 is responsible for the pharmacologic activity of **Octreotide.** OCT incorporates *D*-Trp^4, which stabilizes the pharmacophoric β-turn along with *D*-Phe^1, and exhibits high-binding affinity for $sstr_2$, along with intermediate-binding affinity to $sstr_3$ and $sstr_5$. In this context, several studies have reflected the importance of the disulfide bond, the bridging unit Cys^2–Cys^7, which provides enhanced metabolic stability and stabilizes the β-turn structure spanning the *D*-Trp^4-Lys^5 residues, which are supposed to be mandatory for the binding to the SSTR.

However, it is well-known that the disulfide bridge is also prone to be attacked by endogenous reducing enzymes or by nucleophilic and basic agents. In the search for more robust octreotide derivatives carrying a stable bridging tether, dicarba-analogs of octreotide have been described in recent years. Moreover, it is known that constrained carba-tethers in cyclic peptides can stabilize helices or β-turn.[90–92]

Due to the high binding affinity and selectivity of somatostatin analogs for sstr2 receptor, they have been widely used in active targeted drug delivery strategies. Indeed, somatostatin analogs have been conjugated to small organic drugs such as Camptothecin[93] or Methotrexate,[94] the latter being one of the first conjugates described with an OCT analog. Moreover, several examples of conjugates with metal-based anticancer complexes (Ru(II),[26,95] Pt(II),[95,96] Ir(III)[97] and Os(II)[95]) have been reported (**Figure 22**). Interestingly, conjugation to cytotoxic and luminescent Ir(III) complexes provides an opportunity for the construction of novel targeted theranostic agents, since they can be used simultaneously as imaging and therapeutic agents.[97]

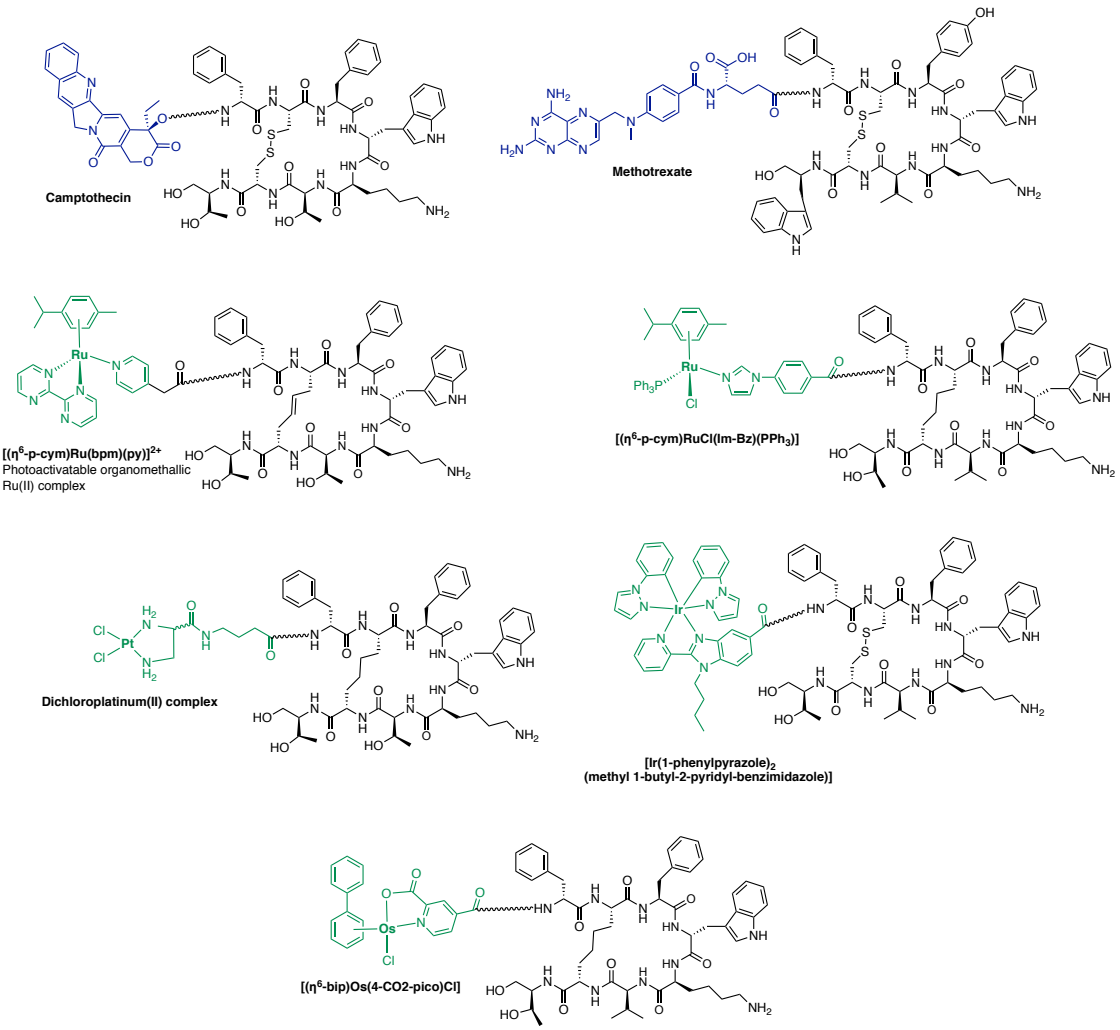

Figure 22 Examples of octreotide-based conjugates and analogs.

Finally, it is worth mentioning that two Octreotide derivatives are being used in the clinics. On the one hand, OctreoScan® when radiolabeled with ^{111}Indium has been approved by the FDA as an imaging agent for the diagnosis of tumor cells and as radiotherapy technique, although it was originally designed for scintigraphy of neuroendocrine tumors. On the other hand, OctreoTher® when radiolabeled with ^{90}Y has exhibited promising results during clinical trials for treating neuroblastosma, childhood brain tumors and gastrointestinal cancer (**Figure 23**).[98,99]

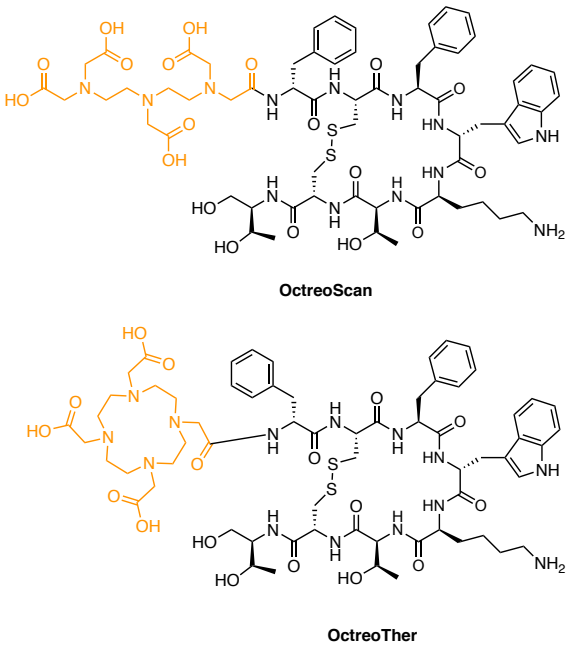

Figure 23 Chemical structures of OctreoScan® and Octreother®.

3. Imaging and caging applications of organic chromophores

3.1. Fluorescence imaging with organic fluorophores

The need for understanding essential recognition events in Chemistry and Biology has directed considerable efforts towards the development of suitable chemical probes. Indeed, the development of efficient fluorescent dyes has facilitated recent advances in cell biology and medical diagnoses imaging. When compared to UV or short wavelength visible light, far-red and near-infrared (NIR) (650-900 nm) light is highly advantageous for bioimaging applications due to minimal photo-damage to biological samples, deep tissue penetration, and minimum interference from background auto-fluorescence by biomolecules in the living systems. Thus, it is of high interest to design and develop fluorescent dyes based on small organic molecules with absorption and emission in the far-red and NIR region. However, the preparation of such fluorescent dyes requires complex design methods and intense synthetic efforts (**Figure 24**).[100–102]

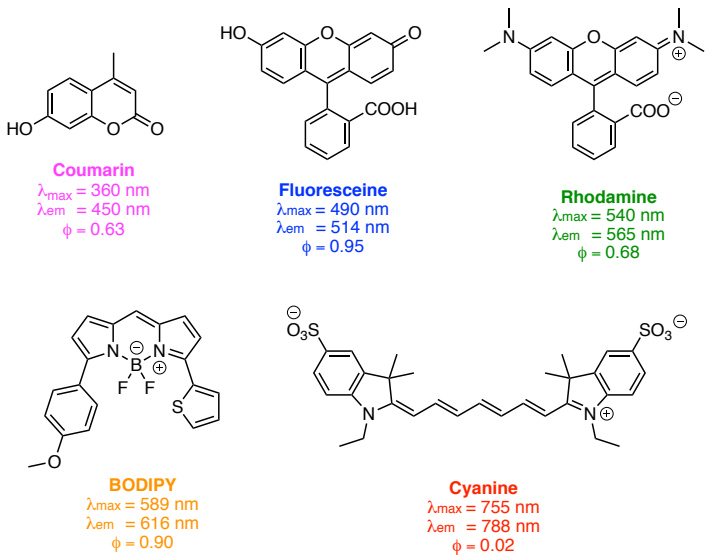

Figure 24 Chemical structure of some representative organic fluorophores.

In this section, we will introduce the importance of fluorescence microscopy, as well as the rationale behind this technique and the concept of fluorescence spectroscopy. Next, we will briefly review some of the most important fluorophores currently used in fluorescence imaging, particularly those based on the coumarin scaffold, which is the main protagonist of this thesis. Finally, we will discuss the conjugation of fluorophores to targeting ligands.

3.1.1. Fluorescence microscopy principles

Fluorescence microscopy requires the use of molecules with fluorescent properties, which are called fluorophores. Fluorescence is the emission of light that occurs within nanoseconds after light absorption by a fluorophore. The fluorescence process begins when a molecule in a singlet electronic ground state (S_0) absorbs a photon of suitable energy. This promotes an electron to higher energy orbitals, which relax quickly to the first singlet excited state (S_1). The decay of the excited state can occur through photon emission (fluorescence) or in a non-radiative process. The non-radiative "quenching" of the fluorophore's excited state can occur through one of a variety of processes, including bond rotation or vibration, molecular collision, and photo induced electron transfer (PET). The excited state can also undergo forbidden inter-system crossing (ITC) to the triplet excited state (T_1) and subsequent relaxation by photon emission (phosphorescence) (**Figure 25**).

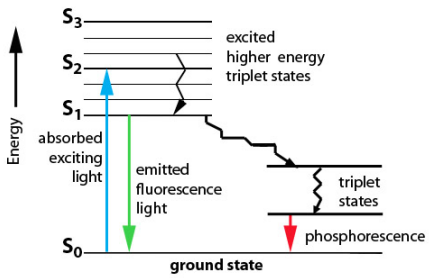

Figure 25 Diagram of Jablonsky.

Fluorescence microscopy can be used to visualize biochemical or biological process by labelling biomolecules with different fluorescent probes. The function of a fluorescence microscope is to irradiate the sample with a desired and specific band of wavelengths, and then to separate the much weaker emitted fluorescence from the excitation light. In a microscope configuration, only the emitted light should reach the detector, so that the resulting fluorescent structures are superimposed with high contrast against a very dark background. By contrast, the goal of confocal microscopy is to reject out-of-focus light from the image. This is achieved with a pinhole aperture that ensures that light reaching the detector comes only from the equivalent (confocal) point in the sample where the excitation light was focused, which leds to a better resolution (**Figure 26**).[100,102–105]

Furthermore, recent advances in fluorescence microscopy techniques offer the possibility of obtaining images of three-dimensional (3D) structures, measure interactions by multicolor co-localization, and record dynamic processes in living cells at the nanometer scale. The enhanced optical resolution allows us to use new microscopy techniques: i) the photoactivated localization microscopy (PALM), ii) stochastic optical reconstruction microscopy (STORM) and iii) ground state depletion microscopy (GSDIM).[105–107]

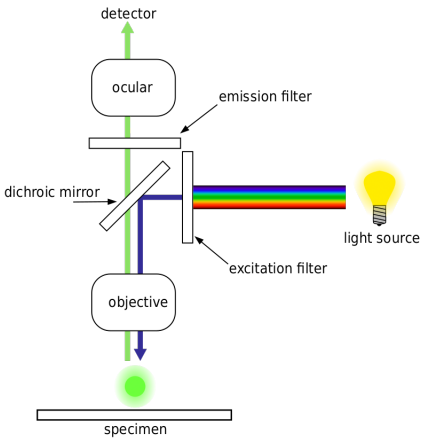

Figure 26 Schematic representation of a fluorescence microscope.

3.1.2. Overview of fluorophores based on organic molecules

Fluorophores based on organic molecules are powerful tools in modern cellular and molecular imaging techniques. In this section, we will introduce some of the most important fluorescent dyes (fluorescein, coumarins, BODIPYs, rhodamines and cyanines; **Figures 27** and **28**).

The main photophysical properties that define the characteristics of a fluorophore include the molar absorption maximum wavelength (**λ_{max}**), the emission maximum wavelength **(λ_{em})**, the extinction coefficient (***ε***), and the fluorescence quantum yield (**Φ**). The difference between **λ_{max}** and **λ_{em}** is termed the "Stokes' Shift". Fluorophores with small Stokes' Shifts are susceptible to self-quenching via energy transfer because the excitation and emission wavelengths overlap. The extinction coefficient (or molar absorptivity) is a measure of the probability of light absorption by the dye. The quantum yield is the ratio of the number of photons emitted to the number of photons absorbed. The relative brightness of fluorophores can be determined by comparing values of Φ x ε, which takes into account both the photons absorbed and the efficiency of the fluorescence process. The main requirements for an ideal fluorophore for optical imaging applications include high photostability, large Stokes' Shifts and brightness. Moreover, other several parameters have also to be considered for use in biological experiments such as solubility in water, tendency to aggregation and toxicity.

Fluorescein (**Figure 27, C**) was first synthesized in 1871 by Baeyer[108] and has played an important role in fluorescence microscopy. Fluorescein was one of the first labels used in immunofluorescence microscopy experiments and is still widely employed in many different biological and biochemical applications. This persistence is a consequence of its synthetic accessibility and the excellent spectroscopic properties of the dye (λ_{max} = 490 nm, ε = 9.3 × 10^4 M^{-1} cm^{-1}), including emission of green light (λ_{em} = 514 nm, Φ = 0.95). Fluorescein structure bears a phenolic pK_a of 6.4 and is highly fluorescent in its phenolate form.

Coumarins (**Figure 27, A and B**) comprise a large class of natural products, pharmacological agents and dyes. Coumarins are classified as benzopyrone organic compounds, although they may also be considered as a subclass of lactones. The prototypical coumarin fluorophore is 4-methyl-7-hydroxy-coumarin (4-methylumbelliferone, 4-MU; **Figure 27, A**), which absorbs UV light (λ_{max} = 360 nm, ε = 1.7 × 10^4 M^{-1} cm^{-1}) and emits blue light (λ_{em} = 450 nm, Φ = 0.63).[109]

The boron difluoride dipyrromethene (**BODIPY**) (**Figure 27, D and Figure 28, D**) dyes have been used in several applications including the development of fluorescent labels for cell imaging, photodynamic therapy, etc. The main characteristic properties of this scaffold include neutral charge, small Stokes' Shifts, and insensitivity of fluorescence to environmental changes. The typical BODIPY scaffold operates on the visible light region (λ_{max} = 505 nm, ε = 9.4 × 10^4 M^{-1} cm^{-1}, λ_{em} = 511 nm, Φ = 0.94).[7,110]

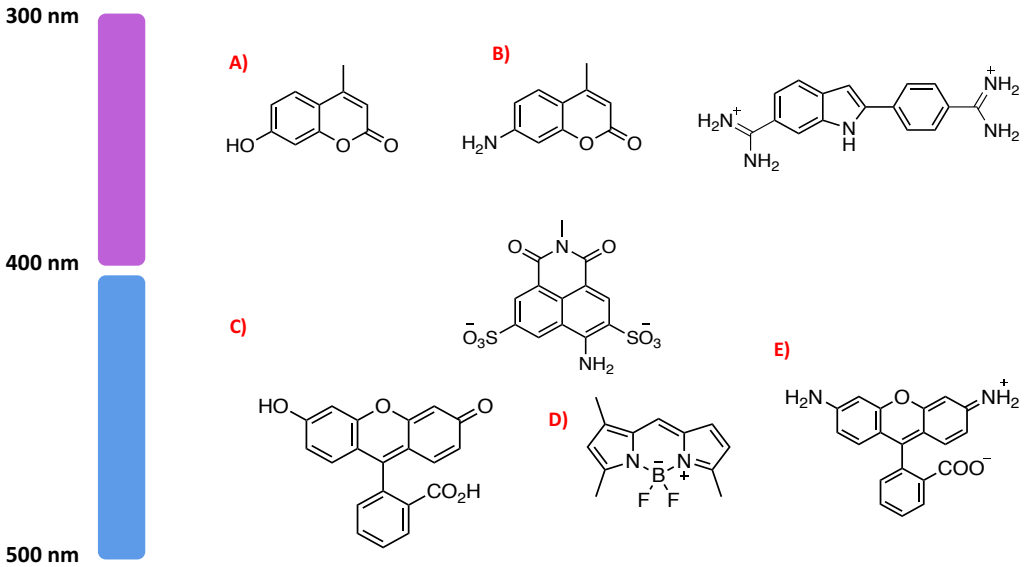

Figure 27 Overview of some representative organic fluorophores absorbing in the 300-500 nm range.

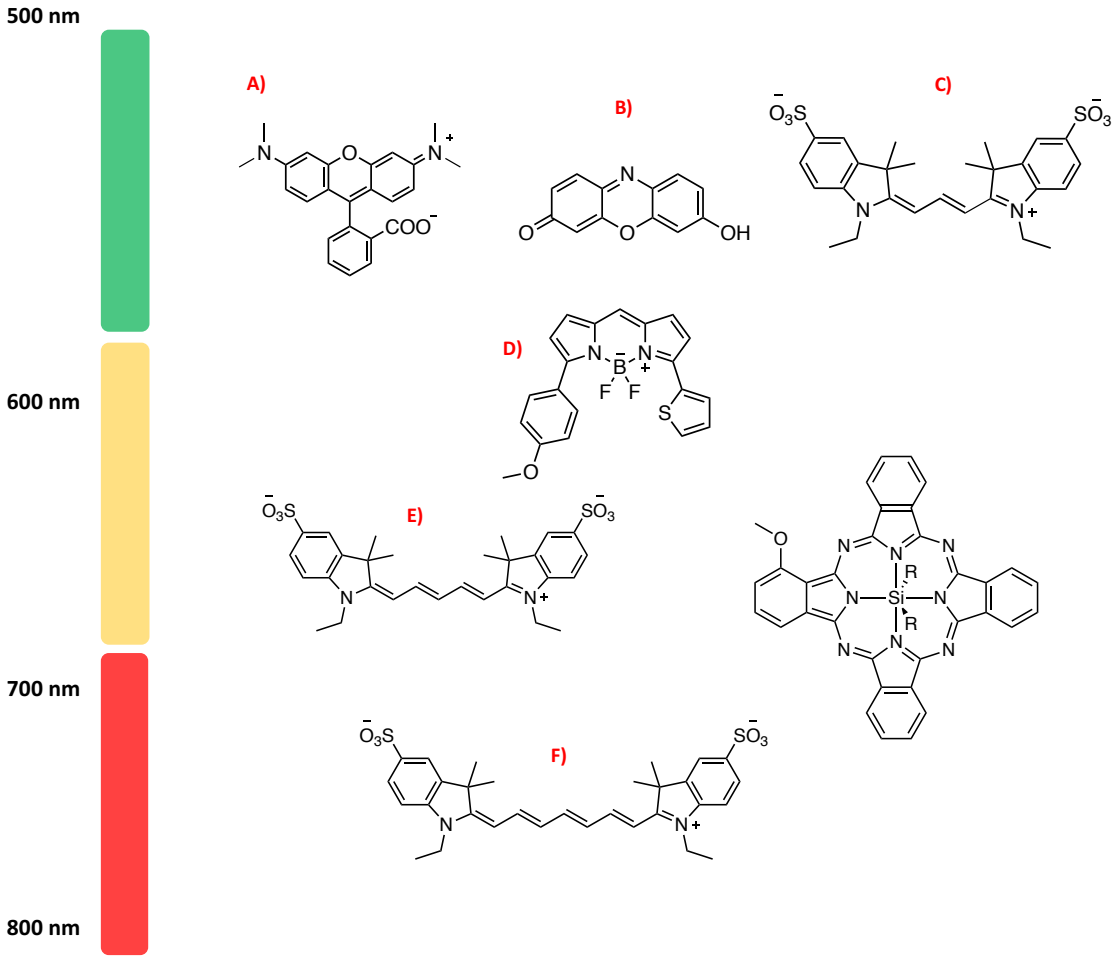

Figure 28 Overview of some representative organic fluorophores absorbing in the 500-800 nm range.

The amino analogs of fluorescein, **Rhodamines** (**Figure 27, E and Figure 28, A**), were first described in the 1880s. Rhodamines offer certain advantages over fluorescein, including low pH-sensitivity, higher photostability, and tunable spectral properties. The conventional rhodamine dye, rhodamine 110 (**Figure 28, A**), has similar optical properties than fluorescein, since absorbs visible light (λ_{max} = 496 nm, ε = 7.4 × 10^4 M^{-1} cm^{-1}) and emits green light (λ_{em} = 517 nm, Φ = 0.92).[110]

Cyanine scaffolds contain two aromatic nitrogenated heterocyclic ring systems linked by a polymethine bridge. Extension of the polymethine chain results in a red-shift of the absorption and emission maxima, with trimethine (**Cy3**, **Figure 28, C**) (λ_{max} = 554 nm, λ_{em} = 568 nm, $\varepsilon = 1.3 \times 10^5$ M^{-1} cm^{-1} and Φ = 0.14), and pentamethine (**Cy5**, **Figure 28, E**) (λ_{max} = 652 nm, λ_{em} = 672 nm, $\varepsilon = 2.0 \times 10^5$ M^{-1} cm^{-1} and Φ = 0.18) being two representative examples of this family of dyes. Such conventional cyanine fluorophores display fluorescence emission in the visible and far-red region.

The heptamethine (**Cy7**, **Figure 28, F**) derivatives display both absortion and emission on the NIR region because of the longer polymethine bridge (λ_{abs} = 755 nm, $\varepsilon = 7.4 \times 10^4$ M^{-1} cm^{-1}, λ_{em} = 778 nm, Φ = 0.02). The lipophilic nature of these dyes limited their utility as cellular membrane probes and DNA stains until the development of sulfonated derivatives. Nowadays, this family of dyes are used for labelling proteins and nucleic acids, and constitutes one of the most widely used fluorophores in biological and biochemical experiments.

The use of a phenoxazine core yields small fluorophores with significant bathochromic shifts when comparised to fluorescein and rhodamine analogs. The most widely used oxazine dye is resorufin (**Figure 28, B**), which absorbs and emits in the yellow range (λ_{max}= 572 nm, $\varepsilon = 5.6 \times 10^4$ M^{-1} cm^{-1}, λ_{em} = 585 nm, Φ = 0.74). Like fluoresceins, resorufin is more fluorescent in its phenolate form (pK_a = 5.8).

Unfortunately, most conventional dyes share some of the problems associated with organic-based fluorophores: poor photostability, low aqueous solubility, low brightness and undesired aggregation. [110–113]

As previously stated suitable fluorophores for cell imaging applications should have high photostability and brightness. Photobleaching can be defined as the loss of fluorescence emission when a fluorophore is continuously irradiated. One of the parameters that can be used to define the photostability of a fluorophore is the fluorescence lifetime (τ_F), since it measures the time a fluorophore spends in the excited state before returning to the ground state by emitting a photon. Fluorophores with small Stokes' Shifts are susceptible to fluorescence quenching via energy transfer and, consequently, show low photostability. On the other hand, the twisted internal charge transfer (TICT) process acts as one of the major non-radiative de-excitation pathways and it is related with the low brightness of some conventional dyes in aqueous solvents.[113-115]

Although water solubility is a key requirement for biological probes, the majority of conventional fluorophores are insoluble in water. For this reason, several synthetic modifications have been explored to improve water solubility including the introduction of charged groups or water-soluble groups such as biopolymers or polyethylene glycol units. Moreover, it is important to emphasize that the photophysical properties of a dye can be strongly affected by the solvent in which is dissolved. Nevertheless, an ideal fluorophore should present high values of quantum yield and brightness in aqueous media.

3.1.3. Coumarin-based fluorophores

Among the palette of fluorescent organic molecules, coumarin scaffolds are ideal candidates to visualize biochemical and biological processes owing to their good cell membrane permeability and well-established photophysical properties. Moreover, coumarins are small compounds that can be easily synthesized and modified both for labeling biomolecules and for improving their photophysical and physicochemical properties. Indeed, the coumarin scaffold can be easily tuned by incorporating electron-donating groups at position 7 (e.g., *N,N*-dialkylamino or hydroxy/alkoxy) that partner with the electron-withdrawing lactone moiety to create a push−pull effect, and then shift the fluorescence emission from blue to cyan. The term push-pull implies a π-scaffold functionalized with an electron-donating group (**EDG or Donor – D**) and an electron-withdrawing group (**EWG or Acceptor – A**). Usually, the donor fragment is based on aliphatic (typically *N,N*-dialkylamino), aromatic or saturared cyclic amines, alcohol or alkoxy (usually methoxy) groups **(Figure 29)**. [116–118]

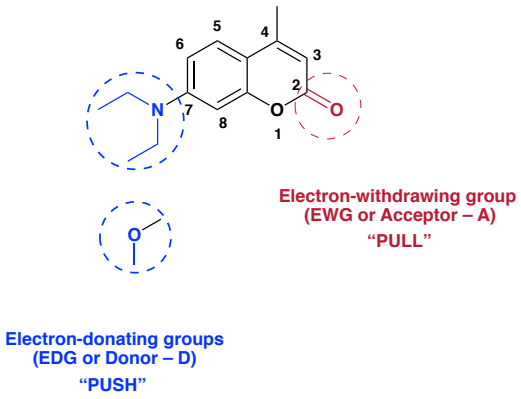

Figure 29 Representation of the push-pull effect over the coumarin scaffold.

This D-π-A system undergoes a photo-induced intramolecular charge-transfer (ICT) state, forming a low-energy molecular orbital. When visible light provides sufficient energy to excite the electrons within this new molecular orbital, these compounds are generally colored. The ICT also generates dipole moments that increase the sensitivity of these fluorophores to polarity and, consequently, they can be considered solvatochromic dyes.

In recent years, many research groups have been working on the development of new push-pull fluorophores based on coumarins to improve their photophysical properties, particularly red-shift their absorption and emission maxima by introducing additional electron-withdrawing groups (EWGs) at positions 3 or 4, such as nitrile, trifluoromethyl or carboxyl.[119] On the same way, several analogs with different EDG groups have been described (**Figure 30**).

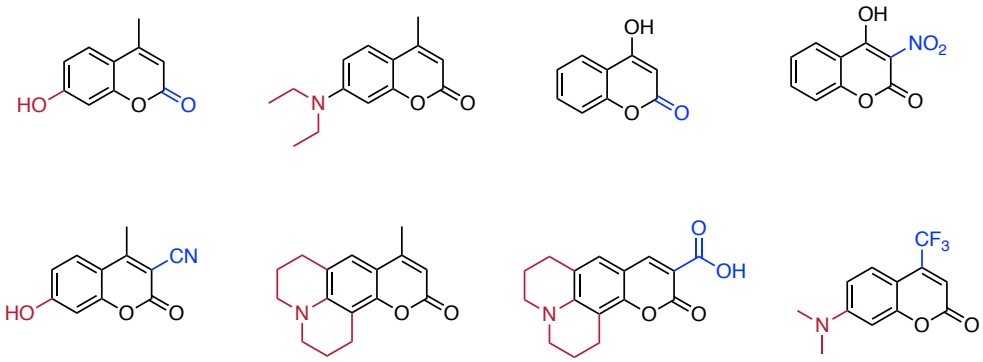

Figure 30 Examples of coumarin based fluorophores.

Alexa fluor 380 (λ_{max} = 346 nm, λ_{em} = 442 nm) (**Figure 31**, **A**) and Alexa fluor 430 (λ_{max} = 433 nm, λ_{em} = 541 nm) (**Figure 31**, **B**) are commercial dyes invented by Molecular Probes and actually commercialized by ThermoFisher. These fluorophores are based on the coumarin skeleton with some modifications. Similarly, other commercially available dyes like Atto 390 (**Figure 31**, **C**) and Atto 425 (**Figure 31**, **D**) are based on the conventional coumarin scaffold. Nevertheless, all these coumarin based fluorophores operate in the UV or blue light region.

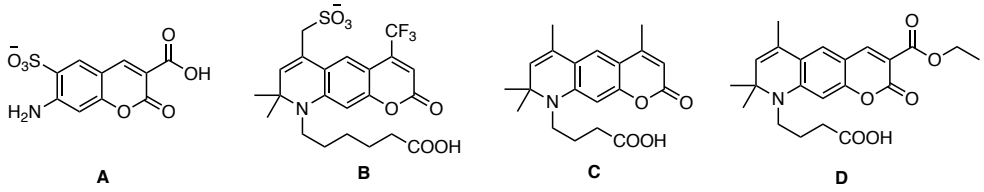

Figure 31 Structures of commercially available coumarin-based dyes.

Dyomics has also developed some coumarin-based dyes for cell imaging, such as DY-480XL (**Figure 32**). These fluorophores exhibit interesting features such large Stokes' Shifts. DY-480XL is based on the conjugation of a *N*-alkylated pyridine at position C3 of the coumarin scaffold. The absorption maximum is located around 500 nm and the emission maximum is centered at 630 nm, but Dyomics do not specify the brightness of the molecule.

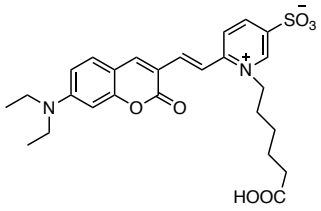

Figure 32 Chemical structure of Dyomics dye (DY-480XL).

Based on these commercial dyes, Hell and collaborators have described several synthetic routes to new 3-heteroaryl coumarins (**Figure 33**) with a polar group attached to the C3 position in the quinolone fragment fused with the coumarin. In addition, they have synthesized analogs with two different polar groups at the C6 position, such as a sulfonate (**Figure 33**, **A**) and phosphate groups (**Figure 33, B**). [120,121] Although such novel synthetic coumarins exhibit promising absorption and emission wavelengths (λ_{max} = 520 nm, λ_{em} = 639 nm), their poor quantum yield (below of 1%) represents an important limitation.

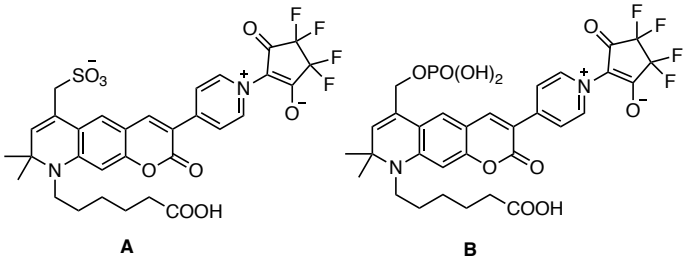

Figure 33 Structures of some coumarin-based derivatives developed by Hell and collaborators.

As previously stated in section 3.1.2, most conventional fluorophores lack of sufficient brightness and photostability for single molecule and fluorescent imaging applications, specially in aqueous media, which is attributed to the TICT process.[114,115] One good example of this phenomenon can be found in coumarin dyes, since the *N,N*-dialkylamino group at position 7 twists out the fluorophore plane upon photoexcitation and forms a non-emissive and short-lived reactive chemical species.

In order to solve this problem, Lavis and collaborators have proposed the replacement of *N,N*-dialkylamino groups by the four-membered azetidine ring in several dyes, including the coumarin scaffold, with the aim of suppressing TITC and increasing the fluorescence quantum yield in polar solvents.[112,113] Indeed, the conventional coumarin (**Figure 34**, **A**) exhibits modest quantum yield (ϕ) in water (ϕ = 0.19) but its azetidinyl analog shows a five-fold increased fluorescent quantum yield (ϕ = 0.96) (**Figure 34**, **B**).[112] Following the same idea, Xu and co-workers have used the three-membered aziridine ring to improve the quantum yield of several dyes, including that of conventional coumarin (ϕ = 0.89) (**Figure 34**, **C**).[114]

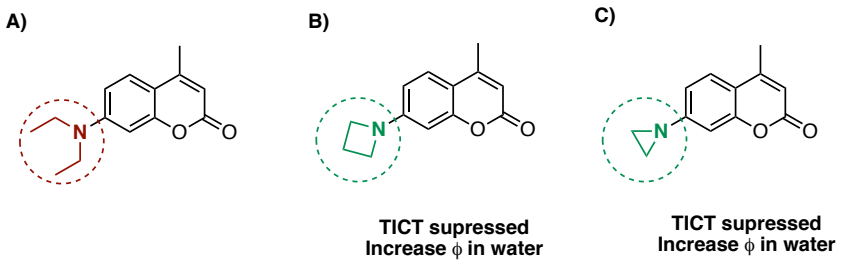

Figure 34 Replacement of the *N,N*- dialkylamino groups in the coumarin scaffold by the four membered azetidine ring and the three membered aziridine ring.

Very recently, Rivera-Fuentes and collaborators have studied in more detail the effect of replacing the *N,N*-dialkylamino group at position 7 of the classical coumarin with azetidine. They have proposed a mechanism of fluorescence quenching that does not involve TICT states but rather H-bond induced nonradiative decay (HBIND).[122] Such unproductive decay channel was efficiently inhibited by azetidinyl substitution.

As previously stated, enormous efforts have been dedicated to red-shift absorption and emission of coumarins by introducing EWGs at positions 3 or 4 while maintaining the electron-withdrawing lactone moiety of the original scaffold. In recent years several groups have demonstrated that absorption and emission maxima of these chromophores can also be red-shifted by modifying the lactone function. Indeed, green light emission was accomplished either through thionation of the carbonyl group (**Figure 35 B**) or by extending the conjugation of the system at position 2 with a dicyanomethylene group (**Figure 35, C**).[123,124]

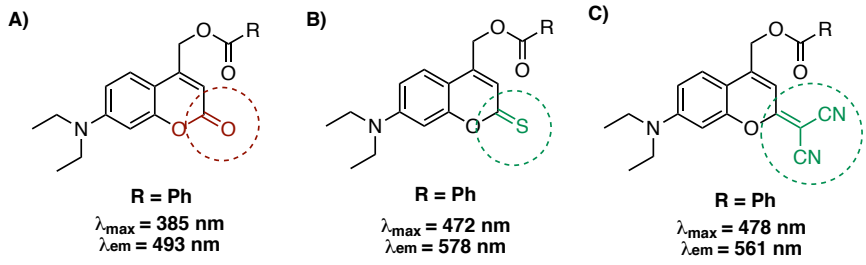

Figure 35 Replacement of the lactone group by thiolactone and dicyanomethylene group.

On the basis of these precedents, our group has recently described the design, synthesis, and spectroscopic characterization of a small library of model coumarinylmethyl derivatives for exploring the effect of replacing one cyano group in the dicyanocoumarin with a phenyl ring containing electron-withdrawing groups (EWGs) at *ortho* and *para* positions with the aim of increasing the push−pull character of the chromophore (**Figure 36**).[125]

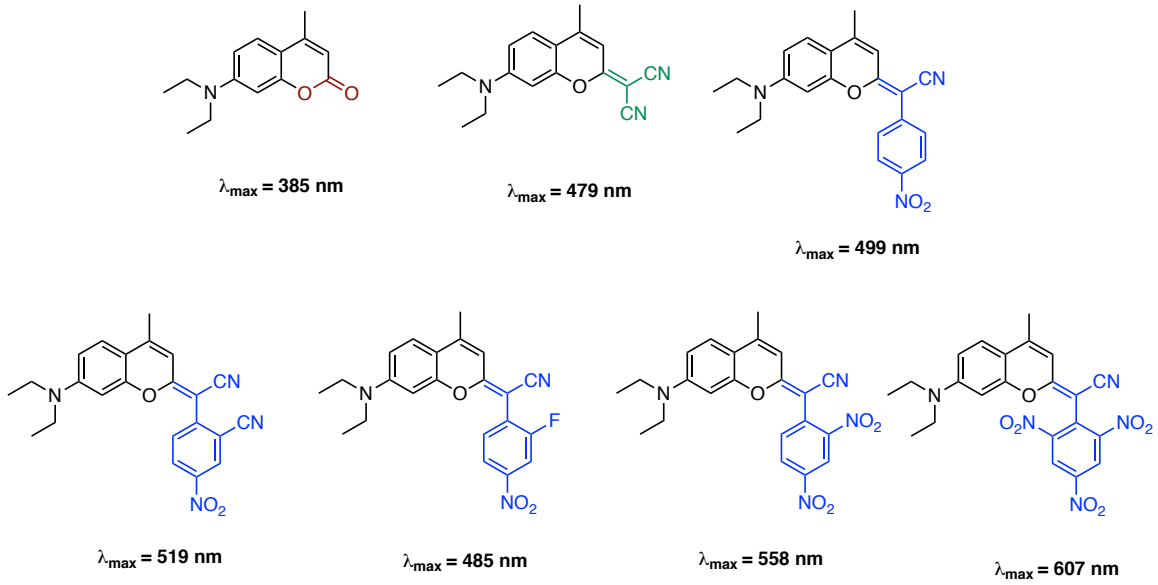

Figure 36 Examples of novel coumarin-based derivatives described by Marchán and collaborators.[125]

Finally, a similar modification of the lactone function has been described recently by Romieu, Richard and collaborators to increase the push−pull character of the chromophore.[126,127] The conjugation of hemicyanine fragments shifted the absorption and emission maxima up to the NIR (**Figure 37**).[128]

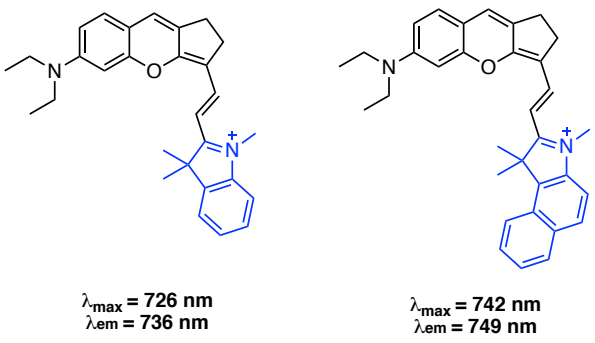

Figure 37 Examples of novel coumarin-based derivatives described by Romieu, Richard and collaborators.[128]

3.1.4. Fluorescence imaging with targeted organic fluorophores

Targeted fluorescence microscopy involves the use of fluorophores synthetically tethered to a targeting moiety (peptides, proteins, antibodies, non-peptidic small-molecules, oligonucleotides, etc.). In this section, we will briefly introduce the main strategies in targeted fluorescence microscopy (mostly the same approaches that are used in targeted drug delivery therapies), focusing on the active strategy and on the key points that should be taken into account for a correct visualization. In addition, we will introduce one of the most important applications of targeted fluorescence microscopy, the fluorescence-guided surgery.

As introduced in the previous sections, fluorescence microscopy allows the visualization of biochemical and biological processes by using a suitable fluorescent probe. **Active targeted fluorescence microscopy** has enabled the specific visualization of some of the molecular events that play key roles in disease processes, including early diagnosis and monitoring of therapeutic responses. When conjugating a fluorescent dye to a targeting ligand, several important parameters such as sensitivity, specificity, delivery, pharmacokinetics and toxicity can be modified depending on the targeting method and the overall chemical composition of the fluorophore.

The stability of a targeted imaging agent is also a determining factor for *in-vivo* experiments. Pharmacokinetic properties can be altered by the size or the charge of the dye, because sometimes large biomolecules (>100 nm) and hydrophobic conjugates bind to plasma proteins and are slowly cleared by the body, hereby increasing the delay (from hours to days) between administration of the targeted fluorophore and the time of imaging.

Fluorophores to be used in ligand targeted fluorescence imaging must have suitable functional groups to facilitate conjugation to different biomolecules. Although commercially available dyes incorporate several types of reactive groups such as carboxyl, *N*-hydroxysuccinimidyl (NHS)-esters, maleimide, amine, azide, iodoacetamide, hydrazine, alkyne, etc **(Figure 38)**, most common conjugation methods are based on the use of NHS-esters since they readily react with amines incorporated in oligonucleotides or with amino groups of proteins and peptides. For example, the ε- amino group of lysine or the *N*-terminal amine allow the formation of chemically stable amide bonds between the dye and peptides or proteins. For labeling thiol groups, the most popular derivatives incorporate maleimides or iodoacetamides. In addition, the azide modification is suitable for reactions with alkynyl groups by using click chemistry, such as the Cu(I)-catalysed azide-alkyne cycloaddition (CuAAc).

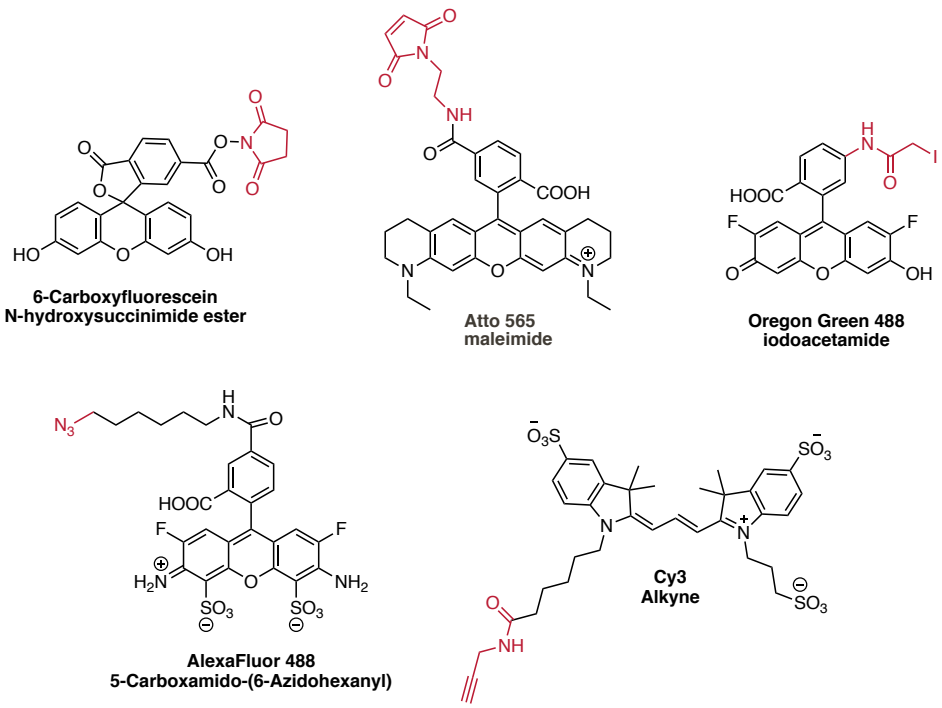

Figure 38 Examples of commercially available dyes suitable for labelling biomolecules.

Finally, **fluorescence-guided surgery** is expected to transform in the near future the way surgeries are performed, through the intraoperative identification of the location of the tumor in real time. One of the main requirements of this approach is the use of fluorophores with absorption and emission in the near-infrared (650 – 900 nm). As we have already introduced, NIR light presents higher tissue-penetration compared with shorter wavelengths. Other advantages of NIR light include minor scattering and photodamage to living cells,[7,129] and the tissues and organs on this range of light do not present autofluorescence (**Figure 39**).[130]

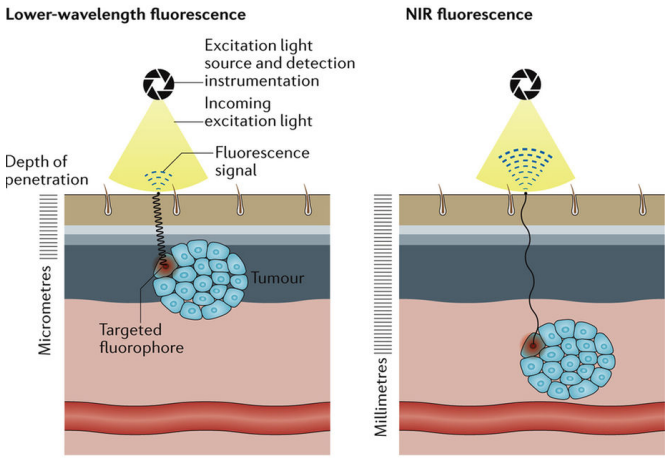

Figure 39 NIR fluorescence is more suitable for *in vivo* imaging applications than UV light.[7]

Nowadays, several ligand targeted fluorophores for **fluorescence-guided surgery** have been evaluated on clinical phases I and II.

- **Bevacizumab-800CW**. This NIR-cyanine dye whose absorption maximum wavelength is centered around 773 nm incorporates a monoclonal antibody as targeting ligand, which presents affinity for the vascular endothelial growth factor (VEGP). It is being evaluated for the diagnosis of several premalignant and malignant diseases, including colorectal, breast and oseophageal cancer.[7,131]

- **OTL38** (**Figure 40**). This fluorescent imaging agent composed by on a folate-based targeting ligand conjugated to a cyanine NIR dye (Cy7). Upon administration, OTL38 binds specifically to FRα expressed mostly on ovarian tumor cells whith allows the selectively delivery of the fluorescent dye to this type of cancer cells.[132]

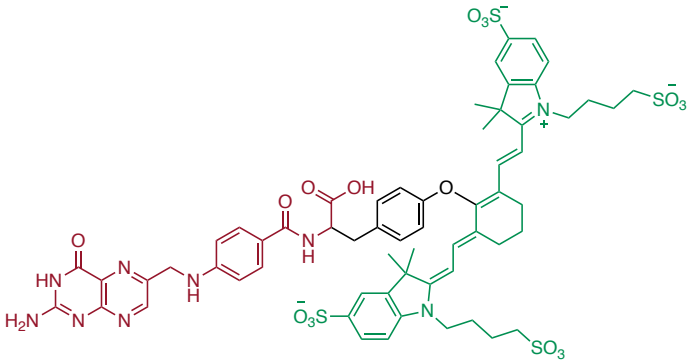

Figure 40 Chemical structure of OTL38.[128]

3.2. Photocontrolling chemical and biological processes with caging groups

As previously introduced in Section 1.3 in the context of photoactivatable metal-based anticancer complexes, light can be used to control with high spatiotemporal precision chemical and biological processes. Indeed, light is an ideal external trigger since it is non-invasive, does not cause sample contamination and its qualitative and quantitative properties can be precisely controlled. Moreover, light can be generated and manipulated with well-established techniques, and there are several methods that can be used to apply light to living systems- from cells to higher organisms.[118,133,134]

Chemical and biological processes can be regulated with light by using i) photolabile protecting groups to irreversibly trigger chemical processes **(Figure 41, A)**, ii) photoswitches for reversible switching **(Figure 41, B)**, and iii) genetically-encoded light-responsive elements (optogenetics). Here, we will introduce only the concept of caged compounds and the mechanism of photo-release of some representative photolabile protecting groups. Next, we will discuss the applications of some conventional caging groups, particularly those based on the coumarin scaffold.

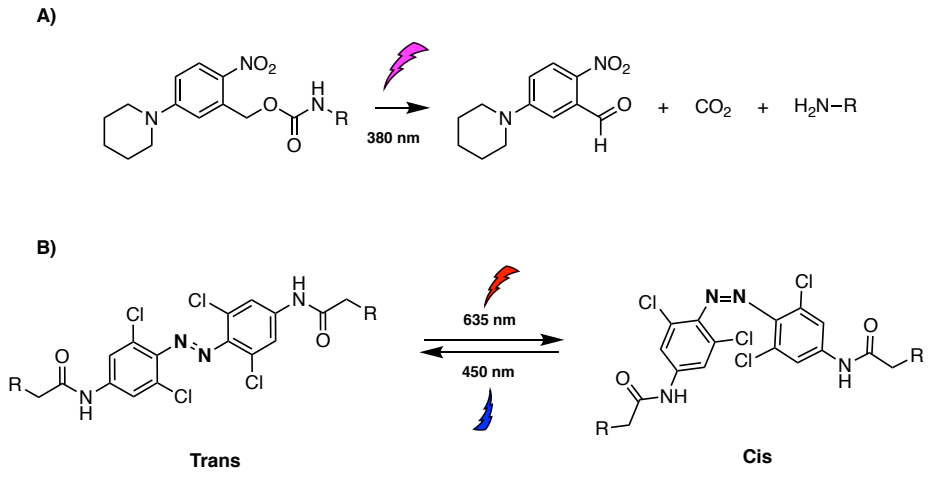

Figure 41 Examples of two strategies used for controlling chemical and biological processes with light.

3.2.1. Photocleavable protecting groups

The use of photocleavable protecting groups (PPGs or caging groups) has received widespread attention in recent years for the regulation of the activity of biologically relevant molecules, including drugs based on small compounds and biomolecules, such as peptides, proteins, and oligonucleotides. It is based on the premise that the activity of a compound can be temporarily deactivated through the protection of a key functional group with a PPG. Hence, removal of the PPG group from the protected compound (usually referred to as a caged compound) upon light irradiation should restore the activity or function of the original molecule (**Scheme 8**).

The use of PPGs that can be uncaged with light of long wavelengths is particularly appealing since offers the possibility to externally control biological processes with non-toxic and deep-tissue-penetrating visible light.[135] Moreover, for the regulation of concurrent processes with light, it is crucial to be able to address them separately in an orthogonal and non-interfering fashion. This can be achieved by employing two or more PPGs with different spectral properties like absorption maximum wavelengths.[116]

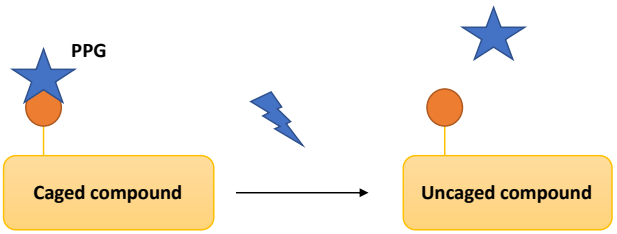

Scheme 8 Schematic representation of the concept of the uncaging process.

The criteria for choosing a PPG will depend on the final application of the caged compound. No single system needs to fulfill all of the following requirements: [117,118]

- The λ_{max} of absorption of the PPGs should be centered around the visible/NIR region, because this light does not interfere with the biological system. In addition, light of long wavelengths, particularly far-red and NIR, penetrates deeper into biological tissues than UV or blue light.

- The photoreaction should be clean and should occur with a high uncaging quantum yield or efficiency, Φ_{Ph}.

- The photochemical by-products accompanying the released bioactive compound should ideally be transparent at the irradiation wavelength to avoid competitive absorption of the excitation wavelengths and should not be toxic. Moreover, they must be biocompatible, and they should not react with the system being investigated.

- The PPG has to be synthetically accessible and stable under physiological conditions.

3.2.2. Overview of common caging groups

Despite the large number of photoremovable protecting groups reported to date, most of them require UV irradiation for triggering photoactivation (*o*-nitrobenzyl derivatives and conventional coumarins). As previously stated, this radiation is not ideal given its known phototoxicity and capacity to interact with endogenous biomolecules. Moreover, the low capacity of penetration of UV light (even in the UVA range) into deep tissues compromises further therapeutic applications. For these reason, many efforts have been devoted in recent years to the development of novel PPGs removable in the visible region of the electromagnetic spectra and even in the NIR, such as non-conventional coumarins, BODIPYs and cyanine derivatives (**Figure 42**).

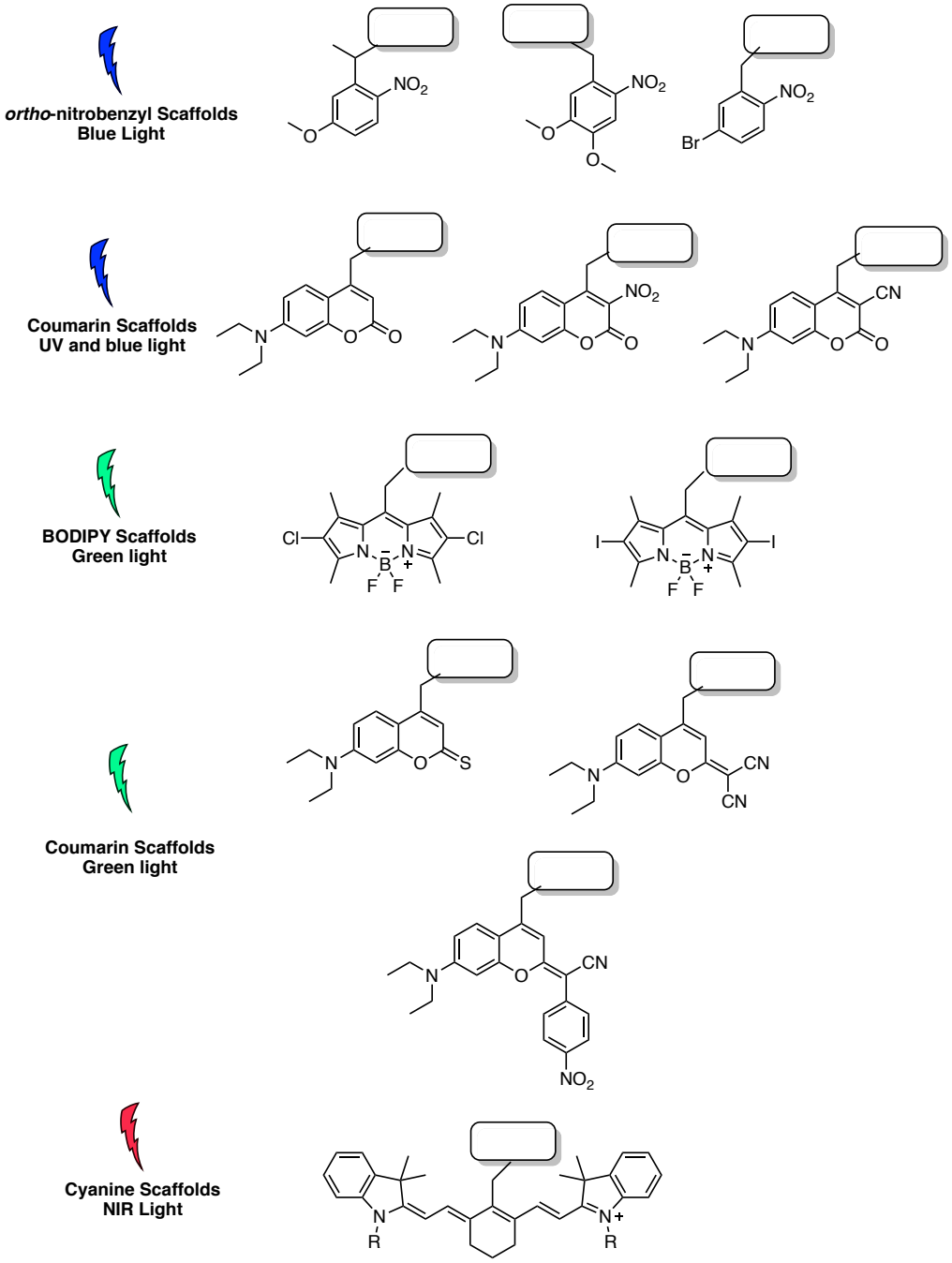

Figure 42 Examples of PPG classified according to the irradiation light required for triggering uncaging.

o-Nitrobenzyl derivatives and their analogs are by far the most widely used photolabile protecting groups in organic synthesis. Various functional groups such as aliphatic alcohols, phenols, carboxylic acids and phosphates can be protected with *o*-nitrobenzyl or nitrophenylethyl groups.[137,138] Their relatively simple structures, which are readily available and convenient for attachment to the target molecules, renders them highly valuable for biological and material science applications. One of the first examples of the use of a PPG for caging a biomolecule was described by Hoffman collaborators in 1978, who caged ATP with *o*-nitrobenzyl. This caged-ATP cannot be hydrolyzed as the covalent attachment of the caging group to the γ-phosphate prevents enzymatic access. However, photolysis breaks the bond between the benzylic carbon of the chromophore and the oxygen atom, liberating the uncaged ATP (**Scheme 9**).[138,139]

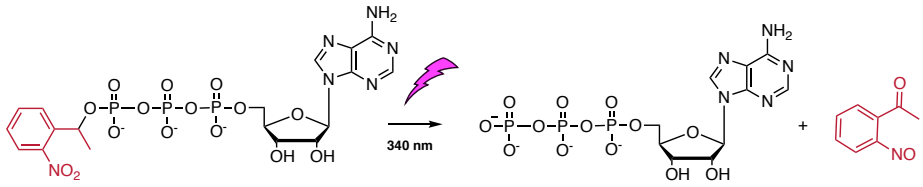

Scheme 9 The exposure of caged-ATP to UV light undergoes efficiency uncaging.

Similarly, Imperialli and collaborators have synthesized peptides containing 1-(2-nitrophenyl)ethyl-caged phosphoserine, phosphothreonine, and phosphotyrosine. Photochemical uncaging of these peptides releases the 2-nitrophenylethyl protecting group to afford the corresponding phosphopeptide (**Scheme 10**).[140]

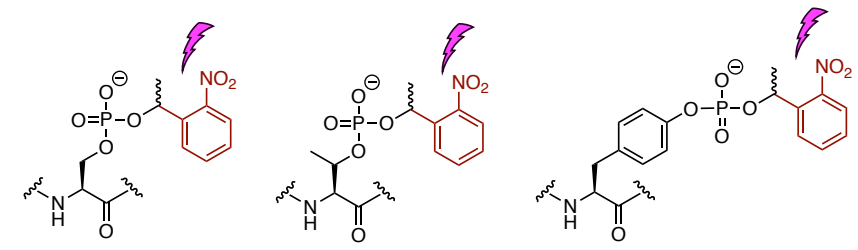

Scheme 10 Examples of caged phosphorylated amino acids.

Gasser and collaborators have also described the use of a photolabile 3-(4,5-dimethoxy-2-nitrophenyl)-2-butyl) ester group to control the anticancer activity of a ruthenium(II) complex with UV light (**Scheme 11**).[141]

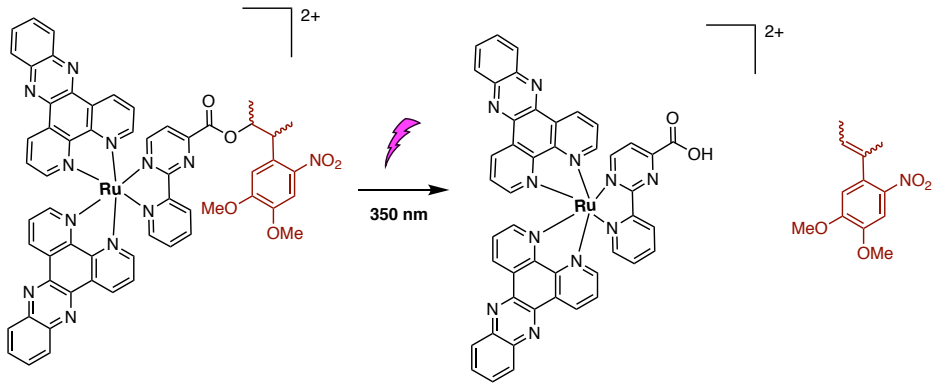

Scheme 11 Example of a caged ruthenium(II) complex.

Coumarins have also been used in various caged compounds. Okamoto and collaborators have described a new RNA-caged system that uses 6-bromo-4-diazomethyl-7-hydroxycoumarin. This coumarin derivative forms a covalent bond with the phosphate moiety of the sugar-phosphate backbone of RNA. The resulting caged RNA undergoes uncaging when exposed to longer UV light (350-365 nm) (**Scheme 12**).[142]

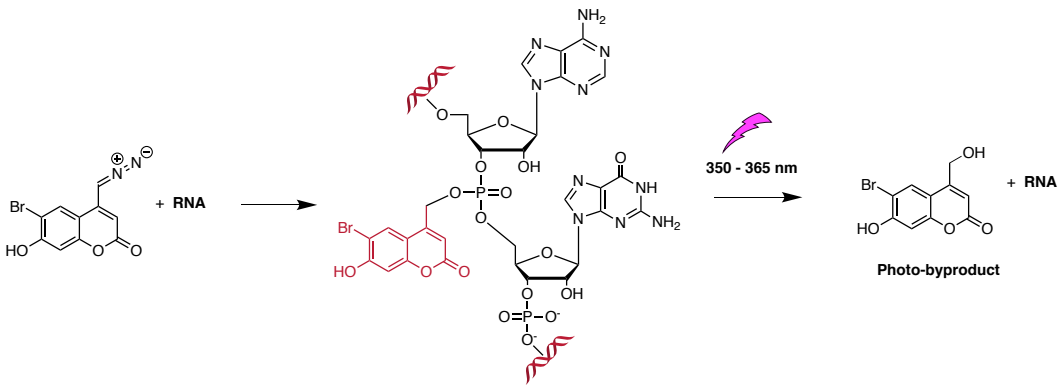

Scheme 12 Irradiation with UV light initiates a photosolvolysis reaction that releases the uncaged mRNA.

BODIPY derivatives have also been explored recently as caging groups removable with visible light.[143-145] Urano and collaborators have developed a BODIPY analog for the protection of phenol, that has been applied to the synthesis of a BODIPY-caged histamine neurotransmitter, which can be photoactivated with green light **(Scheme 13)**.[145]

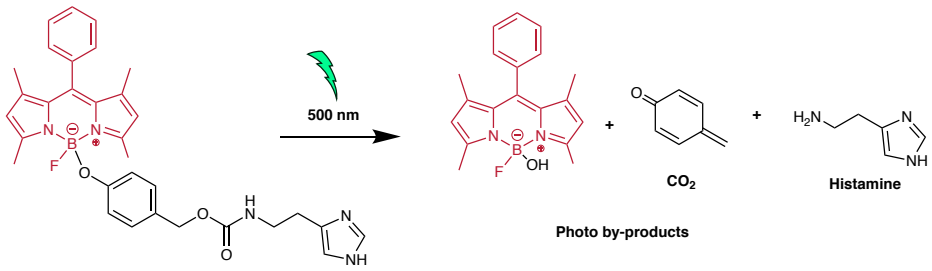

Scheme 13 Uncaging of a BODIPY caged-Histamine derivative with green light.

Finally, Schnermann and collaborators are currently working on the development of caging groups based on the heptamethine cyanine scaffold that can be removed with NIR light.[146-148] Mechanistically, photo-cleavage from the cyanine scaffold occurs through two discrete stages: regioselective photoxidative C-C cleavage (i) followed by intramolecular cyclization (ii) to obtain the uncaged compound (**Scheme 14**).[149,150]

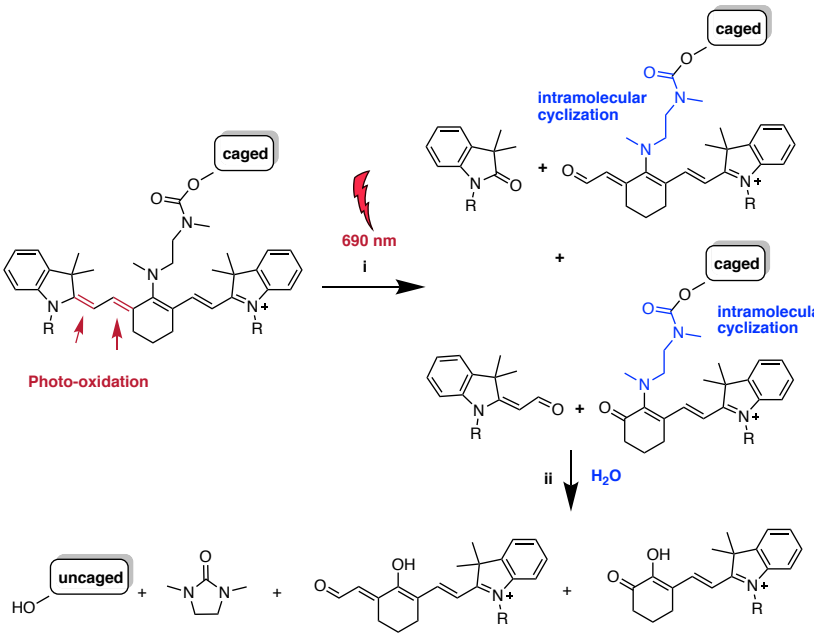

Scheme 14 Uncaging reaction sequence of C4'-dialkylamine-substituted heptamethine cyanines.

3.2.3. Coumarin-based caging groups

The use of coumarins as PPGs has received widespread attention in recent years. Coumarin skeleton offers certain advantages, such as large molar absorption coefficients, high biocompatibility and fast release rates. In addition, coumarin-based caging groups are easily synthesized from commercial precursors and can be attached to the molecule to be caged through different types of bonds, such as ester, carbamate, carbonate and phosphate. Coumarin-caged compounds can be easily obtained from (coumarin-4-yl)methanol or (coumarin-4-yl)bromide precursors (**Figure 43**).

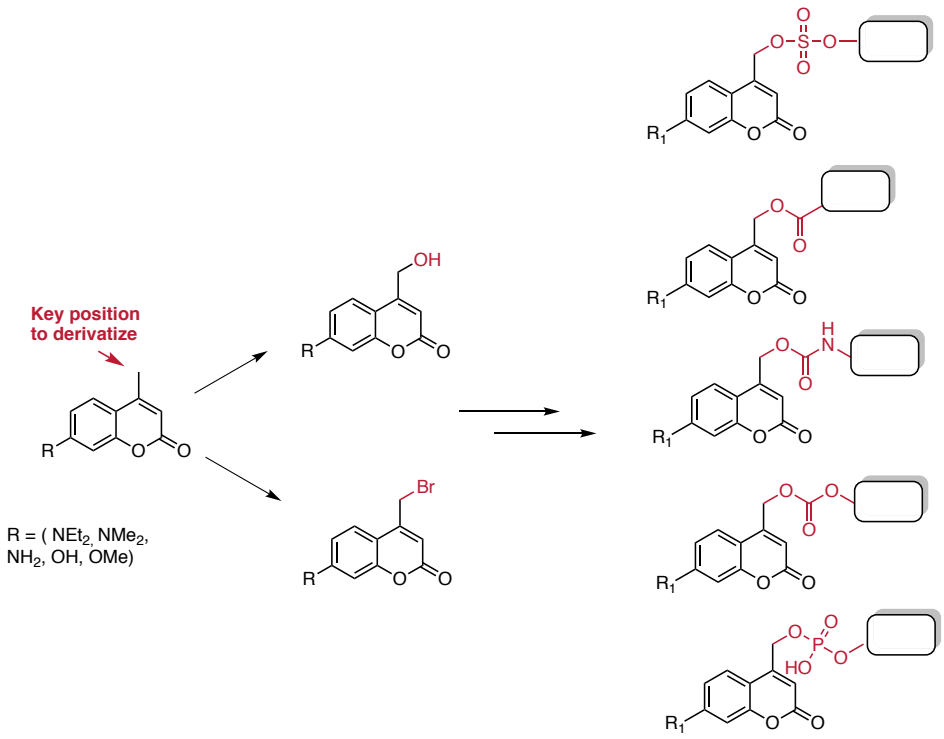

Figure 43 Overview of the different chemical functionalities that can be used to cage a compound with a coumarin derivative.

The mechanism of photorelease of coumarin-4-ylmethyl caged compounds is based on a simple S_N1 reaction. As shown on **Scheme 15**, two processes may occur after initial light absorption: i) relaxation to the lowest excited singlet state followed by heterolysis of the C–caged compound bond, or ii) return to the initial compound by fluorescence or non-radiative deactivation emission. After heterolysis, a tight ion pair ((coumarin-4-yl)methyl cation and leaving group conjugate base) is formed. This key intermediate is then separated and trapped by the polar solvent to give a coumarin by-product and the uncaged compound. The stabilization of the carbocation has been described as a way to avoid recombination.[151]

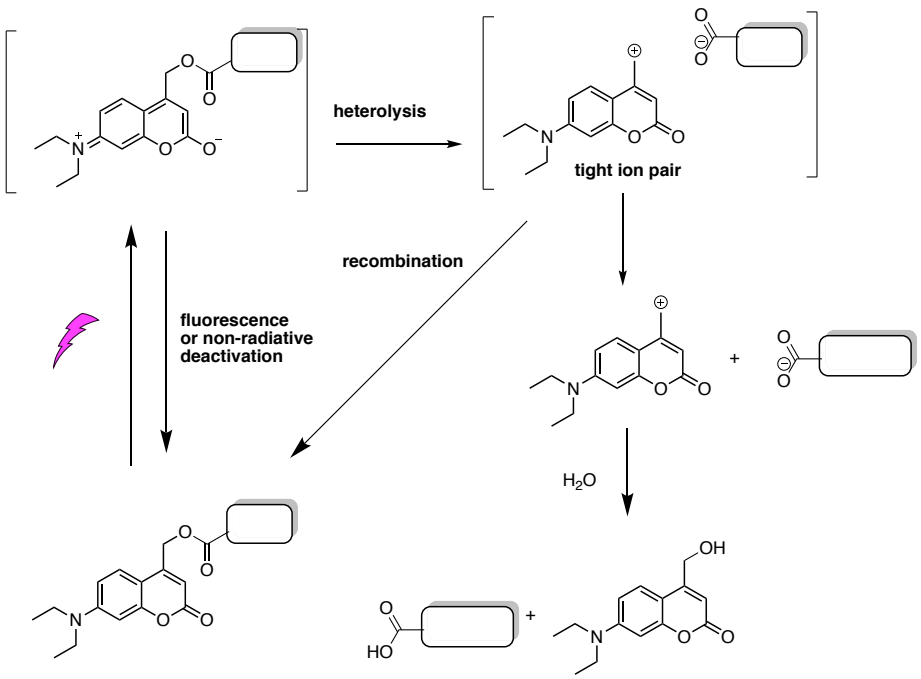

Scheme 15 General mechanism for the photocleavage of (coumarin-4-yl)methyl esters.

Poor leaving groups such as alcohols, phenols, and thiols render (coumarin-4-yl)methyl derivatives resistant to heterolysis. Such groups can be more efficiently released when caged through a carbonate or thiocarbonate linkage. The initially liberated carbonic or thiocarbonic acid is unstable and undergoes decarboxylation to give the free alcohol or thiol. The rates of these decarboxylation reactions are usually quite slow, and subject to both acid and base catalysis. Photorelease of amines from coumarin-carbamates proceeds at slower rates. As in the case of carbonates, the rate-limiting step is decarboxylation of the released carbamate anion, which is more strongly dependent on the pH and on the nature of the released amine.[152]

3.2.4. Overview of coumarin-based caging groups' applications

In this section, we will introduce some examples of coumarin-caged molecules (small organic drugs, peptides, proteins, oligonucleotides), making emphasis on the wavelength of irradiation necessary for triggering uncaging. As shown in **Figure 44**, small structural changes in the coumarin skeleton can lead to significant differences in the absorption maximum (300 – 550 nm). Indeed, the introduction of electron-donating groups (EDG) at the 7-position in combination with the carbonyl or thiocarbonyl group, causes a significant red-shift in absorption. Conversely, changing from the most widely used 7-*N,N*-diethylaminocoumarin towards a slightly less electron-donating 7-di(carboxy-methyl)amino group led to a blue-shift.

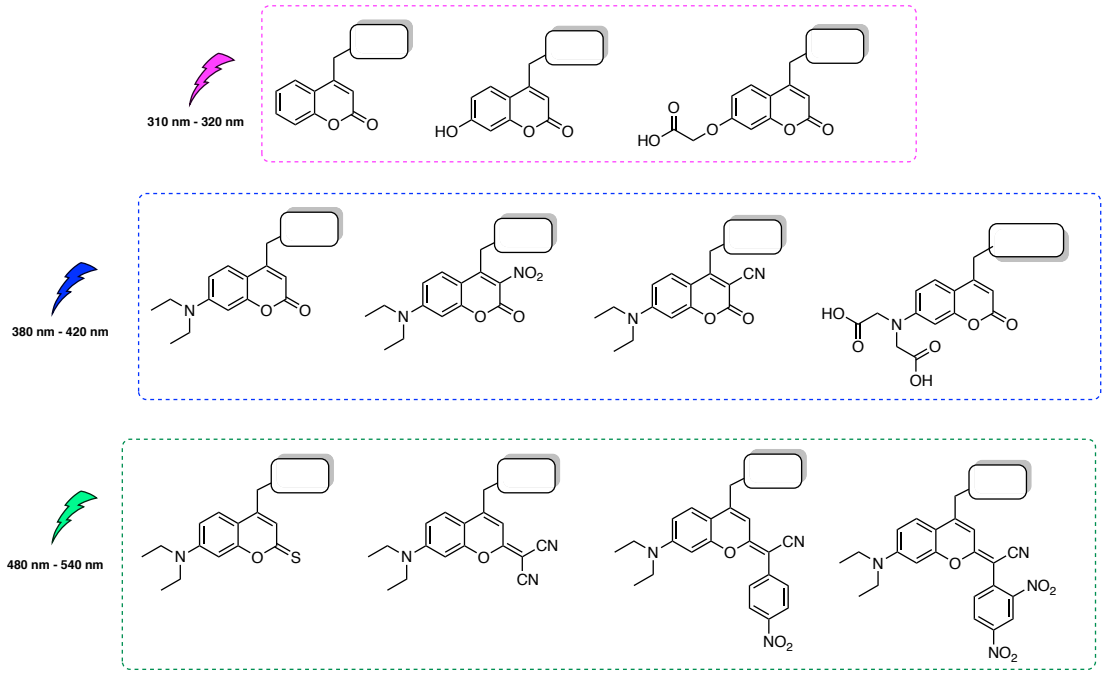

Figure 44 Examples of coumarin-based PPGs classified according to their maximum absorption.

Ellis-Davis and co-workers have studied the effect of introducing several modifications at the position 3 of the coumarin skeleton (cyano, nitro and 4-cyano-phenyl (**Figure 45, A**). In this context, they have incorporated a methylvinylacrylate group and demonstrated that it can be applied to photorelease an intracellular second messenger in living cells, cyclic-AMP (cAMP), with visible light (473 nm) (**Figure 45, B**).[154]

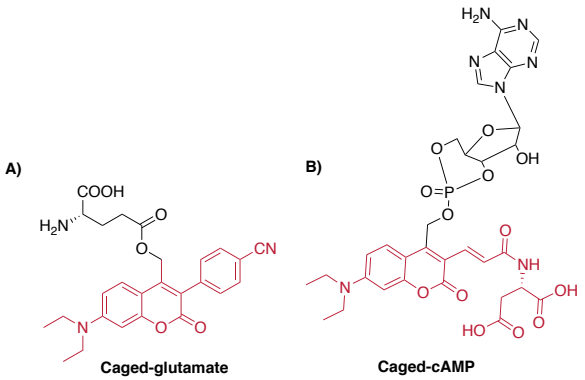

Figure 45 Examples of caged glutamate and cAMP with coumarins modified at position 3.

Similary, they have synthesized caged neurotransmitters that efficiently release γ-aminobutyric acid (GABA) by using one-photon excitation and two-photon excitation.[155,156] The advantages of two-photon excitation are: i) the reduced scattering of the near-IR photons in turbid biological tissues gives a two- to three-fold increase in depth compared with near-UV excitation, and ii) two-photon excitation gives better definition of the focal spot (**Figure 46**).[156-158]

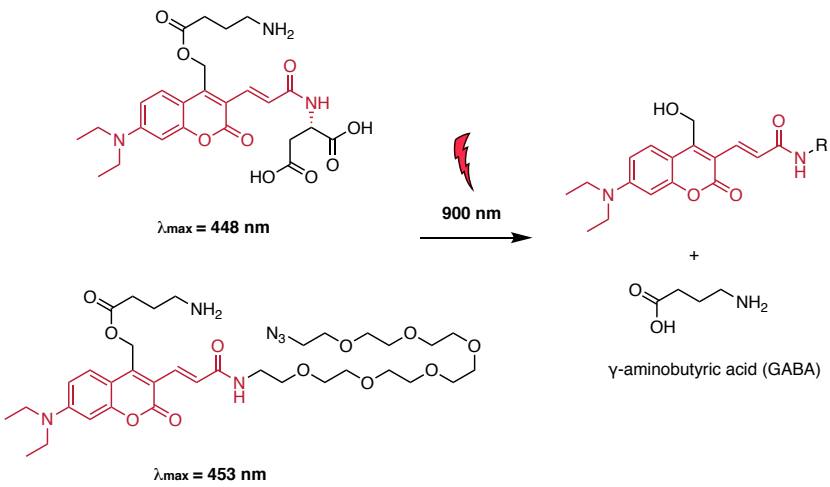

Figure 46 Examples of coumarin-caged GABA under two-photon excitation

Coumarins have also been used to cage amino acids and nucleosides with the aim of synthesizing caged peptides and oligonucleotides, respectively. Del Campo and co-workers have improved the hydrolytic stability of the protected ester bond of coumarin-caged Asp derivatives in basic conditions used in solid-phase peptide synthesis (SPPS) while retaining the good photochemical properties of the PPG.[159] Caged oligonucleotides have already been applied to photoregulate nucleic acid folding, transcription, siRNA function, aptamer function, or DNA nanoarchitecture assembly. Among the large number of examples described in the literature, Heckel and collaborators have caged with coumarin different nucleobases, [160,161] such as Thymine and Guanine, and obtained very relevant results in the uncaging experiments (**Figure 47**).

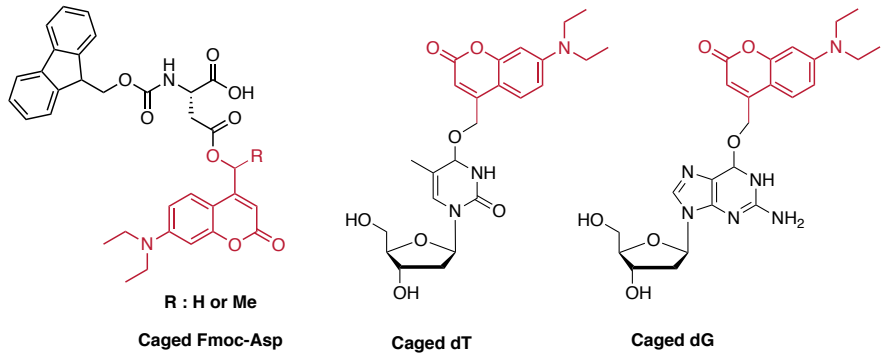

Figure 47 Examples of caged amino acids and nucleosides.

Owing to the potential applications of coumarin scaffolds as caging groups, we can find in the literature several recent examples of the use of light to control the activity of different drugs: Paclitaxel,[162] Progesterone,[163] antibiotics such as benzylpenicillin and fluoroquinolone,[164] and antivirals such as ritonavir[165] (**Figure 48**).

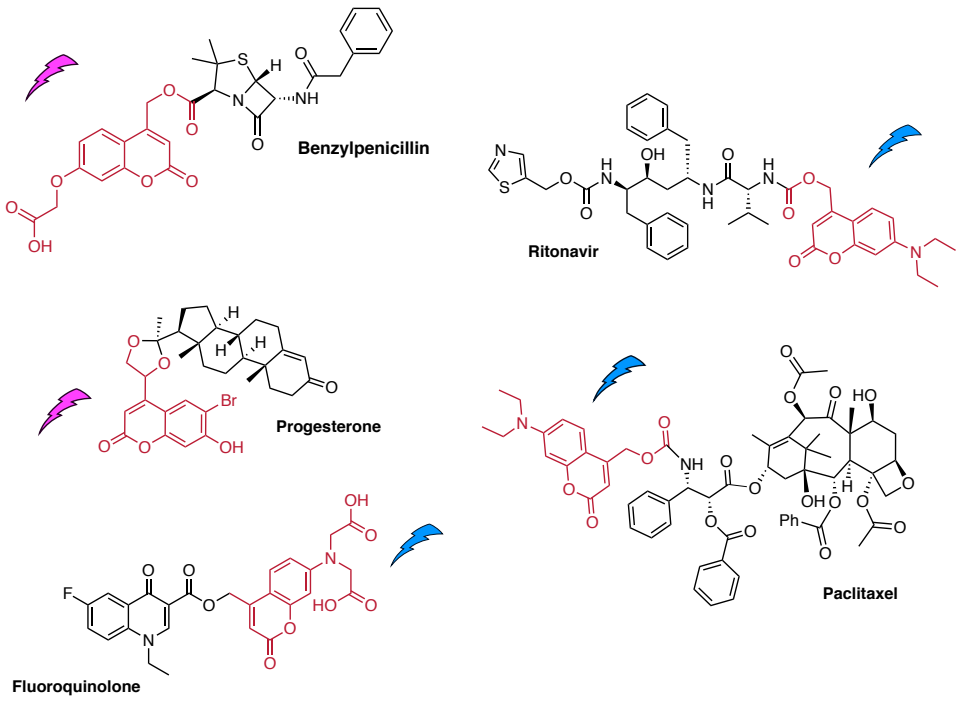

Figure 48 Examples of drugs caged with conventional coumarins.

As previously introduced in section 3.1.3, the replacement of *N,N*-dialkylamino groups with azetidine has been used to increase the fluorescence quantum yield (ϕ) in water of several conventional fluorophores, including the coumarin scaffold. Very recently, Rivera-Fuentes and co-workers have demonstrated that azetidinyl substitution can also be exploited to modulate photochemical processes in coumarin-based caging groups.[122] Indeed, they have prepared and measured the photorelease quantum yield of a series of 7-azetidinyl-4-methyl coumarin esters (**Figure 49, B**) and compared with the corresponding 7-*N,N*-diethylamino derivatives (**Figure 49, A**). Very interestingly, the efficiency of the photorelease reactions of azetidinyl-substituted compounds was higher than that of the corresponding diethylamino coumarins.[122]

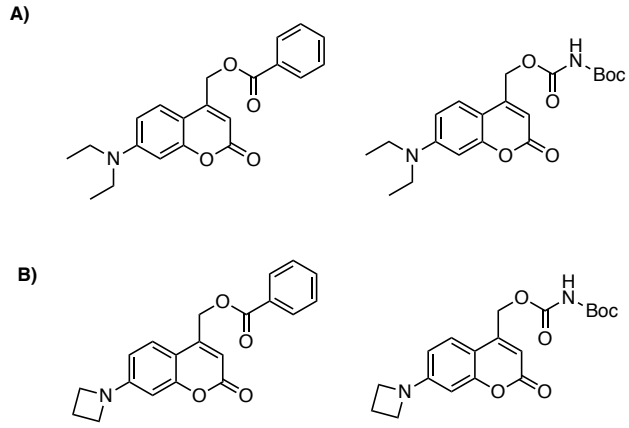

Figure 49 Structures of 7- diethylaminocoumarin and 7-azetidinylcoumarin-caged compounds studied by Rivera-Fuentes and collaborators.[112]

On the basis of the antecedents explained in section 3.1.3 regarding the introduction of EWGs at the coumarin skeleton, the same strategy has been used for designing new coumarin-based PPG with red-shifted absorption.[123-125] In addition, Jullien and collaborators have modified the position 2 of the coumarin skeleton and showed that thiocoumarin (**Figure 50, A**) and dicyanomethylenecoumarin (**Figure 50, B)** can be uncaged with green light.[123]

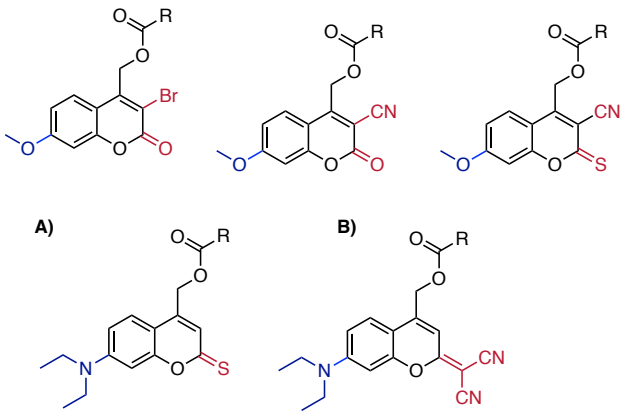

Figure 50 Examples of coumarin-based caging groups described by Jullien and collaborators.[123]

Jullien and collaborators have evaluated a substrate (Ind) acting as an inducer for controlling the activity of target proteins fused to the extensively used modified estrogen receptor ligand-binding domain (ERT2) by using a diethylamino-thiocoumarinylmethyl PPG (**Figure 51, A**).[124] On the other hand, Chen and collaborators have achieved the first inactivation of an organism gene function using a dicyanomethylenecoumarin derivative. (**Figure 51,B**).[166]

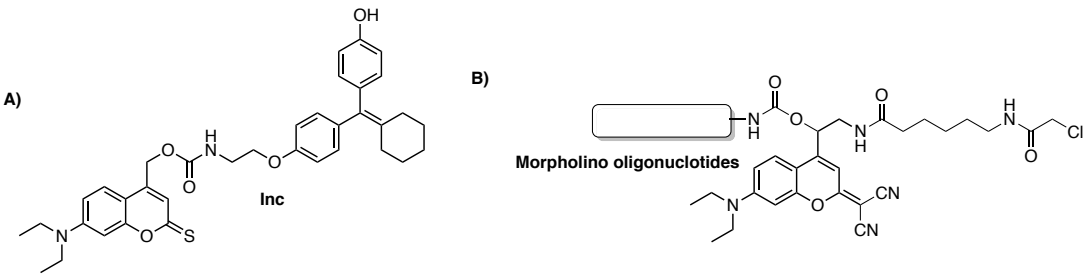

Figure 51 Two examples of caged-biomolecules with non-conventional coumarins.

Finally, our group has recently described the design of novel photocleavable protecting groups based on replacing one cyano group in the dicyanomethylene coumarin with a phenyl ring containing nitro groups at *ortho* and *para* positions. As shown in **Figure 52**, benzoic acid was selected as a model compound to be caged with nitro-, dinitro-, and trinitro- containing coumarinylmethyl derivatives through the formation of an ester bond.[125]

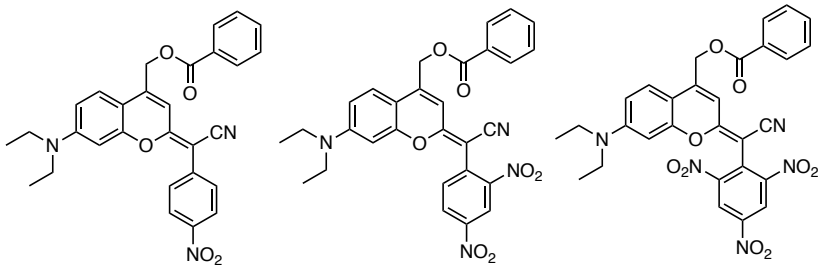

Figure 52 Examples of novel coumarin-based PPGs described by Marchán and collaborators.[125]

4. Objectives

The overall goal of this Thesis was to develop novel chemical tools for the visualization and treatment of cancer by combining the outstanding properties of light with ligand-targeted delivery strategies. On the one hand, light can be used to control, with high spatiotemporal precision, the activation of a molecule (either the release of cytotoxic species from an inactive pro-drug or the removal of a photocleavable protecting group from a key functionality), as well as to visualize biological events *in vivo* by using suitable fluorophores. On the other hand, the conjugation of photoactivatable cytotoxic drugs and/or fluorescent probes to targeting ligands can be used to develop novel highly selective anticancer drugs and imaging agents.

Specifically, we proposed the following three main goals:

1.- Conjugation of a photoactivatable Pt(IV) anticancer pro-drug to targeting ligands

Owing to the potential of photoactivatable Pt(IV) complexes as an alternative to current cisplatin-based anticancer drugs, one of the main objectives of this Thesis was to explore the conjugation of *trans,trans,trans*-$[Pt(N_3)_2(OH)_2(py)_2]$ to targeting ligands whose receptors are overexpressed on tumor cells, with the aim of developing novel anticancer agents with dual selectivity. This main goal can be divided into the following four specific objectives:

1.1. To conjugate a suitable Pt(IV) complex derivative to c(RGDfK), a cyclic RGD-containing peptide that is selectively recognized by $\alpha_V\beta_3$ and $\alpha_V\beta_5$ integrins.
1.2. To conjugate the Pt(IV) complex to a folic acid derivative for targeting folate receptor.
1.3. To study the photoactivation of the Pt(IV)-peptide/folate conjugates under visible light irradiation.
1.4. To investigate the biological properties of the Pt(IV)-c(RGDfK) conjugate (phototoxicity and cellular uptake).

The results related with the Pt(IV)-peptide conjugate project (synthesis, photoactivation and biological evaluation) are discussed in Chapter I of this Thesis (publication A: *Chem. Commun*. **2015**, *51*, 9169-9172). The synthesis of the Pt(IV)-folate conjugate and the results from the photoactivation studies are presented in the summaries' section (12.1.3).

2.- Expanding the scope of applications of dicyanocoumarin-based caging groups: from simple caged models to photocontrolled targeted drug delivery strategies

The approach of using photocleavable protecting groups to regulate the activity of a given molecule has found widespread applications when caging biologically-relevant compounds, from small organic drugs and metal complexes to large biomolecules such as peptides, proteins and oligonucleotides. In such a context, the second main goal of the Thesis was related with dicyanocoumarins, specifically with exploring their efficiency as caging groups and their applicability to the synthesis of caged peptides. These two goals were divided into the following seven specific objectives:

2.1. To design and synthesize a series of 7-*N,N*-diethylamino-dicyanocoumarinylmethyl (DEAdcCM) and 7-*N,N*-diethylamino-dicyanocoumarinylethyl (DEAdcCE) caged model compounds.

2.2. To study the photophysical and photochemical properties of DEAdcCM- and DEAdcCE-caged model compounds.

2.3. To perform sequential uncaging experiments involving dicyanocoumarin-caged compounds.

2.4. To synthesize DEAdcCM- and DEAdcCE-caged aspartic acid monomers suitable for Fmoc-*t*Bu SPPS.

2.5. To study the photophysical and photochemical properties of DEAdcCM- and DEAdcCE-caged aspartic acid monomers.

2.6. To synthesize a dicyanocoumarin-caged cyclic RGD peptide and its conjugate to ruthenocene.
2.7. To study the photolysis of the dicyanocoumarin-caged peptide and its ruthenocenoyl conjugate.

The results related with the synthesis, characterization and photolysis studies of dicyanocoumarin-caged model compounds are presented in publication B in Chapter II (*ChemistryOpen*, **2017**, *6*, 375-384). The work concerning the synthesis and photoactivation of dicyanocoumarin-caged RGD peptides and the ruthenocenoyl conjugate can be found on the publication C (*J. Org. Chem.* **2016**, *81*, 11556-11564).

3. Development of novel coumarin-based fluorophores with far-red and near-infrared emission useful for cell imaging applications

The need for understanding essential recognition events in Chemical Biology has directed considerable efforts in recent years towards the development of novel fluorescent dyes based on small organic molecules. In addition, owing to their potential applications in medical diagnoses and in fluorescence-guided surgery, the availability of ligand-targeted fluorescent probes operating in the far-red and near-infrared region is a priority challenge for combating cancer disease. Hence, the third main goal of this Thesis was to red-shift absorption and emission maxima of the conventional coumarin scaffold, while keeping a low molecular weight, and to explore its conjugation to targeting ligands based on octreotide, a FDA-approved synthetic cyclooctapeptide with high affinity and selectivity for somatostatin subtype-2 receptor ($SSTR_2$). This general goal can be divided into the following six specific objectives:

3.1. To design, synthesize and characterize a new family of coumarin-based scaffolds with an extended π-conjugation system through position 2.
3.2. To synthesize novel push-pull fluorophores (COUPYs) through *N*-alkylation of the pyridine heterocycle incorporated at position 2 of the coumarin scaffold.

3.3. To study the spectroscopic and photophysical properties of COUPY fluorophores in several solvents of different polarities and viscosities.
3.4. To investigate the bioimaging applications of COUPY dyes in living HeLa cells.
3.5. To synthesize conjugatable derivatives of COUPY dyes and to label octreotide with them on a solid-phase.
3.6. To investigate the bioimaging applications of COUPY-octreotide conjugate on $SSTR_2$ overexpressing cells.

The design, synthesis and characterization of COUPY fluorophores together with cell imaging studies in living cells are described in publication D (*J. Org. Chem.* **2018**, *83*, 1185-1195) in Chapter III. The synthesis, characterization and biological evaluation of COUPY-octreotide conjugates are discussed on the publication E (Manuscript submitted for publication) in Chapter III.

5. References

1. Siegel, R. L., Miller, K. D. & Jemal, A. Cancer statistics. *CA Cancer J. Clin.* **66,** 7–30 (2016).
2. Kratz, F., Müller, I. A., Ryppa, C. & Warnecke, A. Prodrug strategies in anticancer chemotherapy. *ChemMedChem* **3,** 20–53 (2008).
3. Allen, T. M. Ligand-targeted therapeutics in anticancer therapy. *Nat. Rev. Cancer* **2,** 750–763 (2002).
4. Temming, K., Schiffelers, R. M., Molema, G. & Kok, R. J. RGD-based strategies for selective delivery of therapeutics and imaging agents to the tumour vasculature. *Drug Resist. Updates.* **8,** 381–402 (2005).
5. Teng, L., Xie, J., Teng, L. & Lee, R. J. Clinical translation of folate receptor-targeted therapeutics. *Expert Opin. Drug Delivery* **9,** 901–908 (2012).
6. Vahrmeijer, A. L., Hutteman, M., van der Vorst, J. R., van de Velde, C. J. H. & Frangioni, J. V. Image-guided cancer surgery using near-infrared fluorescence. *Nat. Rev. Clin. Oncol.* **10,** 507–518 (2013).
7. Zhang, R. R., Schroeder, A.B., Grudzinski, J. J., Rosenthal, E. L., Warram, J.M., Pinchuk, A. N., Eliceiri, K. W., Kuo, J. S. & Weichert, J. P. Beyond the margins: Real-time detection of cancer using targeted fluorophores. *Nat. Rev. Clin. Oncol.* **14,** 347–364 (2017).
8. Nguyen, Q. T. & Tsien, R. Y. Fluorescence-guided surgery with live molecular navigation-a new cutting edge. *Nat. Rev. Cancer* **13,** 653–662 (2013).
9. Kelland, L. The resurgence of platinum-based cancer chemotherapy. *Nat. Rev. Cancer* **7,** 573–584 (2007).
10. Johnstone, T. C., Suntharalingam, K. & Lippard, S. J. The next generation of platinum drugs: targeted Pt(II) agents, nanoparticle delivery, and Pt(IV) prodrugs. *Chem. Rev.* **116,** 3436–3486 (2016).
11. Bruno, P. M., Liu, Y.,Park, G.*,* Murai, J.*,* Koch, C.*,* Eisen, T. J.*,* Pritchard, J. R.*,* Pommier, Y.*,* Lippard, S.J. & Hemann, M. T. A subset of platinum-containing chemotherapeutic agents kills cells by inducing ribosome biogenesis stress. *Nat. Med.* **23,** 461–471 (2017).
12. Johnstone, T. C., Suntharalingam, K. & Lippard, S. J. Third row transition metals for the treatment of cancer. *Philos. Trans. R. Soc.* **373,** 2017-2049 (2015).
13. Johnstone, T. C., Wilson, J. J. & Lippard, S. J. Monofunctional and higher-valent platinum anticancer agents. *Inorg. Chem.* **52,** 12234–12249 (2013).
14. Cheff, D. M. & Hall, M. D. A Drug of Such Damned Nature. Challenges and opportunities in translational platinum drug research. *J. Med. Chem.* **60,** 4517–4532 (2017).
15. Wachter, E., Zamora, A., Heidary, D. K., Ruiz, J. & Glazer, E. C. Geometry matters: inverse cytotoxic relationship for cis/trans-Ru(II) polypyridyl complexes from cis/trans-$[PtCl_2(NH_3)_2]$. *Chem. Commun.* **52,** 10121–10124 (2016).
16. Kratochwil, N. A., Zabel, M., Range, K.-J. J. & Bednarski, P. J. Synthesis and X-ray crystal structure of *trans,cis-[*$Pt(OAc)_2I_2(en)$]: a novel type of cisplatin analog that can be photolyzed by visible light to DNA-binding and cytotoxic species in vitro. *J. Med. Chem.* **39,** 2499–2507 (1996).

17. Wang, D. & Lippard, S. J. Cellular processing of platinum anticancer drugs. *Nat. Rev. Drug Discov.* **4,** 307–320 (2005).

18. Bhargava, A. & Vaishampayan, U. N. Satraplatin: leading the new generation of oral platinum agents. *Expert Opin. Invest. Drugs* **18,** 1787–1797 (2009).

19. Kelland, L. R. An update on satraplatin: the first orally available platinum anticancer drug. *Expert Opin. Invest. Drugs* **9,** 1373–1382 (2000).

20. Gandioso, A., Shaili, E., Massaguer, A., Artigas, G., González-Cantó, A., Woods, J. A & Marchán, V. An integrin-targeted photoactivatable Pt(IV) complex as a selective anticancer pro-drug: synthesis and photoactivation studies. *Chem. Commun.* **51,** 9169–9172 (2015).

21. Smith, N. A. & Sadler, P. J. Photoactivatable metal complexes: from theory to applications in biotechnology and medicine. *Philos. Trans. R. Soc.* **371,** 1995–2008 (2013).

22. Crespy, D., Landfester, K., Schubert, U. S. & Schiller, A. Potential photoactivated metallopharmaceuticals: from active molecules to supported drugs. *Chem. Commun.* **46,** 6651-6662 (2010).

23. Zhao, Y., Woods, J. A., Farrer, N. J., Robinson, K. S., Pracharova, J., Kasparkova, J., Novakova, O., Li, H., Salassa, L., Pizarro, A. M., Clarkson, G. J., Song, L., Brabec, V. & Sadler, P. J. Diazido mixed-amine platinum(IV) anticancer complexes activatable by visible-light form novel DNA adducts. *Chem. - Eur. J.* **19,** 9578–9591 (2013).

24. Farrer, N. J., Woods, J. A., Salassa, L., Zhao, Y., Robinson, K. S., Clarkson, G., MacKay, F. S. & Sadler, P. J. A potent trans-diimine platinum anticancer complex photoactivated by visible light. *Angew. Chem. Int. Ed.* **49,** 8905–8908 (2010).

25. Magennis, S. W., Habtemariam, A., Novakova, O., Henry, J. B., Meier, S., Parsons, S., Oswald, I. D.H., Brabec, V. & Sadler, Peter J. Dual triggering of DNA binding and fluorescence via photoactivation of a dinuclear ruthenium(II) arene complex. *Inorg. Chem.* **46,** 5059–5068 (2007).

26. Barragán, F., López-Senín, P., Salassa, L., Betanzos-Lara, S., Habtemariam, A., Moreno, V.,Sadler, P.J. & Marchán, V. Photocontrolled DNA binding of a receptor-targeted organometallic ruthenium(II) complex. *J. Am. Chem. Soc.* **133,** 14098–14108 (2011).

27. Göttle, A. J., Alary, F., Boggio-Pasqua, M.l, Dixon, I. M., Heully, J. L., Bahreman, A., Askes, S. H.C. & Bonnet, S. Pivotal role of a pentacoordinate 3MC state on the photocleavage efficiency of thioether ligand in ruthenium(II) complexes: A theoretical mechanistic study. *Inorg. Chem.* **55,** 4448–4456 (2016).

28. Van Rixel, V. H. S., Siewert, B., Hopkins, S. L., Askes, S. H. C., Busemann, A., Siegler, M. A. & Bonnet, S. Green light-induced apoptosis in cancer cells by a tetrapyridyl ruthenium prodrug offering two *trans* coordination sites. *Chem. Sci.* **7,** 4922–4929 (2016).

29. Leonidova, A., Pierroz, V., Rubbiani, R., Heier, J., Ferrari, S. & Gasser, G. Towards cancer cell-specific phototoxic organometallic rhenium(I) complexes. *Dalton Trans.* **43,** 4287–4294 (2014).

30. Lee, L. C., Leung, K.. & Lo, K.W. Recent development of luminescent rhenium(I) tricarbonyl polypyridine complexes as cellular imaging reagents, anticancer drugs, and antibacterial agents. *Dalton Trans.* 16357–16380 (2017).

31. Nam, J. S., Kang, M. G., Kang, J., Park, S. Y., Lee, S. C., Kim, H.T., Seo, J. K., Kwon, O.H., Lim, M. H., Rhee, H.W. & Kwon, T. H. Endoplasmic reticulum-localized iridium(III) complexes as efficient photodynamic therapy agents via protein modifications. *J. Am. Chem. Soc.* **138,** 10968–10977 (2016).

32. Mari, C., Pierroz, V., Ferrari, S. & Gasser, G. Combination of Ru(II) complexes and light: new frontiers in cancer therapy. *Chem. Sci.* **6,** 2660–2686 (2015).

33. Tian, X., Zhu, Y., Zhang, M., Luo, L.,Wu, J., Zhou, H., Guan, L., Battaglia, G. & Tian, Y. Localization matters: a nuclear targeting two-photon absorption iridium complex in photodynamic therapy. *Chem. Commun.* **53,** 3303–3306 (2017).

34. Dickerson, M., Sun, Y., Howerton, B. & Glazer, E. C. Modifying charge and hydrophilicity of simple Ru(II) polypyridyl complexes radically alters biological activities: Old complexes, surprising new tricks. *Inorg. Chem.* **53,** 10370–10377 (2014).

35. Fan, W., Huang, P. & Chen, X. Overcoming the Achilles' heel of photodynamic therapy. *Chem. Soc. Rev.* **45,** 6488–6519 (2016).

36. Azzouzi, A. R., Barret, E., Moore, C. M., Villers, A., Allen, C., Scherz, A., Muir, G., De Wildt, M., Barber, N. J.,Lebdai, S. & Emberton, M. TOOKAD®Soluble vascular-targeted photodynamic (VTP) therapy: Determination of optimal treatment conditions and assessment of effects in patients with localised prostate cancer. *BJU Int.* **112,** 766–774 (2013).

37. Pracharova, J., Vigueras, G., Novohradsky, V., Cutillas, N., Janiak, C., Kostrhunova, H., Kasparkova, J., Ruiz, J., & Brabec, V. Exploring the effect of polypyridyl ligands on the anticancer activity of phosphorescent iridium(III) complexes: from proteosynthesis inhibitors to photodynamic therapy Agents. *Chem. - Eur. J.* **24,** 4607–4619 (2018).

38. You, Y., Cho, E. J., Kwon, H., Hwang, J. & Lee, S. E. A singlet oxygen photosensitizer enables photoluminescent monitoring of singlet oxygen doses. *Chem. Commun.* **52,** 780–783 (2016).

39. Kratochwil, N. A., Parkinson, J. A., Bednarski, P. J. & Sadler, P. J. Nucleotide platination induced by visible light. *Angew. Chem. Int. Ed.* **38,** 1460–1463 (1999).

40. Pizarro, A. M., McQuitty, R. J., Mackay, F. S., Zhao, Y., Woods, J.A. & Sadler, P. J. Cellular accumulation, lipophilicity and photocytotoxicity of diazido platinum(IV) Anticancer Complexes. *ChemMedChem* **9,** 1169–1175 (2014).

41. Pracharova, J., Zerzankova, L., Stepankova, J., Novakova, O., Farrer, N. J., Sadler, P. J., Brabec, V., & Kasparkova, J. Interactions of DNA with a new platinum(IV) azide dipyridine complex activated by UVA and visible light: Relationship to toxicity in tumor cells. *Chem. Res. Toxicol.* **25,** 1099–1111 (2012).

42. Butler, J. S., Woods, J. A., Farrer, N. J., Newton, M. E. & Sadler, P. J. Tryptophan switch for a photoactivated platinum anticancer complex. *J. Am. Chem. Soc.* **134,** 16508–16511 (2012).

43. Perfahl, S., Natile, M. M., Mohamad, H. S., Helm, C. A., Schulzke, C., Natile, G. & Bednarski, P. J. Photoactivation of diiodido-Pt(IV) complexes coupled to upconverting nanoparticles. *Mol. Pharm.* **13,** 2346–2362 (2016).

44. Ruggiero, E., Hernández-Gil, J., Mareque-Rivas, J. C. & Salassa, L. Near infrared activation of an anticancer Pt(IV) complex by Tm-doped upconversion nanoparticles. *Chem. Commun.* **51,** 2091–2094 (2015).

45. Castro, S. A. Ruggiero, E., Ruiz-De-Angulo, A., Rezabal, E., Mareque-Rivas, J. C., Lopez, X., López, Gallego, F. & Salassa, L. Riboflavin as a bioorthogonal photocatalyst for the activation of a Pt (IV) prodrug. *Chem. Sci.* **8,** 4619–4625 (2017).

46. Castro, S. A., Cortajarena, A. L., Fernando, L. & Salassa, L. Bioorthogonal Catalytic Activation of Platinum and Ruthenium Anticancer Complexes by FAD and Flavoproteins. *Angew. Chem. Int. Ed.* **57,** 3143–3147 (2018).

47. Wang, X. & Guo, Z. Targeting and delivery of platinum-based anticancer drugs. *Chem. Soc. Rev.* **42,** 202–224 (2013).

48. Srinivasarao, M., Galliford, C. V. & Low, P. S. Principles in the design of ligand-targeted cancer therapeutics and imaging agents. *Nat. Rev. Drug Discov.* **14,** 203–219 (2015).

49. Danhier, F., Breton, A. Le & Préat, V. RGD-based strategies to target αvβ3 integrin in cancer therapy and diagnosis. *Mol. Pharm.* **9,** 2961–2973 (2012).

50. Massaguer, A. , González-Cantó, A., Escribano, E., Barrabés, S., Artigas, G., Moreno, V. & Marchán, V. Integrin-targeted delivery into cancer cells of a Pt(IV) pro-drug through conjugation to RGD-containing peptides. *Dalton Trans.* **44,** 202–212 (2015).

51. Arosio, D. & Casagrande, C. Advancement in integrin facilitated drug delivery. *Adv. Drug Delivery Rev.* **97,** 111–143 (2016).

52. Alvarez-Lorenzo, C. & Concheiro, A. Smart drug delivery systems: from fundamentals to the clinic. *Chem. Commun.* **50,** 7743–7765 (2014).

53. Goodman, S. L., Hölzemann, G., Sulyok, G. A. G. & Kessler, H. Nanomolar small molecule inhibitors for αvβ6, αvβ5, and αvβ3 Integrins. *J. Med. Chem.* **45,** 1045–1051 (2002).

54. Pierschbacher, M. D. & Ruoslahti, E. Cell attachment activity of fibronectin can be duplicated by small synthetic fragments of the molecule. *Nature* **309,** 30-33 (1984).

55. Grant, D. S., Tashiro, K., Segui-Real, B., Yamada, Y., Martin, G. R. & Kleinman, H. K. Two different laminin domains mediate the differentiation of human endothelial cells into capillary-like structures in vitro. *Cell* **58,** 933–943 (1989).

56. Haubner, R., Schmitt, W., Hölzemann, G., Goodman, S. L., Jonczk, A. & Kessler, H Cyclic RGD peptides containing β-turn mimetics. *J. Am. Chem. Soc.* **118,** 7881–7891 (1996).

57. Arap, W., Pasqualini, R. & Ruoslahti, E. Cancer Treatment by targeted drug delivery to tumor vasculature in a mouse model cancer treatment by targeted drug delivery to tumor vasculature in a mouse model. *Science.* **279,** 377-388 (1998).

58. Burkhart, D. J., Kalet, B. T., Coleman, M. P., Post, G. C. & Koch, T. H. Doxorubicin-formaldehyde conjugates targeting αvβ3 integrin. *Mol. Cancer Ther.* **3,** 1593–1605 (2004).

59. Chen, X., Plasencia, C., Hou, Y. & Neamati, N. Synthesis and biological evaluation of dimeric RGD peptide-paclitaxel conjugate as a model for integrin-targeted drug delivery. *J. Med. Chem.* **48,** 1098–1106 (2005).

60. Dal Pozzo, A. Ni, M. H., Esposito, E., Dallavalle, S., Musso, L., Bargiotti, A., Pisano, C., Vesci, L., Bucci, F., Castorina, M., Foderà, R., Giannini, G., Aulicino, C. & Penco, S. Novel tumor-targeted RGD peptide-camptothecin conjugates: Synthesis and biological evaluation. *Bioorg. Med. Chem.* **18,** 64–72 (2010).

61. Mukhopadhyay, S. Barnés, C. M., Haskel, A., Short, S. M., Barnes, K. R & Lippard, S. J. Conjugated platinum (IV) - peptide complexes for targeting angiogenic tumor vasculature. *Bioconjugate Chem.* **19,** 39–49 (2008)

62. Hahn, E. M. Estrada-Ortiz, N., Han, J., Ferreira, V.F.C., Kapp, T.G., Correia, J. D.G., Casini, A. & Kühn, F. E. Functionalization of ruthenium(II) terpyridine complexes with cyclic RGD peptides to target integrin receptors in cancer Cells. *Eur. J. Inorg. Chem.* **2017,** 1667–1672 (2017).

63. Massaguer, A., González-Cantó, A., Escribano, E., Barrabés, S., Artigas, G., Moreno, V. & Marchán, V. Integrin-targeted delivery into cancer cells of a Pt(IV) pro-drug through conjugation to RGD-containing peptides. *Dalton Trans.* **44,** 202–212 (2015).

64. Murphy, E. A., Majeti, B. K., Barnes, L. A., Makale, M., Weis, S. M., Lutu-Fuga, K., Wrasidlo, W. & Cheresh, D. A. Nanoparticle-mediated drug delivery to tumor vasculature suppresses metastasis. *Proc. Natl. Acad. Sci. U. S. A.* **105,** 9343–9348 (2008).

65. Zhan, C., Gu, B., Xie, C., Li, J., Liu, Y. & Lu, W. Cyclic RGD conjugated poly(ethylene glycol)-co-poly(lactic acid) micelle enhances paclitaxel anti-glioblastoma effect. *J. Controlled Release* **143,** 136–142 (2010).

66. Xu, W. Luo, T., Li, P., Zhou, C., Cui, D., Pang, B., Ren, Q. & Fu, S. RGD-conjugated gold nanorods induce radiosensitization in melanoma cancer cells by downregulating αvβ3 expression. *Int. J. Nanomed.* **7,** 915–924 (2012).

67. Yuan, Y., Kwok, R. T. K., Tang, B. Z. & Liu, B. Targeted theranostic platinum(IV) prodrug with a built-in aggregation-induced emission light-up apoptosis sensor for noninvasive early evaluation of its therapeutic responses in situ. *J. Am. Chem. Soc.* **136,** 2546–2554 (2014).

68. Graf, N., Bielenberg, D. R., Kolishetti, N., Muus, C., Banyard, J., Farokhzad, O. C. & Lippard, S. J. αvβ 3 integrin-targeted PLGA-PEG nanoparticles for enhanced anti-tumor efficacy of a Pt(IV) prodrug. *ACS Nano* **6,** 4530–4539 (2012).

69. Nkepang, G., Bio, M., Rajaputra, P., Awuah, S. G. & You, Y. Folate receptor-mediated enhanced and specific delivery of far-red light-activatable prodrugs of combretastatin A-4 to FR-positive tumor. *Bioconjugate Chem.* **25,** 2175–2188 (2014).

70. Aronov, O., Horowitz, A. T., Gabizon, A. & Gibson, D. Folate-targeted PEG as a potential carrier for carboplatin analogs. Synthesis and in vitro studies. *Bioconjugate Chem.* **14,** 563–574 (2003).

71. Xia, W. & Low, P. S. Folate-targeted therapies for cancer. *J. Med. Chem.* **53,** 6811–6824 (2010).

72. Elnakat, H. & Ratnam, M. Distribution, functionality and gene regulation of folate receptor isoforms: Implications in targeted therapy. *Adv. Drug Delivery Rev.* **56,** 1067–1084 (2004).

73. Leamon, C. P. & Reddy, J. A. Folate-targeted chemotherapy. *Adv. Drug Delivery Rev.* **56,** 1127–1141 (2004).

74. Guaragna, A., Chiaviello, A., Paolella, C., Dalonzo, D., Palumbo, G. & Palumbo, G. Synthesis and evaluation of folate-based chlorambucil delivery systems for tumor-targeted chemotherapy. *Bioconjugate Chem.* **23**, 84-96 (2012).

75. Lee, J. W., Lu, J. Y., Low, P. S. & Fuchs, P. L. Synthesis and evaluation of Taxol-folic acid conjugates as targeted antineoplastics. *Bioorg. Med. Chem.* **10,** 2397–2414 (2002).

76. Reddy, J. A. Westrick, E., Vlahov, I., Howard, S. J., Santhapuram, H. K. & Leamon, C. P. Folate receptor specific anti-tumor activity of folate-mitomycin conjugates. *Cancer Chemother. Pharmacol.* **58,** 229–236 (2006).

77. Dhar, S., Liu, Z., Thomale, J., Dai, H. & Lippard, S. J. Targeted single-wall carbon nanotube-mediated Pt(IV) prodrug delivery using folate as a homing device. *J. Am. Chem. Soc.* **130,** 11467–11476 (2008).

78. Gokhale, M., Thakur, A. & Rinaldi, F. Degradation of BMS-753493, a novel epothilone folate conjugate anticancer agent. *Drug Dev. Ind. Pharm.* **39,** 1315–1327 (2013).

79. Maecke, H. R. & Reubi, J. C. Somatostatin receptors as targets for nuclear medicine Imaging and radionuclide treatment. *J. Nucl. Med.* **52,** 841–844 (2011).

80. Aina, O. H., Liu, R., Sutcliffe, J., Marik, J., Pan, C. & Lam, K.S. From combinatorial chemistry to cancer-targeting. *Mol. Pharm.* **4,** 631–651 (2007).

81. Talme, T., Ivanoff, J., Hägglund, M., Van Neerven, R. J.J., Ivanoff, A. & Sundqvist, K. G. Somatostatin receptor (SSTR) expression and function in normal and leukaemic T-cells. Evidence for selective effects on adhesion to extracellular matrix components via SSTR2 and/or 3. *Clin. Exp. Immunol.* **125,** 71–79 (2001).

82. Brazeau, P., Vale, W., Burgus, R., Ling, N., Butcher, M., Rivier, J. & Guillemin, R. Hypothalamic polypeptide that Inhibits the secretion of immunoreactive pituitary growth hormone. *Science* **179,** 77-79 (1973).

83. Weckbecker, G. Lewis, I., Albert, R., Schmid, H. A., Hoyer, D. & Bruns, C. Opportunities in somatostatin research: biological, chemical and therapeutic aspects. *Nat. Rev. Drug Discovery* **2,** 999–1017 (2003).

84. Froidevaux, S. & Eberle, A. N. Somatostatin analogs and radiopeptides in cancer therapy. *Biopolymers* **66,** 161–183 (2002).

85. Patel, Y. C. Somatostatin and its receptor family. *Front. Neuroendocrinol.* **20,** 157–198 (1999).

86. Lewis, I., Bauer, W., Albert, R., Chandramouli, N., Pless, J., Weckbecker, G. & Bruns, C. A novel somatostatin mimic with broad somatotropin release inhibitory factor receptor binding and superior therapeutic potential. *J. Med. Chem.* **46,** 2334–2344 (2003).

87. Bruns, C., Raulf, F., Hoyer, D., Schloos, J., Lübbert, H. & Weckbecker, G. Binding properties of somatostatin receptor subtypes. *Metab. Clin. Exp.* **45,** 17–20 (1996).

88. Janin, Y. L. Peptides with anticancer use or potential. *Amino Acids* **25,** 1–40 (2003).

89. Stone, W. N., Hofling, C. K. & Winslow, W. W. Drug therapy . *Prog. Neurol. Psychiatry* **23,** 563–581 (1968).

90. Stymiest, J. L., Mitchell, B. F., Wong, S. & Vederas, J. C. Synthesis of biologically active dicarba analogues of the peptide hormone oxytocin using ring-closing metathesis. *Org. Lett.* **5,** 47–49 (2003).

91. Addona, D. D., Carotenuto, A., Novellino, E., Piccand, V., Reubi, J. C., Cianni, A. D., Gori, F., Papini, A. M. & Ginanneschi, M. Novel sst5 selective somatostatin dicarba-analogues: synthesis and conformation - affinity relationships. *J. Med. Chem* **51***,* 512–520 (2008).

92. Whelan, A. N., Elaridi, J., Harte, M., Smith, S. V., Jackson, W. R. & Robinson, A. J. A tandem metathesis-hydrogenation route to dicarba analogues of cystine-containing cyclic peptides. *Tetrahedron Lett.* **45,** 9545–9547 (2004).

93. Adams, D. J., Dewhirst, M.W., Flowers, J. L., Gamcsik, M. P., Colvin, O. M., Manikumar, G., Wani, M. C. & Wall, M. E. Camptothecin analogues with enhanced antitumor activity at acidic pH. *Cancer Chemother. Pharmacol.* **46,** 263–271 (2000).

94. Nagy, A., Szoke, B. & Schally, A. V. Selective coupling of methotrexate to peptide hormone carriers through a gamma-carboxamide linkage of its glutamic acid moiety: benzotriazol-1-yloxytris(dimethylamino)phosphonium hexafluorophosphate activation in salt coupling. *Proc. Natl. Acad. Sci. U. S. A.* **90,** 6373- 6376 (1993).

95. Barragán, F., Carrion-Salip, D., Gómez-Pinto, I., González-Cantó, A., Sadler, P. J., De Llorens, R., Moreno, V., González, C., Massaguer, A. & Marchán, V. Somatostatin subtype-2 receptor-targeted metal-based anticancer complexes. *Bioconjugate Chem.* **23,** 1838–1855 (2012).

96. Barragán, F., Moreno, V. & Marchán, V. Solid-phase synthesis and DNA binding studies of dichloroplatinum(II) conjugates of dicarba analogues of octreotide as new anticancer drugs. *Chem. Commun.* **31***,* 4705–4707 (2009).

97. Novohradsky, V., Zamora, A., Gandioso, A., Brabec, V., Ruiz, J. & Marchán, V. Somatostatin receptor-targeted organometallic iridium(III) complexes as novel theranostic agents. *Chem. Commun.* **53,** 5523–5526 (2017).

98. Spradau, T. W., Edwards, W. B., Anderson, C. J., Welch, M. J. & Katzenellenbogen, J. A. Synthesis and biological evaluation of Tc-99m- cyclopentadienyltricarbonyltechnetium-labeled octreotide. *Nucl. Med. Biol.* **26,** 1–7 (1999).

99. Smith, M. C. & Chen, T. OctreoTher TM: ongoing early clinical development of a somatostatin-receptor-targeted radionuclide antineoplastic therapy. *Digestion* **62,** 69–72 (2000).

100. Eggeling, C. & Heilemann, M. Editorial overview: Molecular imaging. *Curr. Opin. Chem. Biol.* **20,** 5-7 (2014).

101. Shcherbakova, D. M. & Verkhusha, V. V. Chromophore chemistry of fluorescent proteins controlled by light. *Curr. Opin. Chem. Biol.* **20,** 60–68 (2014).

102. Lichtman, J. W. & Conchello, J. A. Fluorescence microscopy. *Nat. Methods* **2,** 910–919 (2005).

103. Hamaguchi, Y. Optical microscopy. *Tanpakushitsu Kakusan Koso.* **42,** 1026–1032 (1997).

104. Sanderson, M. J., Smith, I., Parker, I. & Bootman, M. D. Fluorescence Microscopy. *Cold Spring Harb Protoc.* **2014,** 1-36 (2016).

105. Egner, A. & Hell, S. W. Fluorescence microscopy with super-resolved optical sections. *Trends Cell Biol.* **15,** 207–215 (2005).

106. Blom, H. & Widengren, J. STED microscopy-towards broadened use and scope of applications. *Curr. Opin. Chem. Biol.* **20,** 127–133 (2014).

107. Huang, B., Bates, M. & Zhuang, X. Super-Resolution Fluorescence Microscopy. *Annu. Rev. Biochem.* **78,** 993–1016 (2009).

108. Adolf, B. Ueber eine neue Klasse von Farbstoffen. *Berichte der Dtsch. Chem. Gesellschaft* **4,** 555–558 (1871).

109. Sun, W.C., Gee, K. R. & Haugland, R. P. Synthesis of novel fluorinated coumarins: Excellent UV-light excitable fluorescent dyes. *Bioorg. Med. Chem. Lett.* **8,** 3107–3110 (1998).

110. Lavis, L. D. & Raines, R. T. Bright ideas for chemical biology. *ACS Chem. Biol.* **3,** 142-155 (2007).

111. Lavis, L. D. Teaching old dyes new tricks: biological probes built from fluoresceins and rhodamines. *Annu. Rev. Biochem.* **86,** 825–843 (2017).

112. Grimm, J. B., English, B.P., Chen, J., Slaughter, J. P., Zhang, Z., Revyakin, A., Patel, R., Macklin, J. J., Normanno, D., Singer, R. H., Lionnet, T. & Lavis, L. D. A general method to improve fluorophores for live-cell and single-molecule microscopy. *Nat. Methods* **12,** 244–250 (2015).

113. Grimm, J. B., Muthusamy, A. K., Liang, Y., Brown, T. A., Lemon, W. C., Patel, R., Lu, R., Macklin, J. J., Keller, P. J., Ji, N. & Lavis, L. D. A general method to fine-tune fluorophores for live-cell and in vivo imaging. *Nat. Methods* **14,** 987–994 (2017).

114. Liu, X., Qiao, Q., Tian, W., Liu, W., Chen, J., Lang, M. J. & Xu, Z. Aziridinyl fluorophores demonstrate bright fluorescence and superior photostability by effectively inhibiting twisted intramolecular charge transfer. *J. Am. Chem. Soc.* **138,** 6960–6963 (2016).

115. Singha, S., Kim, D., Roy, B., Sambasivan, S., Moon, H., Rao, A. S., Kim, J. Y., Joo, T., Park, J. W., Rhee, Y.M., Wang, T., Kim, K.H., Shin, Y. H., Jung, J. & Ahn, K. H. A structural remedy toward bright dipolar fluorophores in aqueous media. *Chem. Sci.* **6,** 4335–4342 (2015).

116. Yu, H., Li, J., Wu, D., Qiu, Z. & Zhang, Y. Chemistry and biological applications of photo-labile organic molecules. *Chem. Soc. Rev.* **39,** 464–473 (2010).

117. Velema, W. A., Szymanski, W. & Feringa, B. L. Photopharmacology: Beyond proof of principle. *J. Am. Chem. Soc.* **136,** 2178–2191 (2014).

118. Brieke, C., Rohrbach, F., Gottschalk, A., Mayer, G. & Heckel, A. Light-controlled tools. *Angew. Chem. Ind Ed* **51,** 8446–8476 (2012).

119. Nad, S. & Pal, H. Unusual Photophysical Properties of Coumarin-151. *J. Phys. Chem. A* **105,** 1097–1106 (2001).

120. Nizamov, S., Sednev, M. V., Bossi, M. L., Hebisch, E., Frauendorf, H., Lehnart, S. E., Belov, V. N. & Hell, S.W. "Reduced" coumarin dyes with an o-phosphorylated 2,2-dimethyl-4-(hydroxymethyl)-1,2,3,4-tetrahydroquinoline fragment: synthesis, spectra, and STED microscopy. *Chem. - Eur. J.* **22,** 11631–11642 (2016).

121. Nizamov, S., Willig, K. I., Sednev, M. V., Belov, V. N. & Hell, S. W. Phosphorylated 3-heteroarylcoumarins and their use in fluorescence microscopy and nanoscopy. *Chem. - Eur. J.* **18,** 16339–16348 (2012).

122. Bassolino, G., Nançoz, C., Thiel, Z., Bois, E., Vauthey, E. & Rivera-Fuentes, P. Photolabile coumarins with improved efficiency through azetidinyl substitution. *Chem. Sci.* **9,** 387–391 (2018).

123. Fournier, L., Aujard, I., Le Saux, T., Maurin, S., Beaupierre, S., Baudin, J. B. & Jullien, L. Coumarinylmethyl caging groups with redshifted absorption. *Chem. - Eur. J.* **19,** 17494–17507 (2013).

124. Fournier, L., Gauron, C., Xu, L., Aujard, I., Le Saux, T., Gagey-Eilstein, N., Maurin, S., Dubruille, S., Baudin, J.B., Bensimon, D., Volovitch, M., Vriz, S. & Jullien, L. A blue-absorbing photolabile protecting group for in vivo chromatically orthogonal photoactivation. *ACS Chem. Biol.* **8,** 1528–1536 (2013).

125. Gandioso, A., Contreras, S., Melnyk, I., Oliva, J., Nonell, S., Velasco, D., García-Amorós, J. & Marchán, V. Development of green/red-absorbing chromophores based on a coumarin scaffold that are useful as caging groups. *J. Org. Chem.* **82,** 5398-5408 (2017).

126. Ong, M. J. H., Srinivasan, R., Romieu, A. & Richard, J. A. Divergent synthesis of dihydroxanthene-hemicyanine fused near-Infrared fluorophores through the late-stage amination of a bifunctional precursor. *Org. Lett.* **18,** 5122–5125 (2016).

127. Romieu, A. & Richard, J. A. An expedient synthesis of N,N-dialkylamino-dihydroxanthene-pyrylium conjugated near-infrared fluorescent dyes. *Tetrahedron Lett.* **57,** 317–320 (2016).

128. Ong, M. J. H., Debieu, S., Moreau, M., Romieu, A. & Richard, J. A. Synthesis of *N,N*-dialkylamino-nor-dihydroxanthene-hemicyanine fused near-infrared fluorophores and their first water-soluble and/or bioconjugatable analogues. *Chem. - Asian J.* **12,** 936–946 (2017).

129. Cui, S., Yin, D., Chen, Y., Di, Y., Chen, H., Ma, Y., Achilefu, S. & Gu, Y. *In vivo* targeted deep-tissue photodynamic therapy based on near-infrared light triggered upconversion nanoconstruct. *ACS Nano* **7,** 676–688 (2013).

130. Owens, E. A., Henary, M., El Fakhri, G. & Choi, H. S. Tissue-specific near-infrared fluorescence imaging. *Acc. Chem. Res.* **49,** 1731–1740 (2016).

131. Tjalma, J. J., Garcia-Allende, P. B., Hartmans, E., Terwisscha van Scheltinga, A. G., Boersma-van Ek, W., Glatz, J., Koch, M., van Herwaarden, Y. J., Bisseling, T. M., Nagtegaal, I. D., Timmer-Bosscha, H., Koornstra, J. J., Karrenbeld, A., Kleibeuker, J. H., van Dam, G. M., Ntziachristos, V. & Nagengast, W. B. Molecular fluorescence endoscopy targeting vascular endothelial growth factor A for improved colorectal polyp detection. *J. Nucl. Med.* **57,** 480–485 (2016).

132. Low, P. S. & Kularatne, S. A. Folate-targeted therapeutic and imaging agents for cancer. *Curr. Opin. Chem. Biol.* **13,** 256–262 (2009).

133. Mayer, G. & Hechel, A. Biologically active molecules with a 'light switch'. *Angew. Chem. Ind. Ed.* **45,** 4900–4921 (2006).

134. Deiters, A. Principles and applications of the photochemical control of cellular processes. *ChemBioChem* **11,** 47–53 (2010).

135. Bochet, C. G. Wavelength-selective cleavage of photolabile protecting groups. *Tetrahedron Lett.* **41,** 6341–6346 (2000).

136. Hansen, M. J., Velema, W. A., Lerch, M. M., Szymanski, W. & Feringa, B. L. Wavelength-selective cleavage of photoprotecting groups: strategies and applications in dynamic systems. *Chem. Soc. Rev.* **44,** 3358–3377 (2015).

137. Klán, P., Šolomek, T., Bochet, C. G., Blanc, A., Givens, R., Rubina, M., Popik, V., Kostikov, A. & Wirz, J. Photoremovable protecting groups in chemistry and biology: Reaction mechanisms and efficacy. *Chem. Rev.* **113,** 119–191 (2013).

138. Kaplan, J. H., Forbush, B. & Hoffman, J. F. Rapid photolytic release of adenosine 5'-triphosphate from a protected analogue: Utilization by the Na:K pump of human red blood cell ghosts. *Biochemistry* **17,** 1929–1935 (1978).

139. Ellis-Davies, G. C. R. Caged compounds: photorelease technology for control of cellular chemistry and physiology. *Nat. Methods* **4,** 619–628 (2007).

140. Goguen, B. N., Aemissegger, A. & Imperiali, B. Sequential activation and deactivation of protein function using spectrally differentiated caged phosphoamino acids. *J. Am. Chem. Soc.* **133,** 11038–11041 (2011).

141. Joshi, T., Pierroz, V., Mari, C., Gemperle, L., Ferrari, S. & Gasser, G. A Bis(dipyridophenazine)(2-(2-pyridyl)pyrimidine-4-carboxylic acid)ruthenium(II) complex with anticancer action upon photodeprotection. *Angew. Chem. Ind. Ed.* **53,** 2960–2963 (2014).

142. Ando, H., Furuta, T., Tsien, R. Y. & Okamoto, H. Photo-mediated gene activation using caged RNA / DNA in zebrafish embryos. *Nat. Genet.* **28,** 317–325 (2001).

143. Umeda, N., Takahashi, H., Kamiya, M., Ueno, T., Komatsu, T., Terai, T., Hanaoka, K., Nagano, T. & Urano, Y. Boron dipyrromethene as a fluorescent caging group for single- photon uncaging with long-wavelength visible light. *ACS Chem. Biol.* **9,** 2242–2246 (2014).

144. Goswami, P. P., Syed, A., Beck, C. L., Albright, T.R., Mahoney, K.M., Unash, R., Smith, E. A. & Winter, A. H. BODIPY-Derived Photoremovable Protecting Groups Unmasked with Green Light. *J. Am. Chem. Soc.* **137,** 3783–3786 (2015).

145. Sitkowska, K., Feringa, B. L. & Szymański, W. Green-light-sensitive BODIPY photoprotecting groups for amines. *J. Org. Chem.* **83,** 1819–1827 (2018).

146. Nani, R. R., Gorka, A. P., Nagaya, T., Yamamoto, T., Ivanic, J., Kobayashi, H. & Schnermann, M. J. *In vivo* activation of duocarmycin-antibody conjugates by near-infrared Light. *ACS Cent. Sci.* **3,** 329–337 (2017).

147. Sato, K., Gorka, A. P., Nagaya, T., Michie, M.S., Nakamura, Y., Nani, R. R., Coble, V. L.. Vasalatiy, O. V., Swenson, R. E., Choyke, P. L., Schnermann, M. J. & Kobayashi, H. Effect of charge localization on the in vivo optical imaging properties of near-infrared cyanine dye/monoclonal antibody conjugates. *Mol. Biosyst.* **12,** 3046–3056 (2016).

148. Nani, R. R., Gorka, A. P., Nagaya, T., Kobayashi, H. & Schnermann, M. J. Near-IR light-mediated cleavage of antibody-drug conjugates using cyanine photocages. *Angew. Chem. Ind. Ed.* **54,** 13635–13638 (2015).

149. Nani, R. R., Shaum, J. B., Gorka, A. P. & Schnermann, M. J. Electrophile-integrating smiles rearrangement provides previously inaccessible C4'-O-alkyl heptamethine cyanine fluorophores. *Org. Lett.* **17,** 302–305 (2015).

150. Gorka, A. P., Nani, R. R., Zhu, J., Mackem, S. & Schnermann, M. J. A near-IR uncaging strategy based on cyanine photochemistry. *J. Am. Chem. Soc.* **136,** 14153–14159 (2014).

151. Schmidt, R., Geissler, D., Hagen, V. & Bendig, J. Mechanism of photocleavage of (coumarin-4-yl)methyl esters. *J. Phys. Chem. A* **111,** 5768–5774 (2007).

152. Suzuki, A. Z., Watanabe, T., Kawamoto, M., Nishiyama, K., Yamashita, H., Ishii, M., Iwamura, M. & Furuta, T. Coumarin-4-ylmethoxycarbonyls as phototriggers for alcohols and phenols. *Org. Lett.* **5,** 4867–4870 (2003).

153. Hagen, V., Kilic, F., Schaal, J., Dekowski, B., Schmidt, R. & Kotzur, N. [8-[Bis(carboxymethyl)aminomethyl]-6-bromo-7-hydroxycoumarin-4-yl]methyl moieties as photoremovable protecting groups for compounds with COOH, NH_2, OH, and C-O functions. *J. Org. Chem.* **75,** 2790–2797 (2010).

154. Olson, J. P., Banghart, M. R., Sabatini, B. L. & Ellis-Davies, G. C. R. Spectral evolution of a photochemical protecting group for orthogonal two-color uncaging with visible light. *J. Am. Chem. Soc.* **135,** 15948–15954 (2013).

155. Kantevari, S., Matsuzaki, M., Kanemoto, Y., Kasai, H. & Ellis-Davies, G. C. R. Two-color, two-photon uncaging of glutamate and GABA. *Nat. Methods* **7,** 123–125 (2010).

156. Amatrudo, J. M., Olson, J.P., Lur, G., Chiu, C. Q., Higley, M. J. & Ellis-Davies, G.C.R. Wavelength-selective one- and two-photon uncaging of Gaba. *ACS Chem. Neurosci.* **5,** 64–70 (2014).

157. Bort, G., Gallavardin, T., Ogden, D. & Dalko, P. I. From one-photon to two-photon probes: 'caged' compounds, actuators, and photoswitches. *Angew. Chem. Ind. Ed.* **52,** 4526–4537 (2013).

158. Pirrung, M. C., Pieper, W. H., Kaliappan, K. P. & Dhananjeyan, M. R. Combinatorial discovery of two-photon photoremovable protecting groups. *Proc. Natl. Acad. Sci. U. S. A.* **100,** 12548–12553 (2003).

159. Weis, S., Shafiq, Z., Gropeanu, R. A. & Del Campo, A. Ethyl substituted coumarin-4-yl derivatives as photoremovable protecting groups for amino acids with improved stability for SPPS. *J. Photochem. Photobiol. A Chem.* **241,** 52–57 (2012).

160. Rodrigues-Correia, A., Weyel, X. M. M. & Heckel, A. Four levels of wavelength-selective uncaging for oligonucleotides. *Org. Lett.* **15,** 5500–5503 (2013).

161. Menge, C. & Heckel, A. Coumarin-caged dG for improved wavelength-selective uncaging of DNA. *Org. Lett.* **13,** 4620–4623 (2011).

162. Skwarczynski, M., Noguchi, M., Hirota, S., Sohma, Y., Kimura, T., Hayashi, Y. & Kiso, Y. Development of first photoresponsive prodrug of paclitaxel. *Bioorg. Med. Chem. Lett.* **16,** 4492–4496 (2006).

163. Kilic, F., Kashikar, N. D., Schmidt, R., Alvarez, L., Dai, L., Weyand, I., Wiesner, B., Goodwin, N., Hagen, V. & Kaupp, U. B. Caged progesterone: A new tool for studying rapid nongenomic actions of progesterone. *J. Am. Chem. Soc.* **131,** 4027–4030 (2009).

164. Velema, W. A., Van Der Berg, J. P., Szymanski, W., Driessen, A. J. M. & Feringa, B. L. Orthogonal control of antibacterial activity with light. *ACS Chem. Biol.* **9,** 1969–1974 (2014).

165. Schimer, J., Pávová, M., Anders, M., Pachl, P., Šácha, P., Cígler, P., Weber, J., Majer, P., Řezáčová, P., Kräusslich, H. G., Müller, B. & Konvalinka, J. Triggering HIV polyprotein processing by light using rapid photodegradation of a tight-binding protease inhibitor. *Nat. Commun.* **6,** 1–8 (2015).

166. Yamazoe, S., Liu, Q., McQuade, L. E., Deiters, A. & Chen, J. K. Sequential gene silencing using wavelength-selective caged morpholino oligonucleotides. *Angew. Chem. Ind. Ed.* **53,** 10114–10118 (2014).

Results and Discussion

Chapter I: Conjugation of a photoactivatable Pt(IV) pro-drug to targeting ligands

6. Publication A: An integrin-targeted photoactivatable Pt(IV) complex as a selective anticancer pro-drug: synthesis and photoactivation studies (*Chem. Commun*. **2015**, *51*, 9169-9172)

ChemComm

COMMUNICATION

View Article Online
View Journal | View Issue

Cite this: *Chem. Commun.*, 2015, 51, 9169

Received 16th April 2015,
Accepted 23rd April 2015

DOI: 10.1039/c5cc03180j

www.rsc.org/chemcomm

An integrin-targeted photoactivatable Pt(IV) complex as a selective anticancer pro-drug: synthesis and photoactivation studies†

Albert Gandioso,[a] Evyenia Shaili,[b] Anna Massaguer,[c] Gerard Artigas,[a] Alejandro González-Cantó,[a] Julie A. Woods,[d] Peter J. Sadler[b] and Vicente Marchán*[a]

A new anticancer agent based on the conjugation of a photoactivatable Pt(IV) pro-drug to a cyclic RGD-containing peptide is described. Upon visible light irradiation, phototoxicity was induced preferentially in SK-MEL-28 melanoma cancer cells overexpressing $\alpha_v\beta_3$ integrin compared to control DU-145 human prostate carcinoma cells.

The use of visible light has enormous potential in chemotherapy for controlling, at a desired time, the place and dose, and release of cytotoxic species from inert anticancer pro-drugs. For this reason, much effort has been dedicated to the development of photoactivatable metal-based anticancer complexes for improving drug efficacy and reducing toxic side-effects associated with platinum-based chemotherapeutic drugs currently used in clinics.[1] In addition, photoactivation offers the possibility for new mechanisms of action as well as the formation of novel adducts with the final biological target (not only DNA, but also RNA or proteins), which are important variables to overcome inherent or acquired resistance to cisplatin. Among photoactivated metallodrugs, Pt(IV) diazidodihydroxido complexes are particularly promising since they are inert and nontoxic in the dark, but become highly active against a range of cancer cell lines upon irradiation with visible light, including cisplatin-resistant cells (A2780cis).[2] Such Pt(IV) pro-drugs accumulate in tumour cells and bind strongly to DNA by generating adducts distinct from those of cisplatin.[3] Ru(II) arene complexes such as $[(\eta^6\text{-}p\text{-cym})\text{Ru(bpm)(py)}]^{2+}$ or its peptide derivatives can also be activated by visible light to induce the dissociation of the Ru–pyridine bond and the generation of an active species with capacity to react with DNA.[4] A similar pro-drug approach has been described with some Ru polypyridyl complexes masked with thioether groups that can be removed selectively upon visible light irradiation.[5] Very recently, caging groups have also been applied to control the activity of Ru(II) and Re(I) complexes.[6]

Despite these promising examples, it is desirable to improve some of the pharmacological properties of photoactivatable metallodrugs, such as aqueous solubility and cell uptake, as well as higher selectivity against cancer cells. In this context, targeted approaches based on peptide vectors whose receptors are overexpressed on cancer cells in combination with light activation can be used to develop anticancer agents with a dual mechanism of selectivity, such as the conjugates between a photoactivatable Ru(II) arene complex and receptor-binding peptides recently described by us[4b] or a conjugate between a caged Re(I) organometallic complex and bombesin.[6b]

Herein we report the conjugation of a photoactivatable Pt(IV) pro-drug, *trans,trans,trans*-$[Pt(N_3)_2(OH)_2(py)_2]$ (**1**)[2] (Fig. 1), to a cyclic peptide containing the RGD sequence (–Arg–Gly–Asp–), which is selectively recognized by $\alpha_v\beta_3$ and $\alpha_v\beta_5$ integrins. The overexpression of these transmembrane heterodimeric glycoproteins in different tumor cells together with their known relationship with tumor angiogenesis, which is an essential process for tumor growth and metastasis, makes them relevant targets in medicinal chemistry.[7] In fact, RGD-containing peptides have been exploited extensively for tumour imaging and for targeted drug delivery of cytotoxic compounds,[8] including some metal-based anticancer drugs.[4b,9] As recently found by us for conjugates between a Pt(IV) derivative of picoplatin and RGD-containing peptides,[9d] we hypothesize

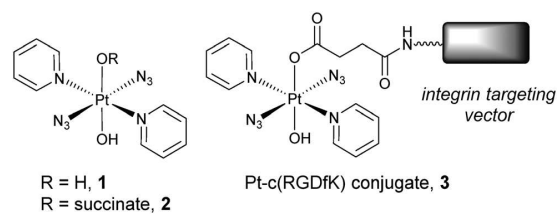

Fig. 1 Structure of *trans,trans,trans*-$[Pt(N_3)_2(OH)_2(py)_2]$ (**1**), *trans,trans,trans*-$[Pt(N_3)_2(OH)(succ)(py)_2]$ (**2**) and the schematic representation of the Pt–c(RGDfK) conjugate (**3**).

[a] *Departament de Química Orgànica and IBUB, Universitat de Barcelona, Barcelona, E-08028, Spain. E-mail: vmarchan@ub.edu*
[b] *Department of Chemistry, University of Warwick, Warwick, CV4 7AL, Coventry, UK*
[c] *Departament de Biologia, Universitat de Girona, Campus Montilivi, Girona, E-17071, Spain*
[d] *Photobiology Unit, Department of Dermatology, Ninewells Hospital, Dundee, DD1 9SY, UK*

† Electronic supplementary information (ESI) available: Experimental procedures, characterization data for conjugate **3**, and results from photoactivation studies. See DOI: 10.1039/c5cc03180j

that the peptide vector will confer complex **1** with selectivity for cancer cells overexpressing pro-angiogenic integrins such as $\alpha_V\beta_3$ and $\alpha_V\beta_5$. The novelty of this approach resides in the use of a photoactivatable Pt(IV) pro-drug since irradiation with visible light directly within the tumour will trigger the release of cytotoxic Pt(II) species from the internalized conjugate (**3** in Fig. 1), thus providing a Pt(IV)-based anticancer agent with dual control over selectivity.

First, one of the axial hydroxyl groups of complex **1** was esterified with succinic anhydride to generate *trans*,*trans*,*trans*-$[Pt(N_3)_2(OH)(succ)(py)_2]$ (**2**) (Fig. 1),[10] which contains a carboxylic acid function suitable for attaching the peptide moiety. As shown in Fig. 2, we selected as a carrier the cyclic pentapeptide c(RGDfK),[11] which is a conjugatable version of Cilengitide, c(RGDf[*N*-Me]V), an antagonist of pro-angiogenic integrins, and currently in clinical phase III trials for the treatment of patients with brain tumors.[12] The incorporation of non-natural D-Phe and [*N*-Me]-Val in the cyclic structure is responsible for increasing both the stability in biological fluids and the higher selectivity for $\alpha_V\beta_3$ integrin over $\alpha_V\beta_5$ and $\alpha_5\beta_1$.[12b] In our case, replacement of *N*-methyl Val by Lys allowed further derivatization of the RGD-containing peptide with a polyethyleneglycol spacer at the ε-NH_2 function. Then, complex **2** was attached to peptide intermediate **4**[9d] by using HATU in the presence of DIPEA in anhydrous DMF for 2 h at RT in the dark. The expected Pt–c(RGDfK) conjugate (**3**) was obtained as a pale yellow solid (54% yield) after purification by reversed-phase HPLC and lyophilisation (Fig. S1, ESI†). Conjugate **3** was unambiguously characterized by high-resolution ESI mass spectrometry and ^{1}H NMR spectroscopy. As shown in Fig. 3 and Fig. S2 (ESI†), an *m*/*z* value consistent with the calculated value of the charged species ($[M + H]^+$) and with the expected isotopic mass distribution pattern of Pt was obtained. In addition, diagnostic signals from the platinum complex (pyridine ligands) and from the peptide moiety (amide NH protons and aromatic protons of D-Phe) in the aromatic region of the ^{1}H NMR spectra confirmed the covalent attachment of the Pt complex to the peptide vector (Fig. 3 and Fig. S3, ESI†).

Next, the efficiency of the photoactivation of Pt–c(RGDfK) conjugate (**3**) in the presence of 5′-GMP (2 mol equiv.) was investigated by HPLC-MS. As shown in Fig. S4 (ESI†), irradiation (λ_{irr} = 420 nm, 11 mW cm^{-2}, 45 min, 37 °C) led to the complete disappearance of **3** and to the formation of a major species that was characterized by HR-ESI-MS as the Pt(II)–GMP adduct, *trans*-$[Pt(N_3)(5'\text{-GMP})(py)_2]^+$ (**6** in Fig. 2) (GMP is considered neutral in all the formulae). In addition, two minor GMP adducts were identified, *trans*-$[Pt(py)_2(5'\text{-GMP})_2]^{2+}$ and $[Pt_2(N_3)(py)_4(5'\text{-GMP})]^+$. The photodissociation of conjugate **3** to form the Pt(II)–GMP adduct as a major product, parallels the behaviour observed for the parent complexes **1**[2a] and **2**,[10] indicating that the attached peptide does not alter the photochemical properties or the type of photoadducts with a model nucleobase. Furthermore, the release of the intact succinate–c(RGDfK) moiety (**5** in Fig. 2) implies that the carrier ligand neither competes with 5′-GMP for binding to the photoreleased Pt(II) species, nor does it form any secondary reactions, being a simple targeting vector of the Pt(IV) pro-drug.

Having established the photoactivation properties of the Pt–c(RGDfK) conjugate, our next objective was to investigate its toxicity towards different cancer cell lines in the presence of visible light to assess the capacity of the peptide vector to deliver the photoactivatable Pt(IV) pro-drug into cancer cells overexpressing integrin receptors. On the basis of flow cytometry studies (Fig. 4), we selected SK-MEL-28 human malignant melanoma cell line as a model to evaluate the phototoxicity of **3** since it expresses high levels of $\alpha_V\beta_3$ integrin

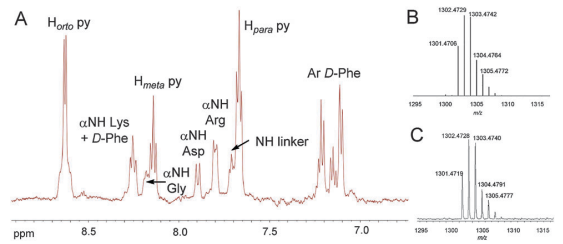

Fig. 3 ^{1}H NMR spectra of conjugate **3** (A) in H_2O/D_2O 9 : 1, showing the region between 6.7 and 9.1 ppm. Expanded HR ESI mass spectrum of the molecular peak of **3** ($[M + H]^+$), calculated (B) and experimental (C).

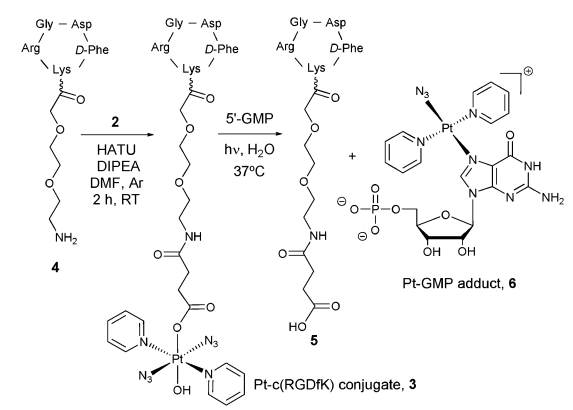

Fig. 2 Schematic representation of the synthesis of the Pt–c(RGDfK) conjugate (**3**) and of the photo-reaction with 5′-GMP.

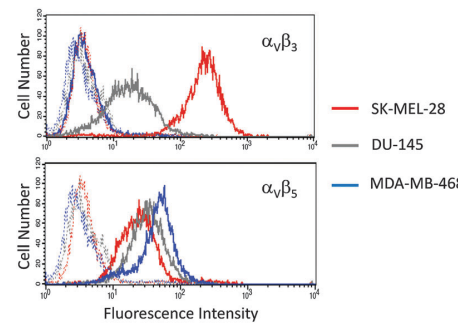

Fig. 4 Expression of $\alpha_V\beta_3$ and $\alpha_V\beta_5$ integrins in SK-MEL-28, DU-145 and MDA-MB-468 cell lines. Representative flow cytometry histograms obtained after the indirect immunofluorescence staining. Solid lines represent the fluorescence intensity of the cells after the incubation with monoclonal antibodies against both integrins followed by incubation with secondary antibody conjugated to Alexa-Fluor 488. Dotted lines indicate the background staining with the secondary antibody alone.

compared with $\alpha_V\beta_5$ integrin (mean cell fluorescence intensity of 217.4 and 23.3 for $\alpha_V\beta_3$ and $\alpha_V\beta_5$ integrins, respectively).[9d] As negative control, the DU-145 human prostate carcinoma cell line was selected since the expression of $\alpha_V\beta_3$ integrin was considerably lower, whereas that of $\alpha_V\beta_5$ integrin was similar (mean cell fluorescence intensity of 16.6 and 31.8 for $\alpha_V\beta_3$ and $\alpha_V\beta_5$ integrins, respectively). As expected, the internalization of the fluorescein-labelled RGD-containing peptide, Fluo-c(RGDfK) (**7**),[9d] was slightly higher in the $\alpha_V\beta_3$ integrin overexpressing SK-MEL-28 cells than in DU-145 (by 1.6-fold when incubated at 10 μM; see Fig. S5, ESI†), which points to the active participation of this integrin receptor in the uptake of the peptide.

The photocytotoxicity of the Pt–c(RGDfK) conjugate (**3**) and of the parent Pt complexes (**1** and **2**) was determined upon irradiation with visible light (λ_{irr} = 420 nm, 5 J cm^{-2}) in both cell lines. The photoactivated dose-dependent inhibition of cell viability for compounds **1–3** towards SK-MEL-28 and DU-145 cells and their phototoxic indices are summarised in Table 1 and the cytotoxicity plots are shown in Fig. S6 (ESI†). First, it is worth noting that the IC_{50} value for complex **1** in SK-MEL-28 was similar to those previously found in other cancer cell lines (IC_{50} = 6.8 μM in HaCaT, 8.3 μM in A2780 or 8.4 μM in OE19, under blue light irradiation),[2b] although the cytotoxicity in DU-145 cells was about 4-fold lower than in the melanoma cancer cell line. Hence, these results confirm the high antitumour efficiency of the Pt(IV) pro-drug against cancer cells of different origin when photoactivated with visible light. Second, the cytotoxic effect of **1** was slightly reduced in SK-MEL-28 (about 1.5-fold) upon derivatization with a succinate group (**2**). This tendency was not reproduced in DU-145, since the cytotoxic effect was increased upon succinylation (IC_{50} = 20 μM for **2** *vs.* IC_{50} = 43 μM for **1**).

As shown in Table 1, the phototoxicity of conjugate **3** in SK-MEL-28 (IC_{50} = 19.5 μM) was similar to that of the parent succinylated complex **2** (IC_{50} = 15.5 μM), whereas the differences in the irradiated mean IC_{50} values were higher in DU-145 cells (IC_{50} = 20 μM for **2** and 54 μM for **3**). This result is in good agreement with the levels of expression of the $\alpha_V\beta_3$ integrin and with the cellular uptake experiments with the fluorescein-labelled peptide, and is consistent with the participation of the receptor in the biological activity of the conjugate. Hence, conjugation to the RGD-containing peptide vector seems to confer selectivity to complex **2** since the anticancer activity is higher in the melanoma cancer cell line that overexpresses $\alpha_V\beta_3$ integrin receptor whereas a lower phototoxicity was found in the human prostate cancer cell line. This difference was increased when conjugate **3** was irradiated with UVA (λ_{irr} = 365 nm, 5 J cm^{-2}) in both cell lines.

Table 1 IC_{50} values of 5 J cm^{-2} visible light or UVA irradiated human DU-145 and SK-MEL-28 cells pretreated with compounds **1–3**

		SK-MEL-28			DU-145		
		IC_{50}[a] (μM)		PI[b]	IC_{50}[a] (μM)		PI[b]
1	420 nm	10.2	(7.9–13.0)	20.8	43.2	(33.0–56.6)	4.9
2	420 nm	15.5	(10.2–23.6)	11.3	20.0	(14.7–27.3)	8.8
3	420 nm	19.5	(13.4–28.2)	3.6	53.9	Wide	1.3
3	365 nm	9.9	(9.5–10.1)	8	56.4	(50.9–61.9)	2.7

[a] IC_{50} is defined as the concentration of compound that inhibits dye uptake by 50%. The lowest value indicates the highest toxicity to cells. [b] PI: phototoxic index.

Interestingly, DU-145 cells treated with aminolevulinic acid (ALA) using the same blue light source were twice more susceptible than SK-MEL-28 cells (irradiated mean IC_{50} values = 0.12 mM and 0.23 mM, respectively). Thus, the melanoma cancer cells were more resistant to the porphyrin-based therapy, but more sensitive to the Pt-based therapy compared to the prostate cancer cells.

Since the cellular uptake of the Pt–peptide conjugate depends both on the level of expression of the pro-angiogenic integrins and on the binding affinity of the RGD-containing peptide towards these receptors, the determination of the intracellular accumulation is of high importance to assess the effect of the peptide conjugation on the biological activity of the Pt(IV) pro-drug as well as to investigate the contribution of each integrin subtype. For this purpose, in addition to SK-MEL-28 and DU-145 cells, we selected the MBA-MD-468 breast adenocarcinoma cell line as positive control for $\alpha_V\beta_5$ integrin. As shown in Fig. 4, the expression of $\alpha_V\beta_5$ integrin was considerably higher than that of $\alpha_V\beta_3$ integrin (mean cell fluorescence intensity of 3.8 and 42.4 for $\alpha_V\beta_3$ and $\alpha_V\beta_5$ integrins, respectively). Then, the three cancer cell lines were exposed to 10 μM solutions of **1–3** in the dark for 1 h, and the intracellular level of platinum was quantified by inductively-coupled plasma mass spectrometry (ICP-MS).

As shown in Fig. 5, the accumulation of platinum after exposure of the three cell lines to Pt–c(RGDfK) conjugate (**3**) (46.6 ± 2 pmol Pt per 10^6 cells in DU-145, 130.7 ± 9 pmol Pt per 10^6 cells in SK-MEL-28 and 166.5 ± 6 pmol Pt per 10^6 cells in MBA-MD-468) was higher than that of complex **1** (26.2 ± 2.4 pmol Pt per 10^6 cells in DU-145, 72.6 ± 1.9 pmol Pt per 10^6 cells in SK-MEL-28 and 73.6 ± 2 pmol Pt per 10^6 cells in MBA-MD-468) or **2** (15.9 ± 2.7 pmol Pt per 10^6 cells in DU-145, 75.4 ± 9.6 pmol Pt per 10^6 cells in SK-MEL-28 and 86.8 ± 7 pmol Pt per 10^6 cells in MBA-MD-468). This clearly indicates that peptide conjugation has a positive effect on the intracellular accumulation of the photoactivatable Pt(IV) pro-drug. Notably, platinum accumulation in SK-MEL-28 cells after exposure to conjugate **3** was higher (about 2.8-fold) than in DU-145 cells, which agree with the higher expression of $\alpha_V\beta_3$ integrin in the human malignant melanoma cell line compared with the prostate carcinoma cell line, as well as with the internalization studies with the fluorescein-labelled peptide.

To our surprise, the intracellular accumulation of **3** in MBA-MD-468 was also higher than in DU-145 cells (about 3.6-fold) despite

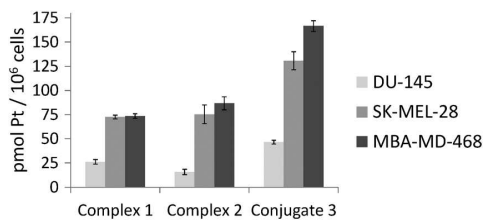

Fig. 5 Cell accumulation of platinum in SK-MEL-28, DU-145 and MBA-MD-468 cells after exposure to compounds **1–3** (10 μM, dark, 1 h). The platinum content is related to the cell number. Errors bars represent the standard deviation of three replicates.

the very low expression of $\alpha_V\beta_3$ integrin in the breast carcinoma cell line. These results and the fact that accumulation of **3** in MBA-MD-468 was about 1.3-fold higher than in SK-MEL-28 points out to the internalization of the Pt–c(RGDfK) conjugate mediated by $\alpha_V\beta_5$ integrin as well. These results are in agreement with the known selectivity of RGD-containing peptides, particularly the cyclic version c(RGDfK), for cancer cells overexpressing $\alpha_V\beta_3$ and $\alpha_V\beta_5$ integrins and suggest in all cases the participation of the peptide in the internalization of the conjugate. The reduced selectivity of conjugate **3** for $\alpha_V\beta_3$ integrin compared with Cilengitide can be attributed to the replacement of [*N*-Me]-Val by the Lys residue where the photoactivatable Pt(IV) complex is attached. Hence, on the basis of the overall results, we can envisage the integrin-mediated internalization and accumulation of the intact Pt–peptide conjugate in cancer cells overexpressing $\alpha_V\beta_3$ and/or $\alpha_V\beta_5$ integrins, where it will be photoactivated to generate cytotoxic Pt(II) species with a capacity to react with nucleic acids, as inferred by the adduct generated with 5′-GMP. Otherwise, a premature activation of the Pt(IV) pro-drug or hydrolysis of the conjugate would lead to similar or even lower Pt accumulation ratios than those obtained with control complexes. Interestingly, a correlation was found between intracellular accumulation of conjugate **3** and phototoxicity (see Table 1): a lower IC_{50} value upon visible light irradiation and a higher phototoxic index was found in the melanoma cancer cells that accumulated a higher amount of the compound compared with prostate carcinoma cells. Notably, the accumulation of **1** and **2** in SK-MEL-28 and MBA-MD-468 cells was also higher than in DU-145, thereby revealing a preference for the melanoma and breast cancer cells. It is also interesting that despite the higher accumulation of conjugate **3** compared with the parent complexes, the phototoxicity was slightly reduced, particularly when compared with **1** in SK-MEL-28. This might be attributable to differences in the quantum yield of the compounds and to the accumulation of the conjugate in intracellular vesicles that might interfere with the interaction of the released Pt(II) species with the target.

In conclusion, our results demonstrate the potential of conjugating photoactivatable metal complexes, such as Pt(IV) pro-drugs, to peptides with the aim of generating receptor-targeted metal-based anticancer drugs with reduced toxic side effects based on dual control over selectivity. The fact that the Pt–c(RGDfK) conjugate can also be internalized by $\alpha_V\beta_5$ integrin opens up the door to delivering such promising anticancer metallodrugs to tumours overexpressing $\alpha_V\beta_5$ integrin[13] or to tumours coexpressing both $\alpha_V\beta_3$ and $\alpha_V\beta_5$ integrins.[7b,14] Such a multi-integrin targeting approach would provide new metal-based anticancer strategies and so benefit a wider range of patients by increasing the number of tumours which can be targeted.[15]

This work was supported by funds from the Spanish *Ministerio de Ciencia e Innovación* (grants CTQ2010-21567-C02-01-02, CTQ2014-52658-R and the RNAREG project, grant CSD2009-00080), the *Generalitat de Catalunya* (2009SGR-208 and XRB), the ERC (grant 247450), EPSRC (EP/F034210/1) and EPSRC (MOAC Doctoral Training Centre, EP/F500378/1). The authors acknowledge helpful assistance of Dr Irene Fernández and Laura Ortiz (MS), Dr Maite Romero (ICP-MS) and Dr M. Antònia Molins (NMR) from CCiTUB.

Notes and references

1 (*a*) C. Moucheron, *New J. Chem.*, 2009, **33**, 235; (*b*) D. Crespy, K. Landfester, U. S. Schubert and A. Schiller, *Chem. Commun.*, 2010, **46**, 6651; (*c*) N. A. Smith and P. J. Sadler, *Philos. Trans. R. Soc., A*, 2013, **371**, 20120519, DOI: 10.1098/rsta.2012.0519.
2 (*a*) N. J. Farrer, J. A. Woods, L. Salassa, Y. Zhao, K. S. Robinson, G. Clarkson, F. S. Mackay and P. J. Sadler, *Angew. Chem., Int. Ed.*, 2010, **49**, 8905; (*b*) Y. Zhao, J. A. Woods, N. J. Farrer, K. S. Robinson, J. Pracharova, J. Kasparkova, O. Novakova, H. Li, L. Salassa, A. M. Pizarro, G. J. Clarkson, L. Song, V. Brabec and P. J. Sadler, *Chem. – Eur. J.*, 2013, **19**, 9578; (*c*) A. M. Pizarro, R. J. McQuitty, F. S. Mackay, Y. Zhao, J. A. Woods and P. J. Sadler, *ChemMedChem*, 2014, **9**, 1169.
3 (*a*) J. Pracharova, L. Zerzankova, J. Stepankova, O. Novakova, N. J. Farrer, P. J. Sadler, V. Brabec and J. Kasparkova, *Chem. Res. Toxicol.*, 2012, **25**, 1099; (*b*) H.-C. Tai, R. Brodbeck, J. Kasparkova, N. J. Farrer, V. Brabec, P. J. Sadler and R. J. Deeth, *Inorg. Chem.*, 2012, **51**, 6830.
4 (*a*) S. Betanzos-Lara, L. Salassa, A. Habtemanriam and P. J. Sadler, *Chem. Commun.*, 2009, 6622; (*b*) F. Barragán, P. López-Senín, L. Salassa, S. Betanzos-Lara, A. Habtemariam, V. Moreno, P. J. Sadler and V. Marchán, *J. Am. Chem. Soc.*, 2011, **133**, 14098.
5 (*a*) R. E. Goldbach, I. Rodriguez-Garcia, J. H. van Lenthe, M. A. Siegler and S. Bonnet, *Chem. – Eur. J.*, 2011, **17**, 9924; (*b*) A. Bahreman, B. Limburg, M. A. Siegler, E. Bouwman and S. Bonnet, *Inorg. Chem.*, 2013, **52**, 9456; (*c*) S. H. C. Askes, A. Bahreman and S. Bonnet, *Angew. Chem., Int. Ed.*, 2014, **53**, 1029.
6 (*a*) T. Joshi, V. Pierroz, C. Mari, L. Gemperle, S. Ferrari and G. Gasser, *Angew. Chem., Int. Ed.*, 2014, **53**, 2960; (*b*) A. Leonidova, V. Pierroz, R. Rubbiani, Y. Lan, A. G. Schmitz, A. Kaech, R. K. O. Sigel, S. Ferrari and G. Gasser, *Chem. Sci.*, 2014, **5**, 4044.
7 (*a*) M. Friedlander, P. C. Brooks, R. W. Shaffer, C. M. Kincaid, J. A. Varner and D. A. Cheresh, *Science*, 1995, **270**, 1500; (*b*) J. S. Desgrosellier and D. A. Cheresh, *Nat. Rev. Cancer*, 2010, **10**, 9; (*c*) L. Auzzas, F. Zanardi, L. Battistini, P. Burreddu, P. Carta, G. Rassu, C. Curti and G. Casiraghi, *Curr. Med. Chem.*, 2010, **17**, 1255; (*d*) D. G. Stupack and D. A. Cheresh, *Curr. Top. Dev. Biol.*, 2004, **64**, 207.
8 (*a*) K. Temming, R. M. Schiffelers, G. Molema and R. J. Kok, *Drug Resist. Updates*, 2005, **8**, 381; (*b*) S. Liu, *Mol. Pharmaceutics*, 2006, **3**, 472; (*c*) F. Danhier, A. Le Breton and V. Préat, *Mol. Pharmaceutics*, 2012, **9**, 2961.
9 (*a*) S. Mukhopadhyay, C. M. Barnés, A. Haskel, S. M. Short, K. R. Barnes and S. J. Lippard, *Bioconjugate Chem.*, 2008, **19**, 39; (*b*) N. Graf, D. R. Bielenberg, N. Kolishetti, C. Muus, J. Banyard, O. C. Farokhzad and S. J. Lippard, *ACS Nano*, 2012, **6**, 4530; (*c*) Y. Yuan, R. T. K. Kwok, B. Z. Tang and B. Liu, *J. Am. Chem. Soc.*, 2014, **136**, 2546; (*d*) A. Massaguer, A. González-Cantó, E. Escribano, S. Barrabés, G. Artigas, V. Moreno and V. Marchán, *Dalton Trans.*, 2015, **44**, 202.
10 E. Shaili, PhD thesis, University of Warwick, 2013.
11 (*a*) K.-E. Gottschalk and H. Kessler, *Angew. Chem., Int. Ed.*, 2002, **41**, 3767; (*b*) F. Gaertner, H. Kessler, H. Wester, M. Schwaiger and A. Beer, *Eur. J. Nucl. Med. Mol. Imaging*, 2012, **39**, S126.
12 (*a*) M. A. Dechantsreiter, E. Planker, B. Mathä, E. Lohof, G. Hölzemann, A. Jonczyk, S. L. Goodman and H. Kessler, *J. Med. Chem.*, 1999, **42**, 3033; (*b*) C. Mas-Moruno, F. Rechenmacher and H. Kessler, *Anti-Cancer Agents Med. Chem.*, 2010, **10**, 753.
13 S. L. Goodman, H. J. Grote and C. Wilm, *Biol. Open*, 2012, **1**, 329.
14 A. Erdreich-Epstein, H. Shimada, S. Groshen, M. Liu, L. S. Metelitsa, K. S. Kim, M. F. Stins, R. C. Seeger and D. L. Durden, *Cancer Res.*, 2000, **60**, 712.
15 H. M. Sheldrake and L. H. Patterson, *J. Med. Chem.*, 2014, **57**, 6301.

Electronic Supplementary Material (ESI) for ChemComm.

Supporting Information

An integrin-targeted photoactivatable Pt(IV) complex as a selective anticancer pro-drug: synthesis and photoactivation studies

Albert Gandioso,[a] Evyenia Shaili,[b] Anna Massaguer,[c] Gerard Artigas,[a] Alejandro González-Cantó,[a] Julie A. Woods,[d] Peter J. Sadler,[b] and Vicente Marchán*[a]

[a]*Departament de Química Orgànica and IBUB, Universitat de Barcelona, Barcelona, E-08028, Spain. E-mail: vmarchan@ub.edu.*

[b]*Department of Chemistry, University of Warwick, Warwick, CV4 7AL, Coventry, UK.*

[c]*Departament de Biologia, Universitat de Girona, Campus Montilivi, E-17071 Girona, Spain.*

[d]*Photobiology Unit, Department of Dermatology, Ninewells Hospital, Dundee, DD1 9SY, UK.*

Table of contents

1. Experimental procedures

1.1. Materials and Methods.

Unless otherwise stated, common chemicals and solvents (HPLC grade or reagent grade quality) were purchased from commercial sources and used without further purification. Peptide grade DMF was purchased from Scharlau. Fmoc-protected amino acids, resins and coupling reagents for solid phase synthesis were obtained from Novabiochem, Bachem or Iris Biotech. Milli-Q water was directly obtained from a Milli-Q system equipped with a 5000-Da ultrafiltration cartridge. All the assayed compounds displayed a purity ≥95%, as determined by HPLC analysis.

Analytical reversed-phase HPLC analyses were carried out on a Jupiter Proteo column (250x4.6 mm, 4 μm, flow rate: 1 mL/min), using linear gradients of 0.045% TFA in H_2O (solvent A) and 0.036% TFA in ACN (solvent B). In some cases, small-scale purification was carried out using the same column. Large-scale purification was carried out on a Jupiter Proteo semipreparative column (250 x 10 mm, 10 μm, flow rate: 3 mL/min), using linear gradients of 0.1% TFA in H_2O (solvent A) and 0.1% TFA in ACN (solvent B). After several runs, pure fractions were combined and lyophilized.

ESI mass spectra (ESI-MS) were recorded on a Micromass ZQ instrument with single quadrupole detector coupled to an HPLC. High resolution electrospray mass spectra (HR ESI MS) were obtained on an Agilent 1100 LC/MS-TOF instrument.

1.2. Cell lines.

The SK-MEL-28 human melanoma, DU-145 human prostate carcinoma and MBA-MD-468 breast adenocarcinoma cell lines were from the American Tissue Culture Collection (ATCC, Rockville, MD, USA). Cells were maintained in Dulbecco's Modified Eagle Medium (DMEM) supplemented with 10% FBS (Gibco-BRL, Grand Island, NY, USA) and 100 U mL^-

[1] penicillin-streptomycin (Gibco-BRL) at 37˚C in a humidified atmosphere containing 5% CO_2. Cell growth and morphology were assessed using an inverted microscope.

1.3. Synthesis of Pt-c(RGDfK) conjugate (3).

To a solution of **2** (6.3 mg, 2.2 mol equiv.) and HATU (4.0 mg, 2.1 mol equiv.) in anhydrous DMF (0.5 mL), DIPEA (5.0 µL, 5.7 mol equiv.) was added. After stirring for 2 min at room temperature, the reaction mixture was added to peptide **4** (5.0 mg, 5.1 µmol) previously dissolved in anhydrous DMF (0.25 mL) and DIPEA (10 µL, 11.4 mol equiv.) under Ar atmosphere. After stirring for 2 h at room temperature under Ar, the solvent was evaporated *in vacuo* and the conjugate was purified by semipreparative HPLC (gradient from 0 to 80% B in 30 min, flow rate: 3 mL/min, R_t = 17.5 min). Overall yield (synthesis + purification): 3.9 mg of a pale yellow solid, 54 %. Characterization: R_t= 18.2 min (analytical gradient: 0 to 80 % in 30 min); HR ESI MS, positive mode: *m/z* 1302.4728 (calcd mass for $C_{47}H_{67}N_{18}O_{14}Pt$ $[M+H]^+$: 1302.4729).

1.4. Integrin expression analysis.

The expression of $\alpha_V\beta_3$ and $\alpha_V\beta_5$ integrins on the cell surface was analyzed by double immuno-fluorescence. The cells were incubated for 30 min at 4˚C with monoclonal antibodies against human $\alpha_V\beta_3$ (clone LM609) (Millipore, Temecula, CA) and $\alpha_V\beta_5$ integrin (sc-81632) (Santa Cruz Biotechnology, Santa Cruz, CA, USA) or medium alone as negative control. After washing with phosphate-buffered saline (PBS) (Gibco-BRL), cells were incubated for additional 30 min at 4˚C with the Alexa-Fluor 488-conjugated goat anti-mouse IgG antibody (Invitrogen, Carlsbad, CA, USA). Next, the cell fluorescence was analyzed using a FACSCalibur flow cytometer (Becton Dickinson Immunocytometry Systems, San Jose, CA, USA) equipped with CellQuest™ software (Becton Dickinson). 10.000 cells were analysed in each experiment. Fluorescence intensity was represented on a four orders of magnitude log scale (1-10.000).

1.5. Internalization experiments with Fluorescein-labeled c(RGDfK) (7).

The uptake efficiency of **7** by SK-MEL-28 and DU-145 cells was quantified by flow cytometry. 60.000 cells were seeded onto 24-well plates and allowed to attach for 24 h. Then, the cells were treated with either **7** at 10 or 50 μM, or medium alone as a control, for 1 h at 37ºC. After washing the cells three times with cold PBS (Gibco), the cells were harvested by trypsinization and the fluorescence of the cells, corresponding to the internalization of **7**, was analysed using a FACSCalibur (Becton Dickinson Immunocytometry Systems). The geometric mean fluorescence of 10.000 cells was determined with the CellQuestTM software (Becton Dickinson).

1.6. Phototoxicity studies.

Cell culture and other chemicals were obtained from Sigma-Aldrich Ltd (Poole, UK). Disposable sterile cell culture plastics were obtained from Greiner Bio-One (Cambridge, UK). All procedures were carried out in a specially adapted photobiology laboratory with ambient light levels measured below 1 lux (Solatell, UK). Phototoxicity was determined according to the OECD 432 guideline with some modification as described below.

For experiments, cells were mycoplasma free and maintained in antibiotic-free conditions in a humidified atmosphere of 5% CO_2/95% air. Cells were seeded at a density of 6-7 x 10^4cells/cm^2 in 96-well plates. Complexes were prepared immediately before use in Earle' Balanced Salt Solution (EBSS) and filter sterilized. Irradiations were performed in optically clear medium and experiments were controlled for light, complex, and handling. Visible light (5 J/cm^2) was delivered by a bank of TL03 fluorescent tubes (λ_{max}: 420 nm) with wavelengths shorter than 400 nm blocked by filtering. Irradiance was measured with a Gigahertz Optik meter calibrated to the source using a spectroradiometer (Bentham Instruments Ltd, UK; mean irradiance 1.3 mW/cm^2 ± 0.1). UVA (5 J/cm^2; λ_{max}: 365 nm) was delivered from a bank of 6ft fluorescent 15500/100W tubes with wavelengths <320 nm blocked. Irradiance was

measured with an International Light meter calibrated to the source using a spectroradiometer (Bentham Instruments Ltd, UK; mean irradiance 1.7 mW/cm^2 ± 0.1). Irradiances were measured through filters and cell culture plate lids. Sham-irradiated cells were treated identically and in parallel with irradiated cells, except that photons were blocked. The viability of DU-145 cells irradiated with visible light was 102.5 ± 6.7%; and of SK-MEL-28 cells was 101.3 ± 6.9%. For UVA this decreased to 71.8% and 85.1%, respectively.

Phototoxicity was determined by neutral red dye uptake 24 hours after irradiation at 540 nm in a Synergy™ 2 plate reader. The concentration of complex required to inhibit dye uptake by 50% (IC_{50} value) was calculated from the log-transformed cytotoxicity curves normalised to untreated cells (Graphpad Prism v.6). Goodness of fit was determined by the 95% confidence interval of the IC_{50} value, and the R2 value. Experiments were performed in triplicate, and independently repeated at least once on cells of differing passage number.

1.7. Platinum accumulation in cancer cells.

For platinum cellular uptake studies, about 1.0 x10^6 SK-MEL-28, DU-145 and MBA-MD-468 cells were plated in 100 mm Petri dishes and allowed to attach for 24 h. Next, the plates were exposed to *trans,trans,trans*-[$Pt(N_3)_2(OH)_2(py)_2$] (**1**), *trans,trans,trans*-[$Pt(N_3)_2(OH)(succ)(py)_2$] (**2**) or to the Pt-c(RGDfK) conjugate (**3**) at a 10 μM concentration. Additional plates were incubated with medium alone as negative control. After 1 h of incubation in the dark at 310 K, the cells were rinsed three times with cold PBS and harvested by trypsinization. The number of cells in each sample was counted manually in a haemocytometer using the trypan blue dye exclusion test. Then the cells were centrifuged to obtain the whole cell pellet for ICP-MS analysis. All experiments were conducted in triplicate.

1.8. ICP-MS analysis.

The whole cell pellets were dissolved in 500 µL of concentrated 72% v/v nitric acid, and the samples were then transferred into wheaton v-vials (Sigma-Aldrich) and heated in an oven at 373 K for 18 h. The vials were then allowed to cool, and each cellular sample solution was transferred into a volumetric tube and combined with washings with Milli-Q water (1.5 mL). Digested samples were diluted 5 times with Milli-Q to obtain a final HNO_3 concentration of approximately 3.6% v/v. Platinum content was analyzed on an ICP-MS Perkin Elmer Elan 6000 series instrument at the Centres Científics i Tecnològics of the Universitat de Barcelona. The solvent used for all ICP-MS experiments was Milli-Q water with 1% HNO_3. The platinum standard (High-Purity Standards, 1000 µg/mL $\pm$ 5 µg/mL in 5% HNO_3) was diluted with 1% HNO_3 to 20 ppb. Platinum standards were freshly prepared in Milli-Q water with 1% HNO_3 before each experiment. The concentrations used for the calibration curve were in all cases 0, 0.2, 0.4, 1, and 2 ppb. The isotope detected was ^{196}Pt and readings were made in triplicate. Rhodium was added as an internal standard at a concentration of 10 ppb in all samples.

1.9. Statistical analysis.

The statistical analysis was performed with the SPSS statistical software for Windows (version 15.0; SPSS Inc., Chicago, IL, USA). Quantitative variables were expressed as mean and standard desviation (SD).

2. Characterization of Pt-c(RGDfK) conjugate (3).

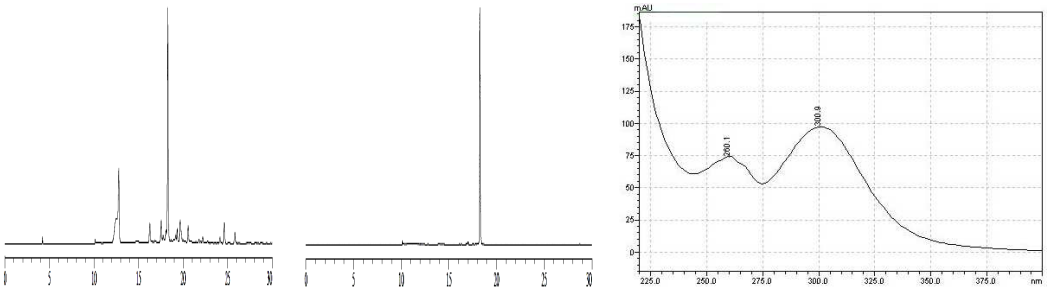

Fig. S1 Reversed-phase HPLC traces for Pt-c(RGDfK) conjugate (**3**): reaction crude (left) and purified (center), and UV-Vis spectrum of the compound in ACN/H_2O solvent (right).

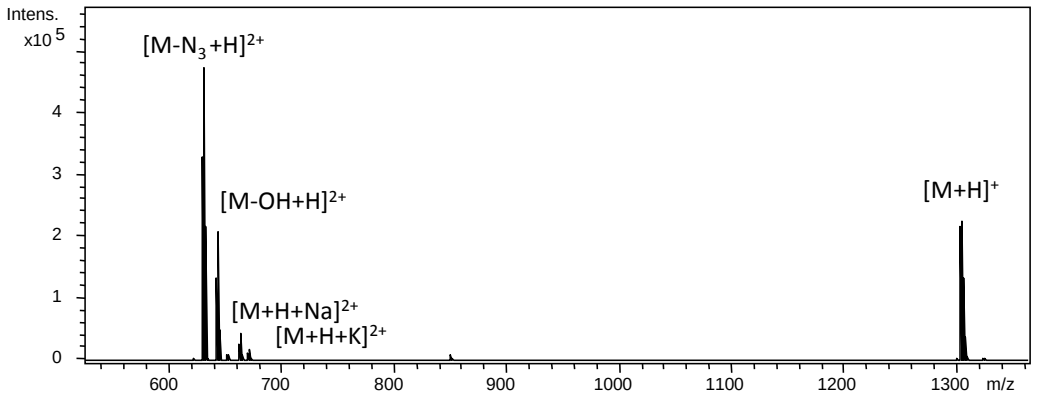

Fig. S2 High-resolution ESI MS of conjugate **3**.

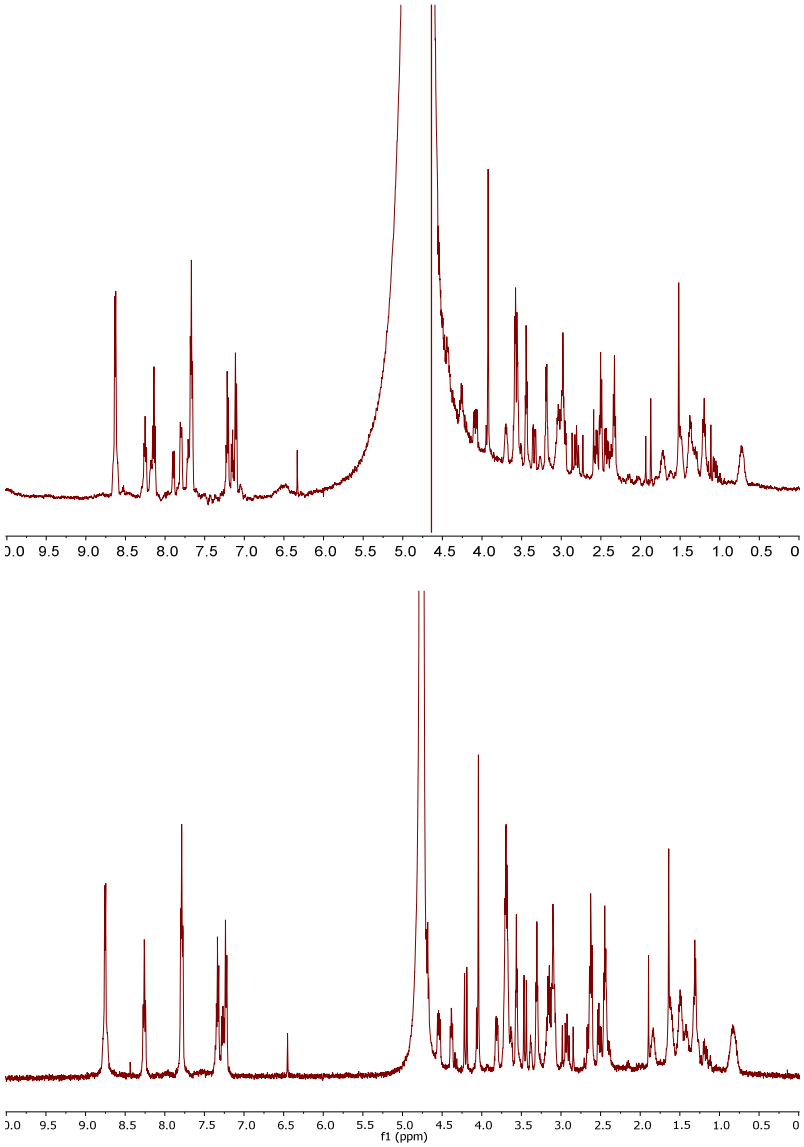

Fig. S3. 500 MHz ^{1}H NMR spectra of conjugate **3** in H_2O/D_2O 9:1 v/v (top) and in D_2O (bottom).

3. Photoactivation of conjugate 3.

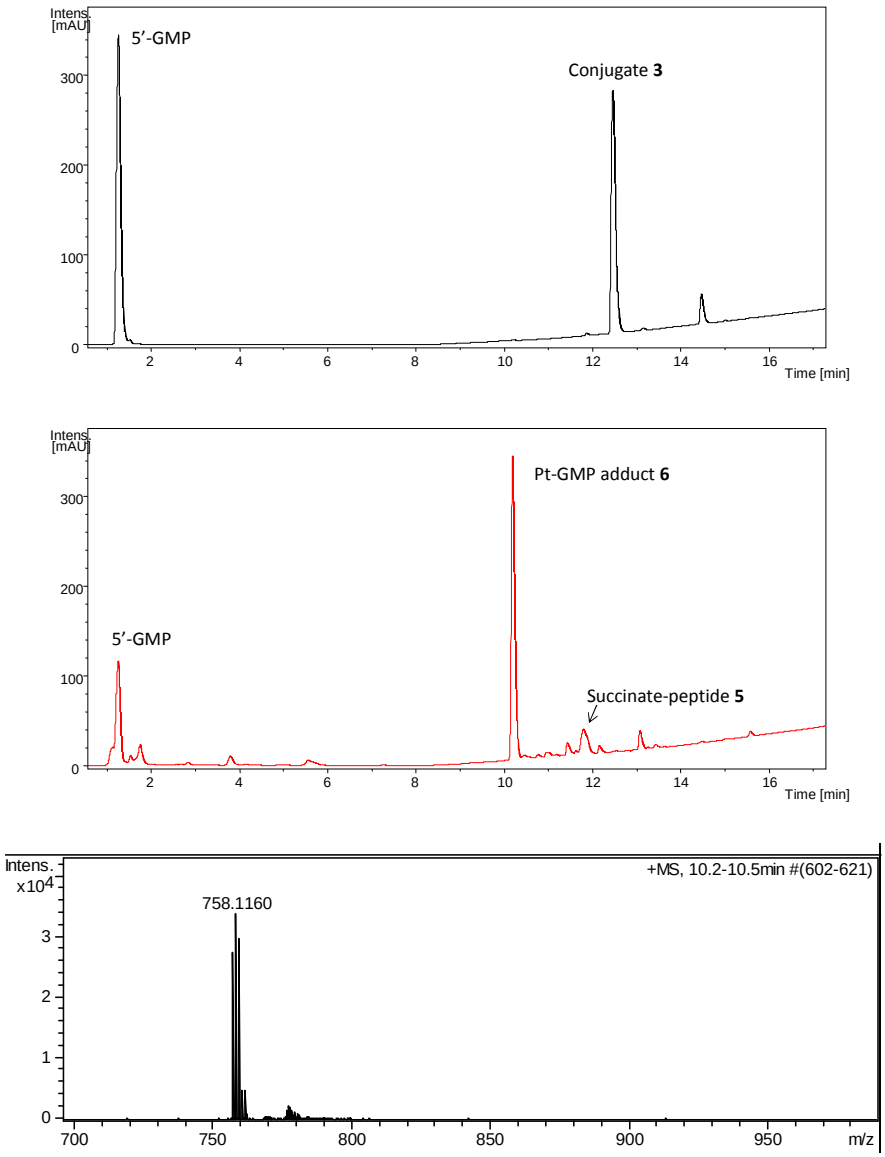

Fig. S4 Reversed-phase HPLC traces for the reaction between 5´-GMP and conjugate **3**: t= 0 (top) and after irradiation with blue light (λ_{irr}= 420 nm, 11 mW cm^{-2}, 45 min, 37ºC) (center). The sample was irradiated using the LZC-ICH2 photoreactor equipped with 420 nm lamps (Luzchem). High-resolution ESI MS of the Pt-GMP adduct **5** (bottom).

4. Cellular uptake of the fluorescein-labelled peptide.

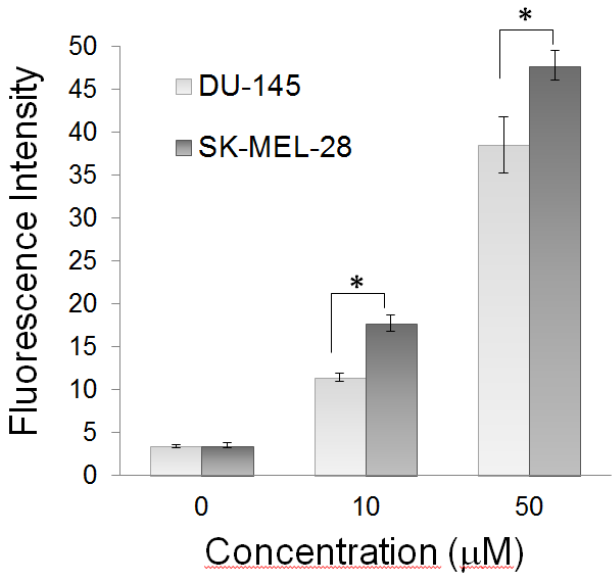

Fig. S5 Intracellular delivery efficiency of Fluo-c(RGDfK) (**7**) in SK-MEL-28 and DU-145 cells. Cells were incubated for 1 h with the peptide at 10 and 50 μM or with medium alone (0 μM) as a control. The fluorescence intensity of the cells, corresponding to the intracellular uptake of the peptides, was determined by flow cytometry. Each column in the graphs represents the mean fluorescence intensity of three independent experiments ± SD. * indicates statistically-significant differences ($P < 0.05$).

5. Cytotoxicity plots

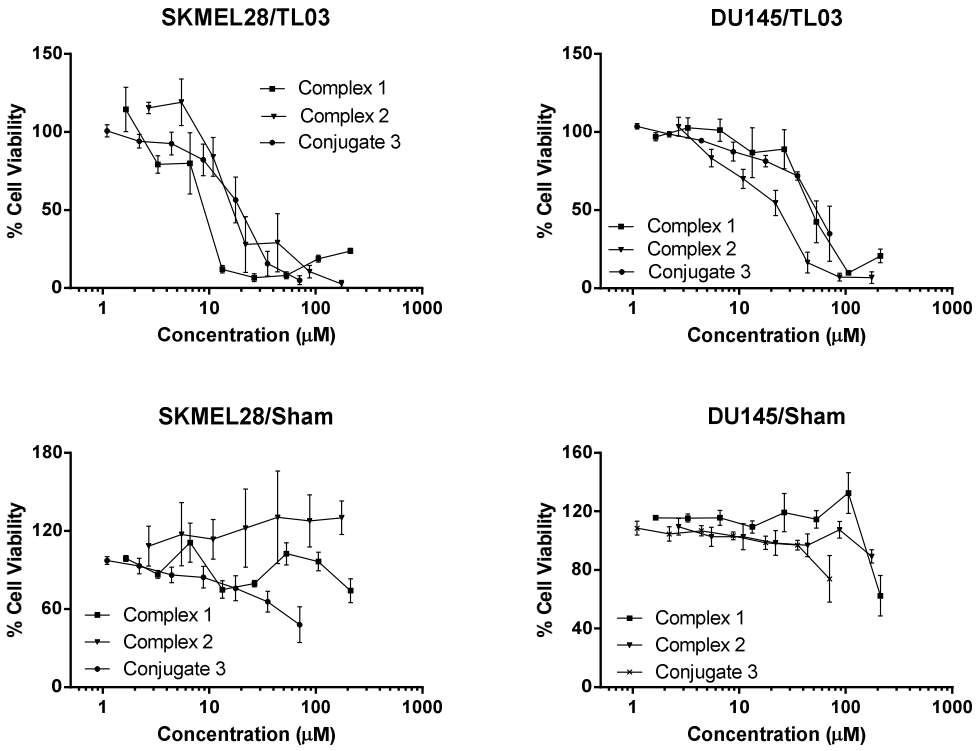

Fig. S6 Cytotoxicity plots with 5 J/cm^2 TL03 irradiation or with sham irradiation. Left hand panel: SK-MEL-28. Right hand panel: DU-145.

Chapter II: Expanding the scope of applications of dicyanocoumarin-based caging groups: from simple caged models to photocontrolled targeted drug delivery strategies

.

.

7. Publication B: Sequential Uncaging with Green Light can be Achieved by Fine-Tuning the Structure of a Dicyanocoumarin Chromophore (*ChemistryOpen*, **2017**, *6*, 375-384)

ChemPubSoc Europe

DOI: 10.1002/open.201700067

Open Access ChemistryOPEN Full Papers

Sequential Uncaging with Green Light can be Achieved by Fine-Tuning the Structure of a Dicyanocoumarin Chromophore

Albert Gandioso,[a] Marta Palau,[a] Alba Nin-Hill,[a, d] Ivanna Melnyk,[a] Carme Rovira,[a, b, d] Santi Nonell,[c] Dolores Velasco,[a, e] Jaume García-Amorós,[a] and Vicente Marchán*[a]

We report the synthesis and photochemical properties of a series of dicyanocoumarinylmethyl (DEAdcCM)- and dicyanocoumarinylethyl (DEAdcCE)-based photocages of carboxylic acids and amines with absorption maximum around 500 nm. Photolysis studies with green light have demonstrated that the structure of the coumarin chromophore as well as the nature of the leaving group and the type of bond to be photocleaved (ester or carbamate) have a strong influence on the rate and efficiency of the uncaging process. These experimental observations were also supported by DFT calculations. Such differences in deprotection kinetics have been exploited to sequentially photolyze two dicyanocoumarin-caged model compounds (e.g., benzoic acid and ethylamine), and open the way to increasing the number of functional levels that can be addressed with light in a single system, particularly when combining dicyanocoumarin caging groups with other photocleavable protecting groups, which remain intact under green light irradiation.

1. Introduction

Light is an excellent non-invasive stimulus for controlling the outcome of molecular processes with high spatiotemporal precision and without causing contamination of the sample.[1] Owing to these extraordinary properties and to the high versatility and efficiency of light, the use of photocleavable protecting groups (PPGs; also commonly referred to as caging groups) have found widespread applications in several fields, from organic synthesis to materials science.[2] In recent years, an exquisite control of complex biological processes has also been achieved by using caged analogs of bioactive compounds (for example, peptides, proteins, oligonucleotides, neurotransmitters, antibiotics, agrochemicals),[3] which can be prepared by modifying an essential functionality with the appropriate PPG. Therefore, activation of the resulting caged compound requires irradiation with light of the appropriate wavelength and intensity to trigger the unmasking of such functionality and, for instance, the recovery of the biological activity of the parent compound.

Among the large number of PPGs reported to date,[2] coumarin derivatives fulfill some of the criteria for an ideal caging group: they are relatively easy to synthesize from commercially available precursors and amenable to structural modifications both to facilitate the attachment of the compound to be caged through different types of bonds (for example, ester, amide, carbamate, or carbonate) and to improve their photophysical and photochemical properties. The latter are important issues as most reported caging groups require UV irradiation for photoactivation, which is toxic and has a poor capacity of penetration in biological tissues. Among the coumarin-based PPGs described to date, those possessing an *N*,*N*-dialkylamino group at position 7 have larger molar extinction coefficients at longer wavelengths than their analogs with hydroxy or methoxy substituents at that position and exhibit moderate to high photochemical quantum yields. Moreover, the replacement of such *N*,*N*-dialkyamino substituents at the 7-position by azetidine, aziridine, or monoalkylated cyclic amines can be used to improve the photophysical properties of coumarin-based fluorophores.[4] Recently, the modification of the carbonyl group of the lactone in the *N*,*N*-diethylamino(coumarin 4-yl)-methyl platform has been proved to be a valuable way to fur-

[a] *A. Gandioso, M. Palau, A. Nin-Hill, I. Melnyk, Dr. C. Rovira, Dr. D. Velasco, Dr. J. García-Amorós, Dr. V. Marchán*
Departament de Química Inorgànica i Orgànica, Secció de Química Orgànica, IBUB (AG, VM)
Universitat de Barcelona, 08028 Barcelona (Spain)
E-mail: vmarchan@ub.edu

[b] *Dr. C. Rovira*
Institució Catalana de Recerca i Estudis Avançats (ICREA)
08010 Barcelona (Spain)

[c] *Dr. S. Nonell*
Institut Químic de Sarrià
Universitat Ramon Llull, 08017 Barcelona (Spain)

[d] *A. Nin-Hill, Dr. C. Rovira*
Institut de Química Teòrica i Computacional (IQTCUB)
Universitat de Barcelona, 08028 Barcelona (Spain)

[e] *Dr. D. Velasco*
Institut de Nanociència i Nanotecnologia (IN2UB)
Universitat de Barcelona, 08028 Barcelona (Spain)

Supporting Information and the ORCID identification number(s) for the author(s) of this article can be found under https://doi.org/10.1002/open.201700067.

ther shift the wavelength of maximum absorption, which can be exploited to trigger uncaging with blue, cyan, or green light.[5] Indeed, dicyanomethylenecoumarin derivatives, which are obtained by conjugating two nitrile groups through position 2 of the coumarin moiety, are particularly attractive as they exhibit a maximum absorption around 500 nm in the 7-diethylamino series (487 nm in a coumarin derivative containing a benzyloxymethyl group at position 4 described by Jullien and co-workers[5c] and 475 nm when this position was occupied by a methyl as described by Granberg and colleagues[6]). Uncaging of dicyanocoumarin-caged cyclic morpholino oligonucleotides has been exploited in the context of gene silencing by Deiters' and Chen's group,[5a] and very recently we have described the synthesis of a dicyanocoumarin-caged RGD peptide for photocontrolled-targeted drug delivery.[5e] Nevertheless, such modifications of the lactone in the *N*,*N*-diethylamino(coumarin 4-yl)methyl platform usually led to a significant reduction of the uncaging quantum yield compared with the parent oxygenated coumarin or its thionated analog,[5c] which could suppose a limitation for future applications of dicyanocoumarins as PPGs.

The mechanism of photocleavage of coumarinylmethyl esters has been well established for the classical 7-(*N*,*N*-diethylamino)coumarin-4-yl)methyl (DEACM) caging group (R = H; see Scheme 1 A).[7] Upon electronic excitation, a solvent-assisted photoheterolytic bond cleavage produces the free carboxylic acid and the corresponding coumarinylmethyl alcohol, which is generated by reaction of the cationic intermediate with water followed by a fast deprotonation. Previous studies have demonstrated that stabilization of this intermediate (by incorporation of electron-donating substituents at the coumarin skeleton) and of the released carboxylate (by decreasing its basicity) have a positive effect on the photocleavage of coumarinylmethyl esters.[7] Recently, del Campo and collaborators have investigated the incorporation of a ethyl group at position 4 of the DEACM moiety (R = Me, see Scheme 1 A) for increasing the stability of the corresponding caged aspartic acid monomer during Fmoc-*t*Bu solid-phase peptide synthesis.[8] Despite the fact that this new caging group, 7-(*N*,*N*-diethylamino)coumarin-4-yl)ethyl (DEACE), generates a secondary cationic intermediate upon the photo S_N1 reaction of the corresponding DEACE-protected Asp derivative, no significant differences were found with respect to the DEACM analog regarding the photochemical properties, particularly the uncaging quantum yield at 360 nm. By contrast, incorporation of this modification in dicyanomethylene-coumarin-caged Asp monomers led to a faster uncaging process with green light (505 nm), which was attributed to the higher stability of the carbocation intermediate.[5e]

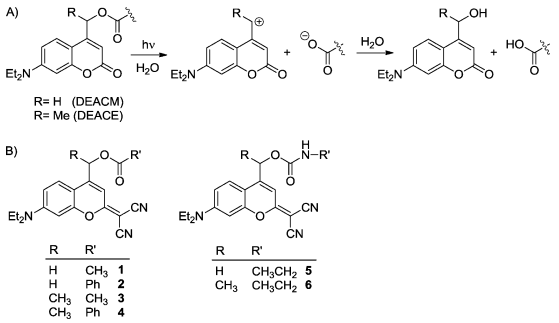

Scheme 1. General mechanism of the photolysis of a DEACM- or DEACE-caged carboxylic acid (A) and structure of the DEAdcCM- and DEAdcCE-caged model compounds synthesized in this work (B).

Taking into account the potential of dicyanocoumarin derivatives as PPGs, in this work we have synthesized a series of *N*,*N*-diethylamino-dicyanocoumarinylmethyl (DEAdcCM)- and dicyanocoumarinylethyl (DEAdcCE)-caged model compounds (**1**–**6**, Scheme 1 B) with the aim of studying their photophysical and photochemical properties, particularly how uncaging is influenced both by the chemical structure of the coumarin chromophore (R = H or Me) and by the nature of the leaving group (that is, aliphatic or aromatic carboxylic acid or amine). Photolysis studies with the corresponding caged model compounds upon irradiation with green light (505 nm) as well as DFT computational calculations have shown that both the structure of the dicyanocoumarin caging group and of the leaving group have a strong influence on the rate and efficiency of the photolysis process. Interestingly, by selecting the appropriate combination of dicyanocoumarin-based caging groups, we have demonstrated that carboxylic acid and amine functionalities can be sequentially released from the corresponding caged compounds by irradiation at 505 nm.

2. Results and Discussion

2.1. Synthesis of DEAdcCM- and DEAdcCE-Caged Model Compounds

As shown in Scheme 2, the synthesis of the DEAdcCM-caged model compounds (**1**, **2**, and **5**) was planned from 4-(acetoxymethyl)-7-(*N*,*N*-diethylamino)-2-thiocoumarin (**11**),[5c] a key intermediate that can be prepared from the commercially available precursor **7** in four steps.[5c,e] Condensation of the thionated coumarin with malononitrile in the presence of triethylamine and silver nitrate afforded 4-(acetoxymethyl)-2-(dicyanomethylene)-7-(*N*,*N*-diethylamino)-coumarin (**1**) in 93% yield after column chromatography. Hydrolysis of the acetyl group with HCl followed by esterification with benzoic acid afforded coumarin derivative **2**. Reaction of the alcohol intermediate **12** with ethyl isocyanate in the presence of triethylamine afforded compound **5** as a model for the protection of primary amines with DEAdcCM through a carbamate linkage. All the compounds were fully characterized by ESI mass spectrometry and ^1H and ^{13}C NMR spectroscopy.

The synthesis of the DEAdcCE-caged model compounds (**3**, **4**, and **6**) is summarized in Scheme 3. First, reaction of the aldehyde **8** with CH_3MgCl in anhydrous THF at low temperature (−78 °C) afforded coumarin alcohol **13** as a racemic mixture.[5e] After esterification with benzoic acid followed by thionation with Lawesson's reagent and condensation with malononitrile,

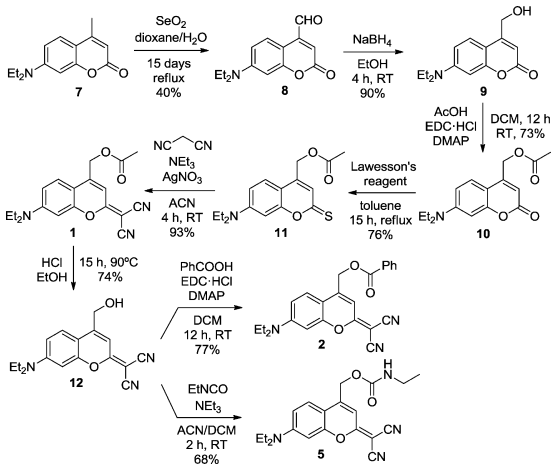

Scheme 2. Synthesis of dicyanocoumarinylmethyl-caged compounds (**1**, **2**, and **5**).

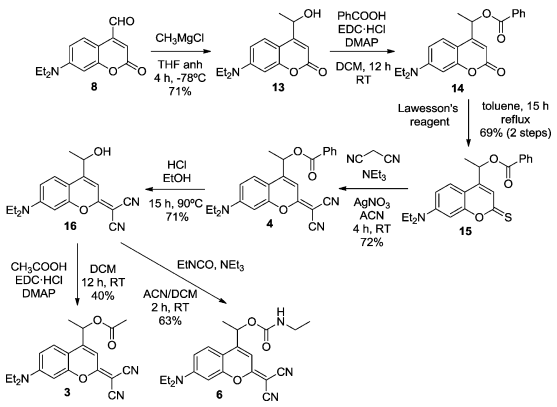

Scheme 3. Synthesis of dicyanocoumarinylethyl-caged compounds (**3**, **4**, and **6**).

the DEAdcCE-caged benzoic acid **4** was obtained. Hydrolysis of **4** followed by esterification with acetic acid or by reaction with ethyl isocyanate, afforded the two remaining DEAdcCE-caged model compounds (**3** and **6**, respectively).

2.2. Absorption and Emission Properties of Dicyanocoumarin Derivatives

The photophysical characterization of the dicyanocoumarin-caged model compounds (**1**–**6**) was carried out in a degassed 1:1 (v/v) mixture of Tris buffer (20 mM, pH 7.5) and MeCN. The UV/Vis absorption and emission spectra of the compounds are shown in Figure 1, and their photophysical properties are reported in Table 1. The maximum absorption wavelength, the shape of the absorption curve, and the molar extinction coefficients of the ester (**1**–**4**) and carbamate (**5**–**6**) derivatives were very similar, and consistent with the values previously reported for **2**.[5c] As shown in Table 1, esterification either with benzoic acid or with acetic acid caused a slight redshift (about 5–11 nm) with respect to the parent coumarin alcohol derivatives (**12** or **16**), and in all cases the presence of the methyl group on the coumarin skeleton caused an additional redshift compared with non-methylated analogs (compare **1** and **3**). A similar bathochromic effect was observed for the emission wavelength of the caged compounds upon excitation at 460 nm when compared with the corresponding coumarin alcohol de-

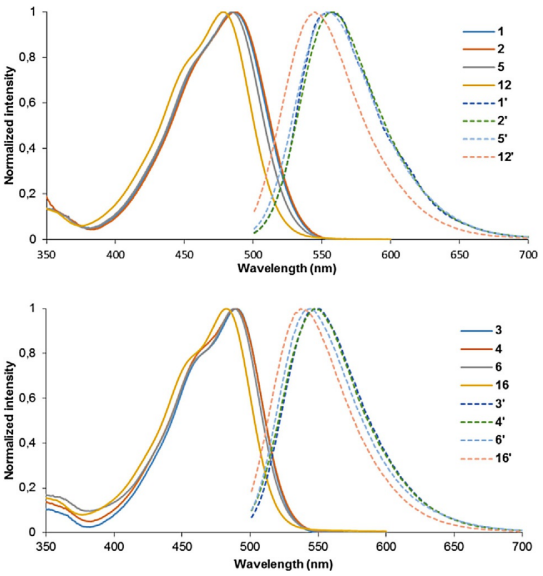

Figure 1. Comparison of the absorption (solid lines) and fluorescence (dotted lines) spectra of DEAdcCM- (top) and DEAdcCE-caged (bottom) model compounds with those of the corresponding dicyanocoumarin alcohols (**12** and **16**, respectively). Solvent: Tris buffer (20 mM, pH 7.5)/MeCN 1:1 (v/v).

Table 1. Photophysical parameters for dicyanocoumarin-caged model compounds (**1**–**6**) and for the corresponding photoreleased coumarin alcohol derivatives (**12** and **16**).[a]

Compound[a]	Absorption		Emission		
	λ_{max} [nm][b]	$\varepsilon(\lambda_{max})$ [$mM^{-1}cm^{-1}$][c]	λ_{Em} [nm][d]	$\Delta\nu$ [cm^{-1}][e]	ϕ_{Em}[f]
1	486	30.4	556	2633	0.17
2	487	32.5	558	2613	0.15
3	489	31.2	549	2193	0.11
4	489	32.0	548	2202	0.11
5	485	32.8	555	2600	0.15
6	488	33.0	544	2067	0.13
12	478	32.5	545	2572	0.17
16	482	33.0	539	2194	0.14

[a] Absorption and emission spectra were recorded in a 1:1 (v/v) mixture of Tris buffer (20 mM, pH 7.5) and MeCN at 25 °C. [b] Wavelength of the absorption maximum. [c] Molar absorption coefficient at λ_{max}. [d] Wavelength of the emission maximum upon excitation at 460 nm. [e] Stokes' shift. [f] Fluorescence quantum yield.

Table 2. Photochemical properties of compounds **1**–**6**.[a]

Caged compound	R	Leaving compound	Uncaging % Caged compound at irradiation time 2 min	5 min	10 min	20 min	k_u [min^{-1}]	ε(505 nm) [mM^{-1}cm^{-1}]	$10^2\times\phi_{Ph}$[b]	ε(505 nm)$\times\phi_{Ph}$ [M^{-1}cm^{-1}]
1	H	AcOH	90	62	22	0	0.125	21.4	0.09 ± 0.03	19
2	H	PhCOOH	55	20	0	0	0.314	23.4	0.15 ± 0.01	34
3	Me	AcOH	28	2	0	0	0.644	22.0	0.28 ± 0.03	62
4	Me	PhCOOH	15	0	0	0	0.948	22.6	0.33 ± 0.00	75
5	H	$EtNH_2$	97	90	79	45	0.036	19.9	0.03 ± 0.01	5
6	Me	$EtNH_2$	71	36	7	0	0.208	21.3	0.12 ± 0.02	25

[a] Data presented: Percent of the starting caged compound at each irradiation time, uncaging first-order rate constant, molar extinction coefficient at the irradiation wavelength, uncaging quantum yield, and uncaging efficiency at 505 nm. [b] Results are the mean ± SDs from two independent experiments.

rivatives. However, the emission maximum was blueshifted in the DEAdcCE compounds with respect to the DEAdcCM counterparts (compare λ_{em} for **1** and **3**). The relative fluorescence quantum yields were calculated by using fluorescein as the standard ($\phi_{Em}=0.92$ in 0.1 M NaOH in water). All the compounds exhibited good quantum yields ($0.11<\phi_F<0.17$) and Stokes' shifts around 2600 cm^{-1} for DEAdcCM derivatives and of 2000–2200 cm^{-1} for the DEAdcCM analogs.

2.3. Photolysis Studies of Dicyanocoumarin-Caged Compounds

From the comparison of the molar extinction coefficients of DEAdcCM- and DEAdcCE-caged model compounds at their respective λ_{max} and at 505 nm (for example, for **1**: $\varepsilon=$ 30.4 mM^{-1}cm^{-1} and 21.4 mM^{-1}cm^{-1}, respectively; see Table 1 and Table 2), we decided to explore the use of green light to carry out the photoactivation studies. Green light is more suitable for biological applications than UV or blue light owing to its reduced photocytotoxicity[9] and deeper optical penetration in tissues.[10] A 505 nm LED source was used for irradiation of solutions of compounds **1**–**6** in a 1:1 (v/v) mixture of Tris buffer (20 mM, pH 7.5) and MeCN at 37 °C, and the course of the uncaging process was monitored by reversed-phase HPLC-ESI MS (see the Experimental Section for further details). As shown in Figure 2, the concentration of all the compounds decreased gradually with time upon irradiation with green light. In the case of DEAdcCM-caged compounds, coumarin alcohol **12** was released as the main photolytic product (Scheme 4). Conversely, photoactivation of DEAdcCE-caged compounds gave coumarin alcohol **16** together with other minor photolytic byproducts, particularly vinyl coumarin **17** (Scheme 4). The formation of this alkene can be explained by a β-elimination reaction from the secondary carbocation intermediate generated upon photoheterolysis of the ester bond (see Scheme 1).

Overall, the results from the photolysis experiments revealed the influence of 1) the structure of the dicyanocoumarin caging group, 2) the nature of the leaving group, and 3) the type of bond photocleaved (ester or carbamate), on the time necessary to release the carboxylic acid or the amine from the corresponding caged compounds. First, it is worth noting that photolysis of DEAdcCE-caged compounds was much faster than that of DEAdcCM (see Figure 2 and Table 2); this result

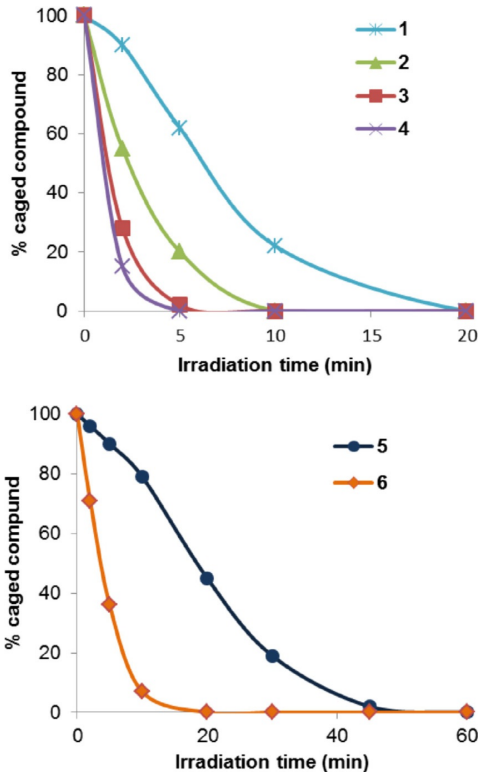

Figure 2. Plot of the temporal evolution of the amount of caged compounds **1**–**4** (top) and **5**–**6** (bottom) in a 1:1 (v/v) mixture of Tris buffer (20 mM, pH 7.5) and MeCN at 37 °C. Irradiation was performed at 505 nm with continuous stirring.

can be attributed to the different stability of the carbocation intermediates (primary or secondary) generated during photoheterolysis of the ester or carbamate bonds in the dicyanocoumarin-caged model compounds. For example, the release of acetic acid from **3** was almost complete after 5 min of irradiation whereas it required 20 min to completely uncage compound **1** ($k_u=0.125$ min^{-1} for **1** vs. $k_u=0.644$ min^{-1} for **3**). Similar trends were found when comparing **2** and **4**, and **5** and **6** (Table 2), in agreement with previous observations with (cou-

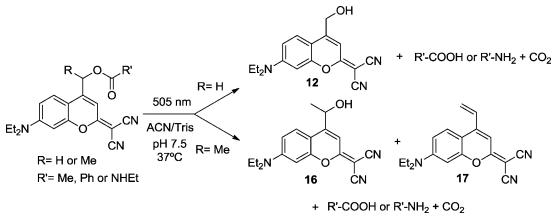

Scheme 4. Photolysis of DEAdcCM- and DEAdcCE-caged model compounds.

marin-4-yl)methyl esters (DEACM).[7] For these compounds, the rate of the overall uncaging process was found to be influenced by the rate constant of the initial heterolytic bond cleavage (see Scheme 1 A), which was higher when the primary coumarinyl carbocation intermediate was stabilized though the incorporation of substituents with strong electron-donating ability (alkoxy or dialkylamino).[7] In our case, the same tendency was observed by shifting the nature of the carbocation intermediate from primary to secondary through the incorporation of a methyl group in the coumarin moiety in a position adjacent to the bond to be photocleaved.

Second, the photocleavage process was also faster with good leaving groups on the molecule to be caged (compare benzoate vs. acetate in Table 2). Again, this can be attributed to the stabilization of the second component of the carbocation–carboxylate ion pair and, consequently, to an increase of the rate constant of the first bond cleavage.[7] As expected, the best combination in terms of uncaging rate ($k_u = 0.948\ min^{-1}$) was obtained for compound **4** as the release of benzoate is accompanied by the formation of a secondary carbocation intermediate. Third, the photolysis of carbamate-coumarin caged amines (**5** and **6**) was much slower than that of the ester analogs (**1** and **2**, respectively), which can be attributed to the lower leaving-group ability of the carbamic acid anion compared with carboxylate. This tendency has been found in other carbonate-, carbamate-, and thiocarbonate-coumarin caged compounds in which the final uncaged product is released after thermal decarboxylation of the intermediate.[11] Nevertheless, our results point out that the introduction of an additional methyl group in the skeleton of other coumarin derivatives could be used to increase the deprotection rate of carbamate-caged amines as well as that of carbonate-caged alcohols and phenols, where photolysis is usually much slower compared with uncaging of ester-caged carboxylic acids.

As shown in Table 2, the uncaging quantum yield (ϕ_{Ph}) of the caged model compounds was also determined upon irradiation at 505 nm (see the Experimental Section for further details). The product of the extinction coefficient at the irradiation wavelength and the quantum yield can be considered as an efficiency parameter of the process ($\varepsilon \times \phi_{Phot}$), for quantifying the uncaging process rate as a function of the photolysis time.[2b,12] In good agreement with results from photolysis studies, the quantum yields for DEAdcCE derivatives were higher than those of the DEAdcCM analogs (compare **1** and **3**, and **2** and **4**), resulting in a high product $\varepsilon \times \phi_{Phot}$.

2.4. Computational Studies

Having stablished how the photolysis rate of the dicyanocoumarin-caged model compounds is influenced by both the introduction of a methyl group in the coumarin moiety next to the bond to be photocleaved and the nature of the leaving group, we decided to get insight into these experimental observations from a theoretical point of view. DFT calculations were carried out with the Gaussian 09 (G09) software package (see the Experimental Section for further details). As previously stated, photocleavage of coumarin-caged compounds proceeds through a photo S_N1 mechanism and the stability of the two components of the resulting ion pair (coumarinyl carbocation and carboxylate) has a strong influence on the rate of the first photocleavage step and, consequently, on the overall rate of the uncaging process.[7] For this reason, we calculated the energy differences between the caged compounds (**1**–**4**) and their corresponding intermediate species. Consistent with the experimental data, DFT calculations predicted that photolysis of DEAdcCE-caged compounds (**3**) gives a small stabilization of the ion pair intermediate ($\Delta E = 1.2\ kcal\,mol^{-1}$) compared with the DEAdcCM (**1**) analogs with the same leaving group (Figure 3, top panel). A similar trend was obtained when comparing **2** and **4** (see Figure S11 in the Supporting Information). On the other hand, the calculations also supported the experimental observations regarding the nature of the leaving group: stabilization of the ion pair generated upon cleavage of

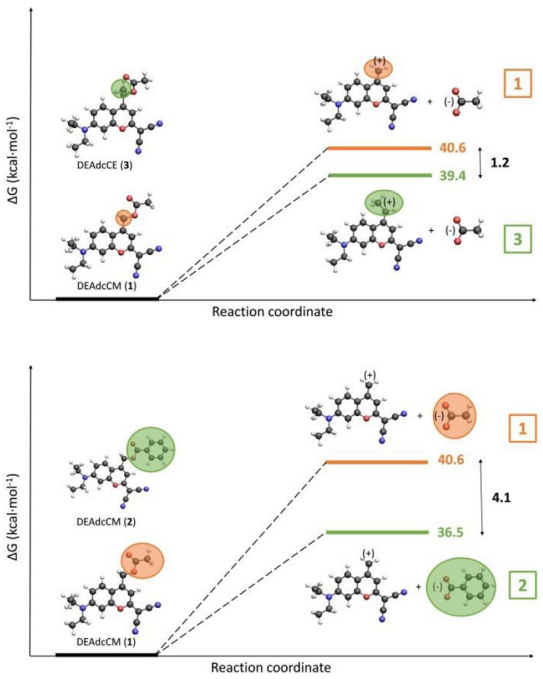

Figure 3. Free energy differences for the transformation of dicyanocoumarin-caged compounds in their respective intermediates (primary or secondary dicyanocoumarinyl carbocation + acetate or benzoate): **1** vs. **3** (top) and **1** vs. **2** (bottom).

the ester bond in **2** was about 4 kcal mol^{-1} higher compared with compound **1** (Figure 3, bottom panel), which agrees with the increased acidity of benzoic acid (pK_a = 4.2) compared with acetic acid (pK_a = 4.76). A similar value was obtained when comparing **3** and **4** (Figure S11 in the Supporting Information).

2.5. Sequential Uncaging Studies

The kinetics of a photodeprotection process depend both on the spectral properties of the PPG (λ_{max} and ε) and on the photolysis quantum yield (ϕ_{Ph}). As found by us and others, the reaction quantum yield can be fine-tuned through the modification of several parameters, including the structure of the chromophore, the nature of the connecting atom in the molecule to be caged, the type of photocleavable bond (ester, carbamate, etc.), and the basicity of the leaving group (aromatic or aliphatic carboxylate).[2b, 3n, 13] With the aim of controlling with light multiple functionalities in a single system, two main approaches have been explored to selectively address several uncaging processes. The first approach relies on using a set of different caging groups, which can be sequentially photolyzed at different wavelengths of light; this method requires the use of two or more PPGs with significantly different spectral properties (λ_{max}, ε, and ϕ_{Ph}). A second approach is well exemplified by the work of Heckel and collaborators,[3n] who demonstrated that selective uncaging can be achieved by irradiation at a single wavelength of light by exploiting the differences in quantum yield (and for instance of deprotection kinetics) of the same PPG when attached to the molecule to be caged through a different connecting atom.

On the basis of the photolysis studies and of the differences in the uncaging quantum yield between DEAdcCM- and DEAdcCE-caged compounds (Table 2), we wondered if sequential uncaging of at least two dicyanocoumarin-protected functionalities in the same reaction mixture could be achieved by irradiating with the same green light source. First, an equimolar mixture of compound **1** (DEAdcCM-caged acetic acid) and **4** (DEAdcCE-caged benzoic acid) as dicyanocoumarin-caged models of aliphatic or aromatic carboxylic acids, respectively, in the presence of uracil as an internal standard, was irradiated at 505 nm. Unfortunately, HPLC analysis revealed (Figure S12 in the Supporting Information) that despite the fact that **4** was completely uncaged in 4 min, about 40% of **1** was also deprotected. However, irradiation at 505 nm of a mixture of **4** (DEAdcCE-caged benzoic acid) and **5** (DEAdcCM-caged ethylamine) demonstrated that a carboxylic acid and an amine can be sequentially uncaged upon irradiation with the same wavelength of light by exploiting the different deprotection kinetics provided by the two dicyanocoumarin caging groups when connected to the caged functionalities through ester or carbamate linkages: **4** was completely uncaged in 3 min leaving >90% of **5** intact (Figure S13 in the Supporting Information). Such as promising results, led us to include compound **10** (see Scheme 2) as a model for the protection of a carboxylic acid with the classical DEACM coumarin, whose absorption at 505 nm is negligible. As shown in Figure 4 and Figure S14 (Supporting Information), upon irradiation at 505 nm of a mixture of **4**, **5**, and **10**, dicyanocoumarin-caged compounds (**4** and **5**) were sequentially uncaged whereas DEACM-caged acetic acid (**10**) remained intact, even after 1 h irradiating at 505 nm (Scheme 5). Hence, the combination of two structurally related dicyanocoumarin caging groups (DEAdcCM and DEAdcCE) with other PPGs with distinct absorption properties (for example, removable with UV or blue light) allows us to increase the number of levels of selectivity that can be addressed with light.

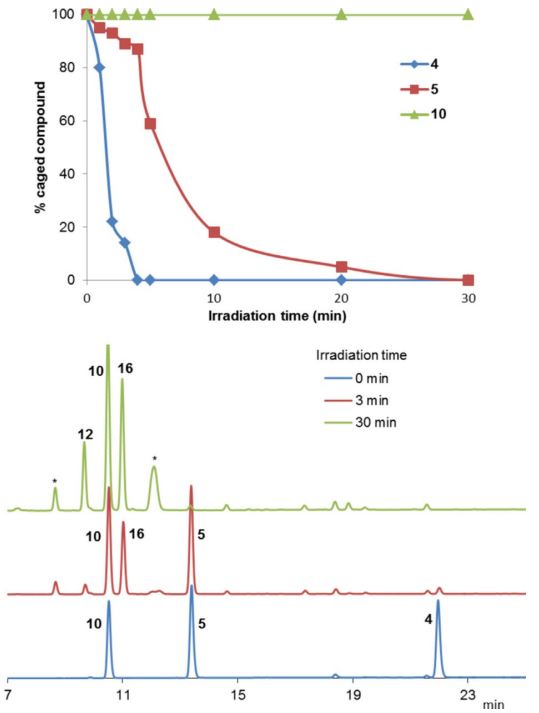

Figure 4. Plot of the temporal evolution of the amount of caged compounds **4**, **5**, and **10** (top) and HPLC chromatograms at a different time (bottom) after irradiation at 505 nm in a 1:1 (v/v) mixture of Tris buffer (20 mM, pH 7.5) and MeCN at 37 °C. *Unidentified coumarin side products.

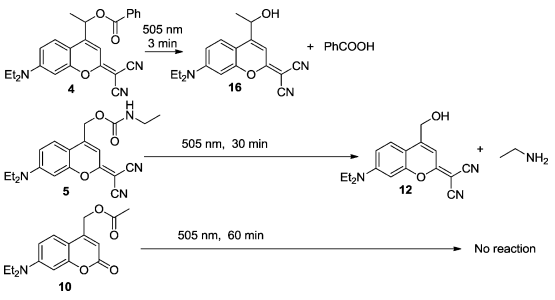

Scheme 5. Schematic representation of the sequential uncaging with green light of two dicyanocoumarin-caged compounds (**4** and **5**) in the presence of DEACM-caged acetic acid (**10**).

3. Conclusions

We have described the synthesis and photophysical properties of novel DEAdcCM- and DEAdcCE-based photocleavable protecting groups and their suitability for caging carboxylic acids and amines through ester and carbamate bonds, respectively. Such chromophores have a maximum absorption around 500 nm, which facilitates uncaging with the biologically compatible green light, which is non-toxic and penetrates deeper into tissues than UV or blue light. Photolysis studies of the corresponding dicyanocoumarin-caged model compounds at 505 nm and DFT calculations have demonstrated that the structure of the coumarin chromophore as well as the nature of the leaving group strongly influence the rate and efficiency of the uncaging process, which has been exploited to sequentially photolyze two dicyanocoumarin-caged model compounds (benzoic acid and ethylamine) in the presence of DEACM-caged acetic acid. Such significant differences in the deprotection kinetics open the way to increasing the number of functional levels that can be addressed with light in a single system, particularly when combining dicyanocoumarin caging groups with other PPGs that remain stable upon irradiation at 505 nm. Finally, our findings on the impact of the stabilization of the carbocation intermediate generated during photoheterolysis of ester or carbamate bonds in dicyanocoumarin-based photocages could be applied to other coumarin-based systems to improve their photochemical properties. Overall, this would increase the potential of known coumarin-based caging groups for designing wavelength-selective systems in which multiple functionalities can be independently addressed by the different wavelengths of light. Work is in progress to extend this approach to other coumarin-based chromophores with improved redshifted properties.

Experimental Section

Materials and Methods

Common chemicals and solvents (HPLC grade or reagent grade quality) were purchased from commercial sources and used without further purification. Aluminium plates coated with a 0.2 mm thick layer of silica gel 60 F_{254} were used for thin-layer chromatography analyses (TLC), whereas flash column chromatography purification was carried out by using silica gel 60 (230–400 mesh). Reversed-phase high-performance liquid chromatography (HPLC) analyses were carried out with a Jupiter Proteo C_{18} column (250× 4.6 mm, 90 Å, 4 μm, flow rate: 1 mL min^{-1}) by using linear gradients of 0.045% trifluoroacetic acid (TFA) in H_2O (A) and 0.036% TFA in MeCN (B). NMR spectra were recorded at 25 °C with a 400 MHz spectrometer by using deuterated solvents. Tetramethylsilane (TMS) was used as an internal reference (0 ppm) for ^{1}H spectra recorded in $CDCl_3$ and the residual signal of the solvent (77.16 ppm) was used for ^{13}C spectra. Chemical shifts are reported in parts per million (ppm) in the δ scale, coupling constants in Hz, and multiplicity as follows: s (singlet), d (doublet), t (triplet), q (quadruplet), qt (quintuplet), m (multiplet), dd (doublet of doublets), td (doublet of triplets), ddd (doublet of doublet of doublets), br (broad signal). Electrospray ionization mass spectra (ESI-MS) were recorded with an instrument equipped with single quadrupole detector coupled to an HPLC, and high-resolution (HR) ESI-MS on a LC/MS-TOF instrument.

Synthesis of DEAdcCM-Caged Model Compounds

Compound 1: Malononitrile (1.1 g, 16.7 mmol) was added to a solution of **11** (1.01 g, 3.32 mmol; see the Supporting Information) in anhydrous MeCN (100 mL). After addition of NEt_3 (9.1 mL, 65.5 mmol) under Ar atmosphere and protection from light, the reaction mixture, which acquired an intense red color, was stirred for 20 min. Then, silver nitrate (1.13 g, 6.66 mmol) was added and stirred at room temperature for 4 h under an Ar atmosphere and protection from light. Finally, the solvent was removed under vacuum and the crude was purified by column chromatography (silica gel, 50–100% CH_2Cl_2 in hexanes, then from CH_2Cl_2 to 0.5% MeOH in CH_2Cl_2), to give 1.04 g (93% yield) of an orange solid. Characterization: TLC: R_f (2.5% MeOH in CH_2Cl_2): 0.60. ^{1}H NMR (400 MHz, $CDCl_3$): δ = 7.33 (1H, d, H5, J = 9.2 Hz), 6.75 (1H, br s, H3), 6.66 (1H, dd, H6, J = 9.2, 2.4 Hz), 6.60 (1H, d, H8, J = 2.4 Hz), 5.24 (2H, d, CH_2, J = 1.0 Hz), 3.45 (4H, q, CH_2 NEt_2, J = 7.2 Hz), 2.21 (3H, s, CH_3), 1.24 ppm (6H, t, CH_3 NEt_2, J = 7.2 Hz); ^{13}C NMR (101 MHz, $CDCl_3$): δ = 171.8, 170.2, 155.0, 151.7, 146.1, 124.9, 114.6, 113.8, 110.6, 106.9, 105.9, 97.4, 61.1, 55.5, 45.0, 20.8, 12.4 ppm; HR ESI-MS (positive mode): m/z = 338.1491 (calcd mass for $C_{19}H_{20}N_3O_3$ $[M+H]^+$: 338.1505).

Compound 12: A solution of HCl in 1,4-dioxane (4 M, 1.5 mL, 6 mmol) was added to **1** (0.80 g, 2.37 mmol) in absolute ethanol (60 mL). The reaction mixture was heated at 90 °C for 12 h. Once the reaction was finished, the solvent was removed under reduced pressure and purified by chromatography column (silica gel, 50–100% of CH_2Cl_2 in hexane, then 0–0.8% of MeOH in CH_2Cl_2) to give 0.52 g of a yellow-orange solid (74% yield). Characterization: TLC: R_f (2.5% MeOH in CH_2Cl_2): 0.62; ^{1}H NMR (400 MHz, $CDCl_3$): δ = 7.34 (1H, d, H5, J = 9.2 Hz), 6.93 (1H, br t), 6.65 (1H, dd, H6, J = 9.2, 2.4 Hz), 6.60 (1H, d, H8, J = 2.4 Hz), 4.88 (2H, d, CH_2, J = 5.8 Hz), 3.45 (4H, q, CH_2 NEt_2, J = 7.2 Hz), 2.06 (1H, t, OH, J = 5.8 Hz), 1.23 ppm (6H, t, CH_3 NEt_2, J = 7.2 Hz); ESI-MS (positive mode): m/z = 295.75 (calcd mass for $C_{17}H_{18}N_3O_2$ $[M+H]^+$: 296.14).

Compound 2: 1-Ethyl-3-(3-dimethylaminopropyl)carbodiimide (EDC)·HCl (51 mg, 0.33 mmol), coumarin **12** (75 mg, 0.25 mmol), 4-dimethylaminopyridine (DMAP; 40 mg, 0.33 mmol), and benzoic acid (45 mg, 0.37 mmol) were dissolved in dry CH_2Cl_2 (2.5 mL) at 0 °C under an Ar atmosphere. After 10 min at 0 °C, the reaction mixture was stirred at room temperature for 4 h in the dark and under Ar. After evaporation under reduced pressure and purification by column chromatography (silica gel, CH_2Cl_2), 78 mg of an orange solid were obtained (77% yield). Characterization: TLC: R_f (5% MeOH in CH_2Cl_2): 0.86; ^{1}H NMR (400 MHz, $CDCl_3$): δ = 8.10 (2H, m, Ph), 7.62 (1H, m, Ph), 7.49 (2H, t, Ph, J = 7.6 Hz), 7.43 (1H, d, H5, J = 9.2 Hz), 6.89 (1H, br s, H3), 6.69 (1H, dd, H6, J = 9.2, 2.4 Hz), 6.62 (1H, d, H8, J = 2.4 Hz), 5.47 (2H, d, CH_2, J = 0.8 Hz), 3.46 (4H, q, CH_2 Et, J = 7.2 Hz), 1.24 ppm (6H, t, CH_3 Et, J = 7.2 Hz); ^{13}C NMR (101 MHz, $CDCl_3$): δ = 171.8, 165.8, 155.1, 151.7, 146.0, 133.8, 129.8, 128.9, 128.8, 125.1, 114.5, 113.8, 110.7, 107.1, 106.4, 97.4, 61.7, 55.6, 45.0, 12.4 ppm; HR ESI-MS (positive mode): m/z = 400.1643 (calcd mass for $C_{24}H_{22}N_3O_3$ $[M+H]^+$: 400.1661).

Compound 5: NEt_3 (95 μL, 0.70 mmol) and ethyl isocyanate (107 μL, 1.35 mmol) were added to a solution of **12** (101 mg, 0.34 mmol) in a mixture of dry MeCN (3 mL) and CH_2Cl_2 (1.8 mL) under an Ar atmosphere. Once the reaction was finished (typically

2–3 h according to TLC), the solvent was removed under reduced pressure and purified by chromatography column (silica gel, 0–0.35% of MeOH in CH_2Cl_2) to give 85 mg of an orange solid (68% yield). Characterization: TLC: R_f (2% MeOH in CH_2Cl_2): 0.50; ^{1}H NMR (400 MHz, $CDCl_3$): δ = 7.33 (1H, d, H5, J = 9.2 Hz), 6.75 (1H, br s), 6.65 (1H, dd, H6, J = 9.2, 2.8 Hz), 6.59 (1H, d, H8, J = 2.8 Hz), 5.26 (2H, br s, CH_2), 4.97 (1H, br s, NH), 3.45 (4H, q, CH_2 NEt_2, J = 7.2 Hz), 3.29 (2H, qt, CH_2 Et, J = 7.2 Hz), 1.23 (6H, t, CH_3 NEt_2, J = 7.2 Hz), 1.20 ppm (3H, t, CH_3 Et, J = 7.2 Hz); ^{13}C NMR (101 MHz, $CDCl_3$): δ = 172.0, 155.1, 154.9, 151.6, 147.3, 124.7, 114.8, 113.9, 110.6, 106.9, 105.1, 97.3, 61.3, 55.2, 44.9, 36.2, 15.1, 12.4 ppm; HR ESI-MS (positive mode): m/z = 367.1752 (calcd mass for $C_{20}H_{23}N_4O_3$ $[M+H]^+$: 367.1770).

Synthesis of DEAdcCE-Caged Model Compounds (3, 4, 6)

Compound 15: EDC·HCl (1.6 g, 10.6 mmol), coumarin **13** (2.52 g, 9.6 mmol),[5e] DMAP (1.3 g, 10.6 mmol), and benzoic acid (1.4 g, 11.6 mmol) were dissolved in dry CH_2Cl_2 (40 mL) at 0 °C under an Ar atmosphere. After 10 min at 0 °C, the reaction mixture was stirred at room temperature for 17 h in the dark and under Ar. Subsequently, the organic solution was diluted with CH_2Cl_2 (60 mL) and washed with saturated NH_4Cl (25 mL), 5% aqueous $NaHCO_3$ (2×25 mL), water (25 mL), and dried over anhydrous Na_2SO_4. After filtration and evaporation under vacuum, the desired product (**14**) was obtained and used without further purification in the next step. Lawesson's reagent (2.5 g, 6.8 mmol) was added to a solution of **14** in toluene (50 mL). The mixture was stirred at 105 °C overnight under an Ar atmosphere and protected from light. Then, the solvent was evaporated under vacuum. After purification by column chromatography (silica gel, 50–65% CH_2Cl_2 in hexane), 2.53 g of an orange solid (69% yield from **13**) was obtained. Characterization: TLC: R_f (5% MeOH in CH_2Cl_2): 0.28; ^{1}H NMR (400 MHz, $CDCl_3$): δ = 8.10 (2H, m, Ph), 7.62 (1H, m, Ph), 7.55 (1H, d, H5, J = 10 Hz), 7.48 (2H, t, Ph, J = 7.6 Hz), 7.16 (1H, s, H3), 6.68 (2H, m, H6 + H8), 6.32 (1H, q, CH-CH_3, J = 6.8 Hz), 3.44 (4H, q, CH_2 NEt_2, J = 7.2 Hz), 1.71 (3H, d, CH-CH_3, J = 6.8 Hz), 1.23 ppm (6H, t, CH_3 NEt_2, J = 7.2 Hz); ^{13}C NMR (101 MHz, $CDCl_3$): δ = 197.4, 165.5, 159.5, 150.9, 147.9, 133.5, 129.8, 129.5, 128.6, 124.9, 119.2, 110.4, 108.0, 97.6, 67.6, 45.0, 21.0, 12.4 ppm. ESI-MS (positive mode): m/z = 382.66 (calcd mass for $C_{22}H_{24}NO_3S$ $[M+H]^+$: 382.15).

Compound 4: A solution of malononitrile (52 mg, 0.79 mmol) and NEt_3 (0.2 mL, 1.54 mmol) in anhydrous MeCN (2 mL) was added to a solution of **15** (202 mg, 0.53 mmol) in MeCN (8 mL) under an Ar atmosphere. The reaction mixture was stirred in the dark for 2 h. Then, $AgNO_3$ (196 mg, 1.15 mmol) was added and stirring was maintained for 2 h. After filtration and removal of the solvent under reduced pressure, the product was purified by column chromatography (silica gel, 0–100% CH_2Cl_2 in hexane) to give 158 mg (72% yield) of an orange solid. Characterization: TLC: R_f (5% MeOH in CH_2Cl_2): 0.63; ^{1}H NMR (400 MHz, $CDCl_3$): δ = 8.09 (2H, m, Ph), 7.61 (1H, m, Ph), 7.54 (1H, d, H5, J = 9.2 Hz), 7.49 (2H, t, Ph, J = 7.6 Hz), 6.85 (1H, s, H3), 6.69 (1H, dd, H6, J = 9.2, 2.6 Hz), 6.61 (1H, d, H8, J = 2.6 Hz), 6.33 (1H, q, CH-CH_3, J = 6.8 Hz), 3.45 (4H, q, CH_2 NEt_2, J = 7.2 Hz), 1.73 (3H, d, CH-CH_3, J = 6.8 Hz), 1.24 ppm (6H, t, CH_3 NEt_2, J = 7.2 Hz); ^{13}C NMR (101 MHz, $CDCl_3$): δ = 172.1, 165.5, 155.4, 152.2, 151.6, 133.7, 129.7, 129.2, 128.7, 125.3, 114.7, 113.9, 110.7, 106.8, 104.6, 97.6, 67.9, 55.3, 45.0, 21.1, 12.5 ppm. HR ESI-MS (positive mode): m/z = 414.1805 (calcd mass for $C_{25}H_{24}N_3O_3$ $[M+H]^+$: 414.1818).

Compound 16: A solution of aqueous HCl (37%, 50 mL, 0.58 mol) was added to **4** (0.24 g, 0.58 mmol) in MeOH (50 mL). The reaction mixture was heated at 90 °C for 15 h. Once the reaction was finished, the solvent was removed under reduced pressure and purified by chromatography column (silica gel, 0–3% of MeOH in CH_2Cl_2) to give 0.13 g of an orange solid (71% yield). Characterization: TLC: R_f (5% MeOH in CH_2Cl_2): 0.40; ^{1}H NMR (400 MHz, $CDCl_3$): δ = 7.46 (1H, d, H5, J = 9.2 Hz), 6.91 (1H, s, H3), 6.66 (1H, dd, H6, J = 9.2, 2.6 Hz), 6.59 (1H, d, H8, J = 2.6 Hz), 5.19 (1H, m, CH-CH_3), 2.10 (1H, d, OH, J = 3.6 Hz), 3.45 (4H, q, CH_2 NEt_2, J = 7.2 Hz), 1.57 (3H, d, CH-CH_3, J = 6.8 Hz), 1.24 ppm (6H, t, CH_3 NEt_2, J = 7.2 Hz); ^{13}C NMR (101 MHz, $CDCl_3$): δ = 172.4, 156.1, 155.2, 151.4, 125.3, 114.9, 114.2, 110.5, 107.0, 104.2, 97.4, 66.0, 54.7, 44.9, 24.0, 12.5 ppm; HR ESI-MS (positive mode): m/z = 310.1542 (calcd mass for $C_{18}H_{20}N_3O_2$ $[M+H]^+$: 310.1556).

Compound 3: Acetic anhydride (85 μL, 0.77 mmol) and DMAP (94 mg, 0.77 mmol) were added to a solution of **16** (47.6 mg, 0.15 mmol) in anhydrous CH_2Cl_2 (4 mL) under an Ar atmosphere. The reaction mixture was stirred in the dark overnight. After removal of the solvent under reduced pressure, the product was purified by column chromatography (silica gel, 0–0.1% MeOH in CH_2Cl_2) to give 21 mg (40% yield) of an orange solid. Characterization: TLC: R_f (1% MeOH in CH_2Cl_2): 0.66; ^{1}H NMR (400 MHz, $CDCl_3$): δ = 7.43 (1H, d, H5, J = 9.2 Hz), 6.72 (1H, s, H3), 6.67 (1H, dd, H6, J = 9.2, 2.4 Hz), 6.60 (1H, d, H8, J = 2.4 Hz), 6.08 (1H, q, CH-CH_3, J = 6.8 Hz), 3.45 (4H, q, CH_2 NEt_2, J = 7.2 Hz), 2.16 (3H, s, CH_3CO), 1.58 (3H, d, CH-CH_3, J = 6.8 Hz), 1.24 ppm (6H, t, CH_3 NEt_2, J = 7.2 Hz); ^{13}C NMR (101 MHz, $CDCl_3$): δ = 172.1, 169.9, 155.3, 152.3, 151.6, 125.2, 114.8, 113.9, 110.7, 106.7, 104.3, 97.6, 67.2, 55.2, 45.0, 21.1, 12.5 ppm; HR ESI-MS (positive mode): m/z = 352.1648 (calcd mass for $C_{20}H_{22}N_3O_3$ $[M+H]^+$: 352.1661).

Compound 6: NEt_3 (600 μL, 4 mmol) and ethyl isocyanate (380 μL, 4.8 mmol) were added to a solution of **16** (62 mg, 0.20 mmol) in a mixture of dry MeCN (2.5 mL) and CH_2Cl_2 (1.5 mL) under an Ar atmosphere. Once the reaction was finished (24 h according to TLC), the solvent was removed under reduced pressure and purified by chromatography column (silica gel, 0–0.75% of MeOH in CH_2Cl_2) to give 42 mg of an orange solid (63% yield). Characterization: TLC: R_f (2% MeOH in CH_2Cl_2): 0.46; ^{1}H NMR (400 MHz, $CDCl_3$): δ = 7.44 (1H, d, H5, J = 9.2 Hz), 6.73 (1H, s, H3), 6.67 (1H, dd, H6, J = 9.2, 2.4 Hz), 6.59 (1H, d, H8, J = 2.4 Hz), 6.03 (1H, q, CH-CH_3, J = 6.8 Hz), 4.90 (1H, br s, NH), 3.45 (4H, q, CH_2 NEt_2, J = 7.2 Hz), 3.24 (2H, qt, NH-CH_2-CH_3, J = 7.2 Hz), 1.55 (3H, d, CH-CH_3, J = 6.8 Hz), 1.23 (6H, t, CH_3 NEt_2, J = 7.2 Hz), 1.17 ppm (3H, t, NH-CH_2-CH_3, J = 7.2 Hz); ^{13}C NMR (101 MHz, $CDCl_3$): δ = 172.3, 155.3, 154.8, 153.5, 151.6, 125.2, 115.0, 114.1, 110.6, 106.8, 104.0, 97.5, 67.2, 54.7, 44.9, 36.1, 15.1, 12.5 ppm; HR ESI-MS (positive mode): m/z = 381.1922 (calcd mass for $C_{21}H_{25}N_4O_3$ $[M+H]^+$: 381.1927).

Photophysical Properties

Absorption spectra were recorded with a Varian Cary 500 UV/Vis/NIR spectrophotometer at 25 °C. Emission spectra were registered in a Photon Technology International (PTI) fluorimeter. Solutions for emission measurements were adjusted to concentrations such that the absorption was around 0.04 at the excitation wavelength (λ_{Ex} = 460 nm). Fluorescence quantum yields, Φ_F, were calculated from Equation (1):

$$\Phi_F = \Phi_F^s \frac{Abs^s}{Abs} \frac{A}{A^s} \frac{n^2}{n_s^2} \quad (1)$$

in which the superscript "s" stands for standard samples, Abs is the absorbance at the excitation wavelength (λ_{Ex}), A is the integrated area of the corresponding emission spectrum, and n is the refractive index of the solvent used.[14] The uncertainty in the experimental value of Φ_F has been estimated to be approximately 10%. The standard fluorophore used for the determination of the fluorescence quantum yield was fluorescein dissolved in aqueous sodium hydroxide (0.1 M) with a reported absolute fluorescence quantum yield, Φ_F, of 0.92.[15] All samples were measured in 1×1 cm quartz cuvettes (Hellma).

Irradiation Experiments

Photolysis studies were performed at 37 °C in a custom-built irradiation setup from Microbeam including a cuvette, thermostated cuvette holder, and a mounted high power LED of 505 nm (100 mW cm^{-2}). In a typical experiment, the irradiation samples contained the dicyanocoumarin-caged model compound (20 μM) and 12 μL of a 30 μM solution of uracil (internal standard) in a 1:1 (v/v) mixture of Tris buffer pH 7.5 and MeCN. After irradiation, the samples were analyzed by reversed-phase HPLC-ESI MS with a Jupiter Proteo C_{18} column (250×4.6 mm, 90 Å, 4 μm, flow rate: 1 mL min^{-1}) by using linear gradients of 0.1% formic acid in H_2O (A) and 0.1% formic acid in MeCN (B).

Uncaging Quantum Yield Determination

The uncaging quantum yield for coumarin derivatives **1**–**6** upon illumination at 505 nm was estimated by comparing the initial rate of photo-uncaging with the rate of photobleaching of (*E*)-2-[1-(2,5-dimethyl-3-furyl-9-ethylidene]-3-isopropylidene succinic anhydride (Aberchrome 540), a well-known chemical actinometer.[16,17] Indeed, the ring-opening back reaction of this particular organic chromophore can be easily exploited for actinometry in the visible region of the electromagnetic spectrum by measuring the decrease in absorbance at 494 nm of a known volume of the red toluene solution, which was previously obtained by irradiating the ring-opened isomer of Aberchrome 540 with UV light (Philips high pressure mercury lamp, 500 W, 320 nm $< \lambda_{Irrad} <$ 390 nm) for 5 min.

The photon flow onto the sample was calculated by using Equation (2):

$$\frac{Nh\nu}{t} = \frac{\Delta A \times V}{\Phi_\lambda \times \varepsilon \times \Delta t} \quad (2)$$

where ΔA is the decrease in absorbance at 494 nm, Δt is the irradiation time, V is the volume of the irradiated solution (3 mL), Φ_λ is the quantum yield for the ring-opening reaction, and ε is the molar absorption coefficient of the ring-closed isomer of Aberchrome 540 at 494 nm (8200 M^{-1} cm^{-1}). The quantum yield for the photobleaching reaction in toluene at 21 °C, was calculated by the following expression [Eq. (3)]:

$$\Phi_\lambda = 0.178 - 2.4 \times 10 - 4\,\lambda_{Ac} \quad (3)$$

where λ_{Ac} is the activation wavelength (in this instance, λ_{Ac} = 505 nm). The photon flow thus determined was 1.05× 10^{-7} Einstein s^{-1}.

The kinetic traces for the uncaging step were fitted to a monoexponential decreasing function and the initial slope was determined by differentiation. The uncaging quantum yield, Φ_{Ph}, was determined by calculating the ratio between the initial slope and the number of absorbed photons by the sample as determined by actinometry.[18]

Computational Calculations

According to the Bell–Evans–Polanyi principle, it can be considered that the changes in the exothermicity of the reaction for two similar dicyanocoumarin-caged compounds is proportional to the differences in reaction activation energies. Thus, we computed the free energy changes associated with the transformation of each compound in its corresponding ion pair intermediate species and compared the results for each pair of similar compounds (that is, differing either in the type of carbocation or anion released in the reaction). All calculations were carried out with the Gaussian 09 (G09) software package.[19] The electronic structures were computed by Density Functional Theory (DFT)[20] by using the B3LYP functional[21] and the 6-31G** basis set.[22] The most stable enantiomers of all chiral centers were chosen for structural optimizations, which were performed in an implicit water solvent (SMD solvation model[23]).

Acknowledgments

This work was supported by funds from the Spanish Ministerio de Economía y Competitividad (grants CTQ2014-52658-R and CTQ2015-65770-P MINECO/FEDER) and the Generalitat de Catalunya (2014SGR187 and XRB). The authors acknowledge the assistance of Dr. Irene Fernández and Laura Ortiz (MS), and Dr. Francisco Cárdenas (NMR) from CCiTUB. A.G. is a recipient fellow of the University of Barcelona.

Conflict of Interest

The authors declare no conflict of interest.

Keywords: caged compounds · coumarins · photolysis · protecting groups · UV/Vis spectroscopy

[1] a) W. A. Velema, W. Szymanski, B. L. Feringa, *J. Am. Chem. Soc.* **2014**, *136*, 2178–2191; b) C. Brieke, F. Rohrbach, A. Gottschalk, G. Mayer, A. Heckel, *Angew. Chem. Int. Ed.* **2012**, *51*, 8446–8476; *Angew. Chem.* **2012**, *124*, 8572–8604; c) G. Mayer, A. Heckel, *Angew. Chem. Int. Ed.* **2006**, *45*, 4900–4921; *Angew. Chem.* **2006**, *118*, 5020–5042; d) A. Deiters, *ChemBioChem* **2010**, *11*, 47–53.

[2] a) P. Klán, T. Solomek, C. G. Bochet, A. Blanc, R. Givens, M. Rubina, V. Popik, A. Kostikov, J. Wirz, *Chem. Rev.* **2013**, *113*, 119–191; b) M. J. Hansen, W. A. Velema, M. M. Lerch, W. Szymanski, B. L. Feringa, *Chem. Soc. Rev.* **2015**, *44*, 3358–3377.

[3] a) M. Zindler, B. Pinchuk, C. Renn, R. Horbert, A. Doebber, C. Peifer, *ChemMedChem* **2015**, *10*, 1335–1338; b) J. Schimer, M. Pávová, M. Anders, P. Pachl, P. Šácha, P. Cígler, J. Weber, P. Majer, P. Řezáčová, H.-G. Kräusslich, B. Müller, J. Konvalinka, *Nat. Commun.* **2015**, *6*, 6461; c) W. A. Velema, J. P. van der Berg, W. Szymanski, A. J. M. Driessen, B. L. Feringa, *ACS Chem. Biol.* **2014**, *9*, 1969–1974; d) J. P. Olson, H.-B. Kwon, K. T. Takasaki, C. Q. Chiu, M. J. Higley, B. L. Sabatini, G. C. R. Ellis-Davies, *J. Am. Chem. Soc.* **2013**, *135*, 5954–5957; e) J. P. Olson, M. R. Banghart, B. L. Sabatini, G. C. R. Ellis-Davies, *J. Am. Chem. Soc.* **2013**, *135*, 15948–15954; f) M. Wirkner, S. Weis, V. San Miguel, M. Álvarez, R. A. Gropeanu, M. Salierno, A. Sartoris, R. E. Unger, C. J. Kirkpatrick, A. del Campo, *ChemBioChem* **2011**, *12*, 2623–2629; g) T. T. Lee, J. R. Garcia, J. I. Paez, A. Singh, E. A. Phelps, S. Weis, Z. Shafiq, A. Shekaran, A. del Campo, A. J. Garcia,

Nat. Mater. **2015**, *14*, 352 – 360; h) M. A. Azagarsamy, K. S. Anseth, *Angew. Chem. Int. Ed.* **2013**, *52*, 13803 – 13807; *Angew. Chem.* **2013**, *125*, 14048 – 14052; i) J. Mosquera, M. I. Sánchez, J. L. Mascareñas, M. E. Vázquez, *Chem. Commun.* **2015**, *51*, 5501 – 5504; j) J. Luo, R. Uprety, Y. Naro, C. Chou, D. P. Nguyen, J. W. Chin, A. Deiters, *J. Am. Chem. Soc.* **2014**, *136*, 15551 – 15558; k) M. Sainlos, W. S. Iskenderian-Epps, N. B. Olivier, D. Choquet, B. Imperiali, *J. Am. Chem. Soc.* **2013**, *135*, 4580 – 4583; l) H. S. Steinert, F. Schäfe, H. R. Jonker, A. Heckel, H. Schwalbe, *Angew. Chem. Int. Ed.* **2014**, *53*, 1072 – 1075; *Angew. Chem.* **2014**, *126*, 1090 – 1093; m) A. Meyer, A. Mokhir, *Angew. Chem. Int. Ed.* **2014**, *53*, 12840 – 12843; *Angew. Chem.* **2014**, *126*, 13054 – 13057; n) A. Rodrigues-Correia, D. Knapp-Bühle, J. W. Engels, A. Heckel, *Org. Lett.* **2014**, *16*, 5128 – 5131; o) A. Rodrigues-Correia, X. M. M. Weyel, A. Heckel, *Org. Lett.* **2013**, *15*, 5500 – 5503; p) J. Hemphill, Q. Liu, R. Uprety, S. Samanta, M. Tsang, R. L. Juliano, A. Deiters, *J. Am. Chem. Soc.* **2015**, *137*, 3656 – 3662; q) J. M. Amatrudo, J. P. Olson, G. Lur, C. Q. Chiu, M. J. Higley, G. C. R. Ellis-Davies, *ACS Chem. Neurosci.* **2014**, *5*, 64 – 70; r) A. M. S. Soares, G. Hungerford, S. P. G. Costa, M. S. T. Gonçalves, *Dyes Pigm.* **2017**, *137*, 91 – 100; s) V. San Miguel, C. G. Bochet, A. del Campo, *J. Am. Chem. Soc.* **2011**, *133*, 5380 – 5388.

[4] a) J. B. Grimm, B. P. English, J. Chen, J. P. Slaughter, Z. Zhang, A. Revyakin, R. Patel, J. J. Macklin, D. Normanno, R. H. Singer, T. Lionnet, L. D. Lavis, *Nat. Methods* **2015**, *12*, 244 – 250; b) J. B. Grimm, B. P. English, H. Choi, A. K. Muthusamy, B. P. Mehl, P. Dong, T. A. Brown, J. Lippincott-Schwartz, Z. Liu, T. Lionnet, L. D. Lavis, *Nat. Methods* **2016**, *13*, 985 – 988; c) X. Liu, Q. Qiao, W. Tian, W. Liu, J. Chen, M. J. Lang, Z. Xu, *J. Am. Chem. Soc.* **2016**, *138*, 6960 – 6963; d) S. Singha, D. Kim, B. Roy, S. Sambasivan, H. Moon, A. S. Rao, J. Y. Kim, T. Joo, J. W. Park, Y. M. Rhee, T. Wang, K. H. Kim, Y. H. Shin, J. Jung, K. H. Ahn, *Chem. Sci.* **2015**, *6*, 4335 – 4342.

[5] a) S. Yamazoe, Q. Liu, L. E. McQuade, A. Deiters, J. K. Chen, *Angew. Chem. Int. Ed.* **2014**, *53*, 10114 – 10118; *Angew. Chem.* **2014**, *126*, 10278 – 10282; b) L. Fournier, C. Gauron, L. Xu, I. Aujard, T. Le Saux, N. Gagey-Eilstein, S. Maurin, S. Dubruille, J.-B. Baudin, D. Bensimon, M. Volovitch, S. Vriz, L. Jullien, *ACS Chem. Biol.* **2013**, *8*, 1528 – 1536; c) L. Fournier, I. Aujard, T. Le Saux, S. Maurin, S. Beaupierre, J.-B. Baudin, L. Jullien, *Chem. Eur. J.* **2013**, *19*, 17494 – 17507; d) A. S. C. Fonseca, A. M. S. Soares, M. S. T. Gonçalves, S. P. G. Costa, *Tetrahedron* **2012**, *68*, 7892 – 7900; e) A. Gandioso, M. Cano, A. Massaguer, V. Marchán, *J. Org. Chem.* **2016**, *81*, 11556 – 11564.

[6] M. A. Kirpichenok, S. K. Gorozhankin, I. I. Granberg, *Chem. Heterocycl. Compd.* **1988**, *24*, 611 – 616.

[7] a) R. Schmidt, D. Geissler, V. Hagen, J. Bendig, *J. Phys. Chem. A* **2007**, *111*, 5768 – 5774; b) R. Schmidt, D. Geissler, V. Hagen, J. Bendig, *J. Phys. Chem. A* **2005**, *109*, 5000 – 5004; c) B. Schade, V. Hagen, R. Schmidt, R. Herbrich, E. Krause, T. Eckardt, J. Bendig, *J. Org. Chem.* **1999**, *64*, 9109 – 9117.

[8] S. Weis, Z. Shafiq, R. A. Gropeanu, A. del Campo, *J. Photochem. Photobiol. A* **2012**, *241*, 52 – 57.

[9] S. L. Hopkins, B. Siewert, S. H. C. Askes, P. Veldhuizen, R. Zwier, M. Heger, S. Bonnet, *Photochem. Photobiol. Sci.* **2016**, *15*, 644 – 653.

[10] a) P. Juzenas, A. Juzeniene, O. Kaalhus, V. Iani, J. Moan, *Photochem. Photobiol. Sci.* **2002**, *1*, 745 – 748; b) S. L. Jacques, *Phys. Med. Biol.* **2013**, *58*, R37 – R61.

[11] a) V. Hagen, B. Dekowski, N. Kotzur, R. Lechler, B. Wiesner, B. Briand, M. Beyermann, *Chem. Eur. J.* **2008**, *14*, 1621 – 1627; b) A. Z. Suzuki, T. Watanabe, M. Kawamoto, K. Nishiyama, H. Yamashita, M. Ishii, M. Iwamura, T. Furuta, *Org. Lett.* **2003**, *5*, 4867 – 4870.

[12] P. P. Goswami, A. Syed, C. L. Beck, T. R. Albright, K. M. Mahoney, R. Unash, E. A. Smith, A. H. Winter, *J. Am. Chem. Soc.* **2015**, *137*, 3783 – 3786.

[13] A. Blanc, C. G. Bochet, *Org. Lett.* **2007**, *9*, 2649 – 2651.

[14] J. R. Lakowicz, *Principles of Fluorescence Spectroscopy, 3rd ed.*, Springer, Singapore, **2006**.

[15] E. D. Korn, *Methods in Membrane Biology, Vol. 4*, Biophysical Approaches, Plenum Press, New York, NY, **1975**.

[16] H. J. Kuhn, S. E. Braslavsky, R. Schmidt, *Pure Appl. Chem.* **2004**, *76*, 2105 – 2146.

[17] M. Montalti, A. Credi, L. Prodi, M. T. Gandolfi, *Handbook of Photochemistry, 3rd ed.*, Chapter 12, CRC Press Taylor & Francis Group, Boca Raton, FL, **2006**.

[18] F. Schäfer, K. B. Joshi, M. A. H. Fichte, T. Mack, J. Wachteitl, A. Heckel, *Org. Lett.* **2011**, *13*, 1450 – 1453.

[19] Gaussian 09, Revision D.01, M. J. Frisch, G. W. Trucks, H. B. Schlegel, G. E. Scuseria, M. A. Robb, J. R. Cheeseman, G. Scalmani, V. Barone, B. Mennucci, G. A. Petersson, H. Nakatsuji, M. Caricato, X. Li, H. P. Hratchian, A. F. Izmaylov, J. Bloino, G. Zheng, J. L. Sonnenberg, M. Hada, M. Ehara, K. Toyota, R. Fukuda, J. Hasegawa, M. Ishida, T. Nakajima, Y. Honda, O. Kitao, H. Nakai, T. Vreven, J. A. Montgomery, Jr., J. E. Peralta, F. Ogliaro, M. Bearpark, J. J. Heyd, E. Brothers, K. N. Kudin, V. N. Staroverov, R. Kobayashi, J. Normand, K. Raghavachari, A. Rendell, J. C. Burant, S. S. Iyengar, J. Tomasi, M. Cossi, N. Rega, J. M. Millam, M. Klene, J. E. Knox, J. B. Cross, V. Bakken, C. Adamo, J. Jaramillo, R. Gomperts, R. E. Stratmann, O. Yazyev, A. J. Austin, R. Cammi, C. Pomelli, J. W. Ochterski, R. L. Martin, K. Morokuma, V. G. Zakrzewski, G. A. Voth, P. Salvador, J. J. Dannenberg, S. Dapprich, A. D. Daniels, Ö. Farkas, J. B. Foresman, J. V. Ortiz, J. Cioslowski, D. J. Fox, Gaussian, Inc. Wallingford CT, **2013**.

[20] P. Hohenberg, W. Kohn, *Phys. Rev. B* **1964**, *136*, B864 – B876.

[21] Y. Zhao, D. G. Truhlar, *Theor. Chem. Acc.* **2008**, *120*, 215 – 241.

[22] *Ab Initio Molecular Orbital Theory*, W. Hehre, L. v. R. Radom, P. Schleyer, J. A. Pople, Wiley, New York, NY, **1986**.

[23] A. V. Marenich, C. J. Cramer, D. G. Truhlar, *J. Phys. Chem. B* **2009**, *113*, 6378 – 6396.

Received: March 30, 2017
Version of record online May 5, 2017

ChemistryOPEN

Supporting Information

Sequential Uncaging with Green Light can be Achieved by Fine-Tuning the Structure of a Dicyanocoumarin Chromophore

Albert Gandioso,[a] Marta Palau,[a] Alba Nin-Hill,[a, d] Ivanna Melnyk,[a] Carme Rovira,[a, b, d] Santi Nonell,[c] Dolores Velasco,[a, e] Jaume García-Amorós,[a] and Vicente Marchán*[a]

open_201700067_sm_miscellaneous_information.pdf

SUPPORTING INFORMATION

Table of contents

1.- Synthesis of compounds 10-11.

4-(Acetoxymethyl)-7-(*N,N*-diethylamino)coumarin (10)

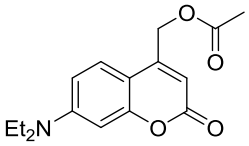

1-Ethyl-3-(3-dimethylaminopropyl)carbodiimide hydrochloride (3.05 g, 15.9 mmol) was added to a solution of 7-(*N,N*-diethylamino)-4-hydroxymethylcoumarin **9**[1] (3.27 g, 13.2 mmol), 4-dimethylaminopyridine (1.94 g, 15.9 mmol) and acetic acid (0.91 mL, 15.9 mmol) in dry DCM (20 mL) at 0ºC under an Ar atmosphere. After 10 min at 0ºC, the reaction mixture was stirred at room temperature for 12 h in the dark and under Ar. Subsequently, the organic solution was washed with HCl 1.2 M (3 x 20 mL), saturated $NaHCO_3$ (3 x 20 mL), and dried over anhydrous Na_2SO_4. After filtration and evaporation under vacuum, the desired product was obtained (2.8 g, yield 73 %) and used without further purification in the next step. Characterization: TLC: R_f (5% MeOH in DCM) 0.77. ^{1}H NMR (400 MHz, $CDCl_3$) δ (ppm): 7.28 (1H, d, *H5*, J= 9.0 Hz), 6.58 (1H, dd, *H6*, J= 9.0 Hz, J= 2.6 Hz), 6.52 (1H, d, *H8*, J= 2.6 Hz), 6.13 (1H, t, *H3*, J= 1.2 Hz), 5.21 (2H, d, *CH_2*, J= 1.2 Hz), 3.41 (4H, q, *CH_2 Et*, J= 7.2 Hz), 2.19 (3H, s, *CH_3*) 1.20 (6H, t, *CH_3 Et*, J 7.2 Hz). ESI-MS, positive mode: *m/z* 289.90 (calcd mass for $C_{16}H_{20}NO_4$ $[M+H]^+$: 290.34).

4-(Acetoxymethyl)-7-(*N,N*-diethylamino)-2-thiocoumarin (11)

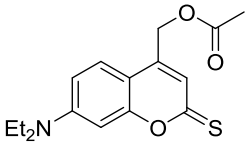

Lawesson's reagent (2.8 g, 7.0 mmol) was added to a solution of **10** (3.0 g 10.4 mmol) in toluene (30 mL). The mixture was stirred at 105ºC overnight under an Ar atmosphere and protected from light. Then, the solvent was evaporated under vacuum. After purification by column chromatography (silica gel, 50-100% DCM in hexane), an orange solid 2.4 g (76% yield) was obtained. Characterization: TLC: R_f (DCM) 0.52. ^{1}H NMR (400 MHz, $CDCl_3$) δ (ppm): 7.34 (1H, d, *H5*, J= 8.8 Hz), 7.06 (1H, s, *H3*,), 6.69-6.64 (2H, m, *H6+H8*), 5.18 (2H, s, *CH_2*), 3.43 (4H, q, *CH_2 Et*, J= 7.2 Hz), 2.19 (3H, s, *CH_3*), 1.22 (6H, t, *CH_3 Et*, J= 7.2 Hz). ^{13}C NMR (101 MHz, $CDCl_3$) δ (ppm): 197.3, 170.4, 159.2, 151.1, 141.9, 124.6, 120.7, 110.5, 108.4, 97.7, 61.1, 45.1, 20.9, 12.5. ESI-MS, positive mode: *m/z* 305.9 (calcd mass for $C_{16}H_{20}NO_3S$ $[M+H]^+$: 306.12).

2.- NMR spectra of DEAdcCM derivatives

4-(Acetoxymethyl)-7-(*N,N*-diethylamino)-2-thiocoumarin (11)

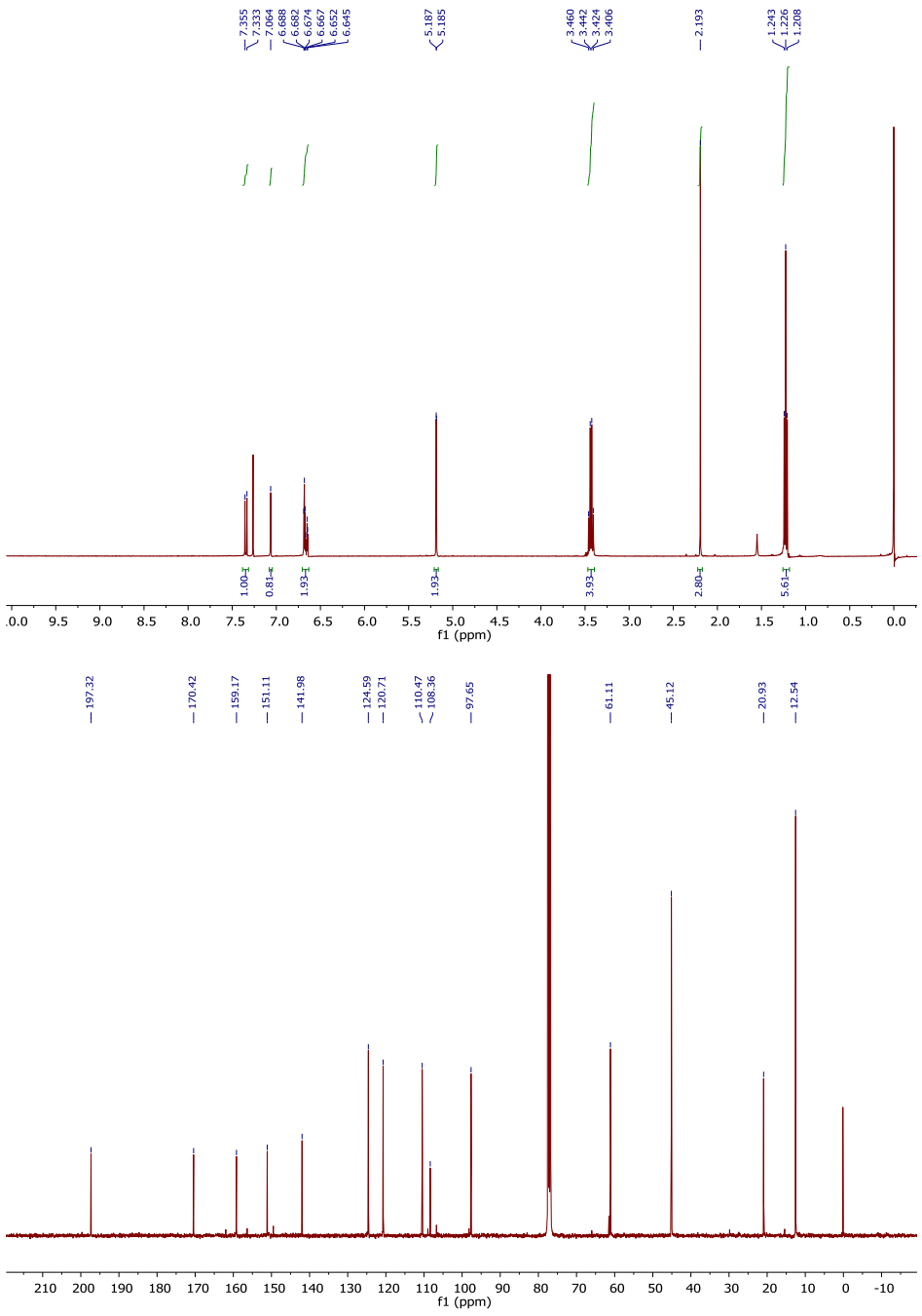

Figure S1. ^{1}H and ^{13}C NMR spectrum of compound **11**.

4-(Acetoxymethyl)-2-(dicyanomethylene)-7-(*N*,*N*-diethylamino)-coumarin (1)

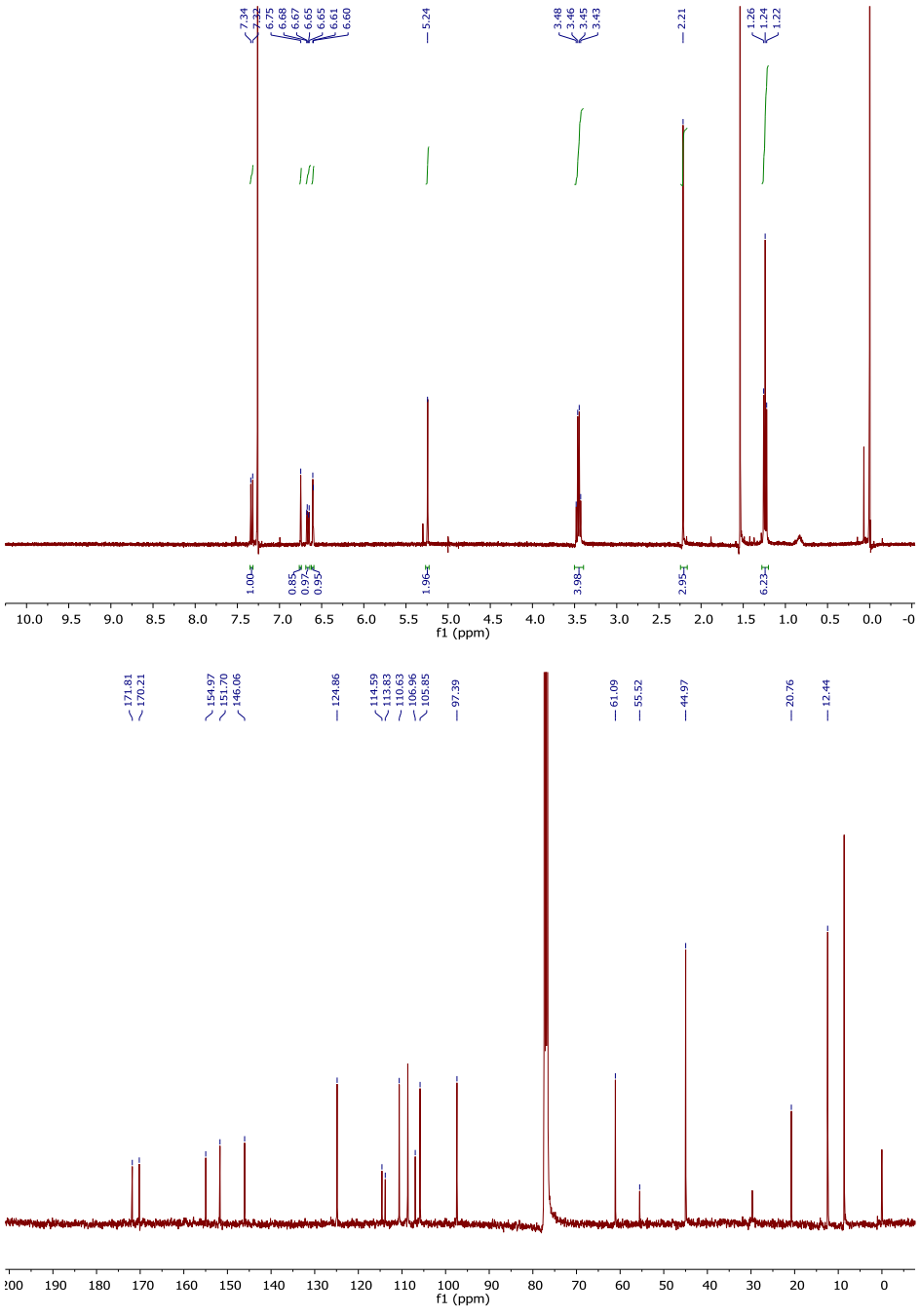

Figure S2. ^{1}H and ^{13}C NMR spectrum of compound **1**.

2-(Dicyanomethylene)-7-(*N*,*N*-diethylamino)-4-(hydroxymethyl)coumarin (12)

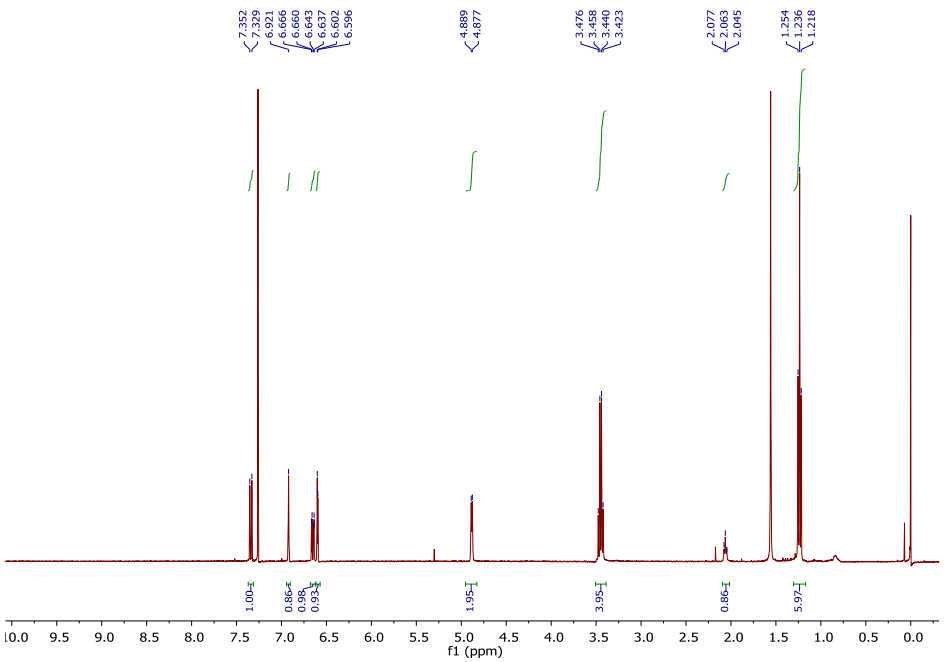

Figure S3. ^{1}H NMR spectrum of compound **12**.

4-(Benzoyloxymethyl)- 2-(dicyanomethylene)-7-(*N,N*-diethylamino)-coumarin (2)

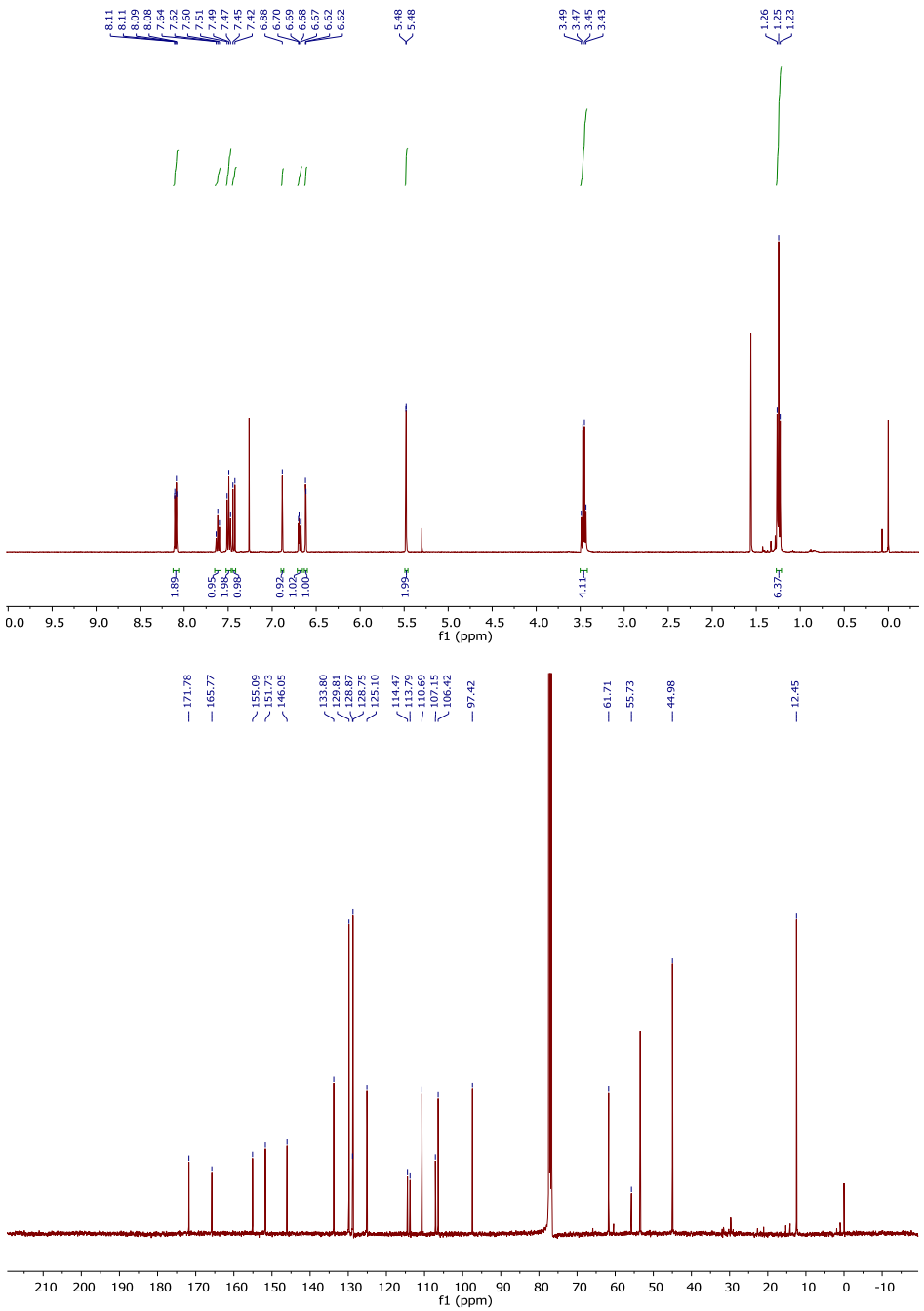

Figure S4. ^{1}H and ^{13}C NMR spectrum of compound **2**.

2-(Dicyanomethylene)-7-(*N,N*-diethylamino)-(coumarin-4-yl)methyl ethylcarbamate (5)

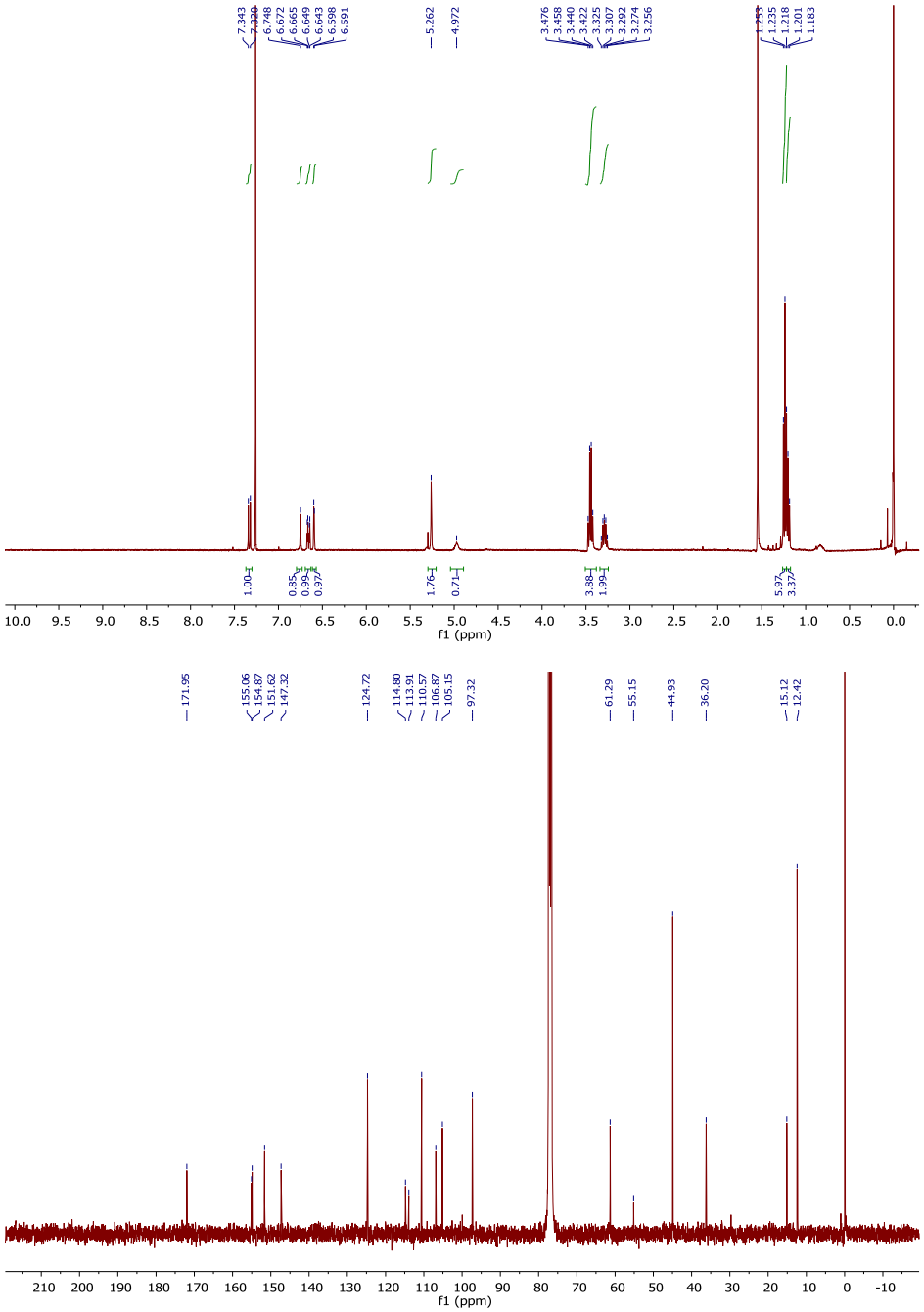

Figure S5. ^{1}H and ^{13}C NMR spectrum of compound **5**.

3.- NMR spectra of DEAdcCE derivatives

4-(Benzoyloxymethyl)-7-(*N,N*-diethylamino)-4-(1-hydroxyeth-1-yl)-2-thiocoumarin (15)

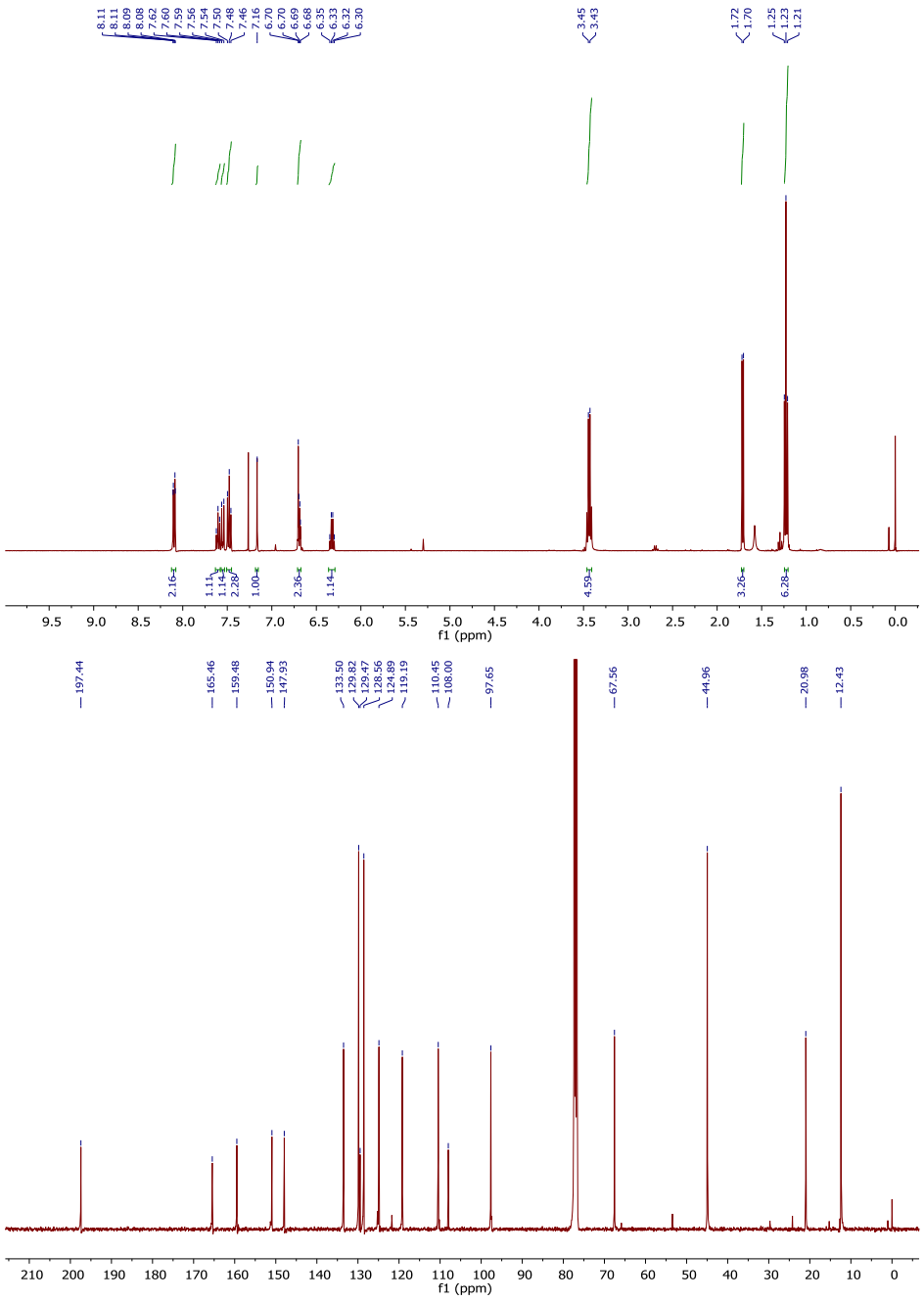

Figure S6. ^{1}H and ^{13}C NMR spectrum of compound **15**.

4-(Benzoyloxymethyl)-2-(dicyanomethylene)-7-(*N,N*-diethylamino)-4-(1-hydroxyeth-1-yl)-coumarin (4)

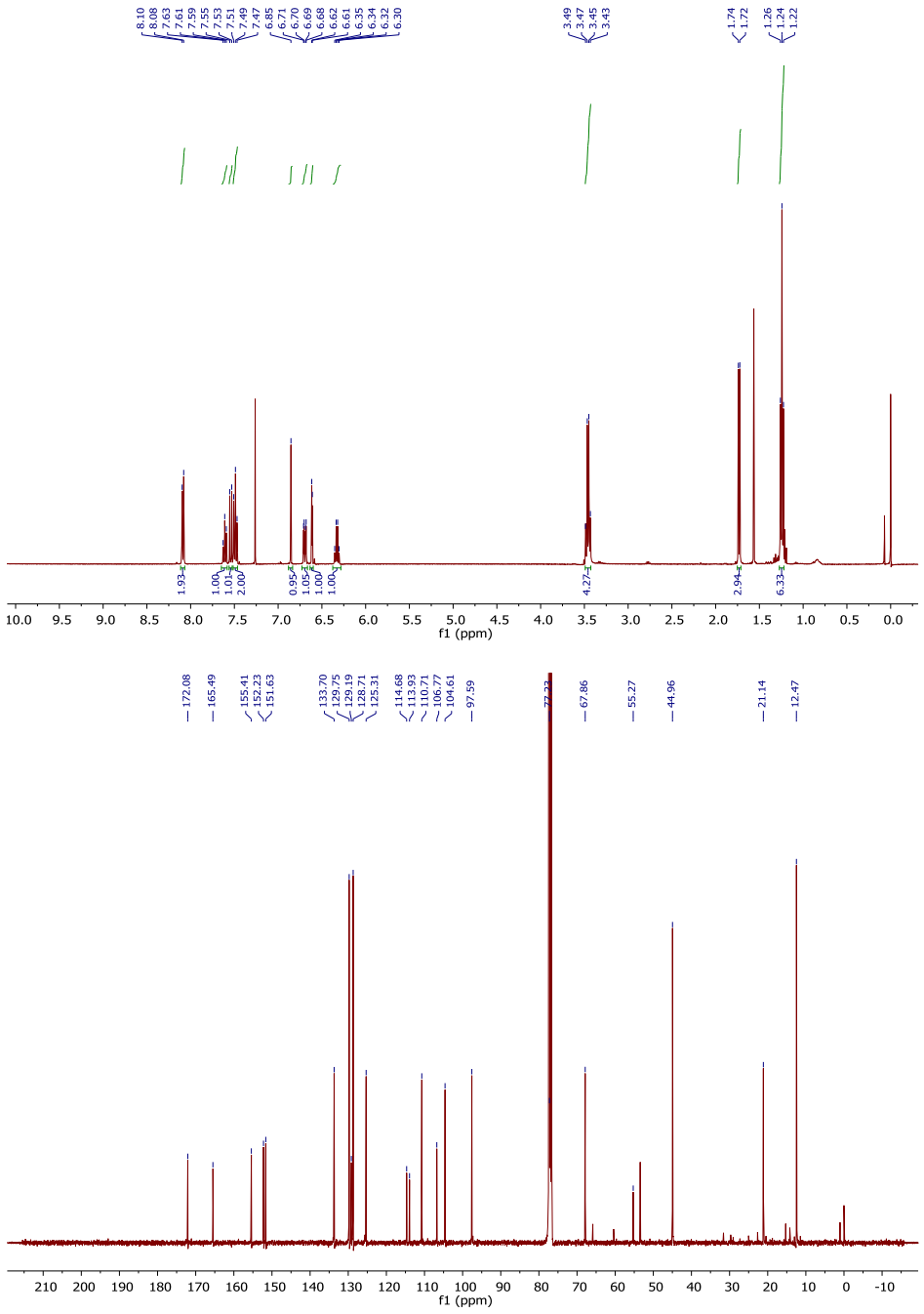

Figure S7. ^{1}H and ^{13}C NMR spectrum of compound **4**.

2-(Dicyanomethylene)-7-(*N,N*-diethylamino)-4-(1-hydroxyeth-1-yl)-coumarin (16)

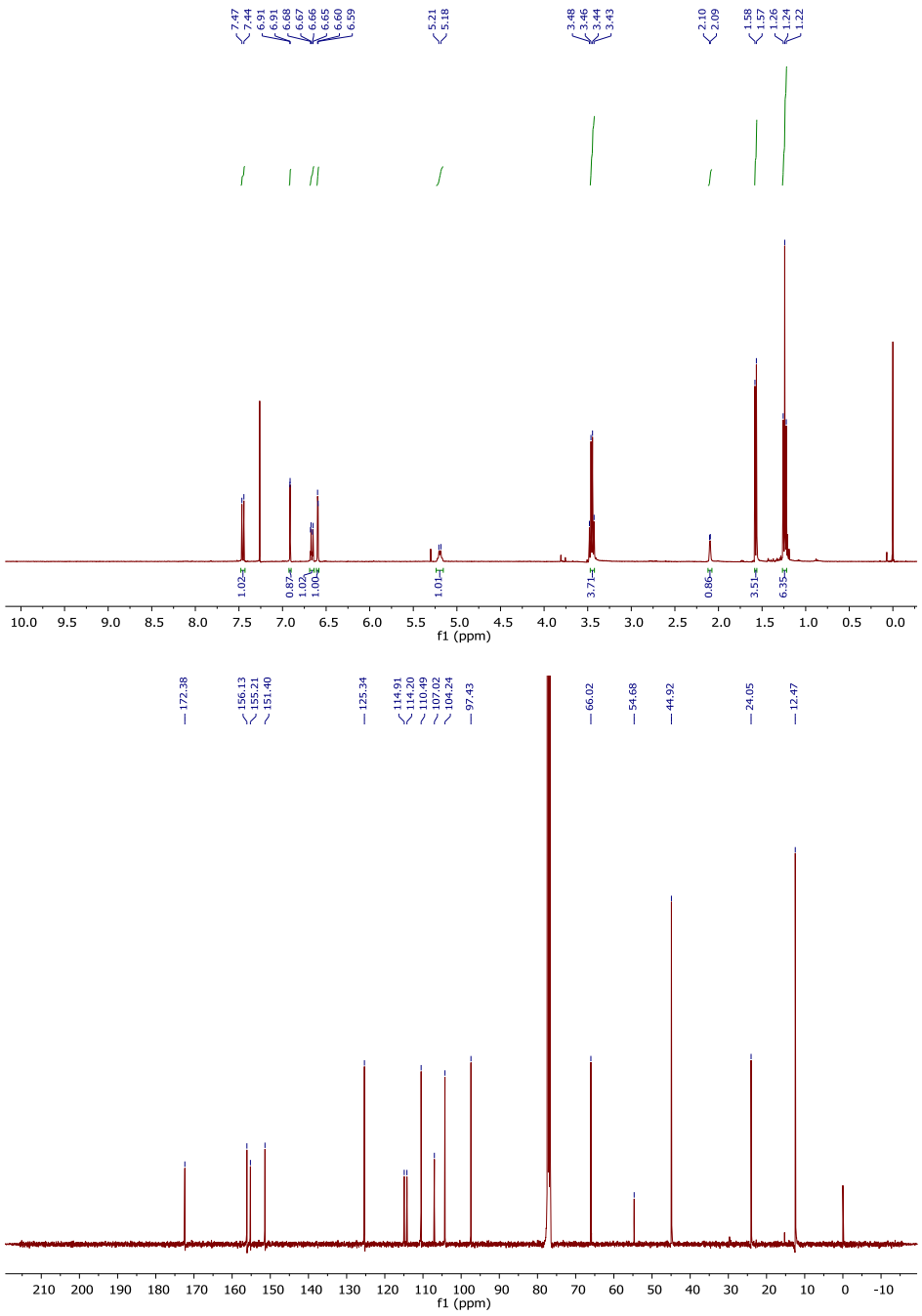

Figure S8. ^{1}H and ^{13}C NMR spectrum of compound **16**.

4-(Acetoxymethyl)-2-(dicyanomethylene)-7-(*N,N*-diethylamino)-4-(1-hydroxyeth-1-yl)-coumarin (3)

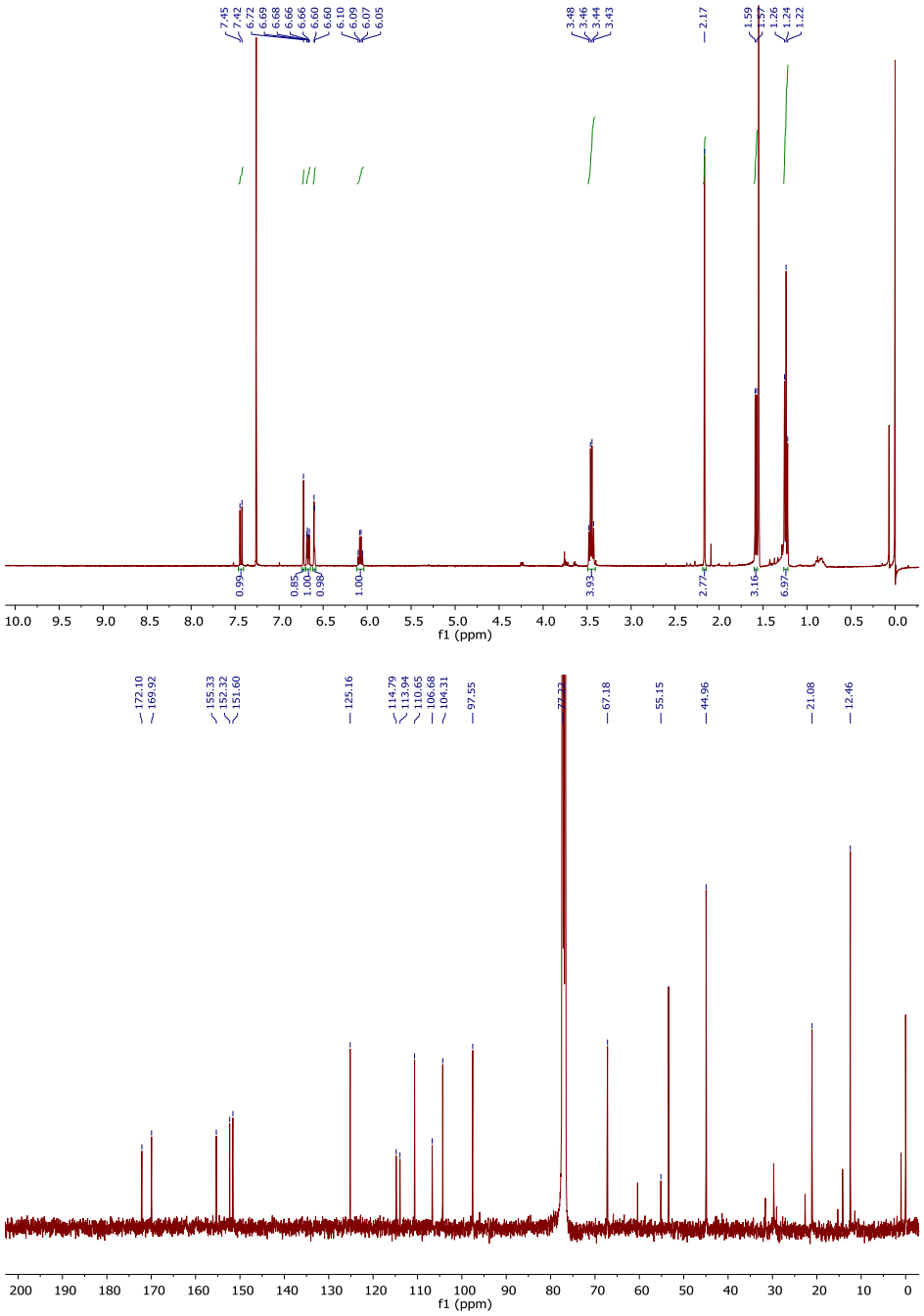

Figure S9. ^{1}H and ^{13}C NMR spectrum of compound **3**.

2-(Dicyanomethylene)-7-(*N,N*-diethylamino)-(coumarin-4-yl)1-ethyl phenylcarbamate

(6)

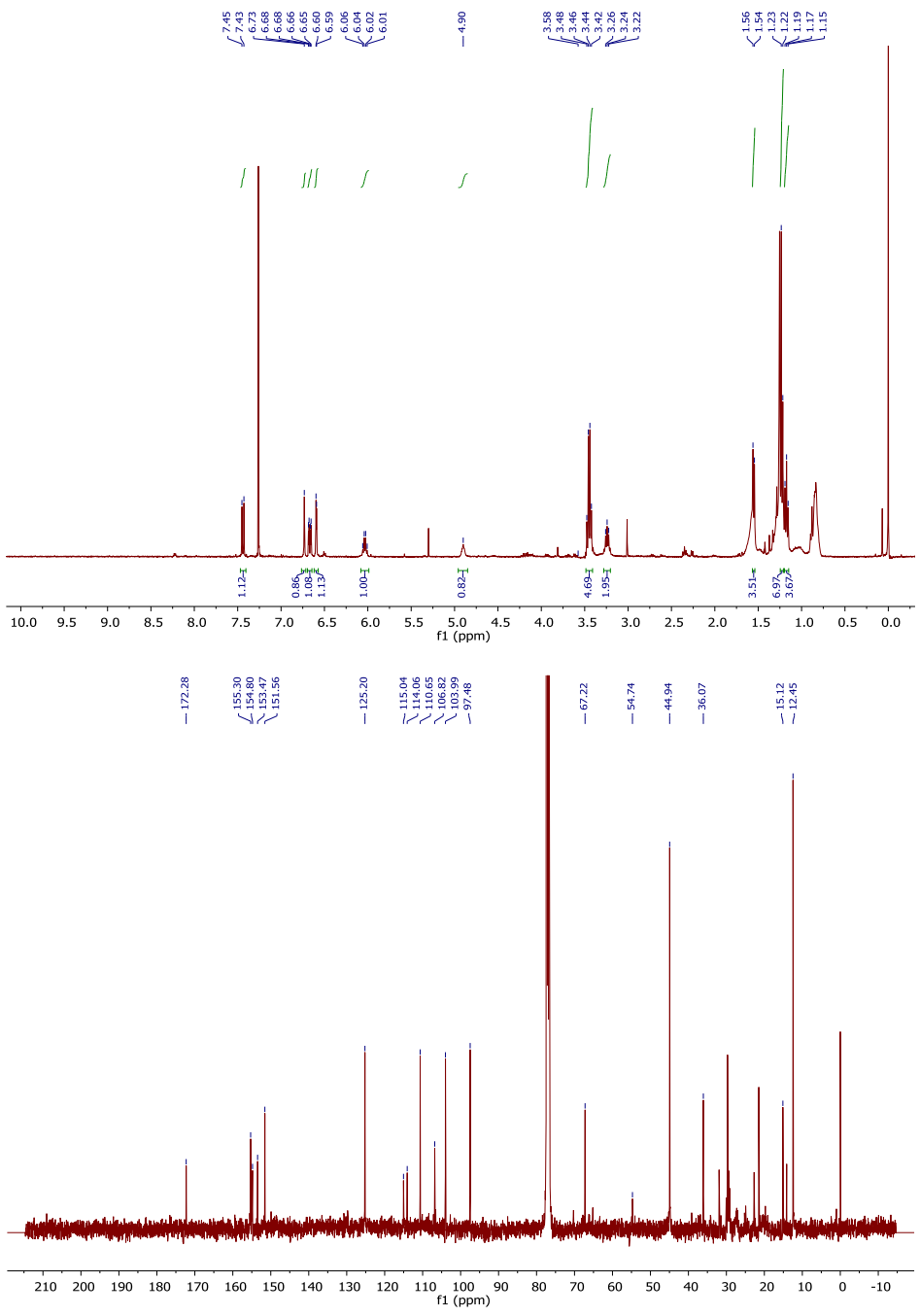

Figure S10. ^{1}H and ^{13}C NMR spectrum of compound **3**.

4.- Computational studies

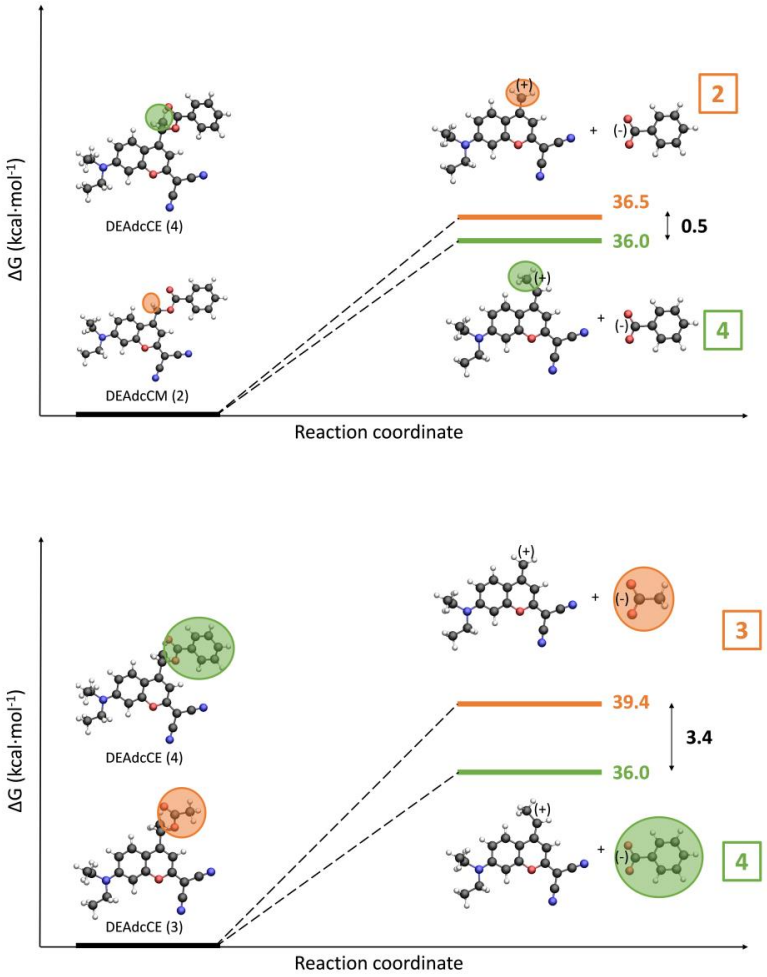

Figure S11. Free energy differences for the transformation of dicyanocoumarin-caged compounds in their respective intermediates (primary or secondary dicyanocoumarinyl carbocation + acetate or benzoate): **2** *vs* **4** (top) and **3** *vs* **4** (bottom).

5.- Sequential uncaging studies of dicyanocoumarin-caged model compounds

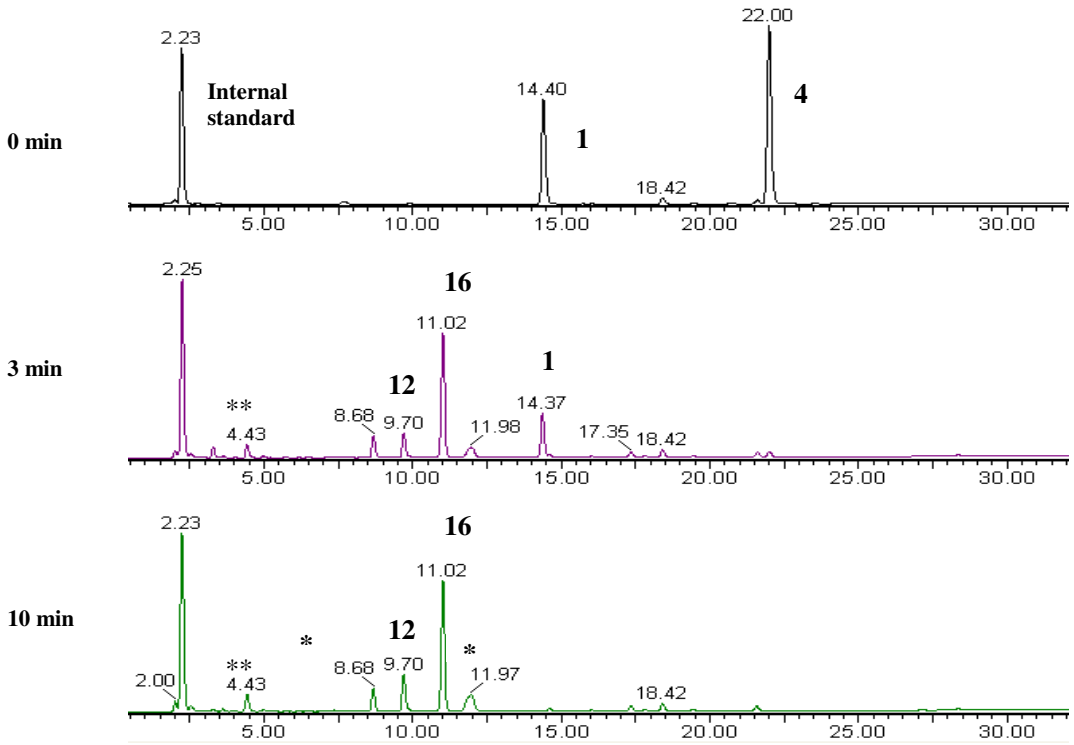

Figure S12. Reversed-phase HPLC-ESI MS traces at 260 nm of a mixture of **1** and **4** at t=0 and after irradiation at 505 nm for 3 and 10 min. *Non-identified coumarin side-products. **Buffer salts.

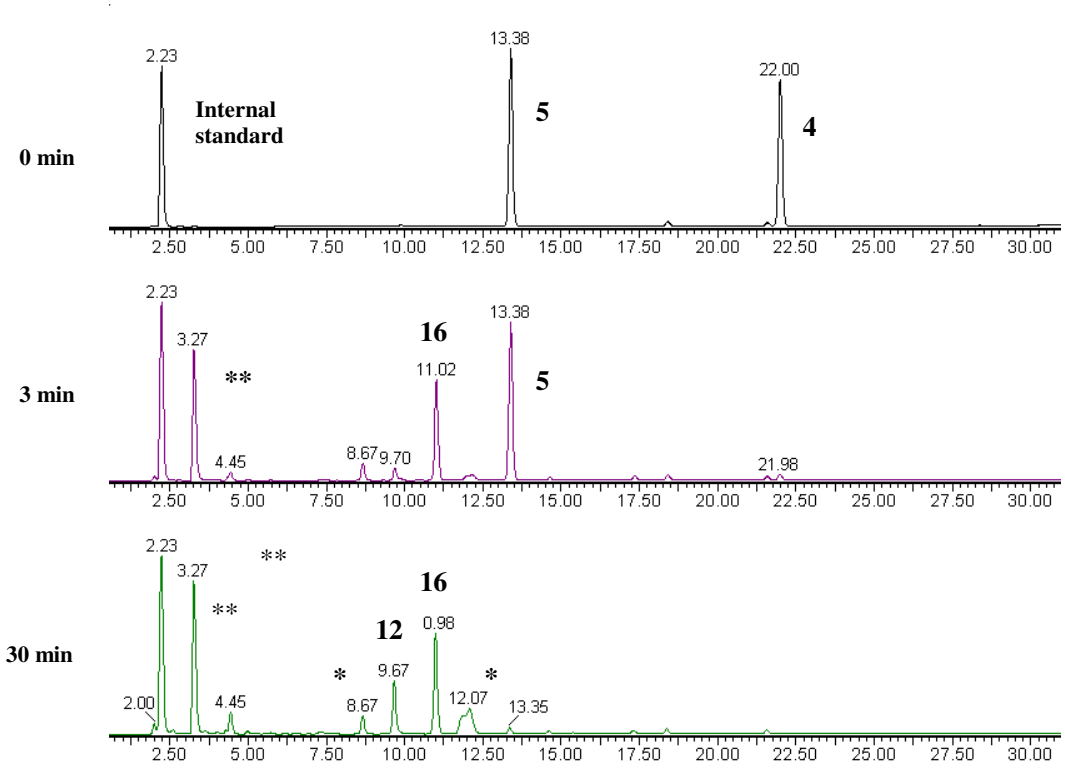

Figure S13. Reversed-phase HPLC-ESI MS traces at 260 nm of a mixture of **4** and **5** at t=0 and after irradiation at 505 nm for 3 and 30 min. *Non-identified coumarin side-products. **Buffer salts.

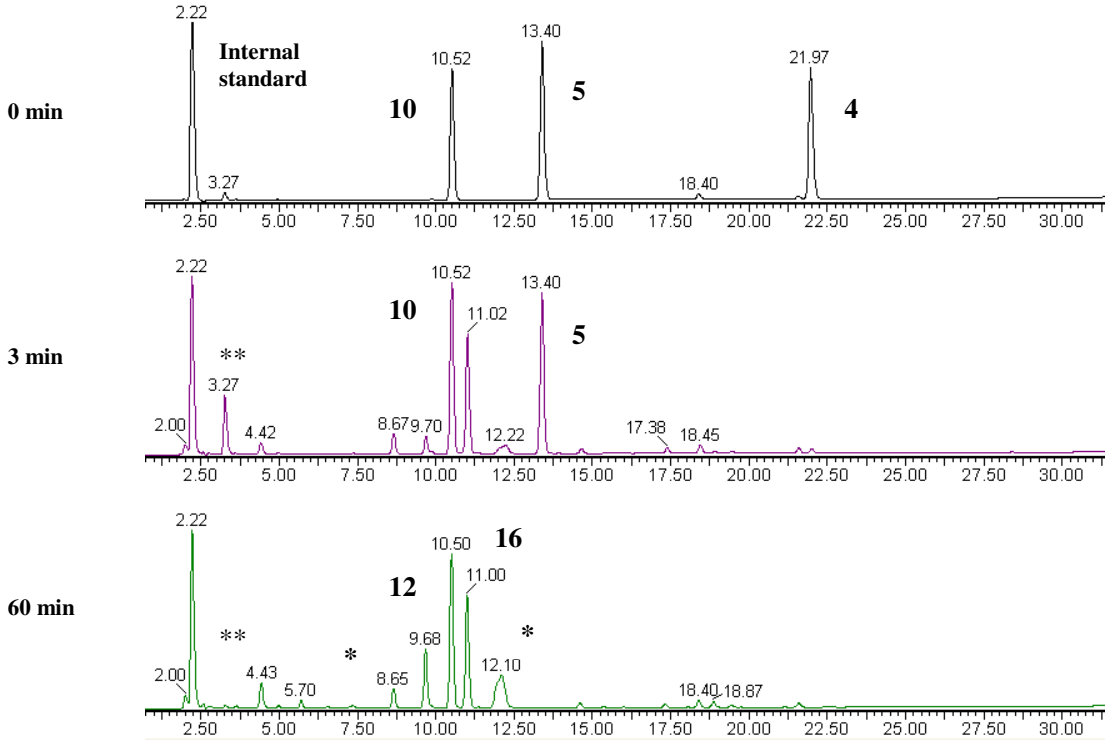

Figure S14. Reversed-phase HPLC-ESI MS traces at 260 nm of a mixture of **4, 5** and **10** at t=0 and after irradiation at 505 nm for 3 and 60 min. *Non-identified coumarin side-products. **Buffer salts.

6.- References

[1] a) A. Gandioso, M. Cano, A. Massaguer, V. Marchán, *J. Org. Chem*. **2016**, *81*, 11556-11564.

8. Publication C: A Green Light-Triggerable RGD Peptide for Photocontrolled Targeted Drug Delivery: Synthesis and Photolysis Studies (*J. Org. Chem.* **2016**, *81*, 11556-11564)

JOC The Journal of Organic Chemistry

Featured Article

pubs.acs.org/joc

A Green Light-Triggerable RGD Peptide for Photocontrolled Targeted Drug Delivery: Synthesis and Photolysis Studies

Albert Gandioso,[†] Marc Cano,[†] Anna Massaguer,[‡] and Vicente Marchán*[,†]

[†]Departament de Química Inorgànica i Orgànica, Secció de Química Orgànica, IBUB, Universitat de Barcelona, E-08028 Barcelona, Spain

[‡]Departament de Biologia, Universitat de Girona, E-17071 Girona, Spain

Supporting Information

ABSTRACT: We describe for the first time the synthesis and photochemical properties of a coumarin-caged cyclic RGD peptide and demonstrate that uncaging can be efficiently performed with biologically compatible green light. This was accomplished by using a new dicyanocoumarin derivative (DEAdcCE) for the protection of the carboxyl function at the side chain of the aspartic acid residue, which was selected on the basis of Fmoc-tBu SPPS compatibility and photolysis efficiency. The shielding effect of a methyl group incorporated in the coumarin derivative near the ester bond linking both moieties in combination with the use of acidic additives such as HOBt or Oxyma during the basic Fmoc-removal treatment were found to be very effective for minimizing aspartimide-related side reactions. In addition, a conjugate between the dicyanocoumarin-caged cyclic RGD peptide and ruthenocene, which was selected as a metallodrug model cargo, has been synthesized and characterized. The fact that green-light triggered photoactivation can be efficiently performed both with the caged peptide and with its ruthenocenyl bioconjugate reveals great potential for DEAdcCE-caged peptide sequences as selective drug carriers in the context of photocontrolled targeted anticancer strategies.

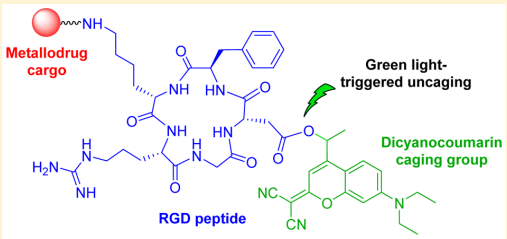

INTRODUCTION

Light can be used to control where, when, and to what extent active species are released from stable, nonbiologically active parent molecules.[1] Besides offering a high level of spatiotemporal control, light does not contaminate the living system, and its wavelength and intensity can be precisely regulated.[2] A promising approach consists of introducing photocleavable protecting groups (PPGs or caging groups)[1b,3] in key positions of the molecule whose biological activity has to be suppressed temporarily. As a result, the active species from the resulting caged compound will be released only upon light irradiation, leading to the expected biological effect at the desired target site. The approach of using caging groups to regulate the activity of molecules with light has found widespread application[1−3] to both cage small compounds[4] and larger biomolecules such as peptides and proteins[5] and oligonucleotides.[6]

Caged peptides can be prepared by introduction of PPGs at the side chain of trifunctional amino acids by taking advantage of the amino (Lys), carboxylate (Asp and Glu), thiol (Cys), and hydroxyl (Ser, Thr, and Tyr and their phosphorylated derivatives) functions.[7] In addition, caging groups have been introduced at the peptide backbone,[8] and very recently, a bisbipyridyl ruthenium(II) complex has been used to cage histidine residues.[9] However, most reported peptide caging groups based on organic chromophores (e.g., *o*-nitrobenzyl derivatives or the first-generation of coumarins) require irradiation with shorter wavelengths (UV or blue light) for uncaging, which compromise in vivo applications due to their poor capacity of penetration into tissues[10] and known photocytotoxicity.[11]

Among receptors overexpressed on tumor cells, integrins are particularly attractive targets since they have been linked to tumor angiogenesis, which is an essential process for tumor growth and metastasis.[12] Moreover, integrins are frequently overexpressed in tumor endothelial cells as well as on various tumor cells. Owing to the ability of some integrin subtypes (especially $\alpha_V\beta_3$) to selectively recognize the tripeptide motif -Arg-Gly-Asp-, RGD-containing peptides, particularly the conjugable version of Cilengitide, c(RGDfK), have been used for tumor imaging and for targeted drug delivery of cytotoxic compounds,[13] including metal-based anticancer agents.[14] In recent years, only a few examples of caged versions of RGD peptides have been described by modifying the Asp residue[7c,e] with a photolabile protecting group or by incorporating an *o*-nitrobenzyl group within the backbone skeleton.[8a] The fact that such caging groups prevent integrin recognition has been exploited to control integrin-mediated cell adhesion to surfaces by using UV light.

Taking into account the potential of caged peptides in photocontrolled targeted drug delivery therapies and as tools to

Received: October 4, 2016
Published: November 9, 2016

DOI: 10.1021/acs.joc.6b02415
J. Org. Chem. 2016, 81, 11556−11564

study and interfere with complex biological processes,[2] triggering the uncaging process with wavelengths of light compatible with biological entities is highly appealing. Here, we report for the first time the solid-phase synthesis of a cyclic RGD-containing peptide that has been caged at the side chain of the Asp residue with a dicyanocoumarin derivative, which allows photoactivation to be efficiently performed with green light (Figure 1). By synthesizing its ruthenocenoyl conjugate,

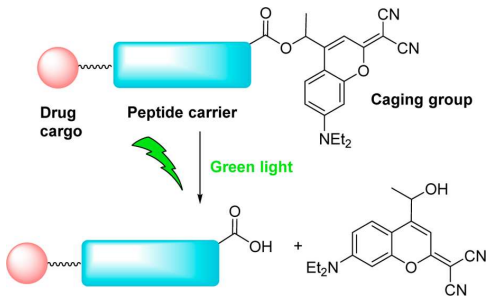

Figure 1. Schematic representation of the uncaging process of a dicyanocoumarin-caged peptide when attached to a drug cargo.

we have also demonstrated that the uncaging process can be triggered in the presence of a metallodrug model cargo, which opens the door to the use of this caged RGD peptide or other dicyanocoumarin-caged peptide sequences in photocontrolled targeted anticancer therapies.

RESULTS AND DISCUSSION

Synthesis and Photochemical Properties of Coumarin-Caged Asp Derivatives. Coumarinylmethyl derivatives have been used to cage carboxylic acid functions through esterification, with the high red-shifted absorption of the 7-(*N*,*N*-diethylamino) series being particularly intersting.[15] Upon irradiation, a solvent-assisted photoheterolysis produces the free carboxylate from the caged carboxylic acid and a solvent-trapped coumarin as a photo byproduct.[16] Recently, del Campo and co-workers[7e] have found that protection of the side chain of Asp during solid-phase peptide synthesis (SPPS) is more convenient with DEACE coumarin (**1**) than with the classical DEACM (**2**) (Scheme 1).[7e] This is because it relies on the steric hindrance provided by the methyl group incorporated in the coumarin moiety that led to an increase of the stability of the ester bond during the Fmoc-removal basic treatment as compared with the parent DEACM. Based on these precedents, we first focused on modifying the lactone function of the *N*-(9-fluorenylmethoxycarbonyl) (Fmoc)-protected Asp derivatives **3** and **4**[7e] (Scheme 1) with the aim of studying (1) if uncaging could be triggered by green light (>500 nm) and (2) their compatibility with Fmoc-tBu solid-phase peptide synthesis (SPPS) procedures for synthesizing a caged cyclic RGD peptide. As shown in Scheme 1, four new caged Asp derivatives have been synthesized by replacing the carbonyl group of the coumarinyl moiety by thiocarbonyl (**5** and **6**) or by dicyanomethylene (**7** and **8**) since both approaches are known to cause a significant red-shift absorption of the coumarin chromophore[15b,17] which has been exploited to uncage model carboxylic acids and amines with blue light.

The synthesis of the new Asp monomers **5**–**8** was planned from **3** and **4**, which were prepared from DEACM and DEACE coumarins following previously reported procedures with minor modifications. The synthesis of the thionated derivatives was carried out by reaction with Lawesson's reagent in toluene at 70 °C for 12 h. Compounds **5** and **6** were isolated by silica gel column chromatography in good yields (81 and 80%, respectively) and fully characterized by UV–vis, HR-ESI MS, and NMR. According to the higher reactivity of Lawesson's reagent for lactones than for esters,[18] thionation occurred exclusively at the coumarin protecting group (DEACM or

Scheme 1. Synthesis of the Coumarin-Caged Fmoc-Protected Asp Derivatives 5–10

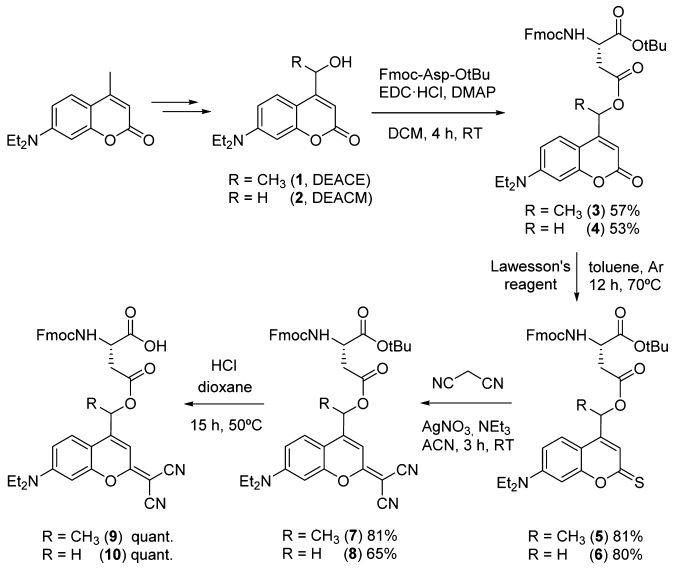

DOI: 10.1021/acs.joc.6b02415
J. Org. Chem. 2016, 81, 11556–11564

DEACE) rather than in the ester or carbamate functions of the amino acid moiety. Indeed, the chemical shift of the carbonyl group of the lactone in the ^{13}C NMR spectra of **4** (δ: 161.7 ppm) was shifted by ca. 36 ppm in **6** (δ: 197.0 ppm) due to thionation, and the adjacent proton in ^{1}H NMR was shifted from 6.1 ppm (**4**) to 7.0 ppm (**6**). Similar effects were observed with compound **5**. The dicyanomethylenecoumarinyl-Fmoc-protected Asp derivatives were obtained by condensation of the respective thionated precursors with malononitrile in the presence of triethylamine and silver nitrate (Scheme 1) in 81% (**7**) and 65% (**8**) yield after silica gel column chromatography and fully characterized by UV−vis, HR ESI MS, and NMR. The purity of the amino acid derivatives was also assessed by reversed-phase HPLC (Figure S1, Supporting Information). It is worth noting that amino acid derivatives **5** and **7** were isolated as a mixture of two diastereomers due to the additional stereogenic center created by the incorporation of the methyl group at the coumarin skeleton.

As a next step, the compatibility of the four Asp monomers with Fmoc-tBu SPPS was studied (Figures S2−S5, Supporting Information). Unfortunately, thionated monomers were not completely stable to the TFA cleavage and deprotection conditions since a considerable amount of desulfurization occurred (about 30% for **5** and 20% for **6**). Both amino acids were also unstable to the typical Fmoc-removing conditions. Reaction of piperidine with the thiolactone was the major side product. By contrast, dicyanomethylenecoumarin-caged Asp monomers (DEAdcCE, **7**, and DEAdcCM, **8**) were found to be stable to the acid and basic treatments typically used in Fmoc-tBu SPPS (Figures S4 and S5) as well as in cell culture medium (DMEM supplemented with 25% fetal bovine serum) after incubation for 1 h at 37 °C (Figure S6). The latter is a prerequisite for exploring the biological applications of coumarin-caged peptides.

On the basis of the stability studies, we selected dicyanomethylenecoumarin (DEAdcCE and DEAdcCM) as a caging group of Asp and focused on studying the photophysical and photochemical properties of **7** and **8** (see Table 1 and Figures 2 and S7−S10). The UV−vis absorption spectra of both compounds are very similar and have an absorbance maximum around 500 nm belonging to $\pi-\pi^*$ transitions of the coumarin chromophore. As shown in Table 1, λ_{max} values were slightly red-shifted with respect the corresponding free dicyanocoumarin alcohols (**11** and **14**; the structures are shown in Scheme 2), which correlates with the tendency previously found in other compounds.[15b] Similarly, the fluorescence emission maxima upon excitation at λ_{max} was also shifted to longer wavelengths in the caged amino acids.

Table 1. Photophysical and Photochemical Properties of the Compounds

	absorption		emission		uncaging		
	λ_{max} [a]	$\varepsilon(\lambda_{max})$ [b]	λ_{em} [c]	$\Delta\nu$ [d]	$10^2\phi$ [e]	$\varepsilon(505)$ [b]	$\varepsilon\phi$ [f]
7	492	30.3	551	59	0.24	24.5	58
8	489	27.5	555	66	0.10	22.5	22
11	483	33.5	545	62			
14	479	28.6	549	70			

[a]Absorption maximum (nm). [b]Extinction coefficient at λ_{max} or at 505 nm (mM^{-1} cm^{-1}). [c]Fluorescence emission maximum upon excitation at λ_{max} (nm). [d]Stokes's shift (nm). [e]Quantum yield for the uncaging process at 505 nm. [f]Efficiency of the uncaging process (M^{-1} cm^{-1}) (see the Supporting Information).

On the basis of the shape of the absorption curve and of the molar extinction coefficients of both DEAdcCM- and DEAdcCE-caged Asp derivatives at their λ_{max} and at 505 nm (Table 1), we decided to evaluate if green light could be used to deprotect them efficiently because it is less harmful to cells and penetrates deeper in tissues than UV or blue light.[10,11] Photolysis studies were carried out by using an LED as a light source, and the course of the uncaging process was monitored by reversed-phase HPLC-ESI MS. As shown in Scheme 2 and in Figures S11 and S12, irradiation at 505 nm induced conversion to the uncaged Fmoc-Asp-OtBu and the corresponding coumarin alcohol derivatives in both cases as the main photolytic byproducts (**11** from **7** and **14** from **8**). The fact that uncaging of **7** was slightly faster compared with that of **8** (2 min vs 5 min, for a complete deprotection) can be attributed to the higher stability of the secondary carbocation intermediate generated during photoheterolysis[16] of the ester bond of **7**. In good agreement with such photolysis studies, the uncaging quantum yield (ϕ) for **7** was higher than for **8** (Table 1), resulting in a high product ($\varepsilon\phi$), thus indicating a higher efficiency for the uncaging process.[1b]

Synthesis of a Dicyanocoumarin-Caged Cyclic RGD Peptide. The next step involved the evaluation of both dicyanomethylenecoumarin derivatives (DEAdcCM and DEAdcCE) as PPGs of the side chain of Asp during the Fmoc-*t*Bu SPPS of a linear pentapeptide containing the RGD sequence (**15** and **16**, respectively; see Scheme 3). First, compounds **7** and **8** were reacted with HCl in dioxane for 15 h at 50 °C to remove the *tert*-butyl group, affording the corresponding caged Asp monomers **9** and **10**, respectively (Scheme 1) suitable for the assembly of the peptide. As shown in Scheme 3, the assembly of the linear tetrapeptide was carried out on 2-chlorotrityl chloride resin using DIPC and HOAt. After incorporation of both Asp monomers (**9** or **10**) and Fmoc removal using standard conditions (20% piperidine in DMF), an acidic treatment was carried out to check the quality of the crude peptide. To our surprise, HPLC-ESI MS analysis (Figures S13 and S14, Supporting Information) revealed that protection of Asp with both dicyanocoumarin derivatives promotes the formation of an aspartimide side product (**17**, Scheme 3). In fact, the use of DEAdcCM monomer (**10**) did not afford the expected peptide (**16**) after standard piperidine treatment but instead the corresponding aspartimide derivative as a major product (Table S1, Supporting Information). In contrast, this undesired cyclization was substantially reduced with monomer **9**, which facilitated peptide **15** to be obtained in a 1:1 ratio with respect **17**. Aspartimide formation is well-known to occur during the piperidine-catalyzed Fmoc removal of peptides containing Asp, and it is very dependent on several factors including the side-chain protecting group of this amino acid and its neighboring residue[19] (D-amino acids are known to increase aspartimide formation, and in our case, D-Phe is adjacent to the dicyanocoumarin-esterified Asp). Since the addition of organic acids to the standard piperidine-based Fmoc deprotection cocktail has been described to reduce the formation of aspartimide side products, we evaluated the use of three additives.[20] As shown in Figures S13 and S14 and in Table S1, HOBt and Oxyma were very effective in reducing this side reaction, particularly when the sterically shielded DEAdcCE monomer (**9**) was used. However, the level of aspartimide was still very high with DEAdcCM monomer (**10**) under the

DOI: 10.1021/acs.joc.6b02415
J. Org. Chem. 2016, 81, 11556−11564

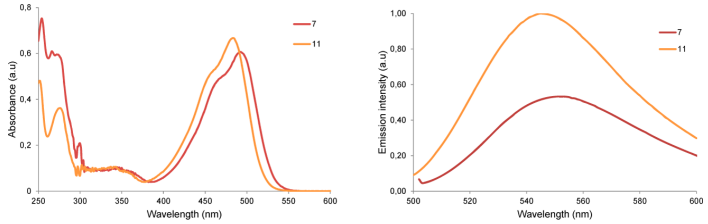

Figure 2. Comparison of the UV−vis spectra (left, 20 μM) and fluorescence emission spectra (right, 50 nM) of DEAdcCE coumarin alcohol (**11**) and of Fmoc-Asp(DEAdcCE)-OtBu (**7**) in Tris buffer pH 7.5/ACN 1:1.

Scheme 2. Photoactivation of Dicyanocoumarin-Caged Asp Monomers

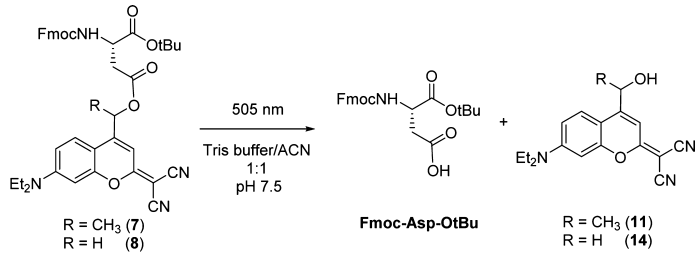

Scheme 3. Evaluation of Aspartimide Formation (17) during Fmoc-tBu SPPS of the Linear Peptide H-Asp(DEAdcCM or DEAdcCE)-D-Phe-Lys-Arg-Gly-OH (15 or 16) by Using Dicyanocoumarin-Protected Asp Monomers (9 or 10, Respectively) Together with Different Fmoc-Removal Conditions

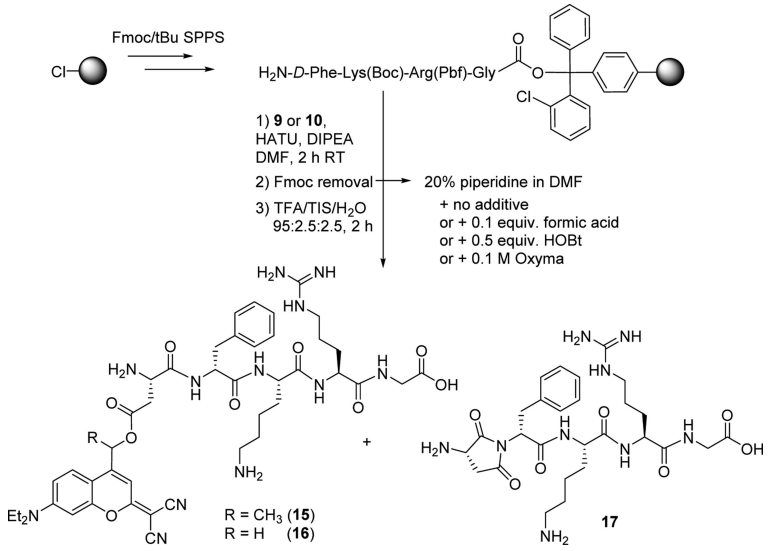

optimal conditions for **9**. The overall results confirm that the steric hindrance provided by the methyl group of DEAdcCE around the β-carboxyl ester in combination with HOBt or Oxyma additives during Fmoc-removal represents the best choice to minimize the nucleophilic attack of the amidate anion at the carbonyl group and, for instance, to reduce aspartimide formation.

Taking into account the synthetic problems encountered with DEAdcCM monomer (**10**) together with its slow photodeprotection rate with green light, we selected DEAdcCE monomer (**9**) to synthesize the target caged cyclic RGD peptide, c(RGD(DEAdcCE)fK) (**18**). As shown in Scheme 4, a Lys building block incorporating a short Boc-protected polyethylene glycol spacer at the ε-NH_2 was used during the assembly of the linear pentapeptide. After cleavage under mild acidic conditions and overnight cyclization with PyBOP, the protected peptide, c[-Arg-(Pbf)-Gly-Asp(DEAdcCE)-D-Phe-Lys(Boc-linker)-] was obtained. Finally, the remaining side chain protecting groups (Boc and Pbf) were eliminated by acidic treatment. Peptide **18** was purified by reversed-phase

DOI: 10.1021/acs.joc.6b02415
J. Org. Chem. 2016, 81, 11556−11564

Scheme 4. Synthesis of the DEAdcCE-Caged Cyclic RGD Peptide (18) and Its Ruthenocenoyl Conjugate (20)

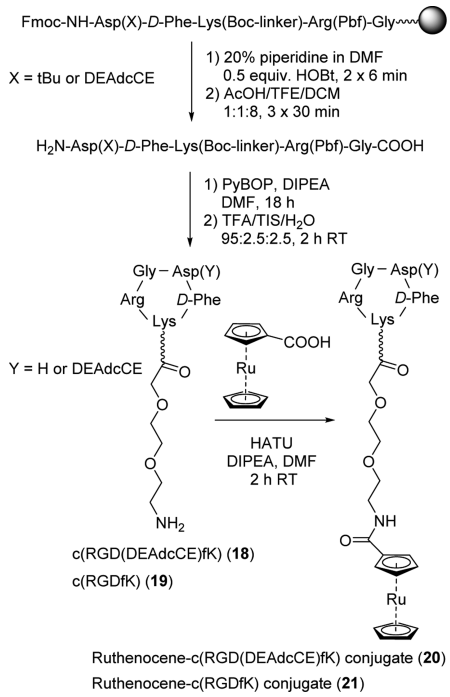

HPLC and characterized by HR ESI-MS (Figures S15 and S16, Supporting Information). Similarly, the noncaged peptide (**19**) was synthesized as a control.[14e]

Synthesis and Photochemical Properties of a Conjugate between Ruthenocene and the Dicyanocoumarin-Caged Cyclic RGD Peptide. Having peptide **18** in hand, we conjugated ruthenocene[21] as a metallodrug model cargo to evaluate the compatibility of a metal complex with uncaging conditions. As shown in Scheme 4, ruthenocene carboxylic acid was attached to **18** by using HATU and DIPEA. Analysis by HPLC-ESI MS showed a main peak (Figure S17) that was isolated and characterized as the expected ruthenocene conjugate (**20**). Similarly, the control ruthenocene–RGD conjugate (**21**) was obtained with peptide **19** (Figure S19). After purification by semipreparative HPLC and lyophilization, the trifluoroacetate salts of **20** (overall yield from **18**: 46%) and **21** (overall yield from **19**: 30%) were obtained as orange and white solids, respectively. In both cases, high-resolution ESI MS analysis afforded m/z values consistent with the calculated value of the charged species ($[M + H]^+$ and $[M + 2H]^{2+}$) and with the appropriate isotopic mass distribution patterns of ruthenium (Figures S18 and S20).

Finally, the photoactivation of the coumarin-caged peptide (**18**) and its ruthenocene conjugate (**20**) was studied. As shown in Figure 3, both compounds strongly absorb in the visible region showing a maximum of absorption at λ_{max}= 496 nm, which was slightly red-shifted with respect monomer **7** (492 nm). Irradiation of **18** at 505 nm caused a fast release of the free peptide **19** (90% after 10 min irradiation at 37 °C in PBS buffer) and the corresponding coumarin alcohol **11** (Figure S21). By contrast, uncaging of conjugate **20** was slightly slower and required 30 min to achieve a similar percentage of deprotection (Figures 3 and S22), which could be attributed both to the different medium employed in the experiments and to the presence of the metal complex. A similar tendency was found when comparing the uncaging quantum yields of the caged peptide ($10^2\phi$ = 0.85) and of the conjugate ($10^2\phi$ = 0.72). Importantly, only ruthenocene–c(RGDfK) conjugate **21** was photoreleased from **20** upon green light irradiation, which indicates that uncaging conditions are completely compatible with the integrity of the bioconjugate. In addition, the stability of the ruthenocenoyl conjugate in cell culture medium (DMEM–25% FBS, 1 h 37 °C; Figure S23) opens the door to using dicyanocoumarin-caged RGD peptides as drug carriers in cells overexpressing $\alpha_V\beta_3$ integrins.

CONCLUSIONS

In summary, we have described for the first time the synthesis and photochemical characterization of a caged cyclic RGD peptide that can be efficiently photoactivated with biologically compatible green light. This was accomplished by using a new dicyanocoumarin derivative (DEAdcCE) for the protection of the carboxyl group at the side chain of the aspartic acid residue, which was selected on the basis of Fmoc-tBu SPPS compatibility and photolysis efficiency. Indeed, the acid and basic stability of dicyanocoumarin-caged Asp monomers (**7** and

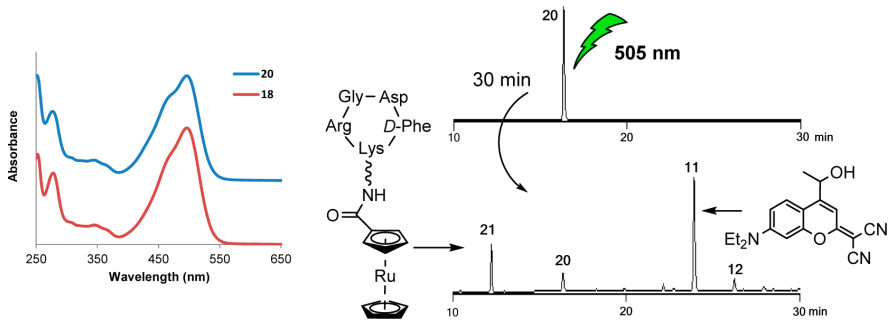

Figure 3. (Left) Comparison of the UV–vis spectra of peptide **18** and its ruthenocene conjugate **20**. (Right) Reversed-phase HPLC traces for the uncaging of conjugate **20** upon irradiation at 505 nm (37 °C, PBS/ACN 8:2) at t = 0 (top) and t = 30 min (bottom). The structure of coumarin derivative **12** is shown in Figure S22 (Supporting Information).

DOI: 10.1021/acs.joc.6b02415
J. Org. Chem. 2016, 81, 11556–11564

8) was found to be substantially higher than that of the thiocoumarin precursors (5 and 6), and among them, the DEAdcCE moiety was preferred over DEAdcCM due to higher uncaging efficiency and reduced aspartimide formation. Minimization of the aspartimide side reaction was accomplished by using acidic additives such as HOBt or Oxyma during the basic Fmoc-removal treatment in combination with the Fmoc-Asp(DEAdcCE)-OH monomer (9) in which the incorporation of a methyl group at the coumarin skeleton near the ester bond linking both moieties led to a steric shielding effect around this functionality.

On the other hand, a conjugate between the coumarin-caged cyclic RGD peptide and ruthenocene, which was selected as a metallodrug model cargo, has been synthesized and characterized. The fact that green-light triggered photoactivation can be efficiently performed both with the caged peptide (18) and with its ruthenocenoyl bioconjugate (21) opens the door to exploring the use of DEAdcCE-caged peptide sequences as selective drug carriers in the context of photocontrolled targeted anticancer strategies. Work is in progress to extend this approach to other coumarin derivatives with improved red-shifted properties, particularly those removable within the optical window of the tissues, as well as to the conjugation between caged peptides and other anticancer agents, including Pt(IV) prodrugs.

EXPERIMENTAL SECTION

Materials and Methods. Unless otherwise stated, common chemicals and solvents including Fmoc-protected amino acids, resins, and coupling reagents for solid-phase synthesis were purchased from commercial sources and used without further purification. Milli-Q water was directly obtained from a Milli-Q system equipped with a 5000 Da ultrafiltration cartridge. Aluminum plates coated with a 0.2 mm thick layer of silica gel 60 F_{254} were used for thin-layer chromatography analyses (TLC), whereas column chromatography purification was carried out using silica gel 60 (230−400 mesh). Analytical reversed-phase HPLC analyses were carried out on a Jupiter Proteo column (250 × 4.6 mm, 4 μm, flow rate: 1 mL/min), using linear gradients of 0.045% TFA in H_2O (solvent A) and 0.036% TFA in ACN (solvent B). In some cases, small-scale purification was carried out using the same column. Large-scale purification was carried out on a Jupiter Proteo semipreparative column (250 × 10 mm, 10 μm, flow rate: 3 mL/min) using linear gradients of 0.1% TFA in H_2O (solvent A) and 0.1% TFA in ACN (solvent B). After several runs, pure fractions were combined and lyophilized. Electrospray ionization mass spectra (ESI-MS) were recorded on an instrument equipped with single quadrupole detector coupled to an HPLC and a high-resolution (HR) ESI-MS on LC/MSTOF instrument. NMR spectra were recorded at 25 °C in a 400 MHz spectrometer using deuterated solvents. Tetramethylsilane (TMS) was used as an internal reference (0 ppm) for ^{1}H spectra recorded in $CDCl_3$ and the residual signal of the solvent (77.16 ppm) for ^{13}C spectra. Chemical shifts are reported in part per million (ppm) in the δ scale, coupling constants in hertz, and multiplicity as follows: s (singlet), d (doublet), t (triplet), q (quadruplet), qt (quintuplet), m (multiplet), dd (doublet of doublets), td (doublet of triplets), ddd (doublet of doublet of doublets), br (broad signal). UV−vis spectra were recorded with a UV−vis−NIR spectrophotometer, and fluorescence measurements were performed on a Quanta-Master fluorimeter. Photolysis studies were performed at 37 °C in a custom-built irradiation setup from Microbeam including a cuvette, a thermostated cuvette holder, and a mounted high power LED of 505 nm (100 mW/cm^2). In a typical experiment, the irradiation samples contained the caged amino acids (20 μM) in a 1:1 (v/v) mixture of Tris buffer pH 7.5 and ACN. After irradiation, the samples were analyzed by reversed-phase HPLC-ESI MS in a Jupiter Proteo C_{18} column (250 × 4.6 mm, 90 Å 4 μm, flow rate: 1 mL/min) using linear gradients of 0.1% formic acid in H_2O (A) and 0.1% formic acid in ACN (B).

Synthesis of the Caged Amino Acid Derivatives. *7-(N,N-Diethylamino)-4-(1-hydroxyeth-1-yl)coumarin (1).*[7e] A solution of 4-carbaldehyde-7-(*N*,*N*-diethylamino)coumarin (2.58 g, 11 mmol) in dry THF (60 mL) was cooled at −78 °C using a mixture of acetone and dry ice and kept under argon atmosphere. Then, a solution of methylmagnesium chloride (6.3 mL, 3 M) in THF was added dropwise, and the reaction mixture was stirred for 2 h at −78 °C in the dark. After that, a second portion of methylmagnesium chloride (3.0 mL) was added. After the mixture was stirred for an additional 2 h at −78 °C in the dark, a saturated aqueous solution of ammonium chloride (50 mL) was added, and the reaction mixture was allowed to reach room temperature. The mixture was extracted with ethyl acetate (3 × 50 mL). The combined organic layers were dried over Na_2SO_4 and filtered, and the solvent was removed under reduced pressure. The red residue was purified by column chromatography (silica gel, 0−3.5% MeOH in DCM). The appropriate fractions were collected, and the solvents were removed to give a 1.94 g (71% yield) of a yellow solid. TLC: R_f (5% MeOH in DCM) 0.31. ^{1}H NMR (400 MHz, $CDCl_3$) δ (ppm): 7.43 (1H, d, J = 9.2 Hz), 6.57 (1H, dd, J = 9.2 Hz, J = 2.6 Hz), 6.50 (1H, d, J = 2.6 Hz), 6.27 (1H, br s), 5.15 (1H, m), 3.41 (4H, q, J = 7.0 Hz), 2.18 (1H, br s), 1.57 (3H, d, J = 6.8 Hz), 1.21 (6H, t, J = 7.0 Hz). ESI-MS, positive mode: m/z 261.55 (calcd mass for $C_{15}H_{20}NO_3$ $[M + H]^+$ 262.14).

7-(N,N-Diethylamino)-4-(hydroxymethyl)coumarin (2).[7e] 4-Carbaldehyde-7-(*N*,*N*-diethylamino)coumarin (3.71 g, 15.1 mmol) and sodium borohydride (0.57 g, 15.1 mmol) were stirred at room temperature for 4 h in ethanol (300 mL) protected from light. After addition of 1 M HCl (80 mL) and dilution with water (50 mL), the red solution was extracted with DCM (3 × 50 mL). The combined organic layers were washed with water (50 mL), dried over anhydrous $MgSO_4$, and filtered. After removal of the solvent under reduced pressure, a yellow solid was obtained (3.31 g, yield 90%) and used without further purification in the next step. TLC: R_f (5% MeOH in DCM) 0.25. ^{1}H NMR (400 MHz, $CDCl_3$) δ (ppm): 7.31 (1H, d, J = 9.2 Hz), 6.57 (1H, dd, J = 9.2 Hz, J = 2.8 Hz), 6.49 (1H, d, J = 2.8 Hz), 6.26 (1H, s, *H3*), 4.83 (2H, s), 3.40 (4H, q, J = 7.2 Hz), 1.20 (6H, t, J = 7.2 Hz). ESI-MS, positive mode: m/z 247.88 (calcd mass for $C_{14}H_{18}NO_3$ $[M + H]^+$ 248.13).

Fmoc-Asp(DEACE)-O^{t}Bu (3).[7e] Fmoc-Asp-O^{t}Bu (2.52 g, 6.12 mmol), 1-ethyl-3-(3-(dimethylamino)propyl)carbodiimide hydrochloride (1.39 g, 7.25 mmol), and DMAP (38 mg, 0.31 mmol) were dissolved in dry DCM (50 mL). A solution of **1** (1.44 g, 5.56 mmol) in dry DCM (50 mL) was added, and the reaction mixture was stirred at room temperature in the dark under argon atmosphere for 4 h. The solvent was removed in vacuum and the crude material was purified via column chromatography (silica gel, 0−1.5% methanol in DCM) to obtain 1.42 g (57% yield) of a yellow crystalline solid. TLC: R_f (5% MeOH in CH_2Cl_2) 0.68. ^{1}H NMR (400 MHz, $CDCl_3$) δ (ppm): 7.75 (2H, t, J = 6.8 Hz), 7.58 (2H. t, J = 6.8 Hz), 7.39 (3H, q, J = 7.2 Hz), 7.31 (2H, t, J = 7.2 Hz), 6.57 (1H, ddd, J = 8.8 Hz, J = 6 Hz, J = 2.4 Hz), 6.50 (1H, dd, J = 5.6 Hz, J = 2.4 Hz), 6.12 (1H, d, J = 4 Hz), 6.06 (1H, m), 5.75 (1H, m), 4.55 (1H, m), 4.35 (2H, m), 4.22 (1H, q J = 6.8 Hz), 3.39 (4H, q, J = 7.2 Hz), 3.02 (2H, m), 1.60 (3H, d, J = 6.4 Hz), 1.56 (1H, s), 1.48 (4H, s), 1.40 (4H, s), 1.19 (6H, dt, J = 7.2 Hz,). ^{13}C NMR (100 MHz, $CDCl_3$) δ (ppm): 170.1, 169.9, 169.5, 169.3, 162.0, 161.9, 156.6, 155.9, 155.1, 154.8, 150.6, 143.9, 143.8, 143.7, 141.2, 127.7, 127.1, 125.2, 124.8, 124.6, 120.0, 119.9, 108.7, 105.5, 105.1, 104.9, 98.0, 83.0, 82.9, 68.4, 68.2, 67.3, 50.9, 50.8, 47.1, 44.7, 36.9, 27.9, 27.8, 20.9, 12.4. ESI-MS, positive mode: m/z 654.9 (calcd mass for $C_{38}H_{42}N_2O_8$ $[M + H]^+$ 654.76).

Fmoc-Asp(DEACM)-O^{t}Bu (4).[7e] Fmoc-Asp-O^{t}Bu (1.83 g, 4.45 mmol), 1-ethyl-3-(3-(dimethylamino)propyl)carbodiimide hydrochloride (1.01 g, 5.27 mmol), and DMAP (25 mg, 0.20 mmol) were dissolved in dry DCM (50 mL). After addition of a solution of **2** (1.01 g, 4.09 mmol) in dry DCM (50 mL), the reaction mixture was stirred at room temperature in the dark under argon atmosphere for 4 h. The solvent was removed under vacuum, and the crude material was purified via column chromatography (silica gel, 0−3% MeOH in

DOI: 10.1021/acs.joc.6b02415
J. Org. Chem. 2016, 81, 11556−11564

DCM) to obtain 1.37 g (53% yield) of a yellow crystalline solid. TLC: R_f (5% MeOH in DCM) 0.74. ^{1}H NMR (400 MHz, $CDCl_3$) δ (ppm): 7.76 (2H, d, J = 7.7 Hz), 7.60 (2H, d, J = 7.2 Hz), 7.39 (2H, t J = 7.2 Hz), 7.31 (3H, m), 6.56 (1H, m), 6.51 (1H, m), 6.12 (1H, s), 5.75 (1H, d, J = 7.6 Hz), 5.24 (2H, m), 4.58 (1H, m), 4.38 (2H, m), 4.23 (1H, t, J = 7.2 Hz), 3.40 (4H, q, J = 7.2 Hz), 3.04 (2H, m), 1.46 (9H, s), 1.19 (6H, t, J = 7.2 Hz). ^{13}C NMR (100 MHz, $CDCl_3$) δ (ppm): 170.3, 169.4, 161.7, 156.3, 155.9, 150.7, 148.8, 143.8, 141.3, 127.7, 127.1, 125.2, 124.4, 120.0, 108.7, 106.8, 105.9, 97.9, 83.1, 67.3, 61.9, 50.9, 47.1, 44.8, 36.8, 27.9, 12.4. ESI-MS, positive mode: m/z 640.95 (calcd mass for $C_{37}H_{41}N_2O_8$ $[M + H]^+$ 641.29).

Fmoc-Asp(DEATCE)-O^{t}Bu (**5**). Lawesson's reagent (0.41 g, 1.01 mmol) was added to a solution of Fmoc-Asp(DEACE)-O^{t}Bu (**3**, 1.10, 1.68 mmol) in toluene (40 mL). After stirring the mixture overnight at 70 °C under an argon atmosphere and protected from light, the solvent was evaporated under reduced pressure, and the resulting orange crude solid was purified via column chromatography (silica gel, 0−1% MeOH in DCM) to obtain 0.91 g (81% yield) of a dark orange solid. Mp: 95−97 °C. TLC: R_f (2% MeOH in DCM) 0.71. ^{1}H NMR (400 MHz, $CDCl_3$) δ (ppm): 7.75 (2H, m), 7.58 (2H, m), 7.40 (3H, m), 7.31 (2H, m), 7.04 (1H, d, J = 6 Hz), 6.65 (2H, m), 6.08 (1H, m), 5.74 (1H, t J = 8 Hz), 4.55 (1H, m), 4.37 (2H, m), 4.23 (1H, m), 3.41 (4H, m), 3.10−2.92 (2H, m), 1.59 (4H, m), 1.48 (4H, s), 1.40 (4H, s), 1.21 (6H, m). ^{13}C NMR (100 MHz, $CDCl_3$) δ (ppm): 197.3, 197.2, 170.1, 170.0, 169.5, 169.3, 159.4, 155.9, 150.9, 147.3, 147.0, 143.9, 143.8, 141.3, 127.7, 127.1, 125.2, 124.8, 124.7, 120.0, 119.3, 119.1, 110.4, 107.8, 97.7, 83.0, 82.9, 68.1, 67.9, 67.3, 67.2, 53.4, 50.8, 50.8, 47.1, 44.9, 37.0, 36.9, 27.9, 27.8, 20.9, 20.8, 12.4. HR ESI-MS, positive mode: m/z 671.2777 (calcd mass for $C_{38}H_{43}N_2O_7S$ $[M + H]^+$ 671.2791). Analytical RP-HPLC (0−100% B in 30 min, 10 min isocratic 100% B; A, 0.1% formic acid in H_2O; B, 0.1% formic acid in ACN; t_R = 32 min).

Fmoc-Asp(DEATCM)-O^{t}Bu (**6**). Lawesson's reagent (1.18 g, 2.92 mmol) was added to Fmoc-Asp(DEACM)-OtBu (**4**, 1 g, 1.56 mmol) in toluene (50 mL). The mixture was stirred overnight at 70 °C under an argon atmosphere and protected from light. After that, the solvent was evaporated under vacuum, and the resulting crude was purified via column chromatography (silica gel, 0−1% MeOH in DCM) to give 0.82 g (80% yield) of a dark orange solid. Mp: 91−94 °C. TLC: R_f (2% MeOH in DCM) 0.71. ^{1}H NMR (400 MHz, $CDCl_3$) δ (ppm): 7.76 (2H, d, J = 7.2 Hz), 7.60 (2H, dm J = 7.2 Hz), 7.40 (2H, t, J = 7.6 Hz), 7.31 (3H, q, J = 6.0 Hz), 7.03 (1H, s), 6.66 (1H, d, J = 2.4 Hz), 6.63 (1H, dd, J = 9.2 Hz, J = 2.4 Hz), 5.74 (1H, d, J = 8.0 Hz), 5.20 (2H, m), 4.58 (1H, m), 4.39 (2H, m), 4.23 (1H, t, J = 7.2 Hz), 3.41 (4H, q, J = 7.2 Hz), 3.05 (2H, m), 1.47 (9H, s), 1.20 (6H, t, J = 7.2 Hz). ^{13}C NMR (100 MHz, $CDCl_3$) δ (ppm): 197.0, 170.3, 169.3, 159.1, 155.9, 151.0, 143.8, 141.3, 141.1, 127.7, 127.1, 125.2, 124.5, 121.0, 120.0, 110.3, 108.2, 97.5, 83.1, 67.3, 61.6, 53.4, 50.9, 47.1, 44.9, 36.8, 27.9, 12.4. HR ESI-MS, positive mode: m/z 657.2623 (calcd mass for $C_{37}H_{41}N_2O_7S$ $[M + H]^+$ 657.2634). Analytical RP-HPLC (30−100% B in 30 min; A, 0.1% formic acid in H_2O; Bm 0.1% formic acid in ACN; t_R = 25.5 min).

Fmoc-Asp(DEAdcCE)-O^{t}Bu (**7**). Silver nitrate (580 mg, 3.42 mmol) was added to a solution of Fmoc-Asp(DEATCE)-OtBu (**5**, 920 mg, 1.37 mmol), malononitrile (453 mg, 6.85 mmol), and triethylamine (670 μL, 4..79 mmol) in dry ACN (80 mL) under an argon atmosphere. The reaction mixture was stirred for 3 h in the dark at room temperature and then concentrated under reduced pressure. The crude was purified by column chromatography (silica gel, 0−0.6% MeOH in DCM) to give 780 mg (81% yield) of a dark orange solid. Mp: 110−113 °C. TLC: R_f (2% MeOH in DCM) 0.65. ^{1}H NMR (400 MHz, $CDCl_3$) δ (ppm): 7.75 (2H, m), 7.57−7.53 (2H, m), 7.45−7.27 (5H, m), 6.70 (1H, m), 6.64 (1H, m), 6.57−6.52 (1H, m), 6.07 (1H, m), 5.73 (1H, br t), 4.56 (1H, m), 4.35 (2H, m), 4.18 (1H, m), 3.46−3.36 (4H, m), 3.02 (2H, m), 1.60 (3H, m), 1.49 (5H, s), 1.40 (4H, s), 1.21 (6H, m). ^{13}C NMR (100 MHz, $CDCl_3$) δ (ppm): 171.9, 170.0, 169.4, 169.2, 155.9, 155.8, 155.3, 151.8, 151.6, 151.5, 151.3, 143.8, 143.7, 141.2, 127.4, 127.0, 125.1, 119.9, 114.6, 113.8, 110.7, 110.6, 106.5, 104.8, 104.4, 97.5, 82.9, 68.3, 67.2, 55.4, 55.3, 50.9, 47.1, 44.9, 36.9, 29.7, 27.9, 27.8, 21.0, 12.4. HR ESI-MS, positive mode: m/z 703.3114 (calcd mass for $C_{41}H_{43}N_4O_7$ $[M + H]^+$ 703.3132). Analytical RP-HPLC (30−100% B in 30 min; A, 0.1% formic acid in H_2O; B, 0.1% formic acid in ACN; t_R = 25.7 and 25.8 min).

Fmoc-Asp(DEAdcCM)-O^{t}Bu (**8**). Silver nitrate (323 mg, 1.90 mmol) was added to a solution of Fmoc-Asp(DEATCM)-OtBu (**6**, 500 mg, 0.76 mmol), malononitrile (352 mg, 5.33 mmol), and triethylamine (370 μL, 2.67 mmol) in dry ACN (40 mL) under an argon atmosphere. The reaction mixture was stirred for 3 h in the dark at room temperature and then concentrated under reduced pressure. The crude was purified by column chromatography (silica gel, 0−0.8% MeOH in DCM) to give 337 mg (65% yield) of a dark orange solid. Mp: 108−110 °C. TLC: R_f (2% MeOH in DCM) 0.74. ^{1}H NMR (400 MHz, $CDCl_3$) δ (ppm): 7.75 (2H, d, J = 7.5 Hz), 7.58 (2H, d, J = 7.4 Hz), 7.39 (2H, t, J = 7.4 Hz), 7.30 (3H, m), 6.73 (1H, s), 6.62 (1H, dd, J = 9 Hz, J = 2.4 Hz), 6.55 (1H, d, J = 2.4 Hz), 5.75 (1H, d, J = 7.6 Hz), 5.23 (2H, q, J = 15 Hz), 4.57 (1H, m), 4.37 (2H, m), 4.20 (1H, t, J = 7.1 Hz), 3.41 (4H, q, J = 7.2 Hz), 3.05 (2H, m), 1.47 (9H, s), 1.21 (6H, t, J = 7.2 Hz). ^{13}C NMR (100 MHz, $CDCl_3$) δ (ppm): 171.6, 170.2, 169.3, 155.9, 155.0, 151.7, 145.2, 143.7, 141.3, 127.7, 127.1, 125.1, 125.0, 120.0, 114.4, 113.7, 110.6, 107.0, 106.5, 97.4, 83.1, 67.2, 61.7, 55.9, 51.0, 47.1, 44.9, 36.9, 27.9, 12.4. HR ESI-MS, positive mode: m/z 689.2977 (calcd mass for $C_{40}H_{41}N_4O_7$ $[M + H]^+$ 689.2975). Analytical RP-HPLC (30−100% B in 30 min; A, 0.1% formic acid in H_2O; B, 0.1% formic acid in ACN; t_R = 24.5 min).

Fmoc-Asp(DEAdcCE)-OH (**9**). A solution of HCl in 1,4-dioxane (20 mL, 100 mmol) was added to Fmoc-Asp(DEAdcCE)-OtBu (**7**, 600 mg, 0.85 mmol). The reaction mixture was stirred in the dark at 50 °C during 15 h and then concentrated under reduced pressure. The compound was used directly in the assembly of the caged peptide. ^{1}H NMR (400 MHz, $CDCl_3$) δ (ppm): 7.75 (2H, d, J = 7.2 Hz), 7.57−7.53 (2H, m), 7.38 (3H, t, J = 7.6 Hz), 7.30−7.27 (2H, m), 6.66−6.64 (2H, m), 6.56−6.53 (1H, m), 6.12−6.05 (1H, m), 5.82 (1H, m), 4.75−4.70 (1H, m), 4.41−4.35 (2H, m), 4.19 (1H, m), 3.66−3.62 (4H, m), 3.11 (2H, m), 1.59 (3H, m), 1.22 (6H, m). ^{13}C NMR (100 MHz, $CDCl_3$) δ (ppm): 172.1, 169.6, 169.1, 155.8, 155.7, 155.2, 151.7, 151.5, 143.5, 143.4, 141.1, 127.6, 126.9, 124.9, 119.8, 115.6, 113.5, 110.7, 106.3, 104.1, 103.9, 97.4, 72.0, 71.0, 67.2, 61.5, 54.8, 49.9, 46.8, 44.8, 42.7, 36.7, 29.5, 21.0, 12.6. HR ESI-MS, positive mode: m/z 647.2518 (calcd mass for $C_{37}H_{35}N_4O_7$ $[M + H]^+$ 647.2506). Analytical RP-HPLC (30−100% B in 30 min; A, 0.1% formic acid in H_2O; B, 0.1% formic acid in ACN; t_R = 23.5 min).

Fmoc-Asp(DEAdcCM)-OH (**10**). A solution of HCl in 1,4-dioxane (5 mL, 25 mmol) was added to Fmoc-Asp(DEAdcCM)-OtBu (**8**, 30 mg, 0.04 mmol). The reaction mixture was stirred in the dark at 50 °C during 15 h and then concentrated under reduced pressure. The compound was used directly in the assembly of the caged peptide. ^{1}H NMR (400 MHz, $CDCl_3$) δ (ppm): 7.75 (2H, d, J = 7.2 Hz), 7.58 (2H, m), 7.39 (2H, t, J = 7.2 Hz), 7.30 (3H, m), 6.70−6.61 (3H, m), 5.88 (1H, m), 5.29 (2H, m), 4.76 (1H, m), 4.40 (2H, m), 4.21 (1H, m), 3.65 (4H, q, J = 7.2 Hz), 3.18 (2H, m), 1.21 (6H, m). ^{13}C NMR (100 MHz, $CDCl_3$) δ (ppm): 172.4, 172.17, 170.1, 156.1, 155.0, 151.7, 146.0, 143.8, 141.4, 127.9, 127.3, 125.2, 125.0, 120.1, 115.8, 113.6, 111.2, 107.1, 105.7, 97.7, 72.4, 71.3, 67.5, 61.8, 55.3, 50.3, 47.2, 45.3, 43.0, 36.9, 12.6. HR ESI-MS, positive mode: m/z 633.2334 (calcd mass for $C_{36}H_{33}N_4O_7$ $[M + H]^+$ 633.2349). Analytical RP-HPLC (30−100% B in 30 min; A, 0.1% formic acid in H_2O; B, 0.1% formic acid in ACN; t_R = 22.7 min).

Synthesis DEAdcCE-Caged RGD Peptide (**18**). Solid-phase peptide syntheses were performed manually in a polypropylene syringe fitted with a polyethylene disk. Standard Fmoc-*t*Bu chemistry was used with 2-chlorotrityl chloride resin (f = 1.5 mmol/g, 100−200 mesh). The following protecting groups were used for the protection of trifunctional amino acids: Boc (N^{ε}-*tert*-butoxycarbonyl, Lys), Pbf (N^G-2,2,4,6,7-pentamethyldihydrobenzofuran-5-sulfonyl, Arg), and ^{t}Bu (*O*-*tert*-butyl, Asp). Fmoc-Asp(DEAdcCE)-OH (**9**) or Fmoc-Asp-(DEAdcCM)-OH (**10**) were used for the synthesis of caged peptides, and Fmoc-Lys(Boc-AEEA)-OH (Boc-AEEA = N^{ε}-(2-(2-(2-(*tert*-butyloxycarbonyl)aminoethoxy)ethoxy)acetyl) was used as spacer. First, the resin was washed with neutral DCM (2 × 5 min and 1 × 30 min), and the loading was reduced to ca. 1 mmol/g by

DOI: 10.1021/acs.joc.6b02415
J. Org. Chem. 2016, 81, 11556−11564

incorporation of Fmoc-Gly-OH (0.7 molar equiv) in the presence of DIPEA (5 molar equiv) in anhydrous DCM for 40 min. After capping with MeOH (1 × 10 min), the following Fmoc-protected amino acids (3 molar equiv) were incorporated with DIPC (3 molar equiv) and HOAt (3 molar equiv) in anhydrous DMF for 2 h. The coupling efficiency was assessed by the ninhydrin test. Fmoc protecting groups were removed with 20% piperidine in DMF (2 × 10 min) in each synthesis cycle except when DEAdcCE or DEAdcCM protection was used for Asp, which required the use of an acidic additive (0.5 equiv of HOBt relative to piperidine). After removal of the final *N*-terminal Fmoc group, linear peptides were released from the support by treatment with AcOH/TFE/DCM 1:1:8 (v/v/v) (3 × 30 min). The collected filtrates were evaporated in vacuo, and several co-evaporations with toluene (4 × 25 mL) were carried out to completely remove acetic acid. The resulting residue was dissolved in a minimum amount of DCM and poured onto cold diethyl ether to precipitate the fully protected linear peptide. The crude was triturated and washed three times with ether. Cyclization was carried out in DMF (ca. 1 mL/mg crude peptide) at pH 8−9 (adjusted with DIPEA) by using PyBOP (1 molar equiv). After being stirred for 18 h at room temperature, the reaction mixture was evaporated in vacuo, and diethyl ether was used to precipitate the peptides. Finally, side-chain deprotection was performed with TFA/TIS/H_2O 95:2.5:2.5 for 2 h at room temperature. After evaporation under reduced pressure, the crude peptide was triturated and washed three times with cold diethyl ether. After purification by semipreparative HPLC (gradient from 0−100% B in 30 min, A, 0.1% TFA in H_2O; B, 0.1% TFA in ACN flow rate: 3 mL/min), the trifluoroacetate salt of the peptide was obtained.

*c(RGD(DEAdcCE)fK) (**18**).* Overall yield (synthesis + purification): 22 mg, 5%. Characterization: Analytical RP-HPLC (0−100% B in 30 min; A, 0.1% formic acid in H_2O; B, 0.1% formic acid in ACN): t_R = 12.7 min. HR ESI MS, positive mode: m/z 1040.5302 (calcd mass for $C_{51}H_{70}N_{13}O_{11}$ $[M + H]^+$ 1040.5318), m/z 520.7698 (calcd mass for $C_{51}H_{71}N_{13}O_{11}$ $[M + 2H]^{2+}$ 520.7698).

Synthesis of Ruthenocenoyl−Peptide Conjugates 20 and 21. *Ruthenocene−c(RGD(DEAdcCE)fK) Conjugate (**20**).* To a solution of ruthenocene carboxylic acid (0.35 mg, 1.3 molar equiv) and HATU (0.51 mg, 1.05 molar equiv) in anhydrous DMF (0.2 mL) was added DIPEA (2 μL, 10 molar equiv). After being stirred for 5 min at room temperature, the reaction mixture was added to peptide **18** (1.0 mg, 0.91 μmol) previously dissolved in anhydrous DMF (0.2 mL) and DIPEA (1 μL, 5 molar equiv). After being stirred for 2 h at room temperature and protected from light, the solvent was evaporated in vacuo, and the conjugate was purified by semipreparative HPLC (gradient from 50 to 100% B in 30 min, flow rate: 3 mL/min, t_R = 9.5 min). Overall yield (synthesis + purification): 0.57 mg of a orange solid, 46%. Characterization: t_R = 16.4 min (analytical gradient: 0−100% in 30 min; A, 0.1% formic acid in H_2O; B, 0.1% formic acid in ACN); HR ESI MS, positive mode: m/z 1298.4928 (calcd mass for $C_{62}H_{78}N_{13}O_{12}Ru$ $[M + H]^+$ 1298.4936).

*Ruthenocene−c(RGDfK) Conjugate (**21**).* To a solution of ruthenocene carboxylic acid (0.48 mg, 1.3 molar equiv) and HATU (0.72 mg, 1.05 molar equiv) in anhydrous DMF (0.2 mL) was added DIPEA (2.4 μL, 10 molar equiv). After being stirred for 5 min at room temperature, the reaction mixture was added to peptide **19** (1 mg, 1.33 μmol) previously dissolved in anhydrous DMF (0.2 mL) and DIPEA (1.2 μL, 5 molar equiv). After being stirred for 2 h at room temperature, the solvent was evaporated in vacuo, and the conjugate was purified by semipreparative HPLC (gradient from 0 to 100% B in 30 min, flow rate: 3 mL/min, t_R = 14.9 min). Overall yield (synthesis + purification): 0.42 mg of a white solid, 30%. Characterization: t_R = 12.2 min (analytical gradient: 0−100% in 30 min; A, 0.1% formic acid in H_2O; B, 0.1% formic acid in ACN); HR ESI MS, positive mode m/z 1007.3561 (calcd mass for $C_{44}H_{61}N_{10}O_{11}Ru$ $[M + H]^+$: 1007.3565).

■ ASSOCIATED CONTENT

Supporting Information

The Supporting Information is available free of charge on the ACS Publications website at DOI: 10.1021/acs.joc.6b02415.

Characterization data (HPLC traces, NMR, MS, UV−vis, and fluorescence) of the compounds (PDF)

■ AUTHOR INFORMATION

Corresponding Author

*E-mail: vmarchan@ub.edu.

ORCID

Vicente Marchán: 0000-0002-1905-2156

Notes

The authors declare no competing financial interest.

■ ACKNOWLEDGMENTS

This work was supported by funds from the Spanish grants CTQ2014-52658-R and CSD2009-00080 and the Generalitat de Catalunya (2014SGR187 and XRB). We acknowledge helpful assistance by Dr. Irene Fernández and Laura Ortiz (MS) and Dr. Francisco Cárdenas (NMR) from CCiTUB. A.G. was a recipient fellow of the University of Barcelona.

■ REFERENCES

(1) (a) Brieke, C.; Rohrbach, F.; Gottschalk, A.; Mayer, G.; Heckel, A. *Angew. Chem., Int. Ed.* **2012**, *51*, 8446−8476. (b) Hansen, M. J.; Velema, W. A.; Lerch, M. M.; Szymanski, W.; Feringa, B. L. *Chem. Soc. Rev.* **2015**, *44*, 3358−3377. (c) Velema, W. A.; Szymanski, W.; Feringa, B. L. *J. Am. Chem. Soc.* **2014**, *136*, 2178−2791. (d) Szymański, W.; Beierle, J. M.; Kistemaker, H. A. V.; Velema, W. A.; Feringa, B. L. *Chem. Rev.* **2013**, *113*, 6114−6178.

(2) (a) Lee, H.-M.; Larson, D. R.; Lawrence, D. S. *ACS Chem. Biol.* **2009**, *4*, 409−427. (b) Deiters, A. *ChemBioChem* **2010**, *11*, 47−53.

(3) Klan, P.; Solomek, T.; Bochet, C. G.; Blanc, A.; Givens, R.; Rubina, M.; Popik, V.; Kostikov, A.; Wirz, J. *Chem. Rev.* **2013**, *113*, 119−191.

(4) (a) Mayer, G.; Heckel, A. *Angew. Chem., Int. Ed.* **2006**, *45*, 4900−4921. (b) Noguchi, M.; Skwarczynski, M.; Prakash, H.; Hirota, S.; Kimura, T.; Hayashia, Y.; Kisoa, Y. *Bioorg. Med. Chem.* **2008**, *16*, 5389−5397. (c) Schimer, J.; Pávová, M.; Anders, M.; Pachl, P.; Šácha, P.; Cígler, P.; Weber, J.; Majer, P.; Řezáčová, P.; Kräusslich, H.-G.; Müller, B.; Konvalinka, J. *Nat. Commun.* **2015**, *6*, 6461−6468. (d) Velema, W. A.; van der Berg, J. P.; Szymanski, W.; Driessen, A. J. M.; Feringa, B. L. *ACS Chem. Biol.* **2014**, *9*, 1969−1974. (e) Olson, J. P.; Kwon, H.-B.; Takasaki, K. T.; Chiu, C. Q.; Higley, M. J.; Sabatini, B. L.; Ellis-Davies, G. C. R. *J. Am. Chem. Soc.* **2013**, *135*, 5954−5957. (f) Furuta, T.; Wang, S. S.-H.; Dantzker, J. L.; Dore, T. M.; Bybee, W. J.; Callaway, E. M.; Denk, W.; Tsien, R. Y. *Proc. Natl. Acad. Sci. U. S. A.* **1999**, *96*, 1193−1200. (g) Schönleber, R. O.; Bendig, J.; Hagen, V.; Giese, B. *Bioorg. Med. Chem.* **2002**, *10*, 97−101. (h) Agarwal, H. K.; Janicek, R.; Chi, S.-H.; Perry, J. W.; Niggli, E.; Ellis-Davies, G. C. R. *J. Am. Chem. Soc.* **2016**, *138*, 3687−3693.

(5) (a) Azagarsamy, M. A.; Anseth, K. S. *Angew. Chem., Int. Ed.* **2013**, *52*, 13803−13807. (b) Gautier, A.; Gauron, C.; Volovitch, M.; Bensimon, D.; Jullien, L.; Vriz, S. *Nat. Chem. Biol.* **2014**, *10*, 533−541.

(6) (a) Steinert, H. S.; Schäfer, F.; Jonker, H. R.; Heckel, A.; Schwalbe, H. *Angew. Chem., Int. Ed.* **2014**, *53*, 1072−1075. (b) Meyer, A.; Mokhir, A. *Angew. Chem., Int. Ed.* **2014**, *53*, 12840−12843. (c) Rodrigues-Correia, A.; Knapp-Bühle, D.; Engels, J. W.; Heckel, A. *Org. Lett.* **2014**, *16*, 5128−5131. (d) Hemphill, J.; Liu, Q.; Uprety, R.; Samanta, S.; Tsang, M.; Juliano, R. L.; Deiters, A. *J. Am. Chem. Soc.* **2015**, *137*, 3656−3662.

(7) (a) Bourgault, S.; Létourneau, M.; Fournier, A. *Peptides* **2005**, *26*, 1475−1480. (b) Bourgault, S.; Létourneau, M.; Fournier, A. *Peptides* **2007**, *28*, 1074−1082. (c) Petersen, S.; Alonso, J. M.; Specht, A.; Duodu, P.; Goeldner, M.; del Campo, A. *Angew. Chem., Int. Ed.* **2008**, *47*, 3192−3195. (d) Wirkner, M.; Weis, S.; San Miguel, V.; Alvarez, M.; Gropeanu, R. A.; Salierno, M.; Sartoris, A.; Unger, R. E.; Kirkpatrick, C. J.; del Campo, A. *ChemBioChem* **2011**, *12*, 2623−2629. (e) Weis, S.; Shafiq, Z.; Gropeanu, R. A.; del Campo, A. *J. Photochem.*

DOI: 10.1021/acs.joc.6b02415
J. Org. Chem. 2016, 81, 11556−11564

Photobiol., A **2012**, *241*, 52−57. (f) Sainlos, M.; Iskenderian-Epps, W. S.; Olivier, N. B.; Choquet, D.; Imperiali, B. *J. Am. Chem. Soc.* **2013**, *135*, 4580−4583. (g) Sainlos, M.; Iskenderian-Epps, W. S.; Olivier, N. B.; Choquet, D.; Imperiali, B. *J. Am. Chem. Soc.* **2013**, *135*, 4580−4583. (h) Nomura, A.; Uyeda, T. Q. P.; Yumoto, N.; Tatsu, Y. *Chem. Commun.* **2006**, 3588−3590. (i) Pan, P.; Bayley, H. *FEBS Lett.* **1997**, *405*, 81−85. (j) Lawrence, D. S. *Curr. Opin. Chem. Biol.* **2005**, *9*, 570−575. (k) Karas, J. A.; Scanlon, D. B.; Forbes, B. E.; Vetter, I.; Lewis, R. J.; Gardiner, J.; Separovic, F.; Wade, J. D.; Hossain, M. A. *Chem. - Eur. J.* **2014**, *20*, 9549−9552. (l) Kotzur, N.; Briand, B.; Beyermann, M.; Hagen, V. *Chem. Commun.* **2009**, 3255−3257.

(8) (a) Ohmuro-Matsuyama, Y.; Tatsu, Y. *Angew. Chem., Int. Ed.* **2008**, *47*, 7527−7529. (b) Jiménez-Balsa, A.; Pazos, E.; Martínez-Albardonedo, B.; Mascareñas, J. L.; Vázquez, M. E. *Angew. Chem., Int. Ed.* **2012**, *51*, 8825−8829. (c) Grunwald, C.; Schulze, K.; Reichel, A.; Weiss, V. U.; Blaas, D.; Piehler, J.; Wiesmuller, K. H.; Tampe, R. *Proc. Natl. Acad. Sci. U. S. A.* **2010**, *107*, 6146−6151. (d) Nandy, S. K.; Agnes, R. S.; Lawrence, D. S. *Org. Lett.* **2007**, *9*, 2249−2252. (e) Johnson, E. C.; Kent, S. B. *Chem. Commun.* **2006**, 1557−1559.

(9) Mosquera, J.; Sánchez, M. I.; Mascareñas, J. L.; Vázquez, M. E. *Chem. Commun.* **2015**, *51*, 5501−5504.

(10) Kalka, K.; Merk, H.; Mukhtar, H. *J. Am. Acad. Dermatol.* **2000**, *42*, 389−413.

(11) (a) Brash, D.; Rudolph, J.; Simon, J.; Lin, A.; Mckenna, G.; Baden, H.; Halperin, A.; Ponten, J. *Proc. Natl. Acad. Sci. U. S. A.* **1991**, *88*, 10124−10128. (b) Protic-Sabljic, M.; Tuteja, N.; Munson, P.; Hauser, J.; Kraemer, K.; Dixon, K. *Mol. Cell. Biol.* **1986**, *6*, 3349−3356. (c) Jacques, S. L. *Phys. Med. Biol.* **2013**, *58*, R37−R61. (d) Hopkins, S. L.; Siewert, B.; Askes, S. H. C.; Veldhuizen, P.; Zwier, R.; Heger, M.; Bonnet, S. *Photochem. Photobiol. Sci.* **2016**, *15*, 644−653.

(12) (a) Desgrosellier, J. S.; Cheresh, D. A. *Nat. Rev. Cancer* **2010**, *10*, 9−22. (b) Auzzas, L.; Zanardi, F.; Battistini, L.; Burreddu, P.; Carta, P.; Rassu, G.; Curti, C.; Casiraghi, G. *Curr. Med. Chem.* **2010**, *17*, 1255−1299. (c) Mas-Moruno, C.; Fraioli, R.; Rechenmacher, F.; Neubauer, S.; Kapp, T. G.; Kessler, H. *Angew. Chem., Int. Ed.* **2016**, *55*, 7048−7067.

(13) Arosio, D.; Casagrande, C. *Adv. Drug Delivery Rev.* **2016**, *97*, 111−143.

(14) (a) Mukhopadhyay, S.; Barnés, C. M.; Haskel, A.; Short, S. M.; Barnes, K. R.; Lippard, S. J. *Bioconjugate Chem.* **2008**, *19*, 39−49. (b) Graf, N.; Bielenberg, D. R.; Kolishetti, N.; Muus, C.; Banyard, J.; Farokhzad, O. C.; Lippard, S. J. *ACS Nano* **2012**, *6*, 4530−4539. (c) Yuan, Y.; Kwok, R. T. K.; Tang, B. Z.; Liu, B. *J. Am. Chem. Soc.* **2014**, *136*, 2546−2554. (d) Barragán, F.; López-Senín, P.; Salassa, L.; Betanzos-Lara, S.; Habtemariam, A.; Moreno, V.; Sadler, P. J.; Marchán, V. *J. Am. Chem. Soc.* **2011**, *133*, 14098−14108. (e) Massaguer, A.; González-Cantó, A.; Escribano, E.; Barrabés, S.; Artigas, G.; Moreno, V.; Marchán, V. *Dalton Trans.* **2015**, *44*, 202−212. (f) Gandioso, A.; Shaili, E.; Massaguer, A.; Artigas, G.; González-Cantó, A.; Woods, J. A.; Sadler, P. J.; Marchán, V. *Chem. Commun.* **2015**, *51*, 9169−9172. (g) Soler, M.; Feliu, L.; Planas, M.; Ribas, X.; Costas, M. *Dalton Trans.* **2016**, *45*, 12970−12982.

(15) (a) Hagen, V.; Dekowski, B.; Kotzur, N.; Lechler, R.; Wiesner, B.; Briand, B.; Beyermann, M. *Chem. - Eur. J.* **2008**, *14*, 1621−1627. (b) Fournier, L.; Aujard, I.; Le Saux, T.; Maurin, S.; Beaupierre, S.; Baudin, J.-B.; Jullien, L. *Chem. - Eur. J.* **2013**, *19*, 17494−17507.

(16) Schmidt, R.; Geissler, D.; Hagen, V.; Bendig, J. *J. Phys. Chem. A* **2007**, *111*, 5768−5774.

(17) (a) Kirpichenok, M. A.; Gorozhankin, S. K.; Grandberg, I. I. *Chem. Heterocycl. Compd.* **1988**, *24*, 611−616. (b) Fournier, L.; Gauron, C.; Xu, L.; Aujard, I.; Le Saux, T.; Gagey-Eilstein, N.; Maurin, S.; Dubruille, S.; Baudin, J.-B.; Bensimon, D.; Volovitch, M.; Vriz, S.; Jullien, L. *ACS Chem. Biol.* **2013**, *8*, 1528−1536. (c) Fonseca, A. S. C.; Soares, A. M. S.; Gonçalves, M. S. T.; Costa, S. P. G. *Tetrahedron* **2012**, *68*, 7892−7900. (d) Yamazoe, S.; Liu, Q.; McQuade, L. E.; Deiters, A.; Chen, J. K. *Angew. Chem., Int. Ed.* **2014**, *53*, 10114−10118.

(18) Jesberger, M.; Davis, T. P.; Barner, L. *Synthesis* **2003**, 1929−1958.

(19) Subirós-Funosas, R.; El-Faham, A.; Albericio, F. *Tetrahedron* **2011**, *67*, 8595−8606.

(20) (a) Michels, T.; Dölling, R.; Haberkorn, U.; Mier, W. *Org. Lett.* **2012**, *14*, 5218−5221. (b) Subirós-Funosas, R.; El Faham, A.; Albericio, F. *Biopolymers* **2012**, *98*, 89−97.

(21) Gross, A.; Habig, D.; Metzler-Nolte, N. *ChemBioChem* **2013**, *14*, 2472−2479.

DOI: 10.1021/acs.joc.6b02415
J. Org. Chem. 2016, 81, 11556−11564

SUPPORTING INFORMATION

A green light-triggerable RGD peptide for photocontrolled targeted drug delivery: synthesis and photolysis studies

Albert Gandioso,[a] Marc Cano,[a] Anna Massaguer,[b] Vicente Marchán*[,a]

[a]Departament de Química Inorgànica i Orgànica
Secció de Química Orgànica, IBUB
Universitat de Barcelona
Martí i Franquès 1-11
E-08028 Barcelona (Spain)
Fax: + (34) 93 339 7878
E-mail: vmarchan@ub.edu

[b]Departament de Biologia
Universitat de Girona
Campus Montilivi
E-17071 Girona (Spain)

Table of contents

1.- HPLC analysis of coumarin-caged Asp derivatives (5-10)

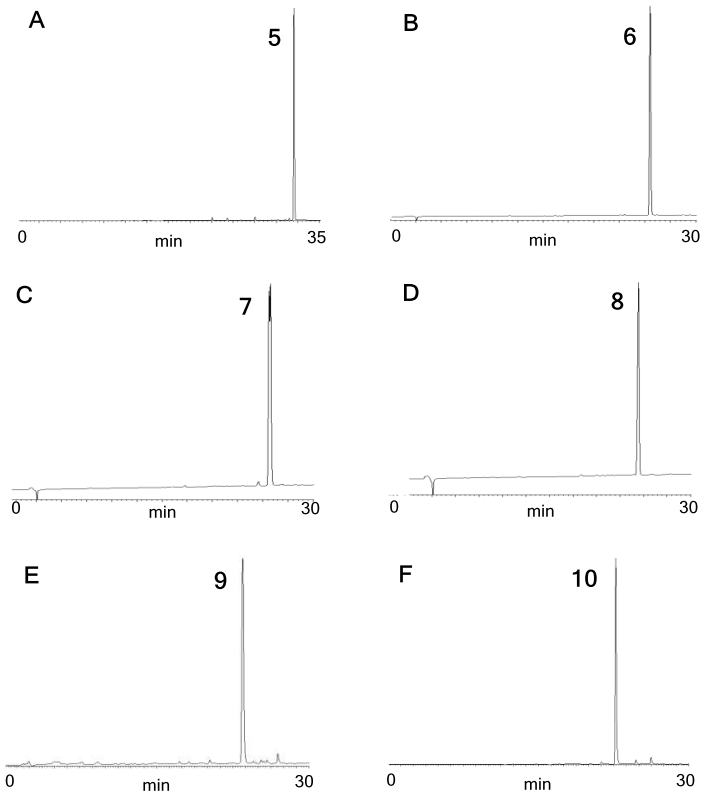

Figure S1. Reversed-phase HPLC-ESI MS traces of the purified coumarin-caged Asp derivatives (**5-10**).

2.- Stability studies of thiocoumarin-caged Asp derivatives (5 and 6)

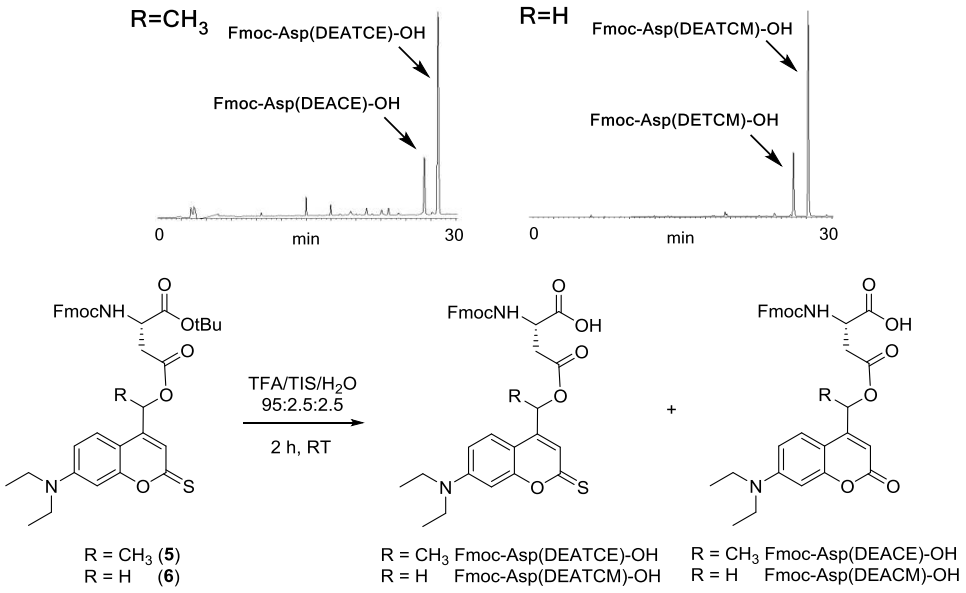

Figure S2. Reversed-phase HPLC-ESI MS traces (top) of the reaction between thionated amino acid derivatives **5** and **6** with the TFA/TIS/H_2O deprotection cocktail for 2 h at RT (bottom).

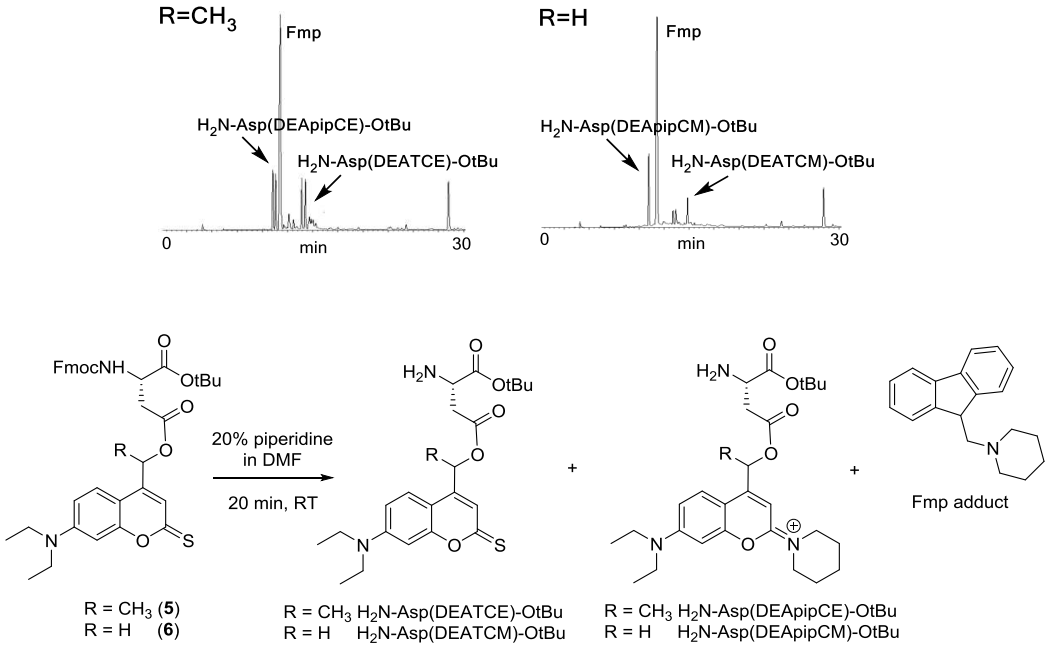

Figure S3. Reversed-phase HPLC-ESI MS traces (top) of the reaction between thionated amino acid derivatives **5** and **6** with 20% piperidine in DMF solution for 20 min at RT (bottom).

3.- Stability studies of dicyanocoumarin-caged Asp derivatives (7 and 8)

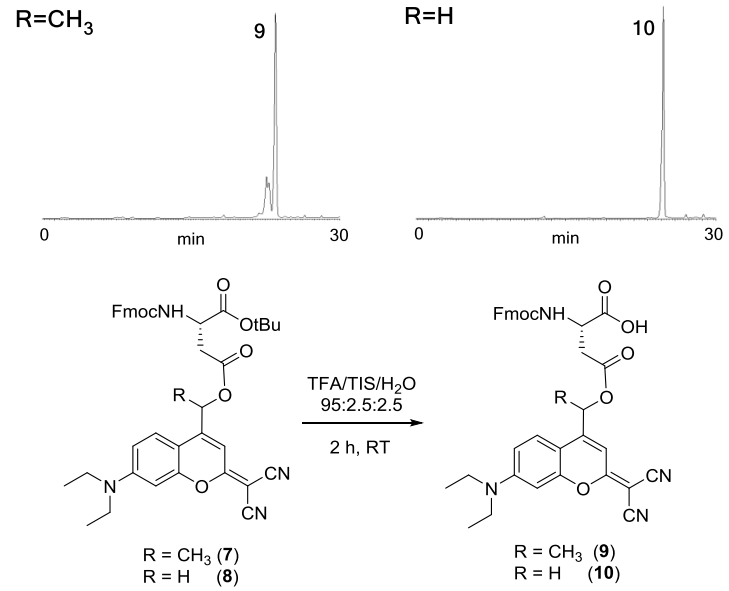

Figure S4. Reversed-phase HPLC-ESI MS traces (top) of the reaction between amino acid derivatives **7** and **8** with the TFA/TIS/H_2O deprotection cocktail for 2 h at RT (bottom).

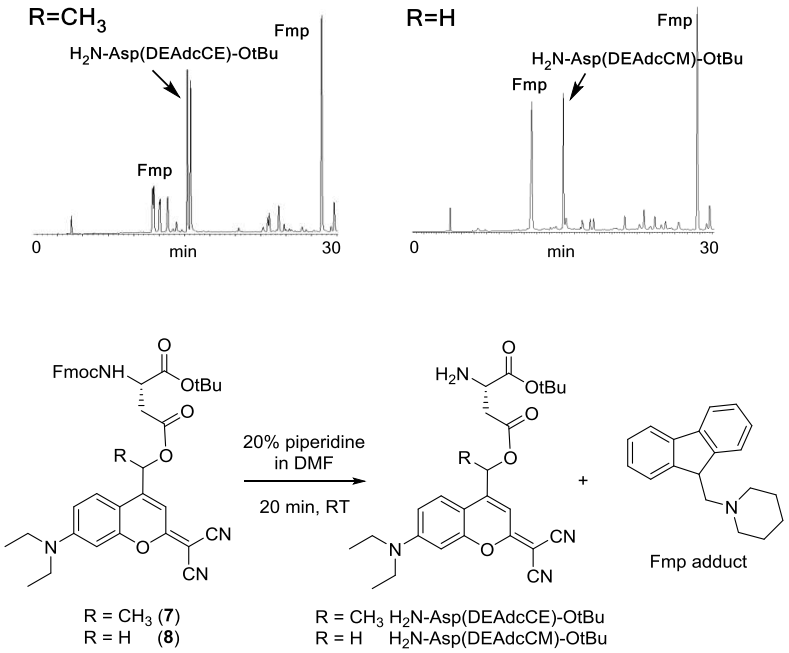

Figure S5. Reversed-phase HPLC-ESI MS traces (top) of the reaction between amino acid derivatives **7** and **8** with 20% piperidine in DMF solution for 20 min at RT (bottom).

4.- Stability studies of dicyanocoumarin-caged Asp derivatives (7-10) in cell culture medium

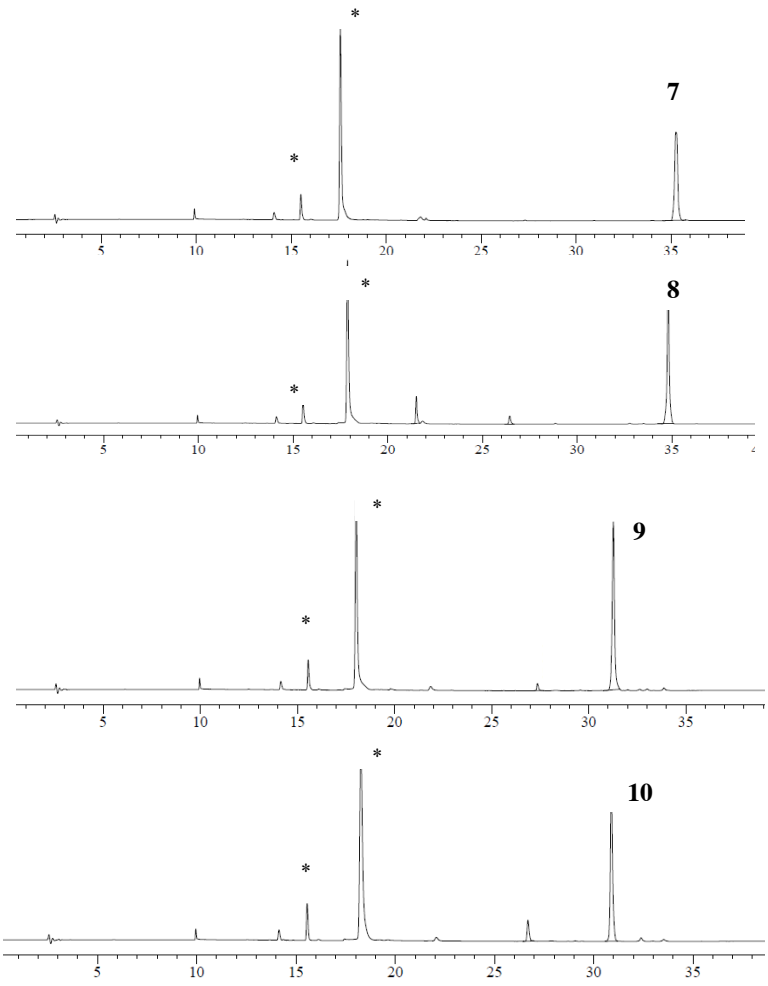

Figure S6. Reversed-phase HPLC traces (detection wavelength: 500 nm) of dicyanocoumarin-caged Asp derivatives (**7-10**) after incubation in DMEM supplemented with 25% fetal bovine serum for 1 h at 37ºC. * These peaks were present in the DMEM-25% FBS.

5.- UV-vis and fluorescence spectra of dicyanocoumarin-caged Asp derivatives (7 and 8)

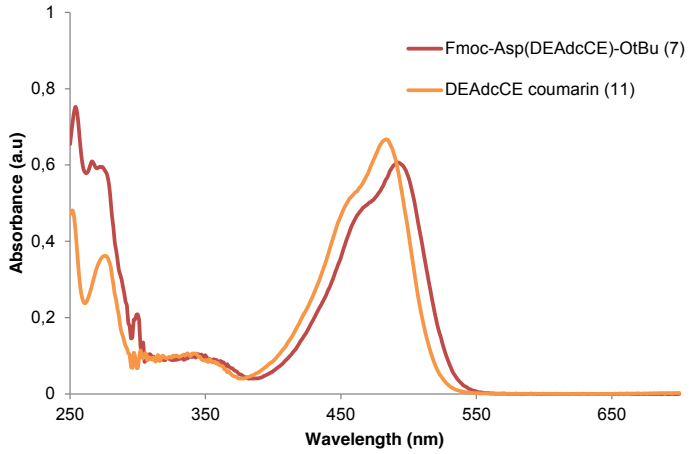

Figure S7. UV-vis spectra of DEAdcCE coumarin (**11**) and of Fmoc-Asp(DEAdcCE)-OtBu (**7**) in Tris buffer pH 7.5/ACN 1:1 (20 μM).

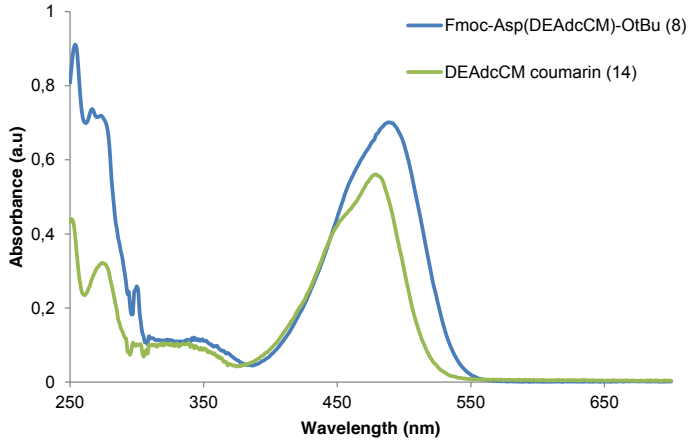

Figure S8. UV-vis spectra of DEAdcCM coumarin (**14**) and of Fmoc-Asp(DEAdcCM)-OtBu (**8**) in Tris buffer pH 7.5/ACN 1:1 (20 μM).

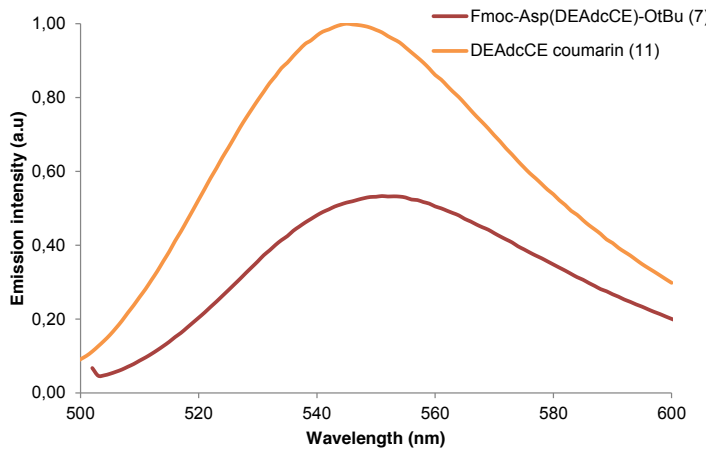

Figure S9. Fluorescence emission spectra of DEAdcCE coumarin (**11**) and of Fmoc-Asp(DEAdcCE)-OtBu (**7**) in Tris buffer pH 7.5/ACN 1:1 (50 nM).

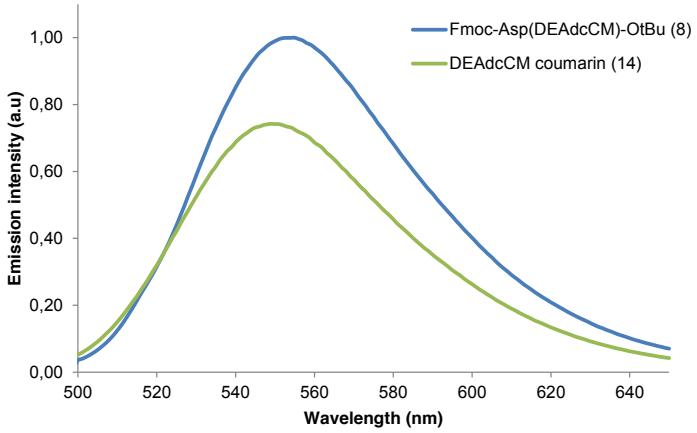

Figure S10. Fluorescence emission spectra of DEAdcCM coumarin (**14**) and of Fmoc-Asp(DEAdcCM)-OtBu (**8**) in Tris buffer pH 7.5/ACN 1:1 (50 nM).

6.- Photoactivation studies of dicyanocoumarin-caged Asp derivatives (7 and 8)

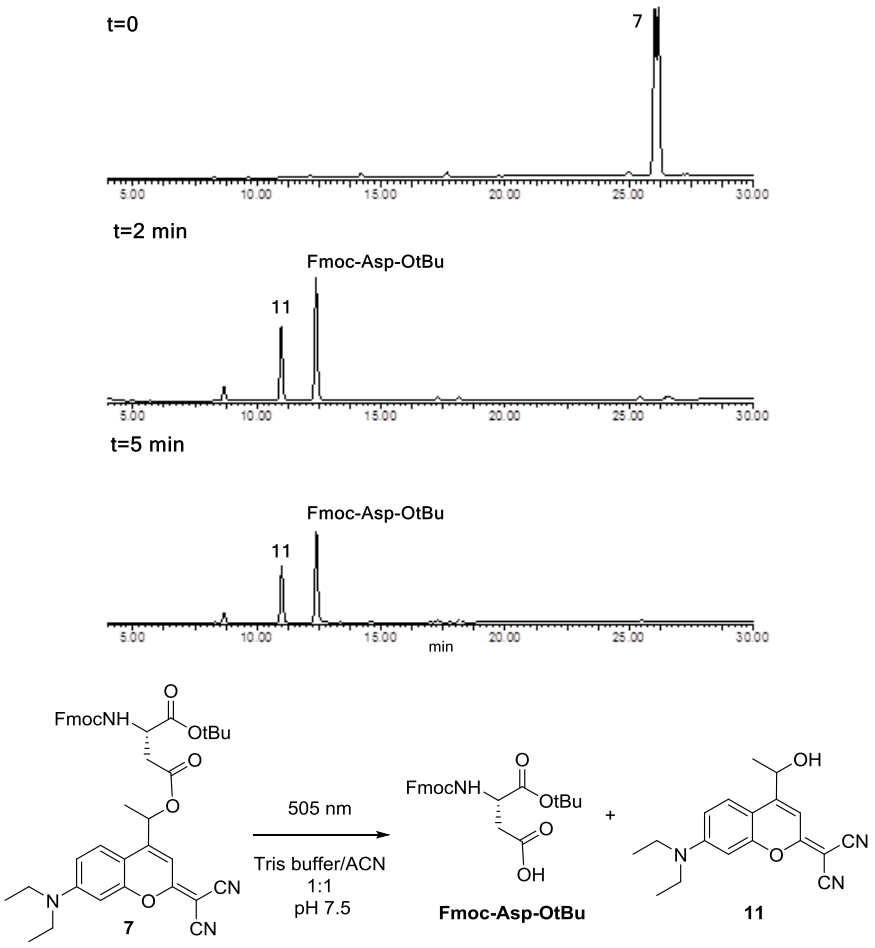

Figure S11. Reversed-phase HPLC-ESI MS traces at 260 nm (top) of the photoactivation of **7** at t=0 and after irradiation at 505 nm for 2 and 5 min (LED source, Tris buffer pH 7.5/ACN 1:1) and structure of the photoproducts (bottom). Compound **7** appears as two peaks in the HPLC trace since it contains a mixture of the two diasteoisomers.

.

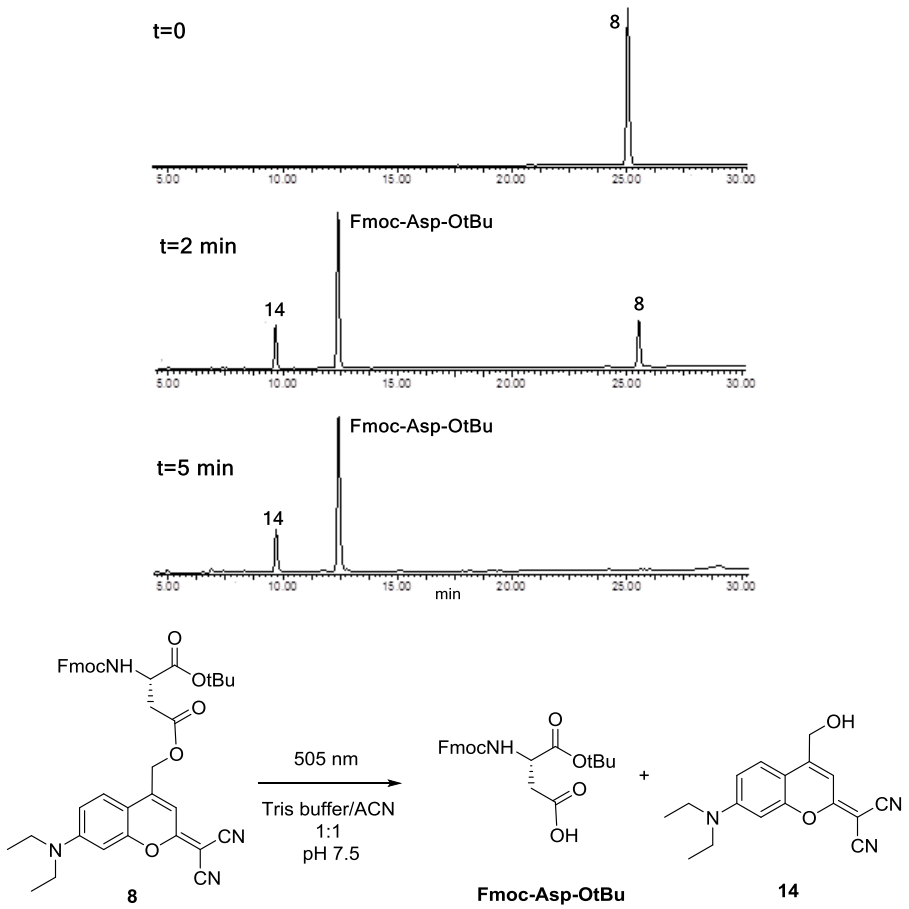

Figure S12. Reversed-phase HPLC-ESI MS traces at 260 nm (top) of the photoactivation of **8** at t=0 and after irradiation at 505 nm for 2 and 5 min (LED source, Tris buffer pH 7.5/ACN 1:1) and structure of the photoproducts (bottom)

7.- Evaluation of aspartimide formation during SPPS with 9 and 10

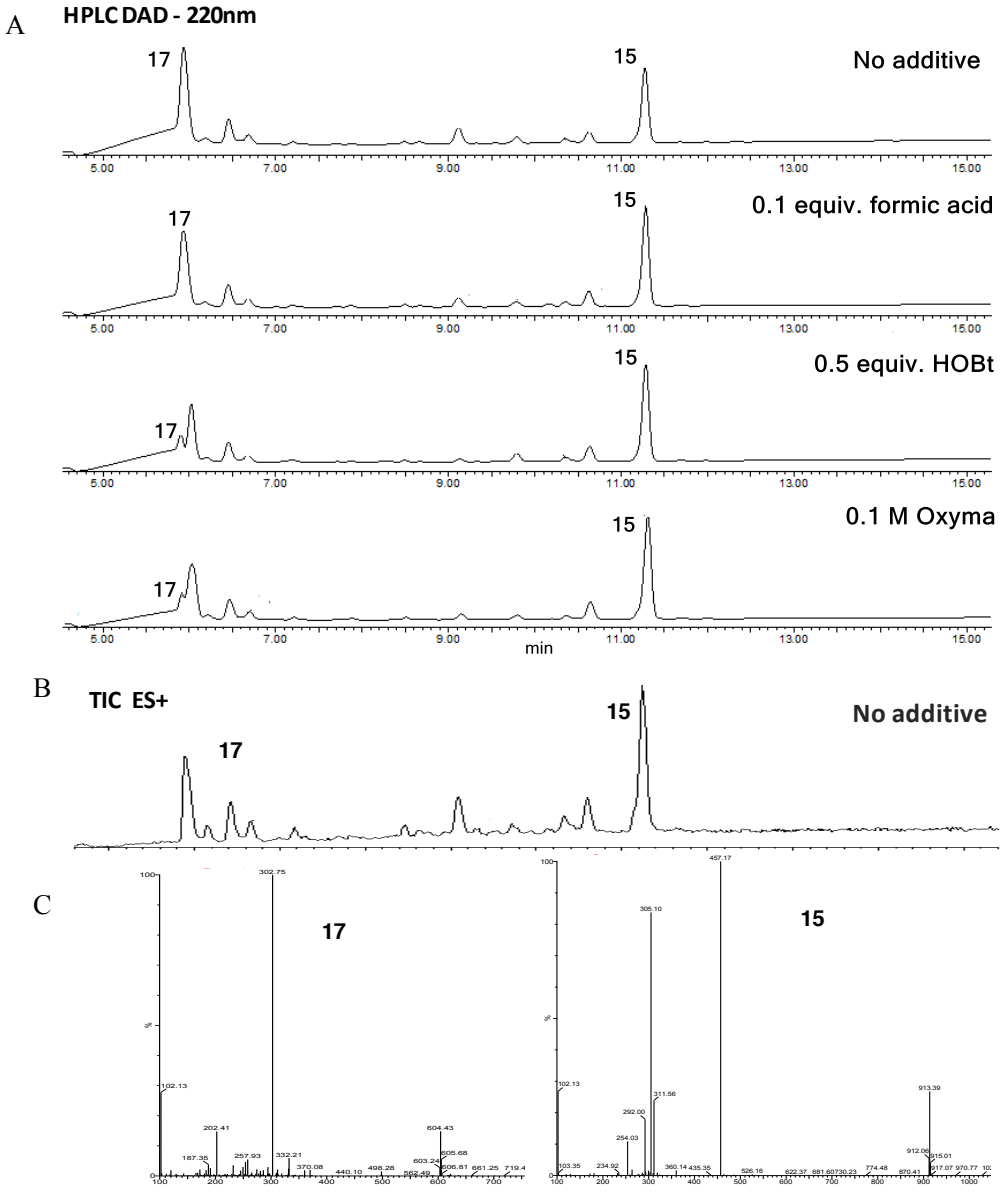

Figure S13. Evaluation by reversed-phase HPLC-ESI MS of aspartimide formation during Fmoc-tBu SPPS of the linear peptide H-Asp(DEAdcCE)-*D*-Phe-Lys-Arg-Gly-OH (**15**) by using dicyanocoumarin-protected Asp monomer **9** together with different Fmoc-removal conditions: HPLC traces (A), TIC analysis of the assay in the absence of additive (B) and ESI MS spectra of peptide **15** and of the aspartimide side-product **17** (C).

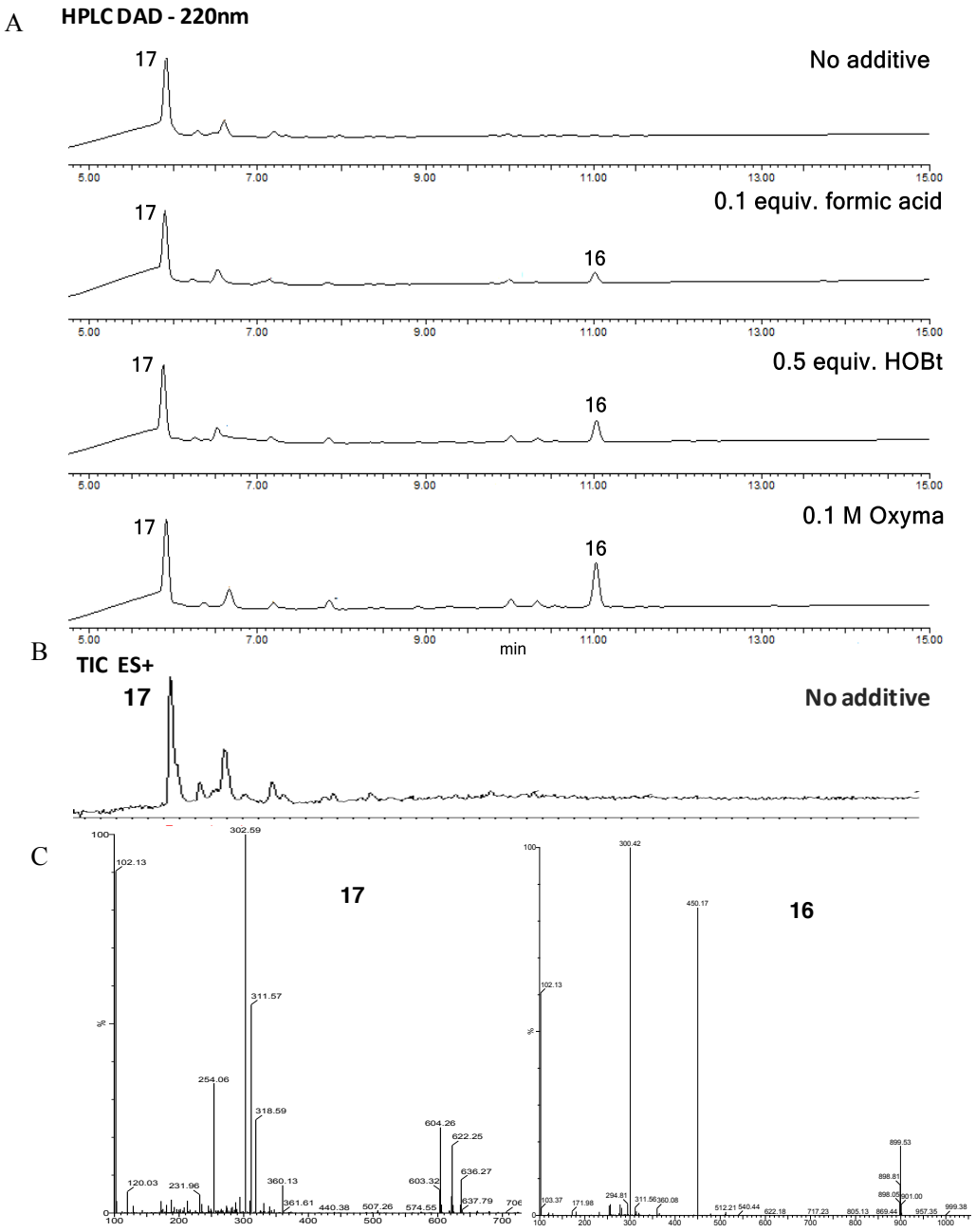

Figure S14. Evaluation by reversed-phase HPLC-ESI MS of aspartimide formation during Fmoc-tBu SPPS of the linear peptide H-Asp(DEAdcCM)-*D*-Phe-Lys-Arg-Gly-OH (**16**) by using dicyanocoumarin-protected Asp monomer **10** together with different Fmoc-removal conditions: HPLC traces (A), TIC analysis of the assay in the absence of additive (B) and ESI MS spectra of peptide **16** and of the aspartimide side-product **17** (C).

Table S1. Evaluation of aspartimide formation during Fmoc removal with piperidine of Fmoc-Asp(DEAdcCM or DEAdcCE)-*D*-Phe-Lys(Boc)-Arg(Pbf)-Gly-2-Cl-Trt-Resin in the presence of various acidic additives.

		Fmoc removal conditions: 20% piperidine in DMF + additive (mol equiv. relative to piperidine) or in 0.1 M Oxyma in DMF, 2 x 10 min			
Asp monomer	Peptide[a]	No additive	+ 0.1 equiv. formic acid	+ 0.5 equiv. HOBt	+ 0.1 M Oxyma
9	**15**	47	58	93	93
	17	53	42	7	7
10	**16**	0	14	24	41
	17	100	86	76	59

[a]Relative yields (%) determined by reversed-phase HPLC (UV detection at 220 nm).

Table S2. MS characterization data of compounds **15**, **16** and **17**.

Compound	Exp. *m/z* $[M+H]^+$	Calc. *m/z* $[M+H]^+$	
15	913.4	913.47	$C_{45}H_{61}N_{12}O_9$
16	899.4	899.45	$C_{44}H_{59}N_{12}O_9$
17	604.2	604.32	$C_{27}H_{42}N_9O_7$

8.- Synthesis and characterization of DEAdcCE-caged RGD peptide (18)

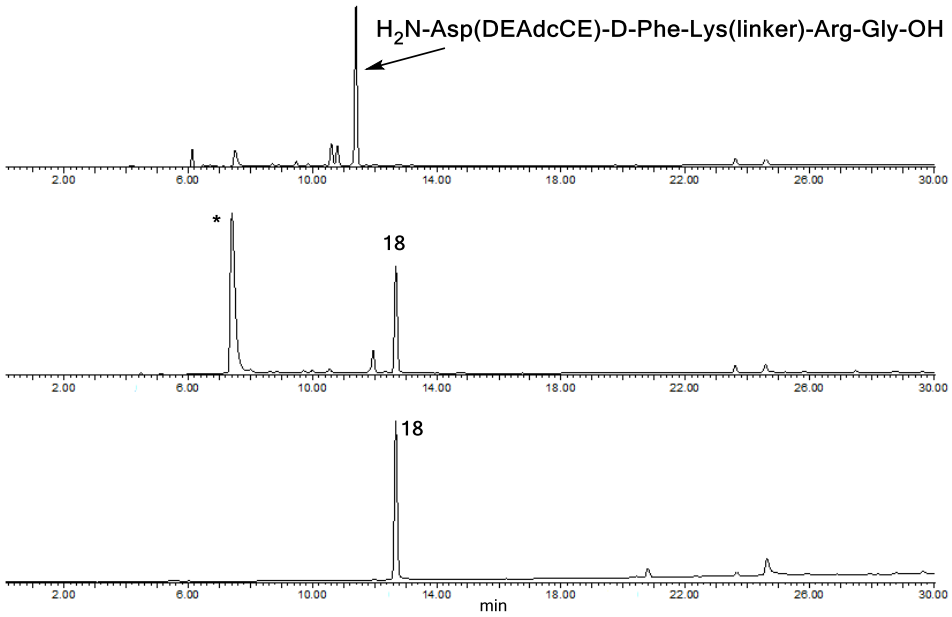

Figure S15. Reversed-phase HPLC traces of the crude linear peptide H_2N-Asp(DEAdcCE)-*D*-Phe-Lys(linker)-Arg-Gly-OH obtained after deprotection of an aliquot of peptide-resin before cyclization (top), of crude cyclic peptide **18** (center; * corresponds to PyBOP) and of the pure peptide **18** (bottom).

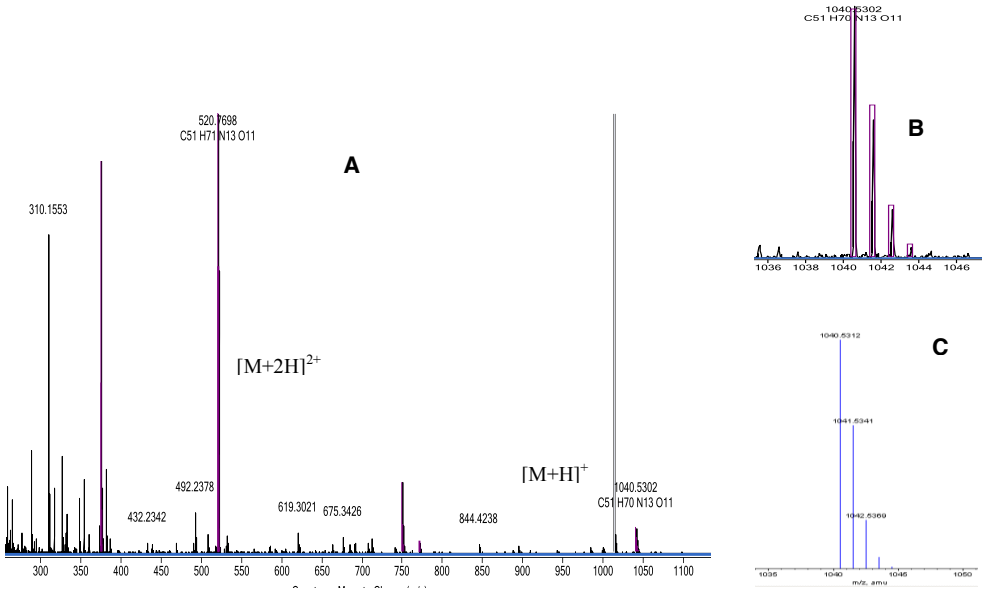

Figure S16. High resolution ESI MS of peptide **18**: experimental (A, B) and calculated (C).

9.- Synthesis and characterization of ruthenocenoyl-peptide conjugates (20 and 21)

Ruthenocene-c(RGD(DEAdcCE)fK) conjugate (20).

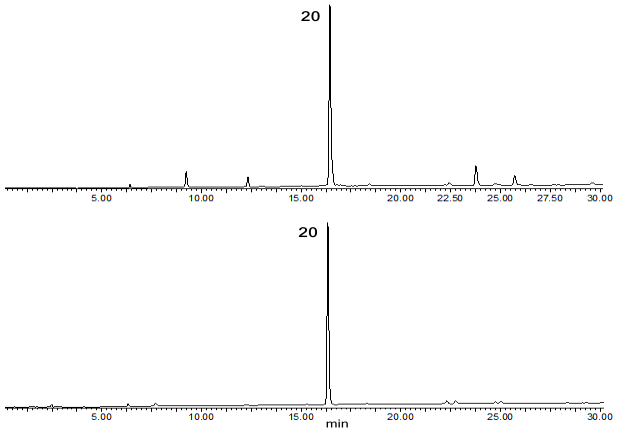

Figure S17. Rreversed-phase HPLC traces for conjugate **20**: reaction crude (top) and purified (bottom).

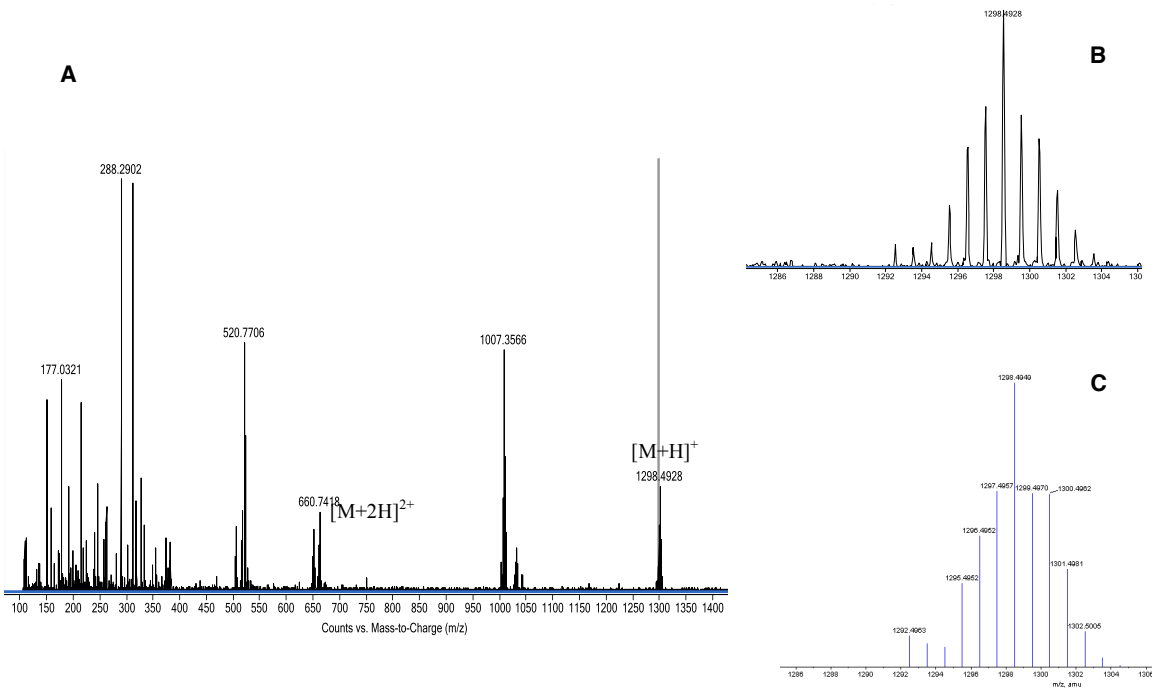

Figure S18. High resolution ESI MS of conjugate **20**: experimental (A, B) and calculated (C).

Ruthenocene-c(RGDfK) conjugate (21).

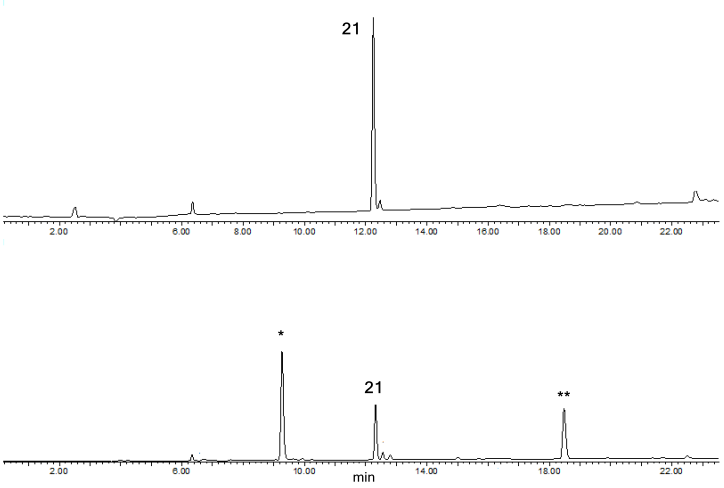

Figure S19. Reversed-phase HPLC traces for conjugate **21**: reaction crude (bottom) and purified (top). *PyBOB coupling reagent; **Ruthenocene carboxylic acid.

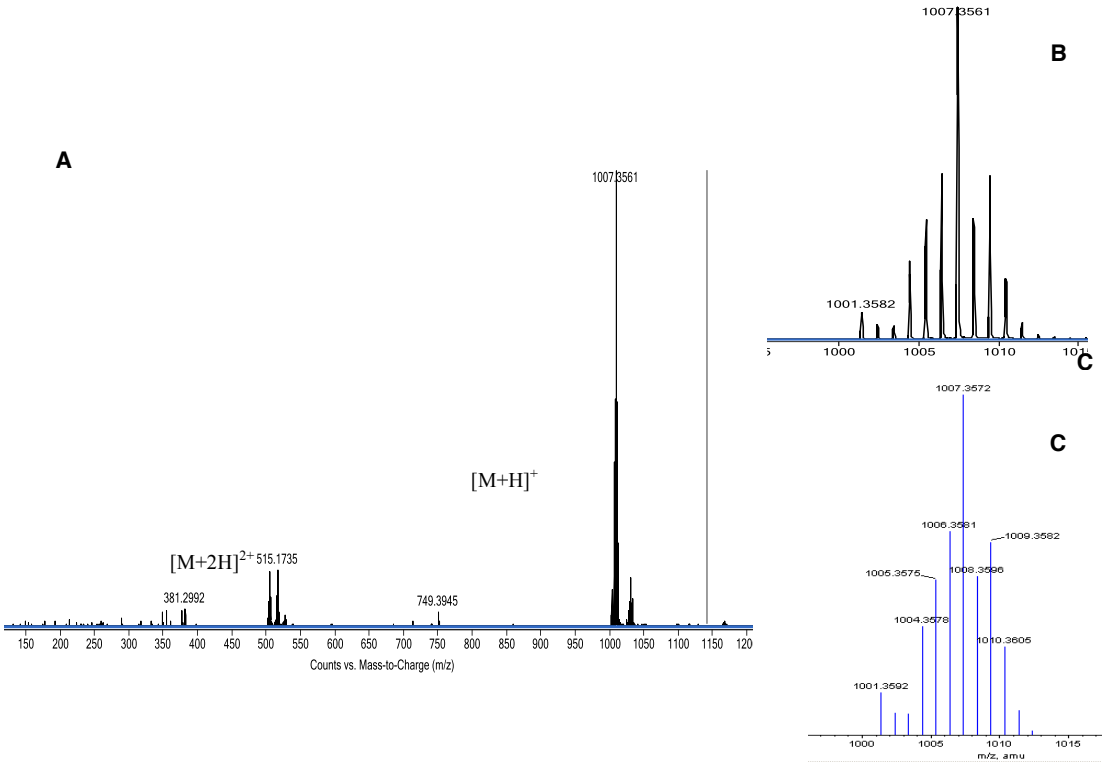

Figure S20. High resolution ESI MS of conjugate **21**: experimental (A, B) and calculated (C).

10.- Photoactivation studies of DEAdcCE-coumarin-caged peptide (18)

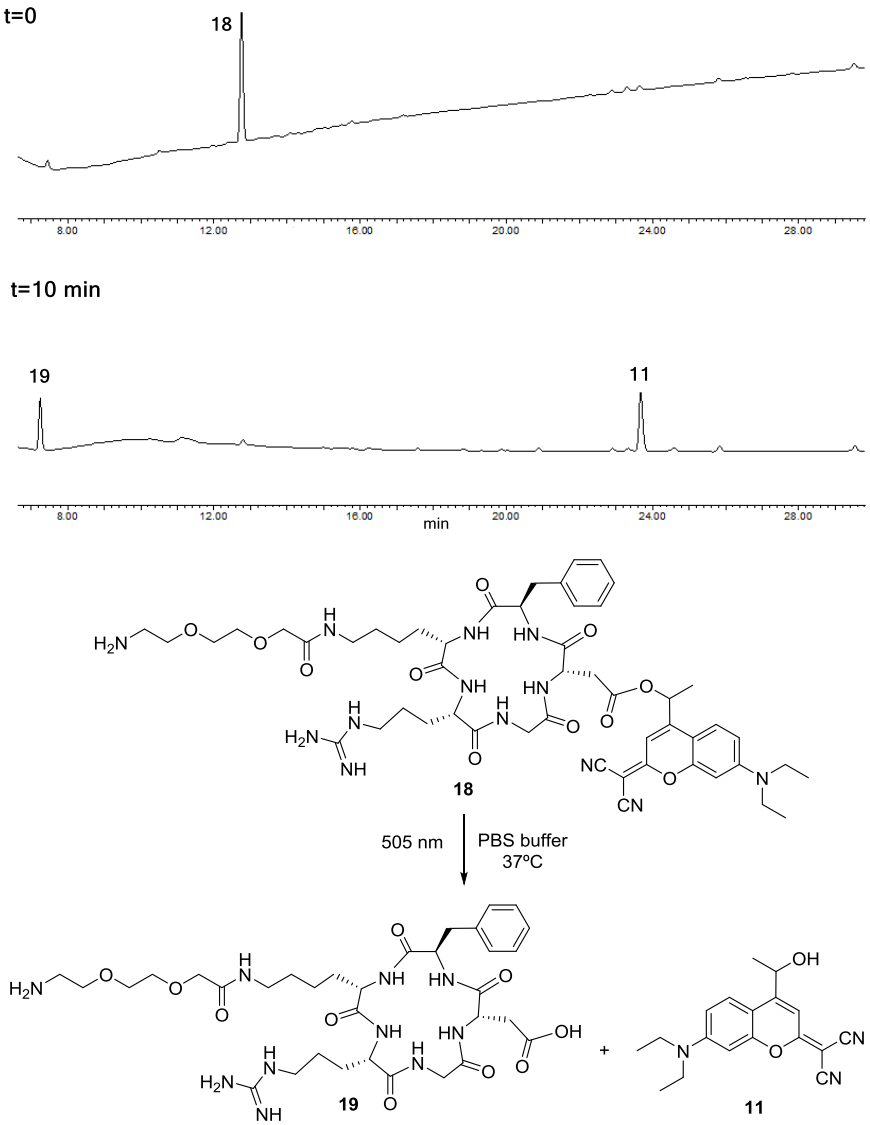

Figure S21. Reversed-phase HPLC-ESI MS traces at 220 nm (top) of the photoactivation of peptide **18** (505 nm LED, PBS pH 7.0) and structure of the products (bottom).

11.- Photoactivation studies of ruthenocenoyl-coumarin-caged peptide conjugate (20)

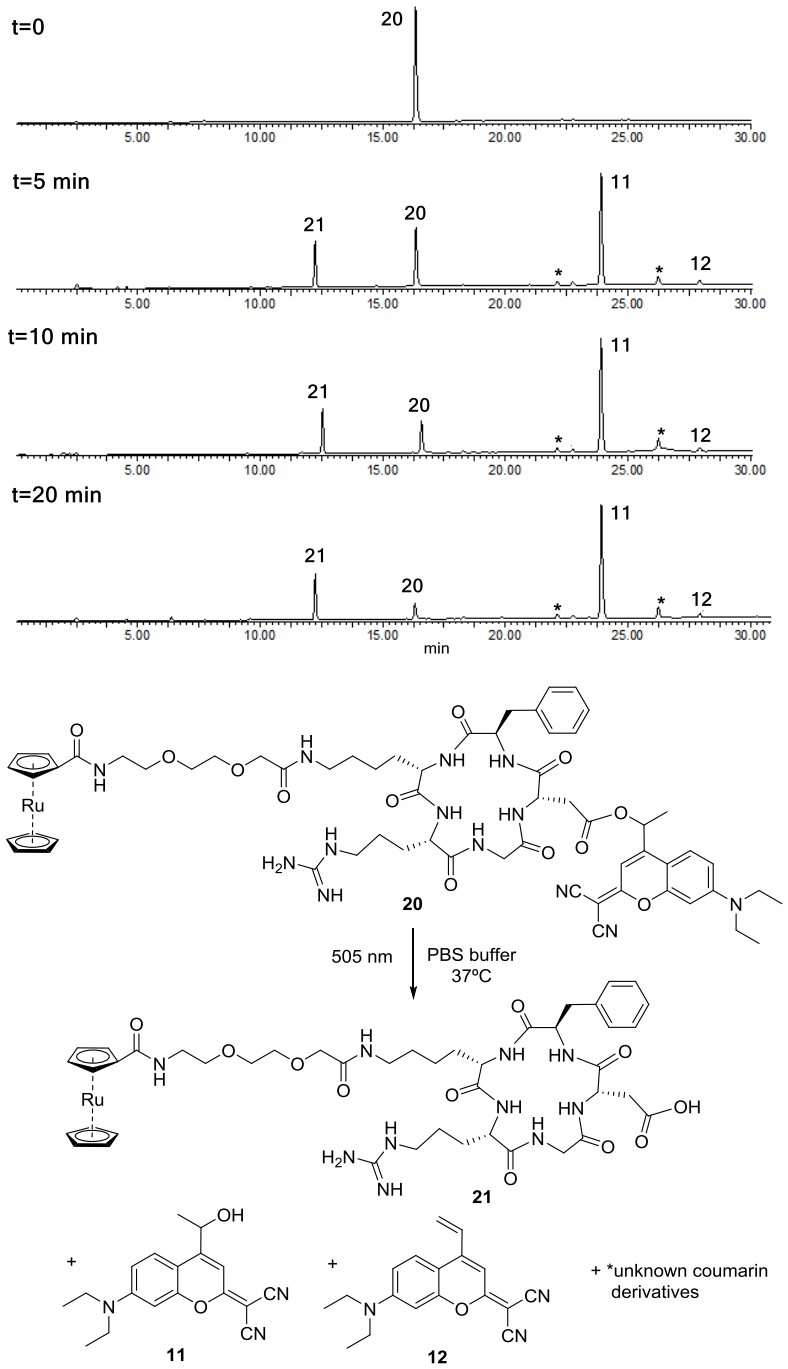

Figure S22. Reversed-phase HPLC-ESI MS traces at 260 nm (top) of the photoactivation of conjugate **20** (505 nm LED, PBS pH 7.0/ACN 8:2) and structure of the products (bottom).

12.- Stability of conjugate 21 in cell culture medium

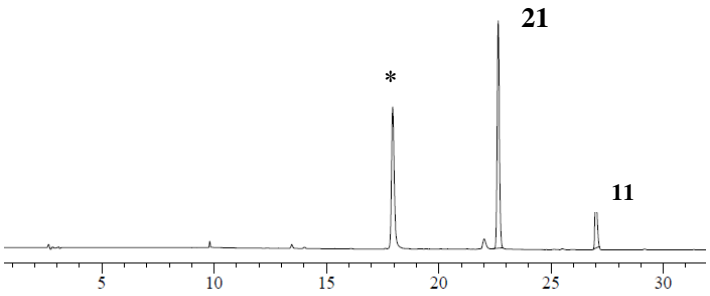

Figure S23. Reversed-phase HPLC trace (detection wavelength: 500 nm) of ruthenocene-dicyanocoumarin-caged peptide conjugate (**21**) after incubation in DMEM supplemented with 25% fetal bovine serum for 1 h at 37ºC. * These peaks were present in the DMEM-25% FBS.

13.- Uncaging Quantum Yield Determination

Uncaging quantum yield was determined by irradiation at 505 nm with a LED source. Solutions of the caged amino acids and of Aberchrome 540, which was used as actinometer, in a 1:1 (v/v) mixture of Tris buffer pH 7.5 and ACN with matched absorbances at the irradiation wavelength, were irradiated with the LED in a thermostated cuvette at 37°C. The efficiency of the photochemical process was estimated from the following equation[1]

$$\Delta(OD)sample = \frac{\Phi sample * \text{Ɛ}sample}{\Phi standard * \text{Ɛ}standard}\Delta(OD)standard$$

where $\Phi_{standard}$ $(0.0568)^2$ is the quantum yield of its reversible photocyclization of *Aberchrome 540* excited at 505 nm, Φ_{sample} is the efficiency of the photolysis process, $\varepsilon_{standard}$ is the molar extinction coefficient of *Aberchrome 540* at 505 nm (8200 $M^{-1}cm^{-1}$)[3] and ε_{sample} is the molar extinction coefficient of the caged amino acids at 505 nm (see Table 1). $\Delta(OD)_{sample}$ and $\Delta(OD)_{standard}$ correspond to the absorbance changes of the compounds and of *Aberchrome 540*, respectively.

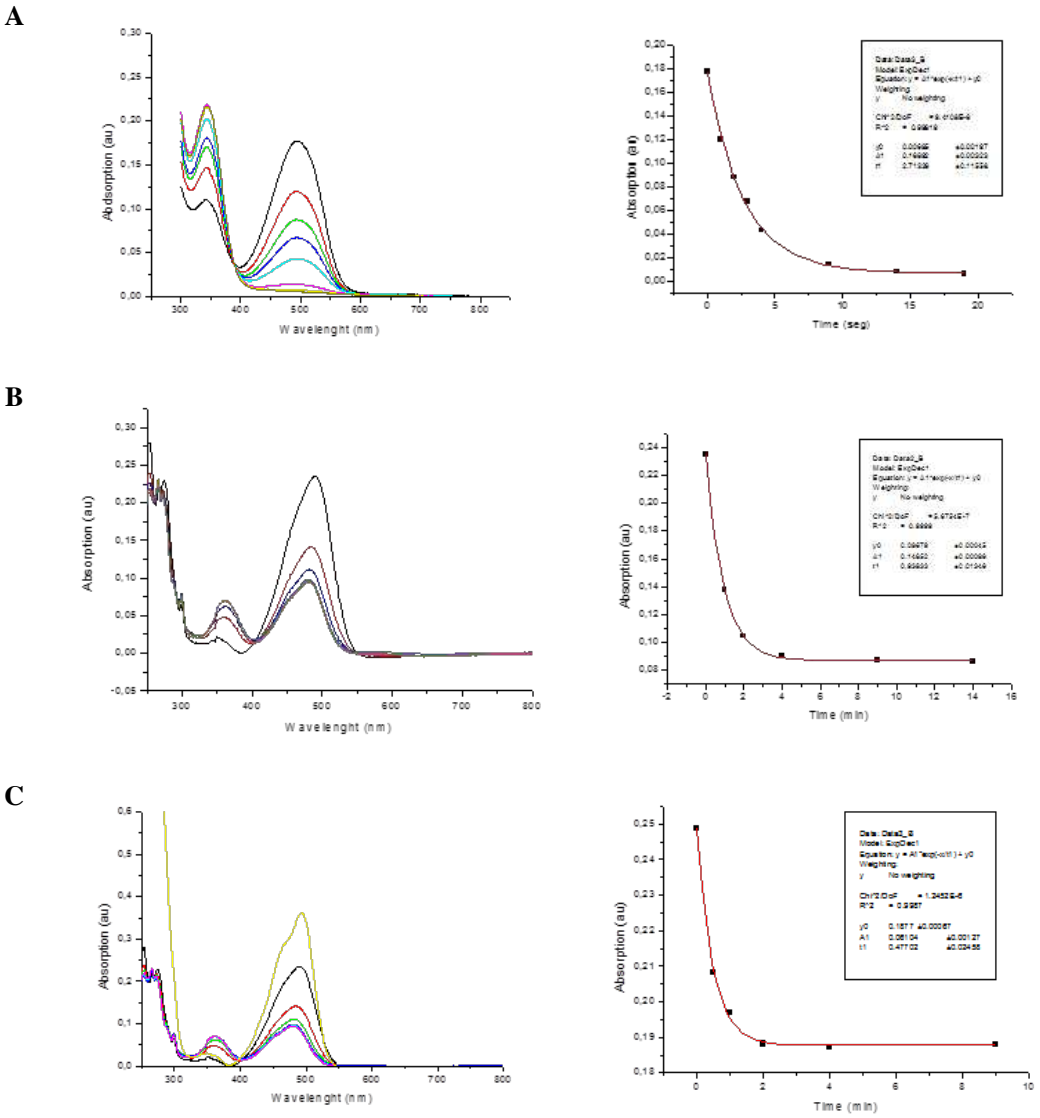

Figure S24. Temporal evolution of the absorbance of *Aberchrome 540* (A), **7** (B) and **8** (C) upon irradiation at 505 nm for different times (left), and exponential relationship between the absorbance at the maximum absorption and the time of irradiation (right).

14.- NMR SPECTRA OF THE COMPOUNDS

4-Carbaldehyde-7-(*N*,*N*-diethylamino)coumarin

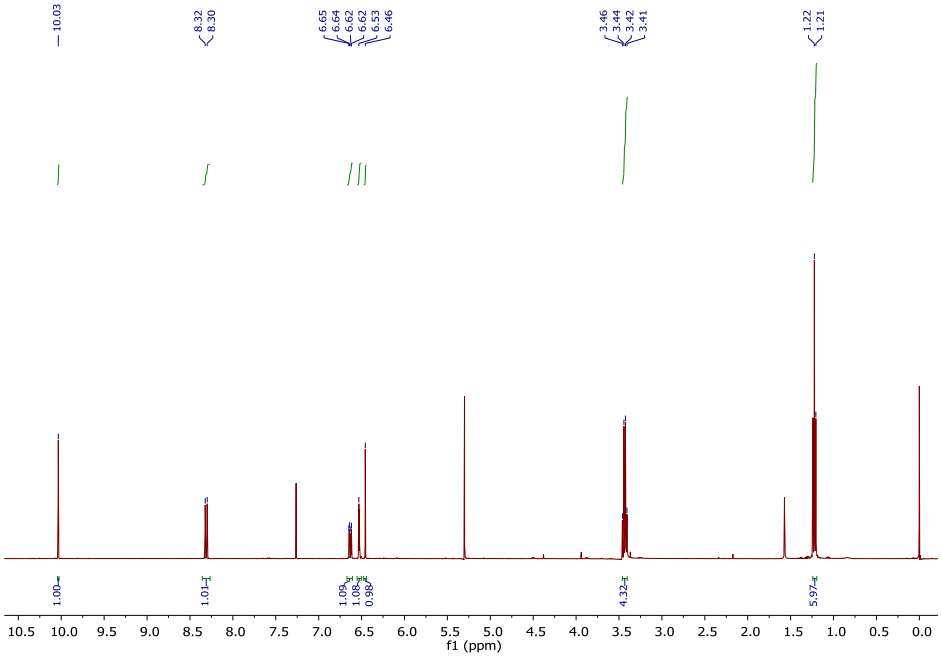

Figure S25. [1]H NMR spectrum of 4-carbaldehyde-7-(*N*,*N*-diethylamino)coumarin.

7-(*N*,*N*-diethylamino)-4-(1-hydroxyeth-1-yl)-coumarin (1)

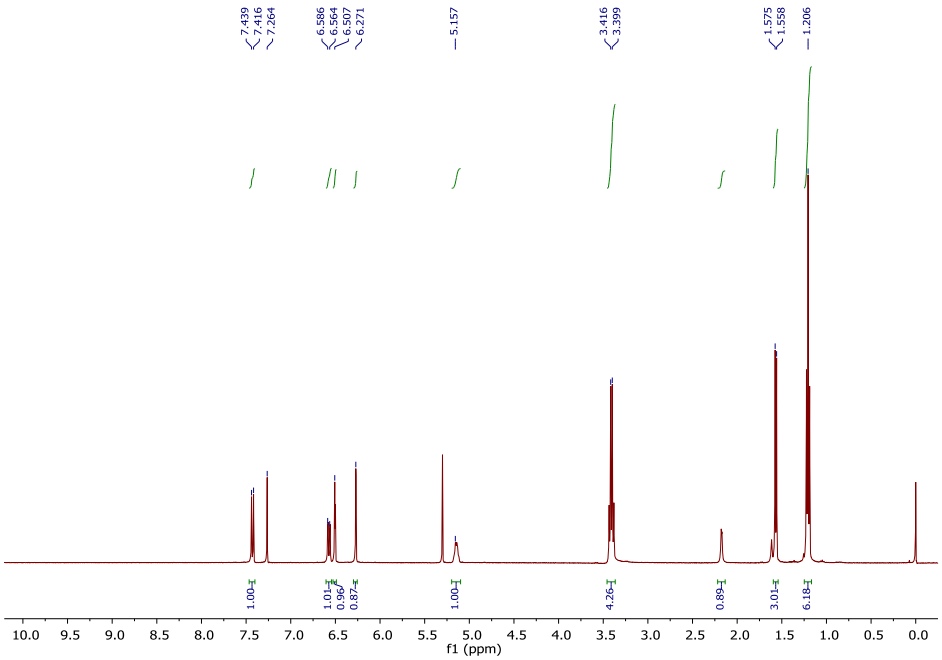

Figure S26. [1]H NMR spectrum of compound **1**.

7-(*N*,*N*-Diethylamino)-4-hydroxymethylcoumarin (2)

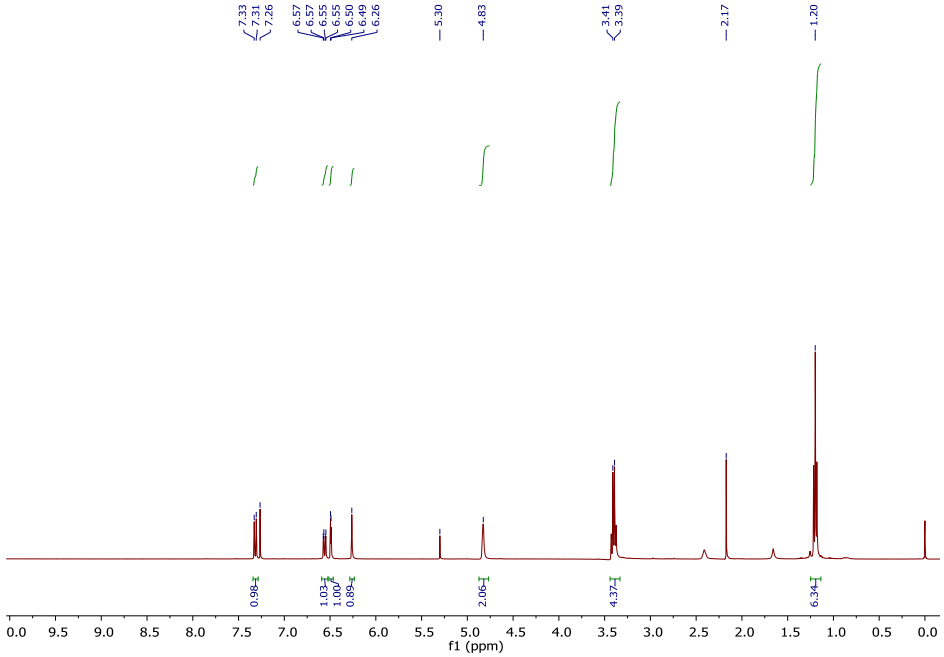

Figure S27. ^{1}H NMR spectrum of compound **2**.

Fmoc-Asp(DEACE)-O^{t}Bu (3)

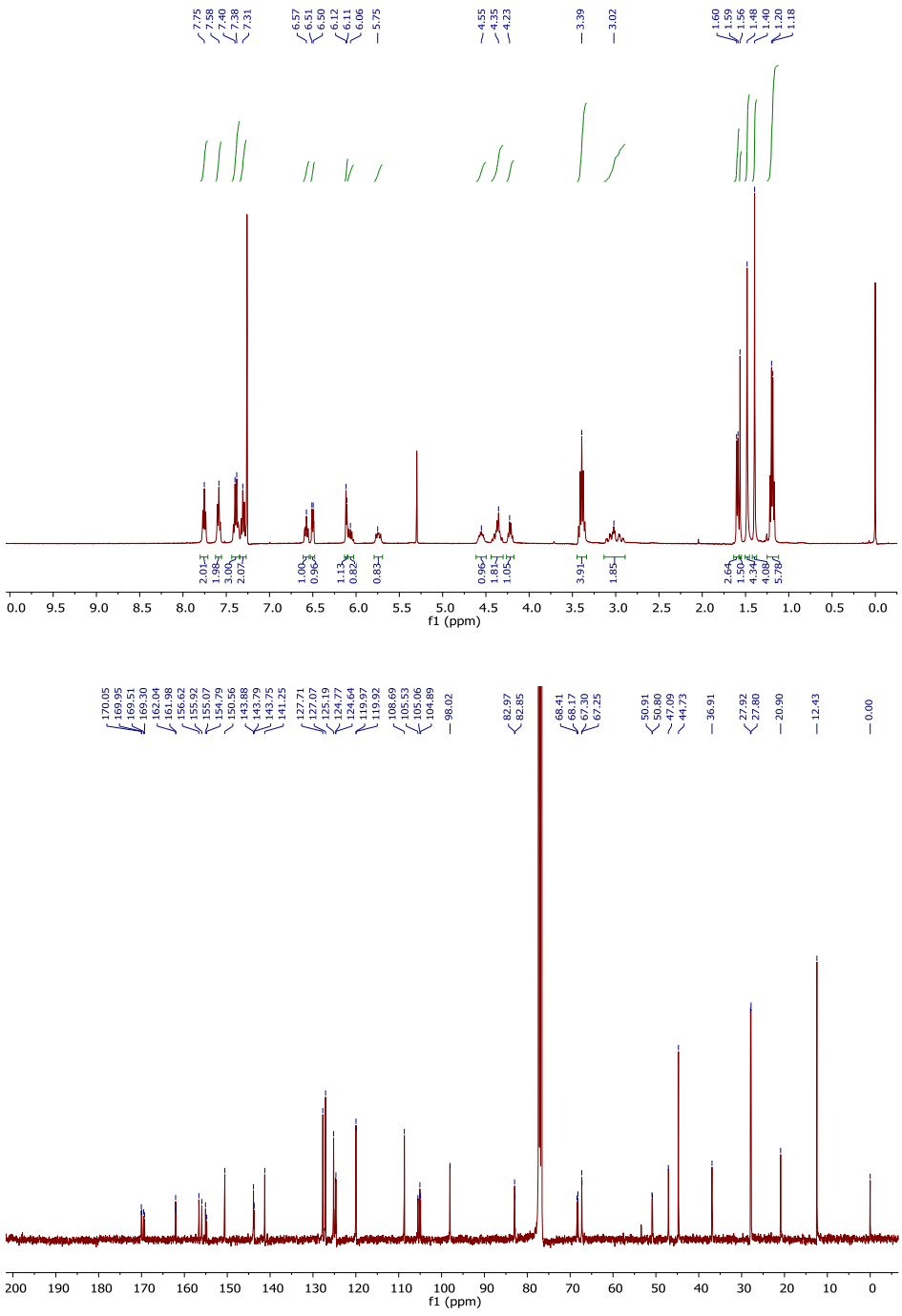

Figure S28. ^{1}H and ^{13}C NMR spectrum of compound **3**.

Fmoc-Asp(DEACM)-O^{t}Bu (4)

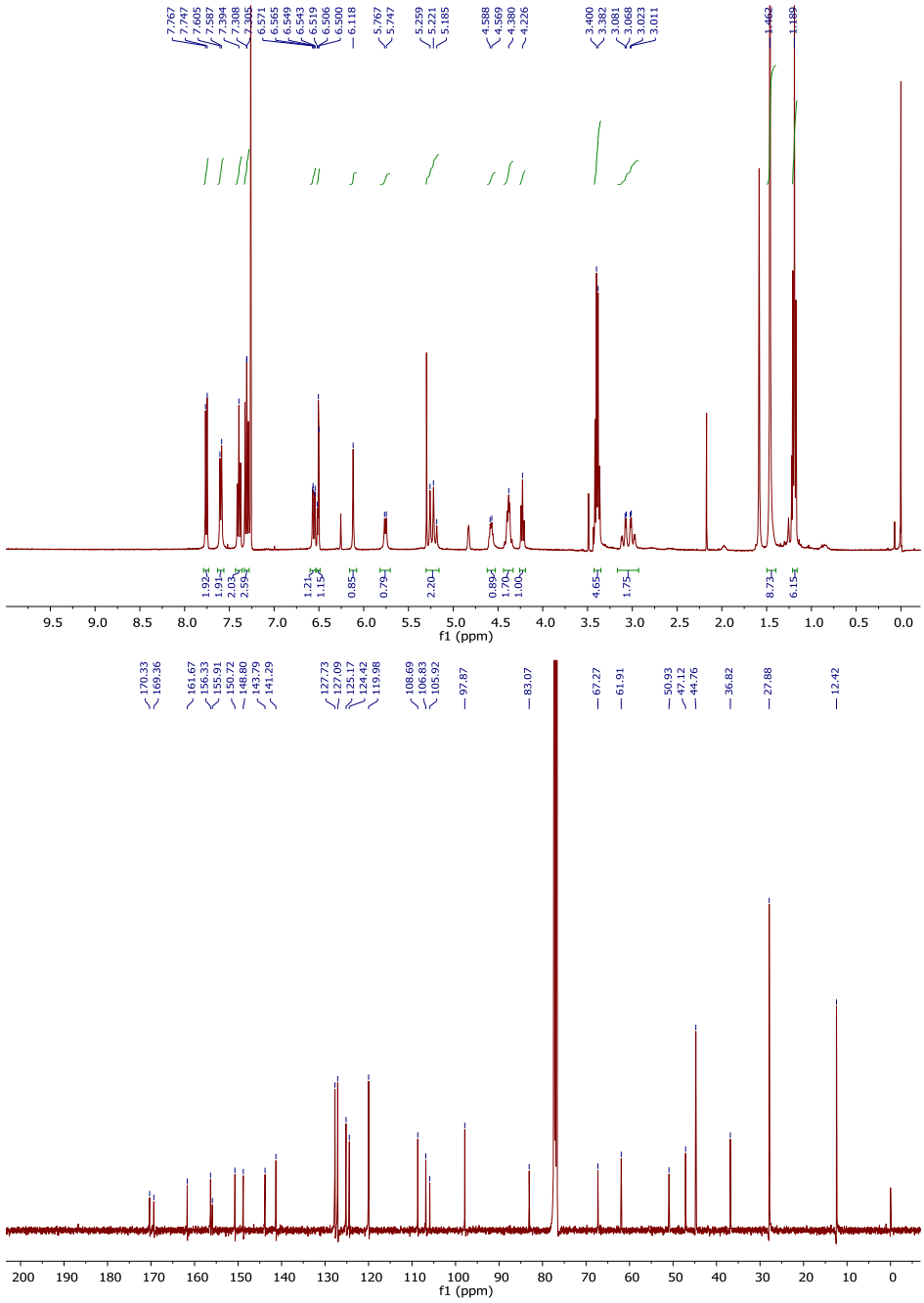

Figure S29. ^{1}H and ^{13}C NMR spectrum of compound **4**.

Fmoc-Asp(DEATCE)-O^{t}Bu (5)

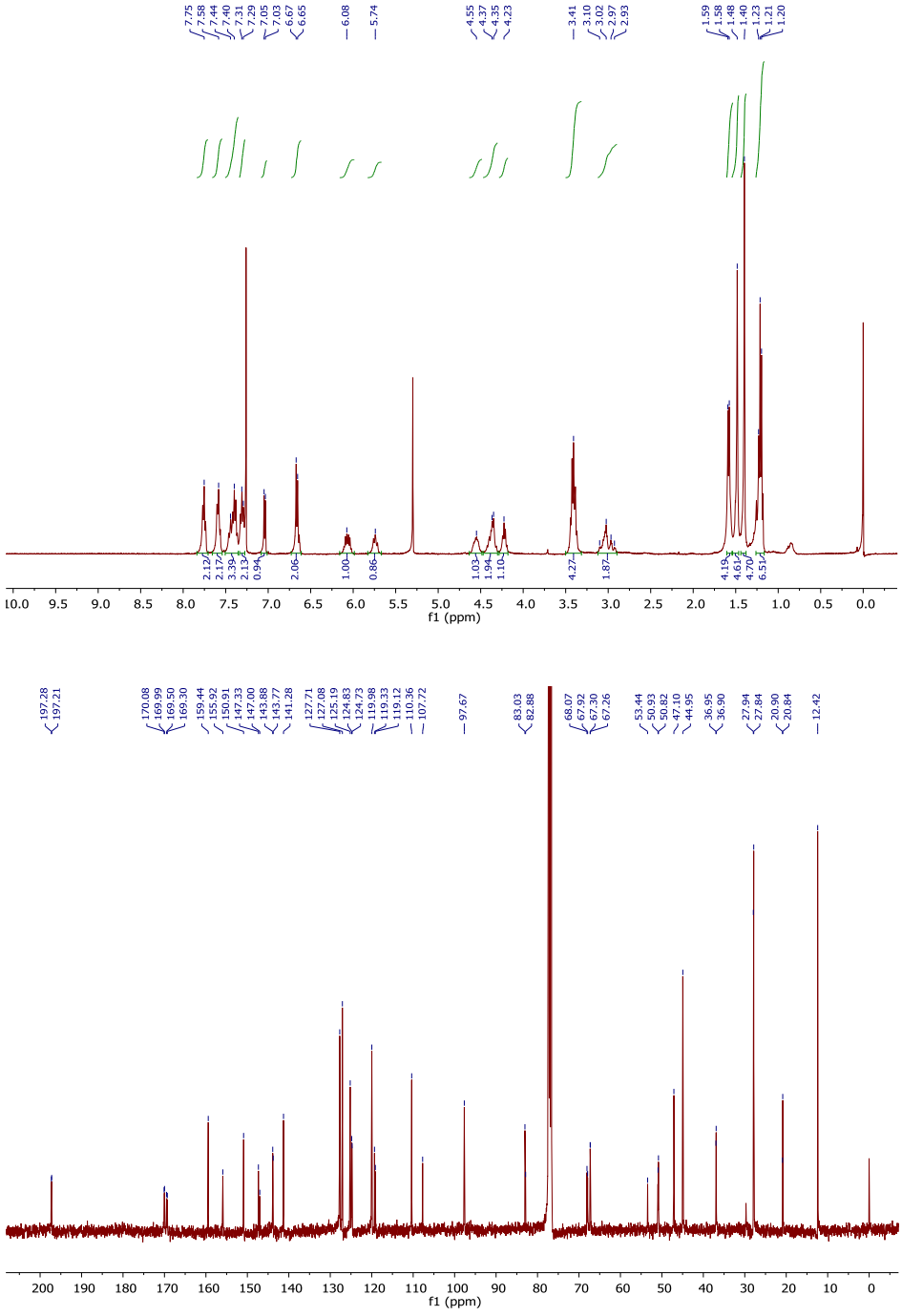

Figure S30. ^{1}H and ^{13}C NMR spectrum of compound **5**.

Fmoc-Asp(DEATCM)-O^{t}Bu (6)

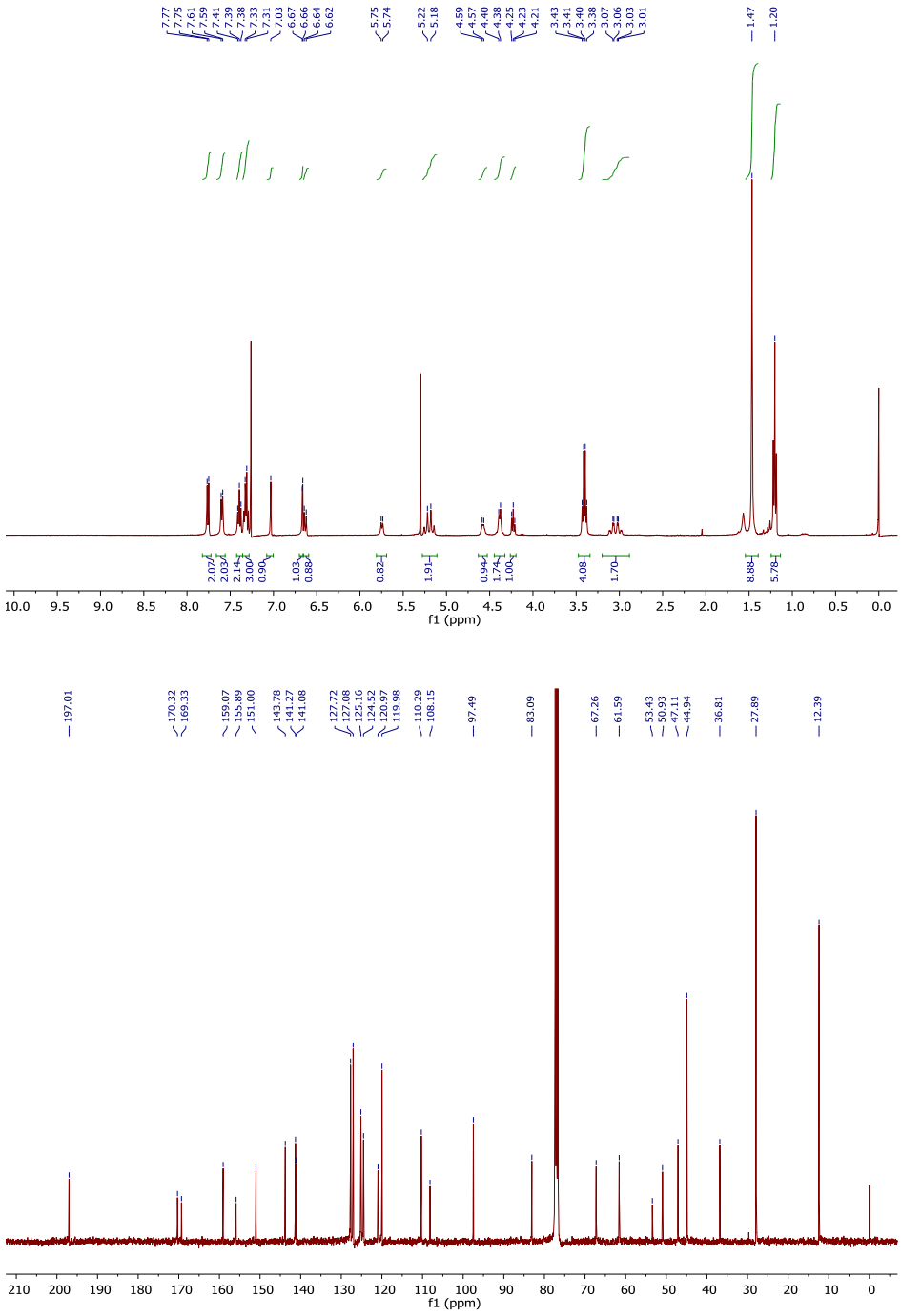

Figure S31. ^{1}H and ^{13}C NMR spectrum of compound **6**.

Fmoc-Asp(DEAdcCE)-O^{t}Bu (7)

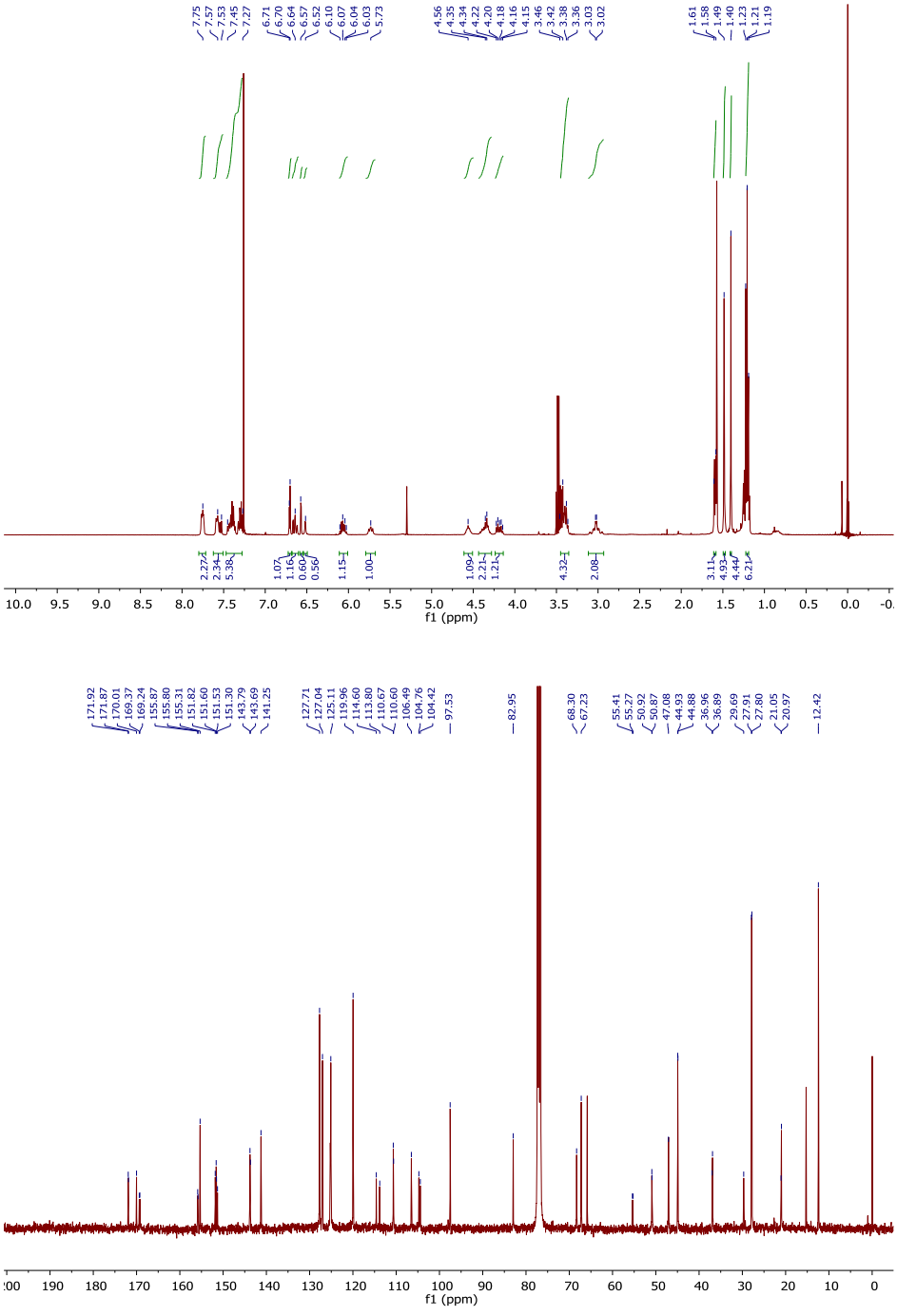

Figure S32. ^{1}H and ^{13}C NMR spectrum of compound **7**.

Fmoc-Asp(DEAdcCM)-O^{t}Bu (8)

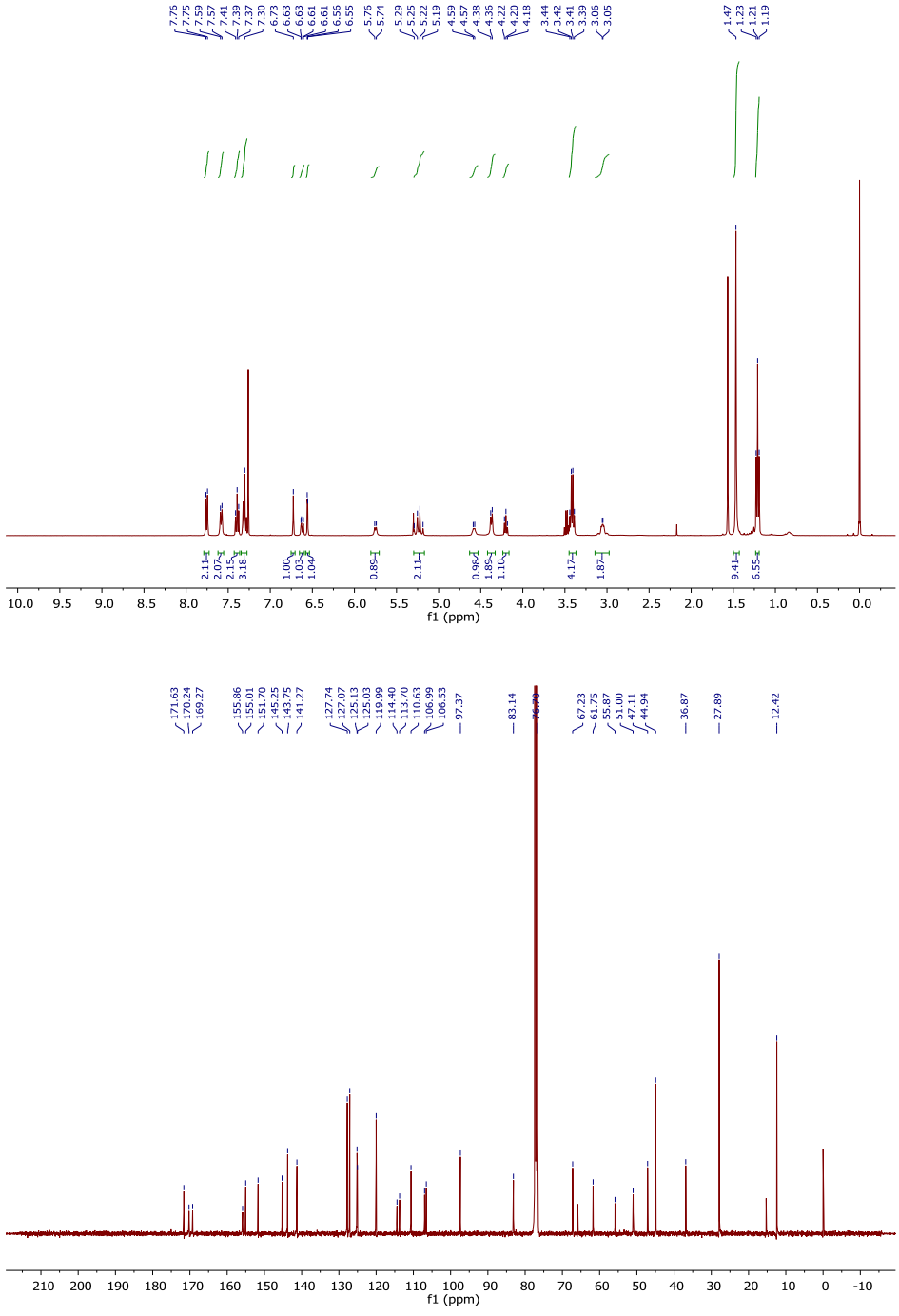

Figure S33. ^{1}H and ^{13}C NMR spectrum of compound **8**.

Fmoc-Asp(DEAdcCE)-OH (9)

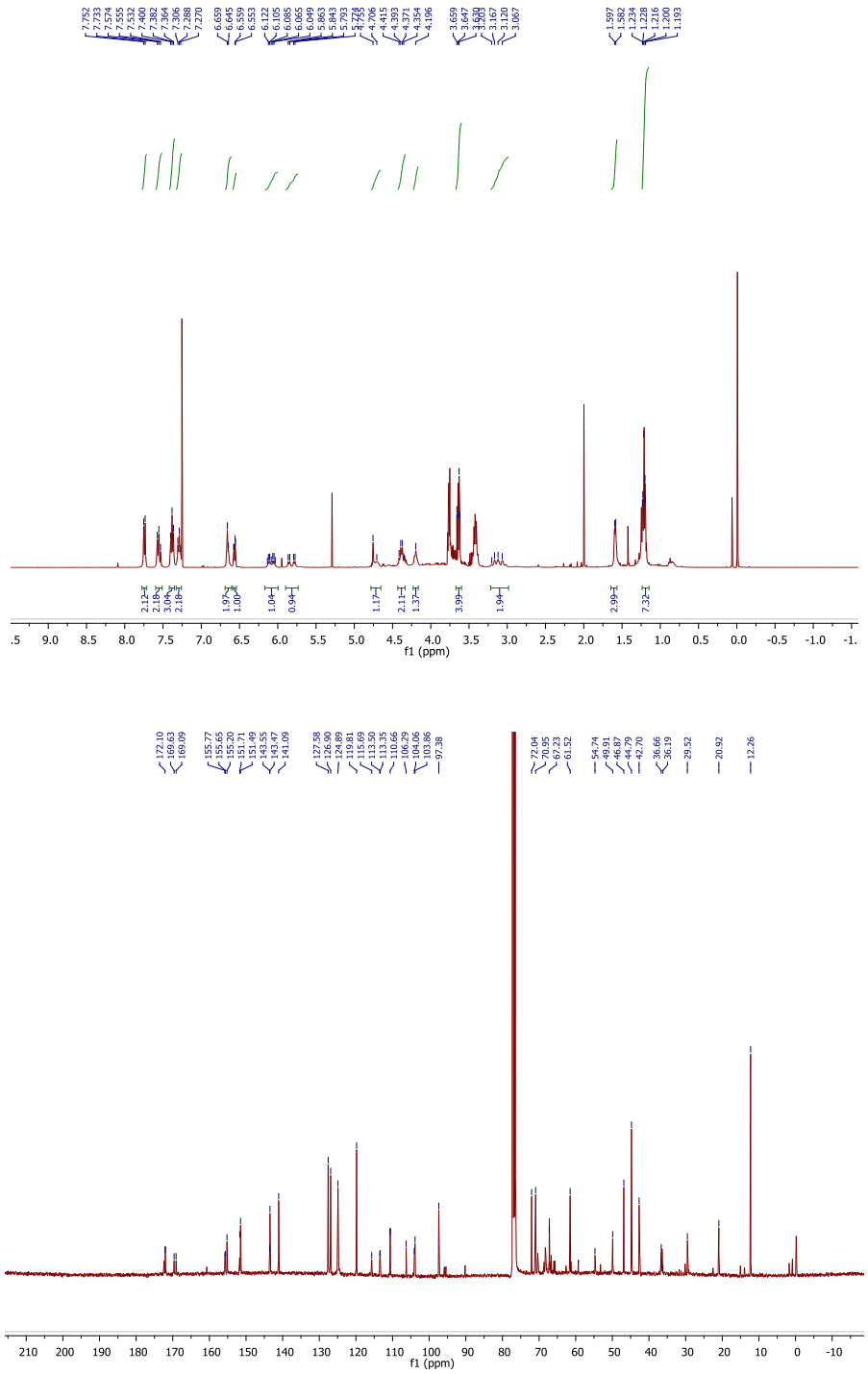

Figure S32. ^{1}H and ^{13}C NMR spectrum of compound **9**.

Fmoc-Asp(DEAdcCM)-OH (10)

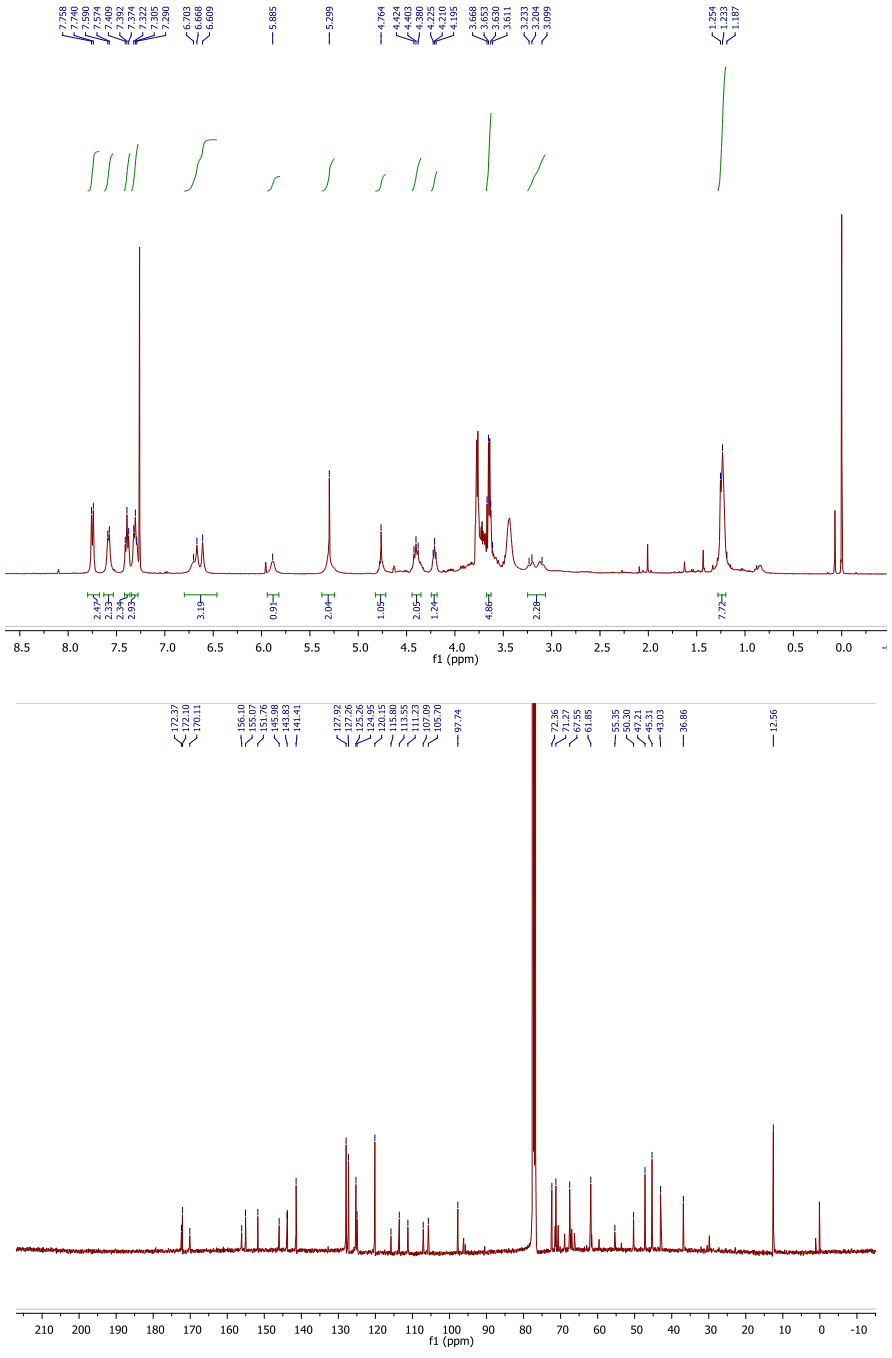

Figure S34. ^{1}H and ^{13}C NMR spectrum of compound **10**.

15.- References

1.- T. Yamaguchi, Y. Kobayashi and J. Abe. *J*. *Am*. *Chem*. *Soc*. **2016**, *138*, 906-913.

2.- M. Montalti, A. Credi, L. Prodi and M. T. Gandolfi, Chemical actinometry, Handbook of Photochemistry, Taylor & Francis Group, Boca Raton, Florida, 3rd ed, 2006, pp. 601–616.

3.- H. J. Kuhn1, S. E. Braslavsky and R. Schmidt. *Pure Appl*. *Chem*. **2004**, *76*, 2105–2146.

Chapter III: Development of novel coumarin-based fluorophores with far-red and near-infrared emission useful for cell imaging applications

9. Publication D: Redesigning the Coumarin Scaffold into Small Bright Fluorophores with Far-Red to Near-Infrared Emission and Large Stokes Shifts Useful for Cell Imaging (*J. Org. Chem.* **2018**, *83*, 1185-1195)

JOC The Journal of Organic Chemistry
Cite This: J. Org. Chem. 2018, 83, 1185−1195
Article
pubs.acs.org/joc

Redesigning the Coumarin Scaffold into Small Bright Fluorophores with Far-Red to Near-Infrared Emission and Large Stokes Shifts Useful for Cell Imaging

Albert Gandioso,[†,‡] Roger Bresolí-Obach,[§] Alba Nin-Hill,[†,∥] Manel Bosch,[⊥] Marta Palau,[†] Alex Galindo,[†] Sara Contreras,[†] Anna Rovira,[†] Carme Rovira,[†,#,∥] Santi Nonell,[§] and Vicente Marchán*[,†,‡]

[†]Secció de Química Orgànica, Departament de Química Inorgànica i Orgànica, Universitat de Barcelona, Martí i Franquès 1-11, E-08028 Barcelona, Spain

[‡]Institut de Biomedicina de la Universitat de Barcelona (IBUB), E-08028 Barcelona, Spain

[§]Institut Químic de Sarrià, Universitat Ramon Llull, E-08017 Barcelona, Spain

[∥]Institut de Química Teòrica i Computacional (IQTCUB), E-08028 Barcelona, Spain

[⊥]Unitat de Microscòpia Òptica Avançada, Centres Científics i Tecnològics, Universitat de Barcelona, E-08028 Barcelona, Spain

[#]Institució Catalana de Recerca i Estudis Avançats (ICREA), E-08010 Barcelona, Spain

Supporting Information

ABSTRACT: Among the palette of previously described fluorescent organic molecules, coumarins are ideal candidates for developing cellular and molecular imaging tools due to their high cell permeability and minimal perturbation of living systems. However, blue-to-cyan fluorescence emission is usually difficult in *in vivo* applications due to the inherent toxicity and poor tissue penetration of short visible light wavelengths. Here, we introduce a new family of coumarin-based fluorophores, nicknamed COUPY, with promising photophysical properties, including emission in the far-red/near-infrared (NIR) region, large Stokes shifts, high photostability, and excellent brightness. COUPY fluorophores were efficiently synthesized in only three linear synthetic steps from commercially available precursors, with the *N*-alkylation of a pyridine moiety being the key step at the end of the synthetic route, as it allows for the tuning of the photophysical properties of the resulting dye. Owing to their low molecular weights, COUPY dyes show excellent cell permeability and accumulate selectively in nucleoli and/or mitochondria of HeLa cells, as their far-red/NIR fluorescence emission is easily detected at a concentration as low as 0.5 μM after an incubation of only 20 min. We anticipate that these coumarin scaffolds will open a way to the development of novel coumarin-based far-red to NIR emitting fluorophores with potential applications for organelle imaging and biomolecule labeling.

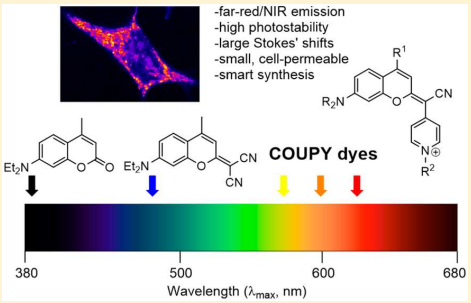

INTRODUCTION

Fluorophores based on organic molecules are powerful tools in modern cellular and molecular imaging techniques as well as for the *in vivo* detection and/or quantification of biologically relevant species.[1] Among them, far-red and near-infrared (NIR) fluorophores are particularly interesting since emission at longer wavelengths exhibits several appealing features, such as deep tissue penetration, minimal autofluorescence interference, and low light scattering, while minimizing photodamage to living cells compared to UV and blue light.[2] Despite the large number of previously described far-red/NIR fluorescent dyes, most are far from being ideal due to suboptimal photophysical parameters (e.g., small Stokes shifts and poor photostabilities) and physicochemical properties (e.g., low aqueous solubilities and undesirable aggregations)[3] due to their large sizes and structural complexity, the latter being a consequence of the necessity of extending π-conjugation to red-shift absorption and emission. Most commercially available far-red or NIR fluorophores are derived from cyanines,[4] which are also highly polar, making them cell impermeable and not completely suitable for use in live cells. Consequently, it is important to develop new fluorophores based on low molecular weight scaffolds operating in the optical window of the tissues with high cell permeability and minimal perturbations of the living system.[5] Ideally, such small scaffolds should be amenable to smart structural modifications to easily tune their absorption and emission properties on demand, preferably at the late synthetic stages,[6] as well as for facilitating conjugation to

Received: October 20, 2017
Published: December 28, 2017

DOI: 10.1021/acs.joc.7b02660
J. Org. Chem. 2018, 83, 1185−1195

Scheme 1. Rational Design of the New Coumarin-Based Fluorophores Synthesized in This Work

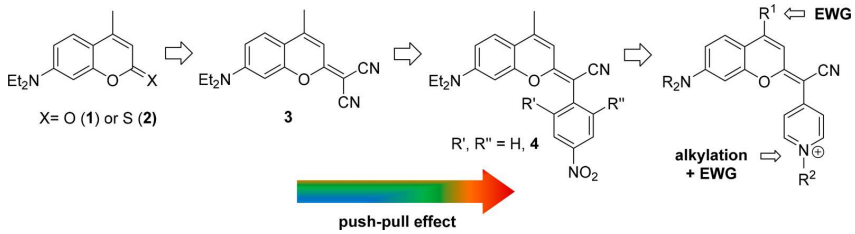

Scheme 2. Synthesis of Coumarin Fluorophores 9–12

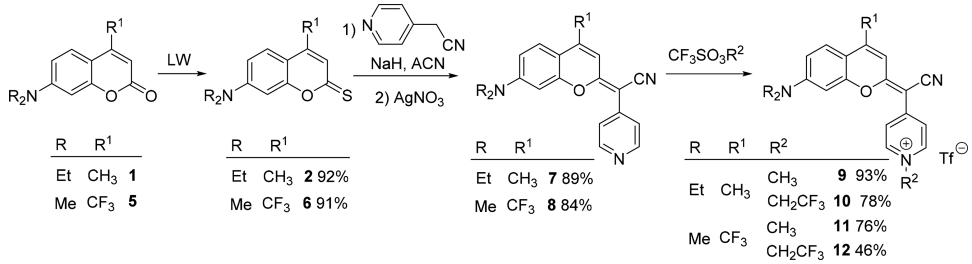

biomolecules such as lipids, peptides, proteins, oligonucleotides, and antibodies.

Among the palette of fluorescent organic molecules,[1,3a] coumarin scaffolds are ideal candidates for this purpose owing to their good cell membrane permeability and well-established photophysical properties. The fluorescence emission of basic coumarin scaffolds (e.g., compound **1** in Scheme 1, usually referred to as Coumarin 1) can be shifted from blue to cyan by incorporating electron-donating groups at position 7 of the coumarin skeleton (e.g., *N,N*-dialkylamino or hydroxy/alkoxy) that partner with the electron-withdrawing lactone moiety to create a push–pull effect. On the basis of this premise, great efforts have been devoted to red-shift the emission of coumarins by introducing additional electron-withdrawing groups (EWGs) at positions 3 and/or 4 (CN, CF_3, carboxyl), by extending the π-conjugation system through position 3 with methine, carbonyl, or heteroaryl linkages,[7] or by fusion of aromatic cycles,[8] including other fluorescent scaffolds such as rhodamine[9] or BODIPY.[7b,10]

Despite huge synthetic efforts dedicated to the coumarin scaffold, little work has been devoted to modifying the lactone function. Thionation of the carbonyl group (e.g., compound **2** in Scheme 1) is known to cause significant red-shift, leading to blue absorption ($\lambda_{max} \sim 470$ nm) and green light emission ($\lambda_{em} \sim 550$ nm) in the 7-*N,N*-diethylamino series.[11] Similarly, extending the conjugation of the system at position 2 via the incorporation of a dicyanomethylene group (e.g., compound **3** in Scheme 1) has been reported to induce similar bathochromic effects in both absorption and emission in several systems,[12] including dicyanocoumarin-caged morpholino oligonucleotides[12c] and RGD-containing peptides.[12d] Very recently, we have reported for the first time the synthesis of coumarin derivatives in which one cyano group in coumarin **3** was replaced by a phenyl ring containing EWGs at *ortho* and *para* positions to increase the push–pull character of the chromophore (e.g., compound **4** in Scheme 1).[13] Although such modifications red-shifted absorption into the green-to-red region and allowed us to obtain new caging groups that could be photoremoved with visible light, the incorporation of several strong EWGs such as nitro was found to have a negative effect on the fluorescence emission of the compounds.[13]

With the aim of further red-shifting absorption and emission of the coumarin scaffold while keeping a low molecular weight, we focused on replacing one cyano group in dicyanomethylenecoumarin **3** by pyridine (Scheme 1). We reasoned that this modification could increase the π-conjugation and the push–pull character of the chromophore, which would result in a large bathochromic shift in absorption and emission bands. The electron-deficient pyridine heterocycle offers many other attractive features, such as the possibility of tuning its electronic properties through the incorporation of EWG substituents as well as *N*-alkylation. The latter is an important advantage since the resulting positive charge on the nitrogen atom would lead to an increased electron-withdrawing effect and, consequently, to a large intramolecular charge-transfer effect along the coumarin skeleton. On the basis of this rational design, here we introduce a new family of coumarin-based fluorophores, nicknamed COUPY, which shows promising photophysical properties, including large Stokes shifts, large photostability, brightness, and emission in the far-red/NIR region. Importantly, their photophysical properties were easily tuned by selecting the appropriate combination of the *N*-alkylating group at the pyridine moiety (CH_3 or CH_2CF_3) and the substituent at position 4 (CH_3 or CF_3), while keeping a low molecular weight (MW 340–440). Rapid access to COUPY dyes occurred in only three linear synthetic steps from cheap, commercially available precursors. Moreover, excellent cell permeability was found in HeLa cells, where the compounds accumulated selectively in nucleoli and/or mitochondria.

RESULTS AND DISCUSSION

Design, Synthesis, and Characterization of COUPY Scaffolds. The synthesis of the new fluorophores was designed from commercially available Coumarin 1 (**1**) (Scheme 2). We

DOI: 10.1021/acs.joc.7b02660
J. Org. Chem. 2018, 83, 1185–1195

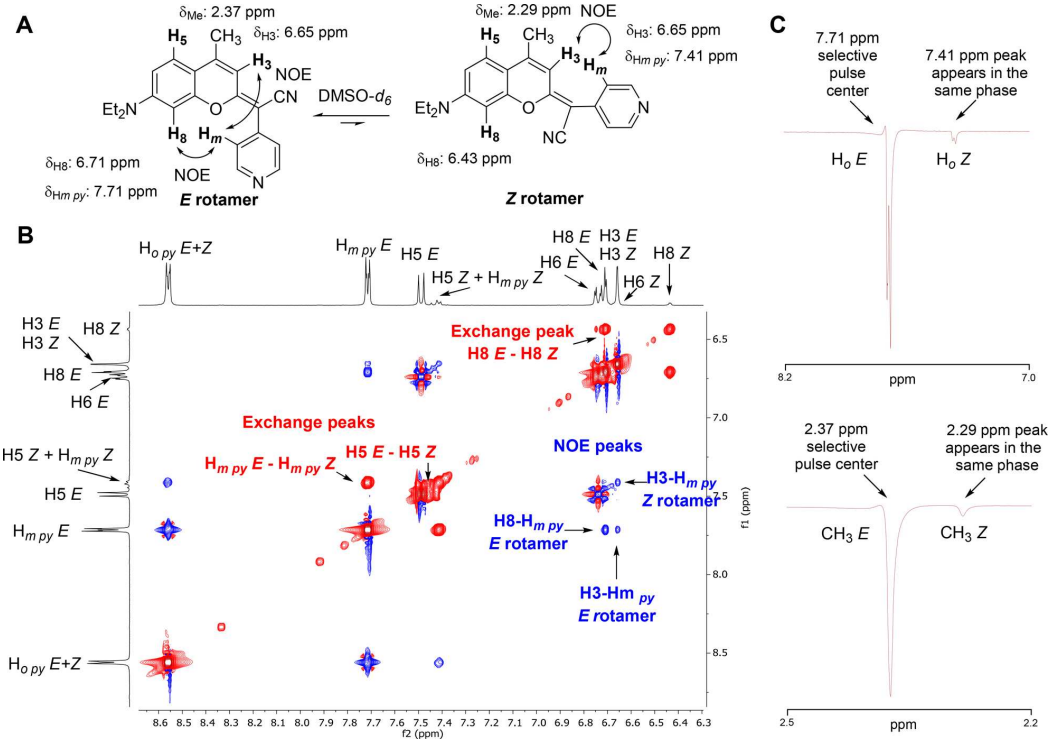

Figure 1. (A) Structures of the *E* and *Z* rotamers of coumarin **7** with some diagnostic NOE cross-peaks indicated. (B) Expansion of the 2D NOESY spectrum (t_m = 500 ms, 25 °C) of **7** in DMSO-d_6 showing exchange cross-peaks between rotamer resonances of the same sign as the diagonal. (C) 1D gradient NOE spectrum of coumarin **7** with an initial selective pulse at 7.71 ppm (top) or at 2.37 ppm (bottom) conduces new peaks of the same phase at 7.41 ppm or at 2.39 ppm, respectively, implying chemical exchange and, for instance, the existence of rotamers.

also selected Coumarin 152 (**5**) because the incorporation of strong EWGs such as CF_3 at position 4 of the coumarin skeleton is known to increase the photostability of the dye when compared to that of the unsubstituted derivative[14] and to induce a pronounced red-shift of the absorption and emission bands by enhancing its "push−pull" character.[7b,c,15] This modification has been applied in a coumarin-based, commercially available dye (AlexaFluor 430) and in the xanthene skeleton for developing deep-red and NIR dyes.[9b,16] Since we and others have demonstrated the utility of thiocoumarin derivatives for introducing the dicyanomethylene functionality within the coumarin skeleton,[12b−e] we first synthesized thiocoumarins **2**[13] and **6** by reaction with Lawesson's reagent (LW, Scheme 2). To our delight, condensation with 4-pyridylacetonitrile in the presence of a strong base followed by treatment with silver nitrate afforded coumarins **7** and **8** in excellent yields after silica column chromatography (89% and 84%, respectively). Full characterization was carried out by high resolution ESI mass spectrometry and NMR (^{1}H, ^{13}C, and ^{19}F), and the purity was assessed by reversed-phase HPLC-MS (Figure S1), revealing a single peak in both cases.

Interestingly, the ^{1}H NMR spectrum of coumarin **7** shows the presence of two sets of proton signals in $CDCl_3$ and in DMSO-d_6 in an ∼90:10 ratio (see Figure 1), and the same duplicity was found in the ^{13}C NMR spectra. Full assignment of the ^{1}H NMR spectrum by using 2D COSY and NOESY experiments (Figures 1 and S3 and S4) confirmed the presence of two species in slow equilibrium in the solution on the chemical shift time scale. As shown in Figure 1B, the presence of chemical exchange cross-peaks between the resonances of the two species in the 2D NOESY spectrum accounts for the existence of *E* and *Z* interconverting rotamers around the exocyclic C═C bond with an exchange rate (k_{ex}) of approximately <10 s^{-1}. It should be mentioned that noticeable exchange cross-peaks were observed only in DMSO-d_6 and not in $CDCl_3$. Further evidence of the dynamic interconversion of the two species was provided by 1D-selective chemical exchange experiments (Figure 1C).[17] The existence of rotamers instead of diastereomers can be attributed to the strong push−pull character of the compounds: the exocyclic C═C bond connecting C-2 of the coumarin moiety and C-4 of the pyridine cannot be considered a pure double bond, but a double bond with partial single bond character due to π-delocalization. The presence of diagnostic NOE cross-peaks, such as the one between the H-3 proton of the coumarin in the minor rotamer and the meta protons of the pyridine (Figure 1), allowed us to conclude that the *E* rotamer was the one preferred (thus the one usually drawn in the manuscript). A similar behavior was found for the 4-trifluoromethylcoumarin analogue (**8**), in which an ∼93:7 mixture of the two rotamers was identified in solution by NMR (Figures S5 and S6). Again, ^{1}H−^{1}H NOESY experiments allowed us to conclude that the *E* rotamer was the major species in solution.

DOI: 10.1021/acs.joc.7b02660
J. Org. Chem. 2018, 83, 1185−1195

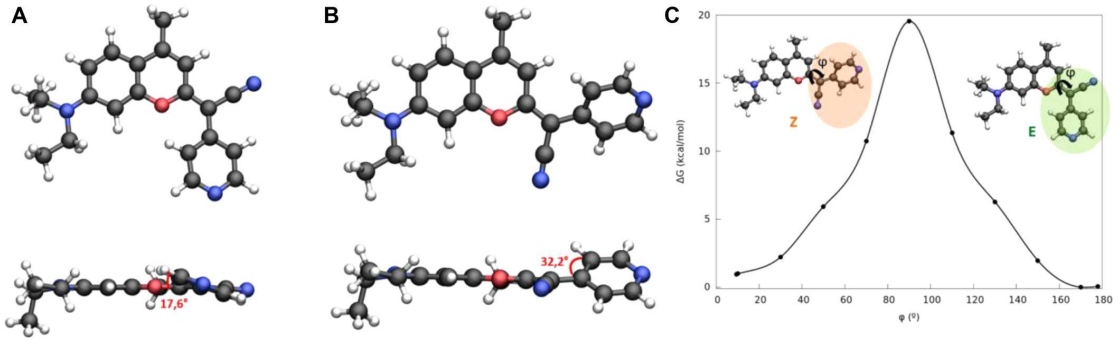

Figure 2. DFT optimized structures of rotamers *E* (A) and *Z* (B) of coumarin **7**, and the energy profile resulting from rotating the φ dihedral angle from the *Z* rotamer to the *E* rotamer (C).

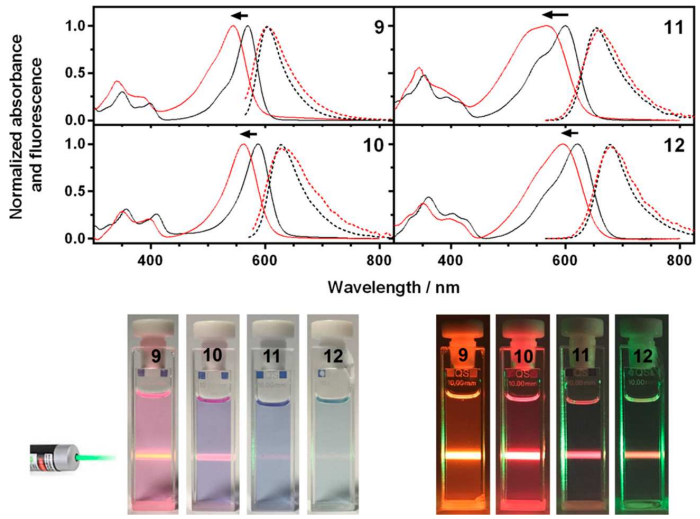

Figure 3. Top: Comparison of the normalized absorption (solid lines) and fluorescence (dotted lines) spectra of COUPY dyes (compounds **9**–**12**) in DCM (black lines) and in H_2O (red lines). Bottom: Photographic images of coumarin derivatives **9**–**12** (5 μM) in DCM in daylight (left) and in the dark (right) upon irradiation with a green light laser (532 nm).

Having established by NMR the existence of rotamers in solution for the two coumarin scaffolds, we decided to get some additional insights into these experimental observations from a theoretical point of view. DFT calculations were carried out with a Gaussian09 (G09) software package (see Figures S11–S16 and Tables S1–S5). As shown in Figure 2, the core of coumarin scaffold **7** is essentially planar in the optimized structures of the two rotamers, by being the pyridine moiety slightly twisted. The C–C and C–N bond lengths determined by DFT calculations confirmed strong electronic delocalization along the π-conjugated system, from the electron-donating NEt_2 group to the pyridine and nitrile. Notably, the value of the exocyclic C=C bond length (1.40 Å) is between a single (1.45 Å) and double (1.33 Å) $C(sp^2)$–$C(sp^2)$ bond (Table S3). The calculated rotational energy barrier (19.6 kcal/mol, Figure 2C) enables interconversion under normal conditions, and the calculated probability of obtaining *E* and *Z* rotamers was approximately 84% and 16%, respectively, which is in good agreement with the experimental ratio determined by NMR. Moreover, a good correlation between the charges of the atoms calculated using the electrostatic potential (ESP) fitting method (Table S4 and Figure S13) and the expected electronic delocalization of the system was found.

Synthesis and Photophysical Characterization of COUPY Fluorophores. To our delight, analysis by UV–HPLC–MS of coumarin derivatives **7** and **8** (Figure S1) revealed a strong bathochromic shift (63 and 85 nm, respectively) of their absorption maximum compared with that of the parent dicyanocoumarin **3** (λ_{max} = 478 nm in **3** vs λ_{max} = 541 nm in **7** and λ_{max} = 563 nm in **8**) and even with respect to that of coumarin **4** (λ_{max} = 499 nm).[13] This red-shift can be attributed to the increased push–pull character of the conjugated π-electron system of the chromophore due to the replacement of the nitrile group in **3** or the *p*-nitrophenyl in **4** by pyridine, which was assumed to be protonated during HPLC analysis under acidic conditions (0.1% trifluoroacetic acid). Such encouraging results led us to synthesize *N*-alkylated pyridinium analogues to obtain pH-independent fluorophores based on the two COUPY scaffolds. As shown in Scheme 2, reaction of **7** with methyl trifluoromethanesulfonate afforded

DOI: 10.1021/acs.joc.7b02660
J. Org. Chem. 2018, 83, 1185–1195

Table 1. Photophysical Data of the Coumarin Derivatives 9−12 in Different Solvents

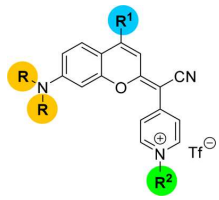

R/R^1	compd	R^2	solvent	λ_{abs} (nm)	ε (mM^{-1} cm^{-1})	λ_{em} (nm)	Stokes shift (nm)	Φ_F	τ_F (ns)
R = Et, R^1 = CH_3	**9**	CH_3	H_2O	543	31	605	62	0.15	1.0
			ACN	548	75	609	61	0.18	1.4
			DCM	569	67	607	38	0.70	5.4
	10	CH_2CF_3	H_2O	562	33	631	69	0.026	0.5
			ACN	567	43	636	69	0.12	1.2
			DCM	588	51	628	40	0.31	2.9
R = Me, R^1 = CF_3	**11**	CH_3	H_2O	567	13	662	95	0.019	0.3
			ACN	569	47	668	99	0.023	0.2
			DCM	600	34	657	57	0.054	0.7
	12	CH_2CF_3	H_2O	595	6.9	683	88	0.046	0.5
			ACN	597	26	689	92	0.12	1.4
			DCM	621	24	679	58	0.25	3.5

N-methylpyridinium-coumarin derivative **9** as a purple solid with excellent yield and purity after a simple precipitation without the need for further purification. Using this simple method, we readily prepared coumarin **10** by using the commercially available 2,2,2-trifluoroethyl trifluoromethanesulfonate as the alkylating reagent with the aim of causing an additional red-shift of the maximum absorption because of the strong electron-withdrawing character of the CF_3 group. Following the optimized procedures, we synthesized the 4-trifluoromethyl analogues **11** and **12** from coumarin scaffold **8** (Scheme 2). The four new coumarin derivatives were isolated as purple (**9**−**11**) and dark blue (**12**) solids; they were fully characterized by HR ESI-MS and 1D (^{1}H, ^{13}C, and ^{19}F) and 2D NMR, and their purity was assessed by HPLC analysis (Figure S2). It is worth noting that the *E* rotamer was the major species in solution for coumarin derivatives **9**, **10**, and **12** as inferred by 2D NOESY experiments (Figures S7−S10), while 8% of rotamer *Z* was identified in solution for coumarin **11**.

Having at hand four new coumarin derivatives, we investigated their photophysical properties (absorption and emission spectra, molar absorption coefficients (ε), fluorescence quantum yields (Φ_F), and fluorescence lifetime (τ_F)) in several solvents of different polarities and viscosities (H_2O, phosphate buffer saline (PBS), methanol (MeOH), glycerol, acetonitrile (ACN), dichloromethane (DCM), and toluene). The UV−vis absorption and emission spectra are shown in Figures 3 and S17 and S18, and their photophysical properties are summarized in Tables 1 and S6. All of the compounds showed an intense absorption band in the yellow-red part of the visible spectrum, with absorption maxima ranging from 569 nm (**9**, DCM) to 621 nm (**12**, DCM), which provided intensely colored solutions (Figure 3). As expected, from the **7** and **8** coumarin derivatives, replacement of the CH_3 group at position 4 of the coumarin skeleton by the strong electron-withdrawing CF_3 group caused a significant red-shift (from 21 to 33 nm, depending on the solvent) in the wavelength at the absorption maximum. A similar effect was observed when comparing *N*-methylated compounds with the corresponding *N*-trifluoroethylated analogues, as exemplified by the far-red absorption of the compound containing two CF_3 groups (**12**). The positions of the maxima for the *N*-methylated compounds were not modified by changing the pH beyond a small amount (Figure S19). By contrast, the spectroscopic properties of the nonmethylated compounds (e.g., **7**) were strongly influenced by the pH of the media, which correlates well with the protonation state of the pyridine moiety. However, a striking observation was made that all the compounds showed negative solvatochromism, i.e., the absorption maxima shifted to the blue when solvent polarity increased (e.g., for **9**, λ_{abs} = 543 nm in H_2O and 569 nm in DCM) which sets them apart from conventional coumarin derivatives.[18] This suggests that COUPY dyes have a smaller dipole moment in the excited state than in the ground state, in agreement with the computational results (Figure S13). For **9**−**12**, the difference between ground and excited state dipole moments is in the range of −4.8 to −6.1 D (Table S6 and Figure S21).[19] The molar absorption coefficients (ε) were also influenced by the polarity of the solvent, showing hyperchromism in less polar solvents, and by the nature of the R^1 substituent, 4-CF_3 coumarins exhibited ε values smaller than those of the 4-CH_3 analogues.

Very interestingly, coumarin derivatives **9**−**12** showed emission in the far-red to NIR region (Figures 3 and S18), with the emission maximum ranging from 609 nm (**9**, ACN) to 689 nm (**12**, ACN), which again demonstrated that the incorporation of CF_3 groups into the coumarin skeleton was highly positive for red-shifting the emission. In contrast with the absorption maximum shift, the effect of solvent polarity on the compounds' emission maxima was minimal in all the solvents studied (Tables 1 and S6). This indicates that the states initially populated by light absorption and those responsible for emission are different. As a result, the Stokes shifts of all the dyes in polar solvents were considerably larger than those of classical 7-dialkylaminocoumarins, particularly those of the 4-CF_3 derivatives (e.g., 62 nm for **9** vs 95 nm for **11** in H_2O).

Coumarins **9** and **10** exhibited excellent Φ_F in the less-polar solvents DCM and toluene (0.31−0.70), while its Φ_F decreased

DOI: 10.1021/acs.joc.7b02660
J. Org. Chem. 2018, 83, 1185−1195

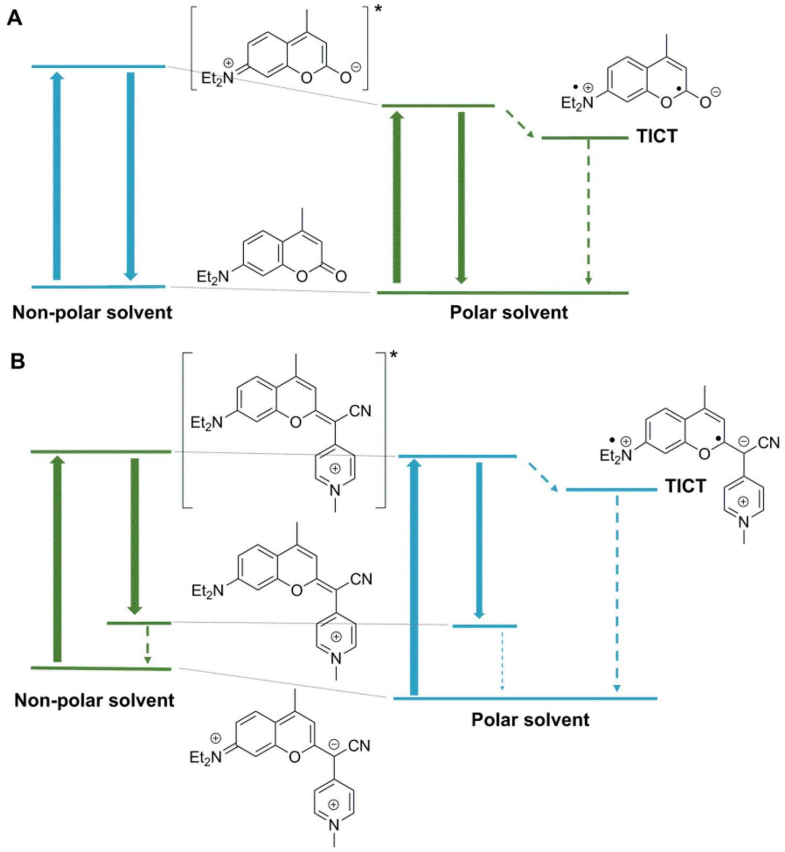

Figure 4. Distinct solvatochromism in (A) conventional coumarins and (B) the new COUPY dyes, as exemplified with compounds **1** and **9**.

in polar protic and nonprotic polar solvents (0.10−0.18). Fluorescence quenching in polar solvents might be a consequence of the formation of a twisted intramolecular charge-transfer (TICT) excited state, which should be more stable in polar media.[20,21] TICT states are known to relax rapidly by nonradiative decay pathways, thereby decreasing the fluorescence yields in polar media. For **9**−**12**, this hypothesis was supported by the observation of Φ_F enhancement in glycerol compared to methanol (Table S6). These two solvents have a similar polarity, and only the high viscosity of glycerol could prevent the twisting out of the 7-alkylamino group from the coumarin plane, thereby reducing the formation of the TICT and enhancing the fluorescence yield.[22] Further confirmation was obtained by time-resolved fluorescence spectroscopy, where the fluorescence lifetime was found to be longer in less-polar and viscous solvents, indicating that the competing deactivation channel had been arrested (Figure S20). Despite its decrease in polar solvents, it is worth noting that the Φ_F values of dyes **9** and **10** are still higher (e.g., Φ_F = 0.15 for **9** in H_2O) than those of the unmodified coumarin **1** (e.g., Φ_F = 0.058 in H_2O)[21c] or even of the parent dicyanocoumarin derivative **3** (e.g., Φ_F = 0.05 for **3**[13] vs Φ_F = 0.15 for **9** in MeOH). Thus, the replacement of one cyano group in **3** by *N*-alkylpyridinium not only red-shifts its absorption and emission but also improves the photophysical parameters relevant for cell imaging purposes, such as Stokes shift, Φ_F, and brightness.

In the case of the 4-CF_3 series (**11** and **12**), Φ_F values were reduced with respect to those of the 4-CH_3 analogues, even in nonpolar solvents such as DCM (e.g., 0.25 for **12** vs 0.70 for **9**), which led to even lower values in polar solvents (e.g., 0.05 in water for **12**). This is not a surprising result since the introduction of strong electron-withdrawing groups like CF_3 in coumarin or xanthene derivatives[9b,16] is known to generate dyes with longer absorption and emission wavelengths, but with reduced Φ_F, which is a phenomenon that typically occurs with NIR fluorescent dyes. Even so, the Φ_F values of **11** and **12** in glycerol were considerably high (Φ_F = 0.16 for **11** and 0.26 for **12**; Table S6), which suggests that if TICT formation could be prevented this would further improve the Φ_F of COUPY scaffolds emitting in the far-red/NIR region.

Finally, the photostability of coumarins **9**−**12** in water was studied under green LED irradiation (520 ± 18 nm; Figure S22). Although the incorporation of the two CF_3 moieties decreases the photostability of **12**, the other COUPY dyes (**9**−**11**) are photostable up to light fluences larger than 20 J/cm^2, which is more than one order of magnitude above typical fluences used for cell imaging purposes.[2d]

To summarize, the introduction of a pyridinium moiety in COUPY scaffolds changes the accepted vision of the photo-

DOI: 10.1021/acs.joc.7b02660
J. Org. Chem. 2018, 83, 1185−1195

physics of coumarins dyes (panel A in Figure 4).[18] Thus, in conventional coumarins, photoexcitation leads to a charge-transfer state that is stabilized in polar solvents, leading to both red-shifted absorption and emission. By contrast, the ground state of COUPY dyes **9**−**12** is slightly more polar than the excited state (see Table S4 and Figure S13), leading to blue-shifts in the absorption spectra. However, the position of the emission wavelength is essentially insensitive to the solvent polarity, indicating that no substantial dipole moment changes occur (panel B in Figure 4). As a result, COUPY dyes show larger Stokes shifts in polar solvents, which adds to their potential value for fluorescence imaging applications. In both cases, formation of TICT states in polar solvents leads to faster nonradiative decay of the excited state, which can be arrested by increasing the solvent viscosity.

Fluorescence Imaging of COUPY Dyes in Living Cells. Once the promising photophysical properties of the fluorescent dyes based on COUPY scaffolds were demonstrated, we investigated their potential applications for cellular imaging. First, the cellular uptake of coumarin **9** was studied in HeLa cells by confocal microscopy by irradiation with a yellow light laser (λ_{ex} = 561 nm). To our delight, fluorescence after 20 min of incubation was clearly observed in different cellular organelles, confirming uptake by cells. At 0.5 and 1 μM coumarin **9** (Figure 5A and B, respectively), mitochondria and intracellular vesicles were stained and also, although less intensely, the nucleoli. At 2 μM (Figure 5C) the same pattern of staining was observed but with stronger fluorescence intensity. Similar results were obtained after incubation of HeLa cells with coumarins **10** and **11** (Figure S23), although no significant fluorescence was detected in nucleoli in the case of coumarin **11**, which suggests a higher preference for mitochondria. Interestingly, the fluorescence detected in the mitochondria with coumarin **9** disappeared shortly after continuous irradiation of the cells with the excitation laser (Figures 5D and S23) and left more apparent the staining of nucleoli, cytoplasm, and vesicles (see below). On the basis of the higher red-shifted absorption of coumarin **12**, this dye could be visualized after irradiation with red light (λ_{ex} = 633 nm), although in this case fluorescence was detected only in vesicles inside the cells (Figure S24). The overall results suggest that COUPY dyes have excellent cell plasma and nuclear membrane permeability, and that they can be used for bioimaging applications in living cells at a concentration as low as 0.5 μM by incubation for a short period of time.

In order to confirm the subcellular localization of coumarin **9**, we performed co-localization experiments in HeLa cells using specific markers for mitochondria and nuclei (MitoTracker Green FM and Hoechst 33342, respectively). As shown in Figure 6, the fluorescence emission of coumarin **9** and of Mitotracker displayed superimposable distributions, which confirmed that COUPY dyes accumulate in the mitochondria. Similar results were obtained from co-localization experiments with coumarins **10** and **11** and MitoTracker Green FM (Figure S25). On the other hand, coumarin **9** detected inside the nuclei was observed where Hoechst staining was lacking (Figure 6, arrowheads), thus confirming the accumulation of the compound inside the nucleoli as Hoechst does stain the nucleus, but not the nucleolus, of cells. These results are in good agreement with previous findings on the accumulation of positively charged fluorophores in these organelles, such as the dicationic bisamidine MitoBlue reported by Vázquez and Mascareñas[23] and other far-red/NIR emitting dyes,[5,9b,15,24]

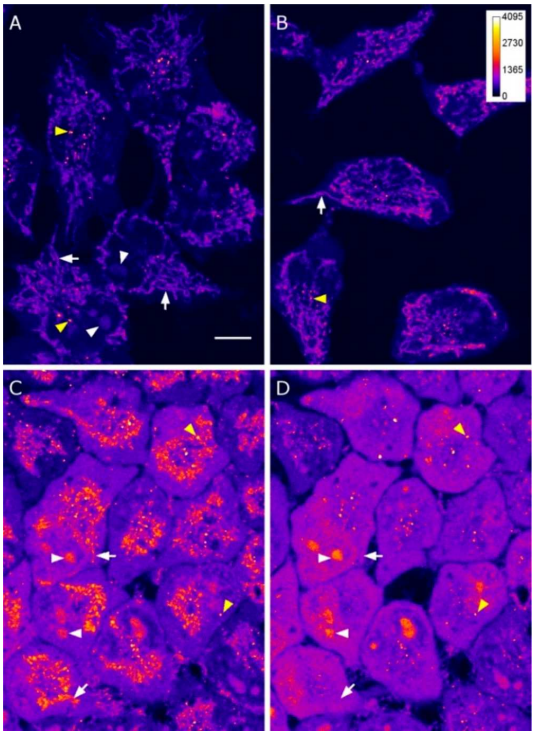

Figure 5. Cellular uptake of coumarin **9**. Single confocal planes of HeLa cells incubated with different concentrations of **9** for 20 min at 37 °C: (A) 0.5 μM, (B) 1 μM, and (C and D) 2 μM. D) Same cells as in C after 3 min of 561 nm laser irradiation. White arrows point out mitochondria, white arrowheads nucleoli, and yellow arrowheads vesicle staining. All images are color coded using the Fire lookup table from Fiji (intensity calibration bar in the upper right corner in B). Scale bar: 10 μm. All images are at the same scale.

including some pyridinium-containing compounds that accumulate preferably in mitochondria.[25] Examples of the simultaneous localization of far-red/NIR fluorescent dyes in mitochondria and nucleoli are scarce,[15,26,27] particularly with regard to low molecular weight, organic compounds that rapidly and efficiently accumulate in nucleoli.

We next evaluated the photostability of coumarin **9** after incubation in HeLa cells by continuous irradiation with a high-energy laser beam of a confocal microscope (λ_{ex} = 561 nm). Besides good cell membrane permeability, photobleaching (the irreversible destruction of an excited dye) is another important parameter for imaging-related biological applications of fluorophores since it can strongly limit their detectability. As it was previously observed, continuous exposure of coumarin **9** to the excitation wavelength caused the decrease of mitochondria signal after 1−2 min (Figures S23 and S26). This intensity decrease, however, was followed by an increment of the fluorescence intensity in nucleoli and in the cytoplasm of cells (see Figures S23 and S26). It is worth noting that this process cannot be attributed to photodegradation of the dye since it was not accompanied by a reduction of the overall fluorescence signal, and it suggests diffusion of the unaltered coumarin dye outside of the mitochondria upon light stress, which then accumulates in the nucleoli and cytoplasm. By

DOI: 10.1021/acs.joc.7b02660
J. Org. Chem. 2018, 83, 1185−1195

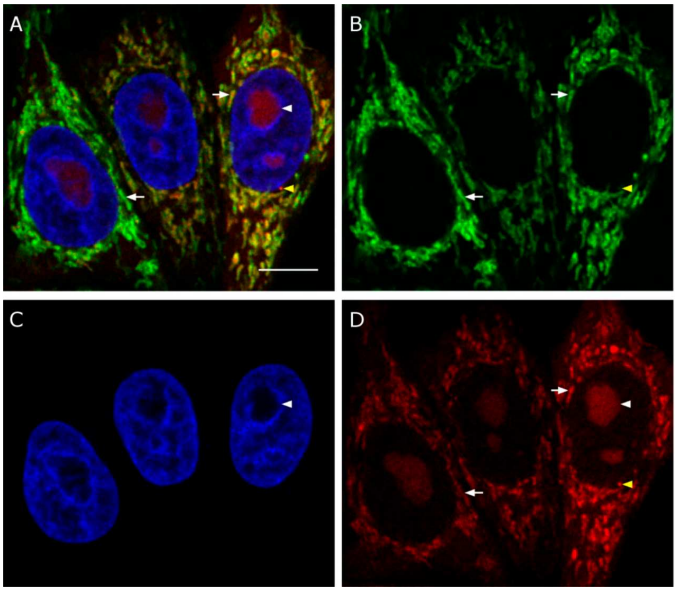

Figure 6. Co-localization studies. Single confocal plane of HeLa cells incubated with coumarin **9** (0.5 μM, red), Mitotracker Green FM (0.1 μM, green), and Hoechst 33342 (1 μg/mL, blue). (A) Overlay of the three staining images. (B, C, and D) Mitotracker Green FM, Hoechst 33342, and coumarin **9** staining, respectively. White arrows point out mitochondria, white arrowheads nucleoli, and yellow arrowheads vesicle staining. Scale bar: 10 μm.

contrast, this redistribution phenomenon was not observed with **10** and **11** (see Figures S23 and S26). The higher photostability of coumarins **10** and **11** compared with that of **9**, particularly that of **11** (see fluorescence bleaching studies in Figure S22), indicates that incorporation of CF_3 groups in COUPY scaffolds at the 4-position of the coumarin skeleton not only allows red-shifting absorption and emission but also reduces photobleaching considerably. Finally, we also evaluated the retention of coumarin **9** after cell fixation using paraformaldehyde (4%) and cell permeabilization using Triton X100. After 10 min of fixation at rt, coumarin **9** was not detected in mitochondria, although it was still observed in cytoplasm and nucleoli (Figure S27). After cell permeabilization, fluorescence was barely observed (Figure S27).

■ CONCLUSIONS

In summary, we have developed a novel family of push−pull fluorophores based on novel coumarin scaffolds, nicknamed COUPY, with promising photophysical properties and great potential for cell imaging applications. Such coumarin scaffolds (**7** and **8**) were readily prepared from commercially available precursors (Coumarin 1 and Coumarin 152, respectively) in only two linear synthetic steps, the condensation of a thiocoumarin derivative with 4-pyridylacetonitrile being the key step. Subsequent *N*-alkylation of the pyridine moiety allowed the rapid and efficient synthesis of a novel class of low molecular weight fluorophores whose photophysical properties were tuned by selecting the appropriate combination of the *N*-alkylating group (CH_3 or CH_2CF_3) and the substituent at position 4 (CH_3 or CF_3). Notably, COUPY dyes (**9**−**12**) show emission in the far-red/NIR region, large Stokes shifts in polar media, moderate-to-high fluorescence quantum yields, high photostability, and excellent brightness, which are the result of the reordering of the polar and nonpolar electronic states as compared to conventional coumarins. Interestingly, NMR spectroscopy revealed the existence of rotamers in solution, and these experimental observations were supported by computational studies. Owing to their low molecular weight, COUPY dyes show excellent cell permeability and accumulate selectively in nucleoli and/or mitochondria of HeLa cells, with their far-red/NIR fluorescence emission easily detected at a concentration as low as 0.5 μM.

Taking into account the promising photophysical properties and excellent cell permeability of the fluorophores described in this work, we anticipate that COUPY scaffolds could be used as a basis to synthesize novel NIR emitting probes for a wide range of biological applications, including organelle imaging, biomolecule labeling, cancer imaging, and fluorescence-guided surgery. Work is in progress in our laboratory to increase the red-shifted properties of COUPY scaffolds with the aim of shifting absorption and emission into the NIR, as well as for improving brightness in aqueous media. This work will be reported in due course.

■ EXPERIMENTAL SECTION

Materials and Methods. Unless otherwise stated, common chemicals and solvents (HPLC grade or reagent grade quality) were purchased from commercial sources and used without further purification. Aluminum plates coated with a 0.2 mm thick layer of silica gel 60 F_{254} were used for thin-layer chromatography analyses (TLC), whereas flash column chromatography purification was carried out using silica gel 60 (230−400 mesh). Reversed-phase high-performance liquid chromatography (HPLC) analyses were carried out on a Jupiter Proteo C_{18} column (250 × 4.6 mm, 90 Å 4 μm, flow rate: 1 mL/min) using linear gradients of 0.045% TFA or 0.1% formic acid in H_2O (A) and 0.036% TFA or 0.1% formic acid in ACN (B). NMR spectra were recorded at 25 °C in a 400 MHz spectrometer

DOI: 10.1021/acs.joc.7b02660
J. Org. Chem. 2018, 83, 1185−1195

using the deuterated solvent as an internal deuterium lock. Tetramethylsilane (TMS) was used as an internal reference (0 ppm) for ^{1}H spectra recorded in $CDCl_3$, and the residual protic signal of the solvent (77.16 ppm) was used for ^{13}C spectra. The residual protic signal of methanol and DMSO was used as a reference in ^{1}H and ^{13}C NMR spectra recorded in CD_3OD and DMSO-d_6, respectively. Chemical shifts are reported in parts per million (ppm) of the δ scale; coupling constants are in hertz, and the multiplicity is as follows: s (singlet), d (doublet), t (triplet), q (quartet), qt (quintuplet), m (multiplet), dd (doublet of doublets), dt (doublet of triplets), ddd (doublet of doublet of doublets), br (broad signal), etc. The proton signals of the *E* and *Z* rotamers were identified by simple inspection of the ^{1}H spectrum, and the rotamer ratio was calculated by peak integration. 2D-NOESY spectra were acquired in DMSO-d_6 with mixing times of 300 and 500 ms. The 1D gradient NOE spectra were obtained in a 400 MHz spectrometer using a Gaussian selective pulse and a 0.5 s mixing time with a standard 1D gradient NOE pulse sequence. Electrospray ionization mass spectra (ESI-MS) were recorded on an instrument equipped with a single quadrupole detector coupled to an HPLC, and high-resolution (HR) ESI-MS on a LC/MS-TOF instrument.

Synthesis and Characterization of (Coumarin-4-yl)methyl Derivatives (7, 9, and 10). *2-(Cyano(4-pyridine)methylene)-7-(N,N-diethylamino)-4-methyl-coumarin (7).* Compound **2**[13] (1 g, 4.04 mmol) was added to a solution of 4-pyridylacetonitrile hydrochloride (1.25 mg, 8.12 mmol) and NaH (60% dispersion in mineral oil, 2.4 g, 60 mmol) in dry ACN (20 mL) under an Ar atmosphere and protected from light. After the mixture was stirred for 2 h at room temperature, silver nitrate (1.45 g, 8.22 mmol) was added, and the reaction mixture was stirred at room temperature for 2 h under an Ar atmosphere and protected from light. The crude product was evaporated under reduced pressure and purified by column chromatography (silica gel, 0−2% MeOH in DCM) to give 1.19 g of red solid (yield 89%). Mp: 173−175 °C. TLC: R_f (10% MeOH in DCM) 0.65. ^{1}H NMR (400 MHz, $CDCl_3$) δ: (major rotamer) 8.57 (2H, d, *py*, J = 6.4 Hz), 7.72 (2H, d, *py*, J = 6.4 Hz), 7.32 (1H, d, *H5*, J = 9.2 Hz), 6.73 (1H, br q, *H3*, J = 0.8 Hz), 6.58 (1H, dd, *H6*, J = 9.2 Hz, J = 2.4 Hz), 6.44 (1H, d, *H8*, J = 2.4 Hz), 3.45 (4H, q, CH_2 *Et*, J = 7.2 Hz), 2.33 (3H, d, CH_3, J = 0.8 Hz), 1.24 (6H, t, CH_3 *Et*, J = 7.2 Hz). ^{13}C NMR (101 Hz, $CDCl_3$) δ: (major rotamer) 163.5, 154.4, 150.6, 150.1, 149.8, 144.0, 141.0, 125.4, 120.7, 119.9, 112.3, 109.9, 109.1, 96.9, 81.3, 44.7, 18.4, 12.5. HR-ESI MS, positive mode: m/z 332.1761 (calcd mass for $C_{21}H_{22}N_3O$ $[M + H]^+$ 332.1757). Analytical HPLC (30 to 100% B in 30 min, TFA additive: t_R = 13.5 min).

2-(Cyano(1-methyl(4-pyridin-1-ium))methylene)-7-(N,N-diethylamino)-4-methyl-coumarin Triflate (9). Methyl trifluoromethanesulfonate (48 μL, 0.42 mmol) was added to a solution of **7** (70 mg, 0.21 mmol) in DCM (30 mL). The mixture was stirred overnight at room temperature under an Ar atmosphere and protected from light. After the removal of the major part of the solvent, the triflate salt was precipitated with diethyl ether. The product was centrifuged and washed with diethyl ether and vacuum-dried to give 96 mg of purple solid (yield 93%). TLC: R_f (DCM) 0.53. ^{1}H NMR (400 MHz, CD_3OD) δ: (major rotamer) 8.45 (2H, d, *py*, J = 7.4 Hz), 8.21 (2H, d, *py*, J = 7.4 Hz), 7.73 (1H, d, *H5*, J = 9.2 Hz), 7.02−6.96 (3H, m, *H3*+*H6*+*H8*), 4.20 (3H, s, CH_3-*py*), 3.61 (4H, q, CH_2 *Et*, J = 7.2 Hz), 2.56 (3H, s, CH_3), 1.29 (6H, t, CH_3 *Et*, J = 7.2 Hz). ^{19}F NMR (376.5 MHz, CD_3OD) δ: −80.2 (3F, s, *Tf*). ^{13}C NMR (101 Hz, DMSO-d_6) δ: (major rotamer) 166.6, 154.7, 152.3, 151.9, 148.5, 143.8, 127.0, 120.7 (q, J = 323 Hz, *Tf*), 120.6, 118.3, 111.7, 110.4, 110.2, 96.4, 77.9, 46.0, 44.2, 18.4, 12.4. HR-ESI MS, positive mode: m/z 346.1912 (calcd mass for $C_{22}H_{24}N_3O$ $[M]^+$ 346.1919). Analytical HPLC (30 to 100% B in 30 min, TFA additive: t_R = 13.5 min).

2-(Cyano(1-(2,2,2-trifluoroethyl)(4-pyridin-1-ium))methylene)-7-(N,N-diethylamino)-4-methyl-coumarin Triflate (10). 2,2,2-Trifluoroethyl trifluoromethanesulfonate (80 μL, 0.54 mmol) was added to a solution of **7** (30 mg, 0.09 mmol) in dry ACN (20 mL). The mixture was stirred at 70 °C for 24 h under an Ar atmosphere and protected from light. Then, most of the solvent was evaporated, and the triflate salt of the compound was precipitated with diethyl ether. The product was centrifuged and washed with diethyl ether and vacuum-dried to give 40 mg of purple solid (yield 78%). TLC: R_f (DCM) 0.53. ^{1}H NMR (400 MHz, CD_3OD) δ: (major rotamer) 8.47 (2H, d, *py*, J = 7.0 Hz), 8.22 (2H, d, *py*, J = 7.0 Hz), 7.78 (1H, d, *H5*, J = 8.8 Hz), 7.08−7.04 (3H, m, *H3*+*H6*+*H8*), 5.32 (2H, q, CH_2−CF_3, J = 8.4 Hz), 3.54 (4H, q, CH_2 *Et*, J = 7.2 Hz), 2.63 (3H, s, CH_3), 1.31 (6H, t, CH_3 *Et*, J = 7.2 Hz). ^{19}F NMR (376.5 MHz, CD_3OD) δ: −73.2 (3F, t, CF_3−CH_2, J = 8.4 Hz), −80.1 (3F, s, *Tf*). ^{13}C NMR (101 Hz, DMSO-d_6) δ: (major rotamer) 167.2, 155.2, 154.5, 152.4, 150.7, 143.6, 127.3, 123.1 (q, J = 280 Hz), 120.7 (q, J = 323 Hz, *Tf*), 120.3, 118.0, 112.6, 110.9, 110.6, 96.3, 78.6, 56.4 (q, J = 34 Hz), 44.3, 18.5, 12.4. HR-ESI MS, positive mode: m/z 414.1788 (calcd mass for $C_{23}H_{23}F_3N_3O$ $[M]^+$ 414.1793). Analytical HPLC (30 to 100% B in 30 min, TFA additive: t_R = 16.1 min).

Synthesis and Characterization of (Coumarin-4-yl)-trifluoromethyl Derivatives (6, 8, 11, and 12). *7-(N,N-Dimethylamino)-4-trifluoromethyl-2-thiocoumarin (6).* 7-(*N*,*N*-Diethylamino)-4-(trifluoromethyl)coumarin (3 g, 11.66 mmol) and Lawesson's reagent (2.65 g, 6.55 mmol) were dissolved in toluene (70 mL) and heated at 100 °C for 15 h. After evaporation under reduced pressure, the red residue was purified by column chromatography (silica gel, 0−50% DCM in hexane) to give 2.91 g of a red solid (yield 91%). Mp: 169−171 °C. TLC: R_f (DCM) 0.50. ^{1}H NMR (400 MHz, $CDCl_3$) δ: 7.53 (1H, dq, J = 9.0 Hz, J = 2 Hz), 7.17 (1H, s), 6.70 (1H, dd, J = 9.0 Hz, J = 2.8 Hz), 6.68 (1H, d, J = 2.4 Hz), 3.10 (6H, s). ^{19}F NMR (376.5 MHz, $CDCl_3$) δ: −63.74 (3F, d, CF_3, J = 2 Hz). ^{13}C NMR (101 Hz, $CDCl_3$) δ: 196.0, 159.5, 153.3, 133.0 (q, J = 32 Hz), 125.8 (q, J = 3 Hz), 122.4 (q, J = 275 Hz), 121.0 (q, J = 6 Hz), 110.8, 105.2, 97.9, 40.1. HR-ESI MS, positive mode: m/z 274.0508 (calcd mass for $C_{12}H_{11}F_3NOS$ $[M + H]^+$ 274.0508).

2-(Cyano(4-pyridine)methylene)-7-(N,N-dimethylamino)-4-trifluoromethyl-coumarin (8). Compound **6** (700 mg, 2.56 mmol) was added to a solution of 4-pyridylacetonitrile hydrochloride (607 mg, 3.94 mmol) and NaH (60% dispersion in mineral oil, 1.5 g, 37.5 mmol) in dry ACN (25 mL) under an Ar atmosphere and protected from light. After the mixture was stirred for 2 h at room temperature, silver nitrate (956 mg, 5.63 mmol) was added, and the reaction mixture was stirred at room temperature for 2 h under an Ar atmosphere and protected from light. The crude product was evaporated under reduced pressure and purified by column chromatography (silica gel, 0−2% MeOH in DCM) to give 765 mg of red solid (yield 84%). TLC: R_f (DCM) 0.53. ^{1}H NMR (400 MHz, $CDCl_3$) δ: (major rotamer) 8.66 (2H, m, *py*), 7.74 (2H, m, *py*), 7.43 (1H, dq, *H5*, J = 9.2 Hz, J = 2 Hz), 7.16 (1H, s, *H3*), 6.61 (1H, dd, *H6*, J = 9.2 Hz, J = 2.4 Hz), 6.47 (1H, d, *H8*, J = 2.4 Hz), 3.12 (6H, s, CH_3). ^{19}F NMR (376.5 MHz, CD_3OD) δ: −64.2 (3F, br s, CF_3). ^{13}C NMR (101 Hz, $CDCl_3$) δ: (major rotamer) 160.5, 154.8, 153.3, 150.3, 139.5, 132.8 (q, J = 32 Hz), 126.1, 122.2 (q, J = 275 Hz), 121.4, 118.2, 112.6 (q, J = 6 Hz), 109.9, 103.8, 97.9, 88.4, 40.4. HR-ESI MS, positive mode: m/z 358.1155 (calcd mass for $C_{19}H_{15}F_3N_3O$ $[M + H]^+$ 358.1162). Analytical HPLC (30 to 100% B in 30 min, TFA additive: t_R = 13.4 min).

2-(Cyano(1-methyl(4-pyridin-1-ium))methylene)-7-(N,N-dimethylamino)-4-trifluoromethyl-coumarin Triflate (11). Methyl trifluoromethanesulfonate (19 μL, 0.17 mmol) was added to a solution of **8** (30 mg, 0.08 mmol) in DCM (20 mL), and the mixture was stirred at room temperature overnight under an Ar atmosphere and protected from light. Then, most of the solvent was removed, and the triflate salt of the compound was precipitated with diethyl ether. The product was centrifuged and washed with diethyl ether and vacuum-dried to give 36 mg of a purple solid (yield 76%). TLC: R_f (DCM) 0.53. ^{1}H NMR (400 MHz, DMSO-d_6) δ: (major rotamer) 8.76 (2H, d, *py*, J = 7.2 Hz), 8.32 (2H, d, *py*, J = 7.2 Hz), 7.54 (1H, dq, *H5*, J = 9.2 Hz, J = 2 Hz), 7.10 (1H, d, *H8*, J = 2.4 Hz), 7.06 (1H, s, *H3*), 7.00 (1H, dd, *H6*, J = 9.2 Hz, J = 2.4 Hz), 4.28 (3H, s, CH_3-*py*), 3.17 (6H, s, CH_3). ^{19}F NMR (376.5 Mz, CD_3OD) δ: −65.22 (3F, d, CF_3, J = 2 Hz), −80.16 (3F, s, *Tf*). ^{13}C NMR (101 Hz, DMSO-d_6) δ: (major rotamer) (the trifluoroacetate salt of the compound was used for recording ^{13}C NMR spectrum) 164.6, 158.0 (q, J = 34 Hz, *TFA*), 155.0, 154.0, 146.9, 144.8, 134.6 (q, J = 32 Hz), 125.5, 122.6, 121.8 (q, J = 276 Hz), 117.1, 116.2

DOI: 10.1021/acs.joc.7b02660
J. Org. Chem. 2018, 83, 1185−1195

(q, J = 296 Hz, *TFA*), 112.1, 109.8 (q, J = 5.8 Hz), 103.3, 98.0, 84.3, 46.8. HR-ESI MS, positive mode: m/z 372.1315 (calcd mass for $C_{20}H_{17}F_3N_3O$ $[M]^+$ 372.1323). Analytical HPLC (30 to 100% B in 30 min, TFA additive: t_R = 13.1 min).

*2-(Cyano(1-(2,2,2-trifluoroethyl)(4-pyridin-1-ium))methylene)-7-(N,N-dimethylamino)-4-trifluoromethyl-coumarin Triflate (**12**).* 2,2,2-Trifluoroethyl trifluoromethanesulfonate (122 μL, 0.84 mmol) was added to a solution of **8** (50 mg, 0.14 mmol) in dry ACN (20 mL). The mixture was stirred at 70 °C for 24 h under an Ar atmosphere and protected from light. The crude product was evaporated under reduced pressure and purified by column chromatography (silica gel, 0−10% MeOH in DCM) to give 38 mg of a dark blue solid (yield 46%). TLC: R_f (DCM) 0.53. ^{1}H NMR (400 MHz, CD_3OD) δ: (major rotamer) 8.74 (2H, d, *py*, J = 7.0 Hz), 8.47 (2H, d, *py*, J = 7.0 Hz), 7.69 (1H, dq br, *H5*, J = 9.2 Hz), 7.28 (1H, s, *H3*), 7.16 (1H, d, *H8*, J = 2.4 Hz), 7.09 (1H, dd, *H6*, J = 9.2 Hz, J = 2.4 Hz), 5.49 (2H, m, CH_2−CF_3), 3.25 (6H, s, CH_3). ^{19}F NMR (376.5 Hz, CD_3OD) δ: −64.98 (3F, s, CF_3), −73.05 (3F, t, CH_2−CF_3, J = 8.3 Hz), −80.16 (3F, s, *Tf*). ^{13}C NMR (101 Hz, DMSO-d_6) δ: (major rotamer) 166.0, 155.4, 154.3, 149.6, 144.9, 135.7 (q, J = 32 Hz), 125.7, 122.9 (q, J = 280 Hz), 122.6, 121.8 (q, J = 277 Hz), 120.7 (q, J = 323 Hz, *Tf*), 117.0, 113.0, 109.3, 104.0, 98.0, 84.2, 56.9 (q, J = 34 Hz), 39.8. HR-ESI MS, positive mode: m/z 440.1190 (calcd mass for $C_{21}H_{16}F_6N_3O$ $[M]^+$ 440.1192). Analytical HPLC (30 to 100% B in 30 min, TFA additive: R_t = 15.3 min).

Photophysical Characterization of Coumarin Derivatives 9−12. For photophysical measurements, all solvents used were spectroscopic grade. Absorption spectra were recorded in a Varian Cary 6000i spectrophotometer (Varian, Palo Alto, CA) at room temperature. Molar absorption coefficients (ε) were determined by direct application of the Beer−Lambert law, using solutions of **9−12** in each solvent with concentrations ranging from 10^{-6} to 10^{-5} M. Emission spectra were registered in a Fluoromax-4 spectrofluorometer (Horiba Jobin-Ybon, Edison, NJ).

Fluorescence quantum yields (Φ_F) were measured by a comparative method using cresyl violet in ethanol (CV; $\Phi_{F,ref}$ = 0.54 ± 0.03) as a reference.[28] Then, optically matched solutions of **9−12** and CV were excited, and the fluorescence spectra were recorded. The absorbance of sample and reference solutions was set below 0.1 at the excitation wavelength, and Φ_F values were calculated using eq 1:

$$\Phi_{F,Sample} = \frac{Area_{Sample}}{Area_{Ref}}\left(\frac{\eta_{Sample}}{\eta_{Ref}}\right)^2 \Phi_{F,Ref} \quad (1)$$

where $Area_{Sample}$ and $Area_{Ref}$ are the integrated fluorescence for the sample and the reference, respectively, and η_{Sample} and η_{Ref} are the refractive indices of the sample and reference solutions, respectively.

Time-resolved fluorescence decays were registered with a time-correlated single photon counting system (Fluotime 200, PicoQuant GmbH, Berlin, Germany). The samples were excited at 504 nm by means of a picosecond-pulsed LED working at a 10 MHz repetition rate. Fluorescence decays were acquired at the emission maxima, and they were analyzed using PicoQuant FluoFit c4.6.5 data analysis software. The counting frequency was always kept below 1%.

The dipole moment ($\Delta\mu$) differences between the ground (μ_g) and excited states (μ_e) for **9−12** have been estimated from the Lippert−Mataga equation (eq 2):[29]

$$\text{Stokes shift} = \overline{\nu}_a - \overline{\nu}_f = \frac{2}{hca_0^3}\left(\frac{\varepsilon - 1}{2\varepsilon + 1} - \frac{n^2 - 1}{2n^2 + 1}\right)(\mu_e - \mu_g)^2 = \left(\frac{2}{hca_0^3}\right)\Delta f \Delta\mu^2 \quad (2)$$

where h is Planck's constant, c is the velocity of light, and a_0 is the radius of the Onsager cavity around the fluorophore. The parameters ε and n are the solvent dielectric constant and refractive index, respectively, which are grouped in the term Δf. The Onsager radius was taken as half of the average distance between the push−pull moieties of the COUPY's fluorophores as described by Mukherjee et al.[30]

Photostability studies were performed by monitoring fluorescence bleaching of a 5 μM **9−12** aqueous solution irradiated with green LED light (520 ± 18 nm; 6.7 mW cm^{-2}; LED Par 64 Short V2 lamp (Showtec, Kerkrade, The Netherlands)).

Cell Culture and Treatments. HeLa cells were maintained in DMEM (Dulbecco's Modified Eagle's Medium) containing low glucose (1 g/L) and supplemented with 10% fetal calf serum (FCS), 50 units/mL penicillin−streptomycin, and 2 mM L-glutamine (all components from Biological Industries). For cellular uptake experiments and posterior observation under the microscope, cells were seeded on glass bottom dishes (P35G-1.5−14-C, Mattek). Twenty-four hours after cell seeding, the cells were incubated for 20 or 30 min at 37 °C with the required concentration of coumarins **9−12** in supplemented DMEM. Then, the cells were washed three times with DPBS (Dulbecco's phosphate-buffered saline, Gibco) to remove the excess of the compounds and kept in low glucose DMEM without phenol red (Gibco) for fluorescence imaging. Unless otherwise stated, no fixation was carried out.

For co-localization experiments, HeLa cells were treated with **9** (0.5 μM) and MitoTracker Green FM (0.1 μM, Life Technologies) for 30 min at 37 °C in non-supplemented DMEM. After removal of the medium and three washes with DPBS, cells were incubated for 10 min at 37 °C with Hoechst 33342 (1 μg/mL, Life Technologies) in supplemented DMEM. Finally, cells were washed and kept in low glucose DMEM without phenol red (Gibco) for fluorescence imaging. Co-localization experiments with **10** and **11** were carried out with a higher concentration of dye (2 μM). Quantitative analysis of the co-localization of coumarins **9−11** and MTG resulted in Pearson's correlation coefficients on the order of 0.73−0.80 (SD < 0.09).

For fixation studies, HeLa cells were treated with **9** (1 μM) for 30 min at 37 °C. After removal of the medium and three washes with DPBS, cells were fixed with 4% paraformaldehyde (Sigma) in PBS for 15 min at room temperature. Then, cells were washed again and kept in DPBS for their observation under a microscope. Finally, cells were washed and treated with 0.5% Triton X100 in PBS for 10 min at room temperature. Cells were washed and kept again in PBS for their observation under a microscope.

For photostability studies, HeLa cells were incubated with the compounds (2 μM, 30 min at 37 °C) and kept in low glucose DMEM without phenol red (Gibco) for fluorescence imaging.

■ ASSOCIATED CONTENT

Supporting Information

The Supporting Information is available free of charge on the ACS Publications website at DOI: 10.1021/acs.joc.7b02660.

HPLC traces and UV−vis absorption and emission spectra; results from DFT and fluorescence imaging studies; and 1D NMR (1H, ^{13}C, and ^{19}F), MS, and selected 2D NMR spectra (PDF)

■ AUTHOR INFORMATION

Corresponding Author

*E-mail: vmarchan@ub.edu.

ORCID

Carme Rovira: 0000-0003-1477-5010
Santi Nonell: 0000-0002-8900-5291
Vicente Marchán: 0000-0002-1905-2156

Notes

The authors declare no competing financial interest.

■ ACKNOWLEDGMENTS

This work was supported by funds from the Spanish Ministerio de Economía y Competitividad (CTQ2013-48767-C3-1-R,

DOI: 10.1021/acs.joc.7b02660
J. Org. Chem. 2018, 83, 1185−1195

CTQ2014-52658-R, CTQ2014-55174-P, CTQ2015-71896-REDT, and CTQ2016-78454-C2-1-R) and from the Generalitat de Catalunya (SGR2014-987). The authors acknowledge the helpful assistance of Dr. Irene Fernández and Laura Ortiz (MS) and Dr. Francisco Cárdenas (NMR) from CCiTUB. The authors acknowledge Dr. Montserrat Terrazas from the Institut de Recerca Biomèdica de Barcelona for supplying HeLa cells. A.Gandioso was a recipient fellow of the University of Barcelona (APIF) and A.N.-H. of the Generalitat de Catalunya (FI-AGAUR). R.B.-O. thanks the European Social Funds and the SUR del DEC de la Generalitat de Catalunya for a predoctoral fellowship (2017 FI_B2 00140).

REFERENCES

(1) (a) Lavis, L. D.; Raines, R. T. *ACS Chem. Biol.* **2008**, *3*, 142−155. (b) Lavis, L. D.; Raines, R. T. *ACS Chem. Biol.* **2014**, *9*, 855−866. (c) Zheng, Q.; Juette, M. F.; Jockusch, St.; Wasserman, M. R.; Zhou, Z.; Altman, R. B.; Blanchard, S. C. *Chem. Soc. Rev.* **2014**, *43*, 1044−1056.

(2) (a) Frangioni, J. V. *Curr. Opin. Chem. Biol.* **2003**, *7*, 626−634. (b) Owens, E. A.; Henary, M.; El Fakhri, G.; Choi, H. S. *Acc. Chem. Res.* **2016**, *49*, 1731−1740. (c) Guo, Z.; Park, S.; Yoon, J.; Shin, I. *Chem. Soc. Rev.* **2014**, *43*, 16−29. (d) Haque, A.; Faizi, M. S. H.; Rather, J. A.; Khan, M. S. *Bioorg. Med. Chem.* **2017**, *25*, 2017−2034. (e) Wagner, M.; Weber, P.; Bruns, T.; Strauss, W. S. L.; Wittig, R.; Schneckenburger, H. *Int. J. Mol. Sci.* **2010**, *11*, 956−966.

(3) (a) *Handbook of Fluorescent Probes and Research Chemicals*, 9th ed.; Spence, M. T. Z., Ed.; Molecular Probes, Inc.: Eugene, OR, 2002. (b) Nani, R. R.; Kelley, J. A.; Ivanic, J.; Schnermann, M. J. *Chem. Sci.* **2015**, *6*, 6556−6563. (c) Vendrell, M.; Zhai, D.; Er, J. C.; Chang, Y. T. *Chem. Rev.* **2012**, *112*, 4391−4420.

(4) (a) Mishra, A.; Behera, R. K.; Behera, P. K.; Mishra, B. K.; Behera, G. B. *Chem. Rev.* **2000**, *100*, 1973−2011. (b) Gorka, A. P.; Schnermann, M. J. *Curr. Opin. Chem. Biol.* **2016**, *33*, 117−125. (c) Gorka, A. P.; Nani, R. R.; Schnermann, M. J. *Org. Biomol. Chem.* **2015**, *13*, 7584−7598.

(5) Cheng, Y.; Li, G.; Liu, Y.; Shi, Y.; Gao, G.; Wu, D.; Lan, J.; You, J. *J. Am. Chem. Soc.* **2016**, *138*, 4730−4738.

(6) (a) de Moliner, F.; Kielland, N.; Lavilla, R.; Vendrell, M. *Angew. Chem., Int. Ed.* **2017**, *56*, 3758−3769. (b) Ong, M. J. H.; Srinivasan, R.; Romieu, A.; Richard, J.-A. *Org. Lett.* **2016**, *18*, 5122−5125.

(7) (a) Long, L.; Li, X.; Zhang, D.; Meng, S.; Zhang, J.; Sun, X.; Zhang, C.; Zhou, L.; Wang, L. *RSC Adv.* **2013**, *3*, 12204−12209. (b) Schill, H.; Nizamov, S.; Bottanelli, F.; Bierwagen, J.; Belov, V. N.; Hell, S. W. *Chem. - Eur. J.* **2013**, *19*, 16556−16565. (c) Nizamov, S.; Willig, K. I.; Sednev, M. V.; Belov, V. N.; Hell, S. W. *Chem. - Eur. J.* **2012**, *18*, 16339−16348. (d) Nizamov, S.; Sednev, M. V.; Bossi, M. L.; Hebisch, E.; Frauendorf, H.; Lehnart, S. E.; Belov, V. N.; Hell, S. W. *Chem. - Eur. J.* **2016**, *22*, 11631−11642.

(8) Roubinet, B.; Massif, C.; Moreau, M.; Boschetti, F.; Ulrich, G.; Ziessel, R.; Renard, P. Y.; Romieu, A. *Chem. - Eur. J.* **2015**, *21*, 14589−14601.

(9) (a) Chen, J.; Liu, W.; Zhou, B.; Niu, G.; Zhang, H.; Wu, J.; Wang, Y.; Ju, W.; Wang, P. *J. Org. Chem.* **2013**, *78*, 6121−6130. (b) Niu, G.; Liu, W.; Wu, J.; Zhou, B.; Chen, J.; Zhang, H.; Ge, J.; Wang, Y.; Xu, H.; Wang, P. *J. Org. Chem.* **2015**, *80*, 3170−3175.

(10) (a) Bochkov, A. Y.; Akchurin, I. O.; Dyachenko, O. A.; Traven, V. F. *Chem. Commun.* **2013**, *49*, 11653−11655. (b) Niu, G.; Liu, W.; Xiao, H.; Zhang, H.; Chen, J.; Dai, Q.; Ge, J.; Wu, J.; Wang, P. *Chem. - Asian J.* **2016**, *11*, 498−504.

(11) (a) Fonseca, A. S. C.; Soares, A. M. S.; Goncalves, M. S. T.; Costa, S. P. G. *Tetrahedron* **2012**, *68*, 7892−7900. (b) Fournier, L.; Gauron, C.; Xu, L.; Aujard, Is.; Le Saux, T.; Gagey-Eilstein, N.; Maurin, S.; Dubruille, S.; Baudin, J.-B.; Bensimon, D.; Volovitch, M.; Vriz, S.; Jullien, L. *ACS Chem. Biol.* **2013**, *8*, 1528−1536.

(12) (a) Kirpichenok, M. A.; Gorozhankin, S. K.; Grandberg, I. I. *Chem. Heterocycl. Compd.* **1988**, *24*, 611−616. (b) Fournier, L.; Aujard, I.; Le Saux, T.; Maurin, S.; Beaupierre, S.; Baudin, J.-B.; Jullien, L. *Chem. - Eur. J.* **2013**, *19*, 17494−17507. (c) Yamazoe, S.; Liu, Q.; McQuade, L. E.; Deiters, A.; Chen, J. K. *Angew. Chem., Int. Ed.* **2014**, *53*, 10114−10118. (d) Gandioso, A.; Cano, M.; Massaguer, A.; Marchán, V. *J. Org. Chem.* **2016**, *81*, 11556−11564. (e) Gandioso, A.; Palau, M.; Nin-Hill, A.; Melnyk, I.; Rovira, C.; Nonell, S.; Velasco, D.; García-Amorós, J.; Marchán, V. *ChemistryOpen* **2017**, *6*, 375−384.

(13) Gandioso, A.; Contreras, S.; Melnyk, I.; Oliva, J.; Nonell, S.; Velasco, D.; García-Amorós, J.; Marchán, V. *J. Org. Chem.* **2017**, *82*, 5398−5408.

(14) Fletcher, A. N.; Bliss, D. E. *Appl. Phys.* **1978**, *16*, 289−295.

(15) Corrie, J. E. T.; Munasinghe, V. R. N; Rettig, W. *J. Heterocycl. Chem.* **2000**, *37*, 1447−1455.

(16) Niu, G.; Liu, W.; Zhou, B.; Xiao, H.; Zhang, H.; Wu, J.; Ge, J.; Wang, P. *J. Org. Chem.* **2016**, *81*, 7393−7399.

(17) Hu, D. X.; Grice, P.; Ley, S. V. *J. Org. Chem.* **2012**, *77*, 5198−5202.

(18) Liu, X.; Cole, P. G.; Waddell, P. G.; Lin, T.-C.; Radia, J.; Zeidler, A. *J. Phys. Chem. A* **2012**, *116*, 727−737.

(19) Ravi, M.; Soujanya, T.; Samanta, A.; Radhakrishnan, T. P. *J. Chem. Soc., Faraday Trans.* **1995**, *91*, 2739−2742.

(20) Grabowski, Z. R.; Rotkiewicz, K.; Rettig, W. *Chem. Rev.* **2003**, *103*, 3899−4032.

(21) (a) Grimm, J. B.; English, B. P.; Chen, J.; Slaughter, J. P.; Zhang, Z.; Revyakin, A.; Patel, R.; Macklin, J. J.; Normanno, D.; Singer, R. H.; Lionnet, T.; Lavis, L. D. *Nat. Methods* **2015**, *12*, 244−250. (b) Grimm, J. B.; English, B. P.; Choi, H.; Muthusamy, A. K.; Mehl, B. P.; Dong, P.; Brown, T. A.; Lippincott-Schwartz, J.; Liu, Z.; Lionnet, T.; Lavis, L. D. *Nat. Methods* **2016**, *13*, 985−988. (c) Liu, X.; Qiao, Q.; Tian, W.; Liu, W.; Chen, J.; Lang, M. J.; Xu, Z. *J. Am. Chem. Soc.* **2016**, *138*, 6960−6963. (d) Singha, S.; Kim, D.; Roy, B.; Sambasivan, S.; Moon, H.; Rao, A. S.; Kim, J. Y.; Joo, T.; Park, J. W.; Rhee, Y. M.; Wang, T.; Kim, K. H.; Shin, Y. H.; Jung, J.; Ahn, K. H. *Chem. Sci.* **2015**, *6*, 4335−4342.

(22) Haidekker, M. A.; Brady, T. P.; Lichlyter, D.; Theodorakis, E. A. *Bioorg. Chem.* **2005**, *33*, 415−425.

(23) Sánchez, M. I.; Martínez-Costas, J.; Mascareñas, J. L.; Vázquez, M. E. *ACS Chem. Biol.* **2014**, *9*, 2742−2747.

(24) Zheng, K.; Lin, W.; Huang, W.; Guan, X.; Cheng, D.; Wang, J.-Y. *J. Mater. Chem. B* **2015**, *3*, 871−877.

(25) (a) Li, C.; Plamont, M.-A.; Aujard, I.; Le Saux, T.; Jullien, L.; Gautier, A. *Org. Biomol. Chem.* **2016**, *14*, 9253−9261. (b) Rosania, G. R. G.; Lee, J. W. J.; Ding, L. L.; Yoon, H.-S. H.; Chang, Y.-T. Y. *J. Am. Chem. Soc.* **2003**, *125*, 1130−1131.

(26) Liu, W.; Zhou, B.; Niu, G.; Ge, J.; Wu, J.; Zhang, H.; Xu, H.; Wang, P. *ACS Appl. Mater. Interfaces* **2015**, *7*, 7421−7427.

(27) Martin, R. M.; Ter-Avetisyan, G.; Herce, H. D.; Ludwig, A. K.; Lättig-Tünnemann, G.; Cardoso, M. D. *Nucleus* **2015**, *6*, 314−325.

(28) Magde, D.; Brannon, J. H.; Cremers, T. L.; Olmsted, J. *J. Phys. Chem.* **1979**, *83*, 696−699.

(29) (a) Lippert, V. E. Z. *Elektrochem.* **1957**, *61*, 962−975. (b) Mataga, N.; Kaifu, Y.; Koizumi, M. *Bull. Chem. Soc. Jpn.* **1956**, *29*, 465−470.

(30) Mukherjee, S.; Chattopadhyay, A.; Samanta, A.; Soujanya, T. *J. Phys. Chem.* **1994**, *98*, 2809−2812.

DOI: 10.1021/acs.joc.7b02660
J. Org. Chem. 2018, 83, 1185−1195

SUPPORTING INFORMATION

Redesigning the coumarin scaffold into small bright fluorophores with far-red to NIR emission and large Stokes' shifts useful for cell imaging

Albert Gandioso,[†,‡] Roger Bresolí-Obach,[§] Alba Nin-Hill,[†,φ] Manel Bosch,[⊥] Marta Palau,[†] Alex Galindo,[†] Sara Contreras,[†] Anna Rovira,[†] Carme Rovira,[†,ξ,φ] Santi Nonell[§] and Vicente Marchán[†,‡,*]

[†]Secció de Química Orgànica, Departament de Química Inorgànica i Orgànica, Universitat de Barcelona, Martí i Franquès 1-11, E-08028 Barcelona (Spain)
E-mail: vmarchan@ub.edu

[‡]Institut de Biomedicina de la Universitat de Barcelona (IBUB), E-08028 Barcelona (Spain)

[§]Institut Químic de Sarrià, Universitat Ramon Llull, E-08017 Barcelona (Spain)

[φ]Institut de Química Teòrica i Computacional (IQTCUB), E-08028 Barcelona (Spain)

[⊥]Unitat de Microscòpia Òptica Avançada, Centres Científics i Tecnològics, Universitat de Barcelona, E-08028 Barcelona (Spain)

[ξ]Institució Catalana de Recerca i Estudis Avançats (ICREA), E-08010 Barcelona (Spain)

Table of contents

1.- Reversed-phase HPLC analysis of compounds 7-12

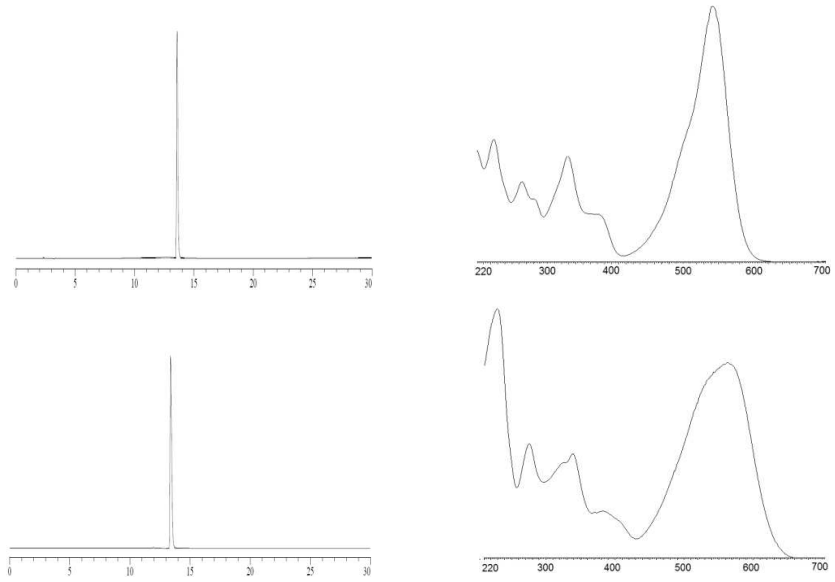

Figure S1. Reversed-phase HPLC traces (left) and UV-vis spectra (right) of coumarins **7** (top) and **8** (bottom).

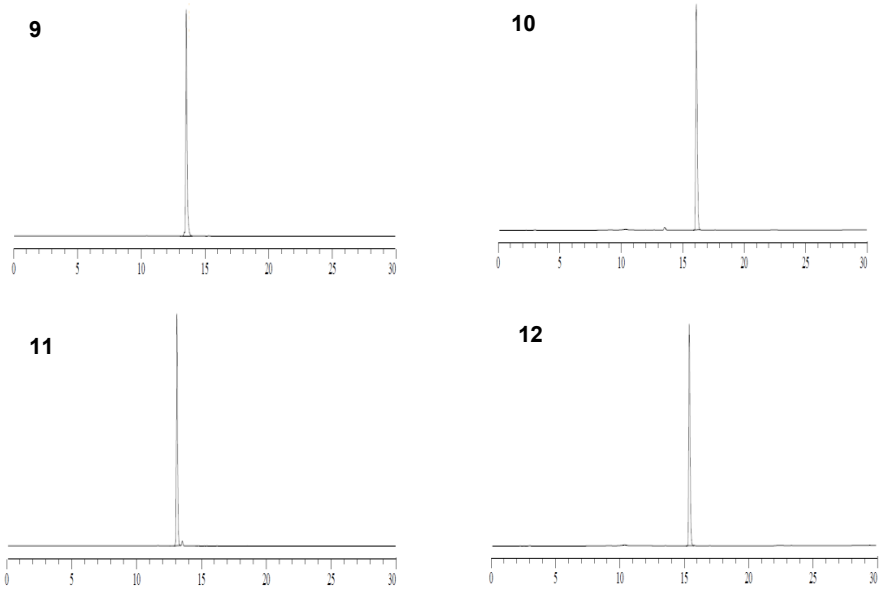

Figure S2. Reversed-phase HPLC traces of coumarins **9-12**.

2- 2D NMR characterization of COUPY scaffolds 7 and 8

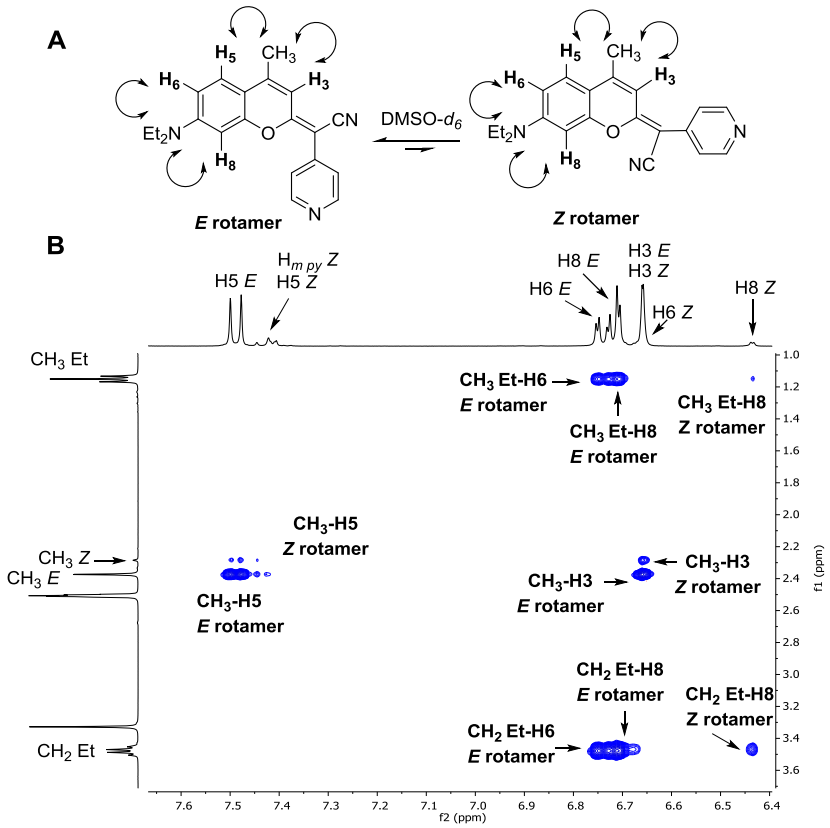

Figure S3. A) Structure of *E* and *Z* rotamers of coumarin **7** with some diagnostic NOE cross-peaks indicated. B) Expansion of the NOESY spectrum (t_m = 500 ms) of **7** in DMSO-d_6 at 298 K.

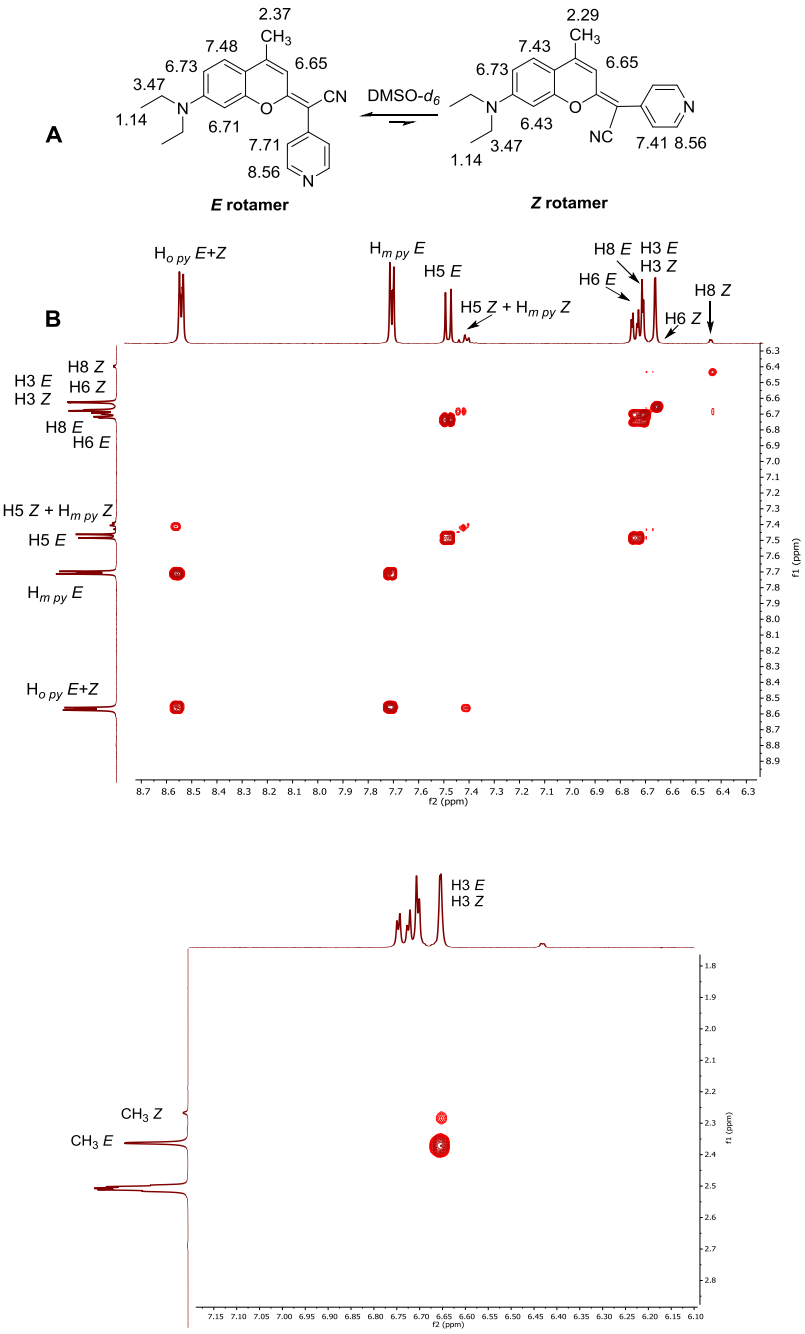

Figure S4. Expansion of the COSY spectrum of coumarin **7** in DMSO-d_6 at 298 K.

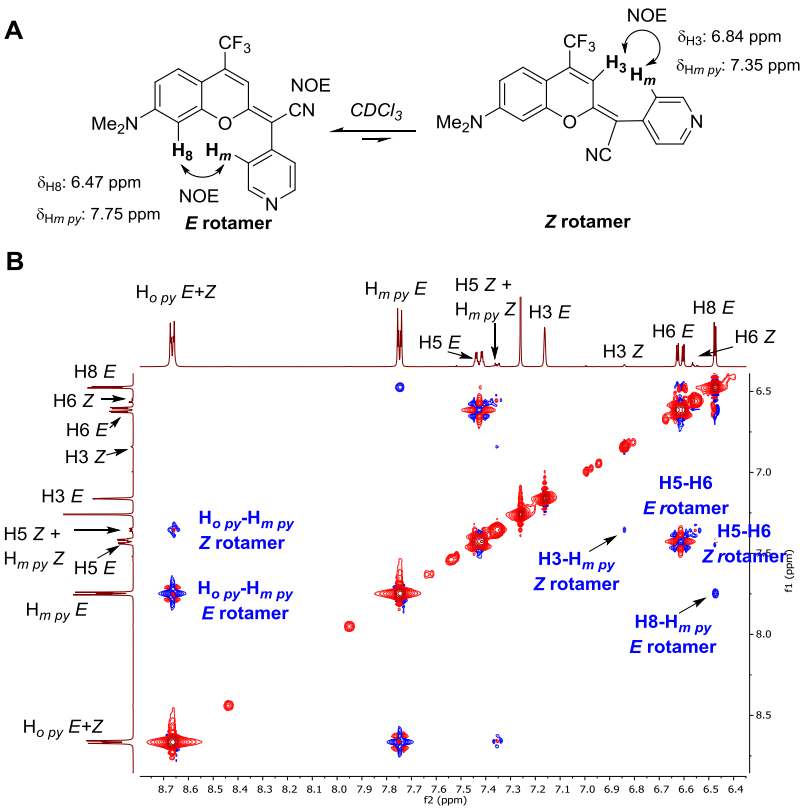

Figure S5. A) Structure of *E* and *Z* rotamers of coumarin **8** with some diagnostic NOE cross-peaks indicated. B) Expansion of the NOESY spectrum (t_m = 500 ms) of **8** in $CDCl_3$ at 298 K.

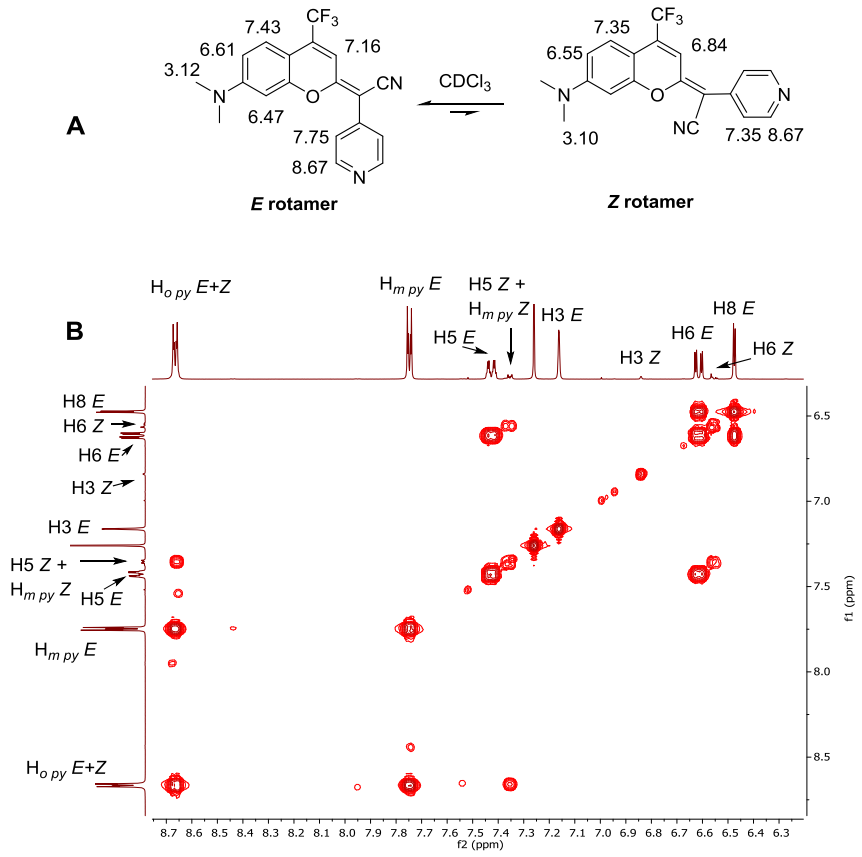

Figure S6. Expansion of the COSY spectrum of coumarin **8** in $CDCl_3$ at 298 K.

3- 2D NMR characterization of COUPY dyes 9-12

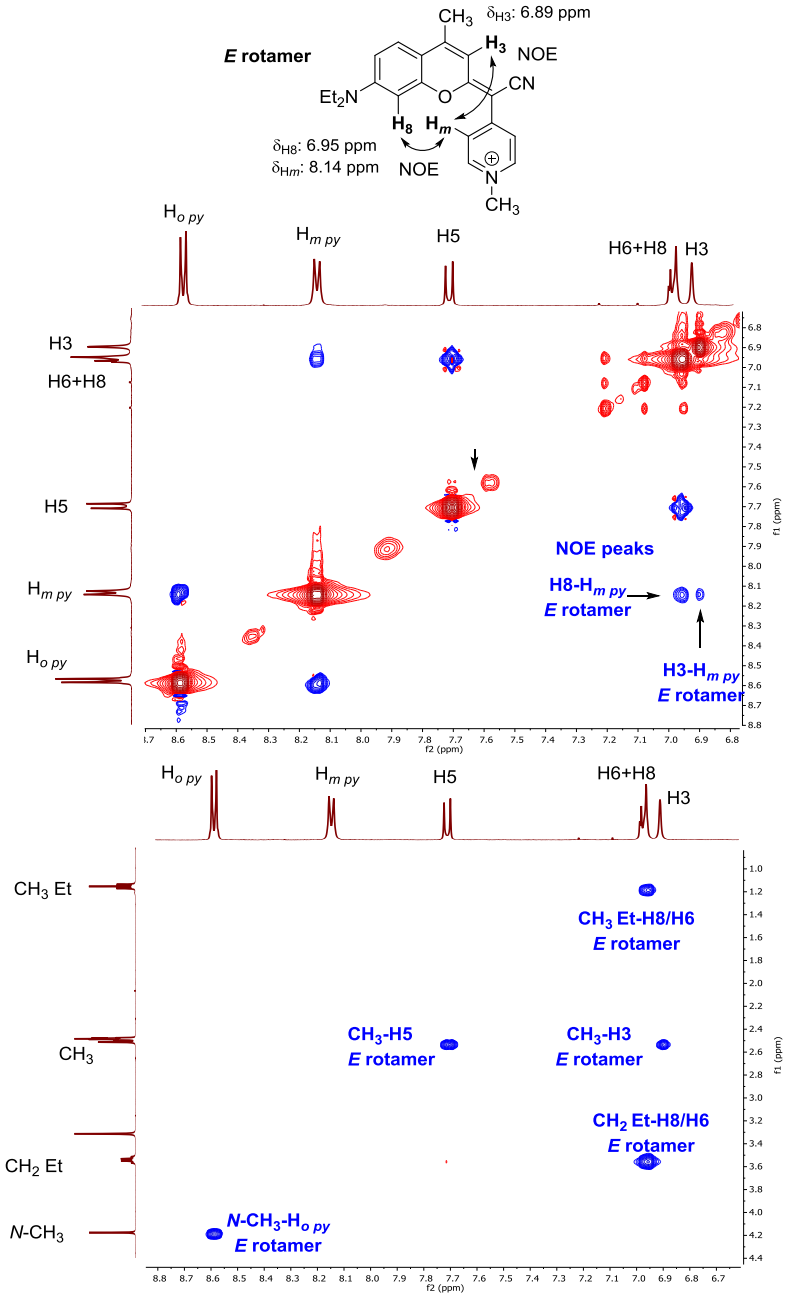

Figure S7. Structure of *E* rotamer of coumarin **9** with some diagnostic NOE cross-peaks indicated, and expansions of the NOESY spectrum (t_m = 500 ms) of **9** in DMSO-d_6 at 298 K.

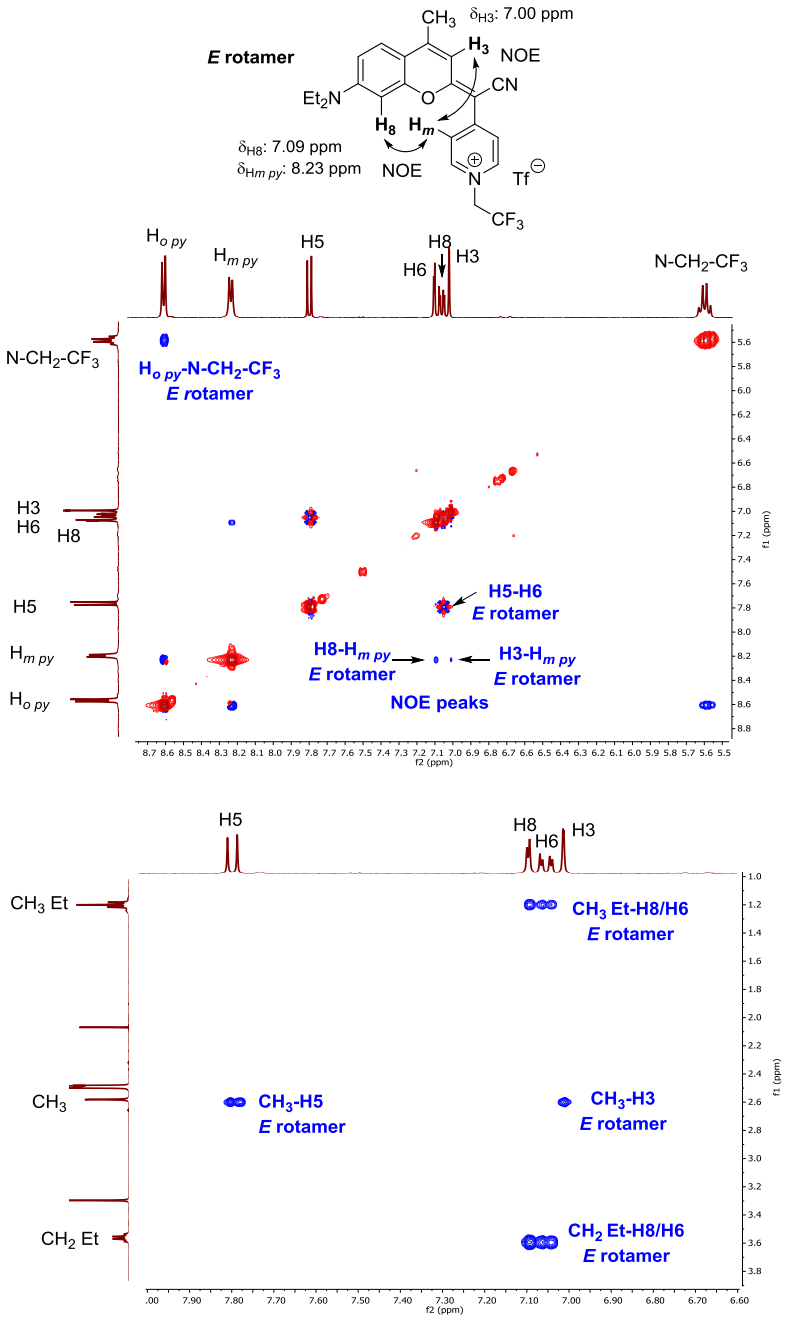

Figure S8. Structure of *E* rotamer of coumarin **10** with some diagnostic NOE cross-peaks indicated, and expansions of the NOESY spectrum (t_m = 500 ms) of **10** in DMSO-d_6 at 298 K.

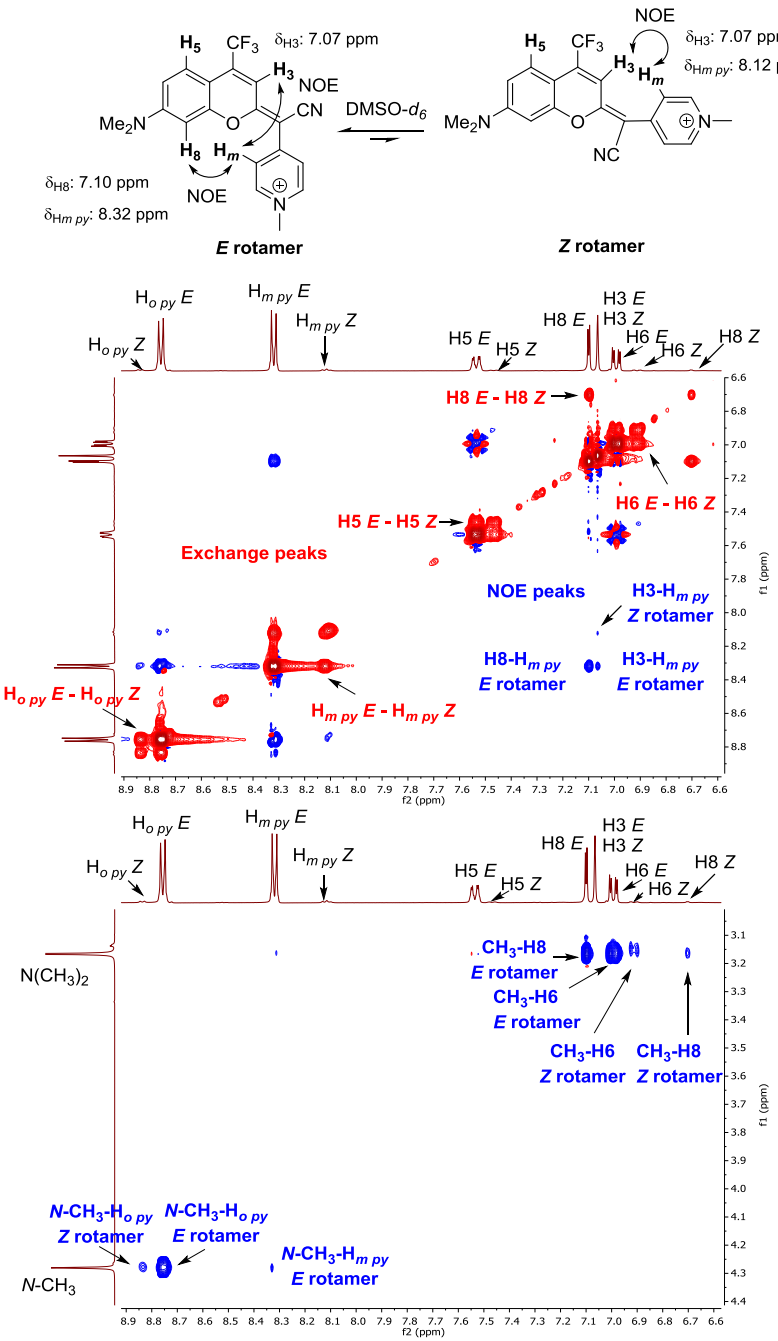

Figure S9. Structure of *E* and *Z* rotamers of coumarin **11** with some diagnostic NOE cross-peaks indicated, and expansions of the NOESY spectrum (t_m = 500 ms) of **11** in DMSO-d_6 at 298 K showing exchange cross-peaks between rotamer resonances of the same sign as the diagonal.

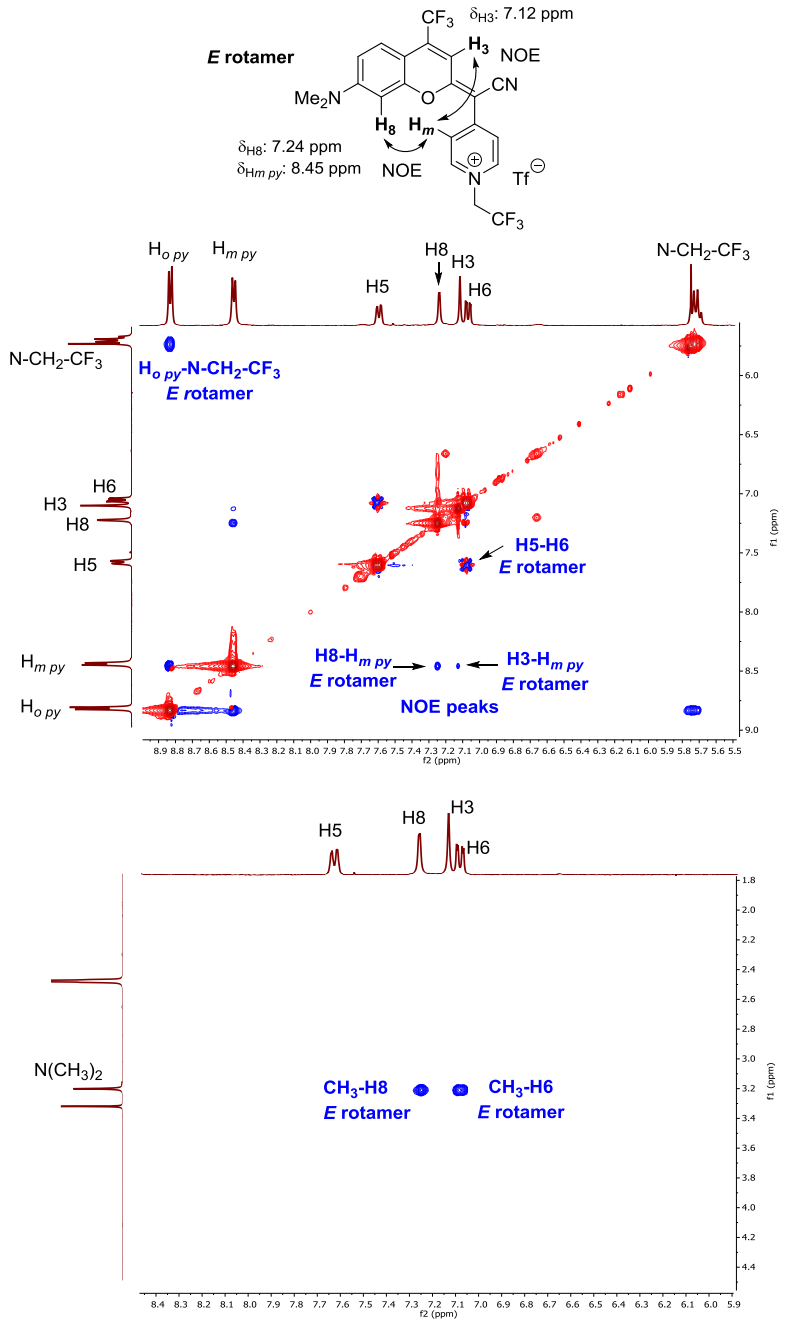

Figure S10. Structure of *E* rotamer of coumarin **12** with some diagnostic NOE cross-peaks indicated, and expansions of the NOESY spectrum (t_m = 500 ms) of **12** in DMSO-d_6 at 298 K.

4.- Computational calculations with coumarins 7 and 9

All calculations were carried out with Gaussian09 (G09) software package.[1] The electronic structures were computed by Density Functional Theory (DFT)[2] using the B3LYP[3,4] functional and the 6-31G** basis set.[5] For the excited states calculations the TDDFT method was used.[6] The calculations were performed in an implicit DMSO solvent (SMD solvation model).[7] The charges of the atoms in the compounds were determined using the electrostatic potential (ESP) fitting method.[8]

4.1.- Energy profiles

The energy profiles of the compounds **7** and **9** going from *Z* rotamer (~ 10º) to *E* rotamer (~ 178º) is represented in Figure S11.

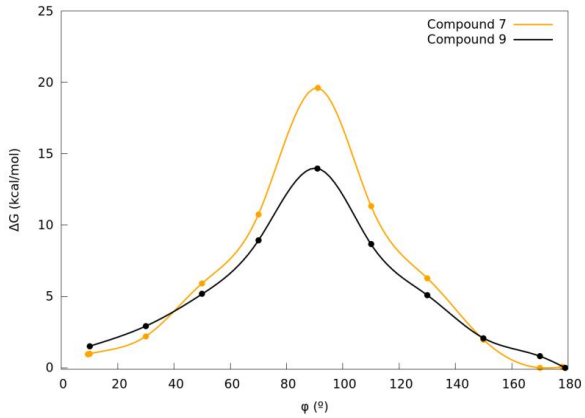

Figure S11. Energy profiles resulting from rotating the φ dihedral angle from the *Z* to the *E* rotamer.

Table S1. Free energy differences with respect the most stable rotamer (*E*). Energy units are indicated in kcal/mol.

φ (º)	**7**	**9**
Z	1.0 (9.4 º)	1.5 (10 º)
10	1.0	1.5
30	2.2	2.9
50	5.9	5.2
70	10.7	8.9
TS	19.6	14.0
110	11.3	8.7
130	6.3	5.1
150	2.0	2.1
170	0.0	0.8
E	0.0 (178.3 º)	0.0 (178.9 º)

4.2.- Kinetic and thermodynamic properties

Following the Transition State Theory (TST) and using the Eyring equation, disregarding the transmission coefficient, the rate constant of the rotational process can be calculated as follows:

$$k = \frac{K_B T}{h} e^{\frac{-\Delta G^{\neq}}{RT}} \quad (1)$$

Approximating to a first order reaction the half-time life corresponds to:

$$t_{1/2} = \frac{\ln(2)}{k} \quad (2)$$

And finally, knowing the energy difference between the two most stable states, the *E* and *Z* rotamers, we can obtain the ratio of probabilities to find the system in one or the other state using the Boltzmann distribution equation:

$$\frac{p_i}{p_j} = e^{\frac{E_j - E_i}{K_B T}} \quad (3)$$

The results obtained for the two compounds are shown in Table S3.

Table S2. Kinetic and thermodynamic properties for coumarins **7** and **9**.

Compound	k **(s^{-1})**	$t_{1/2}$ **(s)**	**Probability *E*/*Z* rotamers (%)**
7	0.046	15	84.4/15.6
9	510	0.0014	92.6/7.4

4.3.- Bond length analysis

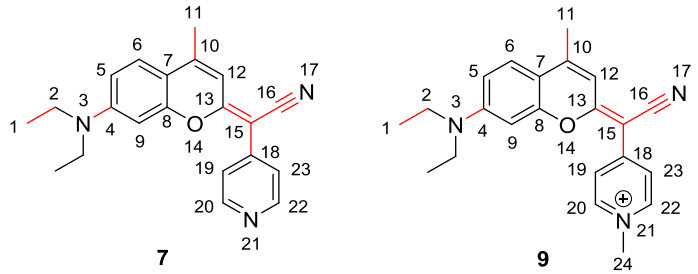

Figure S12. Structure of the *E* rotamer of coumarins **7** and **9** with the numbering indicated in Table S2. The bonds analyzed in Table S3 are represented in red.

Table S3. Representative C-C and C-N bond lengths in Å for the *E* rotamer of compounds **7** and **9** in the ground and first excited state (S_1). Analogue values were obtained for the *Z* rotamer.

Bond	**7**	**9**	**7 (S_1)**	**9 (S_1)**
C_1-C_2	1.53	1.53	1.53	1.53
N_3-C_4	1.37	1.37	1.39	1.37
C_{10}-C_{11}	1.50	1.50	1.50	1.50
C_{13}-C_{15}	1.40	1.42	1.48	1.42
C_{15}-C_{16}	1.42	1.42	1.41	1.42
C_{16}-N_{17}	1.17	1.17	1.17	1.17
C_{15}-C_{18}	1.47	1.45	1.44	1.44
N_{21}-C_{24}	-	1.47	-	1.47

4.4.- ESP charges

Table S4. ESP charges of the *E* rotamer of coumarins **7** and **9** in the ground and first excited state (S_1). The values for the *Z* rotamer are of the same order.

Atom Number[a]	7	9	7 (S_1)	9 (S_1)
1	-0.06	-0.05	-0.07	-0.02
2	0.32	0.30	0.32	0.30
3	-0.48	-0.47	-0.51	-0.32
4	0.49	0.49	0.45	0.42
5	-0.42	-0.17	-0.21	-0.12
6	-0.02	0.10	0.08	0.07
7	-0.28	-0.25	-0.26	-0.13
8	0.40	0.40	0.39	0.36
9	-0.49	-0.32	-0.31	-0.22
10	0.42	0.45	0.28	0.31
11	-0.01	-0.01	-0.05	-0.02
12	-0.63	-0.37	-0.27	-0.26
13	0.68	0.68	0.43	0.53
14	-0.31	-0.29	-0.29	-0.31
15	-0.81	-0.72	-0.6	-0.61
16	0.57	0.55	0.57	0.53
17	-0.63	-0.60	-0.56	-0.58
18	0.82	0.57	0.77	0.49
19	-0.71	-0.17	-0.39	-0.15
20	0.49	0.19	0.53	0.12
21	-0.75	0.21	-0.71	0.22
22	0.48	0.19	0.53	0.13
23	-0.70	-0.15	-0.42	-0.15
24	-	0.13	-	0.11

[a] See Figure S12 for the numbering of the atoms.

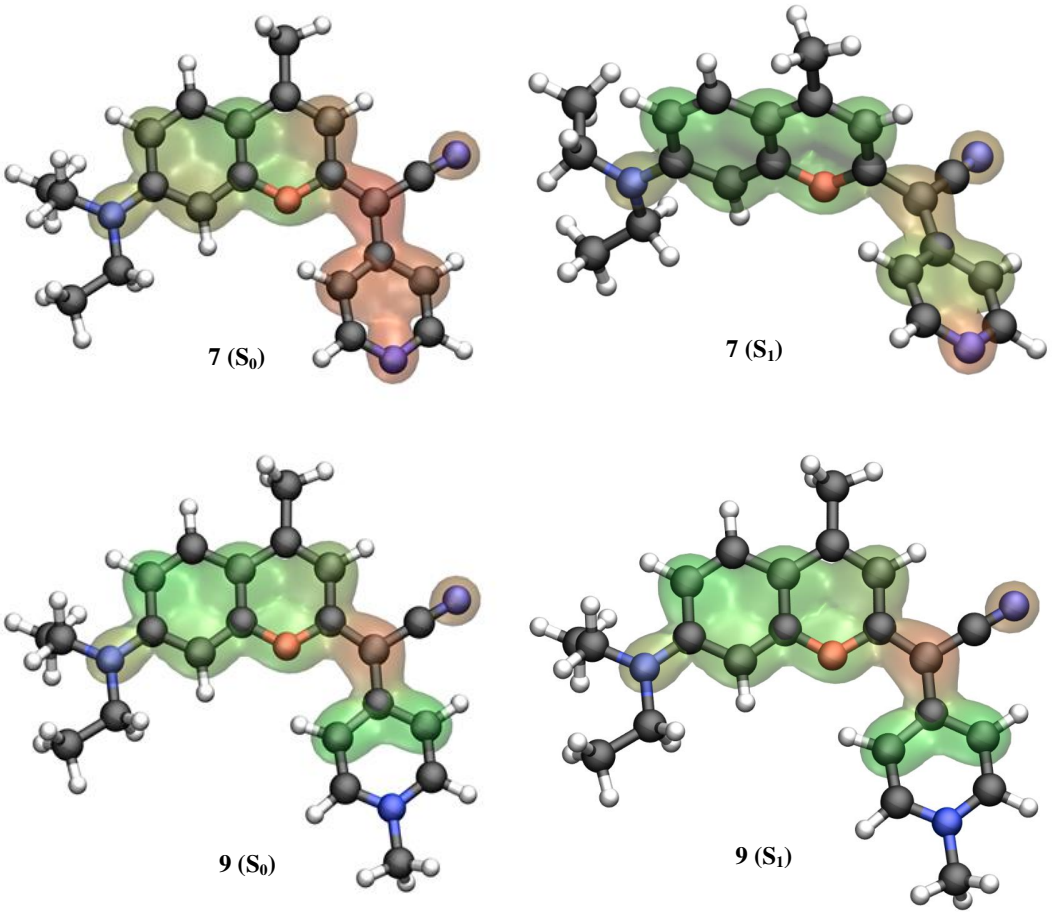

Figure S13. ESP charges distribution for the *E* isomer of compounds **7** and **9** in the ground (S_0) and first excited (S_1) states. The atoms with charges smaller than -0.1, are represented with a transparent surface around it. The color scale goes from green to red through yellow for the less negatively charged to the most negatively charged atoms, respectively.

4.5.- Structural analysis of *E* and *Z* rotamers

Table S5. Dihedral angle of the pyridine moiety respect the plane formed by the core coumarin scaffold.

	7	**9**	**7 (S_1)**	**9 (S_1)**
E	17.6	1.4	92.3	2.3
Z	32.2	22.8	-	-

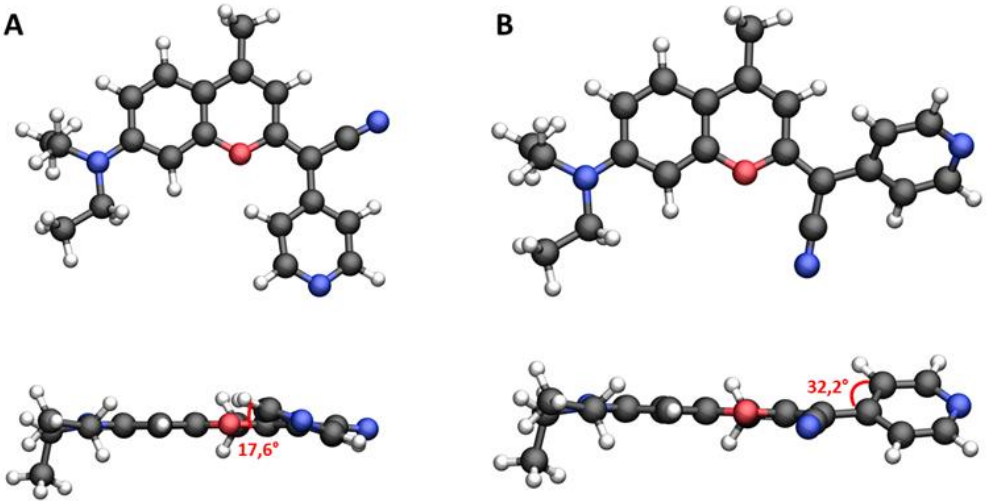

Figure S14. DFT optimized structures of rotamers *E* (A) and *Z* (B) of coumarin **7**.

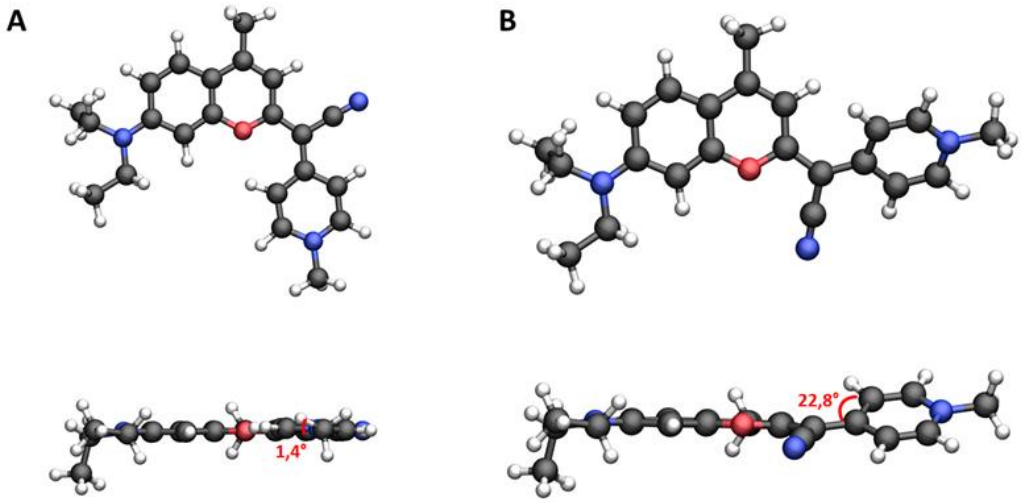

Figure S15. DFT optimized structures of rotamers *E* (A) and *Z* (B) of coumarin **9**.

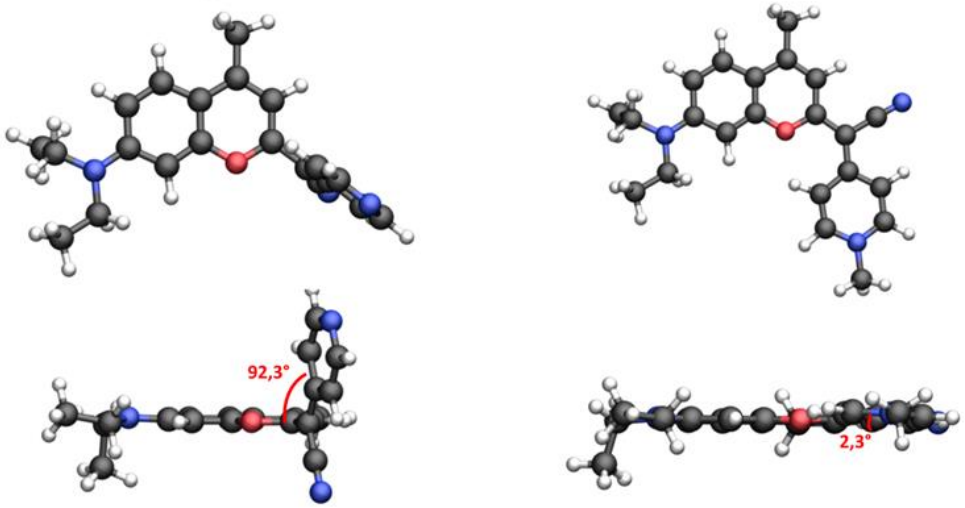

Figure S16. DFT optimized structures of rotamer *E* of coumarins **7** (S_1). (left) and **9** (S_1). (right)

5.- Photophysical characterization of coumarin derivatives 9-12

Table S6. Optical and photophysical properties of the coumarin derivatives **9-12** in different solvents.

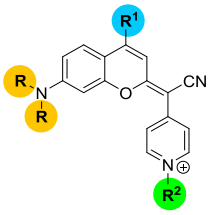

R / R^1	compd	R^2	Solvent	λ_{abs} (nm)	ε ($mM^{-1}cm^{-1}$)	λ_{em} (nm)	Stokes Shift (nm)	Φ_F	τ_F (ns)	$-\Delta\mu$ (Δ)
R = Et $R^1 = CH_3$	**9**	CH_3	H_2O	543	31	605	62	0.15	1.0	5.1
			PBS	545	34	604	59	0.12	0.9	
			MeOH	549	52	606	57	0.15	1.3	
			Glycerol	552	35	606	54	0.49	4.7	
			ACN	548	75	609	61	0.18	1.4	
			DCM	569	67	607	38	0.70	5.4	
			Toluene	566	47	601	35	0.64	4.8	
	10	CH_2CF_3	H_2O	562	33	631	69	0.026	0.5	4.8
			PBS	562	39	630	68	0.018	0.3	
			MeOH	568	56	629	61	0.10	1.1	
			Glycerol	571	42	629	58	0.21	3.4	
			ACN	567	43	636	69	0.12	1.2	
			DCM	588	51	628	40	0.31	2.9	
			Toluene	582	47	625	43	0.54	5.4	
R = Me $R^1 = CF_3$	**11**	CH_3	H_2O	567	13	662	95	0.019	0.3	6.1
			PBS	568	14	660	92	0.022	0.2	
			MeOH	570	28	665	95	0.021	0.2	
			Glycerol	578	8.4	662	84	0.16	2.2	
			ACN	569	47	668	99	0.023	0.2	
			DCM	600	34	657	57	0.054	0.7	
			Toluene	601	20	657	56	0.19	2.4	
	12	CH_2CF_3	H_2O	595	6.9	683	88	0.046	0.5	4.8
			PBS	595	8.3	682	87	0.043	0.5	
			MeOH	597	14	688	91	0.078	0.9	
			Glycerol	605	29	683	78	0.26	1.4	
			ACN	597	26	689	92	0.12	1.4	
			DCM	621	24	679	58	0.25	3.5	
			Toluene	619	18	683	64	0.20	3.3	

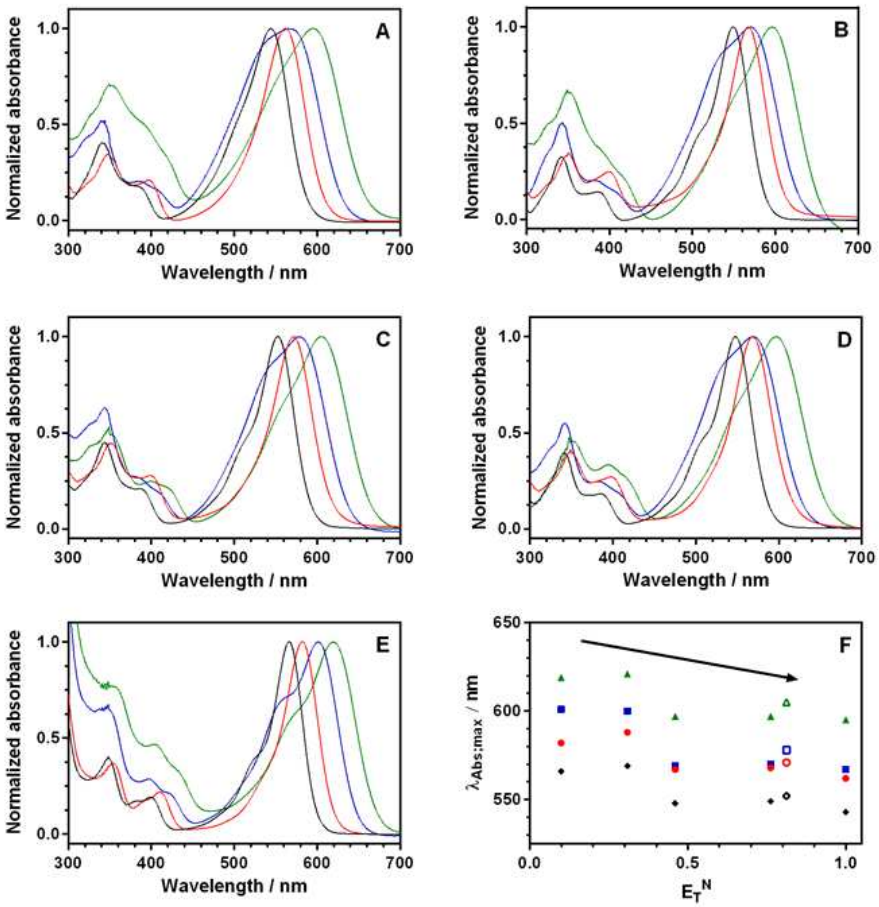

Figure S17. Normalized absorption spectra of COUPY dyes (compounds **9-12**) in PBS buffer (A), MeOH (B), glycerol (C), ACN (D) and toluene (E). (F): Absorbance maximum *vs* solvent polarity (chosen as ETN (a scale based on negatively solvatochromic Reichardt's dye)[9]) for non-viscous (closed symbols) and viscous (glycerol; open symbols) solvents. Fluorophores: **9** (black lines), **10** (red lines), **11** (blue lines) and **12** (green lines).

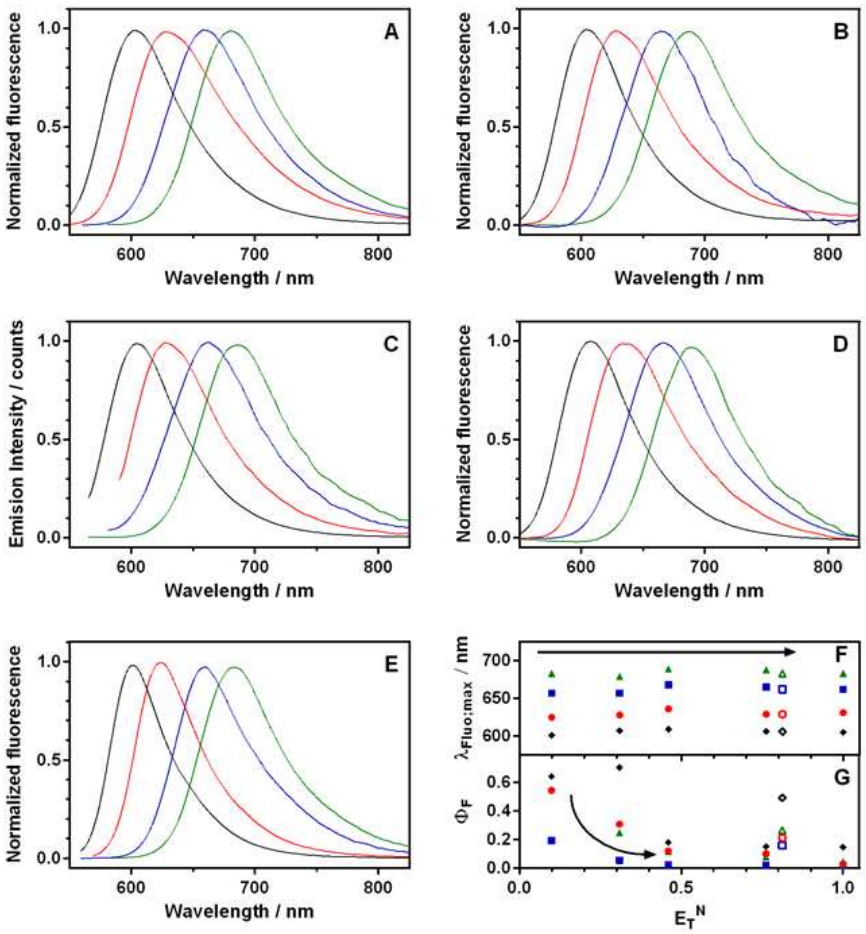

Figure S18. Normalized emission spectra of COUPY dyes (compounds **9-12**) in PBS buffer (A), MeOH (B), glycerol (C), ACN (D) and toluene (E). Fluorescence maximum (F) or Φ_F (G) *vs* solvent polarity (chosen as ETN (a scale based on negatively solvatochromic Reichardt's dye)[9]) for non-viscous (closed symbols) and viscous (glycerol; open symbols) solvents. Fluorophores: **9** (black lines), **10** (red lines), **11** (blue lines) and **12** (green lines).

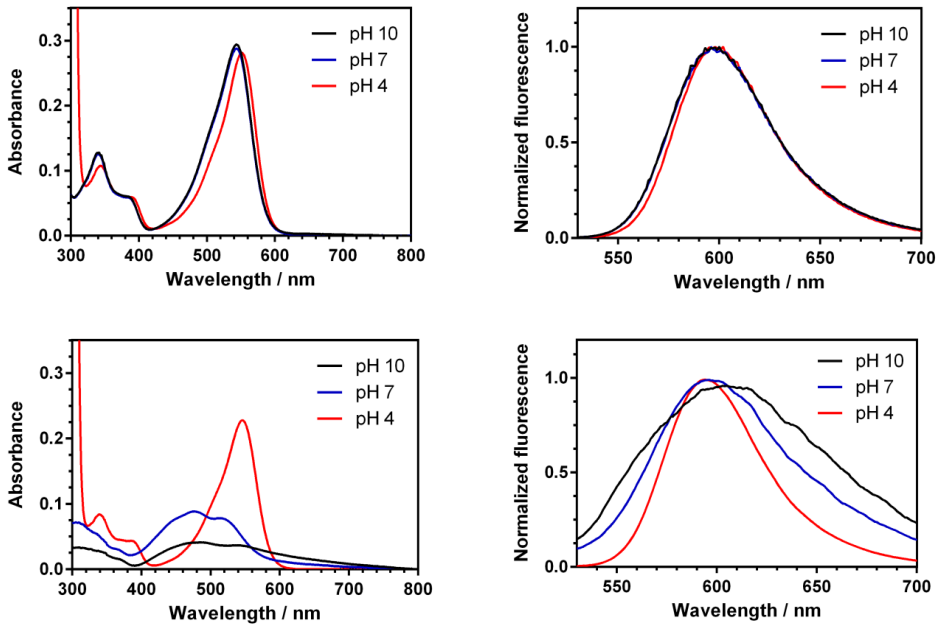

Figure S19. Normalized absorption (left) and emission (right) spectra of coumarins **9** (top) and **7** (bottom) in aqueous solutions of different pH.

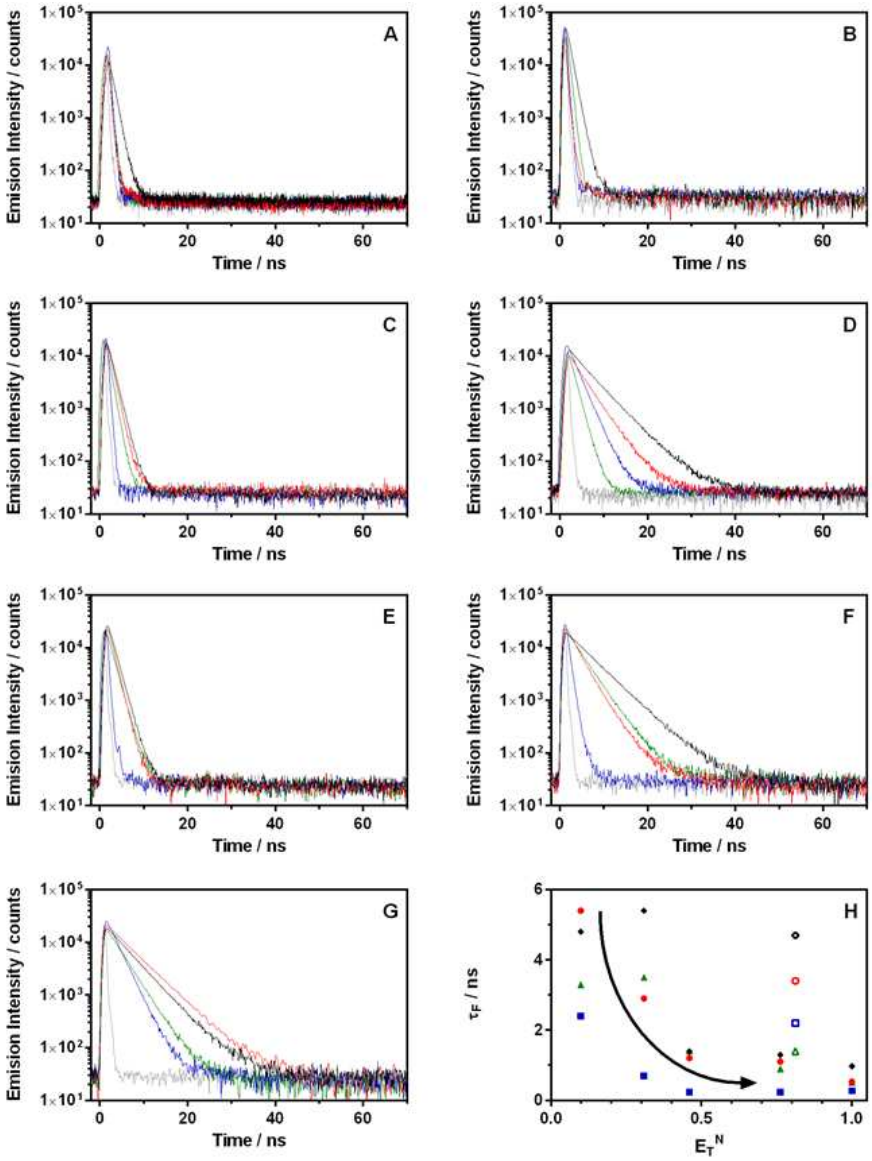

Figure S20. Fluorescence emission decay kinetics of COUPY dyes (compounds **9-12**) in PBS buffer (A), H_2O (B), MeOH (C), glycerol (D), ACN (E), DCM (F) and toluene (G). Fluorophores: **9** (black lines), **10** (red lines), **11** (blue lines) and **12** (green lines). Fluorescence lifetime (G) *vs* solvent polarity (chosen as ETN (a scale based on negatively solvatochromic Reichardt's dye)[9]) for non-viscous (closed symbols) and viscous (glycerol; open symbols) solvents. The grey trace corresponds to the instrument's response function (IRF).

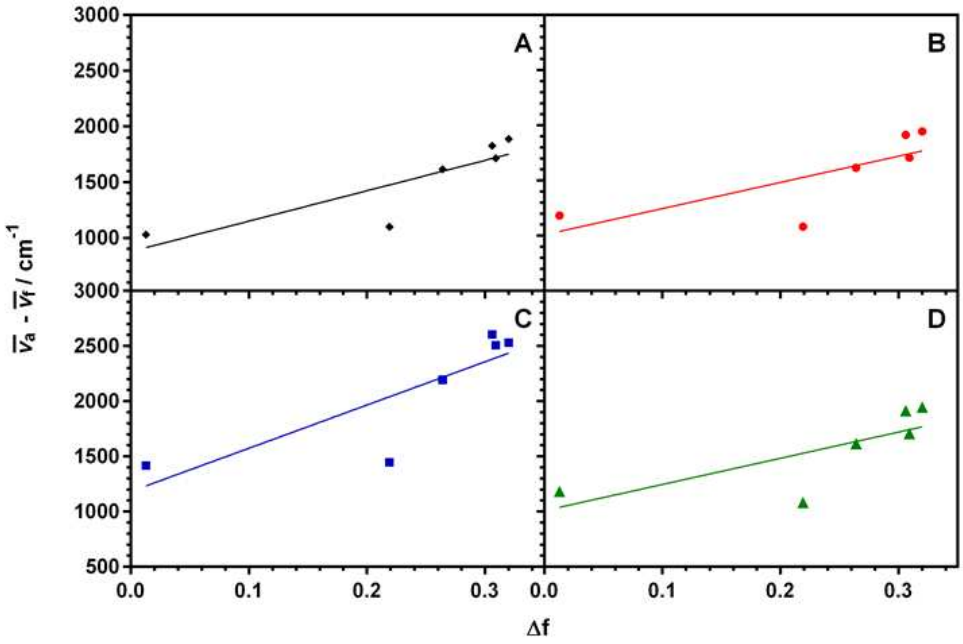

Figure S21. Lippert-Mataga plot for **9** (A), **10** (B), **11** (C) and **12** (D).

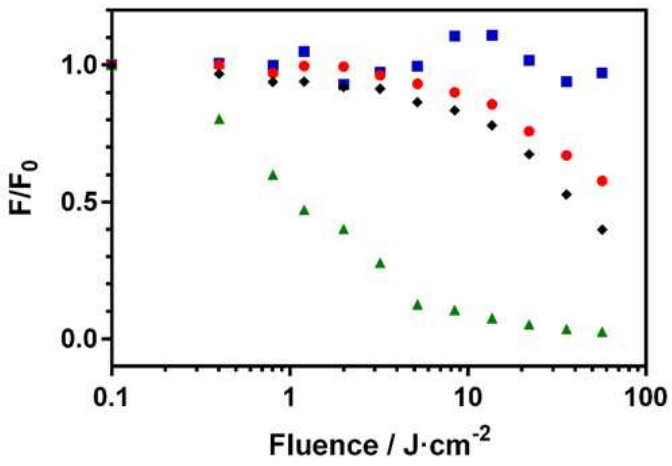

Figure S22. Fluorescence bleaching of 5 μM **9-12** aqueous solution irradiated with green light (520 ± 18 nm). Fluorophores: **9** (black diamonds), **10** (red circles), **11** (blue squares) and **12** (green triangles).

6.- Fluorescence imaging

All microscopy observations were performed using a Leica TCS SP2 confocal microscope equipped with a 405 nm laser diode, an Argon-ion laser, a DPSS 561 nm laser and a HeNe (633 nm) laser. The microscope was also equipped with a full enclosure imaging chamber (Life Imaging Services) connected to a 37ºC heater and a 5% CO_2 providing system. Cells were observed using a 63X 1.2 water immersion objective.

Coumarins **9** to **11** were excited using the DPSS 561 nm laser and detected from 570 to 670 nm. Coumarin **12** was excited with the HeNe laser and detected from 650 to 750 nm. In colocalization studies, Mitotracker Green FM and Hoechst 33342 were observed using the 488 nm laser line of the Argon-ion laser and the 405 nm laser diode respectively.

In photostability studies cells were continuously irradiated every 1.66 s with the DPSS 561 nm laser at 1.31 μW (coumarin **9**) or 3.98 μW (coumarins **10** and **11**) for 10 min. Laser power was measured using a photodetector (model 818-UV, Newport) connected to an optical power meter (model 840-C, Newport).

Image analysis was performed using Fiji[10]. Unless otherwise stated images are colorized using Fire lookup table. In photostability studies mean intensity was measured at each time point in at least 4 different areas of 5 μm^2 at each subcellular compartment (mitochondria, cytoplasm and nucleoli) and also in areas without cells to measure the background. Images were filtered with a median filter of radius 1 to reduce noise before intensity measurements.

Intensity along time graphs (Figure S24) were done with Excel and figure composition was done using Gimp (GNU Image Manipulation Program) version 2.8.18.

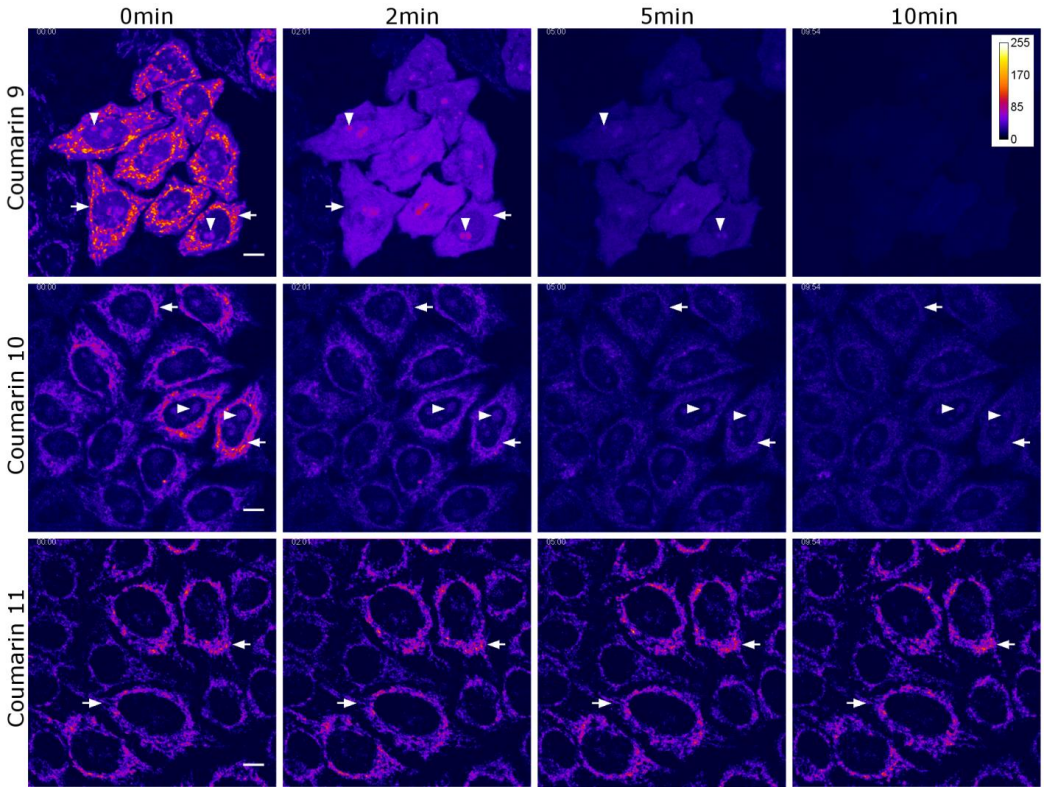

Figure S23. Photostability imaging. Single confocal planes at different time points of image acquisition are shown after incubation of HeLa cells with coumarins **9-11** (1.0 μM) during 30 min at 37 ºC. Images corresponding to coumarins **10** and **11** (centre and bottom rows respectively) were acquired using 3 times more laser power and higher photomultiplier gain to have similar intensities to coumarin **9** (upper row) at time 0. Intensity calibration bar is showed in the upper right corner. White arrows point out mitochondria and white arrowheads nucleoli. Coumarin **11** does not stain nucleoli. Scale bar: 10 μm. All images are at the same scale.

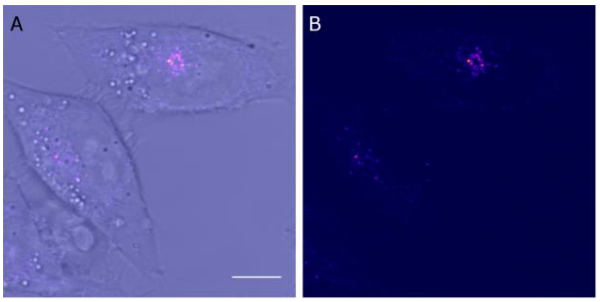

Figure S24. Fluorescence emission of coumarin **12**. Single confocal planes of HeLa cells incubated in with coumarin **12** (1 μM) for 30 min at 37ºC. A) Overlay of transmitted light and fluorescence images. B) Fluorescence emission of coumarin **12** observed only in vesicles inside cells. Scale bar: 10 μm. All images are at the same scale.

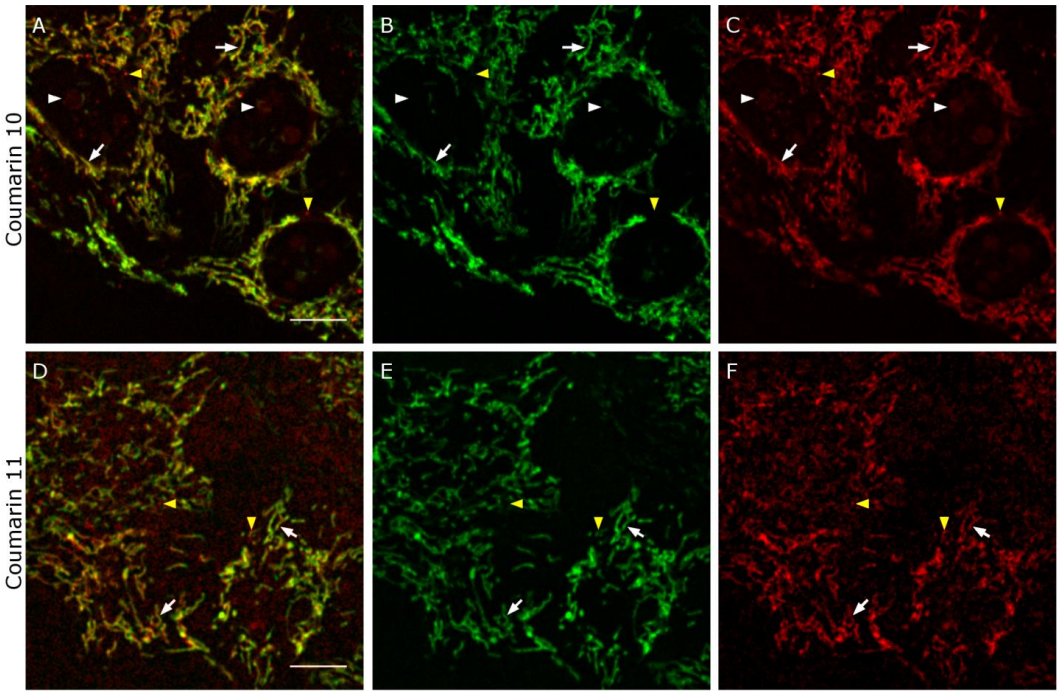

Figure S25. Co-localization studies. Single confocal plane of HeLa cells incubated with coumarin **10** (2 μM A-C) or **11** (2 μM D-F) together with Mitotracker Green FM (0.1 μM). A,D) overlay of the two staining. B,E) Mitotracker Green FM staining. C,F) Coumarin signal. White arrows point out mitochondria, white arrowheads nucleoli and yellow arrowheads vesicles staining. Coumarin signal brightness was enhanced for visualization purposes. Scale bar: 10 μm.

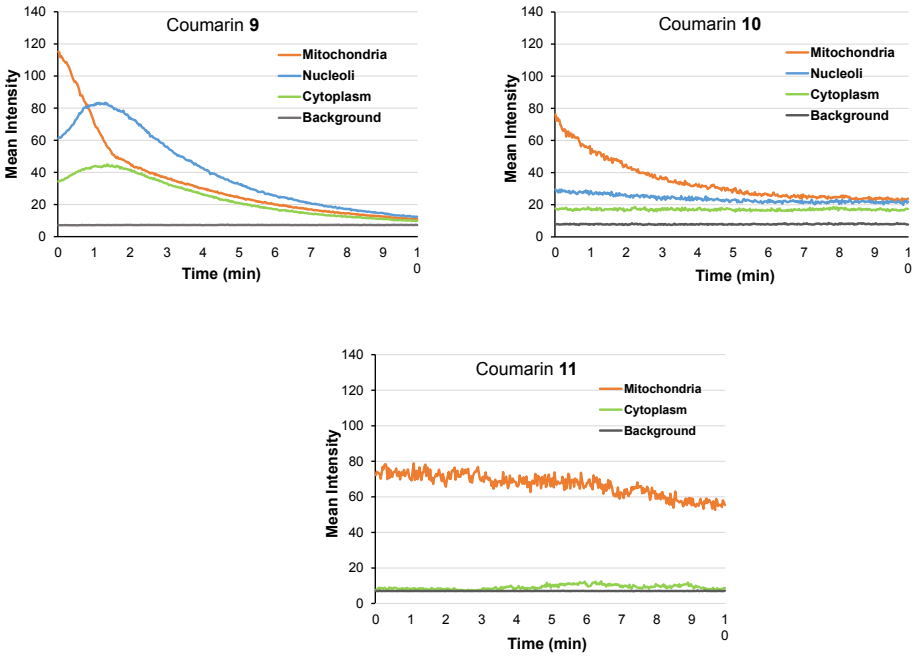

Figure S26. Photostability measurements. Plots of fluorescence intensity (arbitrary units) along time are shown for each coumarin (**9** to **11**) in different subcellular organelle and background. Image acquisition of coumarins **10** and **11** required 3 times more laser power and higher photomultiplier gain to have similar intensities to coumarin **9** at time 0. Intensity fluctuations observed in coumarin **10** and **11** are due to higher photomultiplier gain. Mitochondria signal in coumarin **9** decreases during the first 1.5 min reaching the level of intensity of the cytoplasm; conversely, fluorescence signal in nucleoli and cytoplasm increases during the first 1-1.5 min when it starts decreasing. Coumarin **10** shows a decreasing intensity in the different subcellular organelles, being clearer in mitochondria. In coumarin **11**, intensity in mitochondria is better preserved along the whole experiment; fluorescence in nucleoli was not measured as it was not detected (see Figure S22).

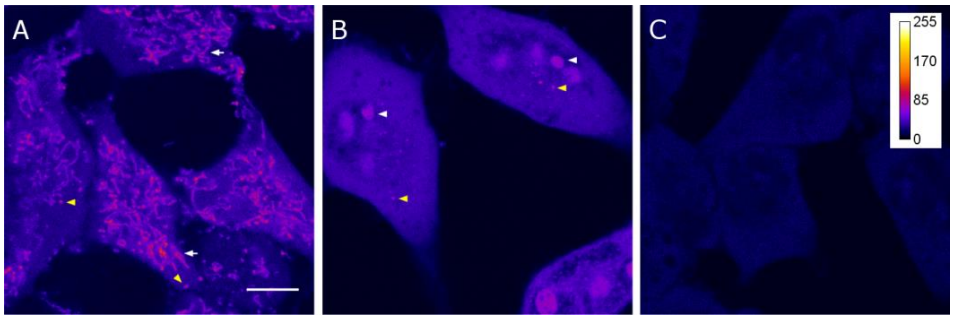

Figure S27. Coumarin **9** (1 μM) fluorescence after fixation and permeabilization. Single confocal planes are shown before A) and after fixation B). Mitochondria staining disappears after fixation but remains in nucleoli and vesicles (B). C) After permeabilization the fluorescence signal is lost. Intensity calibration bar is shown in the upper right corner in C). White arrows point out mitochondria, white arrowheads nucleoli and yellow arrowheads vesicles staining. Scale bar: 10 μm. All images are at the same scale.

7.- ^{1}H, ^{13}C and ^{19}F NMR spectra and HR ESI-MS of the compounds

2-(Cyano(4-pyridine)methylene)-7-(*N,N*-diethylamino)-4-methyl-coumarin (7)

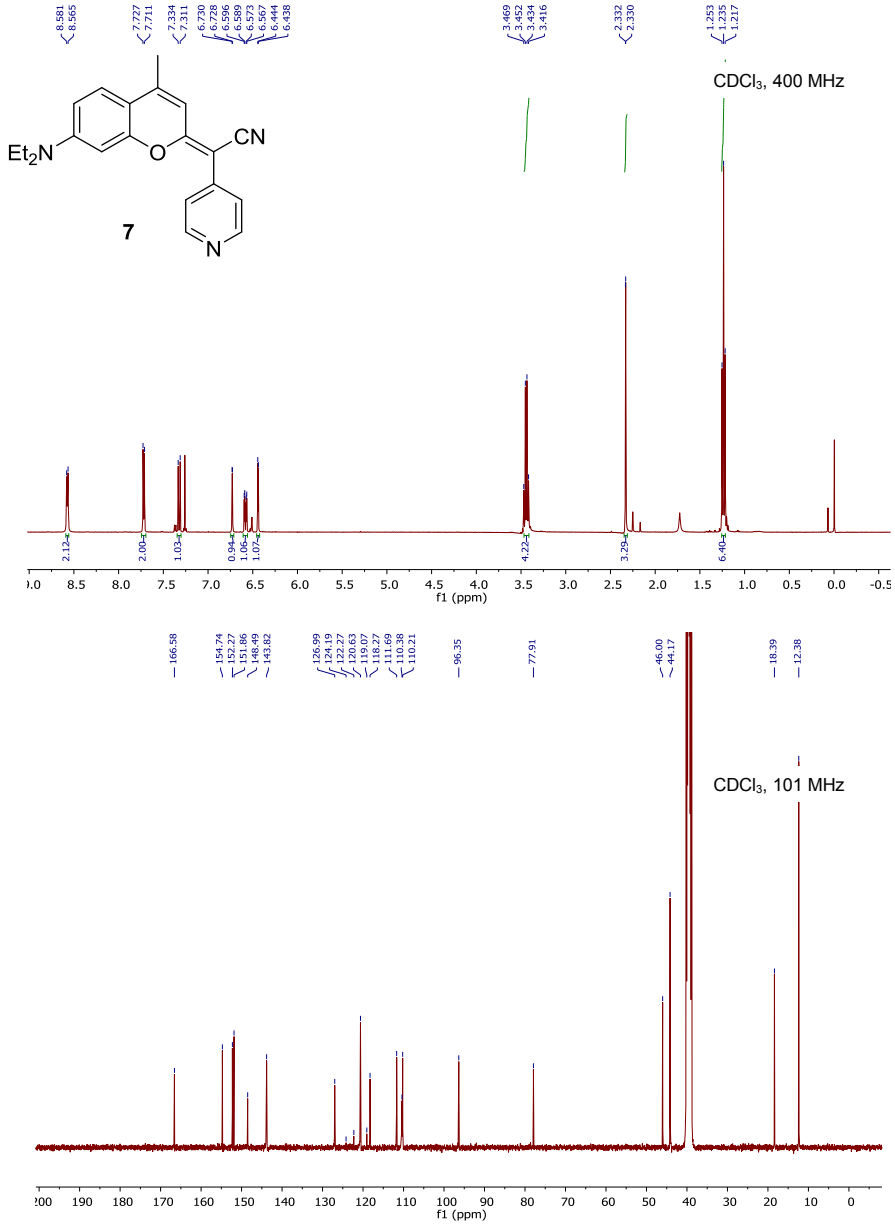

Figure S28. ^{1}H and ^{13}C NMR spectra of compound **7** in $CDCl_3$.

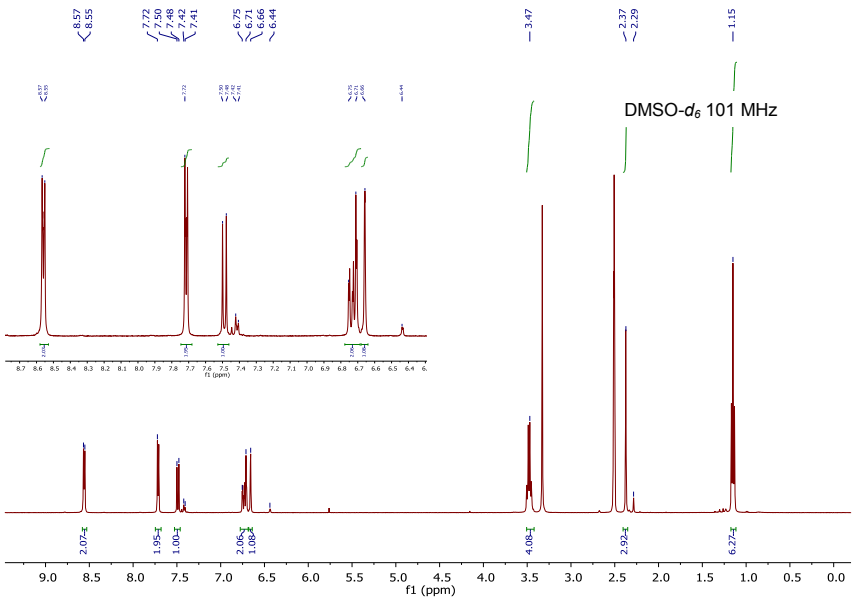

Figure S29. ^{1}H NMR spectrum of compound **7** in DMSO-d_6.

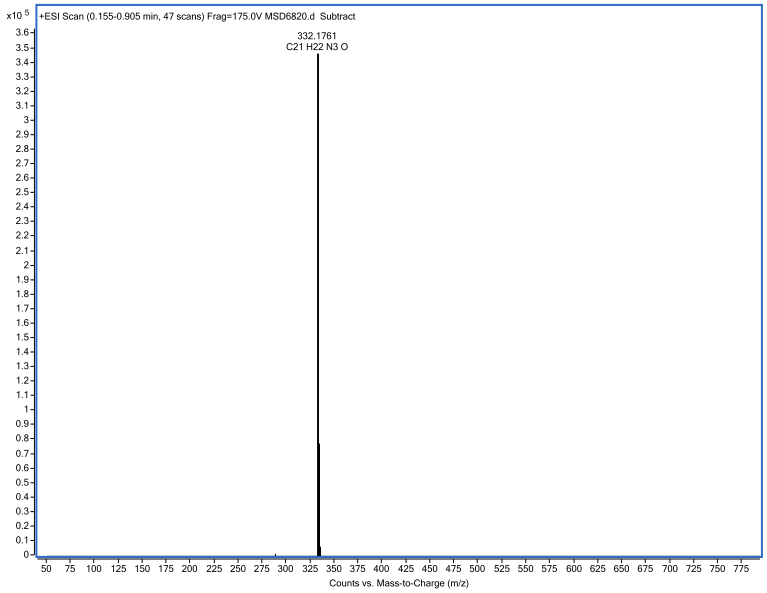

Figure S30. HR ESI-MS spectrum of compound **7**.

2-(Cyano((1-methyl(4-pyridin-1-ium)))methylene)-7-(*N,N*-diethylamino)-4-methyl-coumarin triflate (9)

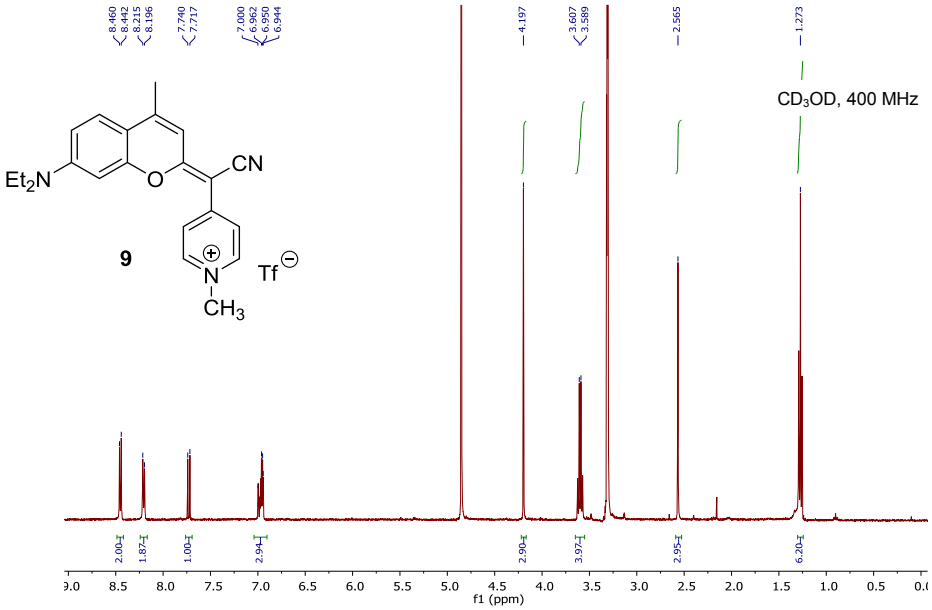

Figure S31. ^{1}H NMR spectrum of compound **9** in CD_3OD.

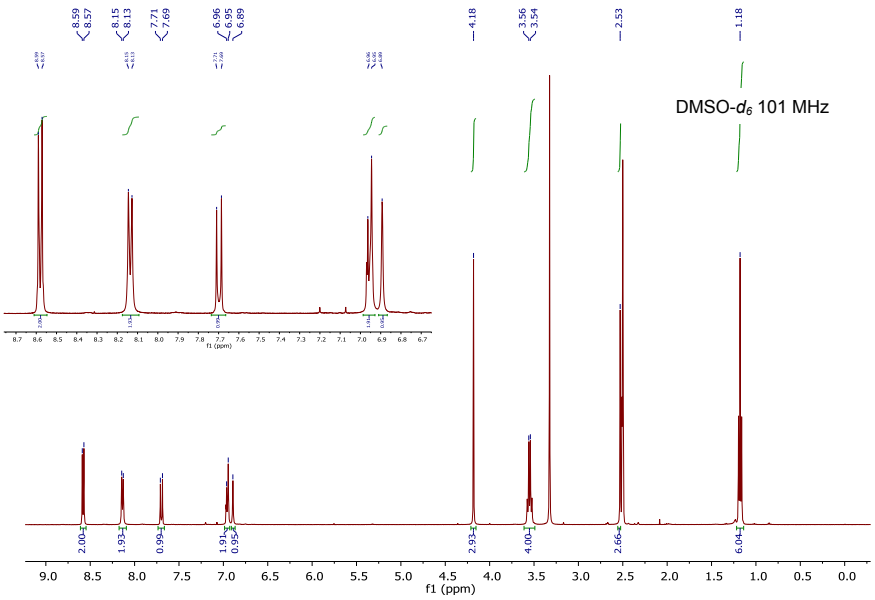

Figure S32. ^{1}H NMR spectrum of compound **9** in DMSO-d_6.

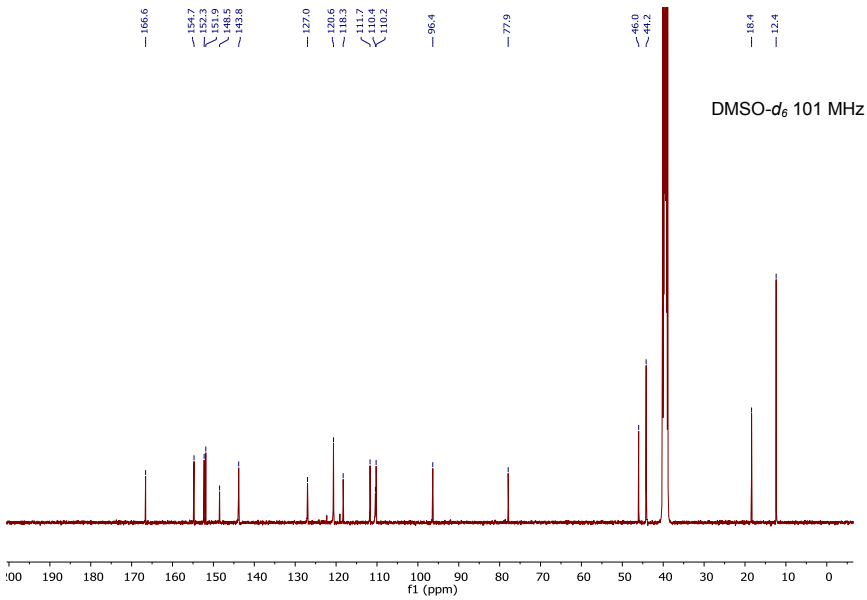

Figure S33. ^{13}C NMR spectrum of compound **9** in DMSO-d_6.

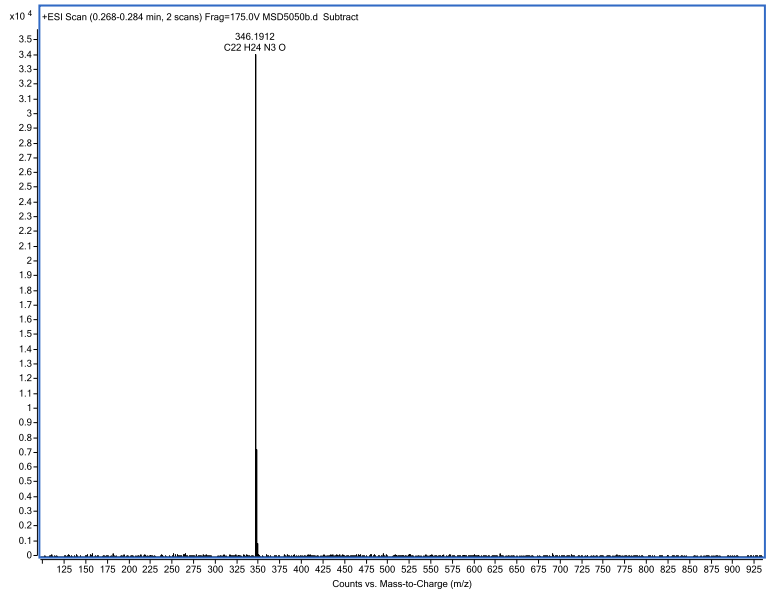

Figure S34. HR ESI-MS spectrum of compound **9**.

22-(Cyano((1-(2,2,2-trifluoroethyl)(4-pyridin-1-ium)))methylene)-7-(*N*,*N*-diethylamino)-4-methyl-coumarin triflate (10)

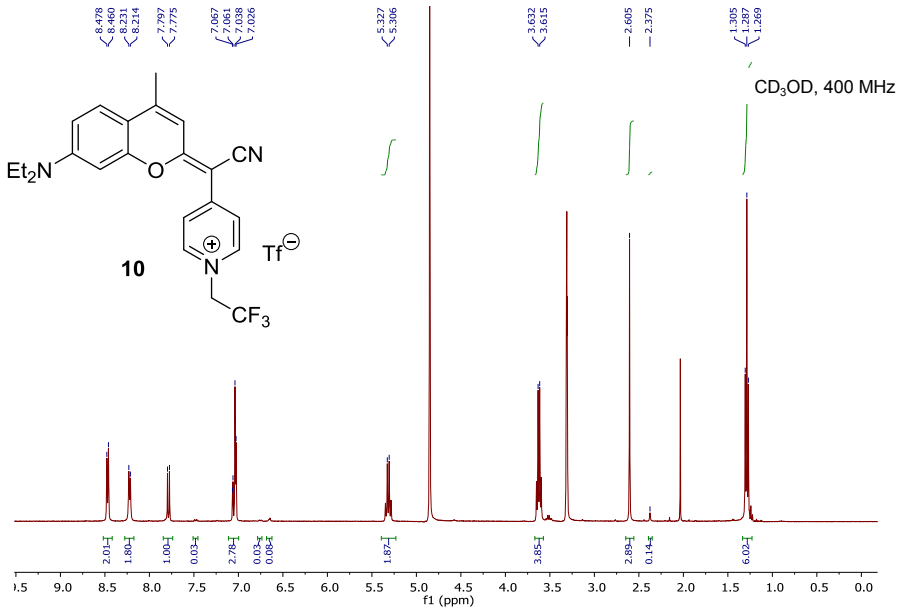

Figure S35. ^{1}H NMR spectrum of compound **10** in CD_3OD.

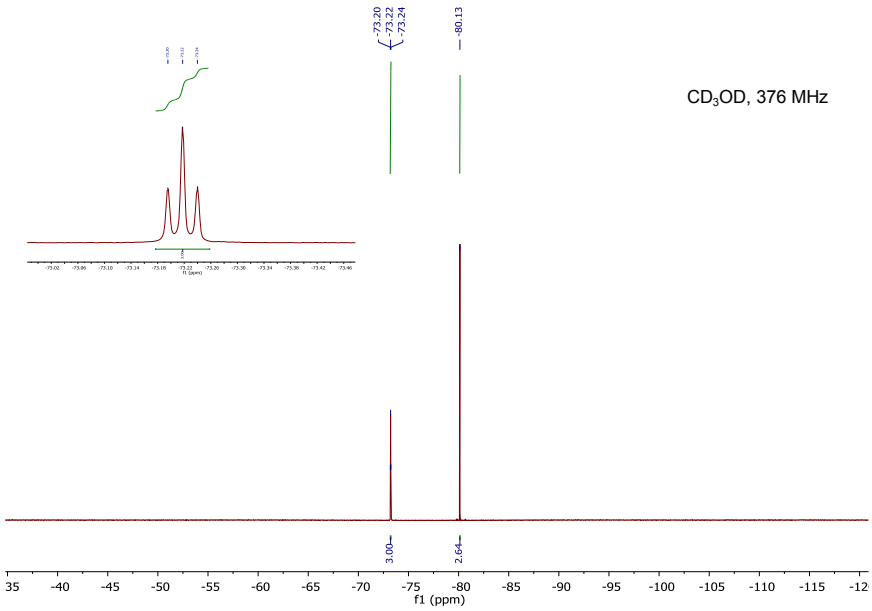

Figure S36. ^{19}F NMR spectrum of compound **10** in CD_3OD.

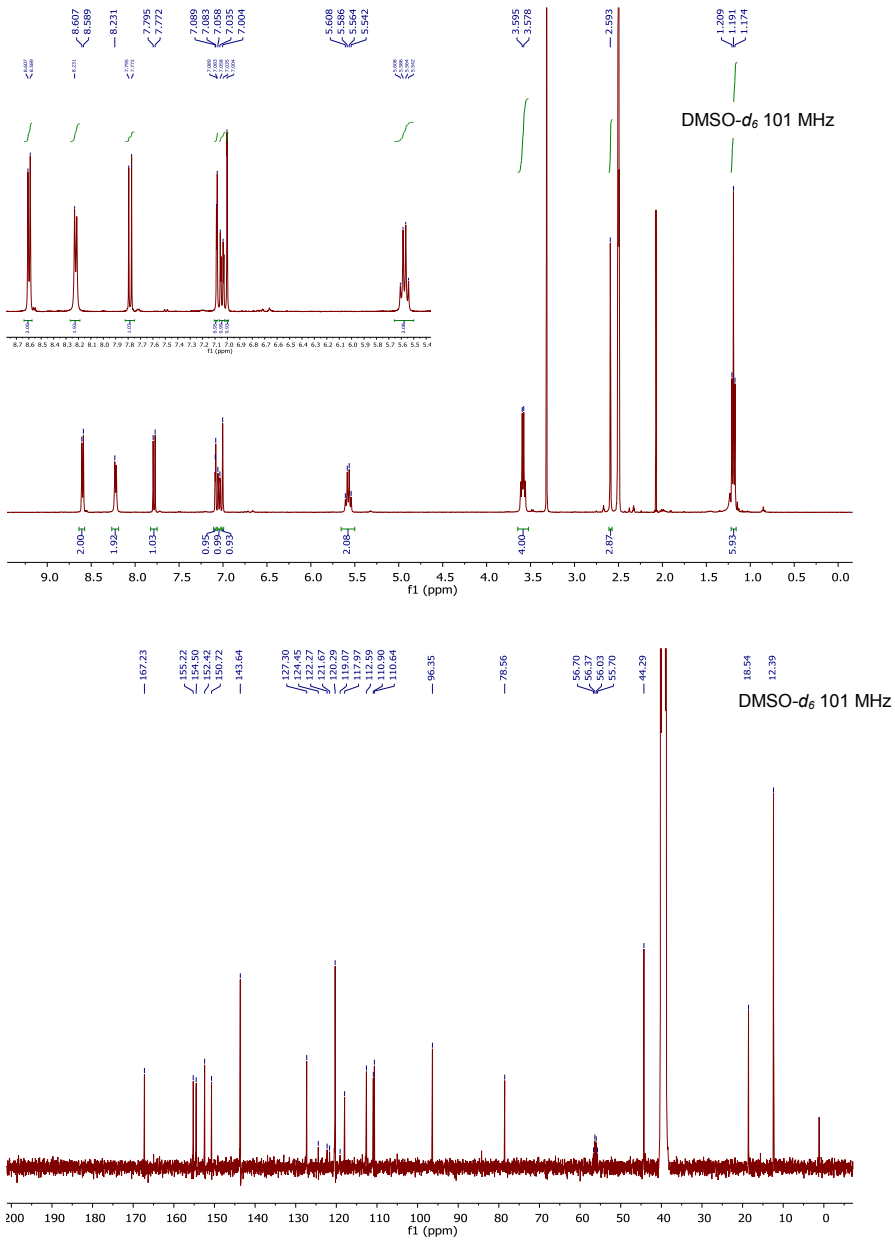

Figure S37. ^{1}H and ^{13}C NMR spectrum of compound **10** in DMSO-d_6.

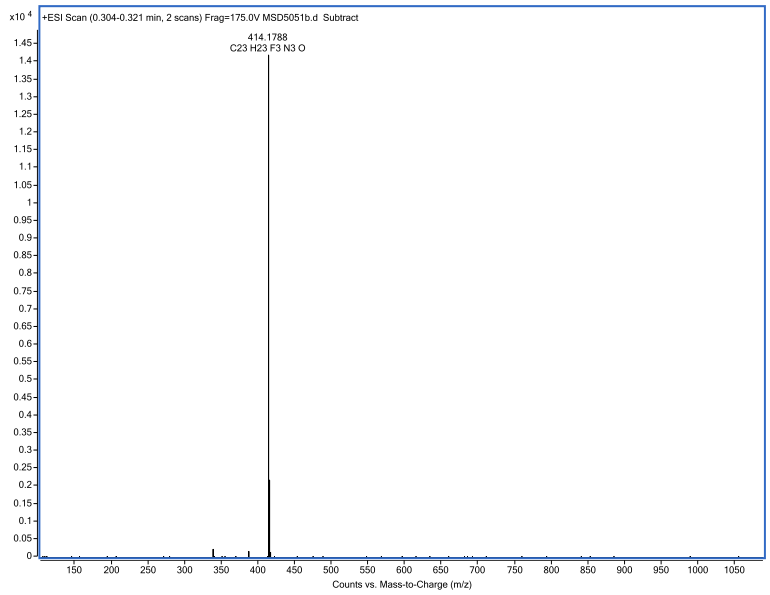

Figure S38. HR ESI-MS spectrum of compound **10**.

7-(*N,N*-Diethylamino)-4-trifluoromethyl-2-thiocoumarin (6)

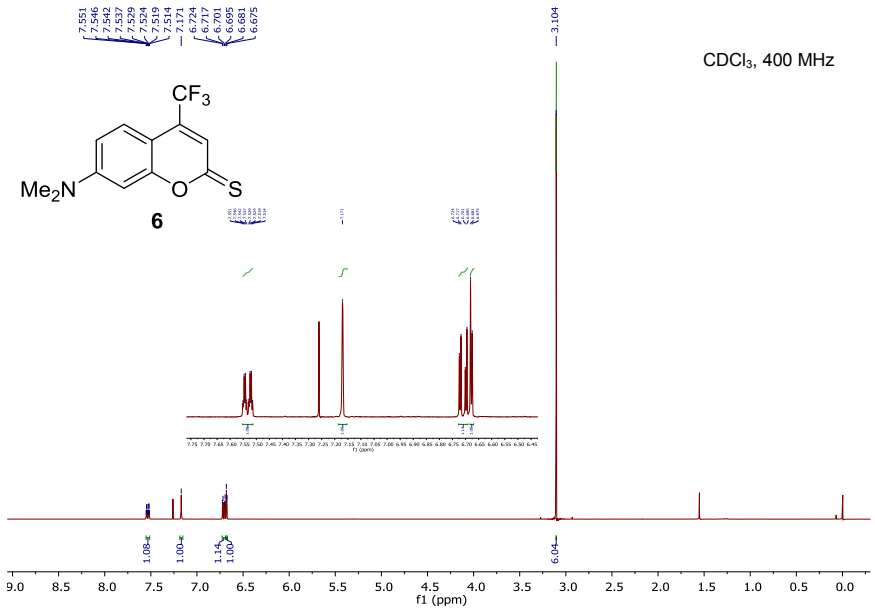

Figure S39. ^{1}H NMR spectrum of compound **6** in $CDCl_3$.

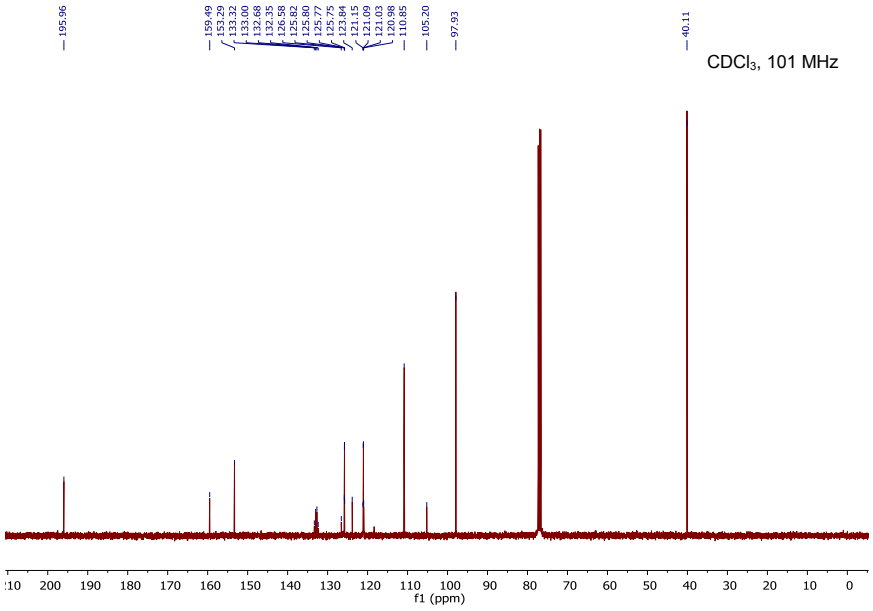

Figure S40. ^{13}C NMR spectrum of compound **6** in $CDCl_3$.

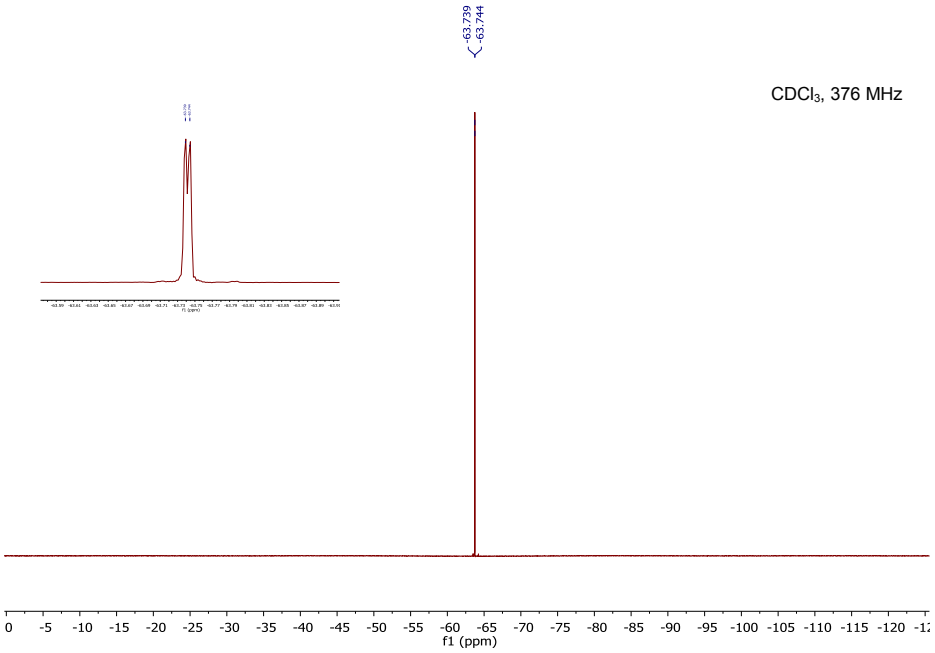

Figure S41. ^{19}F NMR spectrum of compound **6** in $CDCl_3$.

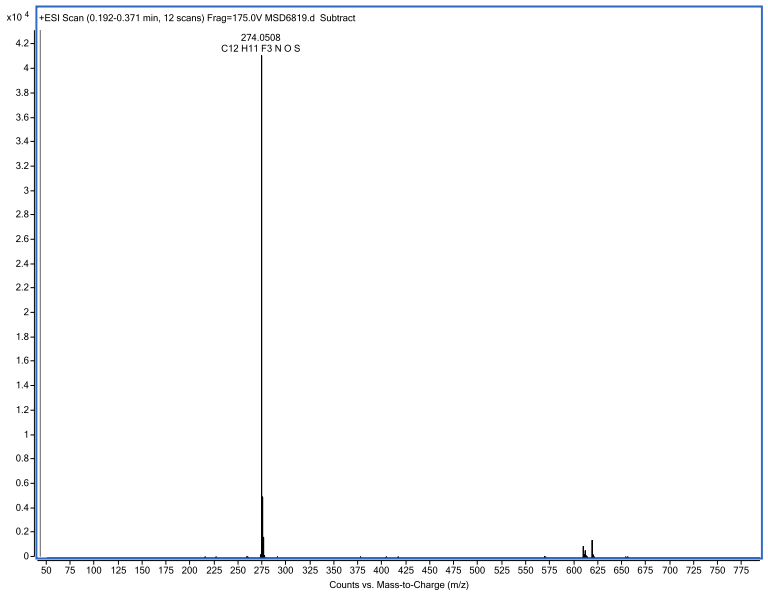

Figure S42. HR ESI-MS spectrum of compound **6**.

2-(Cyano(4-pyridine)methylene)-7-(*N,N*-dimethylamino)-4-trifluoromethyl-coumarin (8)

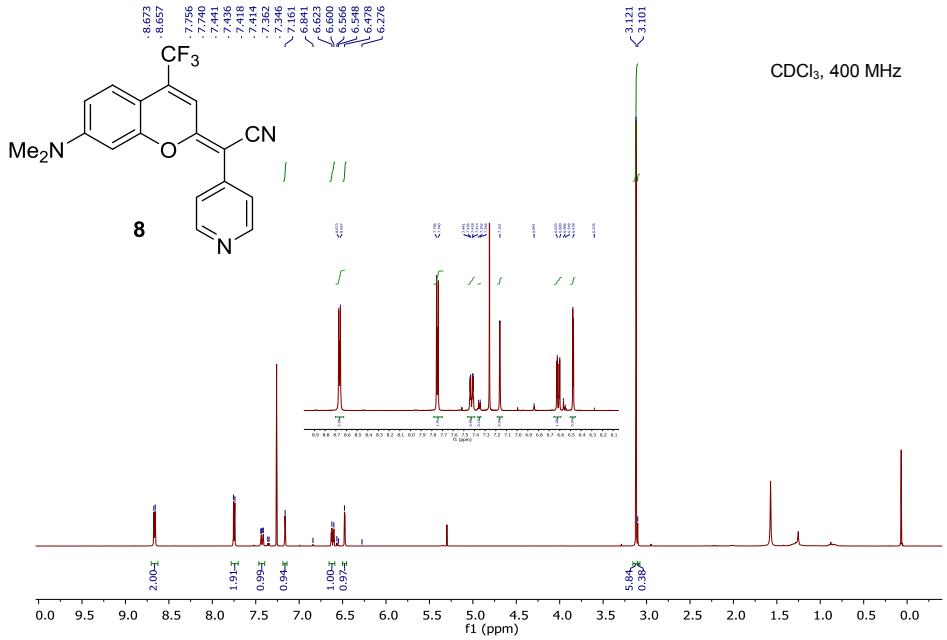

Figure S43. ^{1}H NMR spectrum of compound **8** in $CDCl_3$.

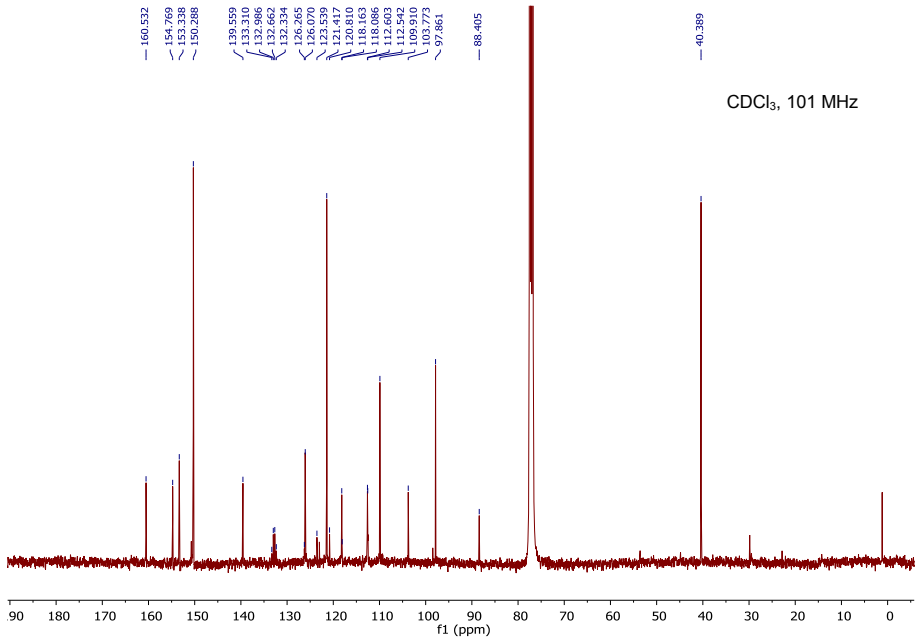

Figure S44. ^{13}C NMR spectrum of compound **8** in $CDCl_3$.

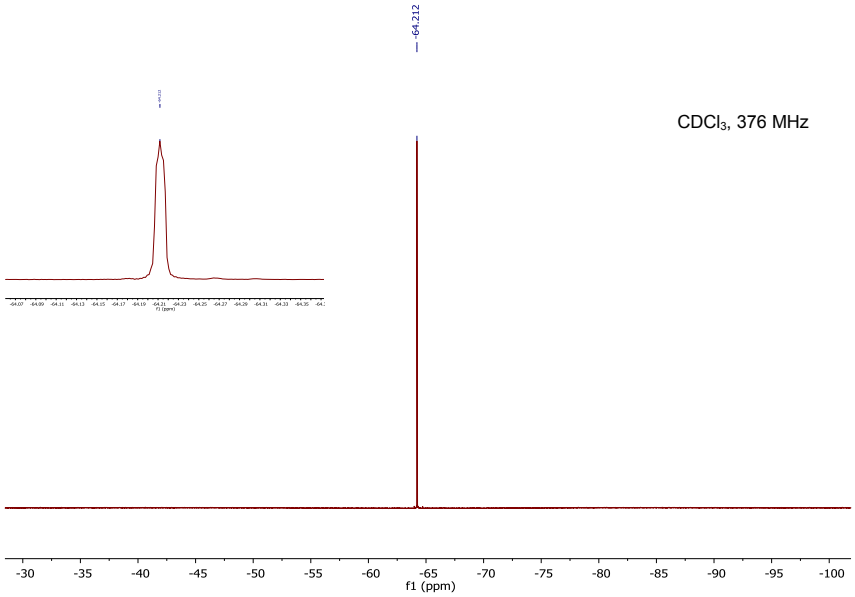

Figure S45. ^{19}F NMR spectrum of compound **8** in $CDCl_3$.

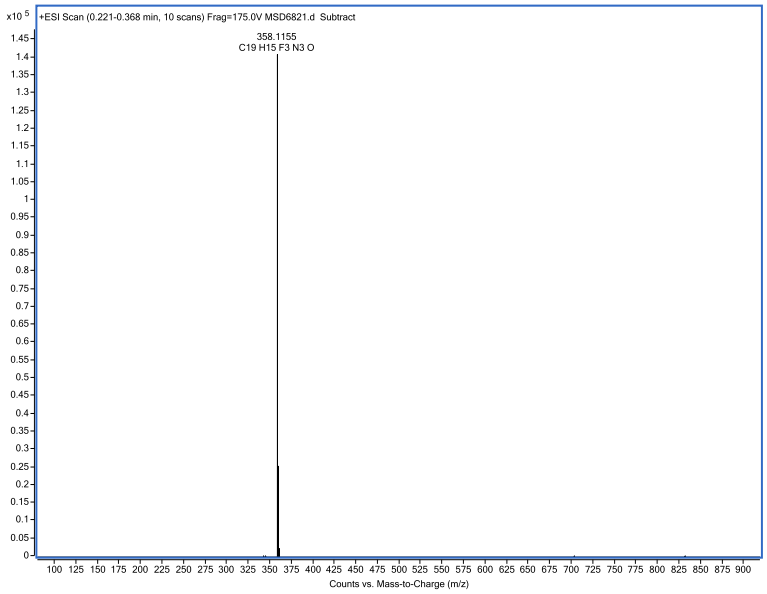

Figure S46. HR ESI-MS spectrum of compound **8**.

2-(Cyano((1-methyl(4-pyridin-1-ium)))methylene)-7-(*N,N*-dimethylamino)-4-trifluoromethyl-coumarin triflate (11)

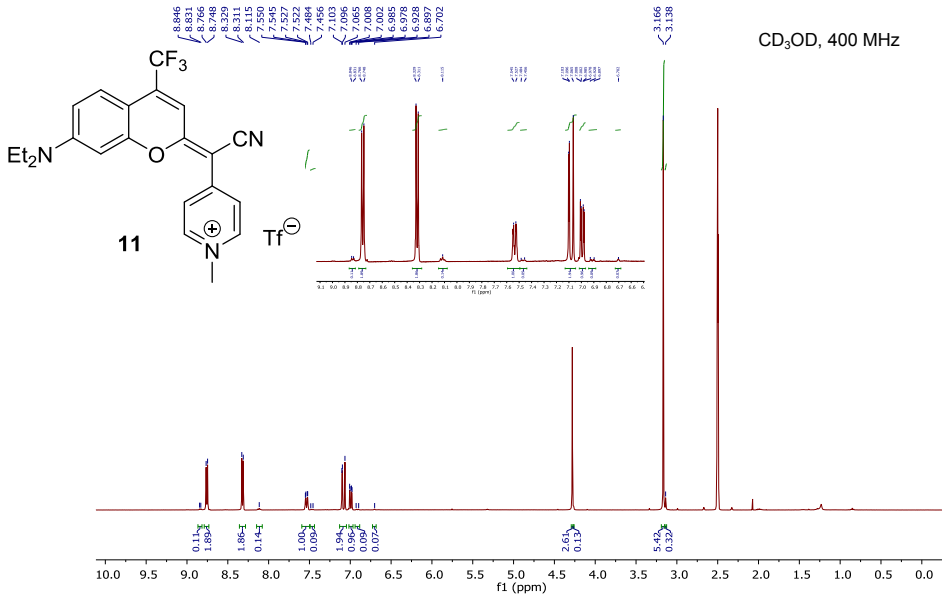

Figure S47. ^{1}H NMR spectrum of compound **11** in DMSO-*d*$_6$.

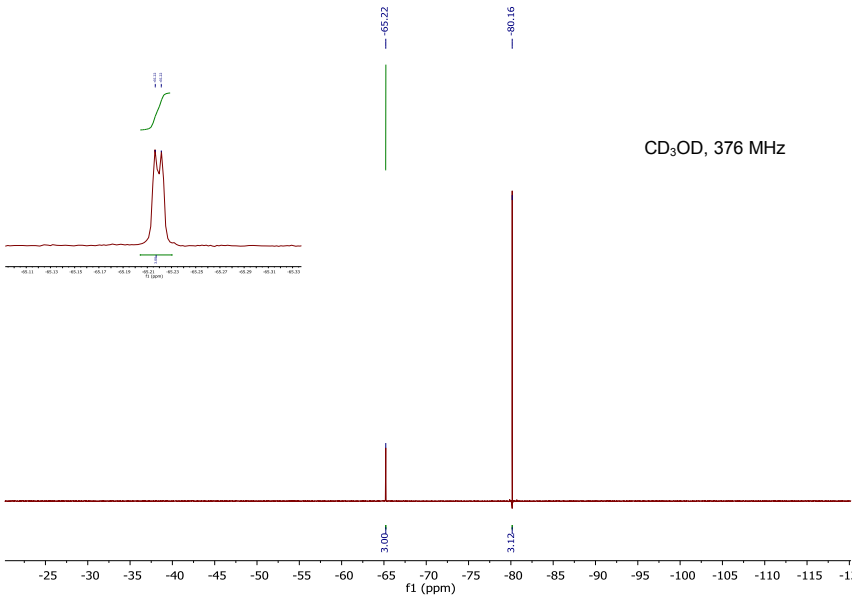

Figure S48. ^{19}F NMR spectrum of compound **11** in CD_3OD.

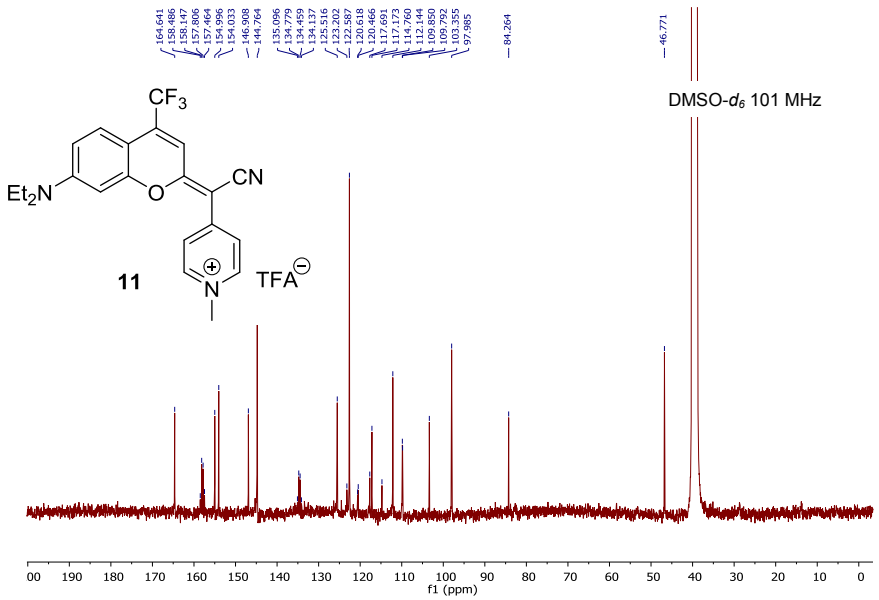

Figure S49. ^{1}H and ^{13}C NMR spectrum of compound **11** in DMSO-d_6.

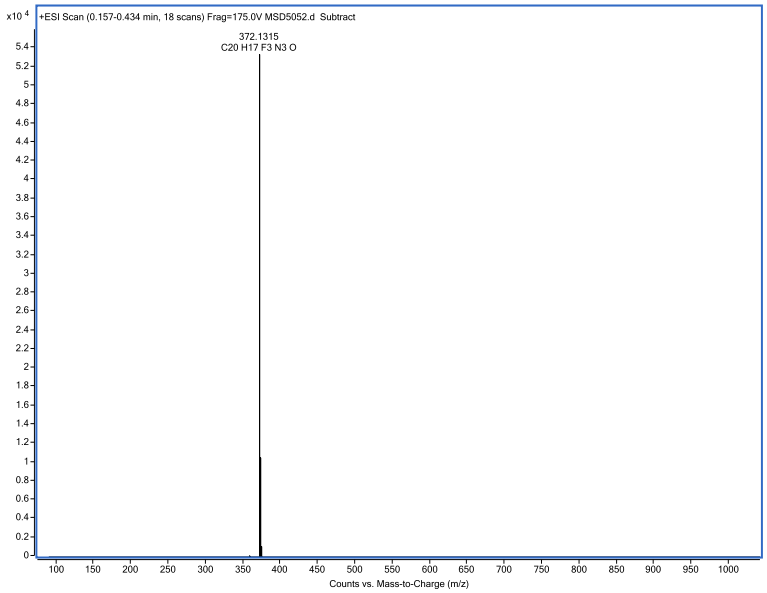

Figure S50. HR ESI-MS spectrum of compound **11**.

2-(Cyano((1-(2,2,2-trifluoroethyl)(4-pyridin-1-ium)))methylene)-7-(*N*,*N*-dimethylamino)-4-trifluoromethyl-coumarin triflate (12)

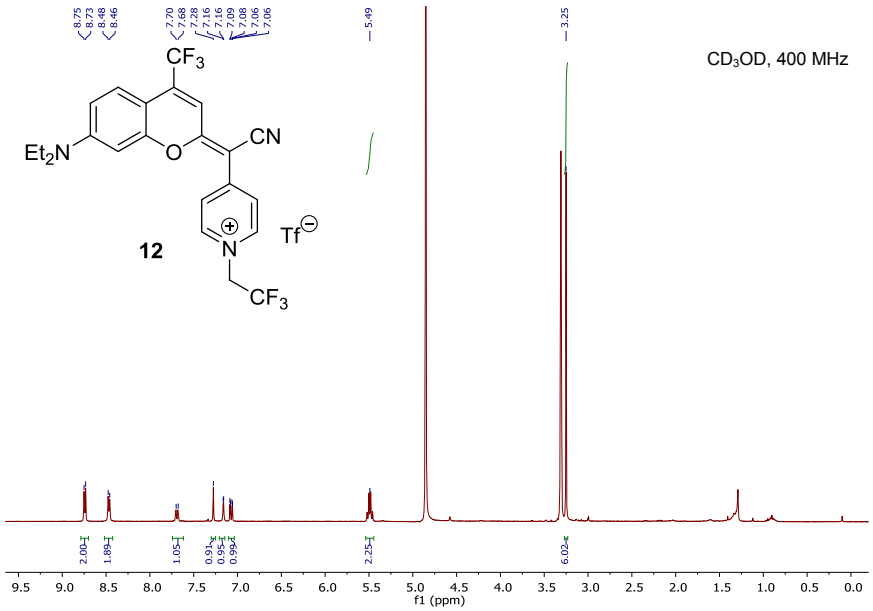

Figure S51. ^{1}H NMR spectrum of compound **12** in CD_3OD.

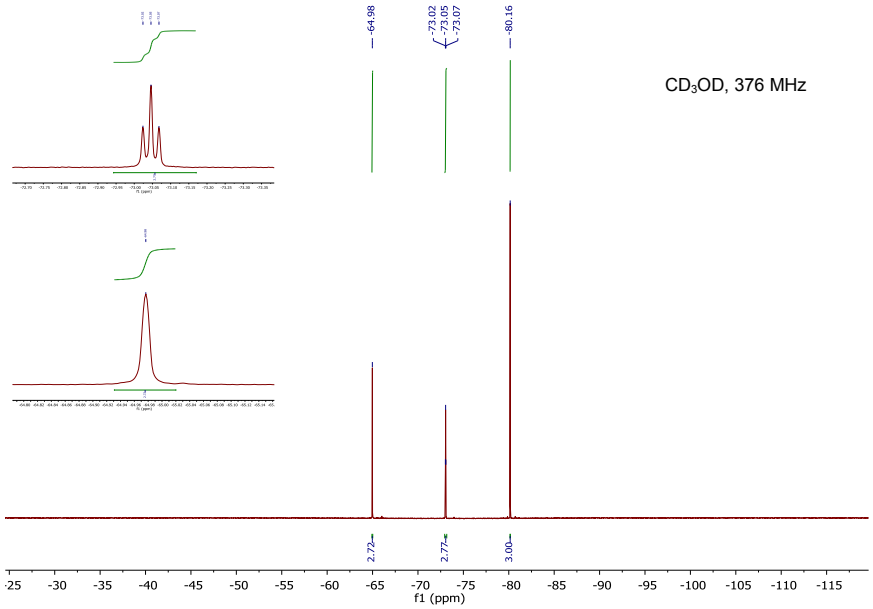

Figure S52. ^{19}F NMR spectrum of compound **12** in CD_3OD.

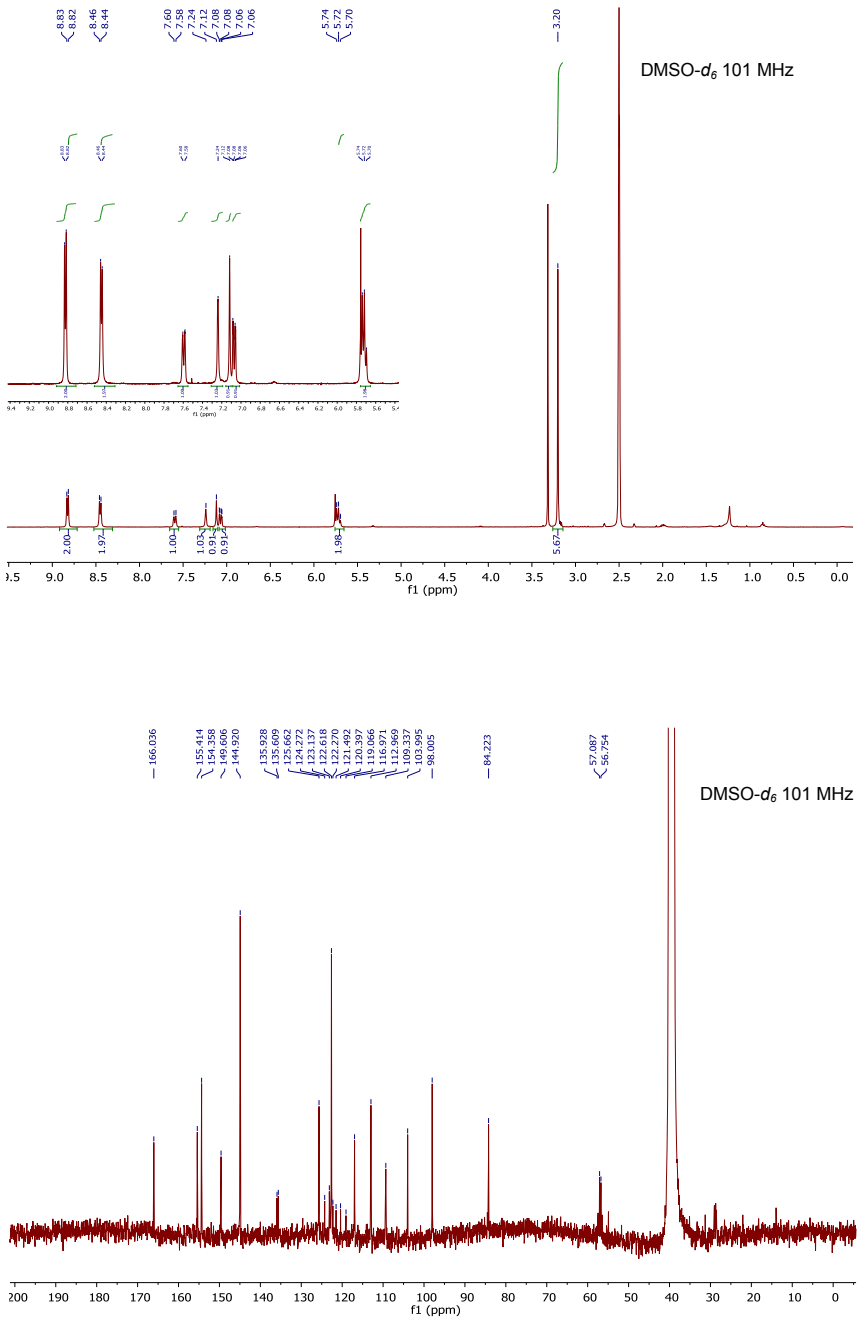

Figure S53. ^{1}H and ^{13}C NMR spectra of compound **12** in DMSO-d_6.

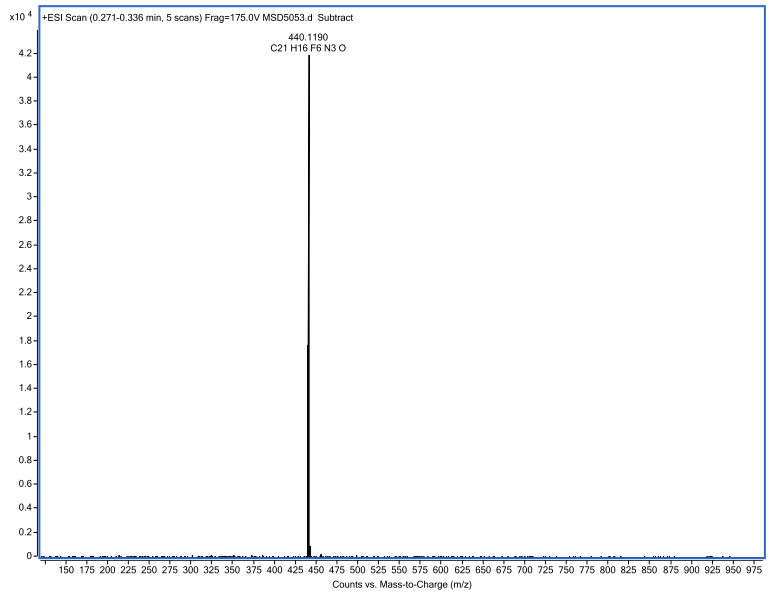

Figure S54. HR ESI-MS spectrum of compound **12**.

8.- Additional DFT results

8.1.- Number of imaginary frequencies and absolute energies

φ (º)	7 (ΔG - Ha)	7 (num imaginary ν)	9 (ΔG - Ha)	9 (num imaginary ν)
Z	-1052.064895	0	-1091.809670	0
10	-1052.064854	0	-1091.809670	0
30	-1052.062911	0	-1091.807419	0
50	-1052.056981	0	-1091.803836	0
70	-1052.049287	0	-1091.797846	0
TS	-1052.035167	1	-1091.789797	1
110	-1052.048351	0	-1091.798275	0
130	-1052.056417	0	-1091.803964	0
150	-1052.063302	0	-1091.808771	0
170	-1052.066427	0	-1091.810786	0
E	-1052.066348	0	-1091.812080	0

Table S7. Absolute free energies (Ha) and the number of imaginary frequencies of compounds **7** and **9** in the ground state (S_0)

φ (º)	7 (ΔG - Ha)	7 (num imaginary ν)	9 (ΔG - Ha)	9 (num imaginary ν)
E	-1051.998069	0	-1091.732275	0

Table S8. Absolute free energies (Ha) and the number of imaginary frequencies of compounds **7** and **9** in the first excited state (S_1)

8.2.- Cartesian coordinates of the optimized structures

8.2.1- Compound **7** (S_0) - Z isomer

46

C	0.802572	-0.054934	1.197515
C	-0.607356	0.178956	1.129178
H	-1.204222	0.183748	2.030771
C	-1.243290	0.399990	-0.073863
H	-2.313972	0.575194	-0.073835
C	-0.544830	0.397870	-1.301628
C	0.839513	0.152326	-1.221180
C	1.509703	-0.076945	-0.030576
H	2.570954	-0.273438	-0.081149
N	1.448399	-0.239726	2.395682
C	0.679189	-0.450324	3.628858
C	0.125950	-1.869526	3.783294
H	-0.130538	0.281913	3.667891
H	1.327031	-0.213177	4.471962
H	-0.555234	-2.126128	2.965838
H	-0.427629	-1.955346	4.724848
H	0.933691	-2.608677	3.796916
C	2.886792	-0.572764	2.370820
C	3.577734	-0.600248	3.729435
H	3.391048	0.179699	1.755441
H	3.035135	-1.540350	1.869080
H	3.489737	0.356569	4.253549
H	4.642620	-0.788175	3.559444
H	3.205140	-1.394913	4.381881
C	-1.132012	0.588082	-2.600443
C	-2.611028	0.798670	-2.743926
H	-3.169576	-0.041050	-2.315214
H	-2.893354	0.902865	-3.793485
H	-2.930086	1.700289	-2.208340
C	-0.317965	0.554124	-3.705388
C	1.082765	0.329184	-3.597703
H	-0.744894	0.659069	-4.693115
O	1.611022	0.122896	-2.356717
C	2.009166	0.236893	-4.638377
C	1.746552	0.548362	-6.056288
C	3.314226	-0.216808	-4.316598
N	4.398680	-0.589520	-4.089209
C	0.880282	1.575985	-6.474999
C	0.706327	1.815889	-7.834946
H	0.369953	2.207977	-5.757914
N	1.330307	1.135364	-8.809375
H	0.035925	2.611704	-8.154934
C	2.175579	0.171207	-8.408835
C	2.414454	-0.153538	-7.078357

H 2.688782 -0.378614 -9.195830
H 3.109291 -0.951953 -6.838951

8.2.2- Compound **7** (S_0) - φ (10º)

46

C 0.802532 -0.054677 1.197140
C -0.607394 0.179122 1.128871
H -1.204115 0.184723 2.030554
C -1.243606 0.398992 -0.074259
H -2.314301 0.574104 -0.074132
C -0.545399 0.395779 -1.302151
C 0.838969 0.150363 -1.221727
C 1.509431 -0.077771 -0.031065
H 2.570686 -0.274202 -0.081672
N 1.448645 -0.238319 2.395361
C 0.679721 -0.447256 3.628973
C 0.125973 -1.866071 3.785186
H -0.129700 0.285362 3.667432
H 1.327916 -0.209443 4.471623
H -0.555640 -2.123299 2.968288
H -0.427265 -1.950663 4.727053
H 0.933421 -2.605528 3.799267
C 2.886956 -0.571663 2.370463
C 3.578051 -0.598606 3.729011
H 3.391327 0.180360 1.754629
H 3.035009 -1.539542 1.869205
H 3.490443 0.358530 4.252605
H 4.642853 -0.786979 3.558999
H 3.205250 -1.392769 4.381953
C -1.132890 0.584583 -2.601068
C -2.612044 0.794274 -2.744453
H -3.170114 -0.045252 -2.314742
H -2.894662 0.897233 -3.794058
H -2.931388 1.696315 -2.209752
C -0.319033 0.549567 -3.706100
C 1.081787 0.325176 -3.598398
H -0.746051 0.653223 -4.693948
O 1.610324 0.120058 -2.357404
C 2.007189 0.228980 -4.639644
C 1.746475 0.546745 -6.056411
C 3.310979 -0.228879 -4.318529
N 4.394225 -0.605361 -4.091604
C 0.882297 1.577588 -6.471644
C 0.710061 1.823505 -7.830704
H 0.372241 2.207312 -5.752370
N 1.333791 1.145999 -8.807455
H 0.041283 2.621770 -8.147974
C 2.176988 0.178725 -8.410166

C	2.414038	-0.152048	-7.080830
H	2.690010	-0.368709	-9.198946
H	3.107263	-0.952682	-6.844178

8.2.3- Compound **7** (S_0) - φ (30º)

46

C	0.800361	-0.060530	1.209991
C	-0.605050	0.198891	1.131514
H	-1.211731	0.190661	2.026443
C	-1.223320	0.462546	-0.071541
H	-2.290702	0.656348	-0.078699
C	-0.510590	0.480416	-1.291553
C	0.868062	0.203916	-1.201888
C	1.520505	-0.068451	-0.010666
H	2.578293	-0.284494	-0.054815
N	1.429058	-0.280322	2.410615
C	0.643585	-0.507009	3.630832
C	0.075510	-1.923645	3.751197
H	-0.159511	0.232127	3.675111
H	1.284306	-0.292161	4.485228
H	-0.598712	-2.157956	2.921310
H	-0.489370	-2.022050	4.684739
H	0.876035	-2.670644	3.759549
C	2.864070	-0.628557	2.396026
C	3.539142	-0.682431	3.761750
H	3.382342	0.127873	1.797456
H	3.007855	-1.590194	1.881817
H	3.453868	0.267763	4.298182
H	4.604126	-0.877903	3.601167
H	3.151591	-1.482786	4.398183
C	-1.080614	0.711058	-2.590062
C	-2.556613	0.931392	-2.747744
H	-3.124631	0.083305	-2.349084
H	-2.823621	1.065756	-3.797871
H	-2.878467	1.820234	-2.192816
C	-0.252794	0.686803	-3.686738
C	1.140862	0.439487	-3.568275
H	-0.662900	0.813385	-4.680212
O	1.651532	0.189512	-2.329902
C	2.047569	0.249565	-4.619495
C	1.927262	0.848957	-5.958217
C	3.262749	-0.418386	-4.322054
N	4.265212	-0.986230	-4.121903
C	1.186789	2.019358	-6.215972
C	1.139613	2.531712	-7.508550
H	0.675122	2.547101	-5.419586
N	1.771440	1.990494	-8.562740

H 0.568031 3.437955 -7.702000
C 2.492442 0.884438 -8.312859
C 2.600560 0.288374 -7.062232
H 3.010383 0.443660 -9.162954
H 3.199181 -0.609553 -6.947801

8.2.4- Compound **7** (S_0) - φ (50º)

46

C 0.813959 -0.068550 1.225686
C -0.582894 0.242224 1.153716
H -1.188873 0.236419 2.049086
C -1.192756 0.550338 -0.041493
H -2.253017 0.779485 -0.043839
C -0.479837 0.567412 -1.262885
C 0.889726 0.240542 -1.179820
C 1.532742 -0.079923 0.004203
H 2.582422 -0.331455 -0.045395
N 1.433499 -0.331136 2.420270
C 0.645076 -0.521293 3.644968
C 0.017787 -1.912108 3.770891
H -0.125146 0.251876 3.691136
H 1.299085 -0.332465 4.495269
H -0.669809 -2.119511 2.944856
H -0.546112 -1.984495 4.707380
H 0.785837 -2.692349 3.776874
C 2.856222 -0.728491 2.400747
C 3.527640 -0.827714 3.765591
H 3.401119 0.018172 1.813613
H 2.964968 -1.686601 1.872074
H 3.480531 0.117657 4.314848
H 4.584067 -1.062999 3.602149
H 3.107543 -1.620489 4.390605
C -1.044016 0.831830 -2.553494
C -2.513407 1.090600 -2.710489
H -3.104450 0.252397 -2.324826
H -2.774120 1.247805 -3.758943
H -2.812394 1.979909 -2.143594
C -0.215764 0.788578 -3.653776
C 1.167432 0.512249 -3.541329
H -0.621005 0.930837 -4.647999
O 1.670900 0.226010 -2.309071
C 2.045544 0.233106 -4.611472
C 2.156257 1.053491 -5.823830
C 3.129887 -0.638331 -4.333233
N 4.012975 -1.385480 -4.158585
C 1.502831 2.294122 -5.978915
C 1.668494 3.017855 -7.154094

H	0.891466	2.709831	-5.186257
N	2.431861	2.626756	-8.188444
H	1.163283	3.976229	-7.263704
C	3.062955	1.449670	-8.036842
C	2.959753	0.644495	-6.909764
H	3.685946	1.125939	-8.869134
H	3.500184	-0.295892	-6.875478

8.2.5- Compound **7** (S_0) - φ (70º)

46

C	0.815582	-0.081184	1.238947
C	-0.577964	0.256407	1.175051
H	-1.181880	0.243413	2.071647
C	-1.184518	0.598741	-0.009948
H	-2.240370	0.846705	-0.006010
C	-0.472242	0.626319	-1.234255
C	0.892687	0.268621	-1.159820
C	1.531542	-0.086565	0.016063
H	2.575326	-0.359836	-0.040964
N	1.430163	-0.373707	2.426288
C	0.643257	-0.564058	3.652695
C	0.002756	-1.949498	3.767776
H	-0.118107	0.216945	3.707850
H	1.302607	-0.389184	4.501733
H	-0.689196	-2.142418	2.941823
H	-0.558950	-2.024293	4.705312
H	0.763099	-2.737189	3.764599
C	2.849276	-0.786119	2.400590
C	3.522741	-0.903300	3.762850
H	3.399822	-0.040367	1.817974
H	2.944979	-1.740897	1.863959
H	3.488117	0.038287	4.319389
H	4.575926	-1.149041	3.594104
H	3.095706	-1.696329	4.382705
C	-1.032019	0.923743	-2.512923
C	-2.494483	1.217766	-2.667948
H	-3.105693	0.385444	-2.301510
H	-2.748030	1.402859	-3.713465
H	-2.774212	2.101614	-2.083127
C	-0.203583	0.867693	-3.620764
C	1.166024	0.566858	-3.518524
H	-0.606021	1.030691	-4.613640
O	1.667368	0.257899	-2.291578
C	2.025178	0.215807	-4.605805
C	2.441547	1.165724	-5.638309
C	2.905271	-0.868491	-4.358591
N	3.605234	-1.797375	-4.222409

C	1.945581	2.487126	-5.707126
C	2.381155	3.337154	-6.715405
H	1.241994	2.859441	-4.970385
N	3.272240	3.001848	-7.665009
H	1.995319	4.354849	-6.756197
C	3.747779	1.745747	-7.597886
C	3.374205	0.812955	-6.639739
H	4.470949	1.463624	-8.361814
H	3.806516	-0.181962	-6.667986

8.2.6- Compound **7** (S_0) - ϕ (TS)

46

C	0.854211	-0.060885	1.093182
C	-0.543910	0.288956	1.035117
H	-1.108385	0.411899	1.948722
C	-1.192996	0.473655	-0.154558
H	-2.242815	0.744356	-0.146775
C	-0.527583	0.312109	-1.402569
C	0.844042	-0.054951	-1.330573
C	1.525668	-0.241269	-0.141724
H	2.564380	-0.532218	-0.197221
N	1.498731	-0.208340	2.282417
C	0.759570	-0.179392	3.554676
C	0.084000	-1.507866	3.900603
H	0.027232	0.629285	3.518776
H	1.461395	0.095526	4.340219
H	-0.648661	-1.795705	3.140138
H	-0.437864	-1.419011	4.859464
H	0.819668	-2.313872	3.986896
C	2.916536	-0.635046	2.268607
C	3.630285	-0.600745	3.614191
H	3.454266	0.028408	1.583907
H	2.980378	-1.647730	1.847711
H	3.637432	0.402118	4.051577
H	4.670942	-0.893248	3.442906
H	3.207175	-1.301055	4.339633
C	-1.114136	0.508399	-2.669859
C	-2.534268	0.960957	-2.819979
H	-3.219312	0.222098	-2.388720
H	-2.791648	1.099302	-3.871375
H	-2.704392	1.904065	-2.289676
C	-0.312285	0.310496	-3.805440
C	1.005525	-0.097829	-3.711009
H	-0.719923	0.483722	-4.794087
O	1.559468	-0.248184	-2.477250
C	1.975320	-0.169447	-4.800426

C	2.768546	0.985602	-5.164189
C	1.695981	-1.138750	-5.779668
N	1.494320	-1.974378	-6.581533
C	2.860300	2.144579	-4.351432
C	3.627405	3.224509	-4.763379
H	2.332239	2.208548	-3.405472
N	4.328190	3.278353	-5.911407
H	3.680784	4.108244	-4.127889
C	4.248339	2.175828	-6.681934
C	3.515520	1.041653	-6.369342
H	4.811599	2.202036	-7.614479
H	3.513781	0.201655	-7.057118

8.2.7- Compound **7** (S_0) - φ (110º)

46

C	0.842754	-0.032913	1.125635
C	-0.554918	0.291607	1.069878
H	-1.123063	0.404602	1.982826
C	-1.206750	0.473359	-0.125796
H	-2.260368	0.730279	-0.115371
C	-0.542751	0.327888	-1.369454
C	0.826875	-0.013849	-1.299586
C	1.514923	-0.191999	-0.111512
H	2.556789	-0.471325	-0.170332
N	1.497913	-0.177935	2.318208
C	0.744590	-0.268337	3.577384
C	0.118462	-1.643907	3.818493
H	-0.020242	0.511057	3.588432
H	1.424519	-0.022829	4.391787
H	-0.591014	-1.905317	3.027023
H	-0.420400	-1.648570	4.772142
H	0.885680	-2.423968	3.858318
C	2.921366	-0.574579	2.294666
C	3.644581	-0.502887	3.634490
H	3.437464	0.095309	1.599960
H	3.014377	-1.590451	1.884303
H	3.596525	0.498963	4.072553
H	4.699053	-0.736752	3.457132
H	3.267075	-1.225514	4.363398
C	-1.131341	0.531759	-2.651733
C	-2.549268	0.999759	-2.786648
H	-3.238594	0.266352	-2.352442
H	-2.816100	1.145130	-3.835101
H	-2.706481	1.942460	-2.251155
C	-0.342017	0.343689	-3.775624
C	0.997294	-0.065848	-3.684174
H	-0.747066	0.528254	-4.763389

O	1.551157	-0.201833	-2.448663
C	1.942047	-0.115809	-4.755124
C	3.086687	0.787420	-4.883496
C	1.408134	-0.636094	-5.959719
N	0.997524	-1.106237	-6.951376
C	3.546722	1.622625	-3.839735
C	4.612222	2.485270	-4.062711
H	3.081991	1.609837	-2.861699
N	5.281005	2.593674	-5.223953
H	4.949382	3.129839	-3.251980
C	4.853184	1.789887	-6.213469
C	3.799516	0.893278	-6.100352
H	5.388579	1.863582	-7.159094
H	3.527177	0.285251	-6.956720

8.2.8- Compound **7** (S_0) - φ (130º)

46

C	0.828806	-0.044759	1.170213
C	-0.568942	0.266393	1.110786
H	-1.147268	0.349197	2.020599
C	-1.212070	0.472407	-0.088495
H	-2.268754	0.717229	-0.080440
C	-0.536961	0.368052	-1.327399
C	0.832208	0.038803	-1.254471
C	1.511820	-0.166521	-0.065463
H	2.556170	-0.437208	-0.122472
N	1.479639	-0.210394	2.365898
C	0.717089	-0.349928	3.614216
C	0.108078	-1.740229	3.812568
H	-0.059763	0.417279	3.641023
H	1.385733	-0.117365	4.441906
H	-0.593318	-1.988929	3.009887
H	-0.436495	-1.779254	4.762299
H	0.885169	-2.511198	3.835669
C	2.904176	-0.599626	2.341630
C	3.620417	-0.547605	3.686385
H	3.420554	0.085884	1.662494
H	3.007310	-1.607320	1.913008
H	3.560224	0.445023	4.143652
H	4.678032	-0.768436	3.510861
H	3.245881	-1.287211	4.399672
C	-1.119812	0.593839	-2.616162
C	-2.545675	1.040357	-2.746834
H	-3.225598	0.293834	-2.320378
H	-2.814242	1.193418	-3.793899
H	-2.716623	1.975749	-2.202349
C	-0.325676	0.440144	-3.732445

C	1.030404	0.051137	-3.637589
H	-0.727605	0.636413	-4.719042
O	1.573241	-0.110213	-2.402048
C	1.947775	-0.016432	-4.711902
C	3.291971	0.573145	-4.743805
C	1.352194	-0.303889	-5.967403
N	0.879609	-0.573936	-7.003260
C	3.918012	1.181584	-3.633575
C	5.174608	1.757375	-3.779984
H	3.438947	1.216683	-2.664678
N	5.880747	1.775814	-4.922812
H	5.641839	2.231841	-2.918256
C	5.291108	1.187260	-5.977480
C	4.039904	0.586314	-5.942790
H	5.853855	1.191384	-6.909718
H	3.645961	0.134976	-6.847116

8.2.9- Compound **7** (S_0) - φ (150º)

46

C	0.821658	-0.058915	1.201931
C	-0.575377	0.247893	1.139797
H	-1.162692	0.300531	2.046118
C	-1.209000	0.484196	-0.060560
H	-2.267471	0.721732	-0.054864
C	-0.523423	0.418800	-1.294747
C	0.845473	0.095638	-1.219633
C	1.515953	-0.140650	-0.031006
H	2.563048	-0.401345	-0.085778
N	1.465674	-0.257507	2.397365
C	0.697013	-0.412754	3.639314
C	0.076936	-1.801321	3.815650
H	-0.075413	0.358879	3.674098
H	1.362913	-0.196716	4.473744
H	-0.621941	-2.034754	3.006224
H	-0.473100	-1.849041	4.761919
H	0.848203	-2.578270	3.832671
C	2.889782	-0.647823	2.368902
C	3.587307	-0.683156	3.723811
H	3.418417	0.075022	1.738570
H	2.996072	-1.628031	1.881295
H	3.537146	0.282453	4.236499
H	4.643688	-0.911504	3.550496
H	3.189463	-1.455484	4.388086
C	-1.101236	0.663741	-2.586630
C	-2.536485	1.081099	-2.716780
H	-3.203901	0.314444	-2.306679
H	-2.803053	1.247511	-3.762407

H	-2.729443	2.003544	-2.157515
C	-0.301495	0.539952	-3.697167
C	1.066931	0.172382	-3.599098
H	-0.702641	0.739053	-4.683328
O	1.600531	-0.014894	-2.364141
C	1.961141	0.072772	-4.677699
C	3.413622	0.301610	-4.653232
C	1.356387	-0.036483	-5.956959
N	0.874724	-0.146621	-7.016716
C	4.121131	0.804267	-3.540449
C	5.489967	1.028851	-3.639740
H	3.621950	1.033619	-2.609496
N	6.226348	0.792321	-4.737589
H	6.024661	1.425312	-2.777968
C	5.554562	0.311608	-5.797078
C	4.189576	0.055582	-5.807056
H	6.141257	0.114797	-6.692945
H	3.732055	-0.334029	-6.710355

8.2.10- Compound **7** (S_0) – φ (170º)

46

C	0.814250	-0.073637	1.216760
C	-0.580543	0.239143	1.153444
H	-1.173428	0.273799	2.057011
C	-1.206377	0.502646	-0.046219
H	-2.264504	0.741959	-0.041601
C	-0.513928	0.462692	-1.276788
C	0.852009	0.132045	-1.201122
C	1.514151	-0.135277	-0.014267
H	2.560318	-0.399909	-0.068121
N	1.453306	-0.294853	2.411769
C	0.679902	-0.461225	3.648937
C	0.053758	-1.849091	3.809374
H	-0.090025	0.312723	3.689193
H	1.343494	-0.256126	4.488053
H	-0.642860	-2.072137	2.995065
H	-0.500132	-1.903898	4.753042
H	0.821846	-2.629283	3.821897
C	2.874952	-0.693014	2.382335
C	3.566477	-0.755163	3.739412
H	3.411077	0.037122	1.766693
H	2.978072	-1.665576	1.878868
H	3.522227	0.202977	4.266432
H	4.621689	-0.989649	3.567121
H	3.159177	-1.534076	4.390029
C	-1.086622	0.725444	-2.569780
C	-2.530168	1.113711	-2.701670

H -3.184400 0.326725 -2.309294
H -2.793715 1.293608 -3.745882
H -2.745737 2.022216 -2.127928
C -0.281722 0.625943 -3.675958
C 1.094145 0.271584 -3.576252
H -0.683259 0.825564 -4.661652
O 1.615579 0.046875 -2.343498
C 1.972198 0.146848 -4.659659
C 3.435086 -0.015300 -4.618018
C 1.378471 0.233170 -5.946474
N 0.906915 0.296597 -7.013989
C 4.236703 0.249938 -3.487858
C 5.616247 0.089981 -3.570550
H 3.807556 0.590784 -2.557014
N 6.275132 -0.310958 -4.669174
H 6.226320 0.302589 -2.694023
C 5.513768 -0.559210 -5.747869
C 4.131181 -0.429198 -5.774567
H 6.037593 -0.884247 -6.645230
H 3.597980 -0.654337 -6.692077

8.2.11- Compound **7** (S_0) - E isomer

46

C 0.768898 0.048704 1.148381
C -0.660265 0.080922 1.091064
H -1.245765 -0.034628 1.992701
C -1.330894 0.253211 -0.101154
H -2.415565 0.272224 -0.091409
C -0.649358 0.397035 -1.329848
C 0.755178 0.348392 -1.260295
C 1.461841 0.173958 -0.081822
H 2.539586 0.128535 -0.143033
N 1.443987 -0.088847 2.336647
C 0.720642 -0.444838 3.564107
C 0.373118 -1.931943 3.672209
H -0.182884 0.165428 3.629571
H 1.334351 -0.146478 4.413465
H -0.264906 -2.256553 2.844148
H -0.162175 -2.124505 4.608537
H 1.277409 -2.549515 3.666113
C 2.913894 -0.219133 2.294260
C 3.615400 -0.205448 3.647672
H 3.305005 0.618966 1.707840
H 3.187906 -1.137036 1.753488
H 3.403084 0.707845 4.212297
H 4.694249 -0.237154 3.465057
H 3.363140 -1.069673 4.268581

C	-1.267560	0.576460	-2.616610
C	-2.761279	0.643633	-2.742368
H	-3.226964	-0.276153	-2.370374
H	-3.062009	0.786748	-3.782199
H	-3.166953	1.469168	-2.146462
C	-0.462929	0.686092	-3.721422
C	0.957959	0.632904	-3.626587
H	-0.900733	0.823387	-4.702293
O	1.516896	0.467775	-2.401068
C	1.838475	0.721000	-4.710868
C	3.310925	0.708142	-4.677747
C	1.232524	0.805253	-5.992341
N	0.752072	0.877659	-7.055189
C	4.087774	0.988091	-3.533926
C	5.476139	0.969873	-3.624309
H	3.630580	1.232671	-2.586542
N	6.165844	0.700040	-4.743624
H	6.066572	1.191671	-2.736663
C	5.427578	0.440382	-5.835647
C	4.038832	0.434173	-5.856125
H	5.976756	0.221694	-6.749928
H	3.526304	0.210945	-6.785788

8.2.12- Compound **7** (S_1) - E isomer

46

C	0.874029	-0.136497	1.311887
C	-0.441528	0.391203	1.202900
H	-1.047398	0.543255	2.085904
C	-0.989124	0.726868	-0.025812
H	-1.996840	1.128657	-0.050230
C	-0.291403	0.560130	-1.240420
C	1.007713	0.014075	-1.116763
C	1.578160	-0.336221	0.097704
H	2.572122	-0.760454	0.073666
N	1.452703	-0.423017	2.537829
C	0.616399	-0.483261	3.741337
C	-0.208219	-1.767158	3.877915
H	-0.038249	0.391511	3.757720
H	1.268093	-0.371547	4.607996
H	-0.892843	-1.896252	3.033517
H	-0.805367	-1.735632	4.796175
H	0.438017	-2.650102	3.927583
C	2.762234	-1.097333	2.548659
C	3.435163	-1.183936	3.915006
H	3.429866	-0.534768	1.888757
H	2.678010	-2.108570	2.120628
H	3.556995	-0.196334	4.371443

H	4.433630	-1.610888	3.776214
H	2.898669	-1.829521	4.615753
C	-0.806268	0.890472	-2.546498
C	-2.177391	1.472044	-2.722947
H	-2.959992	0.799290	-2.347201
H	-2.384426	1.667040	-3.778661
H	-2.292806	2.418606	-2.178257
C	0.037134	0.645412	-3.633318
C	1.299507	0.120198	-3.472909
H	-0.287452	0.873084	-4.643826
O	1.796363	-0.210748	-2.227317
C	2.255430	-0.187050	-4.560014
C	3.249108	0.748654	-5.020519
C	2.172903	-1.473018	-5.125163
N	2.068571	-2.551474	-5.570493
C	3.336938	2.045045	-4.465750
C	4.311579	2.915758	-4.937965
H	2.654250	2.363752	-3.687142
N	5.189404	2.604828	-5.904970
H	4.389727	3.916020	-4.518381
C	5.104121	1.370588	-6.435293
C	4.173812	0.421846	-6.040150
H	5.819918	1.132230	-7.218338
H	4.161417	-0.555708	-6.509762

8.2.13- Compound **9** (S_0) - Z isomer

50

C	0.802457	-0.053416	1.187379
C	-0.611457	0.189226	1.135627
H	-1.193967	0.205316	2.046264
C	-1.263903	0.400370	-0.055428
H	-2.333491	0.579808	-0.043109
C	-0.580086	0.381036	-1.295907
C	0.808066	0.132153	-1.229367
C	1.495314	-0.087363	-0.049159
H	2.555341	-0.286003	-0.111520
N	1.456696	-0.237751	2.373740
C	0.704862	-0.395362	3.626951
C	0.123760	-1.797580	3.824217
H	-0.085775	0.357485	3.659606
H	1.374263	-0.153079	4.451030
H	-0.577125	-2.058006	3.024913
H	-0.414643	-1.848276	4.776873
H	0.915564	-2.553446	3.841421
C	2.897399	-0.569158	2.337112
C	3.596919	-0.616049	3.690183
H	3.397470	0.189490	1.725796

H	3.036265	-1.531100	1.823636
H	3.527960	0.337709	4.222196
H	4.657418	-0.817761	3.509313
H	3.217610	-1.410690	4.338647
C	-1.180523	0.546309	-2.579864
C	-2.659309	0.755593	-2.716082
H	-3.214390	-0.072948	-2.262641
H	-2.950592	0.837103	-3.764779
H	-2.969240	1.669786	-2.197129
C	-0.377058	0.484850	-3.704540
C	1.011893	0.268828	-3.607436
H	-0.829466	0.545808	-4.683753
O	1.557746	0.094040	-2.376840
C	1.954287	0.135300	-4.655881
C	1.758576	0.492657	-6.044205
C	3.215004	-0.420504	-4.305182
N	4.259294	-0.875791	-4.048509
C	0.792694	1.427206	-6.498716
C	0.673876	1.726021	-7.834790
H	0.154095	1.965364	-5.812868
N	1.470274	1.146620	-8.766733
H	-0.048585	2.444566	-8.201545
C	2.431292	0.272512	-8.371603
C	2.596901	-0.057401	-7.050509
H	3.044704	-0.151392	-9.156767
H	3.374768	-0.767337	-6.797707
C	1.345418	1.513338	-10.188752
H	1.596621	0.647420	-10.800738
H	2.027281	2.336764	-10.414103
H	0.318753	1.818076	-10.387971

8.2.14- Compound **9** (S_0) - φ (10º)

50

C	0.805859	-0.057570	1.191408
C	-0.605526	0.197960	1.138360
H	-1.190612	0.208914	2.047442
C	-1.252173	0.429598	-0.052250
H	-2.319984	0.619383	-0.041042
C	-0.564715	0.418542	-1.290531
C	0.820240	0.154731	-1.223181
C	1.501827	-0.085406	-0.043561
H	2.560068	-0.293735	-0.105075
N	1.455532	-0.258452	2.377873
C	0.699369	-0.422901	3.627482
C	0.109842	-1.823389	3.811532
H	-0.087468	0.333640	3.664452
H	1.367697	-0.190963	4.455409

H	-0.590262	-2.073182	3.008132
H	-0.431597	-1.878793	4.762219
H	0.897139	-2.584027	3.824807
C	2.893955	-0.599191	2.342241
C	3.589643	-0.659226	3.696784
H	3.400358	0.160405	1.737324
H	3.028229	-1.558593	1.822772
H	3.524751	0.291494	4.234703
H	4.649452	-0.865954	3.517533
H	3.203789	-1.455779	4.338963
C	-1.158720	0.609345	-2.574413
C	-2.634194	0.840569	-2.711398
H	-3.200991	0.012897	-2.271056
H	-2.921574	0.940927	-3.759564
H	-2.933800	1.751272	-2.180376
C	-0.352773	0.556629	-3.697046
C	1.033717	0.319698	-3.599582
H	-0.802918	0.639673	-4.675373
O	1.572764	0.121823	-2.368932
C	1.984345	0.212929	-4.642126
C	1.774274	0.522963	-6.041510
C	3.255106	-0.316407	-4.285599
N	4.309552	-0.744925	-4.024621
C	0.804349	1.445091	-6.514860
C	0.670216	1.699844	-7.857655
H	0.178371	2.009542	-5.838535
N	1.456785	1.089271	-8.779353
H	-0.053518	2.408318	-8.241789
C	2.421415	0.229427	-8.367905
C	2.602109	-0.057238	-7.037101
H	3.027121	-0.220059	-9.144165
H	3.384967	-0.756764	-6.771200
C	1.277380	1.398929	-10.208975
H	1.908778	0.734029	-10.795706
H	1.561409	2.436988	-10.393622
H	0.231644	1.248063	-10.480566

8.2.15- Compound **9** (S_0) - φ (30º)

50

C	0.823243	-0.067817	1.200673
C	-0.581208	0.227171	1.144701
H	-1.172061	0.229362	2.050028
C	-1.212748	0.507308	-0.042451
H	-2.275232	0.724526	-0.033408
C	-0.516510	0.510694	-1.276840
C	0.861585	0.206317	-1.206994
C	1.527148	-0.085312	-0.030207

H	2.579821	-0.320857	-0.089901
N	1.457648	-0.312294	2.385758
C	0.690825	-0.470426	3.629975
C	0.065032	-1.857238	3.796146
H	-0.076658	0.305351	3.670921
H	1.360952	-0.263849	4.463046
H	-0.637289	-2.080745	2.986929
H	-0.482206	-1.908444	4.743711
H	0.832494	-2.637869	3.805021
C	2.887841	-0.687871	2.354087
C	3.571462	-0.788246	3.712271
H	3.417033	0.069342	1.765939
H	3.001245	-1.641270	1.819200
H	3.529193	0.155483	4.264436
H	4.626427	-1.021331	3.536962
H	3.158713	-1.583604	4.338839
C	-1.099440	0.743634	-2.556514
C	-2.570053	0.998789	-2.699345
H	-3.152820	0.171710	-2.279465
H	-2.847371	1.125455	-3.747333
H	-2.858994	1.903679	-2.152586
C	-0.285141	0.693261	-3.676205
C	1.093315	0.436454	-3.572408
H	-0.719600	0.802789	-4.660516
O	1.621409	0.187056	-2.348460
C	2.021102	0.262445	-4.633626
C	1.935801	0.871998	-5.938744
C	3.194041	-0.481917	-4.336754
N	4.161317	-1.103176	-4.129985
C	1.069612	1.953378	-6.254237
C	1.046978	2.493127	-7.515460
H	0.433177	2.406417	-5.506786
N	1.845458	2.021948	-8.508004
H	0.403033	3.324549	-7.774391
C	2.708015	1.008376	-8.242151
C	2.775624	0.434331	-6.997669
H	3.327612	0.676725	-9.065536
H	3.478609	-0.376260	-6.849423
C	1.787036	2.638282	-9.845273
H	2.375312	2.038097	-10.537297
H	2.192763	3.651146	-9.797864
H	0.749278	2.672386	-10.179619

8.2.16- Compound **9** (S_0) - φ (50º)

50

C	0.832546	-0.091568	1.209765
C	-0.569207	0.225286	1.159757

H	-1.158615	0.221294	2.065957
C	-1.197405	0.535124	-0.019841
H	-2.256083	0.769287	-0.005983
C	-0.501669	0.548524	-1.256526
C	0.872329	0.213987	-1.193364
C	1.533662	-0.107985	-0.022782
H	2.581376	-0.363245	-0.087818
N	1.464024	-0.355491	2.389862
C	0.699892	-0.506151	3.637270
C	0.062641	-1.887460	3.803358
H	-0.059861	0.276775	3.681289
H	1.375347	-0.306496	4.467596
H	-0.644333	-2.103276	2.996080
H	-0.481650	-1.934970	4.752741
H	0.823288	-2.674700	3.808456
C	2.892128	-0.741072	2.354654
C	3.577778	-0.849450	3.711071
H	3.424605	0.014174	1.767160
H	2.996474	-1.693753	1.817141
H	3.544632	0.093538	4.265070
H	4.630367	-1.090417	3.532302
H	3.160405	-1.642824	4.337012
C	-1.081614	0.817532	-2.525821
C	-2.547151	1.099142	-2.666297
H	-3.144388	0.270854	-2.269778
H	-2.818116	1.257346	-3.711563
H	-2.823306	1.994208	-2.097340
C	-0.265134	0.766469	-3.650272
C	1.101813	0.486097	-3.550896
H	-0.690371	0.906239	-4.636115
O	1.628319	0.197818	-2.336504
C	2.006892	0.259873	-4.637606
C	2.138553	1.117444	-5.782330
C	3.020638	-0.709071	-4.418817
N	3.846288	-1.524301	-4.278683
C	1.408225	2.326914	-5.951108
C	1.593612	3.114360	-7.058400
H	0.708960	2.673027	-5.201835
N	2.471501	2.775428	-8.038270
H	1.057518	4.044549	-7.199653
C	3.196637	1.632171	-7.913383
C	3.054854	0.808720	-6.828047
H	3.883851	1.411919	-8.720723
H	3.656008	-0.091435	-6.788769
C	2.695032	3.672193	-9.184506
H	2.935160	3.073133	-10.062725
H	3.522617	4.351071	-8.963796
H	1.787480	4.245718	-9.370143

8.2.17- Compound **9** (S_0) - φ (70º)

50

C	0.839954	-0.117526	1.216964
C	-0.562685	0.209242	1.171707
H	-1.151286	0.193461	2.078224
C	-1.188826	0.541813	0.000360
H	-2.245783	0.782612	0.017691
C	-0.491879	0.570050	-1.238912
C	0.883000	0.221176	-1.180788
C	1.541154	-0.122852	-0.015707
H	2.586462	-0.386565	-0.084400
N	1.466896	-0.400771	2.391295
C	0.705040	-0.550357	3.641309
C	0.063889	-1.929967	3.803583
H	-0.050908	0.235647	3.689223
H	1.384395	-0.355753	4.469466
H	-0.646454	-2.139745	2.997667
H	-0.477199	-1.978722	4.754625
H	0.821826	-2.719730	3.803145
C	2.895560	-0.788468	2.353870
C	3.580235	-0.911442	3.709254
H	3.428820	-0.028524	1.773534
H	2.995782	-1.736053	1.807392
H	3.553303	0.027263	4.270672
H	4.631215	-1.156996	3.527420
H	3.158702	-1.707662	4.328629
C	-1.068632	0.868402	-2.495292
C	-2.527643	1.179555	-2.635656
H	-3.141522	0.347550	-2.273514
H	-2.787212	1.378540	-3.676702
H	-2.793013	2.058057	-2.036937
C	-0.247884	0.814781	-3.627443
C	1.105447	0.522102	-3.532148
H	-0.663385	0.986714	-4.612923
O	1.634819	0.214193	-2.324205
C	2.005107	0.265755	-4.641215
C	2.424890	1.272382	-5.560961
C	2.776283	-0.918452	-4.540758
N	3.391783	-1.912350	-4.495711
C	1.888146	2.594600	-5.566788
C	2.317246	3.526793	-6.472609
H	1.137537	2.895737	-4.846848
N	3.266460	3.238002	-7.404948
H	1.927776	4.537268	-6.488290
C	3.810962	1.990965	-7.429720
C	3.419940	1.017355	-6.551588
H	4.564561	1.815227	-8.187175

H	3.885441	0.042215	-6.629572
C	3.747636	4.280722	-8.324533
H	4.122060	3.808369	-9.232407
H	4.549377	4.853616	-7.851312
H	2.921317	4.945373	-8.576248

8.2.18- Compound **9** (S_0) - φ (TS)

50

C	0.860295	-0.089297	1.165481
C	-0.554705	0.204242	1.128859
H	-1.127395	0.214236	2.045520
C	-1.205028	0.473415	-0.040341
H	-2.266104	0.693277	-0.017312
C	-0.525397	0.463884	-1.295132
C	0.865646	0.151216	-1.243766
C	1.547548	-0.120631	-0.075080
H	2.598240	-0.360591	-0.146161
N	1.502009	-0.322223	2.336991
C	0.757191	-0.450722	3.601670
C	0.144486	-1.837811	3.802310
H	-0.011197	0.323202	3.638260
H	1.443854	-0.224380	4.415135
H	-0.572101	-2.077738	3.010554
H	-0.383246	-1.874148	4.761192
H	0.917054	-2.613077	3.809404
C	2.943860	-0.666495	2.297849
C	3.638526	-0.753625	3.650447
H	3.449207	0.101439	1.703549
H	3.065192	-1.617631	1.763100
H	3.592198	0.191473	4.199531
H	4.693937	-0.975508	3.464164
H	3.240884	-1.552181	4.282487
C	-1.124015	0.716130	-2.538610
C	-2.581411	1.031531	-2.673296
H	-3.189095	0.174940	-2.359190
H	-2.834391	1.274278	-3.706524
H	-2.860355	1.875511	-2.034119
C	-0.308702	0.639633	-3.691696
C	1.026746	0.339276	-3.605385
H	-0.734495	0.809314	-4.672783
O	1.592456	0.101153	-2.397733
C	1.951060	0.158015	-4.741399
C	2.686664	1.221101	-5.302048
C	2.174740	-1.173933	-5.140174
N	2.348849	-2.283344	-5.476513
C	2.542868	2.579504	-4.869604
C	3.278087	3.583179	-5.434641

H	1.845349	2.842174	-4.082884
N	4.174704	3.346578	-6.434656
H	3.185724	4.614284	-5.115770
C	4.341712	2.067186	-6.880550
C	3.635583	1.022767	-6.358335
H	5.066766	1.934224	-7.674284
H	3.808512	0.031706	-6.761384
C	5.013293	4.430863	-6.962457
H	5.220355	4.243412	-8.016525
H	5.954896	4.483721	-6.408673
H	4.479603	5.376057	-6.862799

8.2.19- Compound **9** (S_0) - φ (110º)

50

C	0.890274	-0.052302	1.109742
C	-0.528182	0.200719	1.078045
H	-1.090469	0.247314	2.000107
C	-1.201949	0.387291	-0.098837
H	-2.267952	0.582867	-0.070960
C	-0.542028	0.323944	-1.357284
C	0.852471	0.059951	-1.309482
C	1.561322	-0.121276	-0.137690
H	2.617176	-0.335816	-0.213407
N	1.556881	-0.219648	2.284237
C	0.827191	-0.339141	3.557014
C	0.247288	-1.734865	3.795714
H	0.041194	0.418023	3.584714
H	1.514527	-0.079550	4.360301
H	-0.468223	-2.010734	3.014783
H	-0.273813	-1.761594	4.758631
H	1.037951	-2.491638	3.815691
C	3.001553	-0.542111	2.234755
C	3.719255	-0.565688	3.578359
H	3.486377	0.209864	1.603762
H	3.134373	-1.511108	1.734571
H	3.656854	0.395934	4.096581
H	4.777141	-0.768384	3.384143
H	3.351379	-1.351341	4.244043
C	-1.158282	0.519557	-2.614040
C	-2.611247	0.864722	-2.731612
H	-3.229155	0.051847	-2.333192
H	-2.890939	1.033601	-3.772740
H	-2.851175	1.762811	-2.152616
C	-0.363387	0.417071	-3.762604
C	0.983565	0.100067	-3.685074
H	-0.793738	0.588387	-4.741864
O	1.567774	-0.046226	-2.472143

C	1.916396	0.063356	-4.797420
C	2.964781	1.012492	-4.978342
C	1.486851	-0.696107	-5.911178
N	1.149463	-1.345976	-6.824547
C	3.316520	1.991978	-4.001156
C	4.319680	2.893451	-4.234562
H	2.798846	2.053011	-3.053021
N	5.031419	2.892767	-5.394940
H	4.595518	3.648928	-3.509207
C	4.730711	1.974585	-6.353653
C	3.737798	1.050126	-6.177852
H	5.324714	2.015970	-7.258050
H	3.551870	0.343314	-6.977368
C	6.066186	3.911646	-5.628762
H	6.776534	3.535461	-6.364396
H	6.587715	4.113880	-4.692970
H	5.606062	4.831398	-5.999214

8.2.20- Compound **9** (S_0) - φ (130º)

50

C	0.849179	-0.090564	1.154787
C	-0.571964	0.121166	1.104397
H	-1.151955	0.130425	2.016603
C	-1.231399	0.314342	-0.083101
H	-2.303107	0.478623	-0.068512
C	-0.550680	0.299244	-1.328022
C	0.844218	0.071509	-1.262539
C	1.540147	-0.119114	-0.083468
H	2.602067	-0.306778	-0.146703
N	1.506535	-0.256273	2.338838
C	0.761656	-0.421145	3.596466
C	0.218999	-1.836531	3.805556
H	-0.047749	0.311324	3.624852
H	1.427235	-0.154493	4.415917
H	-0.477409	-2.120950	3.010535
H	-0.314617	-1.893852	4.760419
H	1.030846	-2.570731	3.825641
C	2.957651	-0.542949	2.303472
C	3.660063	-0.561336	3.655566
H	3.432720	0.227007	1.686598
H	3.123060	-1.503225	1.795359
H	3.565483	0.393261	4.182083
H	4.725329	-0.734348	3.473120
H	3.305179	-1.362797	4.309416
C	-1.150844	0.512420	-2.599033
C	-2.611933	0.820697	-2.726442
H	-3.212810	-0.008231	-2.335378

H	-2.888352	0.987192	-3.768953
H	-2.878467	1.710853	-2.146322
C	-0.341741	0.463250	-3.728016
C	1.025525	0.181829	-3.636402
H	-0.761549	0.651283	-4.708563
O	1.585725	0.012821	-2.416735
C	1.949642	0.184369	-4.731892
C	3.215080	0.865157	-4.762149
C	1.396937	-0.228526	-5.972344
N	0.959244	-0.591076	-6.993808
C	3.805310	1.508229	-3.636284
C	5.005114	2.161432	-3.746167
H	3.326838	1.504071	-2.668020
N	5.687026	2.216978	-4.920717
H	5.467928	2.660483	-2.903506
C	5.161503	1.616930	-6.019782
C	3.963386	0.953412	-5.970335
H	5.743650	1.689183	-6.929562
H	3.598608	0.498557	-6.883141
C	6.995782	2.887882	-4.974394
H	7.314253	2.961277	-6.013002
H	7.727509	2.308880	-4.406523
H	6.907481	3.888286	-4.547600

8.2.21- Compound **9** (S_0) – φ (150º)

50

C	0.807311	-0.118642	1.213442
C	-0.609695	0.099845	1.139697
H	-1.207983	0.091707	2.040078
C	-1.244572	0.319333	-0.058595
H	-2.316284	0.485044	-0.061985
C	-0.539737	0.328497	-1.287846
C	0.850636	0.098743	-1.199435
C	1.522532	-0.122815	-0.011318
H	2.585280	-0.311635	-0.056585
N	1.442505	-0.311926	2.407661
C	0.671993	-0.496388	3.646199
C	0.110960	-1.909878	3.818177
H	-0.131314	0.243059	3.674271
H	1.323705	-0.252402	4.483782
H	-0.574571	-2.171669	3.006087
H	-0.439749	-1.980014	4.762503
H	0.914385	-2.653330	3.837735
C	2.889584	-0.616499	2.392406
C	3.565111	-0.674728	3.757075
H	3.387090	0.161234	1.803281
H	3.054058	-1.567076	1.865638

H	3.474109	0.270007	4.301639
H	4.631183	-0.860187	3.592244
H	3.184793	-1.484097	4.386302
C	-1.116425	0.556109	-2.572526
C	-2.579331	0.847857	-2.721930
H	-3.179236	0.013993	-2.340310
H	-2.841319	1.013595	-3.768400
H	-2.862352	1.735852	-2.145924
C	-0.289858	0.525747	-3.681708
C	1.088651	0.267606	-3.566754
H	-0.694657	0.715389	-4.667808
O	1.619563	0.072005	-2.339523
C	2.009057	0.261350	-4.650749
C	3.411969	0.598356	-4.607095
C	1.421241	0.102856	-5.934959
N	0.952338	-0.043050	-6.994652
C	4.120148	0.972025	-3.431673
C	5.448175	1.314283	-3.487541
H	3.638526	1.010305	-2.467241
N	6.143904	1.302407	-4.652949
H	6.001606	1.610166	-2.604730
C	5.509318	0.944898	-5.798688
C	4.182326	0.600158	-5.803173
H	6.108570	0.946551	-6.700466
H	3.734821	0.331367	-6.751984
C	7.580888	1.626287	-4.657866
H	7.872539	1.935716	-5.660719
H	8.155681	0.745301	-4.361866
H	7.764958	2.439270	-3.955497

8.2.22- Compound **9** (S_0) - φ (170º)

50

C	0.765767	-0.118244	1.255001
C	-0.647607	0.107307	1.158836
H	-1.261840	0.091181	2.048255
C	-1.259768	0.344646	-0.048794
H	-2.330757	0.514218	-0.069464
C	-0.533080	0.367088	-1.263966
C	0.853101	0.130895	-1.154091
C	1.502365	-0.110795	0.043022
H	2.565175	-0.302857	0.015960
N	1.380317	-0.327221	2.458868
C	0.587530	-0.538537	3.678715
C	0.031904	-1.958016	3.816381
H	-0.221203	0.194994	3.705082
H	1.221841	-0.304800	4.532556
H	-0.638552	-2.209258	2.988461

H	-0.533958	-2.047649	4.750049
H	0.839043	-2.697490	3.836487
C	2.825569	-0.638432	2.464355
C	3.479300	-0.703905	3.839387
H	3.335303	0.140282	1.887201
H	2.995818	-1.587352	1.936042
H	3.379550	0.238392	4.386725
H	4.547882	-0.889098	3.691126
H	3.088705	-1.515965	4.458684
C	-1.087462	0.601685	-2.559630
C	-2.551939	0.872822	-2.733889
H	-3.148334	0.032102	-2.362124
H	-2.798095	1.035828	-3.784724
H	-2.855210	1.757776	-2.163344
C	-0.243745	0.580260	-3.652066
C	1.139392	0.331860	-3.515428
H	-0.636333	0.763533	-4.643941
O	1.644184	0.119353	-2.280824
C	2.060030	0.298672	-4.592307
C	3.504657	0.250112	-4.532516
C	1.474497	0.375961	-5.886384
N	1.006911	0.433782	-6.954411
C	4.274920	0.273686	-3.338640
C	5.648089	0.247399	-3.383550
H	3.812832	0.324245	-2.366542
N	6.325799	0.198206	-4.556212
H	6.250711	0.269563	-2.484013
C	5.630832	0.170242	-5.722429
C	4.260312	0.196615	-5.737276
H	6.219169	0.128252	-6.630645
H	3.768530	0.178361	-6.701706
C	7.796610	0.120755	-4.568180
H	8.171519	0.635236	-5.452454
H	8.108070	-0.926331	-4.589416
H	8.184956	0.602950	-3.671868

8.2.23- Compound **9** (S_0) - E isomer

50

C	0.802457	-0.053416	1.187379
C	-0.611457	0.189226	1.135627
H	-1.193967	0.205316	2.046264
C	-1.263903	0.400370	-0.055428
H	-2.333491	0.579808	-0.043109
C	-0.580086	0.381036	-1.295907
C	0.808066	0.132153	-1.229367
C	1.495314	-0.087363	-0.049159
H	2.555341	-0.286003	-0.111520
N	1.456696	-0.237751	2.373740
C	0.704862	-0.395362	3.626951
C	0.123760	-1.797580	3.824217
H	-0.085775	0.357485	3.659606
H	1.374263	-0.153079	4.451030
H	-0.577125	-2.058006	3.024913
H	-0.414643	-1.848276	4.776873
H	0.915564	-2.553446	3.841421
C	2.897399	-0.569158	2.337112
C	3.596919	-0.616049	3.690183
H	3.397470	0.189490	1.725796
H	3.036265	-1.531100	1.823636
H	3.527960	0.337709	4.222196
H	4.657418	-0.817761	3.509313
H	3.217610	-1.410690	4.338647
C	-1.180523	0.546309	-2.579864
C	-2.659309	0.755593	-2.716082
H	-3.214390	-0.072948	-2.262641
H	-2.950592	0.837103	-3.764779
H	-2.969240	1.669786	-2.197129
C	-0.377058	0.484850	-3.704540
C	1.011893	0.268828	-3.607436
H	-0.829466	0.545808	-4.683753
O	1.557746	0.094040	-2.376840
C	1.954287	0.135300	-4.655881
C	1.758576	0.492657	-6.044205
C	3.215004	-0.420504	-4.305182
N	4.259294	-0.875791	-4.048509
C	0.792694	1.427206	-6.498716
C	0.673876	1.726021	-7.834790
H	0.154095	1.965364	-5.812868
N	1.470274	1.146620	-8.766733
H	-0.048585	2.444566	-8.201545
C	2.431292	0.272512	-8.371603
C	2.596901	-0.057401	-7.050509
H	3.044704	-0.151392	-9.156767

H	3.374768	-0.767337	-6.797707
C	1.345418	1.513338	-10.188752
H	1.596621	0.647420	-10.800738
H	2.027281	2.336764	-10.414103
H	0.318753	1.818076	-10.387971

8.2.24- Compound **9** (S_1) - E isomer

50

C	0.735563	-0.127750	1.263450
C	-0.682210	0.028976	1.159394
H	-1.309767	-0.023621	2.037765
C	-1.281743	0.243579	-0.064122
H	-2.358975	0.359082	-0.104429
C	-0.539201	0.314768	-1.267498
C	0.862955	0.149182	-1.148470
C	1.494351	-0.067726	0.057915
H	2.567143	-0.195589	0.054091
N	1.353273	-0.331556	2.466113
C	0.567838	-0.492960	3.697116
C	0.044244	-1.921130	3.887967
H	-0.255049	0.223630	3.684367
H	1.202769	-0.214971	4.536011
H	-0.623706	-2.212444	3.072144
H	-0.514305	-1.978107	4.827789
H	0.867561	-2.640216	3.933357
C	2.817425	-0.551221	2.497078
C	3.449038	-0.643289	3.879112
H	3.287891	0.276431	1.956650
H	3.036505	-1.467445	1.933061
H	3.323792	0.279255	4.453042
H	4.522537	-0.799170	3.734605
H	3.070187	-1.484521	4.465127
C	-1.112701	0.537119	-2.573776
C	-2.589306	0.714230	-2.751505
H	-3.144689	-0.164029	-2.397477
H	-2.837405	0.872392	-3.803633
H	-2.962753	1.573897	-2.179998
C	-0.235729	0.578199	-3.642866
C	1.159054	0.412446	-3.503737
H	-0.623468	0.747403	-4.640869
O	1.684167	0.191339	-2.250829
C	2.090746	0.453683	-4.576244
C	3.529065	0.334472	-4.543112
C	1.508864	0.641050	-5.862840
N	1.047799	0.795389	-6.923950
C	4.315744	0.202187	-3.355658
C	5.680462	0.100339	-3.415962

H	3.858849	0.185984	-2.379380
N	6.357566	0.126340	-4.602088
H	6.287525	-0.000132	-2.524797
C	5.645257	0.250880	-5.765349
C	4.282480	0.354805	-5.760710
H	6.224888	0.265215	-6.679848
H	3.786237	0.456168	-6.718264
C	7.813001	-0.044895	-4.644178
H	8.229263	0.593058	-5.425576
H	8.064049	-1.088789	-4.857596
H	8.236229	0.240373	-3.681035

9.- References

(1) Peralta, J.; Ogliaro, F.; Bearpark, M.; Heyd, J.; Brothers, E.; Kudin, K.; Staroverov, V.; Kobayashi, R.; Normand, J.; Raghavachari, K., et al. Gaussian 09, Revision D. 01., **2013**.

(2) Hohenberg, P.; Kohn, W. *Phys. Rev. B* **1964**, *136*, 864-876.

(3) Becke, A. D. *Phys. Rev. A* **1988**, *38*, 3098-3100.

(4) Lee, C.; Yang, W.; Parr, R. G. *Phys. Rev. B* **1988**, *37*, 785-789.

(5) Hehre, W.; Radom, L. v. R. Schleyer, P.; Pople, JA Ab initio molecular orbital theory, **1986**.

(6) Bauernschmitt, R.; Ahlrichs, R. *Chem. Phys. Lett*. **1996**, *256*, 454-464.

(7) Marenich, A. V.; Cramer, C. J.; Truhlar, D. G. *J. Phys. Chem. B* **2009**, *113*, 6378-6396.

(8) Chen, D.-L.; Stern, A. C.; Space, B.; Johnson, J. K. *J. Phys. Chem. A* **2010**, *114*, 10225-10233.

(9) Reichardt, R. Solvatochromic dyes as solvent polarity indicators. *Chem. Rev*. **1994**, *94*, 2319-2358.

(10) Schindelin, J.; Arganda-Carreras, I.; Frise, E.; Kaynig, V.; Longair, M.; Pietzsch, T.; Preibisch, S.; Rueden, C.; Saalfeld, S.; Schmid, B.; Tinevez, J. Y.; White, D. J.; Hartenstein, V.; Eliceiri, K.; Tomancak, P.; Cardona, A. *Nat. Methods* **2012**, *9*, 676-682.

10. Publication E: Straightforward solid-phase approaches for labelling targeting peptides with far-red/NIR emitting coumarin fluorophores (*Manuscript submitted for publication*)

Journal Name

COMMUNICATION

Straightforward solid-phase approaches for labelling targeting peptides with far-red/NIR emitting coumarin fluorophores

Received 00th January 20xx,
Accepted 00th January 20xx

DOI: 10.1039/x0xx00000x

www.rsc.org/

Anna Rovira,[a,‡] Albert Gandioso,[a,‡] Marina Goñalons,[a] Alex Galindo,[a] Anna Massaguer,[b] Manel Bosch,[c] and Vicente Marchán*[a]

Three straightforward solid-phase approaches based on amide-bond formation or Cu(I)-catalyzed azide–alkyne click reaction have been developed for labelling octreotide peptide with a far-red/NIR emitting coumarin dye, and the potential bioimaging applications of the resulting targeted conjugates demonstated in living cells.

Last few decades have witnessed an impressive growth in the development of novel diagnostic and therapeutic technologies against cancer. Even so, this disease is still the second leading cause of death globally. In this context, receptors over-expressed on cancer cells have been exploited to selectively deliver a large variety of cytotoxic drugs into cancer cells with the aim of minimizing toxic side-effects associated with chemotherapy. Ligand-targeted imaging agents also offer great potential in the early detection of cancerous cells, as well as in fluorescence-guided surgery (FGS), which allows resection of solid tumours by the surgeon after illumination of malignancies directly in the operating room.[1] In fact, recent advances in fluorophore chemistry and knowledge of targetable receptors on cancer cells have led to the clinical testing of several targeted fluorophores for intraoperative cancer detection and FGS.[1b,2]

Owing to the potential of fluorophores based on organic molecules in ligand-targeted imaging applications, it is urgent to develop novel low molecular-weight fluorescent probes operating in the far-red and near-infrared (NIR) region, since only the use of non-toxic and high tissue-penetrating radiation will guarantee clinical translation in the next years.[3] Ideally, such fluorophores should be amenable to smart structural modifications to tune, on demand, photophysical (e.g., Stokes' shifts, photostability, brightness, etc.) and physicochemical properties, as well as to facilitate conjugation to a broad variety of targeting ligands (e.g., peptides, proteins, folic acid, monoclonal antibodies (mAb), etc.) by using efficient and chemoselective conjugation chemistries. Although many times forgotten, the biological properties of a targeting ligand should not be impaired by the fluorescent tag. This issue is particularly problematic in the case of short peptide sequences since uptake and subcellular localization may be strongly influenced after conjugation to a fluorophore.[4] In the same way, some structural modifications of cyanine-based dyes alter the mechanism of mAb when conjugated together, and non-specific hydrophobic interactions between EGF receptor and the dye moiety in BODIPY-peptide conjugates were found to reduce peptide-receptor binding specificity.[5] Hence, the choice of the fluorophore cannot be underestimated since constitutes a critical parameter in ligand-targeted imaging applications.

Recently, we have developed a novel family of coumarin-based fluorophores, nicknamed COUPYs, with promising photophysical properties and great potential for imaging applications in living cells.[6] As shown in Scheme 1A, replacement of the carbonyl function in coumarin **1** with the cyano(4-pyridine)methylene moiety (e.g., compound **2**) allowed us to increase the push–pull character of the classical coumarin chromophore, which was easily transformed into pH-independent far-red/NIR-emitting fluorophores through *N*-alkylation of the pyridine heterocycle (e.g., compound **3**). Considering the small size and the easy synthetic accessibility to COUPY dyes, these compounds are potential candidates for

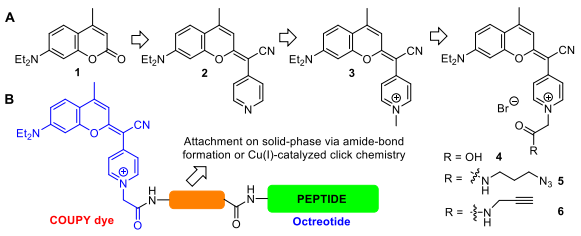

Scheme 1 Rational design of conjugatable versions of COUPY dyes (A) and schematic representation of COUPY-octreotide conjugates (B).

[a] *Departament de Química Inorgànica i Orgànica, Secció de Química Orgànica, IBUB, Universitat de Barcelona, Martí i Franquès 1-11, E-08028 Barcelona (Spain). E-mail: vmarchan@ub.edu*
[b] *Departament de Biologia, Universitat de Girona, E-17071 Girona (Spain).*
[c] *Unitat de Microscòpia Òptica Avançada, Centres Científics i Tecnològics, Universitat de Barcelona, E-08028 Barcelona (Spain)*
† These authors contributed equally to this work.
Electronic Supplementary Information (ESI) available: Details of the synthesis and characterization of the compounds, and results from fluorescence imaging studies. See DOI: 10.1039/x0xx00000x

labelling targeting ligands such as receptor-binding peptides. In such a context, we envisaged that conjugatable versions of COUPY dyes (e.g., compounds **4** to **6** in Scheme 1A) could be obtained from scaffold **2** through *N*-alkylation with adequate reagents, thereby providing suitable functional groups (e.g., carboxylic acid, azide or alkyne) for conjugation via amide-bond formation or copper(I)-catalyzed azide–alkyne cycloaddition reaction (CuAAC), respectively.[7]

Herein, we report for the first time three straightforward solid-phase approaches for the conjugation of coumarin-based COUPY fluorophores to octreotide (Scheme 1B), a FDA-approved peptide that displays high affinity and selectivity for somatostatin receptors, mainly subtype-2 receptor (SSTR2) which is overexpressed on the membrane of various types of malignant cells.[8] This cyclic octapeptide is a promising candidate for developing novel targeted imaging agents for intraoperative cancer detection and FGS since some derivatives, such as [^{111}In-DTPA]- and [^{90}Y-DOTA-Tyr3]-octreotide conjugates, are routinely used in the clinics for molecular imaging and therapy of neuroendocrine tumors, respectively, and several other SSTR2-targeted radiotherapeutics are currently under clinical evaluation.[1a] Octreotide has also been conjugated successfully to several anticancer drugs (both organic compounds and metallodrugs),[9] including Ir(III) complexes useful for theranostic applications.[10]

COUPY fluorophores **4-6** were easily synthesized through *N*-alkylation of **2** (Scheme 2), which was previously obtained by condensation of thiocoumarin **7**[6,11] with 4-pyridylacetonitrile in the presence of NaH followed by treatment with $AgNO_3$.[6] On the one hand, reaction of **2** with methyl bromoacetate afforded intermediate **8** in excellent yield after silica column chromatography (97 %). This compound was transformed into coumarin **4** bearing the carboxylic acid function by acidic hydrolysis (Fig. S1). On the other hand, azido- (**5**) and alkynyl- (**6**) containing fluorophores were synthesized by reaction of **2** with *N*-alkyl bromoacetamide derivatives containing the appropriate functional groups for CuAAC (compounds **9** and **10**, respectively). In both cases, the syntheses proceed efficiently and compounds **5** and **6** were obtained as dark blue solids after purification (96 % and 80 % yields, respectively). Full characterization was carried out by high resolution ESI-MS and 1D (^{1}H and ^{13}C) and 2D NMR, and the purity was assessed by reversed-phase HPLC-MS (Fig. S1), revealing a single peak in all cases. Similarly to the parent COUPY dye **3**,[6] ^{1}H-^{1}H NOESY experiments revealed that the *E* rotamer (as drawn in the manuscript) was the major species in solution (Fig. S2-S4).

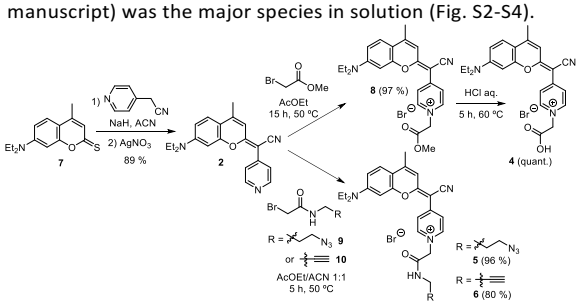

Scheme 2 Synthesis of conjugatable COUPY fluorophores **4-6**.

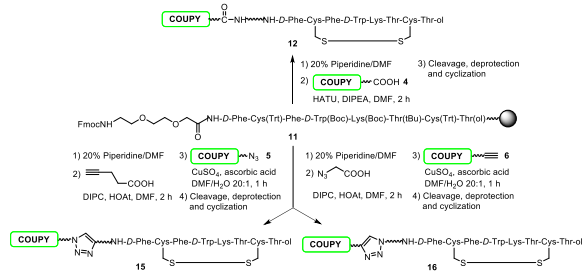

Scheme 3 Schematic representation of the three solid-phase approaches used for the labelling of octreotide with COUPY dyes via amide-bond formation (top) or CuAAC reaction (bottom).

Having at hand the conjugatable COUPY derivatives (**4-6**), we focused on labelling octreotide following a stepwise solid-phase strategy since it allows the regioselective attachment of the fluorescent dye at the *N*-terminal end of the peptide sequence, either through amide-bond formation or by Cu(I)-catalyzed click chemistry. First, the linear octapeptide sequence incorporating a short polyethylenglycol spacer (**11**) was assembled manually on a Rink amide resin-*p*-MBHA using standard Fmoc-*t*Bu methodology (Scheme 3). After coupling of coumarin **4** with HATU in the presence of DIPEA, side-chain deprotection and cleavage from the resin (TFA/TIS/H_2O/EDT 94:2.5:2.5:1, 2.5 h RT) and cyclization via disulfide bond formation in an aqueous buffer (pH 7-8) were carried out. Analysis by HPLC-ESI MS showed a main peak (Fig. S5) that was isolated and characterized as the expected COUPY-octreotide conjugate (**12**). Finally, after purification by semipreparative HPLC and lyophilization, the formate salt of **12** (overall yield 12 %) was obtained as a pink solid and fully characterized by HR ESI-MS and ^{1}H NMR (1D and 2D). As shown in Fig. S6, the obtained *m/z* values are consistent with the calculated values of the charged species $[M]^+$, $[M+H]^{2+}$ and $[M+2H]^{3+}$. In addition, the aromatic region of the ^{1}H NMR spectra in 8:2 H_2O/D_2O-DMSO-d_6 mixtures showed diagnostic peaks from the COUPY fluorophore and the peptide moiety (amide NH protons and aromatic protons of D/L-Phe and D-Trp residues), confirming the covalent attachment of both moieties (Fig. 1). Importantly, conjugate **12** was found stable in cell culture medium (DMEM supplemented with 10 % FBS) after incubation for 24 h (Fig. S7), as well as non-cytotoxic in HeLa cells (Fig. S8). Both pre-requisites are necessary for exploring the bioimaging applications of COUPY-peptide conjugates.

Once demonstrated the compatibility of COUPY dyes with solid-phase peptide synthesis, we investigated the potential applications of coumarin derivatives bearing azide (**5**) and alkynyl (**6**) functional groups for labelling octreotide via CuAAC reaction on solid-phase, since click chemistry is routinely employed for modifying peptides, oligonucleotides, small molecules and polymers.[12] First, the required functional groups were incorporated at the *N*-terminal end of peptide-bound resin **11** by coupling 4-pentynoic acid or 2-azidoacetic acid, which provided alkynyl- (**13**) and azido- (**14**) peptide-bound resins, respectively, (Fig. S9-S10). Click chemistry was

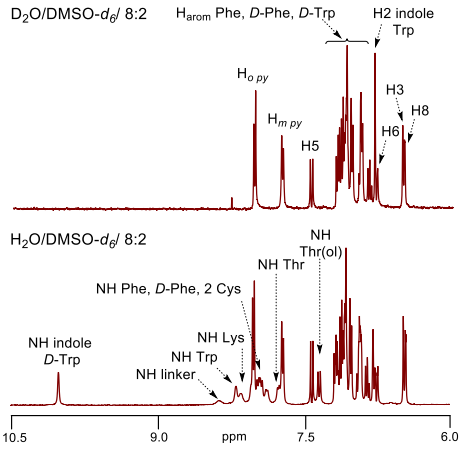

Fig. 1 Aromatic region of the ^{1}H NMR spectra of conjugate **12** in H_2O-DMSO-d_6 8:2 (top) and in D_2O-DMSO-d_6 8:2 (bottom).

investigated by reacting **13** and **14** resins with coumarins **5** and **6**, respectively, in the presence of copper(II) sulfate (3 mol equiv.) and sodium ascorbate (3 mol equiv.) in DMF/H_2O 20:1 for 18 h. To our delight, after cleavage and deprotection, HPLC-MS analysis revealed the formation of the expected linear COUPY-octreotide conjugates. Since no significant side reactions derived of the presence of sodium ascorbate and Cu(I) were detected, we decided not to explore the use of Cu-stabilizing ligands. It is worth noting that most click chemistry procedures reported in the literature for labelling peptides with fluorophores describe the use of long reaction times (12-48 h) and even microwave irradiation.[12] However, we obtained near quantitative conversions after only 1 h of reaction at RT (see Fig. S11 and S14 for the HPLC-MS analyses after 1 h, 4 h and overnight reaction times), independently of the click chemistry approach used (azido-COUPY/alkynyl-peptide resin or alkynyl-COUPY/azido-peptide resin). Finally, after cyclization and purification, clicked COUPY-octreotide conjugates (**15** and **16**) were obtained as pink solids (overall yields 32 % and 13 %, respectively) and characterized by HR ESI-MS (Fig. S13, S16).

The photophysical properties (absorption and emission spectra, molar absorption coefficients (ε), and fluorescence quantum yields (ϕ_F)) of the three COUPY-octreotide conjugates were studied in water and in PBS buffer, and compared with those of their respective coumarin precursors (see Table S1 and Fig. 2 and S17-S20). As expected, all the compounds reproduced the behaviour of the parent coumarin dye **3** and showed an intense absorption band in the yellow-red part of the visible spectrum, being the wavelength absorption maximum slightly red-shifted with respect **3** (e.g., λ_{abs} = 543 nm for **3** *vs* λ_{em} = 555 nm for **5-6** and **8** in H_2O) because of the additional electron-withdrawing effect of ester and amide functions. Similarly, the emission maximum was red-shifted by *ca* 10 nm (e.g., λ_{em} = 605 nm for **3** *vs* λ_{em} = 615 nm for **5-6** and **8** in H_2O) and, consequently, the Stokes's shifts remained around 60-62 nm. An additional red-shift in absorption (*ca* 4-6 nm) and emission (*ca* 3-5 nm) maxima occurred after

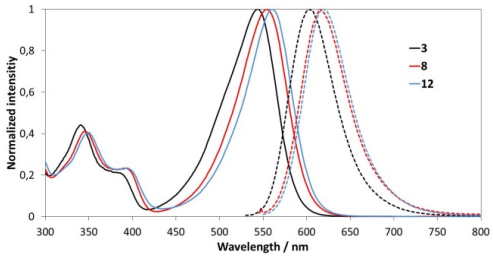

Fig. 2 Comparison of the normalized absorption (solid lines) and fluorescence emission (dotted lines) spectra of coumarins **3** and **8** and of conjugate **12**.

conjugation to octreotide. As shown in Table S1, the ϕ_F of the conjugatable coumarin derivatives (**8** and **5-6**) in aqueous media was reduced when compared with the parent coumarin **3** (e.g., ϕ_F = 0.066 for **5** *vs* ϕ_F = 0.15 for **3** in H_2O). However, it is important to highlight that a clear improvement in the fluorescent quantum yield of these fluorophores was achieved when conjugated to the peptide sequence (e.g., ϕ_F = 0.066 for **5** *vs* ϕ_F = 0.19 for conjugate **15** in H_2O), independently of the chemical conjugation approach used.

Finally, we investigated the potential bioimaging applications of COUPY-octreotide conjugates. As a representative model, we selected conjugate **12** and studied its cellular uptake by confocal microscopy in SSTR2-overexpressing HeLa cells after irradiation with a yellow light laser (λ_{ex} = 561 nm). Interestingly, fluorescent vesicles, mostly-like endosomes, were visible in the cytoplasm of all of the examined cells after 30 min of incubation with **12** at 10 μM concentration, thereby confirming the internalization and accumulation of COUPY-octreotide conjugate in the cells (Fig. 3 and S23). This pattern of staining contrasts with that of coumarin **3** (Fig. S23), which accumulates preferentially in mitochondria and nucleoli,[6] and indicates that the internalization of COUPY-octreotide conjugate is driven exclusively by the peptide moiety and not by the coumarin tag. In order to get more insights into the cellular uptake of the conjugate, we incubated HeLa cells with **12** at 4 $^{\circ}$C for 30 min. As shown in Fig. S24, no staining was observed inside the cytoplasm, which confirms that **12** enters the cells only through an energy-dependent pathway. By contrast, the pattern of staining observed with coumarin **3** was not modified at low temperature (Fig. S24), thereby suggesting internalization of the fluorophore through simple passive diffusion. Overall, these results point out to the participation of SSTR2 in the cellular uptake of conjugate **12** and, more importantly, to the fact that COUPY labeling does not interfere in the peptide-receptor recognition process.

Based on these promising results, we decided to compare the visualization ability of COUPY dyes when conjugated to octreotide with that of two common commercially available fluorophores. For this purpose, we selected 5(6)-carboxyfluorescein, which is one of the most popular fluorescent tags for labelling peptides and is typically excited at 488 nm. In addition, we chose a rhodamine dye, Atto-Rho12, which can be excited with the same yellow light laser

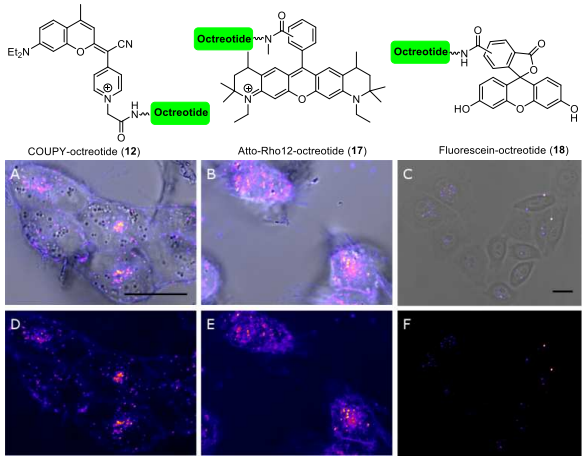

Fig. 3 Comparison of the cellular uptake of COUPY- (**12**), Atto Rho12- (**17**) and Fluorescein- (**18**) octreotide conjugates. Top: structures of conjugates **12** and **17-18**. Bottom: single confocal planes of HeLa cells incubated with **12** (A and D) and **17** (B and E) at 10 μM and **18** (C and F) at 50 μM for 30 min at 37 °C. (A-C) Fluorescence images merged with bright field images. (D-F) Fluorescence images only. All fluorescence images are color coded using the Fire lookup table from Fiji. Scale bar: 20 μm. B,D,E same scale as A. F same scale as C.

(λ_{abs} = 577 nm) than our COUPY fluorophore incorporated in conjugate **12**. Atto-Rho12-octreotide (**17**) was synthesized by reaction of the corresponding succinimidyl ester derivative with octreotide and fluorescein-octreotide (**18**) was prepared by SPPS as previously described.[9a] As shown in Fig. 3, the performance of the COUPY dye when conjugated to octreotide was comparable to that of the rhodamine dye when exciting at 561 nm under similar conditions. By contrast, COUPY fluorophore allowed a much better visualization of HeLa cells than carboxyfluorescein, even at much lower concentrations and, more importantly, with a more convenient excitation wavelength (561 nm *vs* 488 nm). On the other hand, it is worth noting that conjugates involving carboxyfluorescein and Atto-Rho12 dyes (**17** and **18**) were obtained as regiomeric mixtures since both commercially available fluorophores are supplied as mixtures of isomers. However, COUPY-octreotide conjugate **12** was easily obtained as a single product, which represents a suitable alternative to many conventional fluorophores when labeled biomolecules with a well-defined structure are required for biological applications.

In conclusion, we have developed three straightforward solid-phase approaches for labeling peptides on a solid-phase with far-red/NIR emitting coumarins, either by using conventional amide bond formation or by Cu(I)-catalyzed azide–alkyne click reaction. Importantly, octreotide labeling with COUPY dyes allowed visualization of SSTR2-overexpresing living HeLa cells without interfering in the peptide-receptor recognition process. Work is in progress in our laboratory to increase the red-shifted properties of COUPY dyes with the aim of using them in ligand-targeted imaging applications such as fluorescence-guided surgery.

This work was supported by funds from the Spanish *Ministerio de Economía y Competitividad* (grants CTQ2014-52658-R and CTQ2017-84779-R). The authors acknowledge helpful assistance of Dr. Francisco Cárdenas (NMR) and Dr. Irene Fernández and Laura Ortiz (MS) from CCiTUB. A.G. was a recipient fellow of the University of Barcelona.

Conflicts of interest

There are no conflicts to declare.

Notes and references

1 (a) M. Srinivasarao, C. V. Galliford and P. S. Low, *Nat. Rev. Drug Discovery.,* 2015, **14**, 203; (b) R. R. Zhang, A. B. Schroeder, J. J. Grudzinski, E. L. Rosenthal, J. M. Warram, A. N. Pinchuk, K. W. Eliceiri, J. S. Kuo and J. P. Weichert, *Nat. Rev. Clin. Oncol.*, 2017, **14**, 347.

2 (a) E. A. Owens, M. Henary, G. El Fakhri and H. Soo Choi, *Acc. Chem. Res.*, 2016, **49**, 1731; (b) Z. Guo, S. Park, J. Yoon and I. Shin, *Chem. Soc. Rev*. 2014, **43**, 16; c) A. Haque, M. S. H. Faizi, J. A. Rather and M. S. Khan, *Bioorg. Med. Chem*., 2017, **25**, 2017.

3 M. Gao, F. Yu, C. Lv, J. Choo and L. Chen, *Chem. Soc. Rev*. 2017, **46**, 2237.

4 (a) D. Birch, M. V. Christensen, D. Staerk, H. Franzyk and H. M. Nielsen, *BBA Biomembranes,* 2017, **1859**, 2483; (b) C. Zhao, A. Fernandez, N. Avlonitis, G. Vande Velde‖, M. Bradley, N. D. Read and M. Vendrell, *ACS Comb. Sci*., 2016, **18**, 689.

5 (a) K. Sato, A. P. Gorka, T. Nagaya, M. S. Michie, Y. Nakamura, R. R. Nani, V. L. Coble, O. V. Vasalatiy, R. E. Swenson, P. L. Choyke, M. J. Schnermann and H. Kobayashi, *Mol. BioSyst*., 2016, **12**, 3046; (b) N. Zhao, T. M. Williams, Z. Zhou, F. R. Fronczek, M. Sibrian-Vazquez, S. D. Jois and M. G. H. Vicente, *Bioconjugate Chem*., 2017, **28**, 1566.

6 (a) A. Gandioso, R. Bresolí-Obach, A. Nin-Hill, M. Bosch, M. Palau, A. Galindo, S. Contreras, A. Rovira, C. Rovira, S. Nonell and V. Marchán, *J. Org. Chem*., 2018, **83**, 1185; (b) A. Gandioso, M. Palau, R. Bresolí-Obach, A. Galindo, A. Rovira, M. Bosch, S. Nonell and V. Marchán, *J. Org. Chem*., 2018, DOI: 10.1021/acs.joc.8b01422.

7 C. J. Pickens S. N. Johnson, M. M. Pressnall, M. A. Leon and C. J. Berkland, *Bioconjugate Chem*., 2018, **29**, 686.

8 (a) G. Mezo and M. Manea, *Expert Opin. Drug Delivery*, 2010, **7**, 79; (b) A. Janecka, M. Zubrzycka and T. Janecki, *J. Pept. Res*., 2001, **58**, 91; (c) J. C. Reubi, *Endocr. Rev*., 2003, **24**, 389.

9 (a) L.-C. Sun and D. H. Coy, *Drugs Future*, 2008, **33**, 217; (b) F. Barragán, D. Carrion-Salip, I. Gómez-Pinto, C. González-Cantó, P. J. Sadler, R. de Llorens, V. Moreno, C. González, A. Massaguer and V. Marchán, *Bioconjugate Chem*., 2012, **23**, 1838; (c) F. Barragan, V. Moreno and V. Marchán, *Chem. Commun*., 2009, 4705.

10 V. Novohradsky, A. Zamora, A. Gandioso, V. Brabec, J. Ruiz and V. Marchán, *Chem. Commun*., 2017, **53**, 5523.

11 (a) A. Gandioso, M. Palau, A. Nin-Hill, I. Melnyk, C. Rovira, S. Nonell, D. Velasco, J. García-Amorós and V. Marchán, *ChemistryOpen,* 2017, **6**, 375; (b) A. Gandioso, S. Contreras, I. Melnyk, J. Oliva, S. Nonell, D. Velasco, J. García-Amorós and V. Marchán, *J. Org. Chem*., 2017, **82**, 5398.

12 V. Castro, H. Rodríguez and F. Albericio, *ACS Comb. Sci*., 2016, **18**, 1.

SUPPORTING INFORMATION

Straightforward solid-phase approaches for labelling targeting peptides with far-red/NIR emitting coumarin fluorophores

Anna Rovira,[a,‡] Albert Gandioso,[a,‡] Marina Goñalons,[a] Alex Galindo,[a] Anna Massaguer,[b] Manel Bosch,[c] and Vicente Marchán*[a]

[a] Secció de Química Orgànica, Departament de Química Inorgànica i Orgànica, Universitat de Barcelona, Martí i Franquès 1-11, E-08028 Barcelona (Spain)

E-mail: vmarchan@ub.edu

Institut de Biomedicina de la Universitat de Barcelona, (IBUB), E-08028, Barcelona, Spain

[b] Departament de Biologia, Universitat de Girona, E-17071 Girona (Spain)

[c] Unitat de Microscòpia Òptica Avançada, Centres Científics i Tecnològics, Universitat de Barcelona, E-08028 Barcelona (Spain)

‡These authors contributed equally to this work.

Table of contents

1.- Materials and Methods.

Unless otherwise stated, common chemicals and solvents (HPLC grade or reagent grade quality) were purchased from commercial sources and used without further purification. Aluminium plates coated with a 0.2 mm thick layer of silica gel 60 F_{254} were used for thin-layer chromatography analyses (TLC), whereas flash column chromatography purification was carried out using silica gel 60 (230-400 mesh). Reversed-phase high-performance liquid chromatography (HPLC) analyses were carried out on a Jupiter Proteo C_{18} column (250x4.6 mm, 90 Å 4 μm, flow rate: 1 mL/min) using linear gradients of 0.045% TFA or 0.1% formic acid in H_2O (A) and 0.036% TFA or 0.1% formic acid in ACN (B). NMR spectra were recorded at 25 ^{o}C in a 400 MHz spectrometer using the deuterated solvent as an internal deuterium lock. Tetramethylsilane (TMS) was used as an internal reference (0 ppm) for ^{1}H spectra recorded in $CDCl_3$ and the residual protic signal of the solvent (77.16 ppm) for ^{13}C spectra. The residual protic signal of methanol and DMSO was used as a reference in ^{1}H and ^{13}C NMR spectra recorded in CD_3OD and DMSO-d_6, respectively. Chemical shifts are reported in part per million (ppm) in the δ scale, coupling constants in Hz and multiplicity as follows: s (singlet), d (doublet), t (triplet), q (quartet), qt (quintuplet), m (multiplet), dd (doublet of doublets), dt (doublet of triplets), ddd (doublet of doublet of doublets), br (broad signal), etc. The proton signals of the *E* and *Z* rotamers were identified by simple inspection of the ^{1}H spectrum and the rotamer ratio was calculated by peak integration. 2D-NOESY spectra were acquired in DMSO-d_6 with mixing times of 300 and 500 ms. The 1D gradient NOE spectra were obtained in a 400 MHz spectrometer using a Gaussian selective pulse and a 0.5 s mixing time with a standard 1D gradient NOE pulse sequence. Electrospray ionization mass spectra (ESI-MS) were recorded on an instrument equipped with single quadrupole detector coupled to an HPLC, high-resolution (HR) ESI-MS on a LC/MS-TOF instrument.

2.- Synthesis and characterization of coumarin derivatives (4-6 and 8) and compounds 9 and 10.

2-(Cyano(1-(2-methoxy-(2-oxoethyl))(4-pyridin-1-ium))methylene)-7-(*N,N*-diethylamino)-4-methyl-coumarin bromide (8)

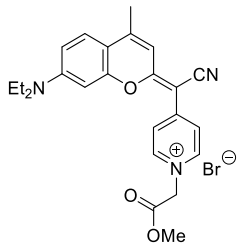

Methyl bromoacetate (140 µL, 1.51 mmol) was added to a solution of coumarin **2**[1] (500 mg, 1.51 mmol) in AcOEt (60 mL). The mixture was stirred for 4 h at 60 ºC under an Ar atmosphere and protected from light. Then, methyl bromoacetate (140 µL, 1.51 mmol) was added again and the reaction mixture was stirred overnight at 60 ºC and protected from light. The crude product was evaporated under reduced pressure and purified by column chromatography (silica gel, 0-8% MeOH in DCM) to give 713 mg of purple solid (yield: 97 %). TLC: R_f (10% MeOH in DCM) 0.55. ^{1}H NMR (400 MHz, DMSO-d_6) δ (ppm): 8.59 (2H, d, J = 7.2 Hz), 8.17 (2H, d, J = 7.2 Hz), 7.70 (1H, d, J = 9.0 Hz), 7.04 (1H, d, J = 2.0 Hz), 6.96 (1H, dd, J = 9.0 Hz, J = 2.8 Hz), 6.89 (1H, s), 5.51 (2H, s), 3.78 (3H, s), 3.56 (4H, q, J = 7.2 Hz), 2.53 (3H, s), 1.18 (6H, t, J = 7.2 Hz). ^{13}C{^{1}H} NMR (101 MHz, DMSO-d_6) δ (ppm): 167.6, 166.8, 154.9, 153.2, 152.1, 149.6, 144.0, 127.0, 120.1, 118.0, 112.1, 110.4, 96.5, 78.2, 58.3, 53.0, 44.2, 18.5, 12.4. HR-ESI MS, positive mode: *m/z* 404.1963 (calcd mass for $C_{24}H_{26}N_3O_3$ $[M]^+$: 404.1969). Analytical HPLC (30 to 100% B in 30 min, formic acid additive: R_t = 7.3 min

2-(Cyano(1-(carboxymethyl)(4-pyridin-1-ium))methylene)-7-(*N,N*-diethylamino)-4-methyl-coumarin bromide (4)

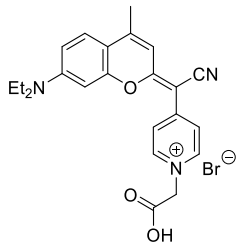

A 1:1 (v/v) mixture of HCl (37 %) and Milli-Q water (170 mL) was added to coumarin **8** (500 mg, 1.03 mmol). The reaction mixture was stirred for 5 h at 60 ºC under an Ar atmosphere and protected from light. After removal of the major part of the solvent, several co-evaporations from acetonitrile were carried out. The crude product was used without further purification

since HPLC-MS analysis revealed that the hydrolysis reaction was quantitative. ^{1}H NMR (400 MHz, DMSO-d_6) δ (ppm): 8.59 (2H, d, J = 7.4 Hz), 8.18 (2H, d, J = 7.4 Hz), 7.72 (1H, d, J = 9.2 Hz), 7.04 (1H, br s), 6.98 (1H, dd, J = 9.2 Hz, J = 2.4 Hz), 6.93 (1H, d, J=2.4 Hz), 5.39 (2H, s), 3.56 (4H, q, J = 7.2 Hz), 2.55 (3H, s), 1.18 (6H, t, J = 7.2 Hz). HR-ESI MS, positive mode: *m/z* 390.1808 (calcd mass for $C_{23}H_{24}N_3O_3$ $[M]^+$: 390.1812). Analytical HPLC (30 to 100% B in 30 min, formic acid additive: R_t = 10.2 min).

_N_-(3-Azidopropyl)-2-bromoacetamide (9)

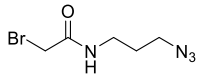

3-Azido-1-propanamine (250 mg, 2.5 mmol) was dissolved in 10 mL of DCM and then 10 mL of saturated aqueous $NaHCO_3$ were added. The mixture was vigorously stirred at -10 ºC and bromoacetyl bromide (1.01 g, 5.0 mmol) was slowly added. The reaction mixture was slowly allowed to warm to room temperature. After stirring for 3 h, the reaction mixture was partially concentrated to remove the organic solvent and then poured into 100 mL of water. The aqueous phase was extracted with AcOEt (2 x 100 mL), and the combined organic phases were washed with saturated $NaHCO_3$ (100 mL), 5 % aqueous HCl solution (100 mL) and saturated NaCl (100 mL). The organic phase was dried over anhydrous Na_2SO_4, filtered and evaporated under reduced pressure. The crude product was purified by column chromatography (silica gel, 0-60 % AcOEt in hexane) to give 364 mg of a pink oil (yield: 66 %). TLC: R_f(hexane/DCM 1:1) 0.5. ^{1}H NMR (400 MHz, $CDCl_3$) δ (ppm): 6.85 (1H, br s), 3.85 (2H, s), 3.37 (4H, m), 1.80 (2H, qt, J = 6.6 Hz). $^{13}C\{^{1}H\}$ NMR (101 MHz, $CDCl_3$) δ (ppm): 165.9, 49.3, 37.9, 29.1, 28.5. HR-ESI MS, positive mode: *m/z* 221.0027 (calcd mass for $C_5H_{10}BrN_4O$ $[M+H]^+$: 221.0033). MS (EI) *m/z* 220 (M^+, 5), 178 (10), 141 (25), 86 (70), 72 (100) (calcd mass for $C_5H_9{}^{79}BrN_4O$ $[M]^+$, 220; calcd mass for $C_5H_9{}^{81}BrN_4O$ $[M]^+$, 222).

2-(Cyano(1-(2-((3-azidopropyl)amino)-2-oxoethyl))(4-pyridin-1-ium))methylene)-7-(*N*,*N*-diethylamino)-4-methyl-coumarin bromide (5)

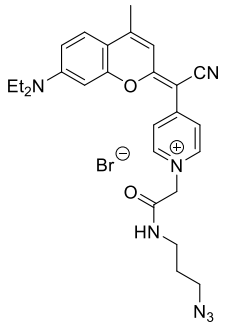

N-(3-Azidopropyl)-2-bromoacetamide (167 mg, 0.75 mmol) was added to a solution of coumarin **2**[1] (250 mg, 0.75 mmol) in a 1:1 mixture of AcOEt and ACN (30 mL), which was previously heated at 50 ºC. After stirring for 2 h at 50 ºC, an additional amount of compound **9** (167 mg, 0.75 mmol) was added and the reaction mixture was stirred for 5 h at 50 ºC. After evaporation under reduced pressure and purification by column chromatography (silica gel, 0-6% MeOH in DCM), 400 mg of a dark purple solid were obtained (yield: 96 %). TLC: R_f (10% MeOH in DCM) 0.45. ^{1}H NMR (400 MHz, DMSO-d_6) δ (ppm): 8.58 (1H, t, J = 5.6 Hz), 8.53 (2H, d, J = 7.4 Hz), 8.16 (2H, d, J = 7.4 Hz), 7.72 (1H, d, J = 9.2 Hz), 7.01 (1H, br s), 6.98 (1H, dd, J = 9.2 Hz, J = 2.4 Hz), 6.93 (1H, s), 5.24 (2H, s), 3.56 (4H, q, J = 7.2 Hz), 3.41 (2H, t, J = 6.8 Hz), 3.21 (2H, q, J = 6.8 Hz), 2.55 (3H, s), 1.71 (2H, qt, J = 6.8 Hz), 1.18 (6H, t, J = 7.2 Hz). ^{13}C{^{1}H} NMR (101 MHz, DMSO-d_6) δ (ppm): 166.8, 165.0, 154.9, 152.8, 152.0, 149.2, 144.2, 127.0, 120.0, 118.2, 111.9, 110.4, 96.4, 78.1, 59.5, 54.9, 48.2, 44.2, 36.3, 28.2, 18.4, 12.3. HR-ESI MS, positive mode: *m/z* 472.2450 (calcd mass for $C_{26}H_{30}N_7O_2$ $[M]^+$: 472.2455). Analytical HPLC (30 to 100% B in 30 min, formic acid additive: R_t = 8.0 min.

2-Bromo-*N*-(prop-2-yn-1-yl)acetamide (10)

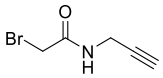

Propargylamine (500 mg, 9.1 mmol) was dissolved in 20 mL of DCM and then 20 mL of saturated aqueous $NaHCO_3$ were added. The mixture was vigorously stirred at -10 ºC and bromoacetyl bromide (3.66 g, 18.2 mmol) was slowly added. The reaction mixture was slowly allowed to warm to room temperature. After stirring for 3 h, the reaction mixture was partially concentrated to remove the organic solvent and then poured into 100 mL of water. The aqueous phase was extracted with AcOEt (2 x 100 mL), and the combined organic phases were washed with saturated $NaHCO_3$ (100 mL), 5 % aqueous HCl solution (100 mL) and saturated NaCl (100 mL). The organic phase was dried over anhydrous Na_2SO_4, filtered and evaporated under

reduced pressure. The crude product was purified by column chromatography (silica gel, 0-60 % AcOEt in hexane) to give 0.87 g of a white solid (yield: 55 %). TLC: R_f (hexane/DCM 1:1) 0.5. ^{1}H NMR (400 MHz, $CDCl_3$) δ (ppm): 6.60 (1H, br s), 3.85 (2H, s), 4.09 (2H, dd, *J* = 5.6 Hz, *J* = 2.4 Hz), 3.90 (2H, s), 2.28 (1H, t, *J* = 2.4 Hz). $^{13}C\{^1H\}$ NMR (101 MHz, $CDCl_3$) δ (ppm): 165.2, 78.6, 72.4, 30.1, 28.8. HR-ESI MS, positive mode: *m/z* 175.9708 (calcd mass for C_5H_7BrNO $[M+H]^+$: 175.9706). MS (EI) *m/z* 175 (M^+, 5), 96 (100), 82 (40), 39 (35) (calcd mass for $C_5H_6{}^{79}BrNO$ $[M]^+$, 175; calcd mass for $C_5H_6{}^{81}BrNO$ $[M]^+$, 177).

2-(Cyano(1-(2-oxo-2-(prop-2-yn-1-ylamino)ethyl))(4-pyridin-1-ium))methylene)-7-(*N*,*N*-diethylamino)-4-methyl-coumarin bromide (6)

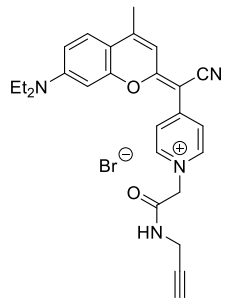

2-Bromo-*N*-(prop-2-yn-1-yl)acetamide (**10**) (42 mg, 0.75 mmol) was added to a solution of coumarin **2**[1] (250 mg, 0.75 mmol) in a 1:1 mixture of AcOEt and ACN (30 mL), which was previously heated at 50 ºC. After stirring for 2 h at 50 ºC, an additional amount of compound **9** (63 mg, 1.12 mmol) was added and the reaction mixture was stirred overnight at 50 ºC. After evaporation under reduced pressure and purification by column chromatography (silica gel, 0-6% MeOH in DCM), 304 mg of a dark purple solid were obtained (yield: 80 %). TLC: R_f (10% MeOH in DCM) 0.60. ^{1}H NMR (400 MHz, DMSO-d_6) δ (ppm): 9.01 (1H, t, *J* = 5.6 Hz), 8.53 (2H, d, *J* = 7.4 Hz), 8.16 (2H, d, *J* = 7.4 Hz), 7.72 (1H, d, *J* = 9.2 Hz), 7.01 (1H, br s), 6.98 (1H, dd, *J* = 9.2 Hz, *J* = 2.4 Hz), 6.93 (1H, s), 5.27 (2H, s), 3.98 (2H, dd, *J* = 5.6 Hz, *J* = 2.4 Hz), 3.57 (4H, q, *J* = 7.2 Hz), 3.23 (1H, t, *J* = 2.4 Hz), 2.55 (3H, s), 1.18 (6H, t, *J* = 7.2 Hz). $^{13}C\{^1H\}$ NMR (101 MHz, DMSO-d_6) δ (ppm): 166.8, 165.0, 154.9, 152.9, 152.0, 149.3, 144.2, 127.0, 120.0, 118.2, 111.9, 110.5, 110.4, 96.4, 80.3, 78.1, 73.8, 59.3, 44.2, 28.4, 18.4, 12.4. HR-ESI MS, positive mode: *m/z* 427.2127 (calcd mass for $C_{26}H_{27}N_4O_2$ $[M]^+$: 427.2129). Analytical HPLC (30 to 100% B in 30 min, formic acid additive: R_t = 7.3 min.

3.- Reversed-phase HPLC analysis of coumarin derivatives 4-6 and 8

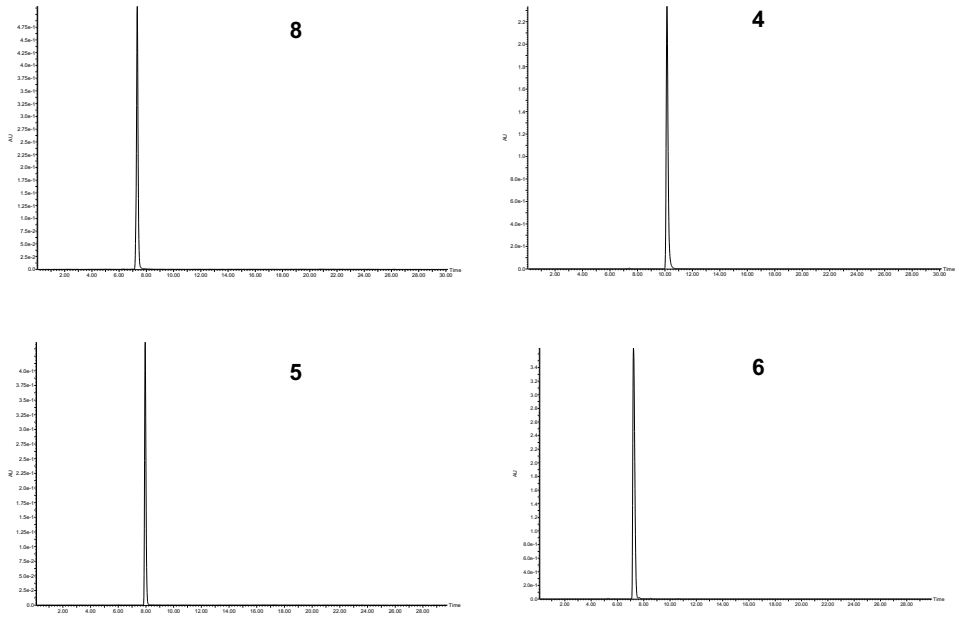

Figure S1. Reversed-phase HPLC traces of coumarins **4-6** and **8**.

4- 2D NMR characterization of coumarin derivatives

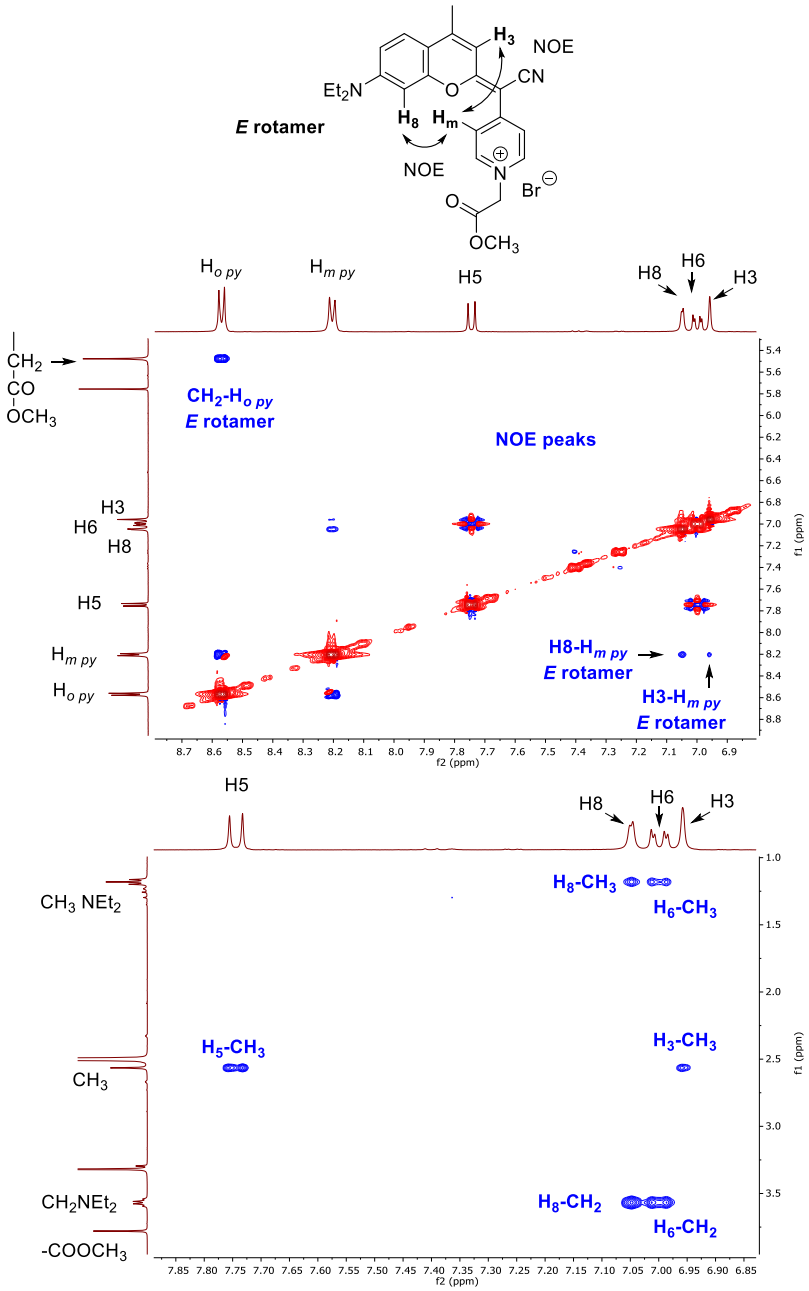

Figure S2. Structure of *E* rotamer of coumarin **8** with some diagnostic NOE cross-peaks indicated, and expansions of the NOESY spectrum (t_m = 500 ms) of **4** in DMSO-d_6 at 298 K.

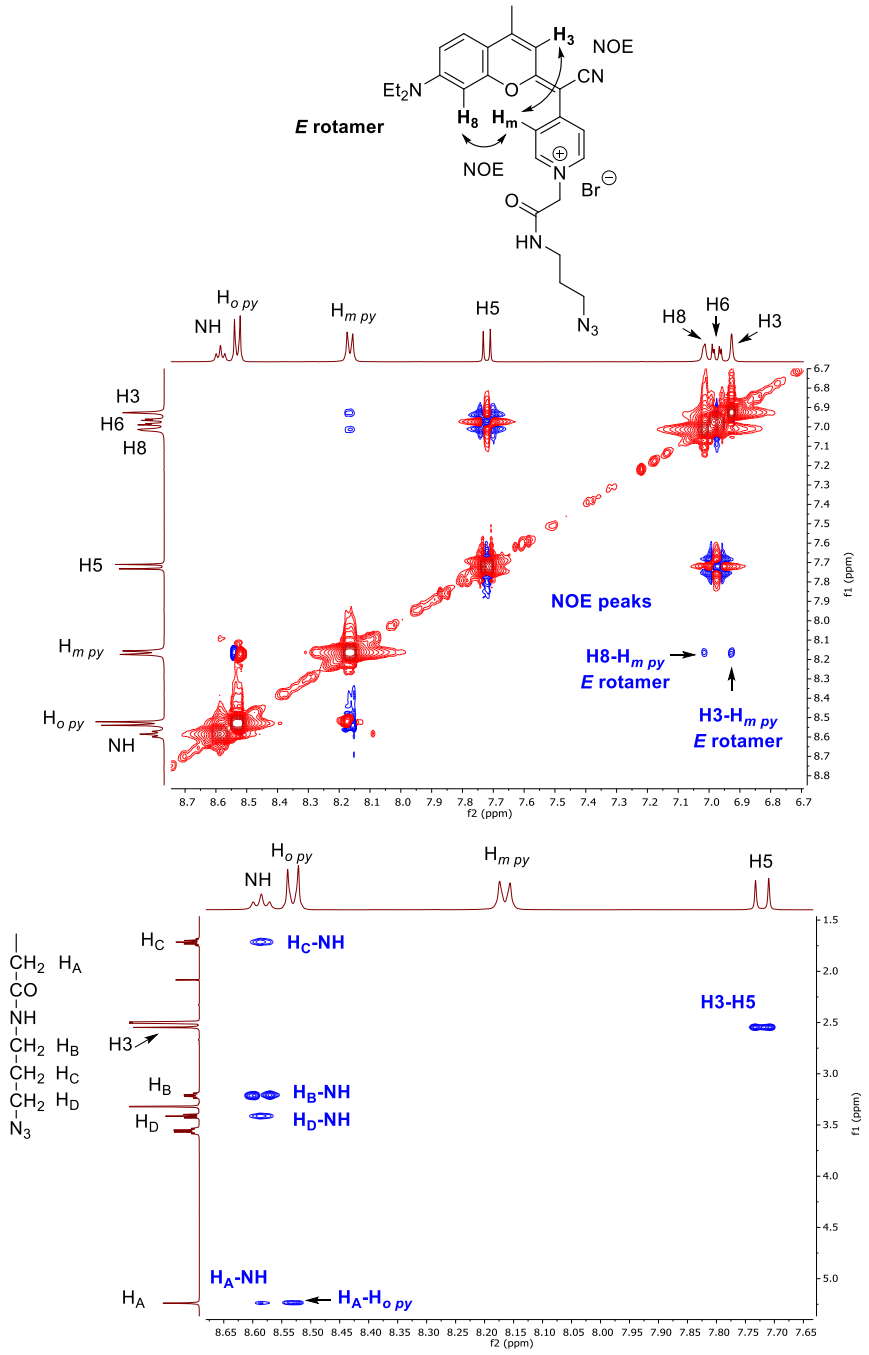

Figure S3. Structure of *E* rotamer of coumarin **5** with some diagnostic NOE cross-peaks indicated, and expansions of the NOESY spectrum (t_m = 500 ms) of **5** in DMSO-d_6 at 298 K.

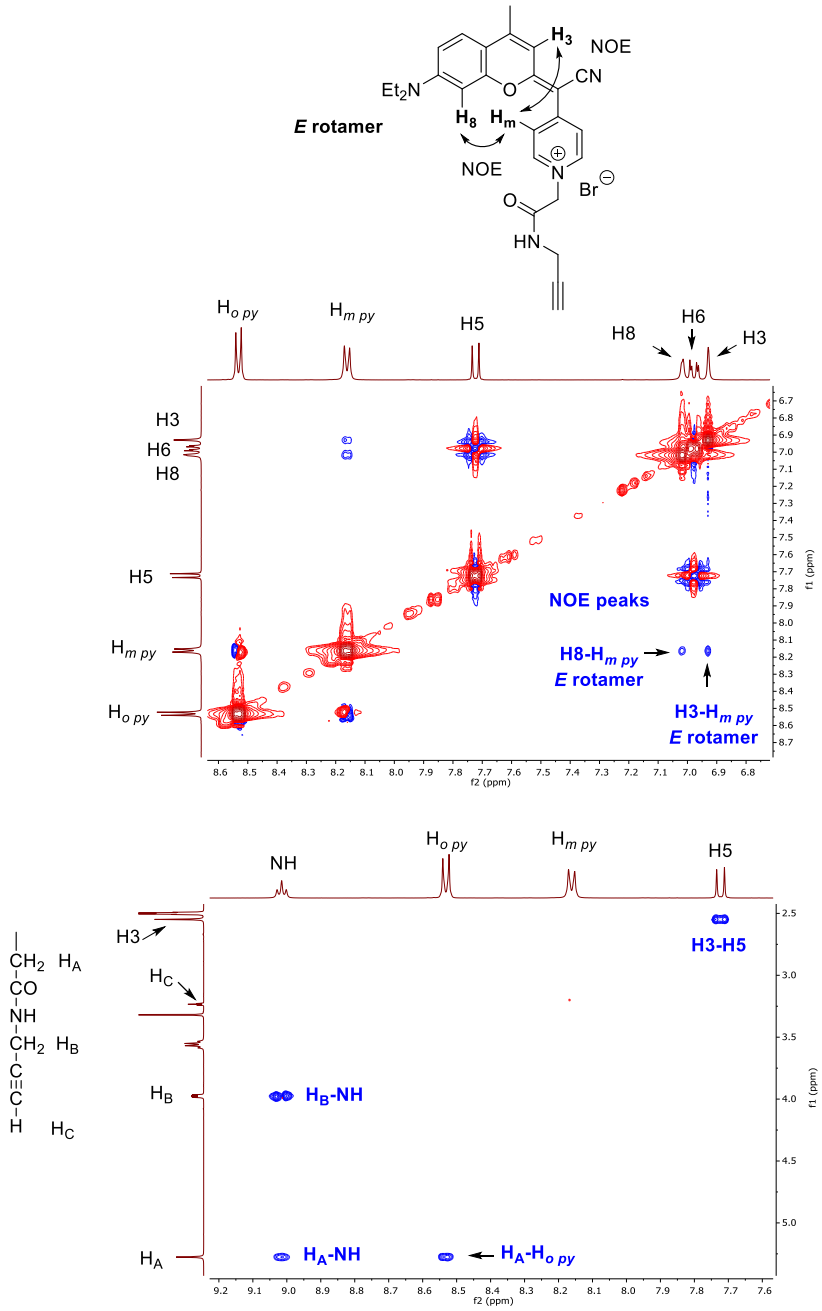

Figure S4. Structure of *E* rotamer of coumarin **6** with some diagnostic NOE cross-peaks indicated, and expansions of the NOESY spectrum (t_m = 500 ms) of **6** in DMSO-d_6 at 298 K.

5.- Synthesis and characterization of COUPY-octreotide conjugates (12, 15 and 16).

5.1. General methods

Fmoc-protected amino acids, resins, and coupling reagents for solid-phase synthesis were obtained from Novabiochem, Bachem, or Iris Biotech. Fmoc-*L*-threoninol *p*-carboxyacetal was synthesized following previously reported procedures.[2] Solid-phase peptide synthesis (SPPS) was performed manually in a polypropylene syringe fitted with a polyethylene disk. Peptides were assembled on a Rink amide resin-*p*-MBHA (f = 0.50 mmol/g, 100−200 mesh) using standard Fmoc/^{t}Bu chemistry with the following side-chain protecting groups: Boc (N^{i}-*tert*-butoxicarbonyl, tryptophan, and N^{ε}-*tert*- butoxycarbonyl, lysine), ^{t}Bu (*O*-*tert*-butyl, threonine), and Trt (*S*-trityl, cysteine).

5.2. Synthesis and characterization of COUPY-octreotide conjugate 12

5.2.1. Octreotide-bound resin 11

*Fmoc-NH-PEG-D-Phe-Cys(Trt)-Phe-D-Trp(Boc)-Lys(Boc)-Thr(tBu)-Cys(Trt)-Thr(ol)-Resin (**11**)*

Octreotide-bound resin **11** was prepared following previously reported procedures.[3] Briefly, the Fmoc-protected *L*-threoninol functionalized as the *p*-carboxybenzaldehyde acetal was anchored to the solid support by using DIPC (3 mol equiv) and HOBt (3 mol equiv) in anhydrous DMF for 3 h and, subsequently, the following Fmoc-protected amino acids as well as the Fmoc-protected PEG spacer, 8-(9-fluorenylmethyloxycarbonyl-amino)-3,6-dioxaoctanoic acid, were incorporated using DIPC (3 mol equiv) and HOAt (3 mol equiv) in anhydrous DMF for 2 h.

5.2.2. COUPY-octreotide conjugate 12

*COUPY-octreotide conjugate (**12**)*

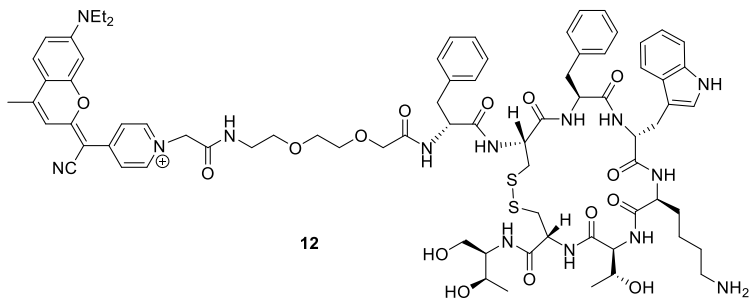

12

After removal of the Fmoc protecting group from peptide-bound resin **11** with 20 % piperidine in DMF (2 x 10 min), coumarin **4** (4 mol equiv.) was coupled by using HATU (3.9 mol equiv.) and DIPEA (2+2 mol equiv.) in anhydrous DMF for 3 h in the dark by using the following

procedure: DIPEA (2 mol equiv.) was first added to a solution of coumarin **4** and HATU in anhydrous DMF and, after stirring for 5 min a RT, the mixture was added to DMF swollen peptide-bound resin **11**; then, DIPEA (2 mol equiv.) was immediately added and the reaction mixture was stirred for 2 h. Cleavage and deprotection of the resulting COUPY-octreotide-bound resin were simultaneously performed by treatment with TFA/H_2O/EDT/TIS 94:2.5:2.5:1 for 2.5 h at RT and protected from light. Most of the TFA was removed by bubbling N_2 into the solution, and the resulting residue was poured onto cold diethyl ether to precipitate the target compound. The solid was isolated by centrifugation, dissolved in H_2O/ACN (9:1) and lyophilized. Cyclisation was accomplished after continuously stirring an aerated solution of the crude material in a 97:3 (v/v) mixture of aqueous NH_4HCO_3 (5%) pH 7-8 and DMSO overnight at RT (1 mL solution per 1 mg of theoretical peptide). As shown in Figure S5, analytical reversed-phase HPLC-MS analysis (10 to 70% B in 30 min, 0.1 % formic acid additive) revealed the presence of a main peak that was characterized as the expected COUPY-octreotide conjugate **12** (R_t = 15.6 min). The solution was lyophilized and the conjugate purified by semipreparative RP-HPLC (gradient from 45 to 70% B in 30 min, A: 0.045 % TFA in H_2O, B: 0.1% TFA in ACN, flow rate: 3 mL/min, R_t = 6 min). Overall yield (synthesis + purification): 2.35 mg of a purple solid (from 27 mg of resin **11**), 12%. HR ESI MS, positive mode: *m/z* 1535.6844 (calcd mass for $C_{78}H_{99}N_{14}O_{15}S_2$ $[M]^+$: 1535.6850), *m/z* 768.3469 (calcd mass for $C_{78}H_{100}N_{14}O_{15}S_2$ $[M+H]^{2+}$: 768.3462). Analytical RP-HPLC (10 to 70% B in 30 min; A, 0.1% formic acid in H_2O; B, 0.1% formic acid in ACN; R_t = 15.6 min).

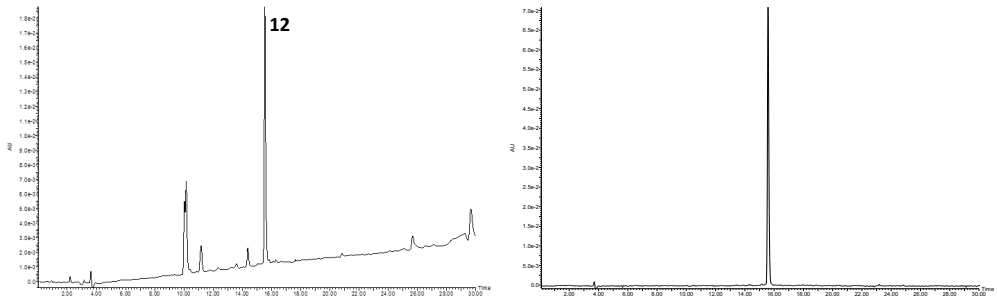

Figure S5. Reversed-phase HPLC traces for COUPY-octreotide conjugate **12**: reaction crude (left) and purified (right).

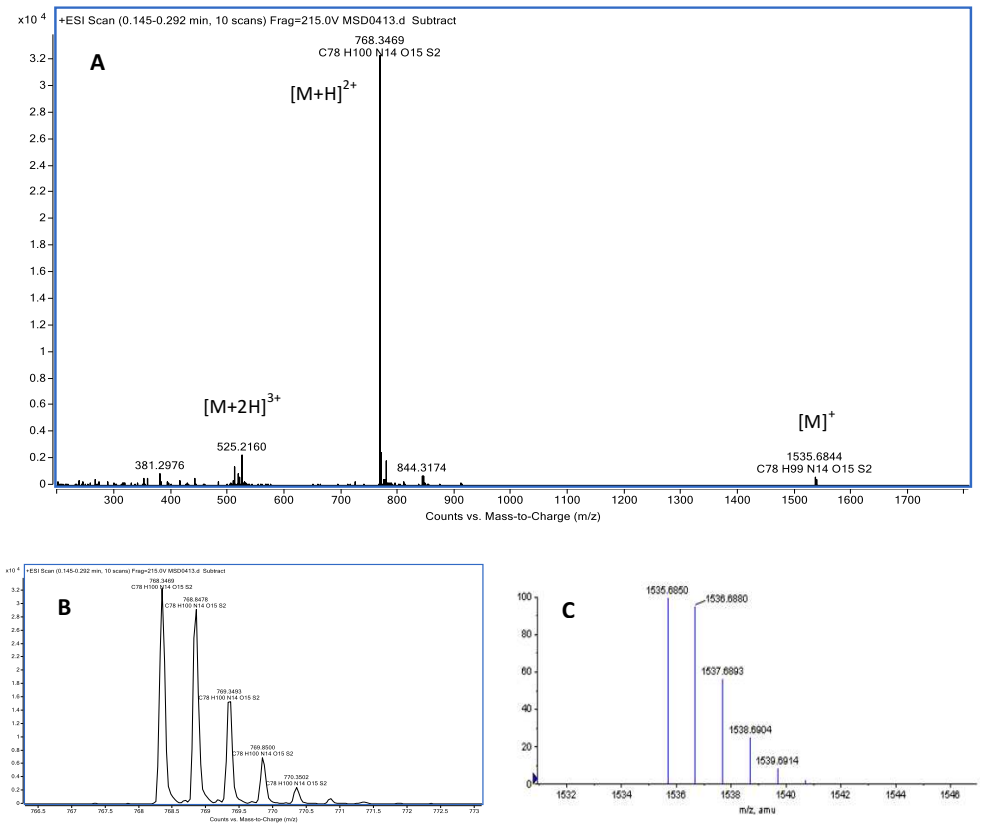

Figure S6. High resolution ESI MS of COUPY-octreotide conjugate **12**: experimental (A, B) and calculated (C).

5.2.3.Stabilty of COUPY-octreotide conjugate 12 in cell medium

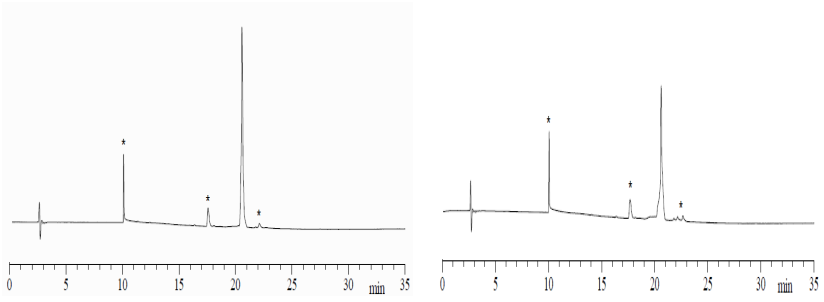

Figure S7. Reversed-phase HPLC traces for COUPY-octreotide conjugate **12** in DMEM-10% FBS at t=0 (left) and after incubation at 37 ºC for 24 h (right). *peaks from the cell medium.

5.2.4. Cytotoxicity studies with conjugate 12

The effect of COUPY-octreotide conjugate **12** in the cell viability was determined by the MTT assay. HeLa cells were seeded onto 96-well plates at a density of 2200 cells per well and allowed to attach for 48 hours. Conjugate **12** was dissolved in DMSO (5%) and Milli-Q water and to obtain the stock solution. Then, the cells were incubated with conjugate **12** diluted in culture medium at concentrations ranging from 0 µM to 100 µM. In parallel, the cells were incubated with the vehicle alone diluted in culture medium at the same concentrations, as control. After 48 h of treatment at 36ºC, the cells were washed with PBS and incubated for 2 additional hours with 100 µL of culture medium together with 10 µL of MTT (Sigma-Aldrich, St. Louis, MO). The medium was discarded and DMSO (Sigma-Aldrich) was added to each well to dissolve the purple formazan crystals. Plates were agitated at room temperature for 10 minutes and the absorbance of each well was determined on a Multiscan Plate Reader (Synergy 4, Biotek, Winooski, USA) at a wavelength of 570 nm. The percentage of viable cells was established by dividing their mean absorbance by the mean absorbance of cells treated with the vehicle alone. Three replicates for each concentration were used, in in three independent experiments.

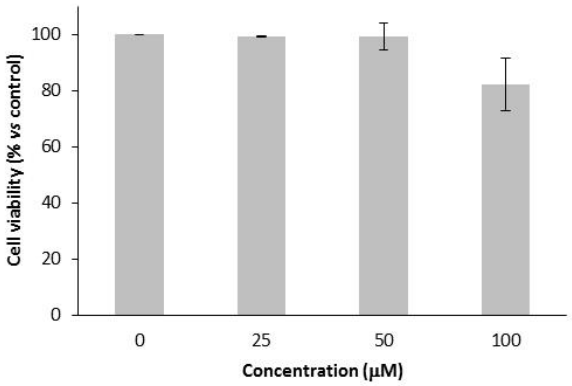

Figure S8. Effect of COUPY-octreotide conjugate **12** in the viability of HeLa cells. Cells were treated for 48 h with the indicated concentrations of each compound and the cell viability was determined by the MTT assay. Each point in the graphs represents the mean of three experiments ± SD.

5.3. Synthesis and characterization of COUPY-octreotide conjugates 15 and 16

5.3.1. Octreotide-bound resins 13 and 14

*Alkynyl-PEG-D-Phe-Cys(Trt)-Phe-D-Trp(Boc)-Lys(Boc)-Thr(tBu)-Cys(Trt)-Thr(ol)-Resin (**13**)*

After removal of the Fmoc protecting group from the peptide-bound resin **11** with 20 % piperidine in DMF (2 x 10 min), 4-pentynoic acid (5 mol equiv.) was coupled by using DIPC (5 mol equiv.) and HOAt (5 mol equiv.) in anhydrous DMF for 2 h. Cleavage and deprotection of an aliquot of the resulting octreotide-bound resin **13** was performed by treatment with TFA/H_2O/EDT/TIS 94:2.5:2.5:1 for 2.5 h. After evaporation of TFA by bubbling with N_2, the crude peptide was precipitated with cold diethyl ether. As shown in Figure S9, reversed-phase HPLC-MS analysis showed the presence of two peaks that were characterized as the linear alkynyl-octreotide (R_t = 15.2 min) and the corresponding disulfide cyclized alkynyl-octreotide (R_t = 14.8 min).

Linear alkynyl-octreotide: LR-ESI MS, positive mode: *m/z* 1246.54 (calcd mass for $C_{60}H_{84}N_{11}O_{14}S_2$ $[M+H]^+$: 1246.56). Analytical HPLC (10 to 70% B in 30 min, 0.1 % formic acid additive: R_t = 15.2 min.

Disulfide cyclized alkynyl-octreotide: LR-ESI MS, positive mode: *m/z* 1244.71 (calcd mass for $C_{60}H_{82}N_{11}O_{14}S_2$ $[M+H]^+$: 1244.55). Analytical HPLC (10 to 70% B in 30 min, 0.1 % formic acid additive: R_t = 14.7 min.

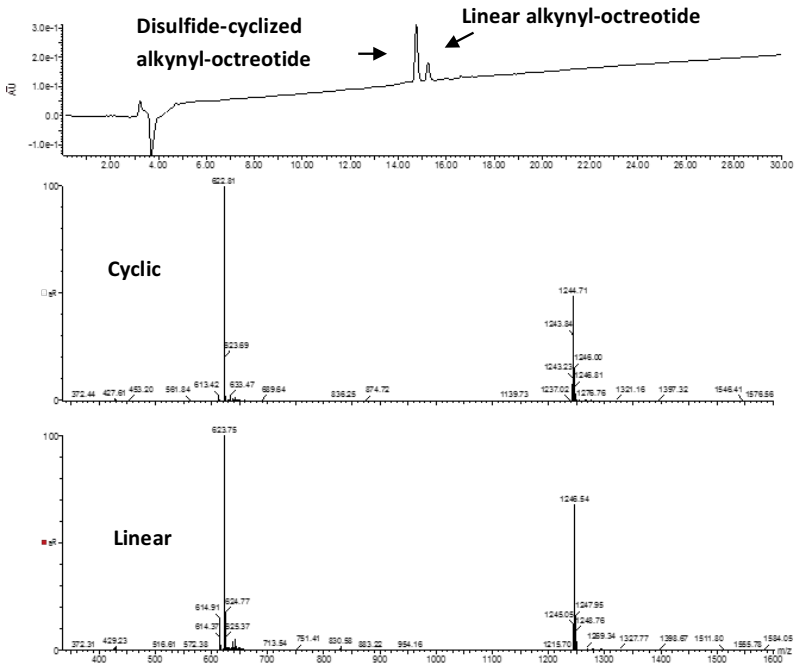

Figure S9. Reversed-phase HPLC traces of the crude mixture after cleavage and deprotection of peptide-bound resin **13**.

*Azido-PEG-D-Phe-Cys(Trt)-Phe-D-Trp(Boc)-Lys(Boc)-Thr(tBu)-Cys(Trt)-Thr(ol)-Resin (**14**)*

After removal of the Fmoc protecting group from the peptide-bound resin **11** with 20 % piperidine in DMF (2 x 10 min), 2-azidoacetic acid (5 mol equiv.) was coupled by using DIPC (5 mol equiv.) and HOAt (5 mol equiv.) in anhydrous DMF for 2 h. Cleavage and deprotection of an aliquot of the resulting octreotide-bound resin **14** was performed by treatment with TFA/H_2O/EDT/TIS 94:2.5:2.5:1 for 2.5 h. After evaporation of TFA by bubbling with N_2, the crude peptide was precipitated with cold diethyl ether. As shown in Figure S10, reversed-phase HPLC-MS analysis showed the presence of two peaks that were characterized as the linear azido-octreotide (R_t = 15.2 min) and the corresponding disulfide cyclized azido-octreotide (R_t = 14.7 min).

Linear azido-octreotide: LR-ESI MS, positive mode: *m/z* 1249.50 (calcd mass for $C_{57}H_{81}N_{14}O_4S_2$ $[M+H]^+$: 1249.55). Analytical HPLC (10 to 70% B in 30 min, 0.1 % formic acid additive: R_t = 15.2 min.

Disulfide cyclized azido-octreotide: LR-ESI MS, positive mode: *m/z* 1247.48 (calcd mass for $C_{57}H_{79}N_{14}O_4S_2$ $[M+H]^+$: 1247.53). Analytical HPLC (10 to 70% B in 30 min, 0.1 % formic acid additive: R_t = 14.7 min.

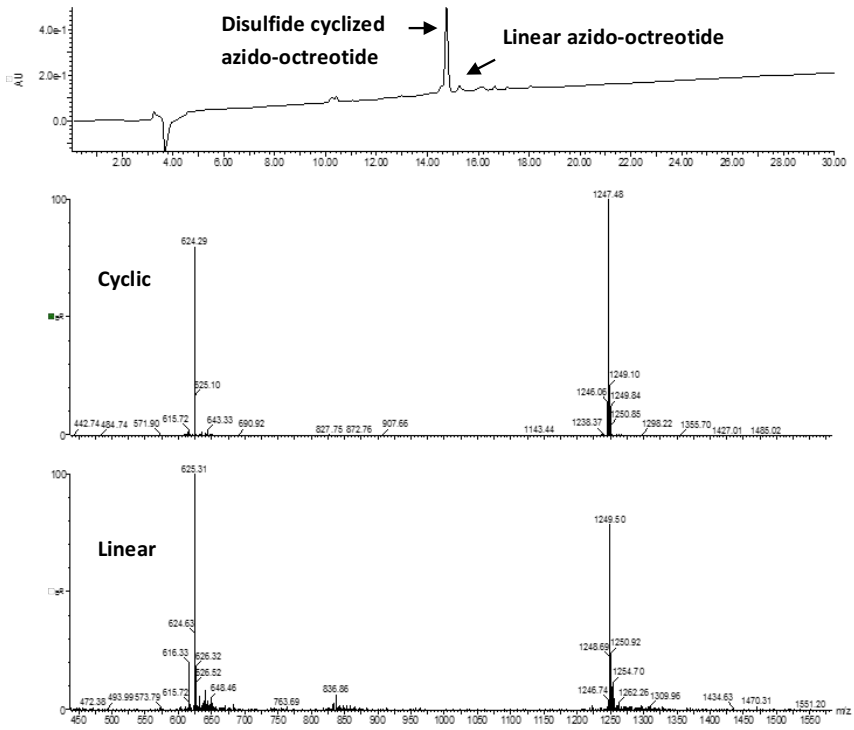

Figure S10. Reversed-phase HPLC traces of the crude mixture after cleavage and deprotection of peptide-bound resin **14**.

5.3.2. COUPY-octreotide conjugates 15 and 16

*COUPY-octreotide conjugate (**15**)*

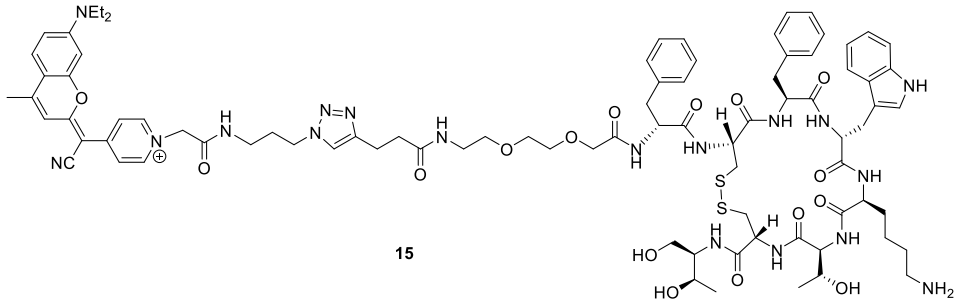

15

After removal of the Fmoc protecting group from alkynyl-peptide-bound resin **13** with 20 % piperidine in DMF (2 x 10 min), 5 mg of the resin were transferred to a 2 mL reaction vial with a magnetic stirrer. Afterwards, a solution of azido-coumarin **5** (4.2 mg, 3 mol equiv.), $CuSO_4$ (1.2 mg, 3 mol equiv.) and sodium ascorbate (1.5 mg, 3 mol equiv.) in 800 µL DMF/H_20 20:1 (v/v) was immediately added to the vial. The suspension was allowed to stir at room temperature for 1 h, 4 or overnight under argon atmosphere in the dark. Then, the resin was filtered off and washed with DMF, DCM and MeOH (5,5,5 x 4 mL). Cleavage, deprotection and cyclisation were carried out as described above for conjugate **12**. As shown in Figure S9, analytical reversed-phase HPLC-MS analysis (10 to 70% B in 30 min, 0.1 % formic acid additive) revealed the presence of a main peak in the three cases that was characterized as the expected COUPY-octreotide conjugate **15** (R_t = 15.4 min). The solution was lyophilized and the conjugate purified by semipreparative RP-HPLC (gradient from 45 to 100% B in 30 min, A: 0.1 % TFA in H_2O, B: 0.1% TFA in ACN, flow rate: 3 mL/min, R_t = 6.5 min). Overall yield (synthesis + purification): 5.23 mg of a purple solid (from 15 mg of resin **13**), 32%. HR ESI MS, positive mode: *m/z* 1715.7912 (calcd mass for $C_{86}H_{111}N_{18}O_{16}S_2$ $[M]^+$: 1715.7861), *m/z* 858.3973 (calcd mass for $C_{86}H_{112}N_{18}O_{16}S_2$ $[M+H]^{2+}$: 858.3970). Analytical RP-HPLC (10 to 70% B in 30 min; A, 0.1% formic acid in H_2O; B, 0.1% formic acid in ACN; R_t = 15.4 min).

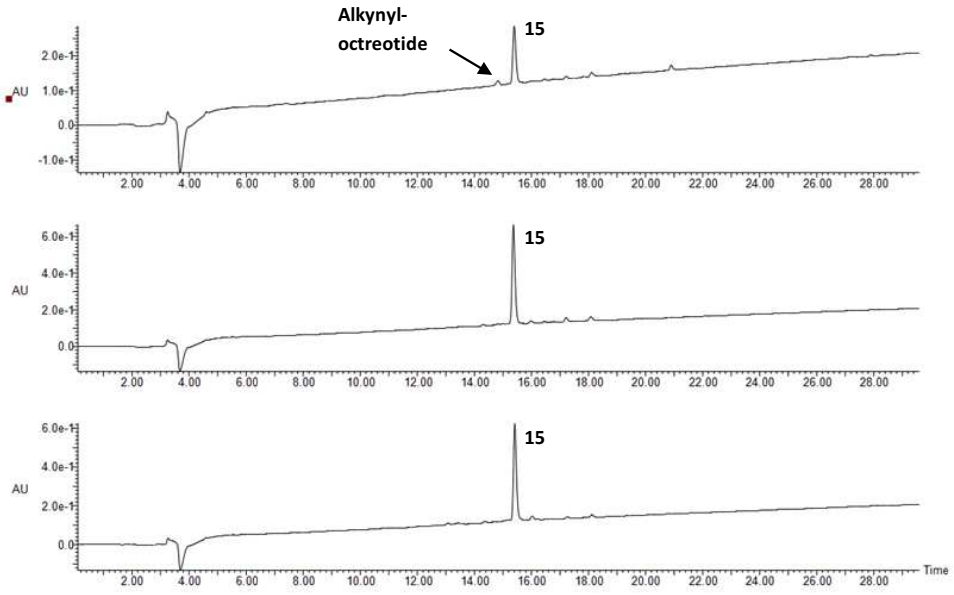

Figure S11. Reversed-phase HPLC traces for click chemistry studies between azido-coumarin **5** and alkynyl-peptide-bound resin **13**. From top to bottom: click chemistry crudes at different reaction times (1 h, 4 h or overnight) after cleavage, deprotection and cyclization.

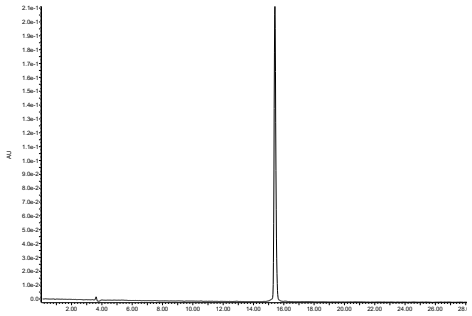

Figure S12. Reversed-phase HPLC analysis of purified COUPY-octreotide conjugate **15**.

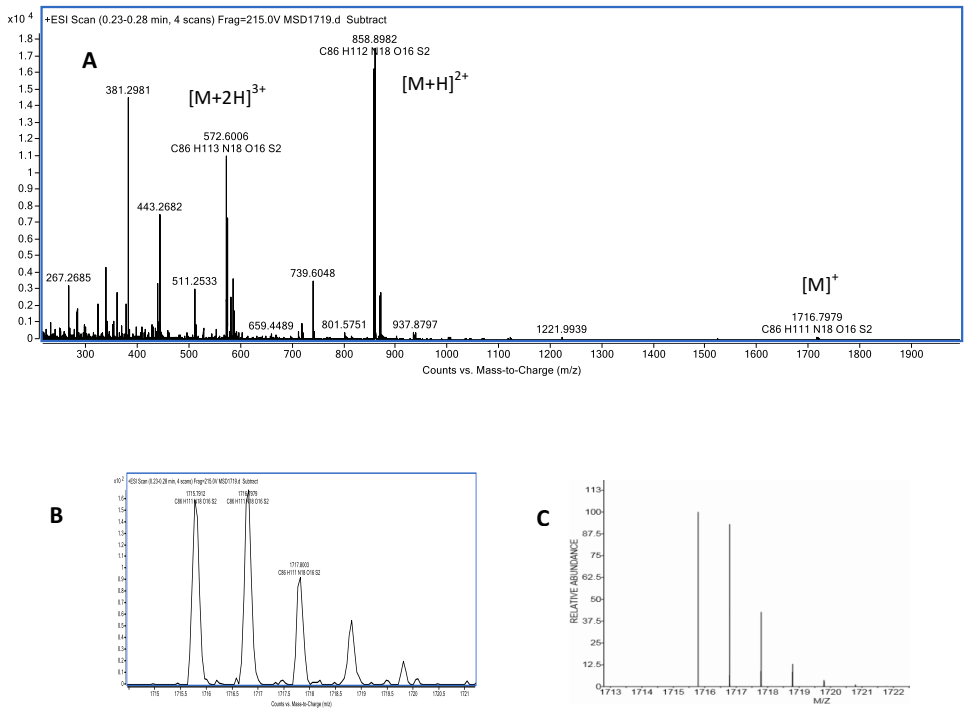

Figure S13. High resolution ESI MS of COUPY-octreotide conjugate **15**: experimental (A, B) and calculated (C).

*COUPY-octreotide conjugate (**16**)*

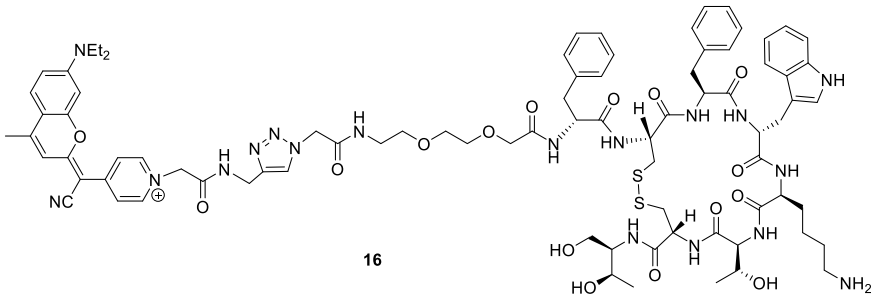

16

After removal of the Fmoc protecting group from azido-peptide-bound resin **14** with 20 % piperidine in DMF (2 x 10 min), 5 mg of the resin were transferred to a 2 mL reaction vial with a magnetic stirrer. Afterwards, a solution of alkynyl-coumarin **6** (3.8 mg, 3 mol equiv.), $CuSO_4$.(1.2 mg, 3 mol equiv.) and sodium ascorbate (1.5 mg, 3 mol equiv.) in 800 µL DMF/$H_2$0 20:1 (v/v) was immediately added to the vial. The suspension was allowed to stir at room temperature for 1 h, 4 or overnight under argon atmosphere in the dark. Then, the resin was filtered off and washed with DMF, DCM and MeOH (5,5,5 x 4 mL). Cleavage, deprotection and cyclisation were carried out as described above for conjugate **12**. As shown in Figure S11, analytical reversed-phase HPLC-MS analysis (10 to 70% B in 30 min, 0.1 % formic acid additive) revealed the presence of a main peak in the three cases that was characterized as the expected COUPY-octreotide conjugate **16** (R_t = 15.3 min). The solution was lyophilized and the conjugate purified by semipreparative RP-HPLC (gradient from 45 to 100% B in 30 min, A: 0.1 % TFA in H_2O, B: 0.1% TFA in ACN, flow rate: 3 mL/min, R_t = 6.5 min). Overall yield (synthesis + purification): 5.23 mg of a purple solid (from 20 mg of resin **14**), 13%. HR ESI MS, positive mode: *m/z* 1673.7388 (calcd mass for $C_{83}H_{105}N_{18}O_{16}S_2$ $[M]^+$: 1673.7392), *m/z* 837.3735 (calcd mass for $C_{83}H_{106}N_{18}O_{16}S_2$ $[M+H]^{2+}$: 837.37.5). Analytical RP-HPLC (10 to 70% B in 30 min; A, 0.1% formic acid in H_2O; B, 0.1% formic acid in ACN; R_t = 15.3 min).

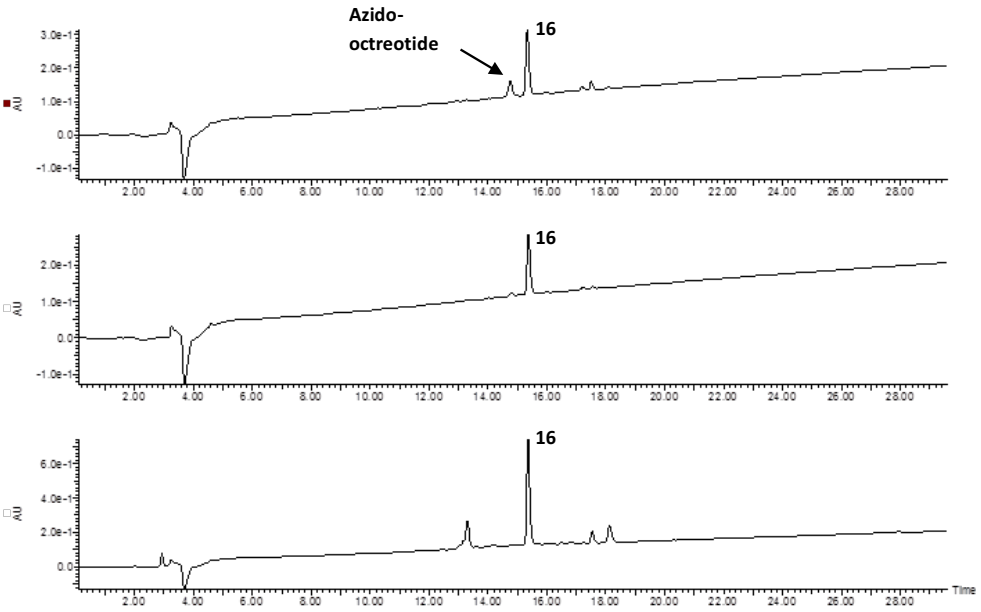

Figure S14. Reversed-phase HPLC traces for click chemistry studies between alkynyl-coumarin **6** and azide-peptide-bound resin **14**. From top to bottom: click chemistry crudes at different reaction times (1 h, 4 h or overnight) after cleavage, deprotection and cyclization.

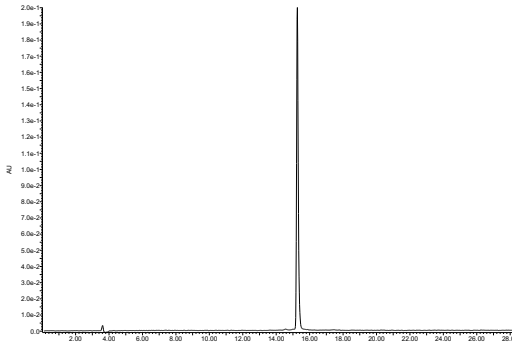

Figure S15. Reversed-phase HPLC analysis of purified COUPY-octreotide conjugate **16**.

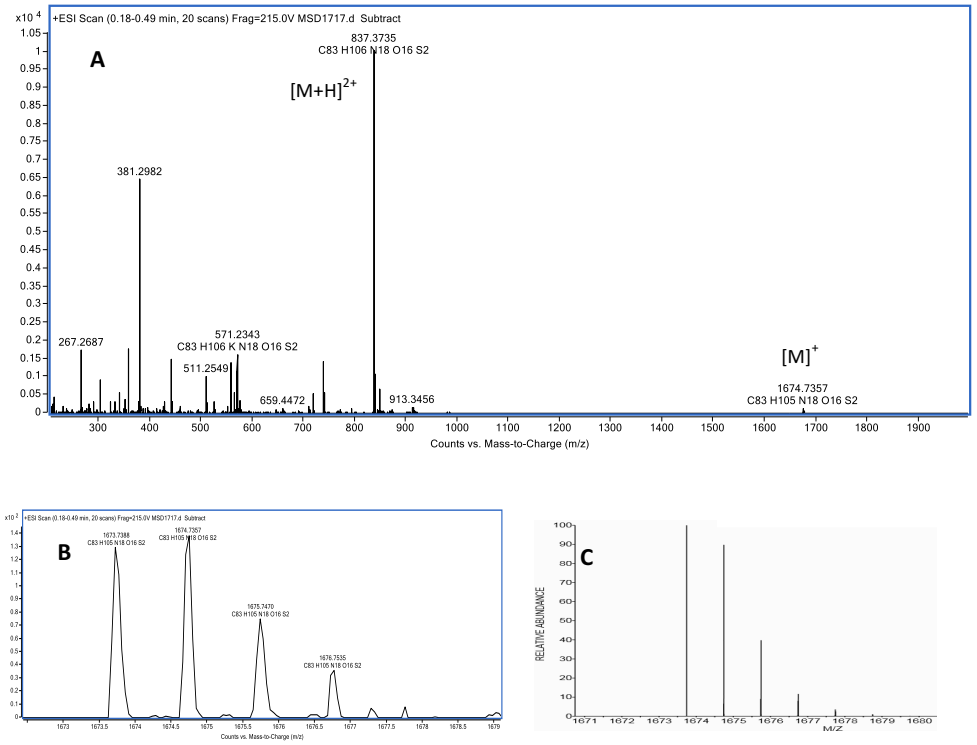

Figure S16. High resolution ESI MS of COUPY-octreotide conjugate **16**: experimental (A, B) and calculated (C).

6.- Photophysical characterization of COUPY dyes (3, 5, 6 and 8) and COUPY-octreotide conjugates (12, 15-16).

Absorption spectra were recorded in a Varian Cary 500 UV/Vis/NIR spectrophotometer at room temperature. Molar absorption coefficients (ε) were determined by direct application of the Beer-Lambert law, using solutions of the compounds in each solvent with concentrations ranging from 10^{-6} to 10^{-5} M. Emission spectra were registered in a Photon Technology International (PTI) fluorimeter. Fluorescence quantum yields (Φ_F) were measured by comparative method using cresyl violet in ethanol (CV; $\Phi_{F;Ref}$ = 0.54 ± 0.03) as reference.[4] Then, optically-matched solutions of the compounds and CV were excited and the fluorescence spectra was recorded. The absorbance of sample and reference solutions was set below 0.1 at the excitation wavelength and Φ_F were calculated using the following equation (1):

$$\phi_{F;Sample} = \frac{Area_{Sample}}{Area_{Ref}} x \left(\frac{\eta_{Sample}}{\eta_{Ref}}\right)^2 x\, \phi_{F;ref} \quad (1)$$

where $Area_{Sample}$ and $Area_{Ref}$ are the integrated fluorescence for the sample and the reference and η_{Sample} and η_{Ref} are the refractive index of sample and reference solutions respectively. The uncertainty in the experimental value of Φ_F has been estimated to be approximately 10%.

Table S1. Photophysical properties of COUPY dyes (**3**, **5**, **6** and **8**) and COUPY-octreotide conjugates (**12**, **15-16**) in PBS buffer and in H_2O. The data for coumarin derivative **3** has been included for comparison purposes.[1]

	Solvent	λ_{abs} (nm)	λ_{em} (nm)	Stokes shift (nm)	ε ($mM^{-1}cm^{-1}$)	ϕ_F
Coumarin **3**	PBS	543	603	60	34	0.14
	H_2O	543	605	62	31	0.15
Coumarin **8**	PBS	554	615	61	48	0.044
	H_2O	555	615	60	48	0.043
Coumarin **5**	PBS	554	616	62	47	0.063
	H_2O	555	615	60	50	0.066
Coumarin **6**	PBS	553	615	62	45	0.045
	H_2O	555	615	60	46	0.061
Conjugate **12**	PBS	561	620	59	24	0.14
	H_2O	561	618	57	27	0.17
Conjugate **15**	PBS	559	620	61	32	0.18
	H_2O	560	618	58	36	0.19
Conjugate **16**	PBS	559	618	59	26	0.14
	H_2O	560	618	58	30	0.19

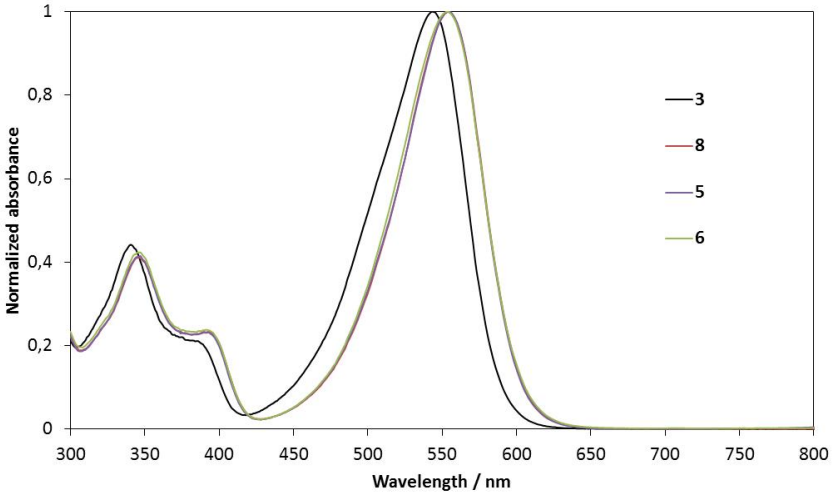

Figure S17. Normalized absorption spectra of coumarins **3**, **5-6** and **8** in PBS buffer.

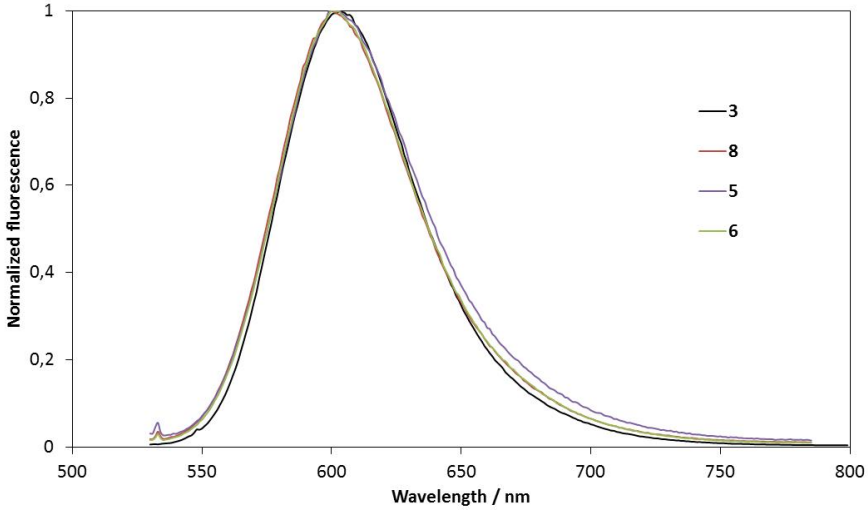

Figure S18. Normalized emission spectra of coumarins **3**, **5-6** and **8** in PBS buffer.

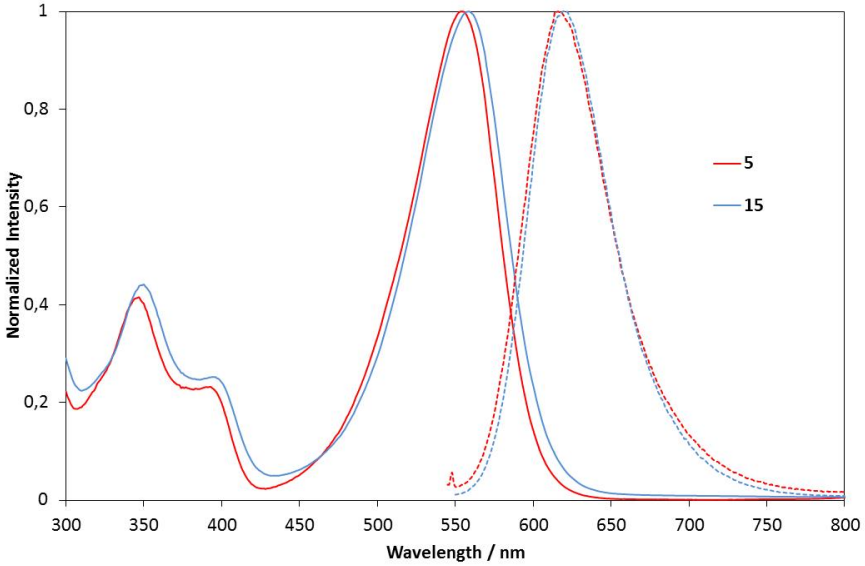

Figure S19. Comparison of the normalized absorption (solid lines) and fluorescence emission (dotted lines) spectra of coumarin **5** and conjugate **15**.

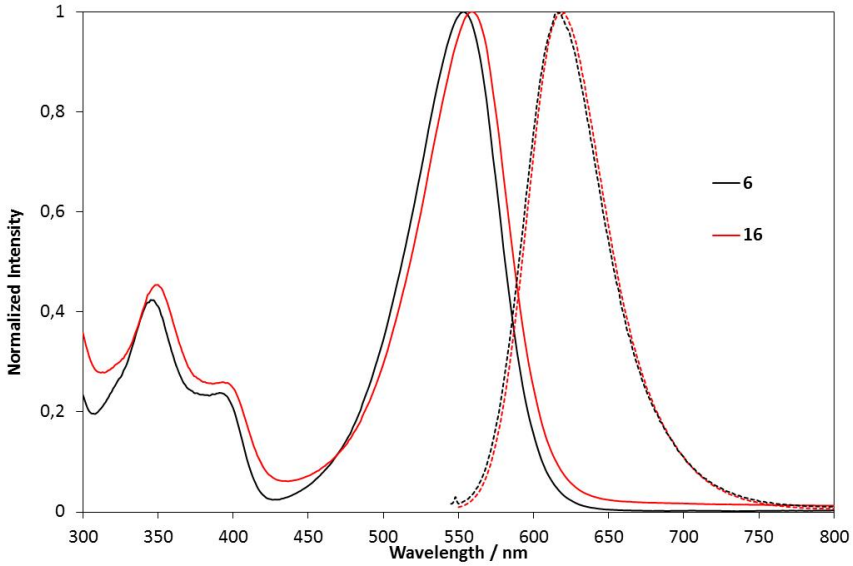

Figure S20. Comparison of the normalized absorption (solid lines) and fluorescence emission (dotted lines) spectra of coumarin **6** and conjugate **16**.

7.- Synthesis and characterization of Atto-Rho12-octreotide conjugate (17).

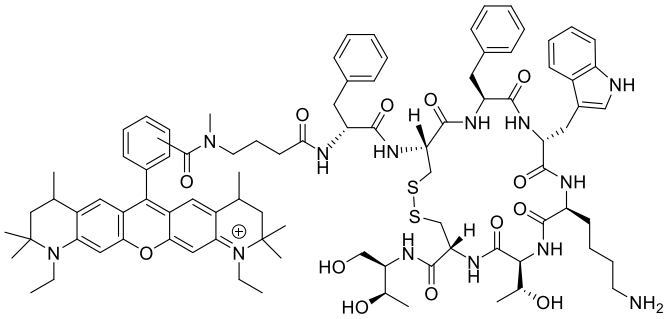

17

Octreotide acetate (Bachem; 1 mg, 0.98 µmol) was allowed to react with Atto Rho12-hexanoic acid *N*-hydroxysuccinimide ester (ATTO Tech; 1 mg, 1.18 µmol) in an aqueous hydrogencarbonate buffer (100 mM, pH 7.5) for 3 h and protected from light. The solution was lyophilized and Atto-Rho12-octreotide conjugate (**17**) was purified by analytical RP-HPLC (gradient from 30 to 100 % in 30 min; A: 0.1 % formic acid in H_2O, B: 0.1% formic acid in ACN, flow rate: 1 mL/min, R_t = 16.7 min). Overall yield (synthesis + purification): 0.4 mg of a pink solid, 25%. Characterization: LR ESI MS, positive mode: *m/z* 1651.65 (calcd mass for $C_{90}H_{116}N_{13}O_{13}S_2^+$: 1650.82).

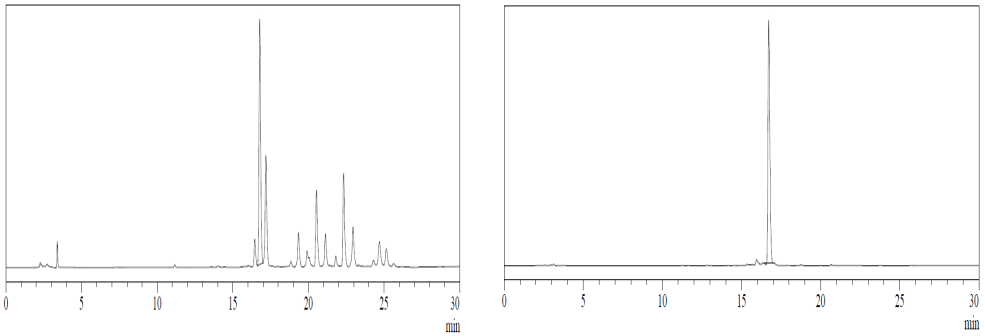

Figure S21. Reversed-phase HPLC traces for Atho Rho12-octreotide conjugate **17**: reaction crude (left) and purified (right).

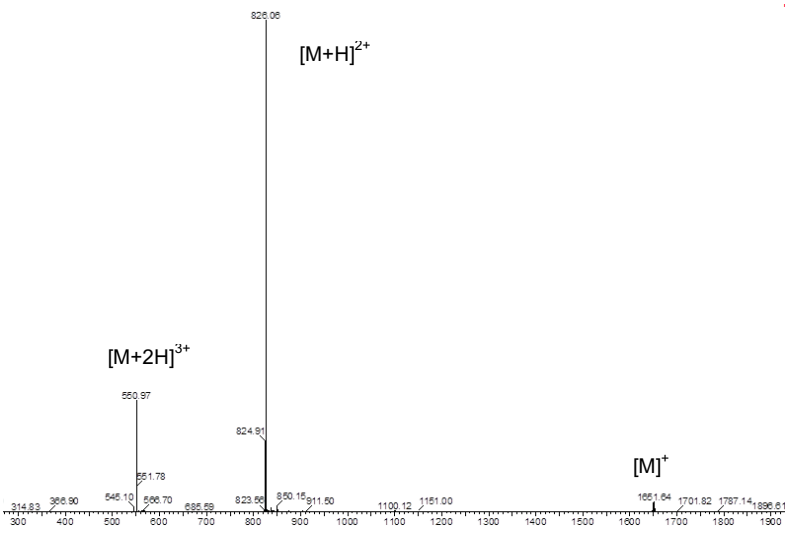

Figure S22. Low resolution ESI MS of Atto Rho12-octreotide conjugate **17**.

8.- Fluorescence imaging

8.1. Cell culture and treatments

HeLa Cells were maintained in DMEM (Dullbecco Modified Eagle Medium) containing low glucose (1 g/L) and supplemented with 10% foetal calf serum (FCS), 50U/mL penicillin-streptomycin and 2 mM *L*-glutamine. For cellular uptake experiments and posterior observation under the microscope, cells were seeded on glass bottom dishes (P35G-1.5-14-C, Mattek). 24 h after cell seeding, cells were incubated for 30 min or 1 h at 37 ºC with coumarin **3** (0.5 μM), COUPY-octreotide **12** (10 μM), Atto Rho12-octreotide **17** (10 μM) or Fluorescein-octreotide **18** (50 μM) in supplemented DMEM. Then, cells were washed three times with DPBS (Dulbecco's Phosphate-Buffered Saline) to remove the excess of the compounds and kept in low glucose DMEM without phenol red for fluorescence imaging. Unless otherwise stated, no fixation was carried out.

8.2. Fluorescence imaging

All microscopy observations were performed using a Zeiss LSM 880 confocal microscope equipped with a 405 nm laser diode, an Argon-ion laser, a 561 nm laser and a 633 nm laser. The microscope was also equipped with a full enclosure imaging chamber (XLmulti S1, Pecon) connected to a 37 ºC heater and a 5% CO_2 providing system. Cells were observed using a 63X 1.2 multi immersion objective. Compounds **3**, **12** and **17** were excited using the 561 nm laser and detected from 570 to 670 nm. Compound **18** was observed using the 488 nm laser line of the Argon-ion laser. Image analysis was performed using Fiji.[5] Unless otherwise stated images are colorized using Fire lookup table.

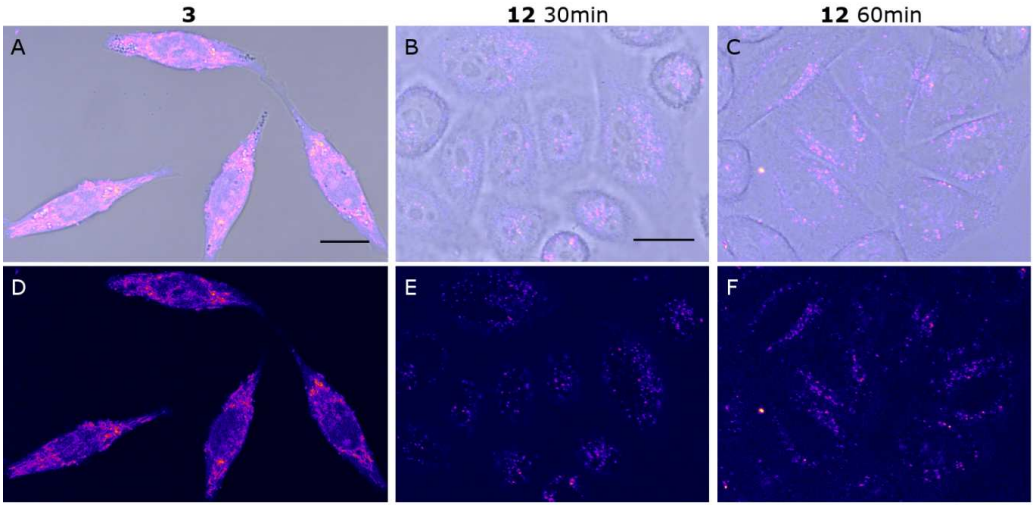

Figure S23. Comparison of the cellular uptake of coumarin **3** and COUPY-octreotide conjugate **12**. Single confocal planes of HeLa cells incubated with **3** at 1 µM for 30 min at 37 °C (A and D) and **12** at 10 µM for 30 min (B and E) or 60 min (C and F) at 37 °C. The compounds were excited at 561 nm and emission detected from 570 to 670 nm. (A-C) Fluorescence images merged with bright field images. (D-F) Fluorescence images only. All fluorescence images are color coded using the Fire lookup table from Fiji. Scale bar: 20 µm. D same scale as A. C,E,F same scale as B.

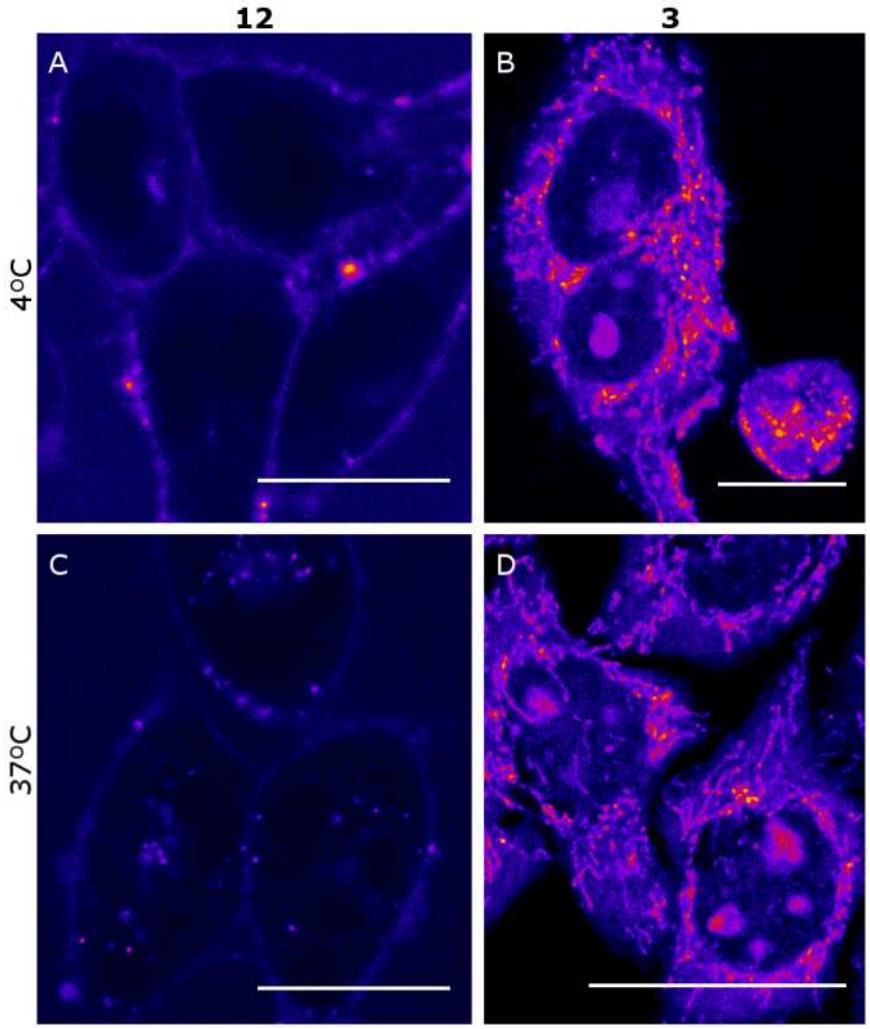

Figure S24. Comparison of the cellular uptake of COUPY-octreotide conjugate **12** and COUPY dye **3**. Single confocal planes of HeLa cells incubated with **12** (A and C) and **3** (B and D) at 10 μM or 0.5 μM, respectively, first at 4 °C for 30 min (A and B) and then incubated at 37 °C for additional 30 min (C and D). The compounds were excited at 561 nm and emission detected from 570 to 670 nm. All images are color coded using the Fire lookup table from Fiji. Scale bar: 20 μm.

9.- ^{1}H, ^{13}C and ^{19}F NMR spectra and HR ESI-MS of the compounds

Coumarin 8

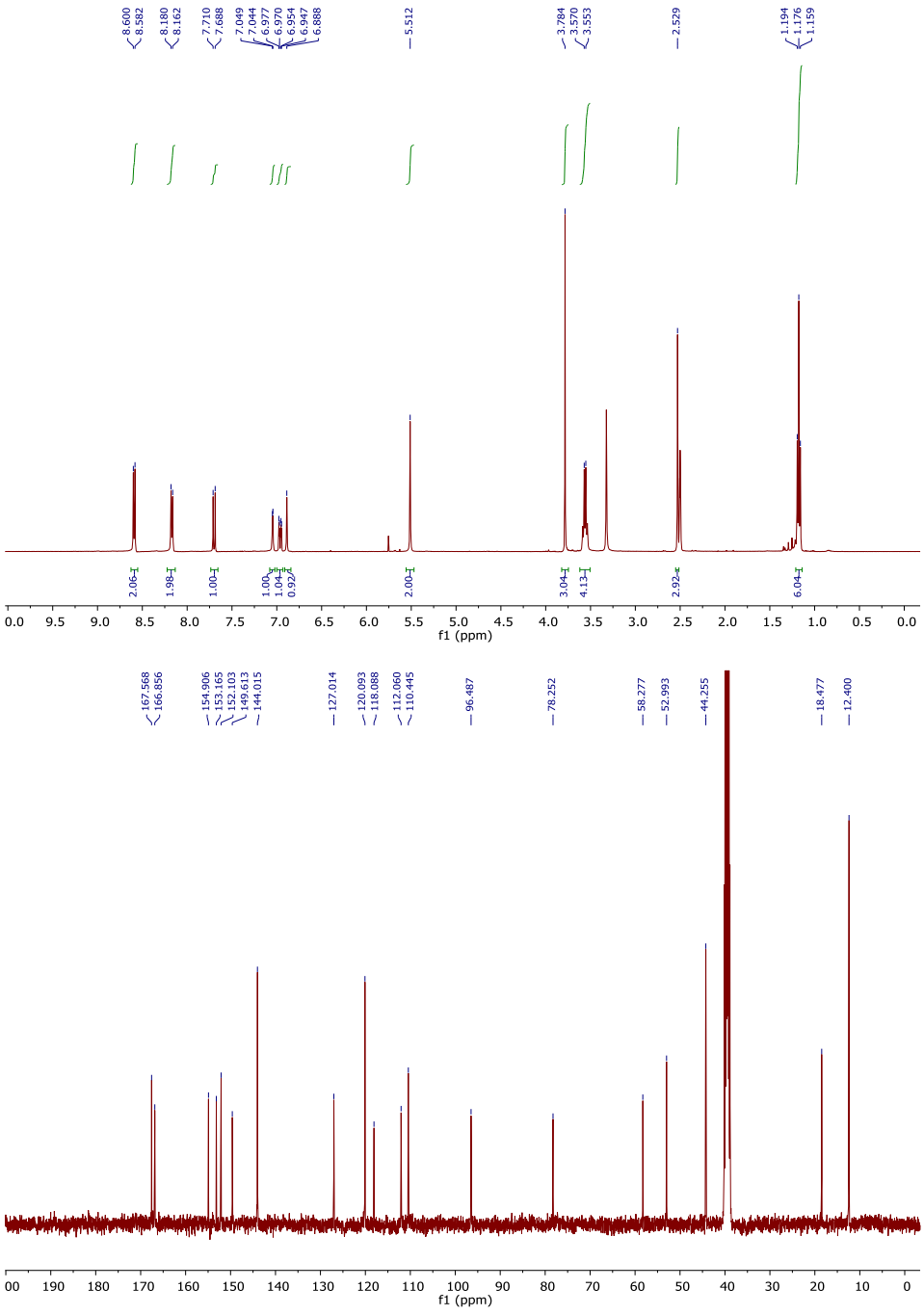

Figure SX. ^{1}H and ^{13}C NMR spectra of compound **8** in DMSO-d_6.

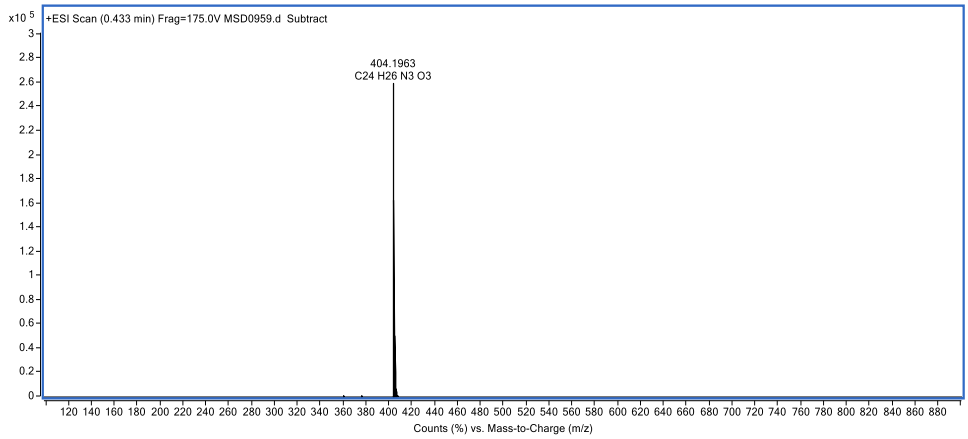

Figure S30. HR ESI-MS spectrum of compound **8**.

Coumarin 4

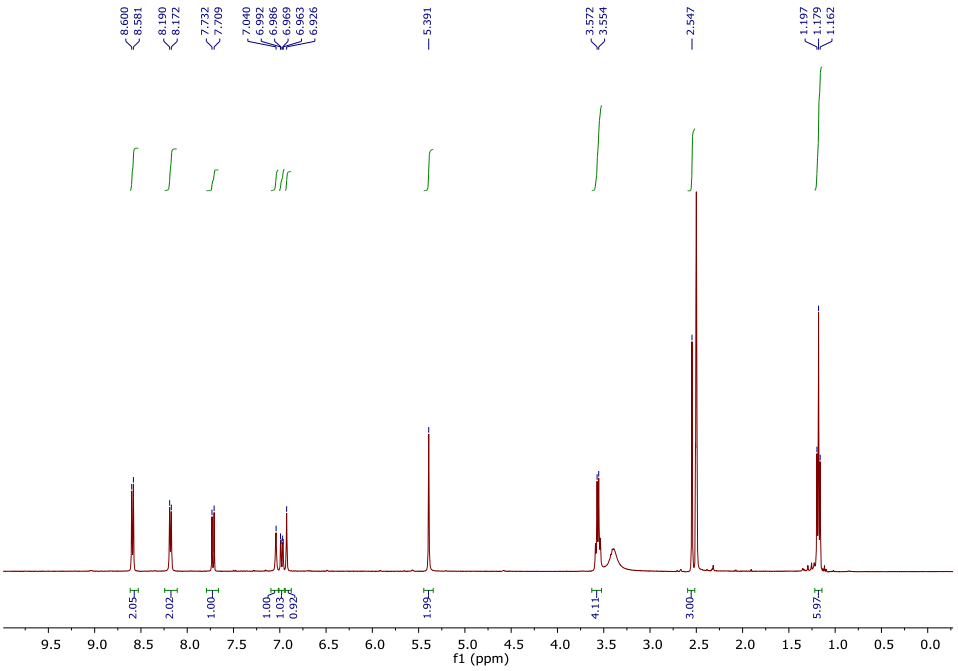

Figure SX. ^{1}H NMR spectra of compound **4** in DMSO-d_6.

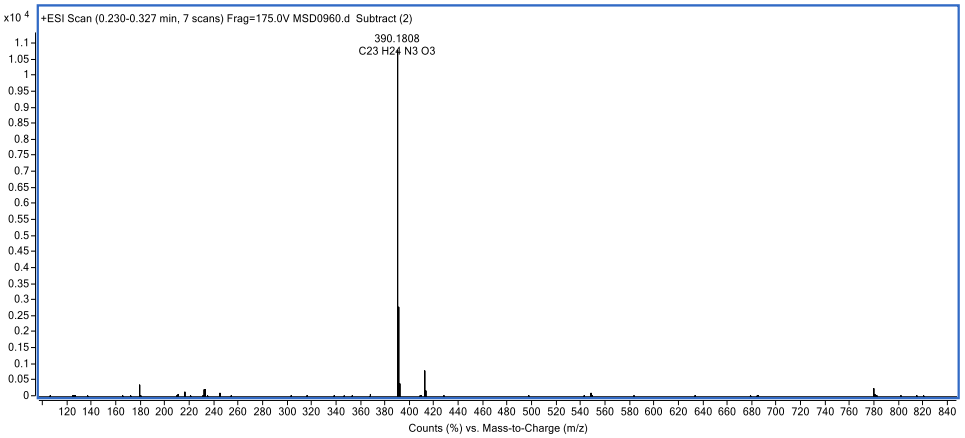

Figure S30. HR ESI-MS spectrum of compound **4**.

***N*-(3-Azidopropyl)-2-bromoacetamide (9)**

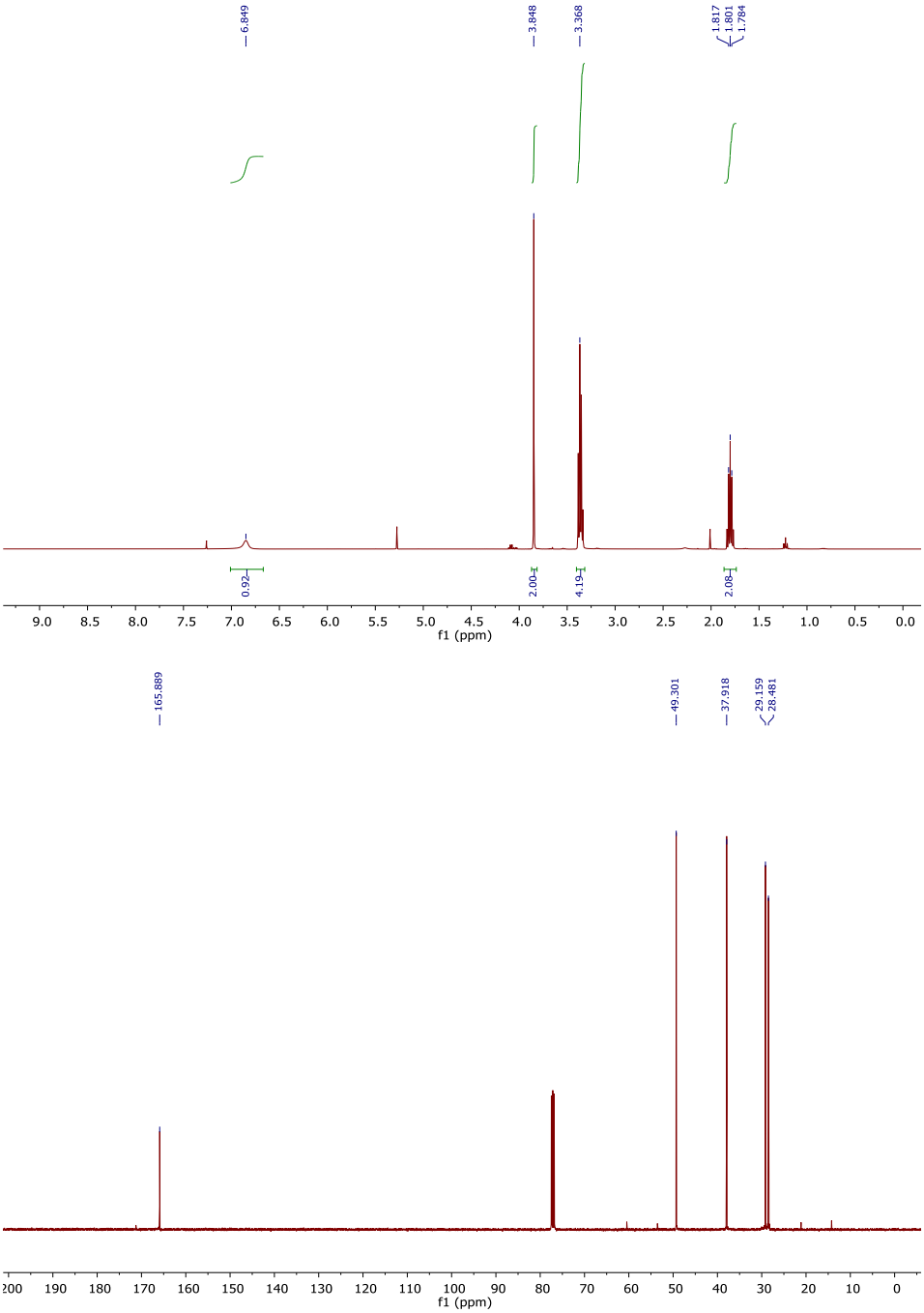

Figure SX. ^{1}H and ^{13}C NMR spectra of compound **9** in $CDCl_3$.

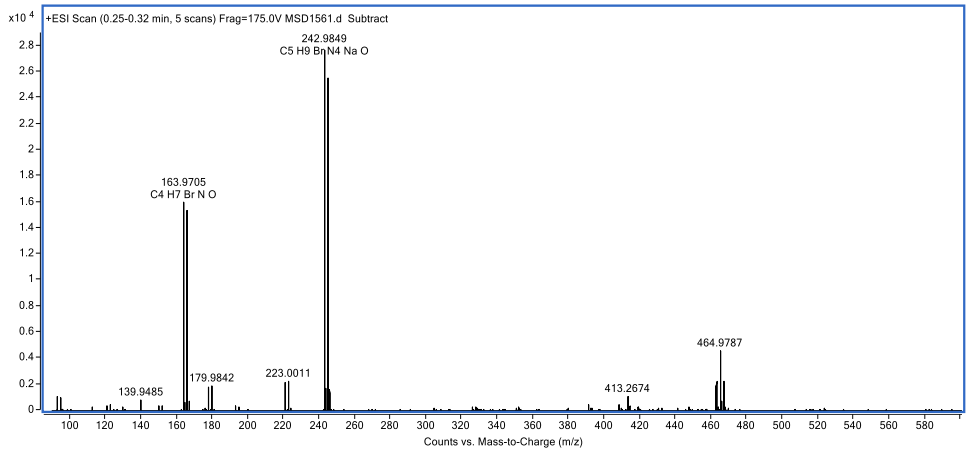

Figure S30. HR ESI-MS spectrum of compound **9**.

Coumarin 5

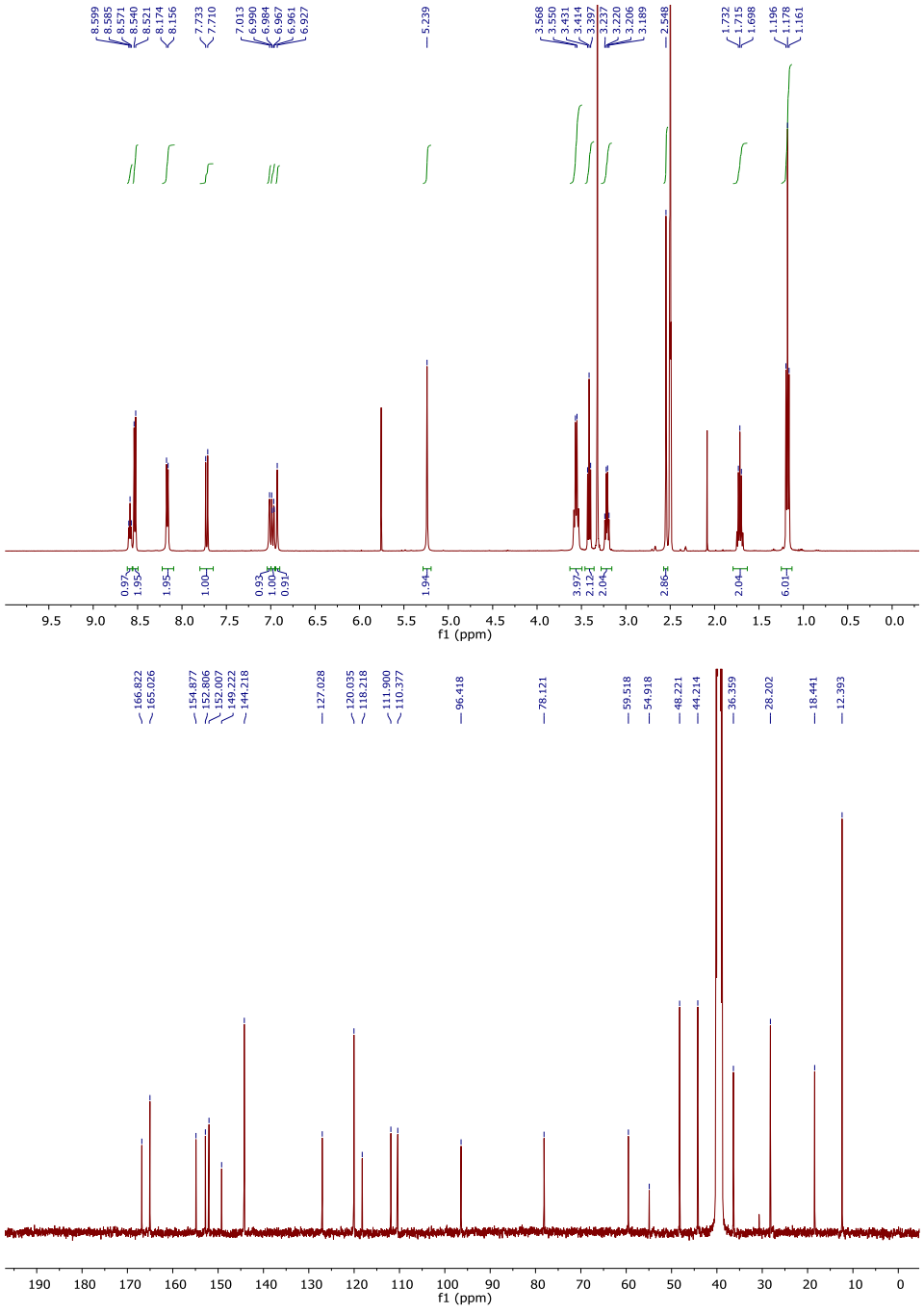

Figure SX. ^{1}H and ^{13}C NMR spectra of compound **5** in *DMSO-d*$_6$.

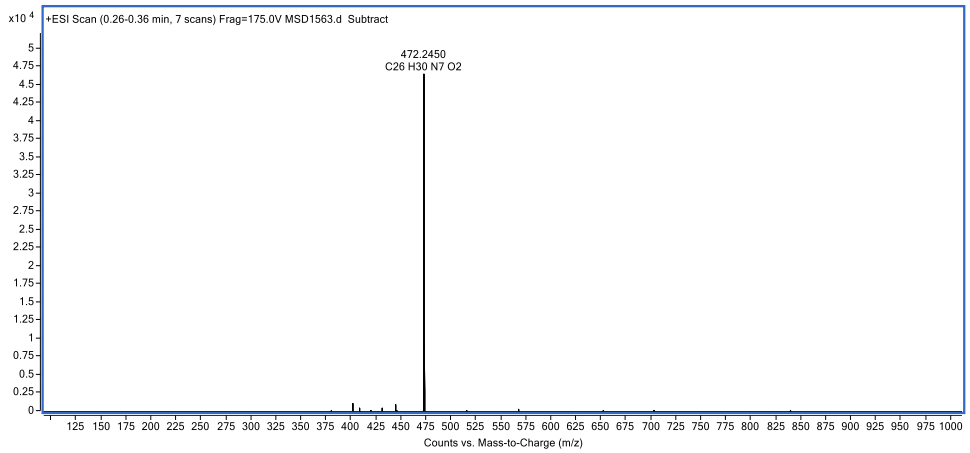

Figure S30. HR ESI-MS spectrum of compound **5**.

2-Bromo-*N*-(prop-2-yn-1-yl)acetamide (10)

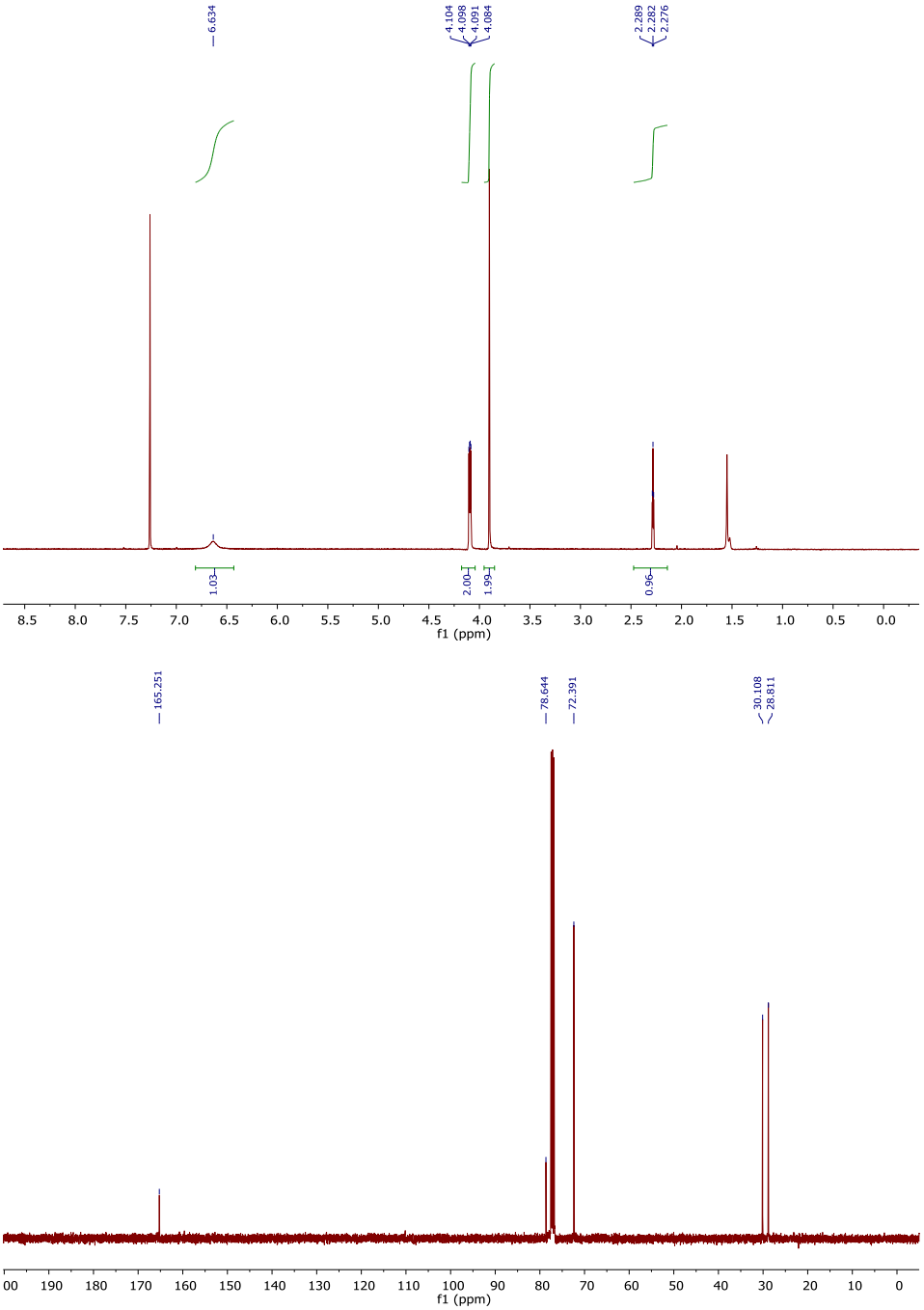

Figure SX. ^{1}H and ^{13}C NMR spectra of compound **10** in $CDCl_3$.

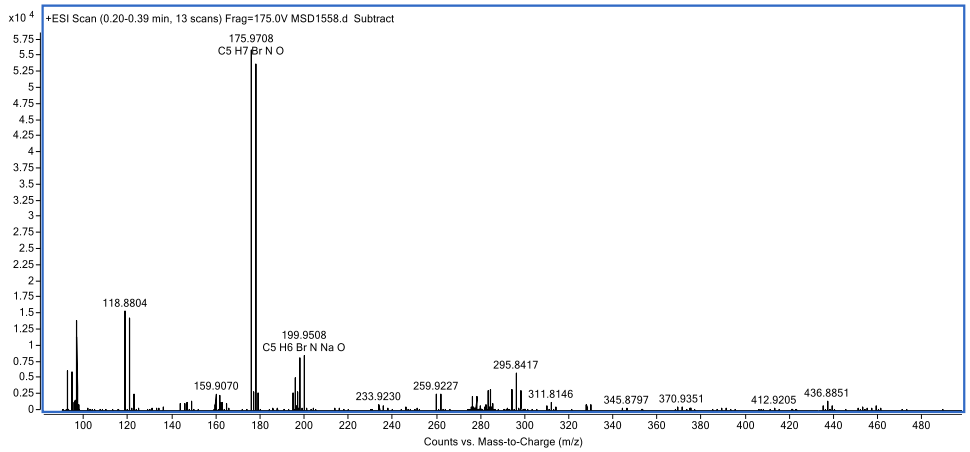

Figure S30. HR ESI-MS spectrum of compound **10**.

Coumarin 6

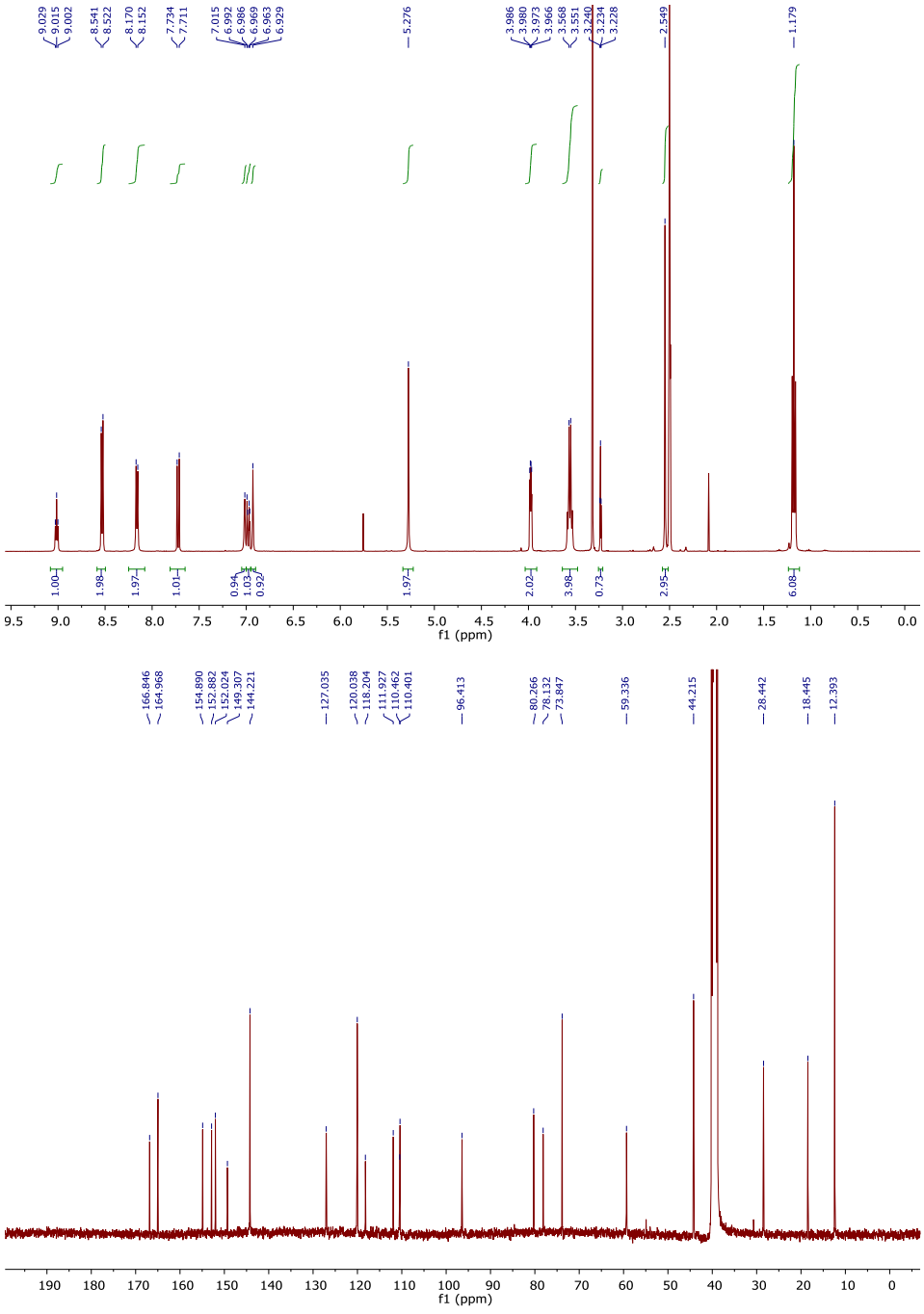

Figure SX. ^{1}H and ^{13}C NMR spectra of compound **6** in *DMSO-d*$_6$.

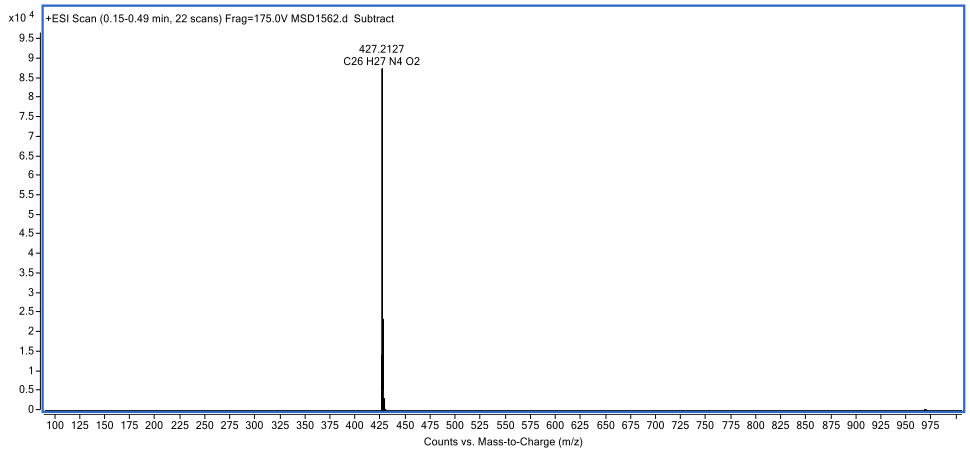

Figure S30. HR ESI-MS spectrum of compound **6**.

10.- References

(1) Gandioso, A.; Bresolí-Obach, R.; Nin-Hill, A.; Bosch, M.; Palau, M.; Galindo, A.; Contreras, S.; Rovira, A.; Rovira, C.; Nonell, S.; Marchán, V. *J. Org. Chem*. **2018**, *83*, 1185−1195.

(2) H.-P. Hsieh, Y.-T. Wu, S.-T. Chen, K.-T. Wang, *Bioorg. Med. Chem*. **1999**, *7*, 1797−1803.

(3) Barragán, F.; Carrion-Salip, D.; Gómez-Pinto, I.; González-Cantó, A.; Sadler, P. J.; de Llorens, R.; Moreno, V.; González, C.; Massaguer, A.; Marchán, V. *Bioconjugate Chem*. **2012**, *23*, 1838−1855

(4) Magde, D.; Brannon, J. H.; Cremers, T. L.; Olmsted, J. *J. Phys. Chem*. **1979**, *83*, 696−699.

(5) Schindelin, J.; Arganda-Carreras, I.; Frise, E.; Kaynig, V.; Longair, M.; Pietzsch, T.; Preibisch, S.; Rueden, C.; Saalfeld, S.; Schmid, B.; Tinevez, J. Y.; White, D. J.; Hartenstein, V.; Eliceiri, K.; Tomancak, P.; Cardona, A. *Nat. Methods* **2012**, *9*, 676−682

Conclusions

11. Conclusions

This Thesis aimed to contribute to the development of novel chemical tools based on the use of light i) to control the release of cytotoxic species from a targeted photoactivatable Pt(IV) pro-drug, ii) to investigate the potential applications of dicyanocoumarin-based photocleavable protecting groups and their removal from key functional groups in caged compounds, and iii) to develop novel coumarin-based fluorescent probes operating in the far-red and the NIR region for bioimaging applications in living cells.

According to the proposed objectives and to the results presented throughout this Thesis, the main conclusions of this work are:

Chapter I:

- The conjugation of two different targeting ligands (a cyclic RGD peptide and folic acid) to a photoactivatable Pt(IV) complex was accomplished.
- The Pt(IV) complex can be efficiently photoactivated with blue light when conjugated to the peptide and the expected Pt(II)-GMP adduct was generated.
- Photoactivation of the Pt(IV)-folate conjugate with blue and green light in the presence of 5'-GMP also conduced to the Pt(II)-GMP adduct. However, the loss of the pterin heterocycle from folic acid together with the formation of a new non-photoactivatable Pt(IV)-folate conjugate occurred after visible light irradiation.
- Biological studies in several cancer cell lines indicated that the phototoxicity of the Pt(IV)-c(RGDfK) conjugate was similar to that of the parent Pt(IV) complex, which confirmed that the photoactivation of the Pt(IV) pro-drug is not affected by peptide conjugation.
- The cellular accumulation of Pt(IV)-c(RGDfK) conjugate in SK-MEL-28 and MDA-MB-468 cells was higher than that of the parent Pt(IV) complex, which suggests selectivity towards tumor cells that overexpress $\alpha_V\beta_3$ and $\alpha_V\beta_5$ integrins.

Chapter II:

- The synthesis of several dicyanocoumarin-caged model compounds (DEAdcCM and DEAdcCE) was accomplished and their suitability for caging carboxylic acids and amines demonstrated.
- The uncaging of dicyanocoumarin-caged model compounds can be achieved with green light, being the efficiency of the photolysis process strongly influenced by i) the structure of the dicyanocoumarin skeleton, ii) the nature of the leaving group, and iii) the type of bond photocleaved (ester or carbamate).
- Photolysis studies with two structurally related dicyanocoumarins revealed that sequential uncaging with green light can be achieved by fine-tuning the structure of the dicyanocoumarin chromophore.
- Two novel dicyanocoumarin-caged aspartic acid derivatives suitable for Fmoc-*t*Bu SPPS (Fmoc-Asp(DEAdcCE)-O*t*Bu and Fmoc-Asp(DEAdcCM)-O*t*Bu) have been synthesized and their chemical stability and photoactivation investigated.
- Although dicyanocoumarin-caged Asp monomers promote the formation of aspartimides during the assembly of the linear RGD-containing peptide on solid-phase following Fmoc-*t*Bu SPPS, the use acidic additives (HOBt or Oxyma) allowed to minimize this side reaction, particularly when the sterically-shielded DEAdcCE monomer was used.
- A dicyanocoumarin-caged cyclic RGD peptide and its ruthenocenoyl conjugate were synthesized and uncaged efficiently with green light.

Chapter III:

- A series of novel coumarin-based fluorophores, nicknamed COUPYs, were easily obtained in only three linear synthetic steps from commercially available precursors.
- The characterization of COUPY scaffolds by 1D and 2D NMR spectroscopy demonstrated the presence of two interconverting rotamers in solution around the exocyclic carbon-carbon bond.

- Besides emission in the far-red to NIR region, COUPY fluorophores exhibit some promising spectroscopical and photophysical properties, including large Stokes' Shifts, high photostability and moderate brightness.
- COUPY dyes showed excellent cell permeability and accumulated selectively in nucleoli and mitochondria of HeLa cells, being their far-red/NIR emission easily detected.
- A conjugatable derivative of COUPY dyes bearing a carboxylic acid group was synthesized through *N*-alkylation of the pyridine heterocycle.
- Octreotide peptide was efficiently labeled with the conjugatable COUPY fluorophore on solid-phase through amide-bond formation, which demonstrates the compatibility of the novel coumarin derivatives with Fmoc/*t*Bu SPPS.
- Cellular uptake experiments by confocal microscopy confirmed the internalization and accumulation of COUPY-octreotide conjugate in SSTR2-overexpressing HeLa cells and that the process is mediated by the receptor.

Summaries

12. Resúmenes de resultados y discusión

12.1 Resumen del capítulo I.

12.1.1 Introducción y objetivos .

La luz presenta un gran potencial a la hora de desarrollar nuevos agentes terapéuticos mucho más selectivos que los actuales, ya que ofrece la posibilidad de controlar dónde, cuándo y en que extensión se produce la activación de un profármaco.[1] En este contexto, los compuestos fotoactivables basado en complejos de Pt(IV) son un buen ejemplo del uso de la luz en el campo de la terapia contra el cáncer. El grupo del Prof. Peter J. Sadler (Universidad de Warwick) describió en 2010 un nuevo profármaco fotoactivable con luz azul, el complejo *trans,trans,trans*-$[Pt(N_3)_2(OH)_2(py)_2]$ (**Esquema 1**). Dicha radiación es más adecuada que la luz UV ya que presenta una mayor capacidad de penetración en los tejidos a la vez de ser menos tóxica.[2,3]

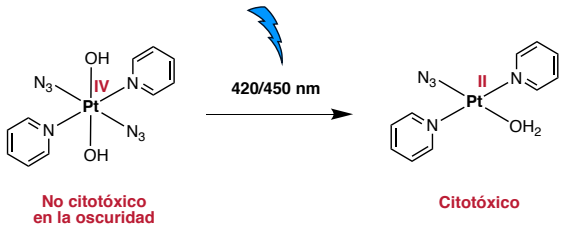

Esquema 1. Esquema general de la reacción de fotoactivación del complejo *trans,trans,trans*-$[Pt(N_3)_2(OH)_2(py)_2]$.

Como se muestra en el **Esquema 2**, *trans,trans,trans*-$[Pt(N_3)_2(OH)_2(py)_2]$ se sintetiza mediante reacción de K_2PtCl_4 con un exceso de piridina, obteniéndose el precursor de Pt(II) *trans,trans*-$[PtCl_2(py)_2]$. Tras el intercambio de los ligandos Cl por N_3, la oxidación de *trans,trans*-$[Pt(N_3)_2(py)_2]$ con H_2O_2 conduce al correspondiente complejo fotoactivable de Pt(IV).[2]

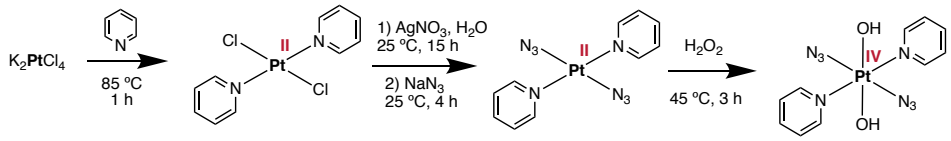

Esquema 2. Esquema general de la síntesis de *trans,trans,trans*-$[Pt(N_3)_2(OH)_2(py)_2]$.

El complejo fotoactivable de Pt(IV) presenta una mayor termoestabilidad que otros complejos descritos por el grupo del Prof. Sadler como, por ejemplo, *trans,trans,trans*-$[Pt(N_3)_2(OH)_2(NH_3)(py)]$ o *trans,trans,trans*-$[Pt(N_3)_2(OH)_2(NH_3)_2]$, además de ser soluble en medio acuoso y estable en la oscuridad. El mecanismo de fotoactivación con luz azul es inducido por la formación de radicales azida que median en el proceso de reducción de Pt(IV) a Pt(II), durante el cual se pierden los dos ligandos axiales (OH) y uno o dos grupos azida. El uso de técnicas espectroscópicas como RMN de ^{1}H y ^{195}Pt y HPLC-MS permitió demostrar la formación de las especies citotóxicas de Pt(II). Así mismo, la realización del experimento de irradiación en presencia de dos equivalentes del nucleótido 5'-GMP confirmó la capacidad de dichas especies para formar aductos con las nucleobases del DNA (**Esquema 3**).[2,3]

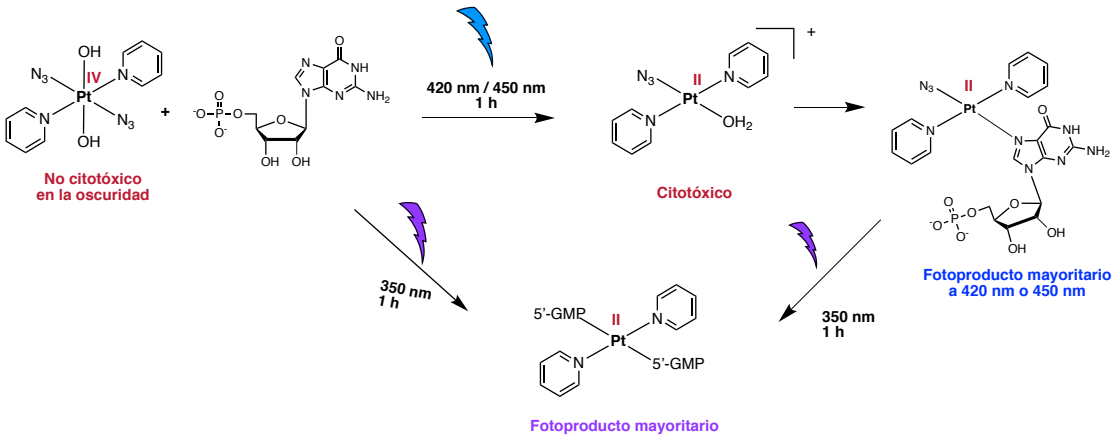

Esquema 3. Reacción de fotoactivación de *trans,trans,trans*-$[Pt(N_3)_2(OH)_2(py)_2]$ en presencia de 5'-GMP.

Estudios posteriores han revelado que los mecanismos mediante los cuales operan dichos complejos fotoactivables de Pt(IV) difieren de los de complejos clásicos de Pt(II) como cisplatino y carboplatino. Así, por ejemplo, las especies generadas tras la irradiación de *trans,trans,trans*-$[Pt(N_3)_2(OH)_2(py)_2]$ inhiben el proceso de transcripción del DNA, debido a su interacción con la RNA polimerasa II, lo que conduce a la muerte celular.[4] Estos hallazgos no excluyen la posibilidad de que otros productos de fotodescomposición también contribuyan a la citotoxicidad del complejo como, por ejemplo, los radicales azida.

Por otro lado, una aproximación ampliamente explorada en el ámbito de la química terapéutica consiste en la conjugación de fármacos anticancerígenos a ligandos que permitan su vehiculización dirigida hacía células tumorales, la estrategia conocida como "*targeted drug delivery*". Así, la sobreexpresión de receptores específicos en la membrana de las células tumorales se puede explotar para internalizar fármacos de manera selectiva en las células malignas sin afectar a las células sanas. Dentro del amplio abanico de receptores sobreexpresados en las células tumorales, son destacables las integrinas y los receptores de ácido fólico y de somatostatina. En cuanto a ligandos selectivos de dichos receptores, cabe mencionar, entre otros, a péptidos, proteínas, anticuerpos y moléculas orgánicas de bajo peso molecular. La interacción entre el receptor y el correspondiente conjugado fármaco-ligando conlleva la internalización vía receptor y es clasificada, por tanto, como una estrategia activa. En cambio, las denominadas estrategias pasivas de vehiculización aprovechan las diferencias morfológicas entre las células tumorales y las células sanas para posibilitar la internalización de los fármacos.

Dentro de las estrategias de vehiculización dirigidas, y basándonos en los antecedentes de nuestro grupo de investigación, en esta tesis nos hemos centrado en el uso de péptidos con la secuencia RGD y en el ácido fólico como ligandos vehiculizadores.

Las integrinas se sobreexpresan en las células cancerígenas y contribuyen a la progresión del tumor y a la metástasis. En el ámbito de la química de péptidos, se ha trabajado intensamente en la mejora de la afinidad y estabilidad de secuencias peptídicas que contienen la tríada de aminoácidos Arginina-Glicina-Ácido Aspártico (**RGD**) (**Figura 1A**), la cual se encuentra en la fibronectina[5] y en otras proteínas de la matriz extracelular.[6] En concreto, el uso de péptidos RGD cíclicos no solo mejora la estabilidad frente a enzimas presentes en el medio celular, sino que la rigidez de su estructura les confiere una mayor afinidad y selectividad hacía determinadas integrinas.[7–10]

Entre los péptidos RGD descritos, destacamos **Cilengitide** (**Figura 1, B**), un pentapéptido cíclico, c(RGDf[*N*-methyl]V), agonista de las integrinas $\alpha v\beta 3$ y $\alpha v\beta 5$ sobreexpresadas en las células tumorales, en especial en células de melanoma y cáncer de mama.[11] Cilengitide presenta también actividad antiangiogénica frente al desarrollo de tumores, por lo que se ha incorporado en fases clínicas avanzadas para el tratamiento del glioblastoma.[12] En este contexto, se han desarrollado diversos derivados de RGD para permitir su conjugación a fármacos. Entre ellos, es destacable el péptido **c(RGDfK) (Figura 1,C)**,[13] que incorpora una Lisina (K) en lugar de Valina (V), lo que ofrece la posibilidad de conjugar fármacos a través del grupo amino de la cadena lateral de este aminoácido.[7–9,14–16] En la literatura se describe un amplio abanico de ejemplos de la conjugación de fármacos anticancerígenos a derivados RGD, tanto fármacos orgánicos[14,17,18] como fármacos basados en metales de transición,[9,19,20] siendo destacables los que incorporan complejos de Pt(II) y Pt(IV).

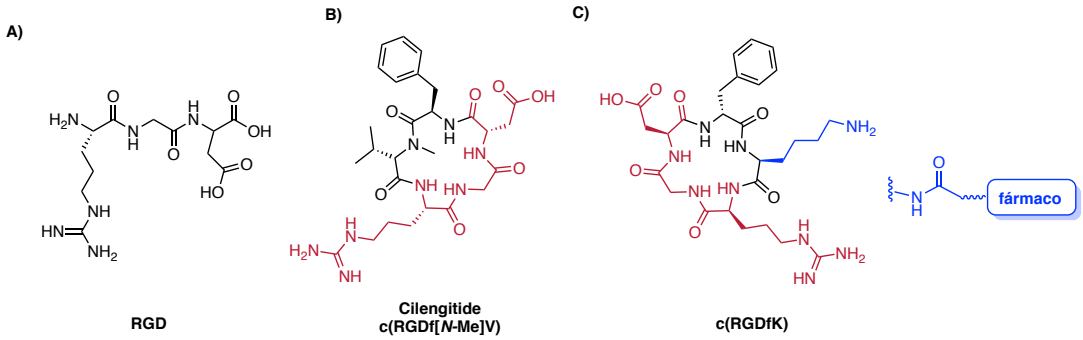

Figura 1. Diferentes ejemplos de estructuras peptídicas que incluyen la secuencia RGD.

Por otro lado, el ácido fólico (**Figura 2**), conocido también como vitamina B9, presenta afinidad por los receptores folato sobreexpresados en las células tumorales.[21–23] A pesar de que el receptor de ácido fólico también se expresa en las células epiteliales sanas, estudios previos han demostrado una mayor afinidad por los receptores en las células malignas.[24] En la literatura encontramos un gran número de ejemplos de conjugación de ácido fólico a fármacos orgánicos[22,25–27] y metálicos.[28,29]

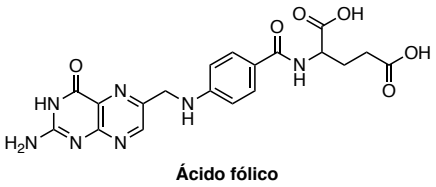

Figura 2. Estructura del ácido fólico.

Con el objetivo de englobar las dos estrategias presentadas, tanto el uso de la luz visible para activar profármacos basados en complejos metálicos como la vehiculización dirigida hacia células tumorales, nos marcamos como primer objetivo de la tesis **la vehiculización dirigida de fármacos fotoactivables hacía células tumorales**. Más concretamente, en colaboración con el Prof. Peter J. Sadler del Departamento de Química de la Universidad de Warwick, se planteó la conjugación del complejo fotoactivable de Pt(IV), *trans,trans,trans*-$[Pt(N_3)_2(OH)_2(py)_2]$, tanto al **péptido c(RGDfK)** como a **ácido fólico** (**Figura 3**). Además de los estudios de fotoactivación de los conjugados de Pt(IV), se realizaron estudios biológicos con el conjugado Pt-c(RGDfK) en colaboración con la Dra. Julie Woods de la Unidad de Fotobiología del Departamento de Dermatología del Hospital Nineweels en Dundee (UK), y con la Dra. Anna Massaguer del Departamento de Biología de la Universitat de Girona (UdG). Los estudios biológicos con el conjugado Pt-Folato están pendientes de realización en el grupo del Prof. Sadler.

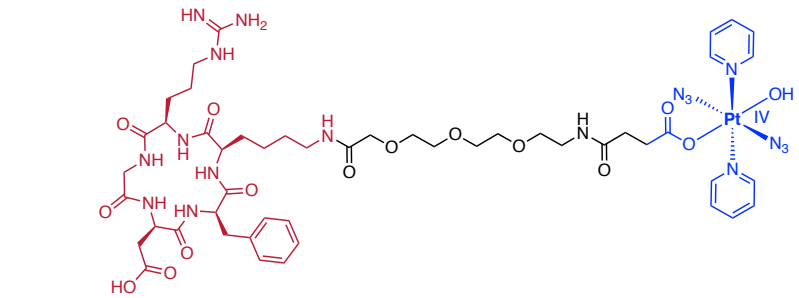

c(RGDfK) y ácido folico
Vehiculización dirigida hacia celulas tumorales que sobreexpresan las integrinas $\alpha v\beta 3$ y $\alpha v\beta 5$ y receptores de ácido fólico, respectivamente.

***trans,trans,trans*-[Pt(N$_3$)$_2$(OH)$_2$(py)$_2$]**
complejo fotoactivable de Pt(IV).

Figura 3. Conjugados objetivo entre el complejo de Pt(IV) y el péptido c(RGDfK) o ácido fólico.

12.1.2. Publicación A: Gandioso, A., Shaili, E., Massaguer, A., Artigas, G., González-Cantó, A., Woods, J. A, Sadler, P. J. & Marchán, V. *An integrin-targeted photoactivatable Pt(IV) complex as a selective anticancer pro-drug: Synthesis and photoactivation studies*. *Chem. Commun.* 51, 9169-9172 (2015).

La preparación del conjugado entre el complejo de Pt(IV) y el péptido c(RGDfK) se planteó en dos fases que incluyeron la síntesis del péptido en fase sólida y su posterior conjugación al complejo de Pt(IV) a través del residuo de lisina en solución. Los estudios de fotoactivación del conjugado se realizaron mediante irradiación con luz azul (420 nm) y los fotoproductos se caracterizaron mediante HPLC-MS. Finalmente, se realizaron ensayos de cito- y fototoxicidad y estudios de acumulación celular en diferentes líneas celulares cancerígenas.

Síntesis del conjugado Pt(IV)-c(RGDfK).

El ensamblaje del péptido se realizó en fase sólida sobre la resina cloruro de 2-clorotritilo siguiendo la estrategia Fmoc/*t*Bu. En primer lugar, se procedió a la elongación de la cadena peptídica a través del acoplamiento de los Fmoc-aminoácidos convenientemente protegidos (Gly, Arg(Pbf), Lys(Alloc), *D*-Phe y Asp(*t*Bu)) usando DIPC y HOBt como agentes acoplantes. Una vez ensamblado el péptido lineal, se desancló del soporte sólido polimérico mediante tratamiento ácido suave (AcOH/TFE/DCM, 1:1:8) y, a continuación, se cicló mediante la formación de un enlace amida entre los extremos *C*- y *N*- terminales. Tras la desprotección ortogonal del grupo Alloc mediante tratamiento con $Pd(PPh_3)_4$ y fenilsilano, se incorporó un espaciador de polietilenglicol (PEG) a través de la cadena lateral del residuo de lisina. Finalmente, tras la eliminación del resto de grupos protectores, Fmoc en condiciones básicas y *t*Bu y Pbf en condiciones ácidas, el péptido **1** se purificó mediante HPLC en fase inversa (**Esquema 4**).

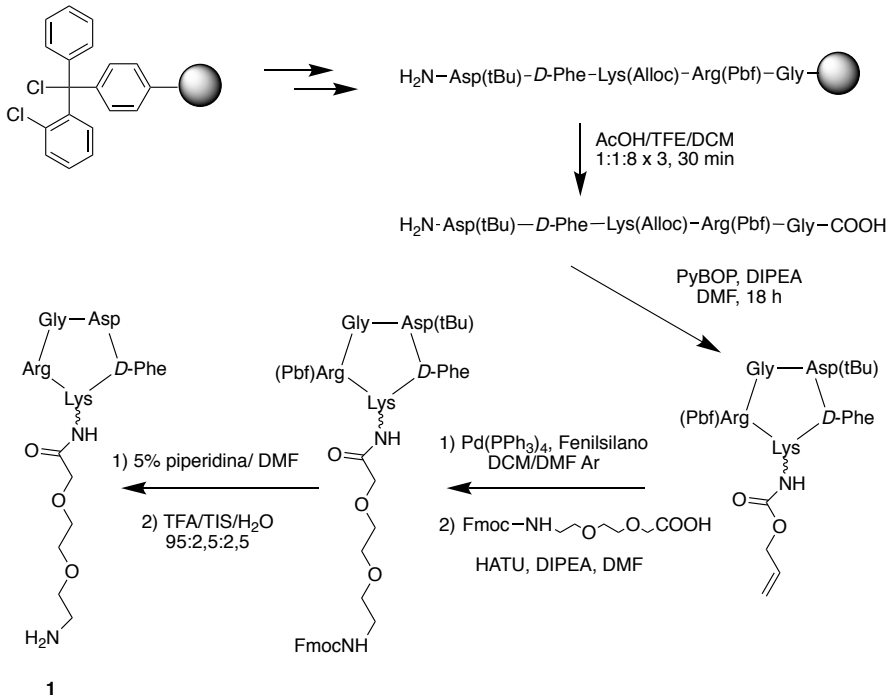

Esquema 4. Esquema de la síntesis del derivado c(RGDfK) que incorpora el espaciador de polietilenglicol.

La conjugación del complejo de Pt(IV) al péptido se planteó a través de la formación de un enlace amida con el extremo amino terminal del espaciador. Para ello, en primer lugar, se sintetizó el complejo *trans,trans,trans*-$[Pt(N_3)_2(OH)(succ)(py)_2]$ (**3**) mediante reacción del complejo **2** con anhídrido succínico. (**Esquema 5, A**). A continuación, se procedió a la preactivación del ácido carboxílico de **3** con HATU y DIPEA en DMF durante 5 minutos y, seguidamente, se hizo reaccionar con el péptido **1** en DMF y DIPEA bajo atmosfera de argón durante 2 horas y protegido de la luz. Finalmente, el conjugado deseado Pt(IV)-c(RGDfK) (**4**) se purificó mediante HPLC en fase inversa y se procedió a su caracterización mediante espectrometría de masas de alta resolución (ESI) y RMN de ^1H (**Esquema 5, B**).

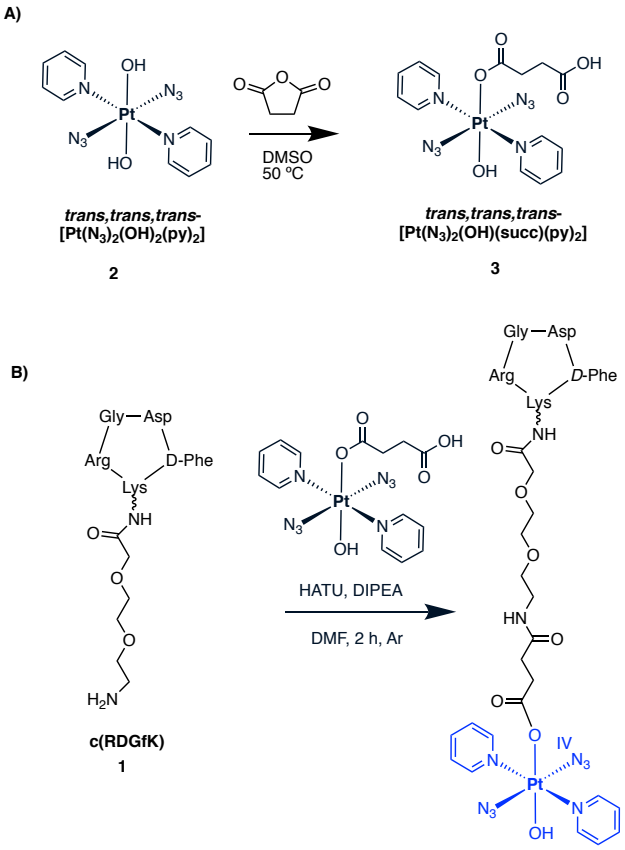

Esquema 5. A) Síntesis del complejo *trans,trans,trans*-$[Pt(N_3)_2(OH)(succ)(py)_2]$, **B)** Síntesis del conjugado c(RGDfK)-Pt(IV).

Estudios de fotoactivación del conjugado Pt(IV)-c(RGDfK).

Los estudios de fotoactivación del conjugado Pt(IV)-c(RGDfK) se realizaron en presencia del nucleótido 5'-GMP (2 equivalentes), y el seguimiento de la reacción se realizó por HPLC-MS para identificar los fotoproductos generados. Tras irradiar a 420 nm durante 45 min a 37 ^{o}C, se observó la completa desaparición del conjugado y la consiguiente formación del péptido libre succinato-c(RGDfK) (**5**) y del aducto de Pt(II)-GMP *trans*-[Pt(N_3)(5'-GMP)$(py)_2]^+$ (**6**), como productos mayoritarios. Además, se observaron otros subproductos minoritarios como *trans*-[Pt(5'-GMP)$_2(py)_2]^{2+}$(**7**) y [$Pt_2(N_3)_2$(5'-GMP)$(py)_4]^+$) (**8**) (**Esquema 6**).

La formación del aducto Pt(II)-5'-GMP confirmó la fotoreduccion de Pt(IV) a Pt(II) y la generación de especies de Pt(II) potencialmente citotoxicas, tal y como habían descrito anteriormente Sadler y colaboradores con el complejo **2**.[2] Además, la aparición del péptido-succinato indica que el vehículo peptídico no altera el mecanismo de fotoactivación del profármaco ya que no se observaron subproductos provenientes del péptido ni fotoproductos diferentes a los descritos por anteriormente.

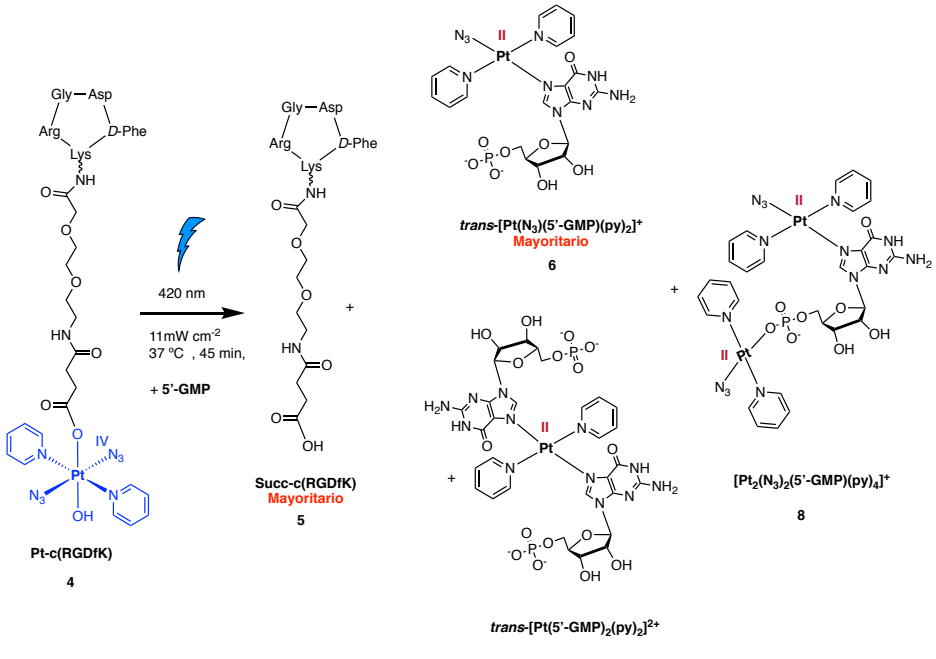

Esquema 6. Reacción de fotoactivación del conjugado Pt(IV)-c(RGDfK) con presencia de 5'-GMP.

Estudios de citotoxicidad y acumulación celular.

Los estudios de citotoxicidad (IC_{50}) bajo irradiación con luz azul (420 nm), tanto de los complejos control, *trans,trans,trans*-[$Pt(N_3)_2(OH)_2(py)_2$] (**2**) y *trans,trans,trans*-[$Pt(N_3)_2(OH)(succ)(py)_2$] (**3**), como del conjugado Pt(IV)-c(RGDfK) (**4**), se realizaron en células tumorales que sobreexpresan las integrinas $\alpha v\beta 3$ y $\alpha v\beta 5$. Para ello, se seleccionaron las siguientes líneas celulares: **SK-MEL-28** que es una línea celular de melanoma que presenta una elevada sobreexpresión de la integrina $\alpha v\beta 3$ y, en menor grado, de $\alpha v\beta 5$, y **DU-145,** que es una línea celular de cáncer de próstata con una expresión de $\alpha v\beta 3$ inferior comparado con SK-MEL-28, pero con niveles similares de $\alpha v\beta 5$.

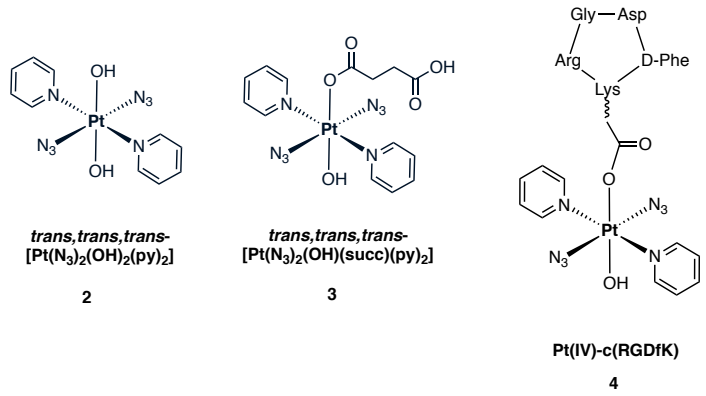

Figura 4. Estructuras de los complejos de Pt(IV) y del conjugado Pt(IV)-c(RGDfK) utilizados en los estudios de citotoxicidad y acumulación celular

Tal y como se muestra en la **Tabla 1**, los complejos **2** y **3** muestran unos valores de IC_{50} similares (10,2 y 15,5 μM**,** respectivamente) en la línea celular **SK-MEL-28.** En el caso del conjugado Pt(IV)-c(RGDfK), se obtuvo un valor de 19.5 μM, lo que refleja una leve pérdida de citotoxicidad en comparación con los complejos control. Por otro lado, en la línea celular **DU-145** se obtuvieron valores de IC_{50} superiores para todos los compuestos estudiados, 43.2 y 20.0 μM para los complejos control **2** y **3,** respectivamente**,** y 53.9 μM para el conjugado **4**. En su conjunto, los valores de IC_{50} del conjugado Pt(IV)-c(RGDfK) tras irradiación confirman que la conjugación del complejo de Pt(IV) al péptido vehiculizador no altera sustancialmente su actividad.

Tabla 1. Valores de citotoxidad de los complejos de Pt(IV) y el conjugado en las líneas celulares SK-MEL-28 y DU-145 bajo irradiación a 420 nm .

	SK-MEL-28 IC_{50} (μM)	DU-145 IC_{50} (μM)
***trans,trans,trans*-[$Pt(N_3)_2(OH)_2(py)_2$] (2)**	10.2 (7.9- 13.0)	43.2 (33.0-56.6)
***trans,trans,trans*-[$Pt(N_3)_2(OH)(succ)(py)_2$] (3)**	15.5 (10.2-23.6)	20.0 (14.7-27.3)
Pt(IV)-c(RGDfK) (4)	19.5 (13.4-28-2)	53.9 (---)

Además, la correlación entre los valores de citotoxicidad del conjugado **4** en ambas líneas celulares y los niveles de expresión de ambas integrinas, sugiere que el mecanismo de internalización del conjugado viene mediado por ellas.

Finalmente, se realizaron estudios de acumulación celular en los que se cuantifica la cantidad de Pt acumulado en las células mediante espectrometría de masas con plasma acoplado inductivamente (ICP-MS). En estos experimentos se incluyó, además de **SK-MEL-28** y **DU-145** un tercera línea celular de adenocarcinoma de cáncer de mama, **MDA-MB-468**, la cual únicamente sobreexpresa la integrina $\alpha v\beta 5$. Como se muestra en la **Figura 5**, para el conjugado Pt(IV)-c(RGDfK) se obtuvieron valores de acumulación de Pt superiores en las líneas células SK-MEL-28 y MDA-MB-468 (130.7 pmol Pt y 166.5 pmol Pt respectivamente) comparado con la línea DU-145 (46.6 pmol Pt). Sin embargo, para los complejos control **2** y **3** se obtuvieron valores de acumulación inferiores, aunque similares entre sí. En su conjunto, estos valores sugieren cierta selectividad mediada por el péptido c(RGDfK).

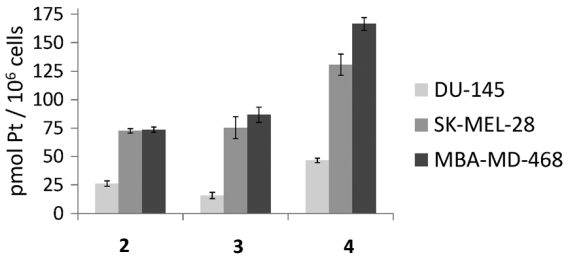

Figura 5. Acumulación de Pt en las diferentes líneas celulares.

12.1.3. Manuscrito en preparación: Gandioso, A. *et al*. A Folate-targeted photoactivatable Pt(IV) complex as a selective anticancer pro-drug: synthesis and photoactivation studies.

A la hora de sintetizar el conjugado Pt(IV)-folato, hay que tener en cuenta que la unión del complejo metálico debe realizarse a través del grupo carboxilato γ y no el α, ya que este último interviene en el reconocimiento con el receptor de ácido fólico. Una vez conjugado el complejo, *trans,trans,trans*-[$Pt(N_3)_2(OH)(succ)(py)_2$] (**3**), se estudió su fotoactivación mediante irradiación a 420 nm y 505 nm, caracterizándose los fotoproductos obtenidos por HPLC-MS (**Esquema 7**).

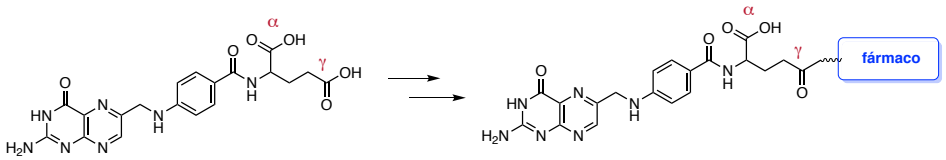

Esquema 7. Esquema general de la conjugación de fármacos a ácido fólico.

Síntesis del conjugado Pt(IV)-Folato.

En primer lugar, se procedió a la incorporación de un espaciador de polietilenglicol (PEG) sobre el grupo ácido carboxílico γ del ácido fólico utilizando *N,N'*-diciclohexilcarbodiimida (DCC), trietilamina y *N*-hidroxisuccinimida (NHS) en DMF y protegido de la luz. Como se muestra en el **Esquema 8**, se obtuvo mayoritariamente el derivado con el espaciador unido al grupo carboxilato γ (**9**), que fue purificado mediante HPLC en fase inversa y caracterizado por espectrometría de masas ESI y RMN de ^{1}H. Finalmente, se sintetizó el conjugado Pt(IV)-folato siguiendo la misma estrategia que con el péptido c(RGDfK). Para ello, se preactivó el complejo de Pt(IV) (**3**) con HATU y DIPEA en DMF durante 5 minutos y, seguidamente, se hizo reaccionar con el derivado de ácido fólico (**9**) en DMF y DIPEA bajo atmosfera de argón durante 2 horas y protegido de la luz. El conjugado Pt(IV)-folato (**10**) deseado se purificó mediante HPLC en fase inversa y se caracterizó mediante EM ESI y RMN ^{1}H (**Esquema 8**).

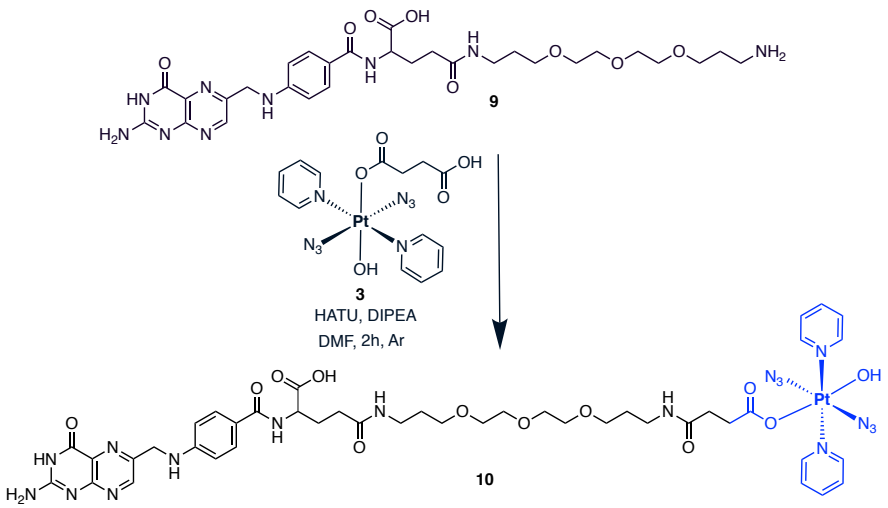

Esquema 8. Síntesis del conjugado Pt(IV)-folato **10**.

Estudios de fotoactivación del conjugado Pt(IV)-folato.

La reacción de fotoactivación del conjugado Pt(IV)-folato en presencia del nucleótido 5'-GMP (2 equivalentes) fue seguida mediante HPLC-MS con el objetivo de identificar los fotoproductos generados. Tras irradiación a 420 nm durante 2 h a 37 °C, se observó la completa desaparición del conjugado **10** junto a la consiguiente formación del aducto de Pt(II)-GMP, (*trans*-[Pt(N_3)(5'-GMP)($py)_2$]$^+$) (**6**) y el derivado de ácido fólico que incorpora el fragmento de succinato proveniente del complejo de platino (**11**) (**Esquema 9**).

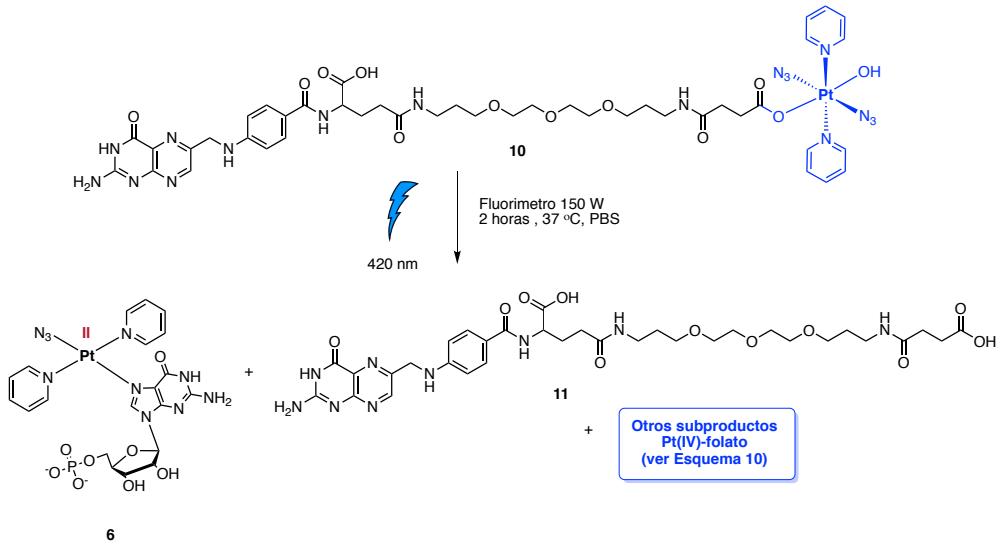

Esquema 9. Reacción de fotoactivación del conjugado Pt(IV)-folato a 420 nm.

Sin embargo, a diferencia de lo ocurrido durante la fotoactivación del conjugado Pt(IV)-c(RGDfK), en este caso sí se identificaron algunos subproductos no esperados. Así, se observó la formación de otros dos "conjugados" mayoritarios que se caracterizaron mediante espectrometría de masas y cuyas estructuras propuestas se muestran en el **Esquema 10**: **i**) un conjugado Pt(IV)-folato en el que se ha perdido el fragmento de pterina del ácido fólico (**12**), y **ii**) un conjugado de Pt(IV)-folato en el que se ha perdido tanto uno de los ligandos azida (N_3) del complejo de Pt(IV), como el fragmento de pterina (**13**).

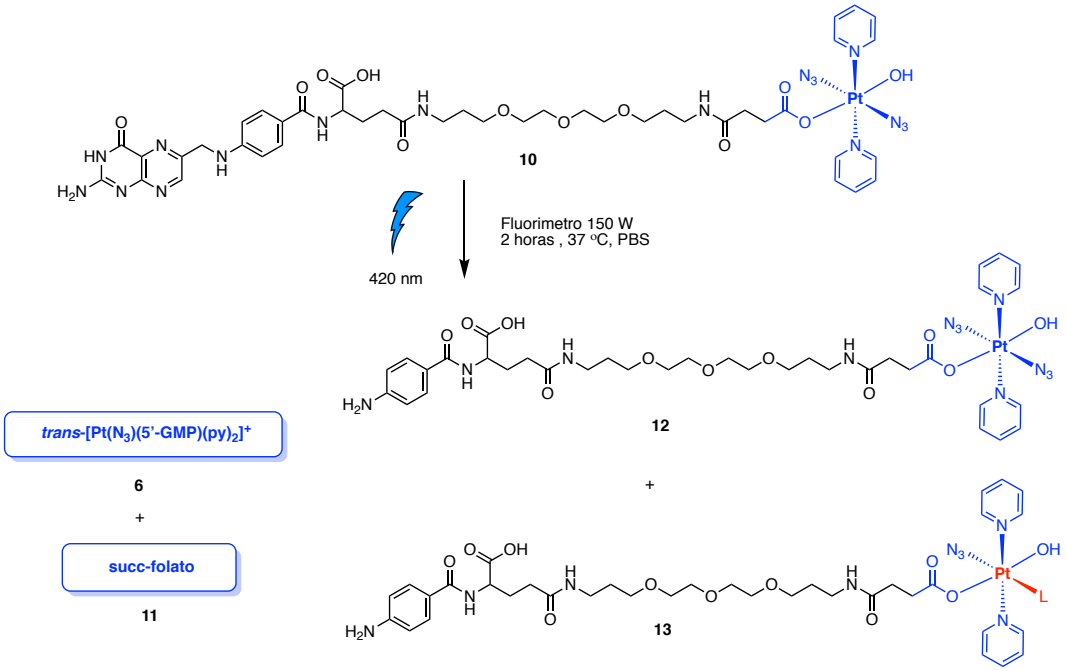

Esquema 10. Reacción de fotoactivación del conjugado Pt(IV)-folato a 420 nm.

Es interesante destacar que la exposición del **conjugado 12** a irradiación con luz azul (420 nm) condujo a la fotoreducción de Pt(IV) a Pt(II) y la consiguiente formación del aducto con 5'-GMP y el derivado de ácido fólico **14** (**Esquema 11, A)**. Sorprendentemente, el **conjugado 13** permaneció inalterado, lo cual se atribuye a la modificación de la esfera de coordinación del platino (**Esquema 11, B)**.

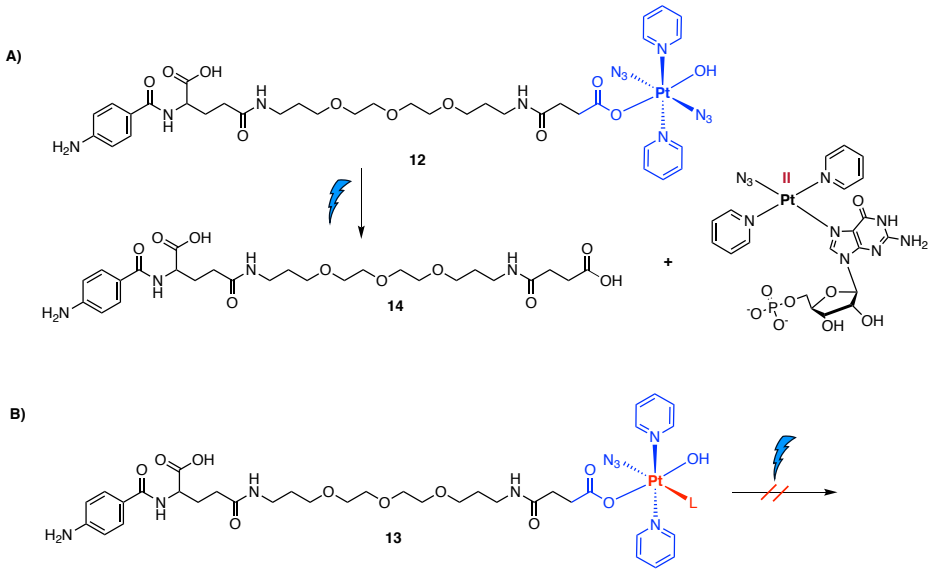

Esquema 11. Resumen de los estudios de fotoactivación de los subproductos obtenidos durante la fotoreacción del conjugado Pt(IV)-folato a 420 nm.

En este contexto, también se exploró la fotoactivación del conjugado Pt(IV)-folato mediante irradiación con un LED de luz verde (505 nm, 100 mW/cm^2) durante 2 h a 37 °C. Se observó la misma tendencia y los mismos subproductos que en los experimentos con luz azul (**Figura 6**), lo cual es un resultado muy positivo ya que la luz verde presenta mayor capacidad de penetración y menor toxicidad que la luz azul.

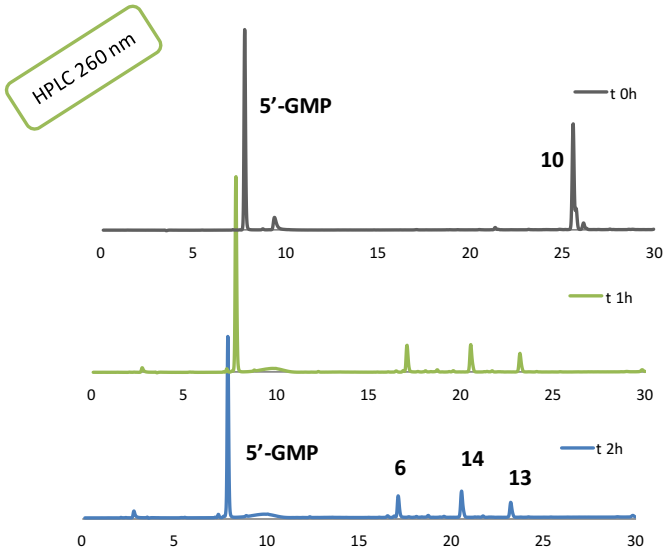

Figura 6. Cromatograma de HPLC-MS de la reacción de fotoactivación del conjugado Pt(IV)-FA a 505 nm.

Finalmente, se planteó la realización de diferentes estudios control para averiguar el porqué de la formación de dos nuevos conjugados durante el proceso de fotoactivación. Por un lado, se irradió ácido fólico durante 2 horas a 420 nm y a 505 nm, observándose que se mantenía estable (**Figura 7**). Por otro lado, se irradió ácido fólico en presencia de *trans,trans,trans*-$[Pt(N_3)_2(OH)_2(py)_2]$ y aquí sí que se observó la pérdida del fragmento de pterina y la correspondiente reducción de Pt(IV) a Pt(II) (**Esquema 12)**, lo que sugiere que los radicales azida o hidroxilo liberados podrían estar involucrados en dicho proceso.

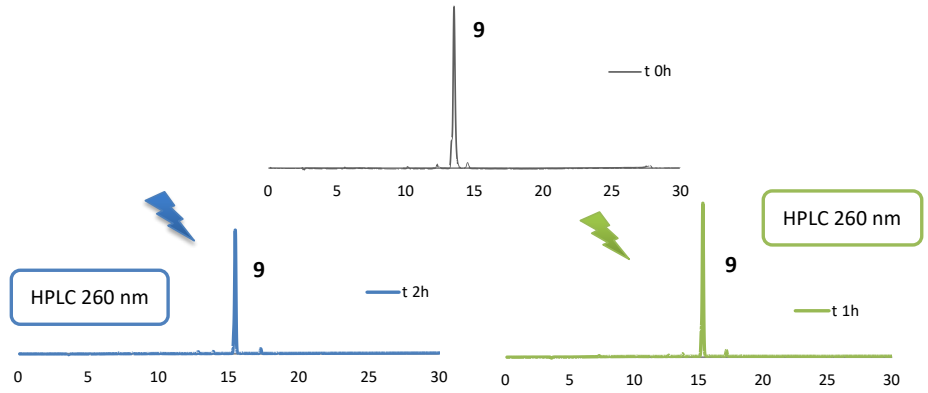

Figura 7. Análisis por HPLC-MS de la estabilidad de ácido fólico tras irradiación con luz azul y verde.

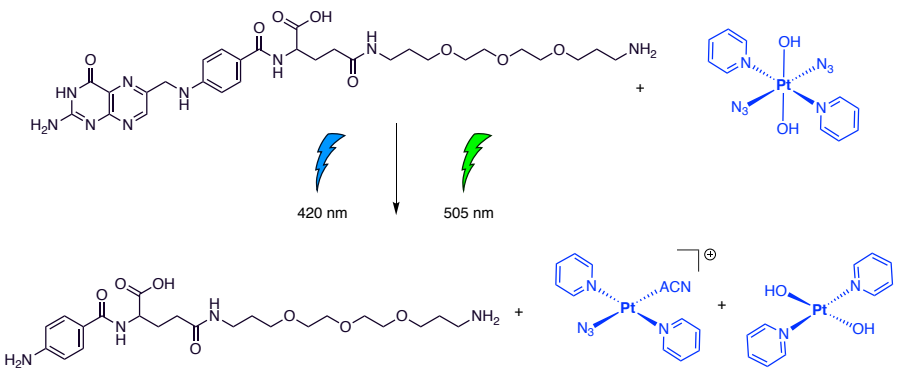

Esquema 12. Fotoactivación del complejo de Pt(IV) *trans,trans,trans*-$[Pt(N_3)_2(OH)_2(py)_2]$ en presencia de ácido fólico.

12.1.4. Conclusiones.

En resumen, el complejo de Pt(IV) se fotoactiva eficientemente con luz visible cuando se conjuga tanto al péptido c(RGDfK) como a ácido fólico, identificándose en ambos casos el aducto esperado Pt(II)-GMP. Sorprendentemente, en el caso del conjugado Pt(IV)-folato también se observó la pérdida del heterociclo de pterina del ácido fólico y la formación de un nuevo conjugado Pt-folato que permanece inalterado a la irradiación con luz azul o verde.

Los estudios biológicos realizados con el conjugado Pt(IV)-c(RGDfK) indican que la fotoxicidad del complejo de Pt(IV) no se ve sustancialmente afectada por la unión al péptido. Además, los estudios de acumulación celular sugieren cierta selectividad en la internalización en células tumorales que sobreexpresan las integrinas $\alpha v\beta 3$ y $\alpha v\beta 5$. En el caso del conjugado Pt(IV)-folato, quedan pendientes los estudios biológicos, los cuales podrán aportar información relevante sobre el papel que podrían desempeñar los productos secundarios de pterina, ya que es conocido que dichos compuestos pueden generan ROS.

12.2 Resumen del capítulo II.

12.2.1 Introducción y objetivos.

Tal y como se ha comentado en el resumen del **capítulo 1**, la luz presenta un gran potencial a la hora de activar profármacos basados en complejos metálicos fotoactivables,[30] pero también cabe destacar su capacidad para regular procesos químicos y biológicos.[31–35] Aunque dicha estrategia no es nueva, sí que lo son los avances que se han desarrollado en los últimos años y que han conducido a nuevas aplicaciones en: i) el uso de grupos protectores fotolábiles para activar la función biológica de una molécula de manera irreversible, ii) el uso de fotoconmutadores químicos para controlar la actividad biológica de una molécula de manera reversible, y iii) el uso de proteínas u otras biomoléculas sensibles a la luz para controlar el material genético, campo conocido como optogenética. Más específicamente, en este segundo capítulo de la Tesis nos hemos centrado en el uso de grupos protectores fotolábiles.

Los grupos protectores fotolábiles (PPGs) han recibido amplia atención en los últimos años para la regulación de la actividad biológica de moléculas, desde fármacos orgánicos hasta metalofármacos y biomoléculas, tales como péptidos, proteínas u oligonucleótidos. Esta estrategia se basa en la premisa de que la actividad biológica de dichos compuestos se puede desactivar temporalmente mediante la protección de un grupo funcional clave con un PPG. Tras irradiación, la eliminación del PPG del compuesto protegido debería al restablecer la actividad o función intrínseca de la molécula (**Figura 9**).[36,37]

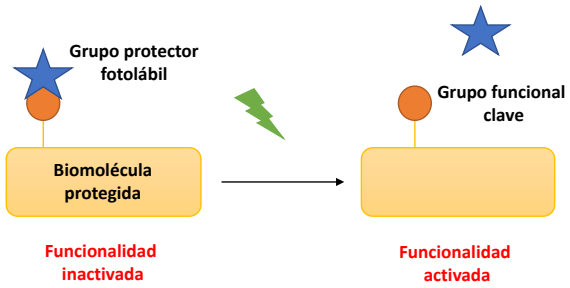

Figura 9. Esquema general del concepto del uso de grupos protectores fotolábiles.

Una gran mayoría de los grupos protectores fotolábiles descritos hasta la fecha requieren irradiación UV para inducir su eliminación (derivados de *o*-nitrobencilo y cumarinas convencionales). Tal y como se ha comentado anteriormente, el uso de la luz UV no es ideal dada su elevada fototoxicidad y su capacidad para interactuar con biomoléculas endógenas, además de su baja capacidad de penetración en los tejidos en comparación con la luz visible o la luz del infrarojo cercano (NIR). Por esta razón, en los últimos años se han dedicado grandes esfuerzos al desarrollo de nuevos PPGs eliminables en la región del visible e incluso en el NIR, como es el caso de algunas cumarinas no convencionales, derivados de BODIPY y de cianina (**Figura 10**).[36,37]

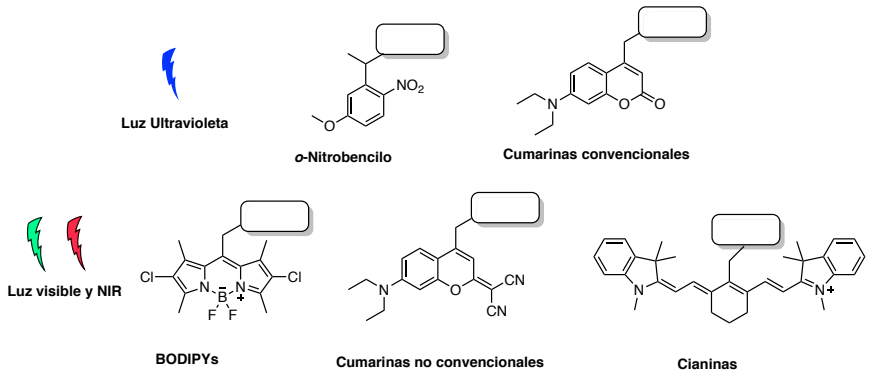

Figura 10. Ejemplos de grupos protectores fotolábiles.

En este contexto, los derivados de **cumarina** son candidatos idóneos para el desarrollo de nuevos **grupos protectores fotolábiles** debido a algunas de sus propiedades, tales como: i) coeficientes de extinción molar (ε) relativamente grandes, ii) alta biocompatibilidad y iii) rendimientos cuánticos de liberación (Φ_{Ph}) moderados. Además, son moléculas orgánicas de tamaño pequeño, fácilmente accesibles sintéticamente y modificables para su uso como PPGs. La derivatización de dichos cromóforos se basa en la oxidación o halogenación del grupo metilo de la posición 4 del esqueleto de cumarina tradicional, de tal manera que se posibilita la protección de grupos funcionales presentes en las moléculas cuya actividad se desea suprimir temporalmente (grupos amino, alcohol, tiol, fosfato y ácido carboxílico), a través de la formación de diferentes tipos de enlace (carbamato, carbonato, ester, etc) (**Esquema 13**).

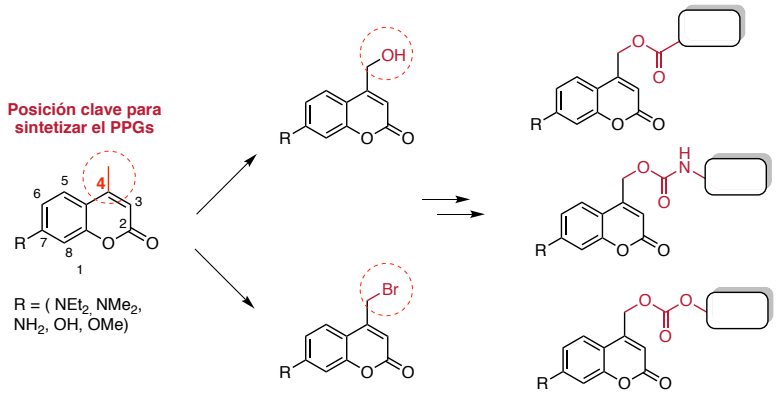

Esquema 13. Ejemplos del uso de cumarinas como grupos protectores fotolábiles.

Como se ha comentado en la introducción general (**Esquema 15, Sección 3.2.3**), la fotodesprotección se produce vía un mecanismo SN_1 y, en el caso de la protección de un ácido carboxílico en forma de éster, se obtienen como fotoproductos el ácido carboxílico libre y el correspondiente derivado de cumarina alcohol si se realiza la fotoactivación en medio acuoso.[38,39]

En la literatura encontramos diferentes ejemplos del uso de cumarinas para la protección de fármacos, proteínas, péptidos, oligonucleótidos, etc.[31,32,34] La longitud de onda necesaria para llevar a cabo la fotodesprotección se sitúa en la región ultravioleta o visible cercano (alrededor de 380 - 420 nm), la cual se puede modular mediante la incorporación de diferentes grupos electro-donadores en la posición 7 o electro-atrayentes en la posición 3 del esquelo de cumarina (**Figura 11**).

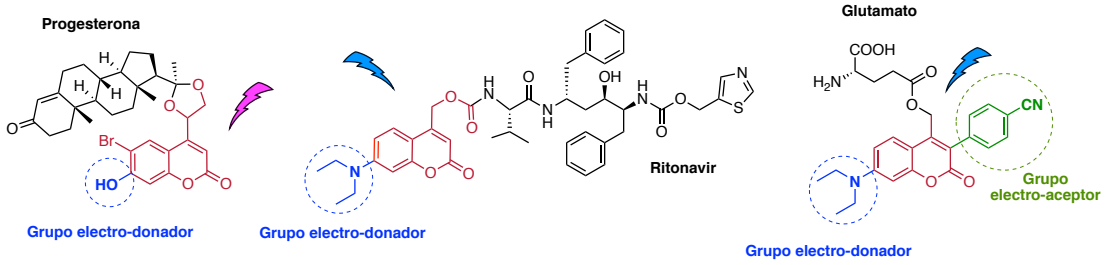

Figura 11. Ejemplos de protección de fármacos con diferentes derivados de cumarina.

Como se ha comentado en la introducción general, en los últimos años se han dedicado grandes esfuerzos a la modificación del esqueleto de cumarina con el objetivo de desplazar el máximo de absorción hacia la zona del visible. En este contexto, son destacables los derivados de tiocumarina y la incorporación del grupo dicianometileno en la posición 2, ya que permitieron desplazar la λ_{max} hasta 480 nm, posibilitando así el uso de luz verde para la liberación de dichos grupos protectores fotolábiles (**Figura 12**).[40]

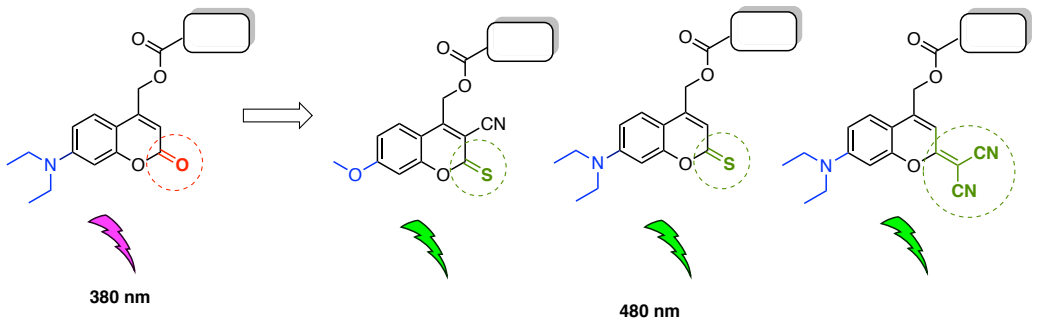

Figura 12. Ejemplos de modificaciones no convencionales en el esqueleto de cumarina.

En base a estos antecedentes, en este capítulo se planteó como principal objetivo la incorporación de un grupo protector fotolábil basado en cumarina en unas de las posiciones clave de reconocimiento de la secuencia peptídica RGD por parte de las integrinas, con el objetivo de controlar la unión péptido-receptor con luz verde. Ahora bien, en primer lugar se abordó **la síntesis de una pequeña biblioteca de análogos de dicianocumarina** con el objetivo de estudiar cómo se ve afectada la fotoliberación con luz verde en función de la estructura del grupo protector y de la naturaleza del grupo saliente (**Figura 13**).

Una vez evaluadas las propiedades fotofísicas y fotoquímicas de los compuestos protegidos modelo, se procedió a **la síntesis de derivados de ácido aspártico que incorporasen dicho grupo PPG en su cadena lateral** y, finalmente, a **la síntesis del péptido c(RGDfK) protegido (Figura 13)**, dónde el reconocimiento por parte de las integrinas quedaría suprimido temporalmente.

Además, también se abordó la conjugación de un metalofármaco modelo, rutenoceno, para poder evaluar el potencial del péptido RGD en terapias fotodirigidas. En este capítulo de la tesis se colaboró con el Dr. Santi Nonell del Instituto Químico de Sarrià de la Universidad Ramón Llull, y con el grupo de la Dra. Carme Rovira de la Universidad de Barcelona.

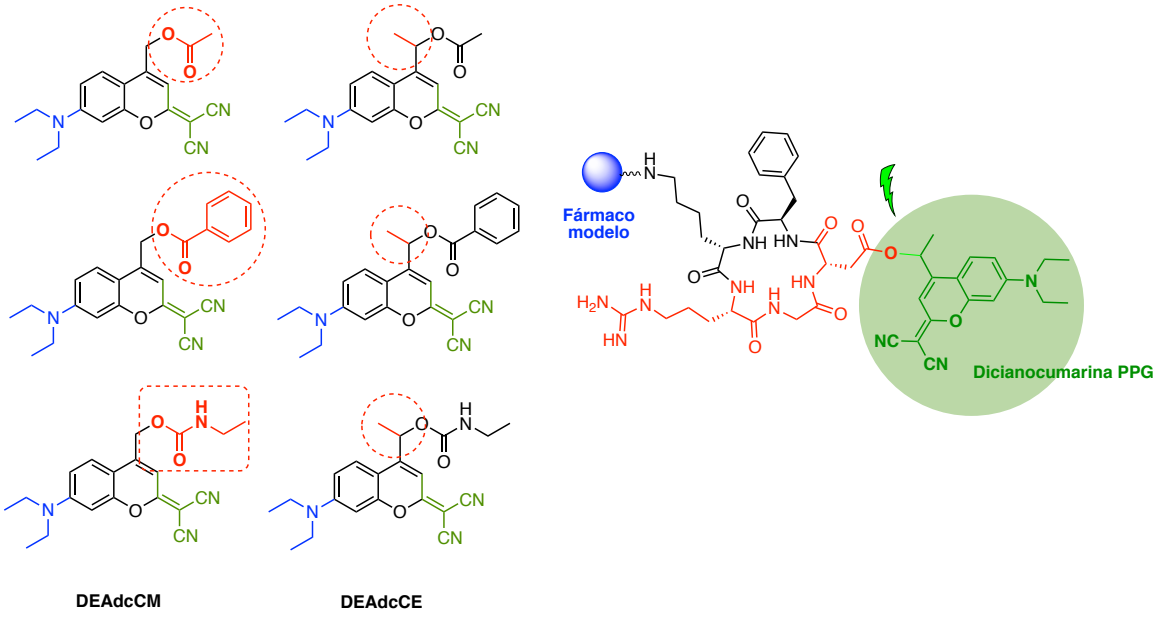

Figura 13. Serie de análogos de 7-*N,N*-dietilamino-dicianocumarina (izquierda) y conjugado protegido con un protector fotolábil basado en dicianocumarina (derecha).

12.1.2 Publicación B: Gandioso, A., Palau, M., Nin-Hill, A., Melnyk, I., Rovira, C., Nonell, S., Velasco, D., García-Amorós, J. & Marchán, V. *Sequential Uncaging with Green Light can be Achieved by Fine-Tuning the Structure of a Dicyanocoumarin Chromophore. ChemistryOpen*, 6, 375–384, (2017).

Como se ha comentado en el apartado anterior, en este artículo se abordó la síntesis de una pequeña biblioteca de derivados de dicianocumarina como modelos de la protección de ácidos carboxílicos y aminas. A continuación, se procedió al estudio de las propiedades fotofísicas y fotoquímicas de cada uno de los compuestos modelo, en particular, como se ve afectado el rendimiento cuántico de liberación **(Φ_{Ph})** en función de si se protegen grupos amino o ácido carboxílico. Asimismo, se estudió cómo se ve afectada la cinética de fotodesprotección por el hecho de incorporar un grupo etilo en la posición 4 del esqueleto de cumarina ya que debería generar un carbocatión secundario.

Síntesis y caracterización de DEAdcCM y DEAdcCE PPGs

La preparación de las 6 moléculas modelo se basó en dos rutas sintéticas muy similares, que únicamente difieren en la incorporación del grupo metilo adicional, tal y como se muestra en el **Esquema 14**.

i. En primer lugar, se procedió a la oxidación de la cumarina **1** con óxido de selenio en una mezcla de dioxano y H_2O a reflujo durante 15 días.

ii. Seguidamente, se procedió a la reducción del aldehído **2** a alcohol siguiendo dos estrategias diferentes. Por un lado, la reducción con $NaBH_4$ (**iia**) condujo a 7-(*N,N*-dietilamino)-4-(1-hidroximetil)cumarina (**3**). Por otro lado, la reacción con CH_3MgCl (**iib**) permitió obtener 7-(*N,N*-dietilamino)-4-(1-hidroxietil)cumarina (**4**).

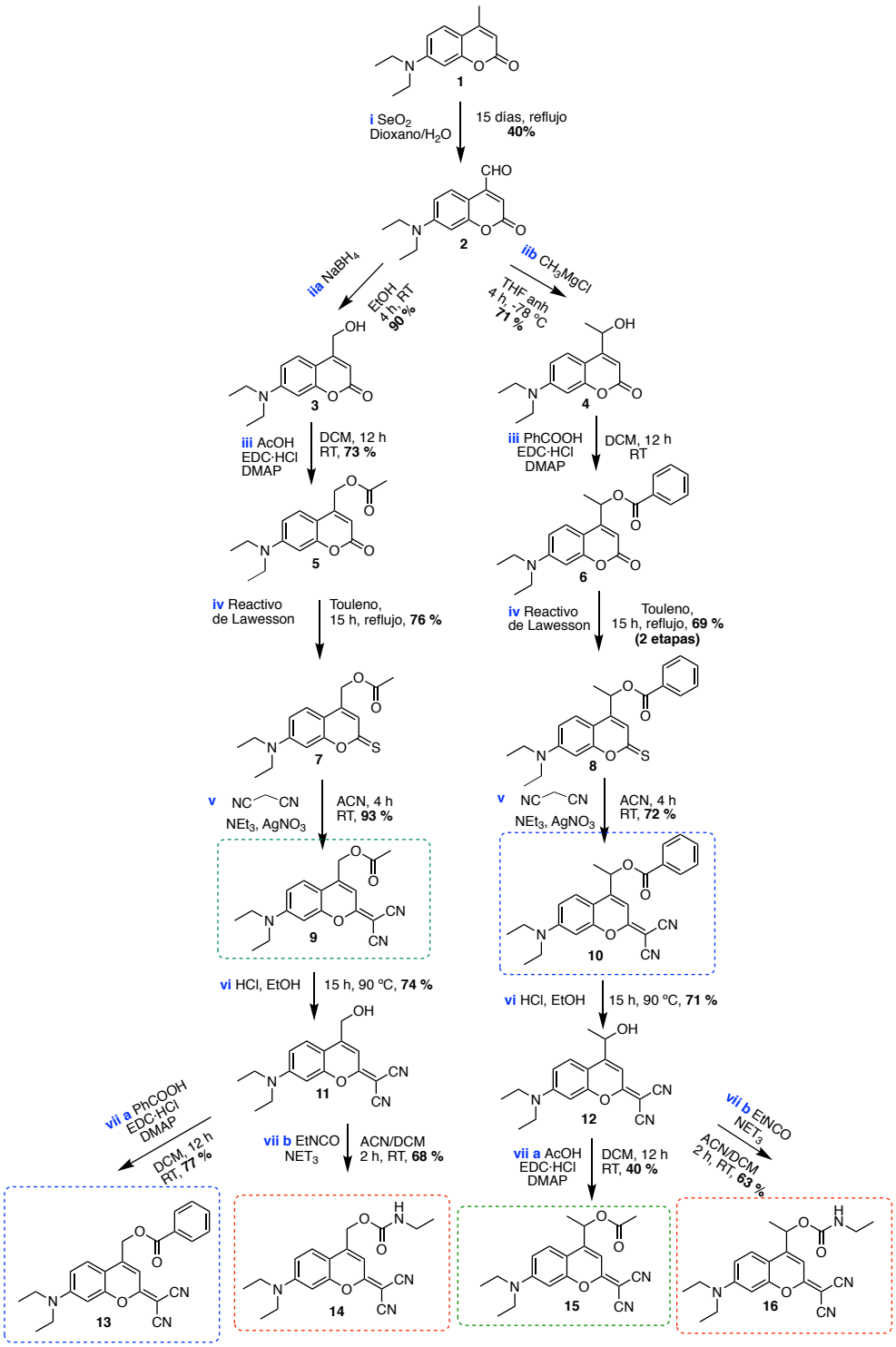

Esquema 14. Resumen de la ruta sintética de los derivados DEAdcCM y DEAdcCE.

iii. Seguidamente se protegió el grupo alcohol mediante esterificación con un ácido carboxílico alifático (**5**) o bien aromático (**6**) utilizando EDC·HCl y DMAP en diclorometano durante 12 h.

iv. La siguiente etapa consistió en la tionación (**7 y 8**) de la lactona mediante reacción con el reactivo de Lawesson en tolueno durante 15 h a reflujo. De acuerdo con la conocida mayor reactividad de este reactivo frente a lactonas, la tionación tuvo lugar exclusivamente en el grupo carbonilo de la lactona (**Esquema 15**).

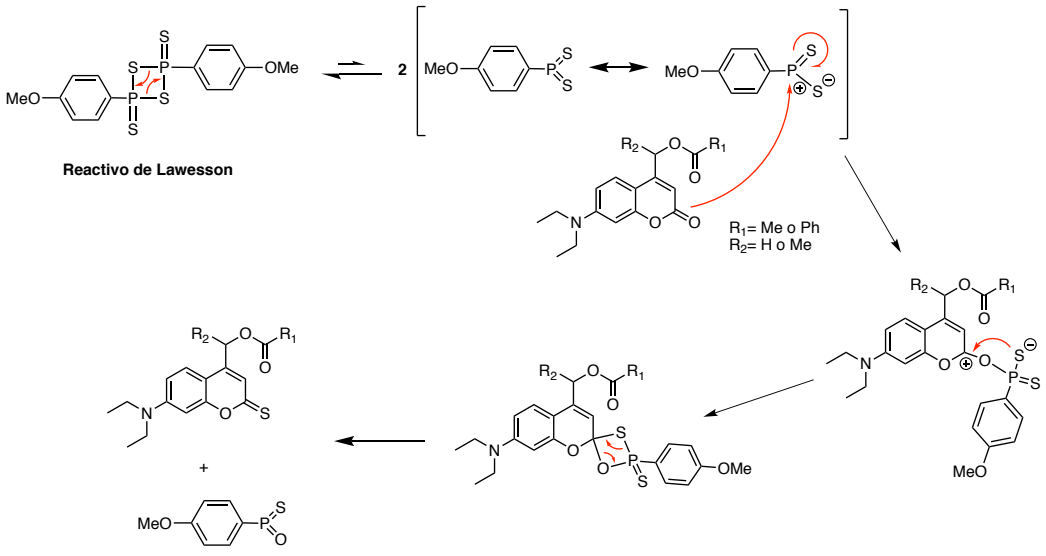

Esquema 15. Mecanismo de reacción de la tionación de una lactona con el reactivo de Lawesson.

v. A continuación, se procedió a la condensación de malononitrilo con los derivados de tiocumarina. Para ello, en primer lugar, se generó el carbanión de malononitrilo con trietilamina que, tras reacción con el derivado de tiocumarina y posterior adición de nitrato de plata, condujo a los derivados deseados **9 (DEAdcCM) y 10 (DEAdcCE) (v).** (**Esquema 16**)

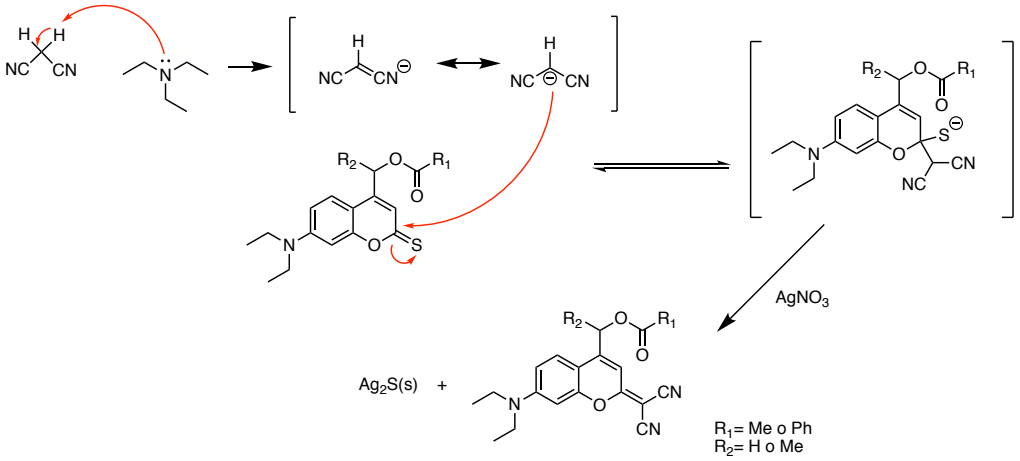

Esquema 16. Mecanismo propuesto para la reacción de la condensación de malononitrilo con los derivados de tiocumarina.

Para la síntesis de los 4 modelos de PPGs restantes, se realizaron dos últimas etapas:

vi. En primer lugar, se hidrolizó el ester de los compuestos **9 y 10** con ácido clorhídrico acuoso para dar los alcoholes correspondientes (**11 y 12**).

vii. Finalmente, la esterificación de **11** y **12** con los ácidos carboxílicos correspondientes permitió obtener los compuestos **13** y **15** (**vii a**), respectivamente. Por otro lado, los derivados carbamato **14 y 16 (vii b)** se obtuvieron por reacción con isocianato de etilo.

Todos los compuestos se purificaron por cromatografía en columna con silica gel y se caracterizaron mediante espectrometría de masas de alta resolución, RMN ^{1}H y RMN ^{13}C.

Una vez obtenidos los compuestos modelo **(9, 10 y 13-16**), se procedió a su caracterización fotofísica (λ_{abs}, λ_{em}, ε, desplazamiento de Stokes y Φ_F), tal y como se indica en la **tabla 1** del artículo. En resumen, todos ellos presentan un máximo de absorción alrededor de 485 nm y valores de coeficientes de extinción molar alrededor de 30 mM^{-1} cm^{-1}. Los máximos de emisión se sitúan sobre los 550 nm, lo que implica unos desplazamientos de Stokes de aproximadamente 65 nm, y presentan rendimientos cuánticos de fluorescencia alrededor de 0,15.

En su conjunto, estos valores permiten considerar a los derivados dicianocumarina como buenos candidatos a PPG eliminables con luz verde, siendo especialmente destacable el desplazamiento del máximo de absorción respecto a las cumarinas convencionales.

Estudios de fotodesproteccíon de los derivados de cumarina DEAdcCM y DEAdcCE.

Los estudios de fotodesprotección de los compuestos protegidos modelo se llevaron a cabo mediante irradiación con un LED de 505 nm (100 mW cm^{-2}). Los experimentos se realizaron en una mezcla 1:1 de tampón Tris pH 7.5 y ACN, previamente desgasado y a 37 °C. El análisis por HPLC-MS reveló la formación de diferentes derivados de cumarina. Por un lado, se identificó el alcohol primario **11** en la serie de DEAdcCM, y el alcohol secundario **12** en la serie de compuesto DEAdcCE junto a la cumarina alqueno (**17**) proveniente de la reacción de β-eliminación desde el carbocatión secundario intermedio (**Esquema 17**).

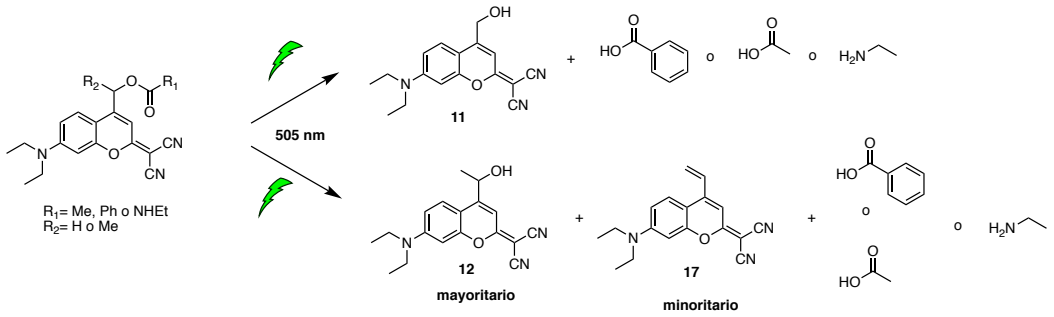

Esquema 17. Reacciones de fotodesprotección de los compuestos modelo de dicianocumarina.

Así mismo, a partir de los datos de HPLC-MS se pudieron representar las cinéticas de desprotección (κ) de cada uno de los compuestos, lo que permitió calcular los rendimientos cuánticos de desprotección. Así, los derivados éster presentan cinéticas de desprotección superiores en comparación con los derivados carbamato. Más concretamente, cuando el grupo saliente es el ácido benzoico la cinética de desprotección es superior, obteniéndose valores de $\kappa = 0.948\ min^{-1}$ y $0.314\ min^{-1}$ para los compuestos **10 y 13,** respectivamente, mientras que los valores para el ácido acético fueron inferiores ($\kappa = 0.644\ min^{-1}$ y $0.125\ min^{-1}$ para los compuestos **15 y 9,** respectivamente) (**Figura 14**).

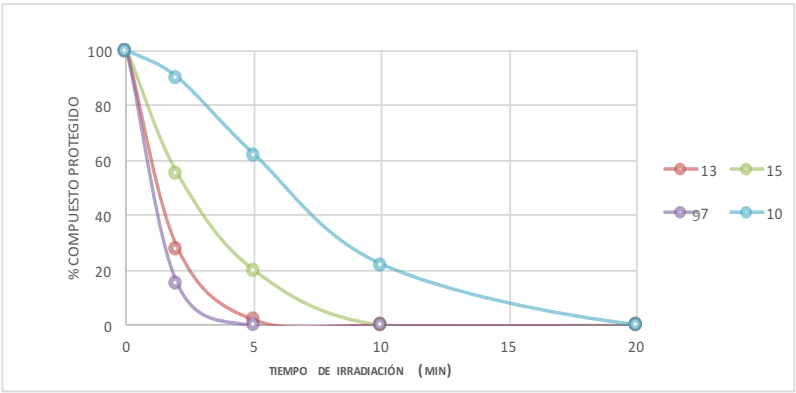

Figura 14. Cinéticas de desprotección de los compuestos **9, 10, 13 y 15**.

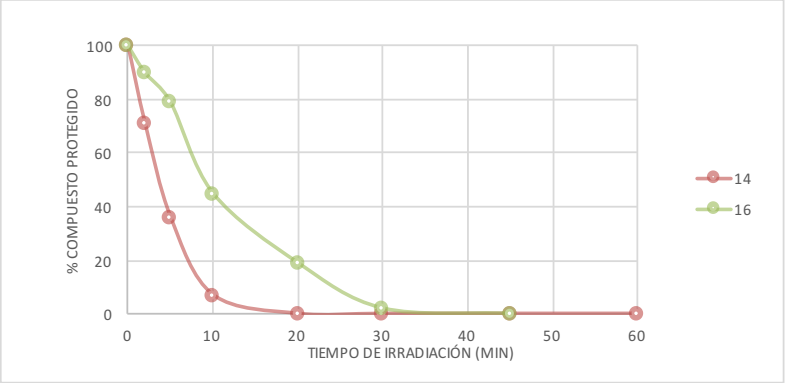

Figura 15 Cinética de desprotección de los compuestos **14 y 16**.

Es de suma importancia destacar las diferencias encontradas en las cinéticas de desprotección en las series DEAdcCM y DEAdcCE. Así, las cineticas de desprotección de los compuestos DEAdcCE son superiores, lo que se atribuye a la mayor estabilidad del carbocation intermedio generado en el mecanismo de fotodesprotección. (secundario *vs* primario).

Estudios secuenciales de fotoliberación.

En base a los buenos resultados obtenidos con los derivados modelo de DEAdcCM y DEAdcCE, se planteó estudiar su aplicabilidad para la fotodesprotección secuencial de aminas y ácidos carboxílicos aprovechando las diferentes cinéticas de desprotección según las estructuras del PPG. Para ello, se estudió la fotodesprotección de los compuestos **5, 10 y 14** con luz verde. Tal y como se muestra en la **Figura 16**, en primer lugar, se desprotegió completamente el compuesto **10** en 2 minutos mientras que los compuestos **5 y 14** permanecían inalterados. Tras 30 minutos de irradiación, el compuesto **14** se desprotegió completamente. Finalmente, se corroboró que el compuesto **5** permanecía inalterado ya que su máximo de absorción se sitúa alrededor de 380 nm (**Figura 16**).

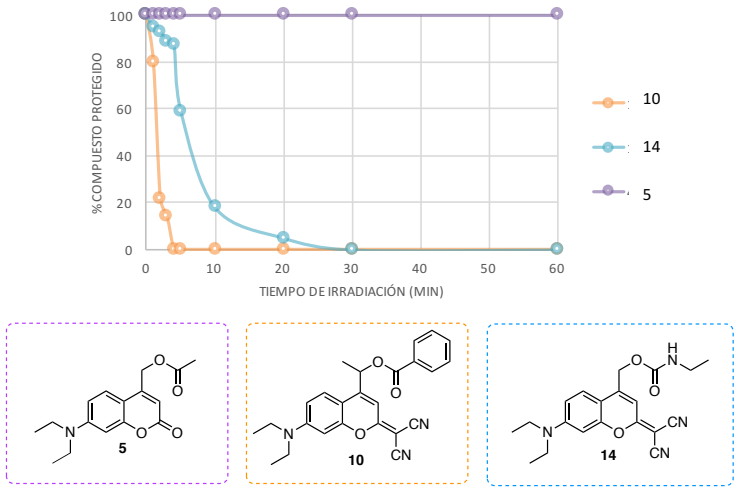

Figura 16. Estudio de desprotección secuencial mediante irradiación con luz verde.

12.2.2. Publicación C: Gandioso, A., Cano, M., Massaguer, A. & Marchán, V. *A Green Light-Triggerable RGD Peptide for Photocontrolled Targeted Drug Delivery: Synthesis and Photolysis Studies. J. Org. Chem.* 81**,** 11556−11564, (2016).

En base a los buenos resultados obtenidos con los derivados de dicianocumarina descritos en el **apartado 12.2.1**, se planteó la protección de la cadena lateral del ácido aspártico de un péptido RGD, la cual está involucrada junto a glicina y arginina en su reconocimiento por parte de ciertas integrinas sobreexpresadas en células tumorales. Tal y como se ha comentado en la **sección 3.2.3 de la introducción general de la Tesis**, en base a los antecedentes descritos por Del Campo y colaboradores, que sintetizaron derivados de Asp protegidos con las cumarinas DEACM y DEACE,[42–44] en nuestro caso nos planteamos la modificación con los análogos de dicianocumarina DEAdcCM y DEAdcCE. Tras evaluar sus propiedades fotofisicas, se seleccionó el mejor candidato para la síntesis en fase solida del péptido c(RGDfK) protegido. Finalmente, se incorporó un metalofármaco modelo, rutenoceno, para explorar su aplicabilidad en estrategias vehiculizantes de fármacos anticancerígenos fotodirigidas (**Figura 17**).

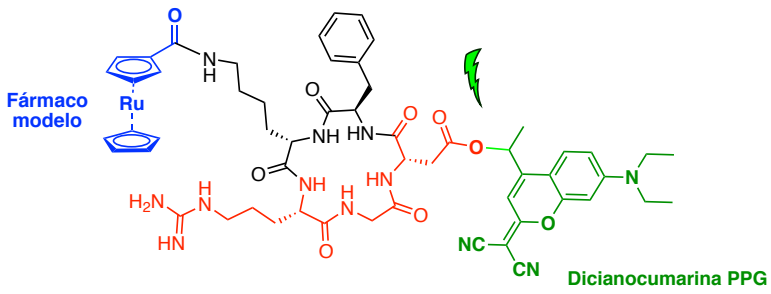

Figura 17. Estructura del péptido c(RGDfK) protegido con el derivados DEAdcCE y conjugado a un metalofármaco modelo.

Síntesis y evaluación de los monómeros DEAdcCM y DEAdcCE-Asp.

Tal y como se muestra en el **Esquema 18**, en primer lugar, se protegió de la cadena lateral de Fmoc-Asp-O*t*Bu con las cumarinas alcohol (**3** y **4**), previamente sintetizadas (**Esquema 14**). Para la reacción de esterificación se utilizó EDC·HCl y DMAP como agentes acoplantes en diclorometano durante 4 h, obteniéndose los derivados de ácido aspártico (**5** y **6**). Seguidamente, se procedió a la tionación de la lactona (**7** y **8**) por reacción con el reactivo de Lawesson (**Esquema 14**). Finalmente, la condensación con malononitrilo condujo a los aminoácidos objetivo, los compuestos **9** y **10**. Todos los compuestos fueron purificados mediante cromatografía en columna con silica gel y caracterizados por espectrometría de masas de alta resolución (ESI-HR), RMN ^{1}H, RMN ^{13}C y espectroscopía UV-Vis.

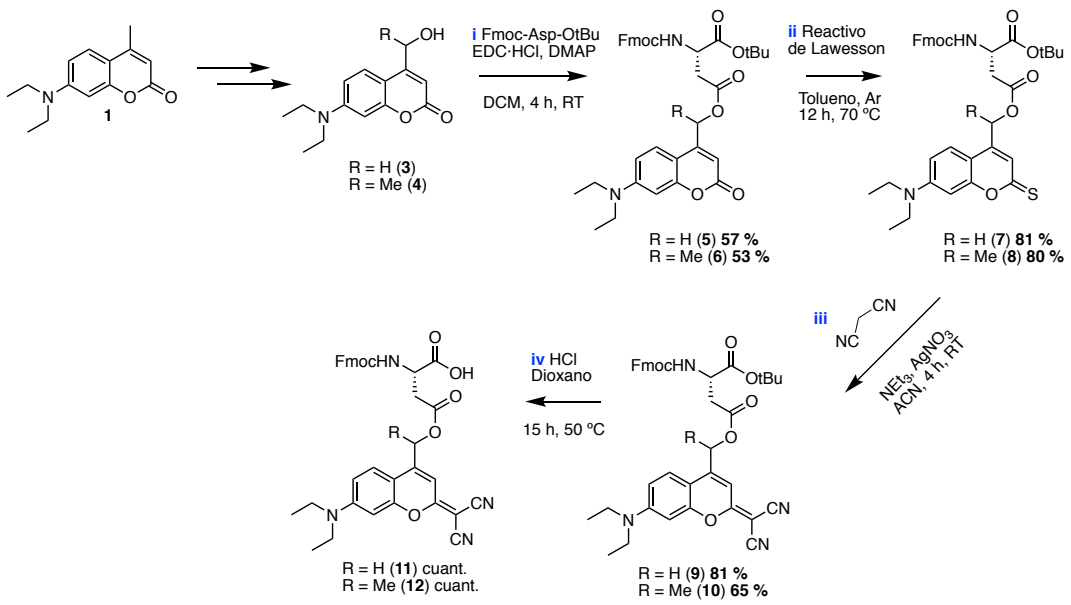

Esquema 18. Síntesis de los derivados de ácido aspártico protegidos con las cumarinas DEAdcCM y DEAdcCE.

A continuación, se investigó la **estabilidad** de los 4 monómeros de Asp modificados (DEATCM, DEATCE, DEAdcCM y DEAdcCE (**7-10,** respectivamente)) en las condiciones habituales de síntesis de péptidos en fase sólida según la estrategia Fmoc-*t*Bu: i) **condiciones ácidas** (TFA/TIS/H_2O 95:2,5;2,5) de desprotección y desanclaje, ii) **condiciones básicas** (20% piperidina en DMF durante 20 min) de desprotección del grupo Fmoc durante la elongación del péptido sobre la resina. Se seleccionaron los 4 monómeros porque todos ellos presentan un máximo de absorción alrededor de 480 nm y serían buenos candidatos para llevar a cabo la fotolisis con luz verde.

Desafortunadamente, los monómeros que incorporan los derivados de tiocumarina **DEATCM** y **DEATCE** no se mostraron completamente estables a los dos tratamientos, encontrándose diferentes subproductos no deseados provenientes de la sustitución del azufre por oxígeno (**14**) en condiciones ácidas. Por otro lado, el tratamiento básico condujo a la formación de un subproducto derivado de la adición de piperidina (**16**), tal y como se muestra en el **Esquema 19**.

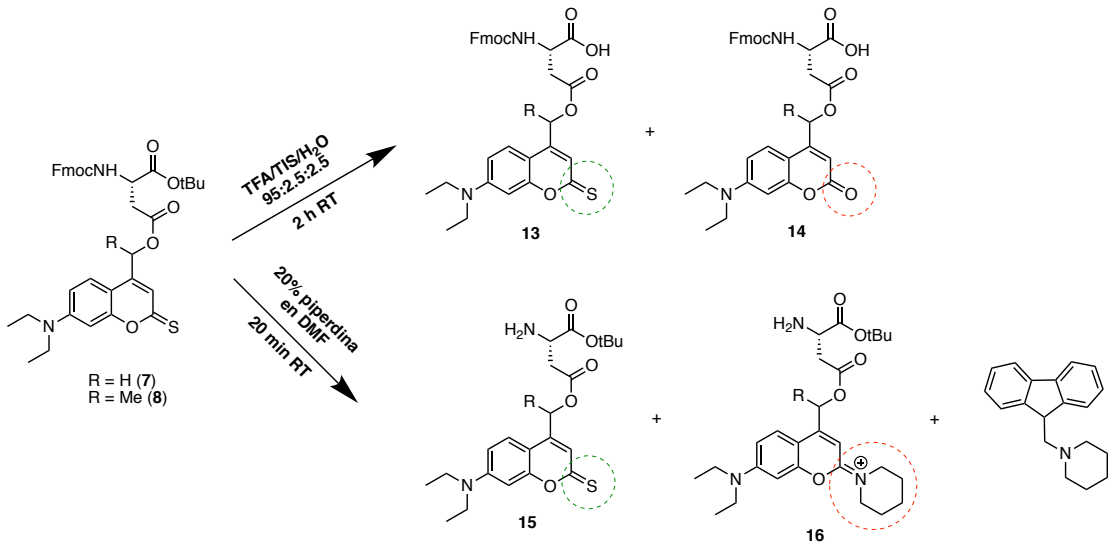

Esquema 19. Estudios de estabilidad de los compuestos **7** y **8** frente a condiciones básicas y ácidas.

En cambio, los monómeros de Asp protegidos con los dos derivados de dicianocumarina (**DEAdcCM** y **DEAdcCE)** sí que se mostraron estables a ambos tratamientos, por lo que se consideraron buenos candidatos para la síntesis en fase sólida del péptido con la secuencia RGD (**Esquema 20**).

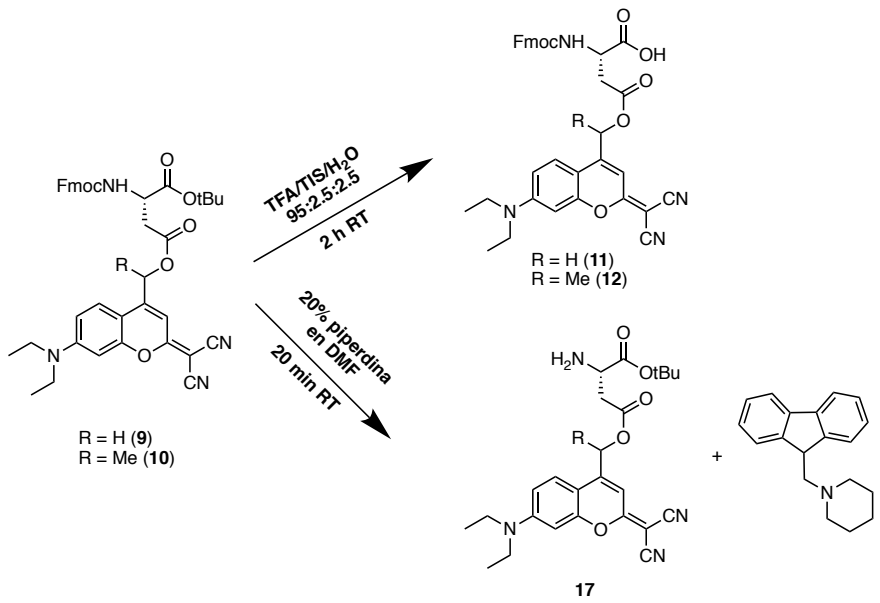

Esquema 20. Estudios de estabilidad de los compuestos **9** y **10** frente a condiciones básicas y ácidas.

A continuación, se procedió a la **caracterización fotoquímica y fotofísica** (λ_{max} , λ_{em},ϕ_F y ε) de los dos monómeros (**9** y **10)**. Es de destacar que los máximos de absorción están ligeramente desplazados (10 nm) respecto a las cumarinas modelo (489 nm para **9** y 492 nm para **10**). Los **estudios de fotólisis** se realizaron mediante irradiación con un LED de 505 nm a 37 °C, y la evolución de la reacción se realizó mediante HPLC-MS. La reacción de fotodesprotección fue completa tras 5 (**9**) y 2 (**10**) minutos de irradiación. Tal y como era de prever, el tiempo de desprotección es inferior en el caso del monómero **10,** lo que se atribuye a la mayor estabilidad del carbocatión secundario intermedio (**Esquema 21**).

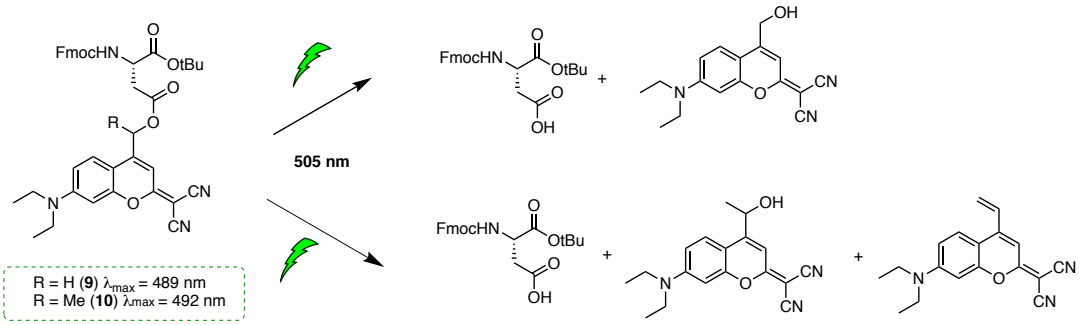

Esquema 21. Subproductos de la fotodesprotección de los monómeros de Asp **9 y 10**.

Síntesis del péptido c(RGD(DEAdcCE)fK).

Una vez comprobada la estabilidad de los dos monómeros de ácido aspártico protegidos con los derivados de dicianocumarina DEAdcCM o DEAdcCE, se procedió a investigar su aplicabilidad a la síntesis del péptido c(RGDfK) protegido en el residuo del Asp. En primer lugar, se ensambló el péptido sobre la resina cloruro de 2-clorotritilo siguiendo la estrategia Fmoc/*t*Bu. La elongación de la cadena peptídica se realizó mediante el acoplamiento secuencial de los aminoácidos Gly, Arg(Pbf), Lys(Boc) y *D*-Phe usando DIPC y HOBt como agentes acoplantes. A continuación, se desprotegió el grupo tBu de los monómeros **9** y **10** mediante tratamiento con ácido clorhídrico en dioxano a 50 °C durante 15 h (**Esquema 18, iv**), obteniéndose los compuestos **11** y **12** respectivamente, que se acoplaron sobre la peptidil-resina con HATU y DIPEA en DMF durante 2 horas. Tras la eliminación del grupo Fmoc terminal con 20% de piperidina en DMF, se procedió al desanclaje y desprotección mediante tratamiento ácido (TFA/TIS/H_2O, 95:2.5:2.5). Sorprendentemente, el análisis por HPLC-MS del crudo del péptido lineal reveló la formación de un subproducto mayoritario no deseado (**Esquema 22,** compuesto **19**) y, en menor proporción, del péptido deseado únicamente en el caso del monómero Asp-(DEAdcCE) (**Esquema 22,** compuesto **18**).

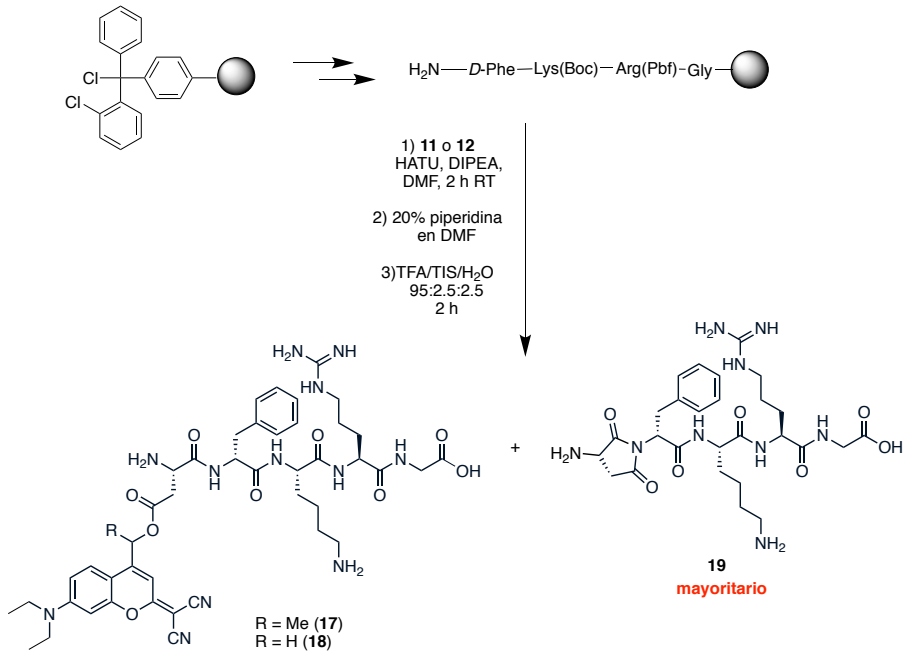

Esquema 22. Estudio preliminar del acoplamiento de los monómeros de ácido aspártico **11** y **12**.

Como se muestra en el **Esquema 22**, el subproducto **19** fue caracterizado por espectrometría de masas como el derivado aspartimida del péptido y que se habría formado durante la desprotección del grupo Fmoc. Dicha reacción secundaria es bien conocida en el ámbito de química de péptidos, ya que el tratamiento con piperidina promueve la ciclación intramolecular en péptidos que contienen residuos de Asp adyacentes a un aminoácido *D*. En nuestro caso, tras el acomplamiento de *D*-Phe se incorporó el derivado Asp protegido con DEAdcCM o DEAdcCE, lo que condujo a la aparición del péptido **19**. Albericio y colaboradores han descrito que el uso de aditivos ácidos (ácido fórmico, HOBt y Oxima) durante el tratamiento básico de desprotección del grupo Fmoc reduce la formación de aspartimidas (**Esquema 23**).[44] Es por ello que se realizaron estudios de desprotección del grupo Fmoc a nivel de peptidil-resina en diferentes condiciones tal y como se muestra en la **Tabla 1**, con el objetivo de reducir esta reacción secundaria.

Tabla 1. Evaluación de la formación de aspartimidas durante el tratamiento de desprotección del grupo Fmoc. * % determinado por HPLC-MS a 220 nm.

		Condiciones de desprotección del grupo Fmoc: 20% piperidina en DMF + aditivo en DMF, 2 x 10 min			
Aspártico protegido	**Péptido**	**Sin aditivo***	**+ 0.1 equiv. Ácido fórmico***	**+ 0.5 equiv. HOBt***	**+ 0.1 M Oxyma***
12	**17**	47	58	93	93
	19	53	42	7	7
11	**18**	0	14	24	41
	19	100	86	76	59

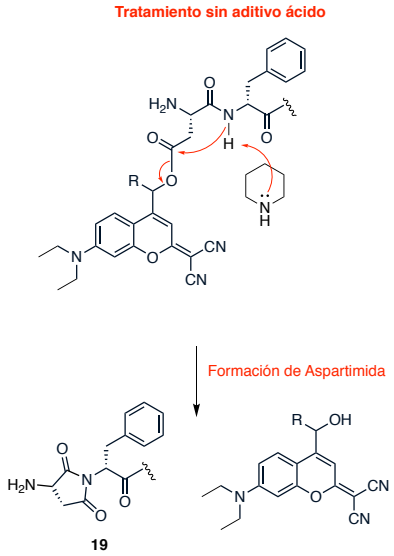

Esquema 23. Mecanismo de formación de Asparimidas.

Como se muestra en la **Tabla 1**, la desprotección del grupo Fmoc en presencia de aditivos ácidos condujo a un aumento en la proporción de los péptidos deseados (**17 y 18**), obteniéndose los mejores resultados en presencia de Oxyma y HOBt. Por otro lado, la incorporación del metilo en la posición α respecto al metilo de la posición 4 de la cumarina en el monómero de Asp(DEAdcCE), además de aumentar la cinética de fotodesprotección, suprime considerablemente la formación de aspartimidas y, por ello, se decidió utilizar únicamente el monómero **12** para la síntesis del péptido protegido **c(RGD(DEAdcCE)fK).**

Así pues, para la síntesis del péptido c(RGDfK) protegido en el residuo de Asp con la dicianocumarina DEAdcCE se siguó la estrategia descrita anteriormente y bajo las condiciones optimizadas (**Esquema 24**). Sin embargo, en esta ocasión se decidió acoplar un residuo lisina (K) que ya incorporaba el espaciador de polietilenglicol unido al ε-NH_2 para la posterior conjugación a fármacos. Una vez ensamblado el péptido lineal, se procedió a su desanclaje del soporte sólido en condiciones ácidas suaves (AcOH/TFE/DCM, 1:1:8 durante 30 min), y posterior ciclación. Finalmente, tras la desprotección del resto de grupos protectores, Boc y Pbf en condiciones ácidas, el péptido deseado (**20**) se aisló mediante purificación por HPLC en fase inversa.

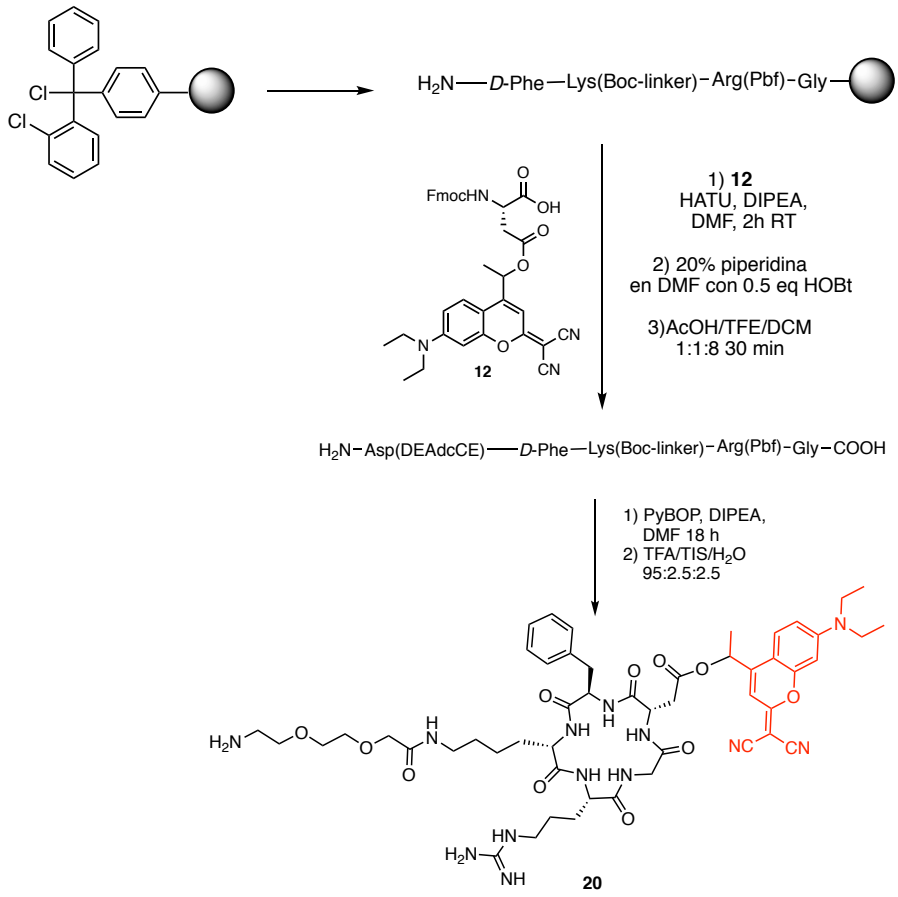

Esquema 24. Sintesis del péptido c(RGD(DEAdcCE)fK)(**20**).

Síntesis del conjugado Rutenoceno-c(RGD(DEAdcCE)fK) y estudios de fotólisis.

Una vez obtenido el péptido **c(RGD(DEAdcCE)fK) (20)**, se planteó su conjugación a rutenoceno como modelo de metalofármaco con el objetivo de controlar su vehiculización con luz verde. En primer lugar, se derivatizó rutenoceno con un grupo carboxilíco para permitir su conjugación al péptido (**Esquema 25**). Para ello, se hizo reaccionar rutenoceno con cloruro de 2-clorobenzoílo y $AlCl_3$, obteniéndose el derivado de rutenoceno **21**, el cual, tras reación con *t*-butóxido de potasio en H_2O durante 24 h, condujo al derivado de rutenoceno **22**, el cual se purificó mediante cromatografía en columna y se caracterizó por EM-ESI y RMN ^1H.

Para la conjugación al péptido, el complejo de Ru(II) se activó HATU y DIPEA en DMF durante 5 minutos, y, seguidamente, se hizo reaccionar con el péptido **20** disuelto en DMF y DIPEA bajo atmosfera de argón durante 2 horas y protegido de la luz. El conjugado deseado Rutenoceno-c(RGD(DEAdcCE)fK) (**23**) se purificó mediante HPLC en fase inversa y se caracterizó mediante espectrometría de masas (ESI) de alta resolución (**Esquema 26**).

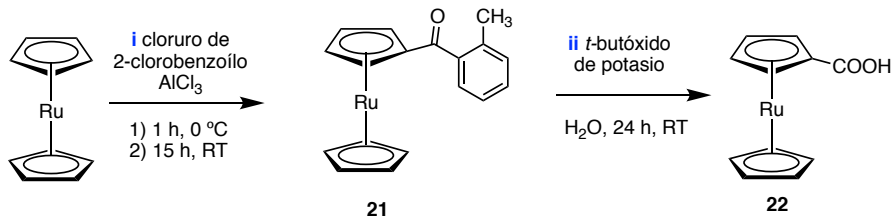

Esquema 25. Síntesis del derivado de Rutenoceno (**22**).

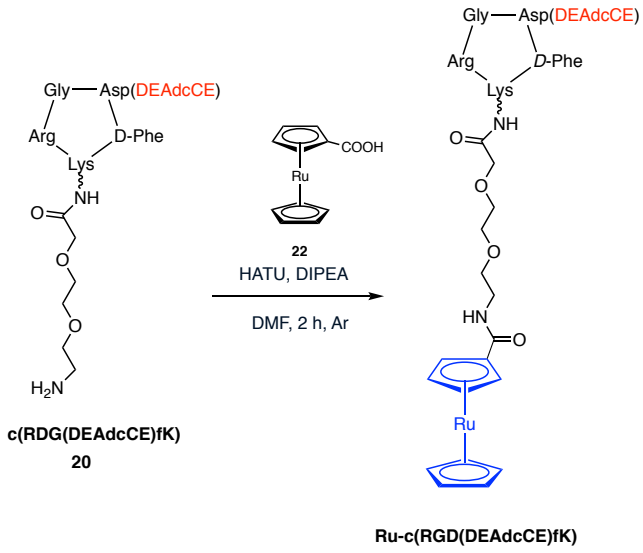

Esquema 26. Síntesis del conjugado Ru-c(RGD(DEAdcCE)fK) (**23**).

Los estudios de fotólisis, tanto del **péptido 20** como del **conjugado 23**, se realizaron mediante irradiación con luz verde (505 nm) en PBS a 37 °C. El análisis por HPLC-MS reveló que la desprotección del péptido **20** era completa a los 15 minutos, obteniéndose el péptido libre c(RGDfK) (**24**) y la cumarina alcohol (**Esquema 27**).

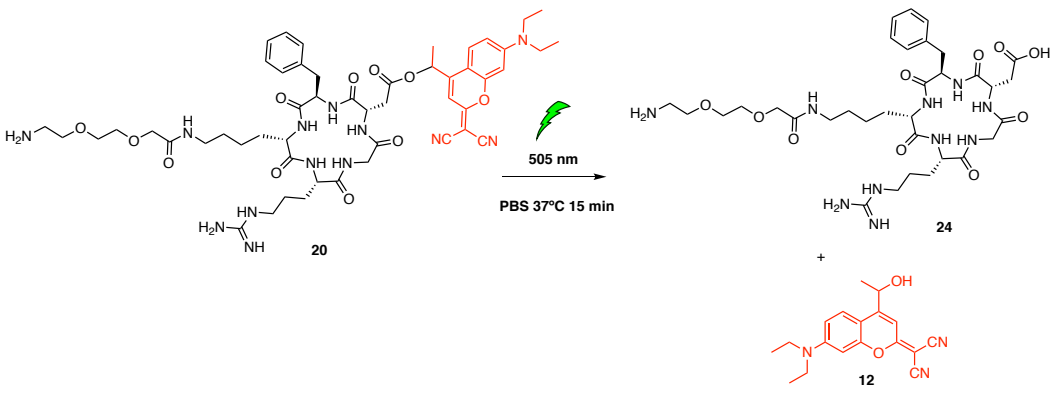

Esquema 27. Fotólisis del péptido c(RGD(DEAdcCE)fK) (**20**).

En el caso del conjugado rutenoceno-c(RGD(DEAdcCE)fK) (**23**), la desprotección fue completa a los 30 minutos, identificándose los siguientes fotoproductos: Rutenoceno-c(RGDfK)(**24**) y las cumarinas **12** y **17** (**Esquema 28**).

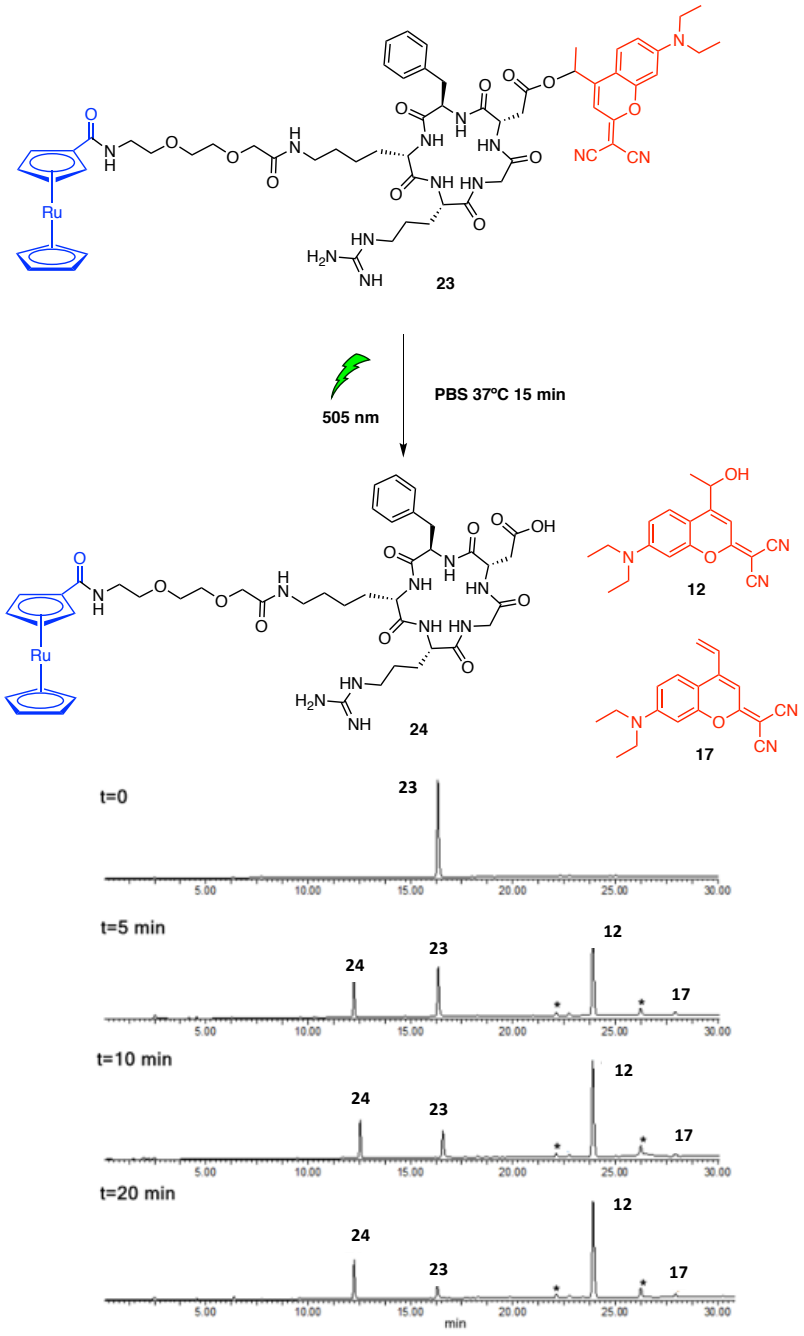

Esquema 28. Fotodesprotección del conjugado Ru-c(RGD(DEAdcCE)fK) (**23**).

12.2.4 Conclusiones.

En resumen, se ha descrito la síntesis y caracterización de nuevos grupos protectores fotolábiles basados en análogos de dicianocumarina, y su aplicación a la protección de ácidos carboxílicos y aminas. Los estudios de fotólisis con luz verde realizados con las moléculas modelo han revelado diferentes aspectos a tener en cuenta a la hora de escoger el derivado de dicianocumarina más adecuado, entre los que destacamos: i) la estructura química del PPG, ii) la naturaleza del grupo saliente, y iii) el tipo de enlace involucrado en la unión del PPG al grupo funcional a proteger.

En base a los resultados obtenidos con los compuestos modelo, se sintetizaron dos nuevos monómeros de ácido aspártico protegidos con los derivados de dicianocumarina, Fmoc-Asp(DEAdcCM)-OtBu y Fmoc-Asp(DEAdcCE)-OtBu, para su posterior uso en la síntesis de un análogo protegido del péptido cíclico c(RGDfK). Los estudios de fotoactivación revelaron que el derivado de Asp protegido con DEAdcCE presenta una cinética de desprotección superior al analógo DEAdcCM. Además, su empleo en combinación con aditivos ácidos como HOBt y Oxyma permitió minimizar la formación de aspartimidas detectada durante el ensamblaje en fase sólida del péptido lineal, lo que condujo a su elección para síntesis del péptido cíclico protegido c(RGDf(DEAdcCE)K). Finalmente, se conjugó dicho péptido a rutenoceno, como modelo de conjugado metalofármaco-péptido fotoactivable para su empleo en terapias fotodirigidas. Los estudios de fotodesprotección, tanto del péptido como del conjugado protegidos con el derivado DEAdcCE, revelaron una desprotección eficaz tras irradiación con luz verde.

12.3 Resumen del capítulo III.

12.3.1 Introducción y objetivos.

La luz puede utilizarse en el ámbito de la química terapéutica como agente externo para controlar procesos biológicos o bien para activar fármacos, tal y como hemos desarrollado en los dos capítulos anteriores.[30,45,46] No obstante, gracias a los avances tecnológicos en el campo de la microscopia de fluorescencia, la luz también puede juegar un papel muy importante en **la visualización de procesos biológicos**. Para ello es necesario disponer de moléculas con propiedades fluorescentes, como son los **fluoróforos orgánicos**. Además, gracias a los avances i) en las tecnologías de visualización, ii) a la disponibilidad de fluoróforos que operan en la zona del infrarrojo cercano, y iii) su posible **conjugación a vehículos a vehículos transportadores**, la visualización de células tumorales en tiempo real en la estrategia conocida como cirugía guiada por fluorescencia presenta un gran potencial en el diagnóstico y tratamiento del cáncer.[47-51]

En las últimas décadas se han desarrollado un gran número de fluoróforos que operan desde la zona ultravioleta del espectro electromagnético hasta los límites entre la zona visible y el infrarrojo cercano, dónde destacan algunos derivados de fluoresceína, cumarina, rodamina, BODIPY y cianina (**Figura 18**).[52-54]

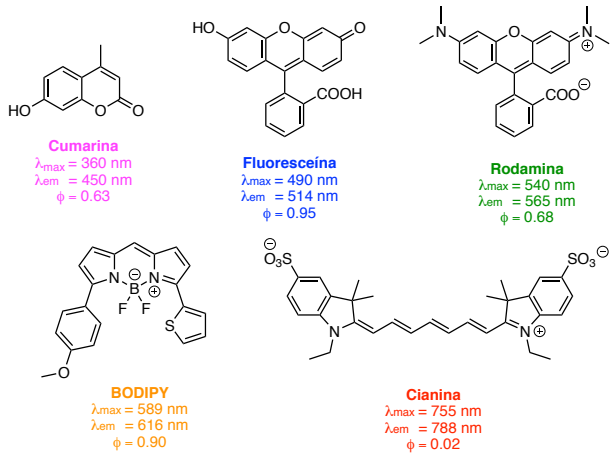

Figura 18. Ejemplos de diferentes fluoróforos con operatividad a lo largo del espectro electromagnético.

Idealmente, los fluoróforos deben reunir ciertas características como, por ejemplo: i) **desplazamientos de Stokes grandes**, ii) **fotoestabilidad** y iii) **buen brillo**. Además, para aplicaciones *in vivo* hay que tener en cuenta algunos parámetros adicionales, tales como la **solubilidad en agua**, la tendencia a la **agregación**, su **rendimiento cuántico de emisión en medio acuoso** y su posible **toxicidad**. Por otro lado, el tipo de luz es también de suma importancia y, por ello, se han dedicado grandes esfuerzos a conseguir desplazar el máximo de absorción de los fluoróforos hacia la zona visible e incluso al **infrarrojo cercano (NIR)**. Ello es debido que la luz en el NIR presenta una **mayor capacidad de penetración en los tejidos** y **menor toxicidad**.

Como se ha comentado anteriormente, la conjugación de fluoróforos a vehículos selectivos de células tumorales, tales como péptidos, proteínas, oligonucleótidos, anticuerpos, o moléculas orgánicas, permite **distinguir y visualizar las células tumorales frente a las células sanas**. Dichas aplicaciones requieren el uso de fluoróforos que, además de reunir las características anteriormente mencionadas, sean fácilmente derivatizables para permitir su conjugación a diferentes grupos funcionales presentes en las biomoléculas en cuestión (**Figura 19**).[55,56]

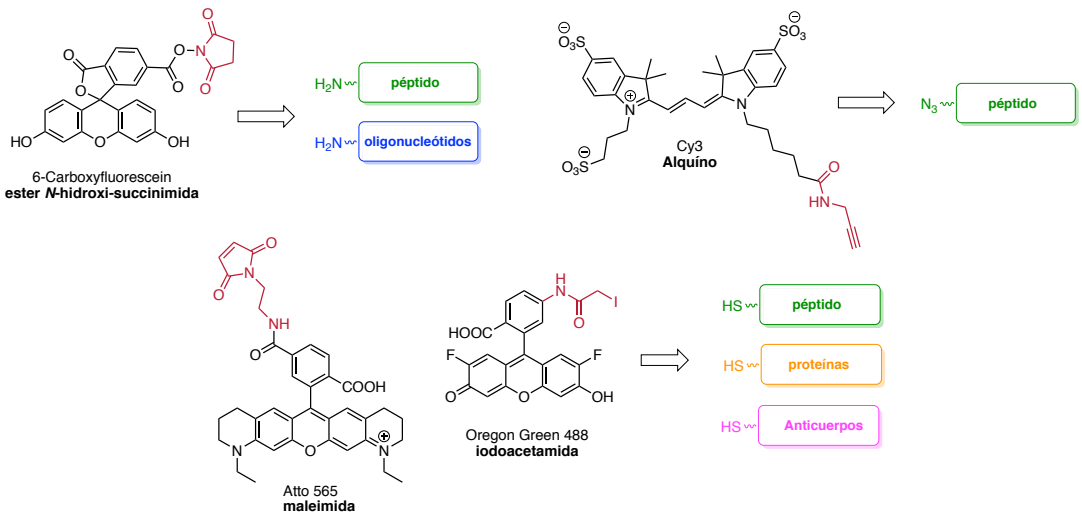

Figura 19. Ejemplos de estrategias de conjugación de fluoróforos comerciales a biomoléculas.

En este contexto, las cumarinas representan un buen punto de partida para desarrollar nuevos fluoróforos con propiedades fotofísicas mejoradas. Además, su estructura simple permite la incorporación de diferentes grupos funcionales que posibilitan la conjugación a vehículos transportadores. En los últimos años, diferentes grupos de investigación, incluido el nuestro, han explorado la introducción de modificaciones en la **posición 2** del esqueleto de cumarina, como son la sustitución del átomo de oxígeno de la lactona por un **azufre** o bien la condensación con **malononitrilo**. Estos nuevos análogos máximos de absorción alrededor de **480 nm**.[40,45,46] Recientemente, en nuestro grupo de investigación también se ha explorado la sustitución de un grupo nitrilo en los derivados de dicianocumarina por **4-nitrofenilo**, lo que ha permitido obtener máximos de absorción alrededor de **600 nm** a través de la incorporación de diferentes grupos electroatrayentes (flúor, nitrilo, nitro) (**Esquema 29**).[57]

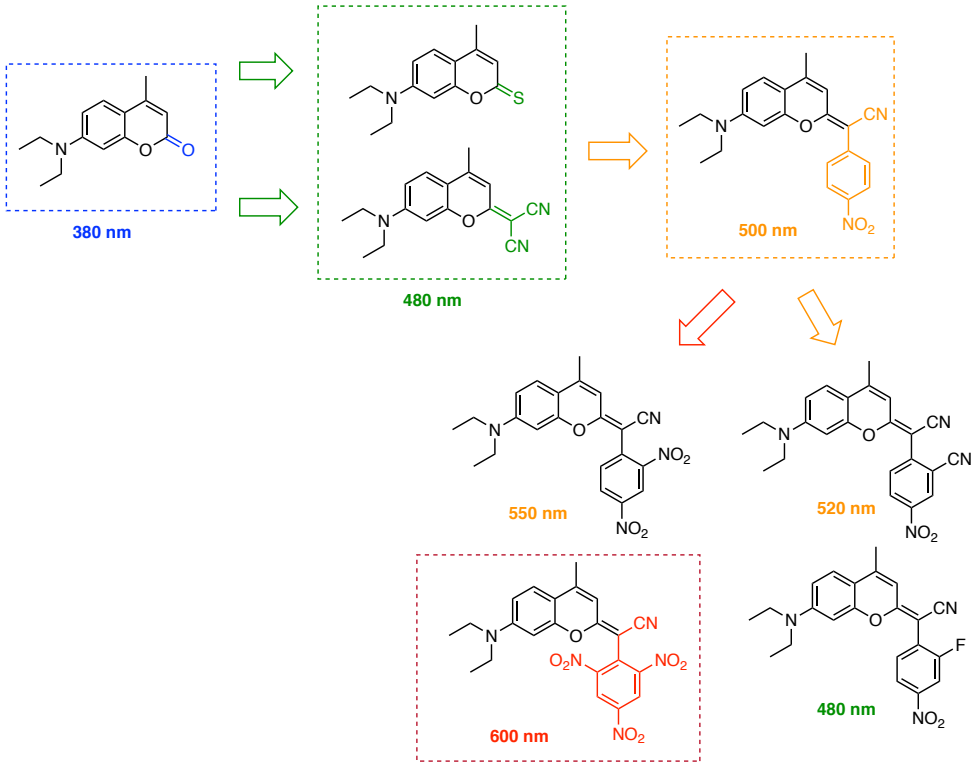

Esquema 29. Desarrollo de nuevas modificaciones en el esqueleto de cumarina.

En base a estos antecedentes, en esta tesis doctoral se ha diseñado y sintetizado una **nueva familia de cumarinas**, en las que el heterociclo de piridina reemplaza al grupo 4-nitrofenilo. La caracterización espectroscópica y fotofísica completa de los nuevos fluoróforos se ha realizado en colaboración con el grupo del Dr. Santi Nonell del Instituto Químico de Sarria de la Universidad Ramon Llull. Además, se han realizado estudios de internalización mediante microscopia confocal bajo la supervisión del Dr. Manel Bosch en la Unidad de Microscopia Óptica Avanzada de la Universidad de Barcelona. Finalmente, se ha derivatizado uno de los nuevos fluoróforos para posibilitar su conjugación a **Octreotide**, un ciclooctapéptido agonista del receptor de la somatostanina que se sobreexpresa en ciertas células tumorales (**Esquema 30**).

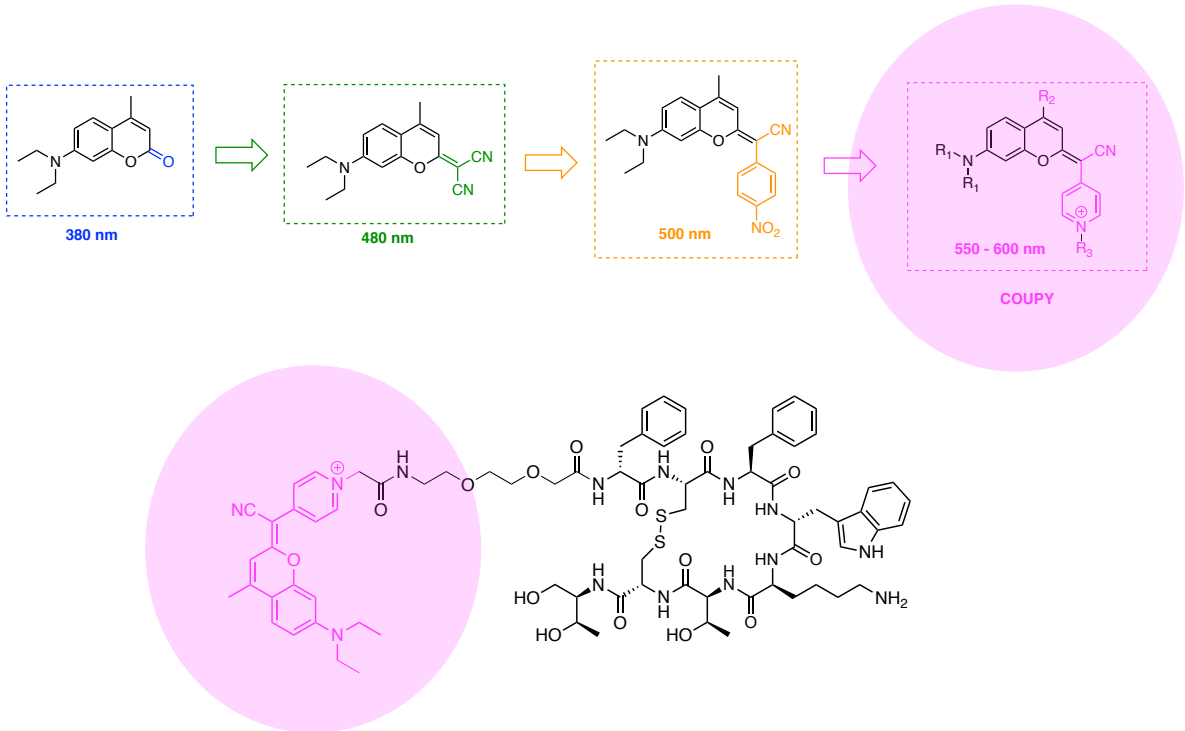

Esquema 30. Síntesis de nuevos fluoróforos basados en cumarina y su conjugación a Octreotide.

12.3.2. Publicación D: Gandioso, A., Bresolí-Obach, R., Nin-Hill, A., Bosch, M., Palau, M., Galindo, A., Contreras, S., Rovira, A., Rovira, C., Nonell, S. & Marchán, V *Redesigning the Coumarin Scaffold into Small Bright Fluorophores with Far-Red to Near-Infrared Emission and Large Stokes Shifts Useful for Cell Imaging. J. Org. Chem.* 83, 1185–1195 (2018).

En este trabajo se describió por primera vez una nueva familia de fluoróforos basados en cumarina con emisión en la región que va del rojo lejano al NIR. En primer lugar, se sintetizaron dos precursores basados en 7-*N,N*-dietilamino-cumarina y 4-trifluorometil-7-*N,N*-dimetilamino-cumarina en los que se modificó la lactona mediante la condensación del fragmento de 4-piridilacetonitrilo. En segundo lugar, se sintetizaron 4 nuevos fluoróforos, denominados COUPY, mediante la *N*-alquilación del anillo piridina con grupos metilo y trifluoroetilo. Finalmente, se procedió a su caracterización fotofísica y la realización de estudios de internalización mediante microscopia confocal en la linea celular HeLa.

Diseño, síntesis y caracterización de los precursores de los fluoróforos COUPY.

En primer lugar, se sintetizaron los derivados de tiocumarina **3** y **4** mediante reacción de las cumarinas **1** y **2** con el reactivo de Lawesson **(Esquema 31, i)**. Seguidamente, se llevó a cabo la condensación de 4-piridilacetonitrilo sobre la tiolactona, en presencia de hidruro de sodio para formar el intermedio correspondiente, seguido de la adición de nitrato de plata lo que condujo a los precursores **5** y **6** (**Esquema 31, ii**). Dichos compuestos se purificaron mediante cromatografía en columna y se caracterizaron mediante espectrometría de masas, RMN ^{1}H y RMN ^{13}C.

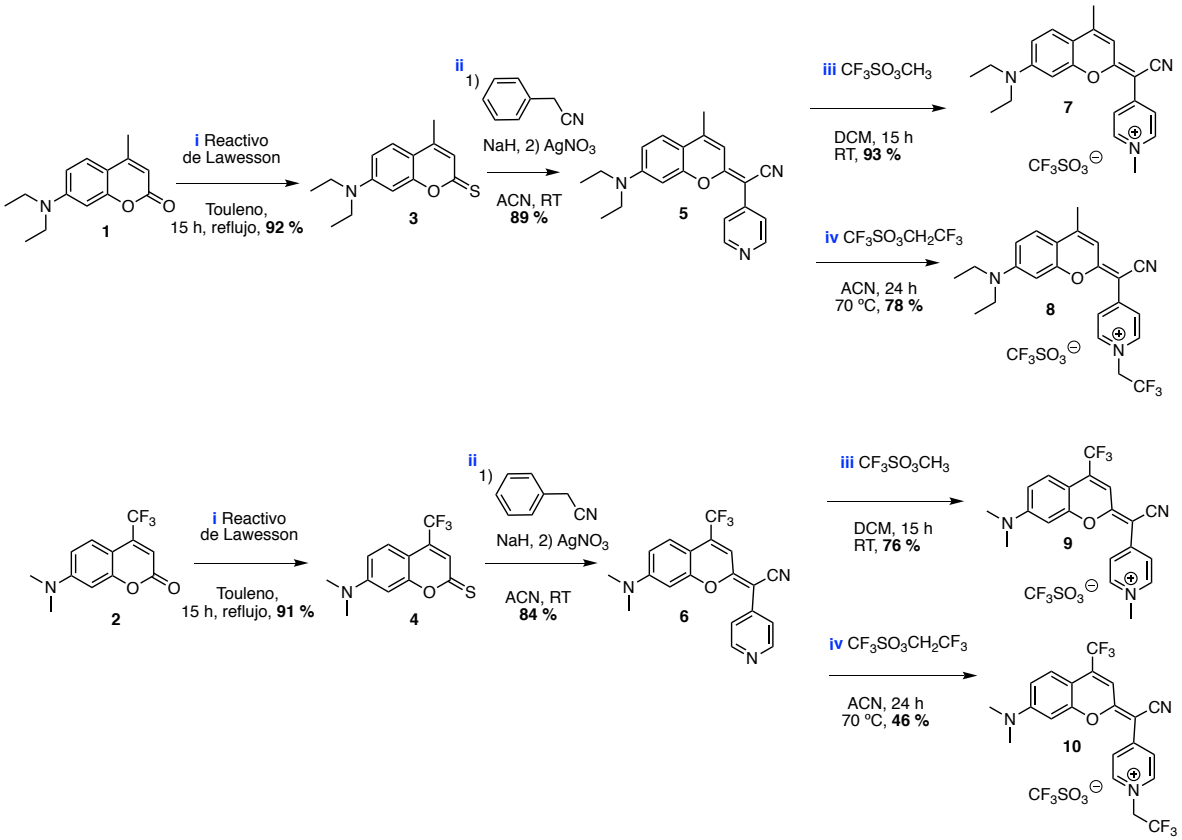

Esquema 31. Ruta sintética seguida para la preparación de los nuevos fluoróforos COUPY.

Sorprendentemente, en los espectros de RMN ^{1}H del compuesto **5** se observaron dos especies en una proporción 90:10. La realización de experimentos de RMN ^{1}H COSY y NOESY permitió confirmar la existencia de dos especies en equilibrio en solución, que fueron caracterizadas como los rotámeros *E* y *Z*. Ello es debido a que el doble enlace exocíclico que une el esqueleto de cumarina con el fragmento de 4-piridilacetonitrilo tiene cierto carácter de enlace sencillo debido a la fuerte deslocalización electrónica a lo largo de la molécula y, por consiguiente, permite la rotación y la formación de dos especies en equilibrio (**Esquema 32).** Dichos resultados fueron corroborados mediante estudios computacionales en colaboración con la Dra. Carme Rovira de la Universidad de Barcelona.

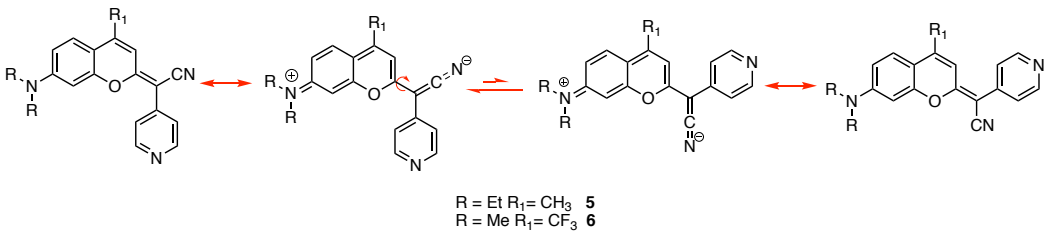

Esquema 32. Rotámetros *E* y *Z* de los precursores COUPY.

Tal y como se muestra en la **Figura 1** del artículo, la presencia de picos de correlación NOE permitió concluir que la especie mayoritaria correspondía al rotámero *E*. Así mismo, la existencia de dos especies en equilibrio también se confirmó mediante experimentos de irradiación 1D NOE selectivos en los que se observó la inversión de la señal del rotámetro *Z* cuando se irradiaba sobre la señal del rotámero *E* y viceversa. Todo ello confirmó la existencia de un equilibrio entre los rotámetros y que no se trataba de diasteroisómeros (**Esquema 33**).

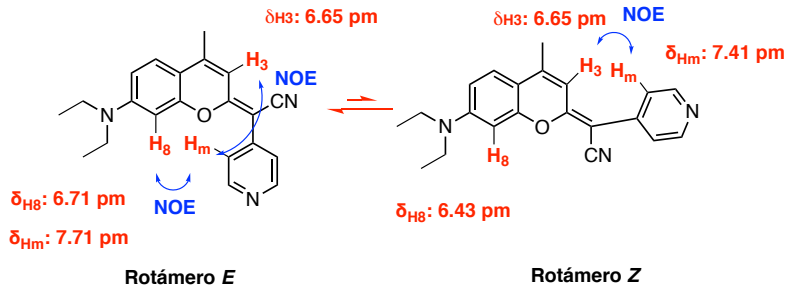

Esquema 33. Estructuras de los rotámeros *E* y *Z* del compuesto **5**.

Síntesis y caracterización de los fluoróforos COUPY.

Una vez sintetizados y caracterizados los precursores **5** y **6**, se procedió a la alquilación del nitrógeno de la piridina. Por un lado, la reacción con trifluorometansulfonato de metilo en DCM a temperatura ambiente durante 15 horas condujo los compuestos **7** y **9** (**Esquema 31, iii**). Por otro lado, la reacción con trifluorometansulfonato de 2,2,2-trifluoroetilo en acetonitrilo a 70 °C durante 15 horas condujo a los compuestos **8** y **10 (Esquema 31, iv)**. Todos ellos se precipitaron y se purificaron mediante columna cromatográfica con silica gel y se caracterizaron mediante espectrometría de masas y RMN ^{1}H, ^{13}C, COSY y NOESY (**Figura 20**).

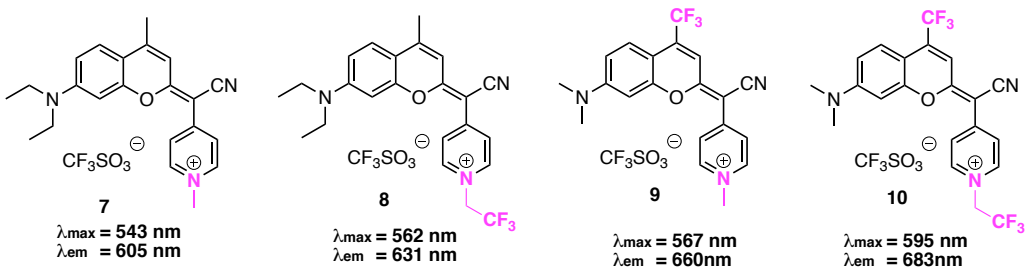

Figura 20. Estructuras de los fluoróforos COUPY. Se indican los máximos de absorción y emisión en H_2O

Algunos de los resultados de la caracterización espectroscópica y fotofísica de los 4 nuevos fluoróforos se recogen en la **tabla 2**: i) máximo de absorción (λ_{max}), ii) máximo de emisión (λ_{em}), iii) desplazamiento de Stokes, iv) coeficiente de extinción molar (ε), v) rendimiento cuántico de fluorescencia (Φ_F) y vi) tiempo de vida media de fluorescencia (τ_F). Todos estos parámetros fueron analizados en disolventes (tampón PBS, H_2O, metanol, glicerol, acetonitrilo, diclorometano y tolueno) de diferente polaridad y viscosidad. Como se muestra en la **tabla 2**, la condensación del fragmento de 4-piridilacetonitrilo en el esqueleto de cumarina desplaza considerablemente los máximos de absorción y emisión hacia la región visible del espectro electromagnético, y en algunos casos, hasta el NIR en comparación con las cumarinas convencionales. Es destacable que la alquilación de la piridina con el grupo trifluoroetilo conduce a un desplazamiento addicional en los máximos de absorción y emisión. Así, el compuesto **7** presenta un máximo de absorción a 543 nm (H_2O) y de emisión a 605 nm (H_2O) mientras que los del compuesto **8** se sitúan alrededor de 562 nm (H_2O) y 631 nm (H_2O), respectivamente

De la misma manera, la sustitución del CH_3 de la posición 4 por CF_3 supone pasar de λ_{max} 562 nm (H_2O) y λ_{em} 631 nm (H_2O) en el compuesto **8** a λ_{max} 595 nm (H_2O) y λ_{em} 683 nm (H_2O) en el compuesto **10**. En general, los desplazamientos de Stokes son relativamente grandes, siendo mayores en los derivados de cumarina con el CF_3 en la posición 4. En cuanto a los rendimientos de fluorescencia, los valores son relativamente buenos en disolventes menos polares. Sin embargo, los Φ_F en disolventes polares (H_2O) son inferiores, probablemente debido al efecto TICT, tal y como sugiere su aumento en disolventes polares más viscosos como el glicerol.

Tabla 2. Propiedades fotofísicas de los derivados de cumarina **7-10**.

	Disolvente	λ_{max} (nm)	ε ($mM^{-1}cm^{-1}$)	λ_{em} (nm)	Stokes (nm)	Φ_F	τ_F (ns)
7	**H_2O**	543	31	605	62	0.15	1.0
	ACN	548	75	609	61	0.18	1.4
	DCM	569	67	607	38	0.70	5.4
8	**H_2O**	562	33	631	69	0.026	0.5
	ACN	567	43	636	69	0.12	1.2
	DCM	588	51	628	40	0.31	2.9
9	**H_2O**	567	13	662	95	0.019	0.3
	ACN	569	47	668	99	0.023	0.2
	DCM	600	34	657	57	0.054	0.7
10	**H_2O**	595	6.9	683	88	0.046	0.5
	ACN	597	26	689	92	0.12	1.4
	DCM	621	24	679	58	0.25	3.5

Estudios de internalización celular de los fluoróforos COUPY mediante microcopia confocal.

En primer lugar, se estudió la internalización de los nuevos derivados de cumarina (**7-10**) en células HeLa a diferentes concentraciones (0.5 µM, 1 µM y 2 µM) tras 30 minutos de incubación. La visualización se realizó mediante microscopía confocal de fluorescencia irradiando con el láser de 561 nm para los compuestos **7-9** y con el de 633 nm para el compuesto **10**. En todos los casos se observó la internalización de los compuestos, siendo el patrón de acumulación muy similar. Como se muestra en la **Figura 21**, para el compuesto **7** se observó la acumulación en las mitocondrias, nucléolo y en ciertas vesículas.

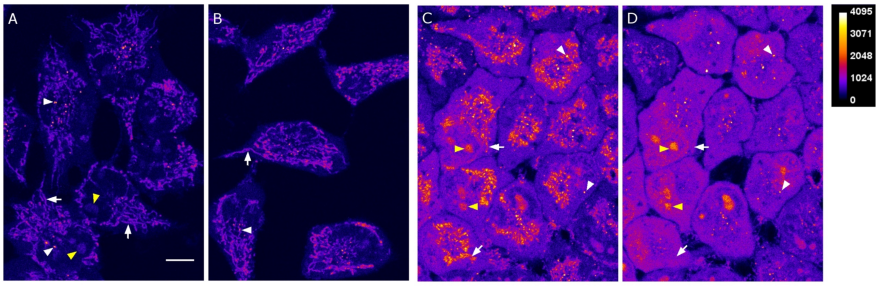

Figura 21. Internalización del compuesto **7** en células a diferentes concentraciones: 0.5 µM (A), 1 µM (B) y 2 µM (C y D).

A continuación, se realizaron estudios de co-localización con los compuestos **7-9** usándose marcadores específicos de mitocondria (MitoTracker Green FM) y núcleo (Hoescht 33342) para confirmar la localización. En el caso de la cumarina **7**, se realizó el **estudio de co-localización** a una concentración 0.5 µM incubándose en presencia Mitotracker green FM (0.1 µM) durante 30 minutos a 37 °C. Tras realizar lavados con PBS, se añadió el marcador de núcleo (1 µg/mL) y se incubó durante 10 minutos a 37 °C.

Dichos marcadores fueron seleccionados ya que debían operar en un rango de absorción diferente al del compuesto **7** (MitroTracker Green se excita a 488 nm y Hoechst 33342 a 405 nm). Tal y como se muestra en la **Figura 22**, se confirmó la localización de la cumarina **7** en las mitocondrias y nucléolo (**Figura 22, B, Rojo**), ya que al irradiar a 488 nm únicamente se observó el marcaje de las mitocondrias debido a MitroTracker Green (**Figura 22, C, Verde**), mientras que al irradiar a 405 se observó marcaje en el núcleo de la célula, pero no en el nucleolo (**Figura 22, D**, **Azul**).

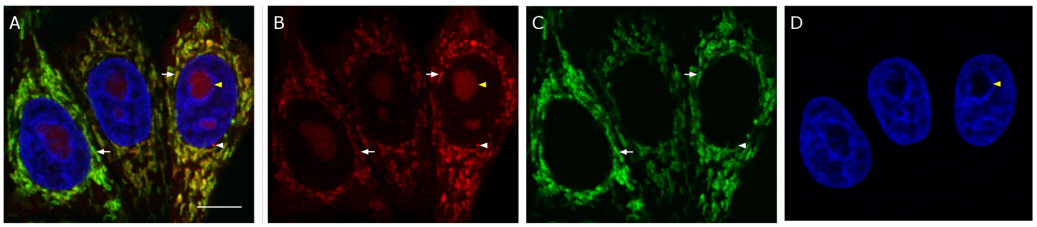

Figura 22. Estudios de co-localización en células HeLa. Compuesto **7** (0,5 µM, rojo, **B**), Mitotracker Green FM (0,1 µM, verde, **C**), y Hoechst 33342 (1 µg/mL, azul, **D**) y superposición de los canales B-D (**A**).

De la misma manera, los resultados de co-localización de las cumarinas **8** y **9** **(Figura 23)** confirmaron la acumulación en mitocondrias.

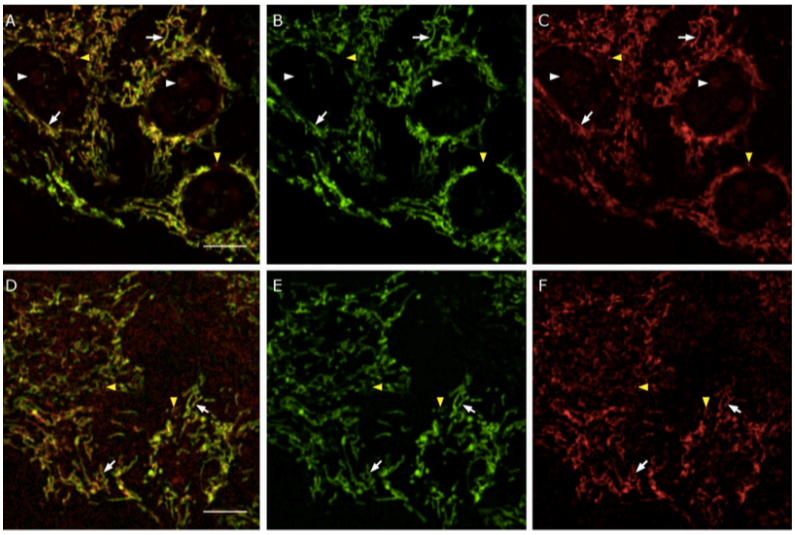

Figura 23. Estudios de co-localización en células HeLa. Internalización de los compuesto **8** y **9** (2 μM, rojo, **C y F**), Mitotracker Green FM (0,1 μM, verde, **B** y **E**) y superposición de los canales B-C y E-F (**A** y **D**).

Así mismo, se realizaron **estudios de foto-estabilidad** de los compuestos **7-9** mediante irradiación con el láser de 561 nm, registrandóse imágenes a diferentes tiempos (**Figura 24**). En el caso de la cumarina **7,** se observó una rápida pérdida de la emisión de fluorescencia a los 5 minutos como consecuencia de la desaparición del marcaje en las mitocondrias y su re-distribución en el citoplasma. En cambio, los derivados **8** y **9** presentaron una fotoestabilidad superior ya que a los diez minutos todavia se identifica un marcaje de las mitocondrias. Por tanto, además de desplazar el máximo hacía el rojo dentro del espectro electromagnético, la alquilación de la piridina con el grupo trifluoroetilo (**cumarina 8**) o la sustitución del CH_3 por CF_3 en la posición 4 (**cumarina 9**) también implica un aumento considerable en la fotoestabilidad de los fluoróforos COUPY.

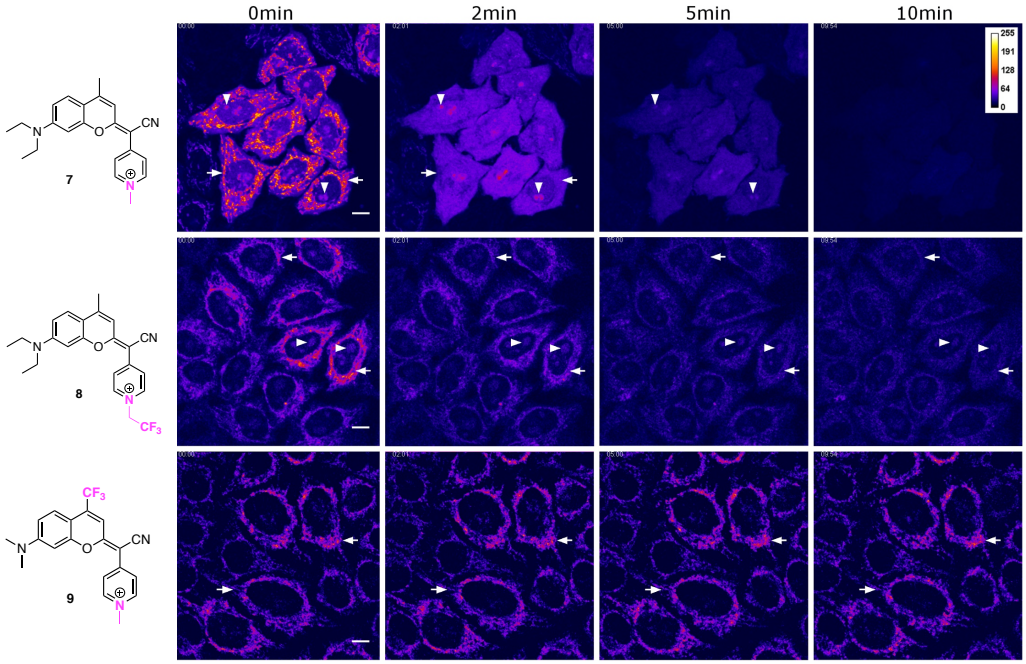

Figura 24. Estudios de fotoestabilidad de los compuestos **7-9** al irradiar a 561 nm en la línea celular HeLa.

Finalmente, se realizaron estudios de permeabilización y fijación con la cumarina **7**, para evaluar su uso como marcador en aquellas técnicas de microscopia de fluorescencia dónde es necesario fijar y/o permeabilizar las células. En el caso del tratamiento con paraformaldehido se observó que el marcaje no se veía alterado tras 10 min de incubación (**Figura 25, A**). Sin embargo, tras la permeabilización de las células con Triton, se observó la pérdida de fluorescencia en las mitocondrias, la cual se extendió por todo el citoplasma (**Figura 25,B**).

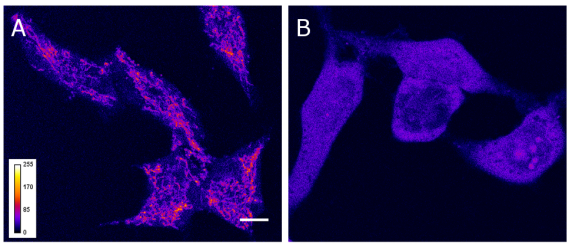

Figura 25. Fijación (A) y permeabilización (B) del compuesto **7** en células HeLa.

12.3.3. Publiación E: Rovira, A., Gandioso, A., Goñalons, M., Galindo, A., Bosch, M. & Marchán, V. *Straightforward solid-phase approaches for labelling targeting peptides with far-red/NIR emitting coumarin fluorophores*. Manuscrito enviado para publicación.

En base a los buenos resultados obtenidos con los nuevos fluoróforos COUPY, se planteó la síntesis de derivados que permitieran su conjugación a un péptido selectivo de células tumorales, y así evaluar su aplicación como marcador de biomoléculas. En primer lugar, se derivatizó el precursor **5** con un grupo ácido carboxílico para permitir su conjugación al extremo amino terminal del péptido Octreotide. A continuación, se realizaron estudios de internalización con el conjugado COUPY-Octreotide en la línea celular HeLa mediante microscopia confocal. Dichos estudios se complementaron con la síntesis y evaluación de dos conjugados fluoróforo-Octreotide que incorporan: i) **carboxifluoresceína**, un fluoróforo comercial usado habitualmente para el marcaje de péptidos y que es excitado con luz verde, y ii) **ATTO-Rho12,** un fluoróforo comercial que presenta un máximo de absorción muy similar al de la cumarina **7**.

Diseño, síntesis y caracterización del derivado COUPY.

En primer lugar, a partir del precursor **5** descrito anteriormente, se alquiló la piridina con bromoacetato de metilo en acetato de etilo a 60 °C durante 15 horas, obteniéndose el producto **11 (Esquema 34)**. Tras purificación por cromatografía en columna, se caracterizó mediante espectrometría de masas, RMN ^{1}H y RMN ^{13}C, no observándose en este caso la presencia de rotámetros. Los datos de caracterización fotofísica de **11** indicaron un desplazamiento hacía el rojo en los máximos de absorción y emisión, con un aumento de 11 nm en comparación con el análogo **7** (λ_{max}= 557 nm ; λ_{em}= 617 nm). Para el posterior acoplamiento al péptido, se hidrolizó el ester de **11** con ácido clorhídrico acuoso a 60 °C durante 5 horas, obteniéndose el compuesto **12** de manera cuantitativa.

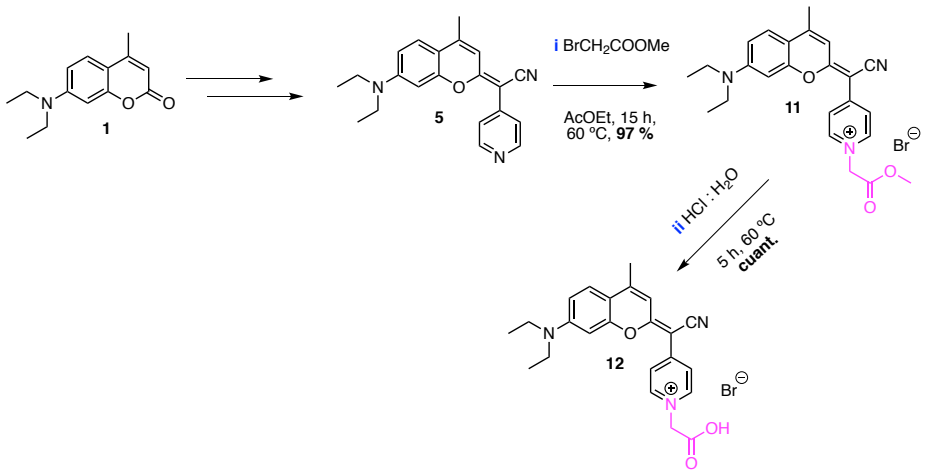

Esquema 34. Síntesis del análogo COUPY para la conjugación a biomoléculas.

Síntesis y caracterización del conjugado COUPY-Octreotide.

El ensamblaje del péptido se realizó en fase sólida sobre la resina Rink Amida siguiendo la estrategia Fmoc/*t*Bu (**Esquema 35**). En primer lugar, se procedió a la elongación de la cadena peptídica utilizando Fmoc-aminoácidos convenientemente protegidos y DIPC y HOBt como agentes acomplantes **(Esquema 35, i)**. Una vez ensamblado el péptido lineal, se procedió al acoplamiento de un espaciador de polietilenglicol **(Esquema 35, ii).** Tras la desprotección del grupo Fmoc del espaciador (20% piperidina en DMF), se acopló el compuesto **12** usando HATU y DIPEA durante 2 horas y protegido de la luz **(Esquema 35, iii**).

Finalmente, tras el desanclaje del péptido del soporte sólido polimérico y eliminación de los grupos protectores mediante tratamiento ácido (TFA/TIS/H_2O: EDT 94;2.5:2.5:1) durante 2 horas **(Esquema 35, iv),** se procedió a la ciclación del mismo formación de un enlace disulfuro entre los residuos de Cys en tampón de hidrogenocarbonato de amonio (5%) a pH=7.8 durante 24 horas (**Esquema 35, v**). El conjugado **13** se obtuvo con un rendimiento del 12% tras purificación por HPLC en fase inversa y se caracterizó mediante espectrometría de masas y RMN ^{1}H.

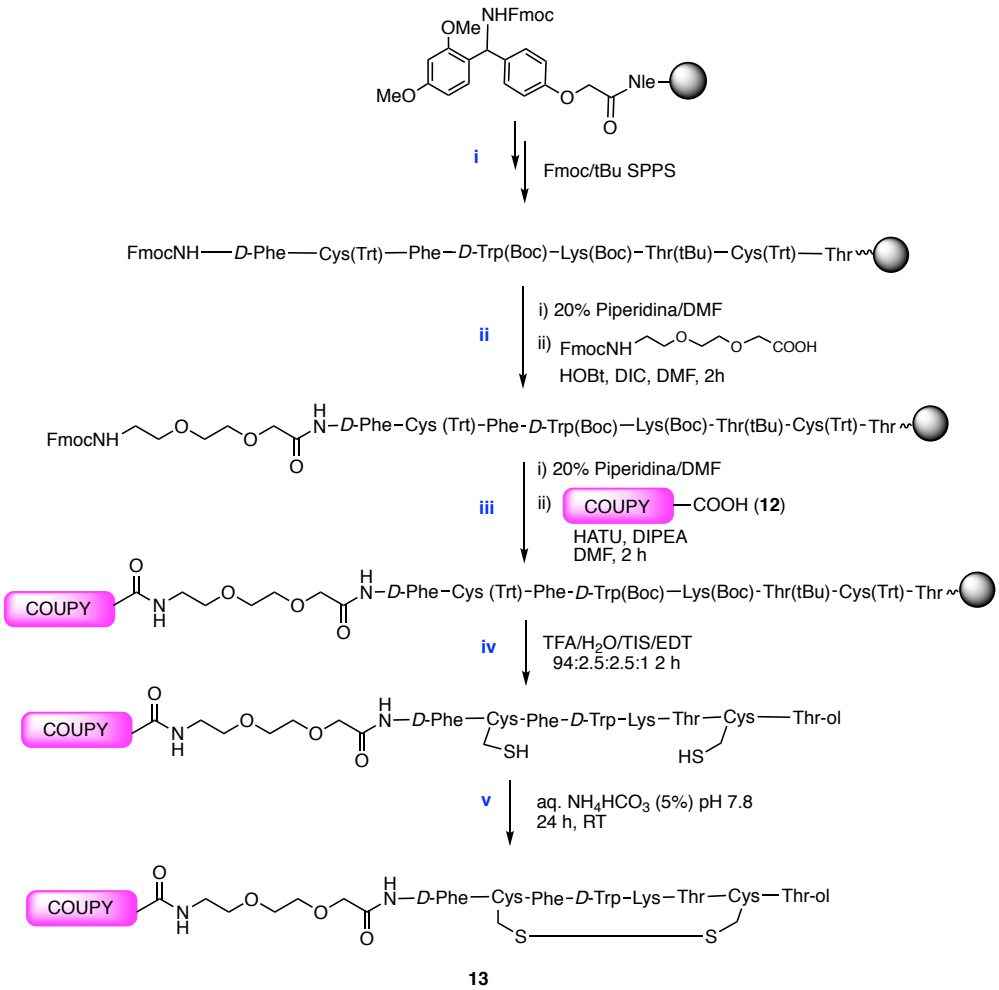

13

Esquema 35. Síntesis del conjugado COUPY-Octreotide (**13**).

Estudios de internalización del conjugado COUPY-OCT mediante microcopia confocal.

Los estudios de internalización del conjugado COUPY-octreotide (**13**) se llevaron a cabo en la línea celular HeLa ya que sobreexpresa el receptor de somatostatina tipo 2, el cual reconoce selectivamente al péptido octreotide. Previamente, se sintetizaron dos péptidos control, marcados con dos fluoróforos comerciales que son usados habitualmente para la visualización de biomoléculas (CarboxiFluoresceína y ATTO-Rho12).

Por un lado, para la síntesis del conjugado CF-Octreotide (Conjugado **14**) se siguió la misma ruta de síntesis en fase sólida que con el conjugado con cumarina. Por otro lado, la síntesis del conjugado con Atto-Rho12 (Conjugado **15**) se realizó en solución, mediante reacción de octreotide con el derivado NHS-AttoRho12 en un tampón de bicarbonato de sodio 100 mM a pH= 7.5 (**Figura 26**).

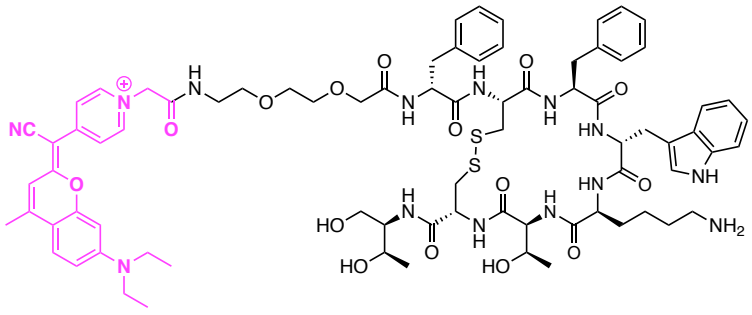

13

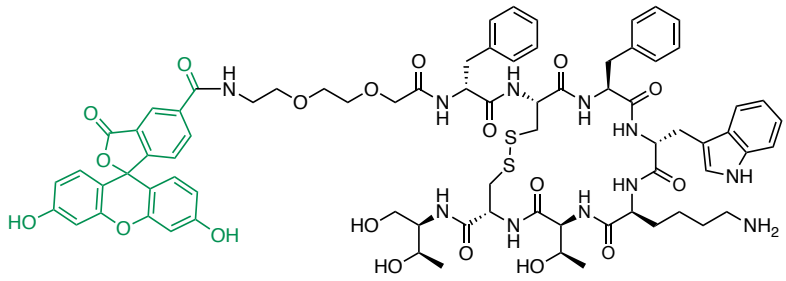

14

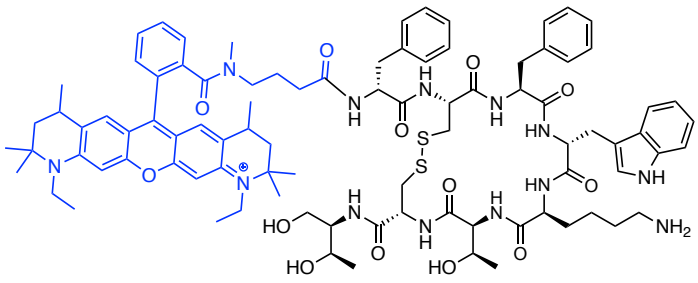

15

Figura 26. Estructura de los conjugados fluoróforo-octreotide.

Una vez sintetizados los dos conjugados control, se realizaron diferentes estudios de internalización. En primer lugar, se incubó el conjugado COUPY-Octreotide **13** a una concentración de 10 µM durante 30 minutos, 1 hora y 2 horas a 37 °C. Además, se incubó la cumarina **7**, anteriormente descrita en la **sección 12.3.2**, para comparar la localización del fluoróforo libre y la del conjugado. La visualización se realizó con el microscopio confocal irradiando con el láser de 561 nm. Tal y como era de esperar, la cumarina **7** se localizó en las mitrocondrias y en el nucleolo (**Figura 27, A y D).**

Sin embargo**,** en el caso del conjugado COUPY-octreotide se observaron vesículas endocíticas a los 30 min en el citoplasma de las células, lo que sugiere internalización mediada por receptor (**Figura 27 B y E)**. Tras incubación a 1 hora y 2 horas, se observaron los mismos resultados, si bien el número de vesículas fue mayor (**Figura 27, C y F).** La diferente localización del fluoróforo libre y del conjugado, demuestran que el fluoróforo no interfiere en el mecanismo de internalización y acumulación de Octreotide en las células.

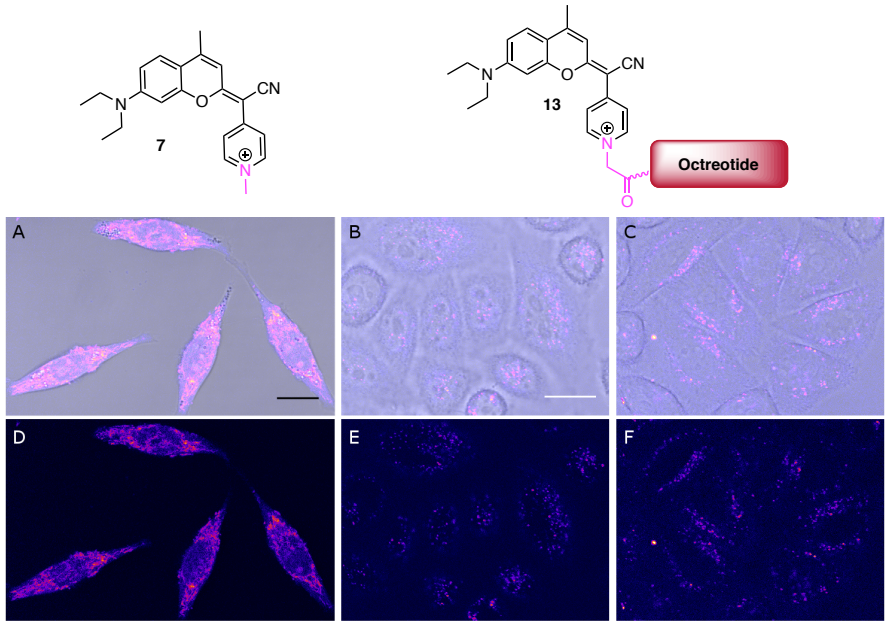

Figura 27. Internalización de fluoróforo **7** a 0.5 µM 30 min (A y D) y del conjugado **13** 10 µM 30 min (B y E) y 1 h (C y F).

A continuación, se revelaron a cabo estudios de internalización de los conjugados control **14** y **15** para determinar si localizan de la misma manera que el de la cumarina **13**. Así, la visualización se realizó con el microscopio confocal irradiando con el láser de 561 nm para los conjugados **13** y **15** (incubación a 10 µM, 30 min), mientras que para el conjugado **14** (incubación 50 µM, 30 min) se utilizó el láser de 488 nm.

En los tres casos se observó el mismo patrón de vesículas dentro del citoplasma de las células. En el caso de AttoRho12-octreotide la intensidad es algo superior (**Figura 28, B y E)** debido que el rendimiento cuántico de fluorescencia del fluoróforo es ligeramente superior al de la cumarina y fluoresceína. En cambio, la intensidad de las vesículas identificadas en el caso del conjugado carboxifluoresceína-octreotide es mucho menor (**Figura 28, C y F).**

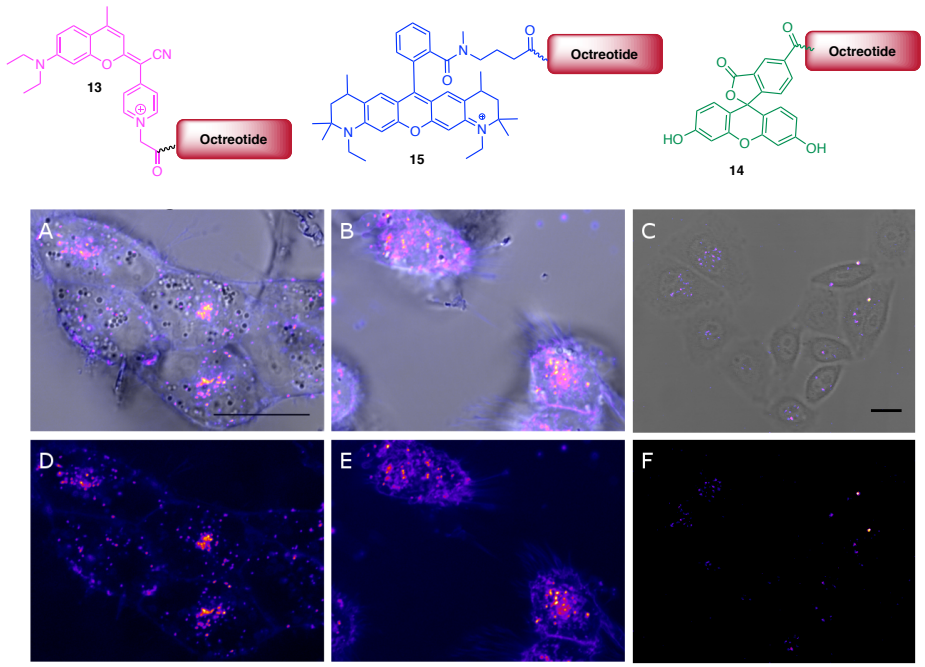

Figura 28. Internalización de los conjugados **13-15** en células Hela. Incubación a 10 µM, 30 min de los conjugado **13** (A y D) y **15** (B y E) y conjugado **14** (C y F) a una concentración de 50 µM, 30 min

Por último, se realizaron experimentos de incubación a 4 °C con los compuestos **7** y **13**, para verificar si el mecanismo de internalización viene mediado por el receptor de somatostatina, ya que los mecanismos de entrada dependientes de energía se inactivan a baja temperatura.

En el caso del conjugado **13**, se observó el marcaje en la membrana de la célula sin la aparición de vesículas en el citoplasma (**Figura 29, A**), lo que surgiere que la internalización es mediada por el receptor. Por otro lado, en el caso de la cumarina **7** se observó la misma tendencia descrita en el apartado **12.3.2**, identificándose únicamente marcaje en las mitocondrias y en el nucleolo (**Figura 29, B**). Finalmente, la incubación del conjugado 13 a 37 °C durante 30 min condujo a la observación de vesículas endocíticas en el citoplasma, lo cual confirmó la entrada vía el receptor de somatostatina (**Figura 29, C**). En cambió la localización de la cumarina **7** no se vió alterada tras incubar a 37 °C **(Figura 29, D).**

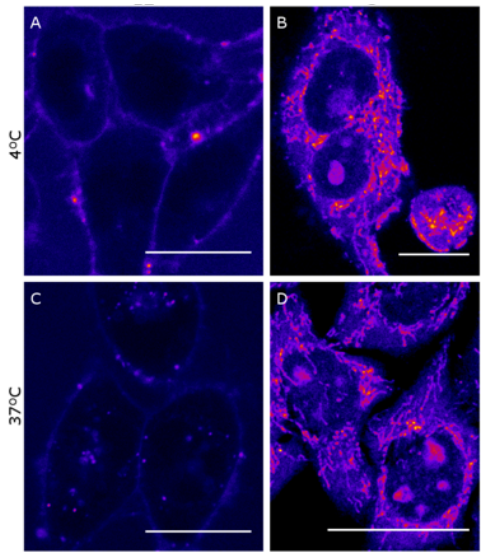

Figura 29. Internalización del conjugado **13** 10 µM (A y C) y del compuesto **7** 0,5 µM (B y D) tras incubación a 4 °C (Superior) y posterior la incubación a 37 °C (Inferior).

12.3.3. Conclusiones.

En resumen, se ha sintetizado una nueva familia de fluoróforos basados en el esqueleto de cumarina, denominados COUPY, a partir de precursores comerciales en tan solo tres etapas sintéticas, y cuyas propiedades fotofísicas pueden ser moduladas mediante la alquilación del heterociclo de piridina presente en la molécula. En algunos casos, los experimentos de RMN de ^{1}H 1D y 2D confirmaron la presencia de dos especies en equilibrio en solución como consecuencia de la rotación en torno al enlace carbono-carbono exocíclico. Además, la caracterización espectroscópica y fotofísica de los nuevos fluoróforos reveló unas propiedades muy prometedoras para su empleo en aplicaciones de bioimagen como son la emisión en la región del espectro electromagnético que va del rojo lejano al infrarrojo cercano, desplazamientos de Stokes relativamente altos y rendimientos cuánticos de fluorescencia moderados. Finalmente, los experimentos de internalización mediante microscopia confocal en células HeLa mostraron una buena capacidad de penetración de los fluoróforos COUPY y una localización selectiva en nucleolo y mitocondrias.

Por otro lado, también se exploró la derivatización de los nuevos fluoróforos COUPY para permitir su conjugación a vehículos selectivos de células tumorales basados en péptidos. Para ello, se sintetizó un análogo que incorpora un grupo carboxilo, y se conjugó satisfactoriamente a octreotide mediante la formación de un enlace amida siguiendo la estrategia Fmoc-*t*Bu de síntesis en fase sólida de péptidos. Finalmente, los estudios de microscopia confocal en células Hela indicaron que la internalización del conjugado COUPY-octreotide viene mediada por el receptor de somatostatina.

12.4 Referencias.

1. Crespy, D., Landfester, K., Schubert, U. S. & Schiller, A. Potential photoactivated metallopharmaceuticals: from active molecules to supported drugs. *Chem. Commun.* **46,** 6651-6662 (2010).
2. Farrer, N. J., Woods, J. A., Salassa, L., Zhao, Y., Robinson, K. S., Clarkson, G., MacKay, F. S. & Sadler, P. J. A potent trans-diimine platinum anticancer complex photoactivated by visible light. *Angew. Chem. Int. Ed.* **49,** 8905–8908 (2010).
3. Zhao, Y., Woods, J. A., Farrer, N. J., Robinson, K. S., Pracharova, J., Kasparkova, J., Novakova, O., Li, H., Salassa, L., Pizarro, A. M., Clarkson, G. J., Song, L., Brabec, V. & Sadler, P. J. Diazido mixed-amine platinum(IV) anticancer complexes activatable by visible-light form novel DNA adducts. *Chem. - Eur. J.* **19,** 9578–9591 (2013).
4. Pracharova, J., Zerzankova, L., Stepankova, J., Novakova, O., Farrer, N. J., Sadler, P. J., Brabec, V., & Kasparkova, J. Interactions of DNA with a new platinum(IV) azide dipyridine complex activated by UVA and visible light: Relationship to toxicity in tumor cells. *Chem. Res. Toxicol.* **25,** 1099–1111 (2012).
5. Pierschbacher, M. D. & Ruoslahti, E. Cell attachment activity of fibronectin can be duplicated by small synthetic fragments of the molecule. *Nature* **309,** 30-33 (1984).
6. Grant, D. S., Tashiro, K., Segui-Real, B., Yamada, Y., Martin, G. R. & Kleinman, H. K. Two different laminin domains mediate the differentiation of human endothelial cells into capillary-like structures in vitro. *Cell* **58,** 933–943 (1989).
7. Temming, K., Schiffelers, R. M., Molema, G. & Kok, R. J. RGD-based strategies for selective delivery of therapeutics and imaging agents to the tumour vasculature. *Drug Resist. Updates.* **8,** 381–402 (2005).
8. Danhier, F., Breton, A. Le & Préat, V. RGD-based strategies to target αvβ3 integrin in cancer therapy and diagnosis. *Mol. Pharm.* **9,** 2961–2973 (2012).
9. Massaguer, A. , González-Cantó, A., Escribano, E., Barrabés, S., Artigas, G., Moreno, V. & Marchán, V. Integrin-targeted delivery into cancer cells of a Pt(IV) pro-drug through conjugation to RGD-containing peptides. *Dalton Trans.* **44,** 202–212 (2015).
10. Arosio, D. & Casagrande, C. Advancement in integrin facilitated drug delivery. *Adv. Drug Delivery Rev.* **97,** 111–143 (2016).
11. Albert, J. M., Cao, C., Geng, L., Leavitt, L., Hallahan, D. E. & Lu, Bo. Integrin $\alpha_v\beta_3$ antagonist Cilengitide enhances efficacy of radiotherapy in endothelial cell and non–small-cell lung cancer models. *Int. J. Radiat. Oncol., Biol., Phys.* **65,** 1536–1543 (2006).
12. Vermorken, J. B., Guigay, J., Mesia, R., Trigo, J. M., Keilholz, U., Kerber, A., Bethe, U., Picard, M, & Brummendorf, T H. Phase I/II trial of cilengitide with cetuximab, cisplatin and 5-fluorouracil in recurrent and/or metastatic squamous cell cancer of the head and neck: findings of the phase I part. *Br. J. Cancer* **104,** 1691-1695 (2011).

13. Schraa, A. J., Schraa, A. J., Kok, R. J., Berendsen, A. D., Moorlag, H. E., Bos, E. J., Meijer, D. K. F., de Leij, L. F. M. H. & *Molema, G.* Endothelial cells internalize and degrade RGD-modified proteins developed for tumor vasculature targeting. *J. Control. Release* **83,** 241–251 (2002).

14. Dal Pozzo, A. Ni, M. H., Esposito, E., Dallavalle, S., Musso, L., Bargiotti, A., Pisano, C., Vesci, L., Bucci, F., Castorina, M., Foderà, R., Giannini, G., Aulicino, C. & Penco, S. Novel tumor-targeted RGD peptide-camptothecin conjugates: Synthesis and biological evaluation. *Bioorg. Med. Chem.* **18,** 64–72 (2010).

15. Danhier, F., Breton, A. Le & Préat, V. RGD-based strategies to target αvβ3 integrin in cancer therapy and diagnosis. *Mol. Pharm.* **9,** 2961–2973 (2012).

16. Mas-Moruno, C. Fraioli, R., Rechenmacher, F., Neubauer, S., Kapp, T. G., Kessler, H. αvβ3 or α5β1 Integrin-Selective Peptidomimetics for Surface Coating. *Angew. Chem. Int. Ed.* **55,** 7048–7067 (2016).

17. Burkhart, D. J., Kalet, B. T., Coleman, M. P., Post, G. C. & Koch, T. H. Doxorubicin-formaldehyde conjugates targeting αvβ3 integrin. *Mol. Cancer Ther.* **3,** 1593–1605 (2004).

18. Chen, X., Plasencia, C., Hou, Y. & Neamati, N. Synthesis and biological evaluation of dimeric RGD peptide-paclitaxel conjugate as a model for integrin-targeted drug delivery. *J. Med. Chem.* **48,** 1098–1106 (2005).

19. Barragán, F., López-Senín, P., Salassa, L., Betanzos-Lara, S., Habtemariam, A., Moreno, V.,Sadler, P.J. & Marchán, V. Photocontrolled DNA binding of a receptor-targeted organometallic ruthenium(II) complex. *J. Am. Chem. Soc.* **133,** 14098–14108 (2011).

20. Hahn, E. M. *et al.* Functionalization of ruthenium(II) terpyridine complexes with cyclic RGD peptides to target integrin receptors in cancer cells. *Eur. J. Inorg. Chem.* **2017,** 1667–1672 (2017).

21. Leamon, C. P. & Reddy, J. A. Folate-targeted chemotherapy. *Adv. Drug Delivery. Rev.* **56,** 1127–1141 (2004).

22. Low, P. S. & Kularatne, S. A. Folate-targeted therapeutic and imaging agents for cancer. *Curr. Opin. Chem. Biol.* **13,** 256–262 (2009).

23. Teng, L., Xie, J., Teng, L. & Lee, R. J. Clinical translation of folate receptor-targeted therapeutics. *Expert Opin. Drug Deliv.* **9,** 901–908 (2012).

24. Elnakat, H. & Ratnam, M. Distribution, functionality and gene regulation of folate receptor isoforms: Implications in targeted therapy. *Adv. Drug Delivery. Rev.* **56,** 1067–1084 (2004).

25. Guaragna, A., Chiaviello, A., Paolella, C., Dalonzo, D., Palumbo, G. & Palumbo, G. Synthesis and evaluation of folate-based chlorambucil delivery systems for tumor-targeted chemotherapy. *Bioconjugate Chem.* (2012).

26. Leamon, C. P. & Reddy, J. A. Folate-targeted chemotherapy. *Adv. Drug Delivery. Rev.* **56,** 1127–1141 (2004).

27. Lee, J. W., Lu, J. Y., Low, P. S. & Fuchs, P. L. Synthesis and evaluation of Taxol-folic acid conjugates as targeted antineoplastics. *Bioorg. Med. Chem.* **10,** 2397–2414 (2002).

28. Giglio, V. Oliveri, V., Viale, M., Gangemi, R., Natile, G., Intini, F. P. & Vecchio, G. Folate-cyclodextrin conjugates as carriers of the platinum(IV) complex LA-12. *ChemPlusChem* **80,** 536–543 (2015).

29. Aronov, O., Horowitz, A. T., Gabizon, A. & Gibson, D. Folate-targeted PEG as a potential carrier for carboplatin analogs. Synthesis and in vitro studies. *Bioconjugate Chem.* **14,** 563–574 (2003).

30. Gandioso, A., Shaili, E., Massaguer, A., Artigas, G., González-Cantó, A., Woods, J. A & Marchán, V. An integrin-targeted photoactivatable Pt(IV) complex as a selective anticancer pro-drug: synthesis and photoactivation studies. *Chem. Commun.* **51,** 9169–9172 (2015).

31. Velema, W. A., Szymanski, W. & Feringa, B. L. Photopharmacology: Beyond proof of principle. *J. Am. Chem. Soc.* **136,** 2178–2191 (2014).

32. Szymański, W., Beierle, J. M., Kistemaker, H. A. V., Velema, W. A. & Feringa, B. L. Reversible photocontrol of biological systems by the incorporation of molecular photoswitches. *Chem. Rev.* **113,** 6114–6178 (2013).

33. Velema, W. A., Van Der Berg, J. P., Szymanski, W., Driessen, A. J. M. & Feringa, B. L. Orthogonal control of antibacterial activity with light. *ACS Chem. Biol.* **9,** 1969–1974 (2014).

34. Hansen, M. J., Velema, W. A., Lerch, M. M., Szymanski, W. & Feringa, B. L. Wavelength-selective cleavage of photoprotecting groups: strategies and applications in dynamic systems. *Chem. Soc. Rev.* **44,** 3358–3377 (2015).

35. Beharry, A. A. & Woolley, G. A. Azobenzene photoswitches for biomolecules. *Chem. Soc. Rev.* **40,** 4422-4436 (2011).

36. Brieke, C., Rohrbach, F., Gottschalk, A., Mayer, G. & Heckel, A. Light-controlled tools. *Angew. Chem. Int. Ed.* **51,** 8446–8476 (2012).

37. Ellis-Davies, G. C. R. Caged compounds: Photorelease technology for control of cellular chemistry and physiology. *Nat. Methods* **4,** 619–628 (2007).

38. Schmidt, R., Geissler, D., Hagen, V. & Bendig, J. Mechanism of photocleavage of (coumarin-4-yl)methyl esters. *J. Phys. Chem. A* **111,** 5768–5774 (2007).

39. Suzuki, A. Z., Watanabe, T., Kawamoto, M., Nishiyama, K., Yamashita, H., Ishii, M., Iwamura, M. & Furuta, *T.* Coumarin-4-ylmethoxycarbonyls as phototriggers for alcohols and phenols. *Org. Lett.* **5,** 4867–4870 (2003).

40. Fournier, L., Aujard, I., Le Saux, T., Maurin, S., Beaupierre, S., Baudin, J. B. & Jullien, L. Coumarinylmethyl caging groups with redshifted absorption. *Chem. - Eur. J.* **19,** 17494–17507 (2013).

41. Weis, S., Shafiq, Z., Gropeanu, R. A. & Del Campo, A. Ethyl substituted coumarin-4-yl derivatives as photoremovable protecting groups for amino acids with improved stability for SPPS. *J. Photochem. Photobiol. A Chem.* **241,** 52–57 (2012).

42. Wirkner, M., Weis, S., San Miguel, V., Álvarez, M., Gropeanu, R.A., Salierno, M., Sartoris, A., Unger, R. E., Kirkpatrick, C. J. & del Campo, A. Photoactivatable caged cyclic RGD peptide for triggering integrin binding and cell adhesion to surfaces. *ChemBioChem* **12,** 2623–2629 (2011).

43. Petersen, S., Alonso, J. M., Specht, A., Duodu, P., Goeldner, M. & del Campo, A. Phototriggering of cell adhesion by caged cyclic RGD peptides. *Angew. Chem. Int. Ed.* **47,** 3192–3195 (2008).

44. Subirós-Funosas, R., El-Faham, A. & Albericio, F. Use of oxyma as pH modulatory agent to be used in the prevention of base-driven side reactions and its effect on 2-chlorotrityl chloride resin. *Biopolymers* **98,** 89–97 (2012)

45. Gandioso, A., Cano, M., Massaguer, A. & Marchán, V. A Green Light-Triggerable RGD Peptide for Photocontrolled Targeted Drug Delivery: Synthesis and Photolysis Studies. *J. Org. Chem.* **81,** (2016).

46. Gandioso, A., Palau, M., Nin-Hill, A., Melnyk, I., Rovira, C., Nonell, S., Velasco, D., García-Amorós, J. & Marchán, V. Sequential Uncaging with Green Light can be Achieved by Fine-Tuning the Structure of a Dicyanocoumarin Chromophore. *ChemistryOpen* **6,** 375-384 (2017).

47. Weber, P. J. A., Bader, J. E., Folkers, G. & Beck-Sickinger, A. G. A fast and inexpensive method for N-terminal fluorescein-labeling of peptides. *Bioorg. Med. Chem. Lett.* **8,** 597-600 (1998).

48. Massou, H., Albigot, R. & Prats, M. Carboxyfluorescein fluorescence experiments. *Biochem Educ.* **28,** 171–173 (2000).

49. Sarder, P., Maji, D. & Achilefu, S. Molecular probes for fluorescence lifetime Imaging. *Bioconjugate Chem.* **26,** 963–974 (2015).

50. Schnermann, M. J. Chemical biology: Organic dyes for deep bioimaging. *Nature* **551,** 176–177 (2017).

51. Grimm, J. B., Muthusamy, A. K., Liang, Y., Brown, T. A., Lemon, W. C., Patel, R., Lu, R., Macklin, J. J., Keller, P. J., Ji, N. & Lavis, L. D.A general method to fine-tune fluorophores for live-cell and in vivo imaging. *Nat. Methods* **14,** 987–994 (2017).

52. Lavis, L. D. Teaching old dyes new tricks: biological probes built from fluoresceins and rhodamines. *Annu. Rev. Biochem.* **86,** 825–843 (2017).

53. Lavis, L. D. & Raines, R. T. Bright ideas for chemical biology. ACS Chem. Biol. **3,** 142-155 (2007).

54. Michie, M. S., Götz, R., Franke, C., Bowler, M., Kumari, N., Magidson, V., Levitus, M., Loncarek, J., Sauer, M. & Schnermann, M. J. Cyanine conformational restraint in the far-red range. *J. Am. Chem. Soc.* **139,** 12406–12409 (2017).

55. Owens, E. A., Henary, M., El Fakhri, G. & Choi, H. S. Tissue-specific near-Infrared fluorescence imaging. *Acc. Chem. Res.* **49,** 1731–1740 (2016).

56. Zhao, C., Fernandez, A., Avlonitis, N., Vande Velde, G., Bradley, M., Read, N.D. & Vendrell, M. Searching for the optimal fluorophore to label antimicrobial peptides. *ACS Comb. Sci.* **18,** 689–696 (2016).

57. Gandioso, A., Contreras, S., Melnyk, I., Oliva, J., Nonell, S., Velasco, D., García-Amorós, J. & Marchán, V. Development of green/red-absorbing chromophores based on a coumarin scaffold that are useful as caging groups. *J. Org. Chem.* **82,** (2017).